DYNAMICAL NETWORKS OF LIFE/DEATH DECISIONS IN A CELL: FROM DNA REPAIR TO CELL DEATH

EDITED BY: Inna N. Lavrik, Nikita Kuznetsov and Vladimir Aleksandrovich Ivanisenko

PUBLISHED IN: Frontiers in Cell and Developmental Biology

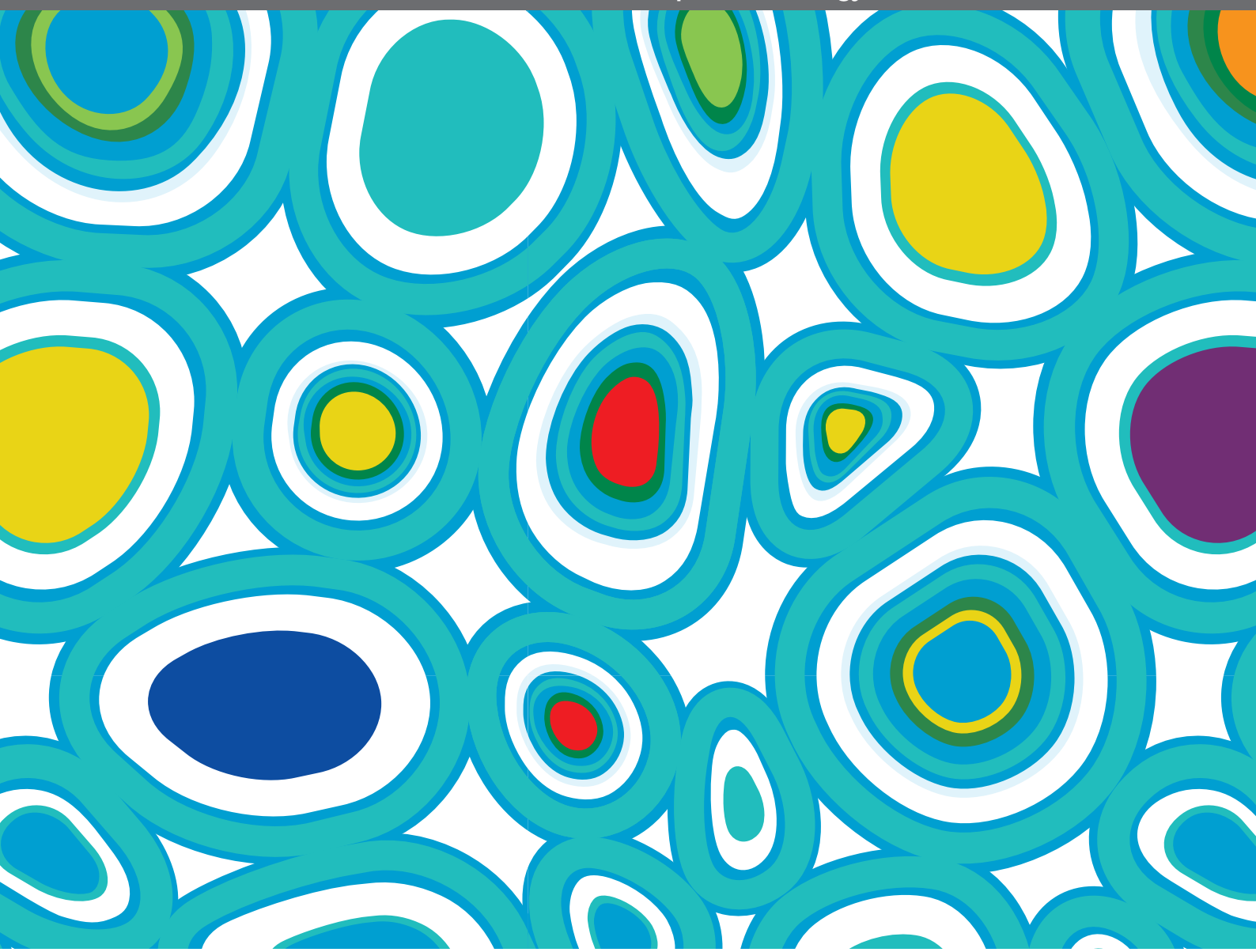

frontiers Research Topics

frontiers

ISSN 1664-8714
ISBN 978-2-88971-211-3
DOI 10.3389/978-2-88971-211-3

About Frontiers

Frontiers is more than just an open-access publisher of scholarly articles: it is a pioneering approach to the world of academia, radically improving the way scholarly research is managed. The grand vision of Frontiers is a world where all people have an equal opportunity to seek, share and generate knowledge. Frontiers provides immediate and permanent online open access to all its publications, but this alone is not enough to realize our grand goals.

Frontiers Journal Series

The Frontiers Journal Series is a multi-tier and interdisciplinary set of open-access, online journals, promising a paradigm shift from the current review, selection and dissemination processes in academic publishing. All Frontiers journals are driven by researchers for researchers; therefore, they constitute a service to the scholarly community. At the same time, the Frontiers Journal Series operates on a revolutionary invention, the tiered publishing system, initially addressing specific communities of scholars, and gradually climbing up to broader public understanding, thus serving the interests of the lay society, too.

Dedication to Quality

Each Frontiers article is a landmark of the highest quality, thanks to genuinely collaborative interactions between authors and review editors, who include some of the world's best academicians. Research must be certified by peers before entering a stream of knowledge that may eventually reach the public - and shape society; therefore, Frontiers only applies the most rigorous and unbiased reviews.
Frontiers revolutionizes research publishing by freely delivering the most outstanding research, evaluated with no bias from both the academic and social point of view. By applying the most advanced information technologies, Frontiers is catapulting scholarly publishing into a new generation.

What are Frontiers Research Topics?

Frontiers Research Topics are very popular trademarks of the Frontiers Journals Series: they are collections of at least ten articles, all centered on a particular subject. With their unique mix of varied contributions from Original Research to Review Articles, Frontiers Research Topics unify the most influential researchers, the latest key findings and historical advances in a hot research area! Find out more on how to host your own Frontiers Research Topic or contribute to one as an author by contacting the Frontiers Editorial Office: frontiersin.org/about/contact

DYNAMICAL NETWORKS OF LIFE/DEATH DECISIONS IN A CELL: FROM DNA REPAIR TO CELL DEATH

Topic Editors:
Inna N. Lavrik, University Hospital Magdeburg, Germany
Nikita Kuznetsov, Institute of Chemical Biology and Fundamental Medicine (RAS), Russia
Vladimir Aleksandrovich Ivanisenko, Russian Academy of Sciences (RAS), Russia

Citation: Lavrik, I. N., Kuznetsov, N., Ivanisenko, V. A., eds. (2021). Dynamical Networks of Life/Death Decisions in a Cell: From DNA Repair to Cell Death. Lausanne: Frontiers Media SA. doi: 10.3389/978-2-88971-211-3

Table of Contents

frontiers in Cell and Developmental Biology

EDITORIAL
published: 16 July 2021
doi: 10.3389/fcell.2021.722426

Editorial: Dynamical Networks of Life/Death Decisions in a Cell: From DNA Repair to Cell Death

*Inna N. Lavrik**

Translational Inflammation Research, Medical Faculty, Center of Dynamic Systems, Otto von Guericke University Magdeburg, Magdeburg, Germany

Keywords: cell death, DNA damage, DNA repair, mitophagy, BER

Editorial on the Research Topic

Dynamical Networks of Life/Death Decisions in a Cell: From DNA Repair to Cell Death

Life/death decisions in the cell are controlled by the intricate balance between cell death and survival signaling pathways. DNA damage induces multifactorial cellular responses: from DNA repair to cell death. In the last years, there has been emerging evidence indicating regulatory crosstalk between these cellular networks. It turned out that core components of cell death networks control DNA repair as well as key regulators of the DNA repair machinery play a major role in the cell death (Boege et al., 2017; Alemasova and Lavrik, 2019; Muller et al., 2020). The crosstalk between these networks is rather complex due to several pathways of DNA repair as well as more than a dozen types of programmed cell death that can be initiated upon DNA damage: apoptosis, necroptosis, autophagy, ferroptosis and paranathosis (Galluzzi et al., 2018). Getting new insights into these intricate machineries and their crosstalk is addressed in this collection. This research is highly important for new directions of development in contemporary biomedicine and paves the way towards drugs development involving targeting cell death and DNA repair networks.

The major part of the collection features the molecular mechanisms of DNA repair, in particular, focusing on base excision repair (BER). A comprehensive overview of the BER pathway in the model organism, *Caenorhabditis elegans* (*C. elegans*) is given by Elsakrmy et al. highlighting BER among other pathways of DNA repair. Another review by Bayken et al. presents state of the art knowledge on the role of BER in the processing of complex DNA structures, which are triggered by oxidative stress and anticancer drugs. Uncovering the structural features of histone-DNA crosslinks and molecular mechanisms of their repair is the subject of the review: by Pachva et al. The latter knowledge plays a key role in the development of novel targeted approaches associated to the induction of DNA repair pathways and DNA damage-induced cell death.

Valuable insights into the molecular mechanisms of the BER machinery are provided by the research articles in this collection. In particular, a detailed analysis of substrate specificity of several key enzymes of the BER pathway is carried out using *in vitro* biochemical systems. The comparison of substrate specificity of human apurinic/apyrimidinic (AP) endonuclease APE1 toward DNA and RNA substrates has allowed finding out new features of APE1 specificity toward DNA and RNA of non-canonical structure (Davletgildeeva et al.). The influence of human tyrosyl-DNA phosphodiesterase 1 (TDP1) and APE1 on the molecular architecture of the AP1 site has been uncovered by Lebedeva et al. This analysis revealed the role of these two enzymes in the crosslinking of 8-oxoguanine-DNA glycosylase (OGG1) to the APE1 site as well as dissected the interplay of OGG1, PARP1, and PARP2 at the initial stages of the BER pathway. The activity of PARP1 and

Edited and reviewed by:
You-Wen He,
Duke University, United States

***Correspondence:**
Inna N. Lavrik
inna.lavrik@med.ovgu.de

Specialty section:
This article was submitted to Cell Death and Survival, a section of the journal Frontiers in Cell and Developmental Biology

Received: *08 June 2021*
Accepted: *14 June 2021*
Published: *16 July 2021*

Citation:
Lavrik IN (2021) Editorial: Dynamical Networks of Life/Death Decisions in a Cell: From DNA Repair to Cell Death. Front. Cell Dev. Biol. 9:722426. doi: 10.3389/fcell.2021.722426

PARP2 in *Arabidopsis thaliana* was compared by Taipakova et al., which allowed unraveling a new type of DNA-modifying activity. Furthermore, a new type of substrate activity of tyrosyl-DNA phosphodiesterase 1 (TDP1) was found by Dyrkheeva et al. Moreover, a comparison of the activity on DNA substrates of endonuclease VIII-like 1 (NEIL1), human 8-oxoguanine-DNA glycosylase (OGG1), endonuclease III (NTH1), prokaryotic formamidopyrimidine-DNA glycosylase (Fpg), and endonuclease VIII (Nei) has been carried out by Kuznetsova et al. These studies identify new distinct and common features of these enzymes, which further underlines the high complexity of the BER machinery and the importance of its investigation in different organisms.

New insights into the other DNA repair pathway, nucleotide excision repair (NER), have been obtained by Petruseva et al. focusing on uncovering the patterns of XPD-p44 interactions with bulky DNA damages. The molecular mechanisms of non-homologous end joining (NHEJ) pathway in cancer cells upon ionizing radiation (IR) are analyzed by Tumia et al. In particular, it has been demonstrated that IR leads to downmodulation of NHEJ repair processes by inhibiting the synthesis of NHEJ repair proteins including Ku70, Ku80, and DNA-PKcs. These findings reveal the molecular basis of the NHEJ repair machinery in cellular responses to drug/radiation-induced DNA damage and development of anti-cancer drugs.

Studies of the autophagic pathway, mitochondrial respiration and cross-talk of autophagy with different forms of cell death also take a prominent place in this collection. The crosstalk of different forms of cell death focusing on the balance between mitophagy and apoptosis is analyzed by Wohlfromm et al. In this study, it was uncovered that the intricate balance between these two pathways might both inhibit and block apoptosis at the earlier and later time points, respectively. The role of HDAC6 in Transactive response DNA-binding protein 43 (TDP-43)-induced neurotoxicity and contribution of autophagy to this pathway and to the development of amyotrophic lateral sclerosis (ALS) is analyzed by Lee et al. The effects of mTOR inhibitors, rapamycin or torin1, on the germination of wheat seeds is analyzed by Smailov et al. Finally, the role of E3 Ubiquitin Ligase Hyd activity in the balance between mitosis and cell death during *Drosophila* oogenesis, is studied by Dorogova et al.

Taken together, this collection provides new insights into life/death decisions in the dynamical networks of DNA damage and cell death, identifies new targets in this network as well as paves the way toward novel therapeutic applications.

AUTHOR CONTRIBUTIONS

The author confirms being the sole contributor of this work and has approved it for publication.

ACKNOWLEDGMENTS

We acknowledge the Wilhelm Sander-Stiftung (2017.008.02), the Center of dynamic systems (CDS), funded by the EU-programme ERDF (European Regional Development Fund), and the DFG (LA 2386) for supporting our work.

REFERENCES

Alemasova, E. E., and Lavrik, O. I. (2019). Poly(ADP-ribosyl)ation by PARP1: reaction mechanism and regulatory proteins. *Nucleic Acids Res.* 47, 3811–3827. doi: 10.1093/nar/gkz120

Boege, Y., Malehmir, M., Healy, M. E., Bettermann, K., Lorentzen, A., Vucur, M., et al. (2017). A dual role of caspase-8 in triggering and sensing proliferation-associated DNA damage, a key determinant of liver cancer development. *Cancer Cell* 32, 342–359 e10. doi: 10.1016/j.ccell.2017.08.010

Galluzzi, L., Vitale, I., Aaronson, S. A., Abrams, J. M., Adam, D., Agostinis, P., et al. (2018). Molecular mechanisms of cell death: recommendations of the Nomenclature Committee on Cell Death 2018. *Cell Death Differ.* 25, 486–541. doi: 10.1038/s41418-017-0012-4

Muller, I., Strozyk, E., Schindler, S., Beissert, S., Oo, H. Z., Sauter, T., et al. (2020). Cancer cells employ nuclear caspase-8 to overcome the p53-dependent G2/M checkpoint through cleavage of USP28. *Mol. Cell.* 77, 970–984 e7. doi: 10.1016/j.molcel.2019.12.023

Conflict of Interest: The author declares that the research was conducted in the absence of any commercial or financial relationships that could be construed as a potential conflict of interest.

frontiers in Cell and Developmental Biology

ORIGINAL RESEARCH
published: 19 August 2020
doi: 10.3389/fcell.2020.00753

eIF3a Regulation of NHEJ Repair Protein Synthesis and Cellular Response to Ionizing Radiation

Rima Tumia[1†], Chao J. Wang[1†], Tianhan Dong[1], Shijie Ma[2], Jenny Beebe[1], Juan Chen[1], Zizheng Dong[2], Jing-Yuan Liu[3] and Jian-Ting Zhang[1,2]*

[1] Department of Pharmacology and Toxicology, Indiana University School of Medicine, Indianapolis, IN, United States,
[2] Department of Cancer Biology, University of Toledo College of Medicine and Life Sciences, Toledo, OH, United States,
[3] Department of Medicine, University of Toledo College of Medicine and Life Sciences, Toledo, OH, United States

Translation initiation in protein synthesis regulated by eukaryotic initiation factors (eIFs) is a crucial step in controlling gene expression. eIF3a has been shown to regulate protein synthesis and cellular response to treatments by anticancer agents including cisplatin by regulating nucleotide excision repair. In this study, we tested the hypothesis that eIF3a regulates the synthesis of proteins important for the repair of double-strand DNA breaks induced by ionizing radiation (IR). We found that eIF3a upregulation sensitized cellular response to IR while its downregulation caused resistance to IR. eIF3a increases IR-induced DNA damages and decreases non-homologous end joining (NHEJ) activity by suppressing the synthesis of NHEJ repair proteins. Furthermore, analysis of existing patient database shows that eIF3a expression associates with better overall survival of breast, gastric, lung, and ovarian cancer patients. These findings together suggest that eIF3a plays an important role in cellular response to DNA-damaging treatments by regulating the synthesis of DNA repair proteins and, thus, eIIF3a likely contributes to the outcome of cancer patients treated with DNA-damaging strategies including IR.

Keywords: eukaryotic initiation factor 3a (eIF3a), DNA repair, radiation, resistance, mRNA translation, protein synthesis, gamma-H2A histone family member X (γ-H2AX)

OPEN ACCESS

Edited by:
Inna N Lavrik,
University Hospital Magdeburg, Germany

Reviewed by:
Ella L Kim,
Johannes Gutenberg University Mainz, Germany
N. Rajendra Prasad,
Annamalai University, India

****Correspondence:***
Jian-Ting Zhang
jianting.zhang@utoledo.edu

† These authors have contributed equally to this work

Specialty section:
This article was submitted to Cell Death and Survival, a section of the journal Frontiers in Cell and Developmental Biology

Received: *27 May 2020*
Accepted: *20 July 2020*
Published: *19 August 2020*

Citation:
Tumia R, Wang CJ, Dong T, Ma S, Beebe J, Chen J, Dong Z, Liu J-Y and Zhang J-T (2020) eIF3a Regulation of NHEJ Repair Protein Synthesis and Cellular Response to Ionizing Radiation. Front. Cell Dev. Biol. 8:753. doi: 10.3389/fcell.2020.00753

INTRODUCTION

Eukaryotic initiation factors (eIFs) are a family of proteins that play important roles in mRNA translation and protein synthesis. Recent growing evidence suggests that eIFs do not just participate in translation initiation of global mRNAs but may also regulate synthesis of a subset of proteins (Dong and Zhang, 2006; Dong et al., 2009). These regulatory functions have been thought to contribute to the potential oncogenic role of eIFs (Hershey, 2015). Indeed, many eIFs were found to have higher expression in human tumors and shown to have oncogenic activity (Yin et al., 2011a). One of these eIFs, eIF3a, has been found to overexpress in many human cancers including cancers of the breast (Bachmann et al., 1997), cervix (Dellas et al., 1998), esophagus (Chen and Burger, 1999), stomach (Chen and Burger, 2004), lung (Pincheira et al., 2001), and bladder (Spilka et al., 2014), and it was thought to be a proto-oncogene. Indeed, knocking down eIF3a expression reversed the malignant phenotype of human cancer cells (Dong et al., 2004) while overexpressing ectopic eIF3a transformed NIH3T3 fibroblast cells (Zhang et al., 2007) *in vitro*.

Interestingly, eIF3a overexpression resulted in cellular sensitivity to cisplatin by regulating nucleotide excision repair (NER) *via* suppressing the synthesis of NER proteins (Liu et al., 2011). It has also been shown that eIF3a upregulation increases cellular sensitivity to anticancer drug doxorubicin, which inhibits topoisomerase II and causes DNA double-strand breaks (DSBs; Yin et al., 2011b). Extensive DSBs induced by various exogenous and endogenous factors are one of the most fatal forms of DNA damages (Helleday et al., 2007; Reynolds et al., 2012) and are used for treating human cancers in the form of chemo and radiation therapy. However, cancer cells with efficient repair of DSBs are able to survive these treatments that cause DSBs using two major mechanisms of repair of DSBs, homologous recombination (HR) and non-homologous end joining (NHEJ; Hartlerode and Scully, 2009; Pardo et al., 2009). While HR repairs the damages using undamaged and symmetrical chromosome as a template during the S or G phase of the cell cycle (Helleday et al., 2007; Branzei and Foiani, 2008), NHEJ repairs DSBs throughout all cell cycle phases and is the major pathway in repairing ionizing radiation (IR)-induced DSBs (van Gent et al., 2001; Rothkamm et al., 2003; Lieber, 2010). The major proteins important in NHEJ repair of DSBs include Ku (Ku70, Ku80) and DNA-PKcs to form the DNA-PK enzyme (Gottlieb and Jackson, 1993; Yaneva et al., 1997; Mari et al., 2006; Uematsu et al., 2007).

In this study, we tested the hypothesis that eIF3a may regulate the cellular response to treatments that cause DSBs by regulating the synthesis of DSB repair proteins. We examined the role of eIF3a in the cellular response to IR because IR is a common and an important strategy for treating many types of human cancers (Hoeijmakers, 2001; Kastan and Bartek, 2004; Lobrich and Jeggo, 2007) and is known to cause DSBs. We found that eIF3a sensitized the cellular response to IR treatments by downregulating NHEJ repair *via* inhibiting the synthesis of NHEJ repair proteins including Ku70, Ku80, and DNA-PKcs. These findings suggest that translational regulation of gene expression and eIF3a play important roles in the cellular response to DNA-damaging treatments and, thus, may underline the molecular basis of their functions in cellular response to drug/radiation-induced DNA damages and in cancer prognosis.

RESULTS

Role of Eukaryotic Initiation Factor 3a in the Cellular Response to Ionizing Radiation Treatment

To determine the potential role of eIF3a in the cellular response to IR, we first knocked down eIF3a expression using siRNA in H1299 cells, which have a high level of endogenous eIF3a (**Figure 1A**) followed by analysis of cellular response to IR using colony formation assay. As shown in **Figures 1B,C**, H1299 cells with eIF3a knockdown (H1299/Si) are significantly more resistant with a 2-fold increase in relative resistance factor (RRF) than the control H1299 cells transfected with scrambled control siRNA (H1299/Scr). To confirm this observaiton, we performed a reverse experiment by using the stable NIH3T3 cells with eIF3a overexpression (NIH3T3/eIF3a) (**Figure 1A**) and tested their response to IR in comparison with the control cells transfected with the empty vector (NIH3T3/Vec). As shown in **Figures 1B,C**, NIH3T3/eIF3a cells are remarkably more sensitive than the control NIH3T3/Vec cells to IR with ∼2-fold reduction in RRF. Thus, eIF3a expression may affect cellular sensitivity to IR treatments.

Effect of Eukaryotic Initiation Factor 3a on Gamma-H2A Histone Family Member X Expression Following Ionizing Radiation Treatment

To investigate how eIF3a affects the cellular response to IR, we tested the hypothesis that eIF3a may regulate the repair of DSBs induced by IR. For this purpose, we first tested the effect of eIF3a on gamma-H2A histone family member X (γ-H2AX) expression, a marker for DSB (Kuo and Yang, 2008), following IR treatment. As shown in **Figure 2A**, little γ-H2AX was detected in either H1299/Si or the control H1299/Scr cells without IR treatments. However, the γ-H2AX level drastically increased following IR treatment in these cells at 20 min after IR treatment. Interestingly, at 6 h after IR, γ-H2AX in H1299/Si cells returned essentially to the basal level while it remained high in the control H1299/Scr cells. We also performed similar experiments using NIH3T3/eIF3a and the control NIH3T3/Vec cells and found that eIF3a overexpression clearly delayed DNA repair, as indicated by the delayed disappearance of γ-H2AX (**Figure 2A**), consistent with the findings using H1299/Si and H1299/Scr cells.

To verify the above findings, we performed immunofluorescence staining of γ-H2AX in the nuclei of these cells at 2 and 6 h after IR exposure. As shown in **Figure 2B**, the high level of punctate staining of γ-H2AX in the nuclei of H1299/Si cells observed at 2 h following IR disappeared at 6 h. However, the punctate staining in the control H1299/Scr cells remained high at 6 h following IR. Similarly, NIH3T3/eIF3a cells retained high levels of γ-H2AX, whereas the control NIH3T3/Vec cells lost γ-H2AX staining at 6 h following IR. These observations are consistent with the results shown using Western blot analysis. Thus, it is possible that eIF3a suppresses the repair of DSB induced by IR.

Effect of Eukaryotic Initiation Factor 3a on DNA Damage Induced by Ionizing Radiation

In the above studies, we used γ-H2AX as a DNA damage marker to evaluate DNA damage and repair. To directly evaluate DNA damage induced by IR in the presence of different levels of eIF3a, we performed neutral comet assay at 2 and 6 h following IR treatment. Cells at 20 min following IR were not tested using this assay because the short time was difficult to control for the comet assay. As shown in **Figure 3A**, H1299/Si cells clearly have significantly lower Olive tail moment than the control H1299/Scr cells at both 2 and 6 h following IR treatment. It is noteworthy that the relative Olive tail moment was reduced at 6 h compared with 2 h following IR in H1299/Si cells while it remained high in H1299/Scr cells, suggesting that little DSBs

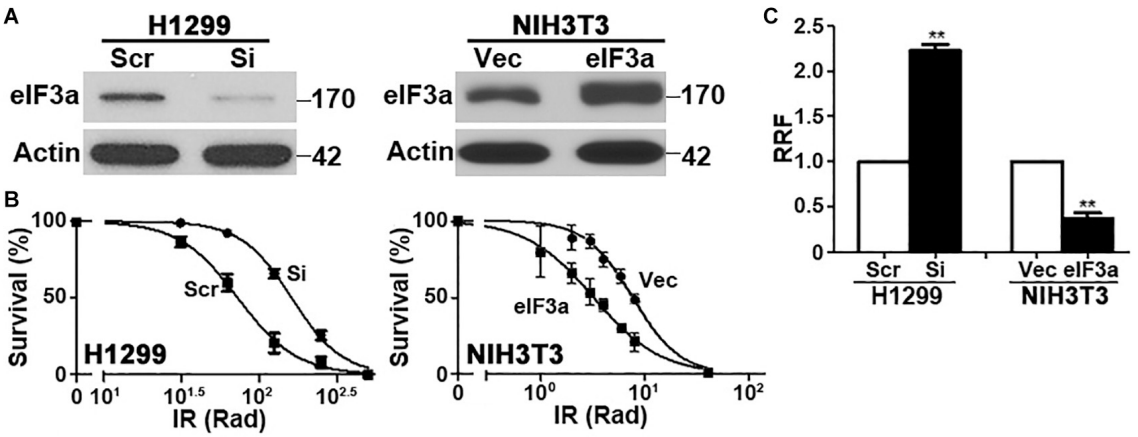

FIGURE 1 | Effect of eukaryotic initiation factor (eIF)3a expression on the cellular response to ionizing radiation (IR). Western blot analyses **(A)** and colony formation assay following IR treatment **(B)** of H1299 cells with transient eIF3a knockdown and NIH3T3 cells with stable eIF3a overexpression compared with their respective control cells. Actin was used as a loading control. Panel **(C)** shows a summary of eIF3a effects on cellular sensitivity to IR treatments. Relative resistance factor (RRF) was derived by dividing the IC_{50} of the test cells by that of their control cells ($n = 3$, $^{**}P < 0.01$).

were repaired in H1299/Scr cells compared with H1299/Si cells. Similarly, NIH3T3/eIF3a cells had significantly higher Olive tail moment than its control NIH3T3/Vec cells (**Figure 3B**) following IR treatment, and less DSBs were repaired in NIH3T3/eIF3a than in the control NIH3T3/Vec cells as indicated by the change in the relative Olive tail moment between 2 and 6 h following IR. Thus, eIF3a likely inhibits the repair of DSBs induced by IR, and cells with high levels of eIF3a retain higher levels of DSBs following IR while cells with lower eIF3a retain lower level of DSBs.

Role of Eukaryotic Initiation Factor 3a in Non-homologous End Joining Repair of Double-Strand Breaks

To determine if eIF3a regulates repairs of DSBs, we next performed host cell reactivation (HCR) assay of NHEJ activity since NHEJ is the main repair pathway of IR-induced DNA damages and it is independent of cell cycle stages as discused above. As shown in **Figure 3C**, H1299/Si cells had a 2-fold increase in NHEJ activity compared with the control H1299/Scr cells. Consistently, the NHEJ activity in NIH3T3/eIF3a cells was decreased by 40% compared with the control NIH3T3/Vec cells (**Figure 3D**). These findings suggest that eIF3a may play an important role in suppressing NHEJ repair of DSBs.

Eukaryotic Initiation Factor 3a Regulates Synthesis of Non-homologous End Joining Repair Proteins

Because eIF3a is known to regulate the synthesis of proteins, we hypothesized that eIF3a may regulate NHEJ repair of DSBs by regulating the synthesis of NHEJ repair proteins. To test this hypothesis, we first performed a Western blot analysis of major proteins involved in NHEJ repair in H1299/Si vs. H1299/Scr and NIH3T3/eIF3a vs. NIH3T3/Vec cells. As shown in **Figures 4A,B**, the expression of DNA-PKcs, Ku70, and Ku80 in H1299/Si cells was drastically increased compared with the control H1299/Scr cells. Consistently, the expression of these genes in NIH3T3/eIF3a cells was dramatically reduced compared with the control NIH3T3/Vec cells. Interestingly, real-time reverse transcription (RT)-PCR analyses showed no change in the mRNA level of these genes, suggesting that the effect of eIF3a on the expression of DNA-PKcs, Ku70, and Ku80 is likely at the protein, not mRNA, level.

Next, we performed pulse labeling and cycloheximide chase experiments to determine the eIF3a effect on the synthesis and degradation of these DNA repair proteins, respectively. As shown in **Figure 5**, eIF3a knockdown using siRNA in H1299 cells (**Figure 5A**) or eIF3a overexpression in NIH3T3 cells (**Figure 5B**) had no effects on the decay of these DNA repair proteins. However, the synthesis of Ku70, Ku80, and DNA-PKcs was dramatically increased in H1299/Si (**Figure 5A**) and reduced in NIH3T3/eIF3a (**Figure 5B**) cells compared with their respective control H1299/Scr and NIH3T3/Vec cells. Thus, eIF3a likely inhibits the synthesis of Ku70, Ku80, and DNA-PKcs proteins, leading to a reduced repair of DSB by the NHEJ pathway.

High Eukaryotic Initiation Factor 3a Expression Benefits Overall Survival of Cancer Patients

The above studies suggest that patients with tumors that have a high level of eIF3a may be more sensitive to treatments that cause DSBs such as radiotherapy and chemotherapy with drugs that cause DSBs. To test this hypothesis, we performed overall survival analysis of breast, gastric, lung, and ovarian cancer patients using information freely available in Kaplan–Meier (KM) plotter. As shown in **Figure 6**, breast, gastric, lung, and ovarian cancer patients with a high eIF3a expression level all had better overall survival than patients with a low eIF3a level. These findings are consistent with the eIF3a function in sensitizing cancer cells to treatment that cause DNA damages.

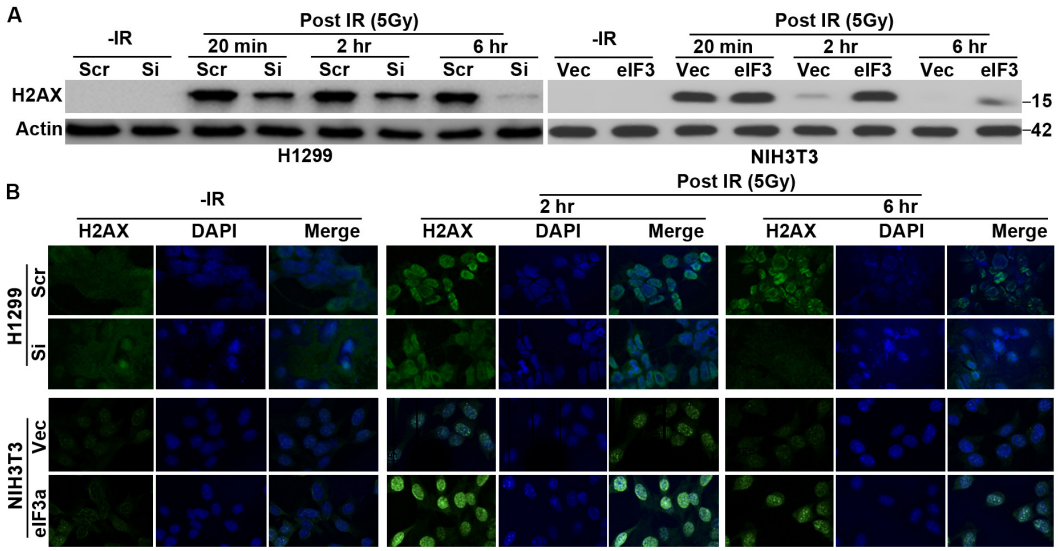

FIGURE 2 | Effect of eukaryotic initiation factor (eIF)3a on ionizing radiation (IR)-induced gamma-H2A histone family member X (γ-H2AX). Western blot **(A)** and immunofluorescence staining **(B)** analyses of γ-H2AX in H1299 cells with transient eIF3a knockdown and in NIH3T3 cells with stable eIF3a overexpression compared with their respective control cells following IR treatments.

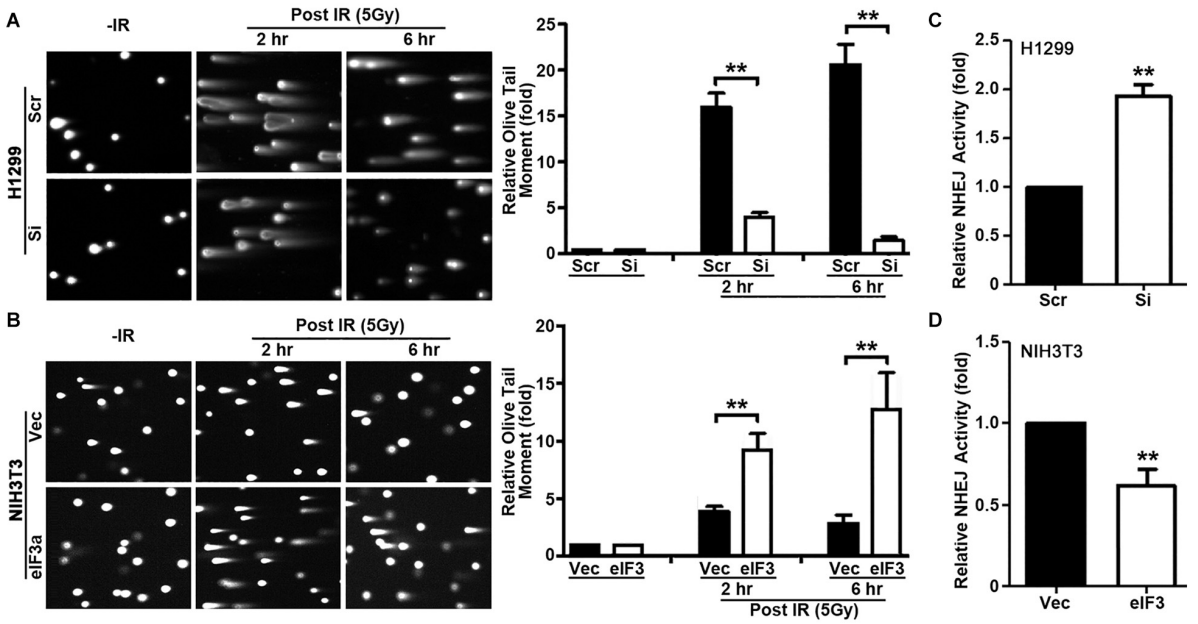

FIGURE 3 | Role of eukaryotic initiation factor (eIF)3a in non-homologous end joining (NHEJ) repair of ionizing radiation (IR)-induced double-strand breaks (DSBs). **(A,B)** Comet assay was used to determine eIF3a effects on the level of DSBs induced by IR in H1299 cells with transient eIF3a knockdown **(A)** and NIH3T3 cells with stable eIF3a overexpression **(B)** compared with their respective control cells. The histograms show the summary of quantitative analysis of Olive tail moment in these cells. **(C,D)** Host cell reactivation assays using reporter constructs were performed using H1299 cells with eIF3a knockdown **(C)** and NIH3T3 cells with eIF3a stable overexpression **(D)** compared with their respective control cells ($n = 3$; $^{**}P < 0.01$).

DISCUSSION

Appropriate combinations of radiation with chemotherapeutic drugs and radiation have resulted in remarkable outcome in cancer treatments. However, resistance to both radiation and anticancer drugs frequently occurs, causing failure in the successful treatment or cure of human cancers. In this study, using cell line models, we show that eIF3a may play important roles in the cellular response to IR with several lines of evidence. Alteration of eIF3a expression not only changes cellular survival

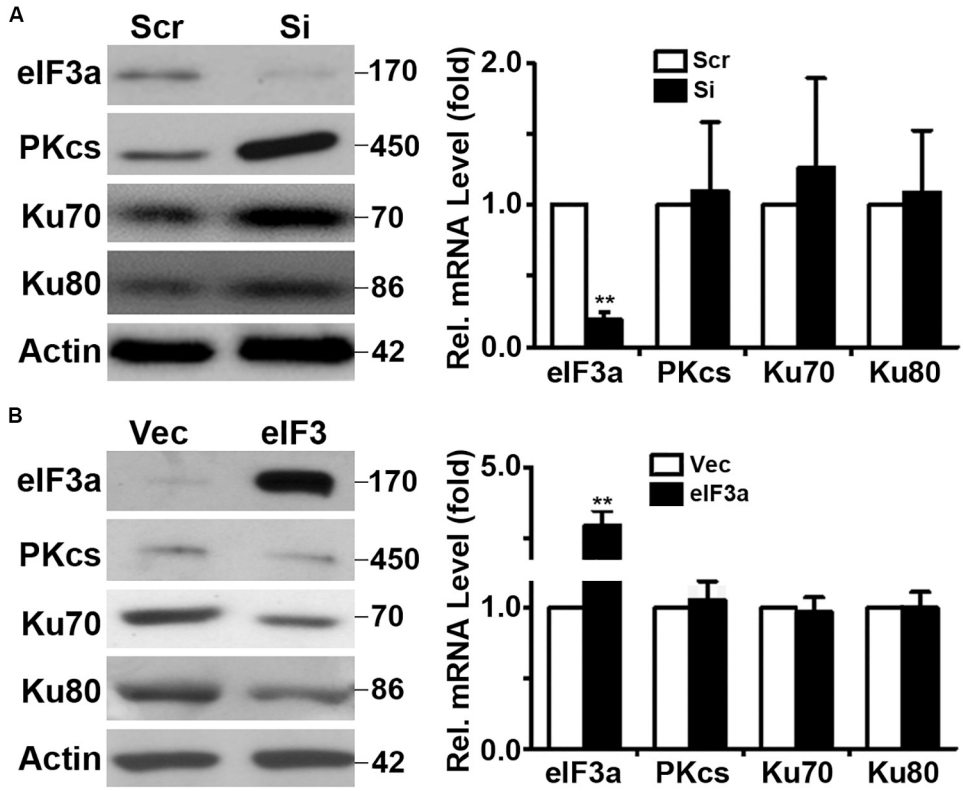

FIGURE 4 | Effect of eukaryotic initiation factor (eIF)3a on expression of genes encoding proteins important for non-homologous end joining (NHEJ) repair. Western blot and real-time reverse transcription (RT)-PCR analyses were performed to determine the effect of eIF3a on the expression of Ku70, Ku80, and DNA-PKcs genes in H1299 cells with transient knockdown **(A)** and NIH3T3 cells with stable eIF3a overexpression **(B)** compared with their respective control cells ($n = 3$; $^{**}P < 0.01$).

following IR treatment, it also affects the levels of DSBs as measured using the comet assay and detecting γ-H2AX, an indicator of DNA damage as well as HCR assay for NHEJ repair activities. Furthermore, eIF3a may regulate the synthesis of DNA repair proteins, Ku70, Ku80, and DNA-PKcs, important for the NHEJ repair pathway. These findings are consistent with the observation that lower eIF3a expression associates with poor prognosis of several cancers in this study and as reported in previous publications (Bachmann et al., 1997; Dellas et al., 1998; Chen and Burger, 1999, 2004; Pincheira et al., 2001; Spilka et al., 2014).

The difference in γ-H2AX protein level between cells with different eIF3a levels was observed early (20 min) following IR treatments. Although eIF3a may sensitize cells from IR-induced DNA damage to reduce the production of γ-H2AX, it is more likely that cells with different eIF3a levels have similar levels of DSBs induced by IR, but the cells with less eIF3a can repair the DSBs much more quickly than the cells with a high eIF3a level, causing the different levels of γ-H2AX in these cells. This difference in repair activity may be due to the difference in the basal level of DNA repair proteins between these cells under different levels of eIF3a regulation. It is noteworthy that DNA-PKcs, the downstream target of eIF3a shown here, has been suggested to phosphorylate H2AX, leading to the production of IR-induced γ-H2AX (Stiff et al., 2004). In this study, although eIF3a knockdown increased the level of DNA-PKcs protein, there is no increase in the basal level of γ-H2AX. In fact, γ-H2AX decreased in eIF3a knockdown cells at 20 min following IR treatment. While this finding is consistent with less DNA damage in eIF3a knockdown cells presumably due to increased NHEJ repair activity, it is inconsistent with possible DNA-PKcs phosphorylation of H2AX. However, because half maximum accumulation of γ-H2AX occurs in 1 min following IR (Rogakou et al., 1998), it is possible that we were unable to detect the IR-induced γ-H2AX increase due to high DNA-PKcs expression with eIF3a knockdown. At 20 min or later after IR when samples were collected, γ-H2AX may have already been reduced due to rapid reduction in DSBs. Future studies are required to test this possibility.

Previously, it has been shown that eIF3a regulates the synthesis of proteins important for NER and cellular response to cisplatin and that eIF3a may bind to the 5′-untranslated region (5′-UTR) of mRNAs encoding DNA repair proteins and, thus, inhibiting translation of these mRNAs to synthesize these proteins (Liu et al., 2011; Yin et al., 2011b, 2013). Together with these previous findings, our current results suggest that eIF3a likely plays an important role in regulating the synthesis of DNA repair proteins that contributes to cellular response to DNA-damaging drugs or radiation (**Figure 7**). In a previous study, we showed that eIF3a knockdown sensitized cancer cells to cisplatin-induced

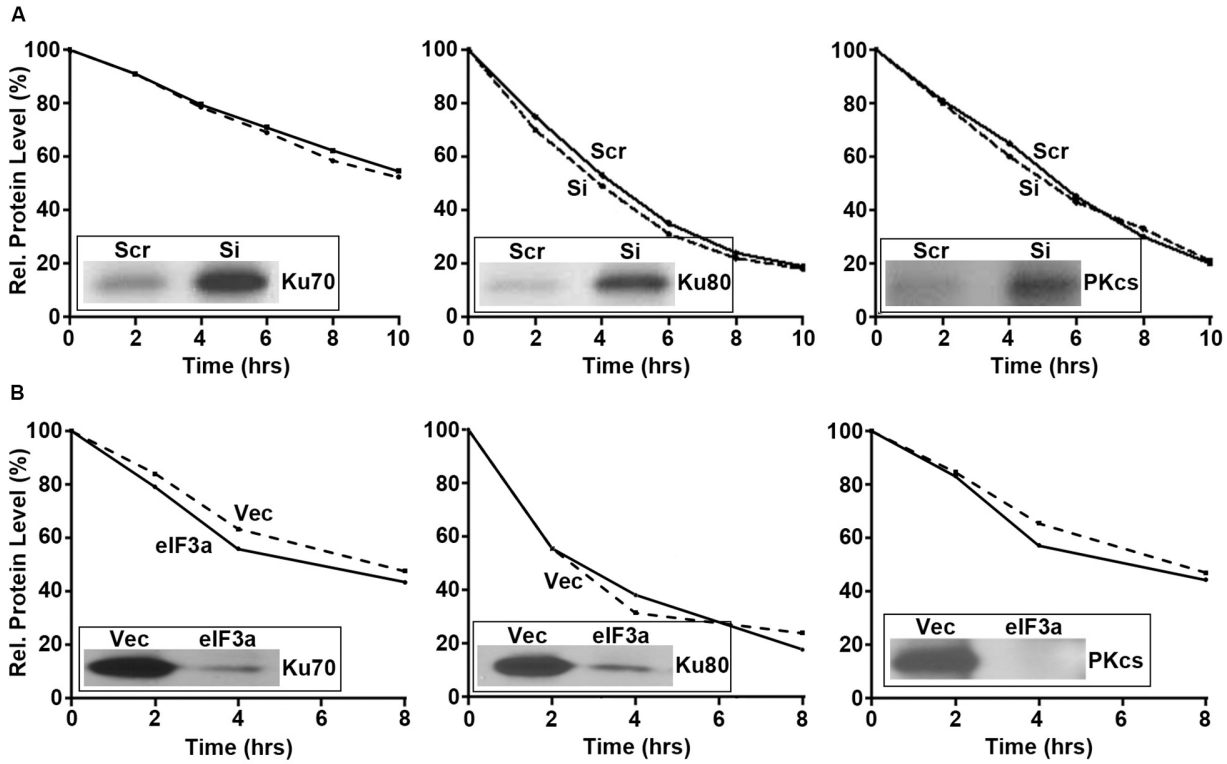

FIGURE 5 | Effect of eukaryotic initiation factor (eIF)3a on the synthesis and degradation of Ku70, K80, and DNA-PKcs. Pulse labeling in combination with immunoprecipitation and cycloheximide chasing were performed to determine the synthesis (insets) and degradation, respectively, of Ku70, Ku80, and DNA-PKcs in H1299 cells with transient eIF3a knockdown **(A)** and NIH3T3 cells with stable eIF3a overexpression **(B)** compared with their respective control cells.

apoptosis (Liu et al., 2011), further supporting the conclusion that eIF3a may contribute to cellular sensitivity to DNA-damaging treatments by suppressing DNA repair and by increasing DNA damage-induced apoptosis. We have also found in the previous study (Liu et al., 2011) that a selected cisplatin-sensitive cell line expressed a higher level of eIF3a compared with the parent cell line, suggesting that cancer cells may alter eIF3a expression to adapt to a DNA-damaging environment by regulating DNA damage repair protein synthesis.

As discussed above, eIF3a may also have oncogenic functions (Dong et al., 2004; Zhang et al., 2007). This oncogenic function may relate to the finding that eIF3a suppresses DNA repair *via* suppressing the synthesis of DNA repair proteins. Reduced DNA damage repair activity due to eIF3a overexpression in normal cells likely reduces the protection against DNA-damaging carcinogens, leading to an increased possibility of carcinogenesis (**Figure 7**). Further studies are required to test this theory.

The fact that eIF3a does not contribute to cellular response to non-DNA-damaging drugs such as *vinca* alkaloid (Yin et al., 2011b) suggests that eIF3a regulation of cellular response to DNA-damaging treatments may be a specific event. Whether eIF3a also regulates the synthesis of proteins important for other DNA repair pathways such as HR for repair of DSBs remains to be determined. Nevertheless, the findings that eIF3a may suppress the synthesis of DNA repair proteins and contribute to the increased sensitivity of cancer cells to DNA-damaging treatments suggest that eIF3a may be developed as a biomarker for precision medicine prescription. Patients with a high level of eIF3a may benefit from DNA-damaging drug and radiation treatment, whereas such treatments may not be as much of a benefit for patients with a low level of eIF3a. Indeed, we observed that patients with a high level of eIF3a expression have significantly better overall survival than patients with a low eIF3a level in breast, gastric, lung, and ovarian cancers. Future studies are also warranted to investigate the possibility to target eIF3a regulation of DNA repair protein synthesis to sensitize resistance to DNA-damaging treatments.

In addition to the regulation in the synthesis of DNA repair proteins, eIF3a has also been observed to possibly regulate the synthesis of p27 and ribonucleotide reductase (Dong and Zhang, 2003; Dong et al., 2004). The findings that eIF3a suppresses the synthesis of DNA repair proteins are against the intuition and belief that eIF3a facilitates translational initiation as a subunit of eIF3 complex, and it would increase protein synthesis in general. Because eIF3a is thought to be a subunit of the eIF3 complex consisting of 13 putative subunits, eIF3a regulation of synthesis of DNA repair proteins may be indirect due to the effect of its upregulation or knockdown on the formation of the complex or sub-complexes of other eIF3 subunits. For example, it is noteworthy that eIF3e was discovered as int-6, a site of mouse mammary tumor virus (MMTV) integration (Asano et al., 1998), suggesting a tumor

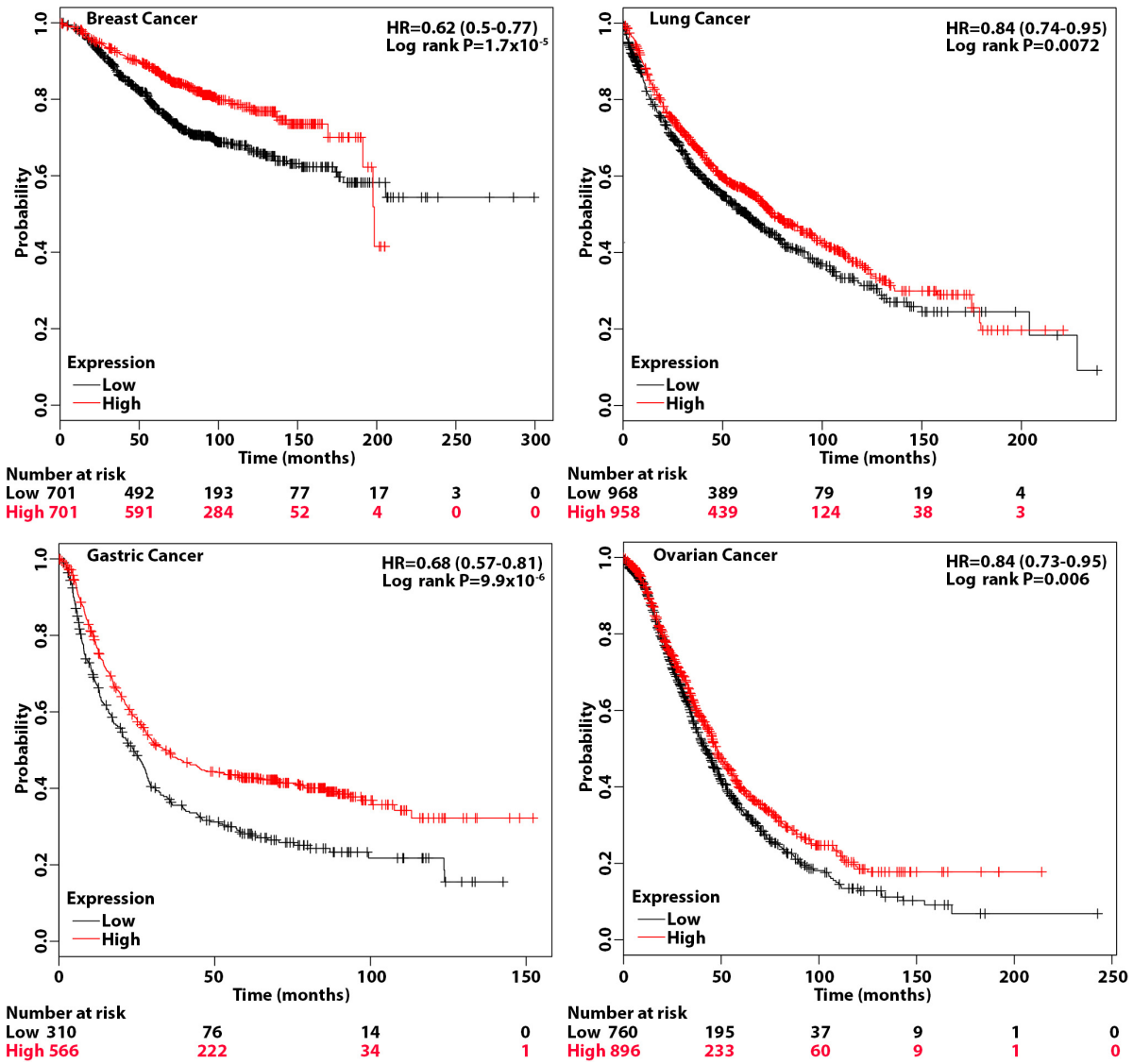

FIGURE 6 | Association of eukaryotic initiation factor (eIF)3a expression with overall survival of breast, gastric, lung, and ovarian cancers. Overall survival analyses were conducted using Kaplan–Meier (KM) plotter with hazard ratio (HR) at 95% confidence intervals and log rank $P < 0.05$ considered significant.

suppressor function. While the role of eIF3e in translational control is not yet established, the studies in yeast support a tumor suppressor role in ameliorating oxidative damage associated with nutritional stress conditions (Udagawa et al., 2008; Nemoto et al., 2010). In mammals, the functional core of eIF3 is defined with eIF3a, b, c, e, f, and h subunits (Masutani et al., 2007), and eIF3a appears to be the docking site for eIF3a:b:i:g sub-complex formation (Zhou et al., 2008; Dong et al., 2013). In light of these previous findings, it is possible that eIF3a knockdown or overexpression changes the spectrum in forming eIF3 sub-complexes including other eIF3 subunits such as eIF3e, which may mediate the regulation of DNA repair protein synthesis.

As an alternative possibility, eIF3a may have an additional regulatory non-canonical function not associated with the eIF3 complex or sub-complexes. The fact that eIF3a suppresses the synthesis of some proteins (e.g., DNA repair proteins) while increasing the synthesis of others (e.g., ribonucleotide reductase) (Dong et al., 2004) and Chk1 (Dong et al., 2020) supports this concept. How eIF3a regulates protein synthesis with its non-canonical activity remains unknown. However, the previous finding that eIF3a can bind to the 5′-UTRs of RPA2 mRNA (Yin et al., 2013) suggests that eIF3a may bind to these mRNAs and suppress the translation of these mRNAs. It also remains to be determined whether this non-canonical activity requires other eIF3 subunits such as eIF3b or eIF3i. Recently, eIF3i has also been shown to be able to regulate the synthesis of cyclooxygenase (COX)2 (Qi et al., 2014), suggesting that other eIF3 subunits may also have non-canonical activity, although it is not clear if they work together. Clearly, more studies are

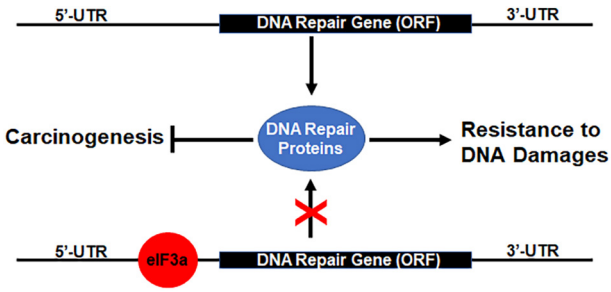

FIGURE 7 | Hypothetical model of eukaryotic initiation factor (eIF)3a regulation of DNA repair protein synthesis relationship with DNA damage resistance and tumorigenesis. Binding of eIF3a to 5′-untranslated regions (5′-UTRs) of mRNAs encoding DNA damage repair proteins inhibits translation and synthesis of DNA repair proteins, leading to sensitization of cancer cells to DNA-damaging treatments and susceptibility of normal cells to DNA-damaging carcinogens.

needed to investigate further the non-canonical function of eIF3 subunits vs. alteration of eIF3 complex/sub-complex formation in regulating protein synthesis.

MATERIALS AND METHODS

Materials

Cell culture media and reagents were purchased from BioSources International (Camarillo, CA), Media Tech (Herndon, CA), or Cambrex (Walkersville, MD). All electrophoresis reagents and polyvinylidene difluoride (PVDF) membranes were purchased from Bio-Rad (Hercules, CA). SYBR Green PCR Master Mix for real-time PCR, the high-capacity cDNA reverse transcription kit, and all primers were purchased from Applied Biosystems-Thermo Fisher (Chicago, IL). Metafectene® pro was purchased from Biontex (San Diego, CA). All other chemicals and reagents were of molecular biology grade from Sigma (St. Louis, MO) or Fisher Scientific (Chicago, IL).

Cell Culture and Survival Assay

Human lung cancer cell line H1299 and NIH3T3 cells were cultured at 37°C with 5% CO_2 in RPMI 1640 and Dulbecco's modified Eagle's medium (DMEM) medium, respectively, supplemented with 10% fetal bovine serum, 100 units/ml penicillin, and 100 μg/ml streptomycin. G418 at 400 μg/ml was also supplemented in the culture of the stable NIH3T3 cells overexpressing eIF3a and vector-transfected controls, which were established in our previous study (Yin et al., 2011b).

Colony formation survival assay was performed following IR treatments as previously described (Li et al., 2010; Wu et al., 2016). Briefly, 100 cells/well were seeded in six-well plates and cultured for 24 h followed by treatments with different doses of IR and continuous culture for 10–14 days with media changed every 2–3 days. At the end of the study, cells were washed with phosphate-buffered saline (PBS), and the colonies were stained with 0.05% (w/v) crystal violet in PBS containing 20% methanol for 15 min at room temperature and counted manually.

Western Blot, Immunofluorescence Staining, and Immunoprecipitation

Western blot analysis and immunofluorescence staining were performed as previously described (Dong and Zhang, 2003; Wu et al., 2016). Briefly, for Western blot analysis, equal amount of proteins from different cells were separated by sodium dodecyl sulfate–polyacrylamide gel electrophoresis (SDS-PAGE), transferred to PVDF membranes, and probed with antibodies specific to eIF3a, γ-H2AX, Ku70, Ku80, DNA-PKcs, and actin control followed by probing with horseradish peroxidase (HRP)-conjugated secondary antibody and enhanced chemiluminescence (ECL) reagents. The signals are captured on X-ray films.

Immunofluorescence staining was performed by culturing cells on glass coverslips, which were washed twice with cold PBS and fixed with acetone/methanol mixture (1:1) for 10 min and blocked in 1% bovine serum albumin (BSA) and 1% normal horse serum in PBS at 4°C for 30 min. The coverslips were then probed with the γ-H2AX-specific antibody for 30 min at 4°C followed by incubation with fluorescein isothiocyanate (FITC)-conjugated secondary antibody at room temperature for 30 min and washed twice with PBS. The cells were counterstained with 4′,6-diamidino-2-phenylindole (DAPI) before viewing on a confocal microscope.

Immunoprecipitation was performed as previously described (Dong and Zhang, 2003). Briefly, cell lysates were first mixed with mouse immunoglobulin G (IgG) and incubated for 2 h at 4°C followed by addition of 50% protein G-agarose slurry and incubation for 3 h at 4°C to remove non-specifically bound proteins by centrifugation. The supernatant was transferred to a new tube and incubated with 5 μg primary antibodies against Ku70, Ku80, or DNA-PKcs at 4°C for 2 h. Finally, 50 μl 50% protein G-agarose beads was added to the mixtures and incubated at 4°C overnight. The immunoprecipitated materials were collected by centrifugation and extensive washing with lysis buffer followed by separation using SDS-PAGE.

Real-Time Reverse Transcription-PCR

Real-time RT-PCR was performed as described previously (Dong et al., 2004, 2005). Briefly, total RNA was extracted using RNeasy Mini Kit (Qiagen, Valencia, CA), and real-time RT-PCR was performed using Power SYBR Green RNA-to-CT 1-Step kit. Data were normalized to an internal control gene, glyceraldehyde-3-phosphate dehydrogenase (GAPDH). The sequences of primers for the PCRs were 5-CATGGCAACTCCAGAGCAG (forward) and GCTCCTTAAACTCATCCACC (reverse) for Ku70; AGAAGAAGGCCAGCTTTGAG (forward) and AGCTGTGACAGAACTTCCAG (reverse) for Ku80; CCGGACGGACCTACTACGACT (forward) and AGAACGACCTGGGCATCCT (reverse) for DNA-PKcs.

Comet Assay

Neutral comet assay was performed as previously described (Wu et al., 2016). Briefly, cells treated with or without IR were embedded in low melting agarose on a microscope slide

followed by lysis at neutral pH and electrophoresis in Tris-borate-ethylenediaminetetraacetic acid (TBE) buffer for 2 h. Comets were observed after staining the cells with SYBR Green I and scoring 120 cells in each sample to measure the Olive tail moment.

Host Cell Reactivation-Based Non-homologous End Joining Assay

Host cell reactivation NHEJ assay was performed using pGL3 reporter plasmid with firefly luciferase gene driven by cytomegalovirus (CMV) promoter as previously described (Wu et al., 2016). Briefly, pGL3 was first linearized by *Hin*dIII digestion and co-transfected into cells along with the control circular pRL-TK reporter plasmid encoding Renilla luciferase followed by determination of both firefly and Renilla luciferase activity. Expression of firefly luciferase is dependent on the repair of the plasmid to regenerate the circular plasmid *via* NHEJ.

Protein Synthesis and Stability Assays

Pulse labeling using [^{35}S]methionine in combination with immunoprecipitation and SDS-PAGE analysis was used to determine the protein synthesis rate as previously described (Dong and Zhang, 2003; Dong et al., 2004). Briefly, cells were washed with PBS and methionine-free media before being subjected to labeling with [^{35}S]methionine (10 μCi/ml) in methionine-free media for 2 h. The cells were then washed with PBS and harvested for cell lysate preparation, immunoprecipitation, and separation by SDS-PAGE. The signals for immunoprecipitated proteins labeled by [^{35}S]methionine were captured by exposing to X-ray films.

The stability of specific proteins was determined using cycloheximide chasing as previously described (Liu et al., 2006). Briefly, cells were treated with 10 μg/ml cycloheximide for different times and harvested for preparation of cell lysates and Western blot analyses. The quantity of each protein at each time point of cycloheximide treatment was determined using the ImageJ software (NIH, USA) and plotted against the treatment time.

Overall Survival Analyses

The KM plotter can assess the effect of 54,675 genes on survival using 10,461 cancer samples, including 5,143 breast, 1,816 ovarian, 2,437 lung, and 1,065 gastric cancer patients with a mean follow-up of 69/40/49/33 months (Lanczky et al., 2016). The analyses on all four cancers were conducted using default parameters, and the hazard ratio (HR) with 95% confidence intervals and log rank $P < 0.05$ considered significant were calculated and shown on the plot.

DATA AVAILABILITY STATEMENT

Publicly available datasets were analyzed in this study. This data can be found here: http://kmplot.com/analysis.

AUTHOR CONTRIBUTIONS

RT performed the experiments and helped to draft the manuscript. CW, TD, JC, JB, SM, and ZD performed the experiments. J-YL performed the data analysis. J-TZ designed the studies, wrote the manuscript, and provided the support. All authors contributed to the article and approved the submitted version.

FUNDING

This study was supported in part by the National Institutes of Health grant R01 CA211904.

ACKNOWLEDGMENTS

Part of this work has been published in the format of the thesis entitled "Role of eIF3a expression in cellular sensitivity to ionizing radiation treatments by regulating synthesis of NHEJ repair proteins" (Tumia, 2015).

REFERENCES

Asano, K., Phan, L., Anderson, J., and Hinnebusch, A. G. (1998). Complex formation by all five homologues of mammalian translation initiation factor 3 subunits from yeast *Saccharomyces cerevisiae*. *J. Biol. Chem.* 273, 18573–18585. doi: 10.1074/jbc.273.29.18573

Bachmann, F., Banziger, R., and Burger, M. M. (1997). Cloning of a novel protein overexpressed in human mammary carcinoma. *Cancer Res.* 57, 988–994.

Branzei, D., and Foiani, M. (2008). Regulation of DNA repair throughout the cell cycle. *Nat. Rev. Mol. Cell Biol.* 9, 297–308. doi: 10.1038/nrm2351

Chen, G., and Burger, M. M. (1999). p150 expression and its prognostic value in squamous-cell carcinoma of the esophagus. *Int. J. Cancer* 84, 95–100. doi: 10.1002/(sici)1097-0215(19990420)84:2<95::aid-ijc1>3.0.co;2-n

Chen, G., and Burger, M. M. (2004). p150 overexpression in gastric carcinoma: the association with p53, apoptosis and cell proliferation. *Int. J. Cancer* 112, 393–398. doi: 10.1002/ijc.20443

Dellas, A., Torhorst, J., Bachmann, F., Banziger, R., Schultheiss, E., and Burger, M. M. (1998). Expression of p150 in cervical neoplasia and its potential value in predicting survival. *Cancer* 83, 1376–1383. doi: 10.1002/(sici)1097-0142(19981001)83:7<1376::aid-cncr15>3.0.co;2-1

Dong, Z., Arnold, R. J., Yang, Y., Park, M. H., Hrncirova, P., Mechref, Y., et al. (2005). Modulation of differentiation-related gene 1 expression by cell cycle blocker mimosine, revealed by proteomic analysis. *Mol. Cell Proteomics* 4, 993–1001. doi: 10.1074/mcp.m500044-mcp200

Dong, Z., Liu, J., and Zhang, J. T. (2020). Translational regulation of Chk1 expression by eIF3a via interaction with the RNA-binding protein HuR. *Biochem. J.* 477, 1939–1950. doi: 10.1042/BCJ20200025

Dong, Z., Liu, L. H., Han, B., Pincheira, R., and Zhang, J. T. (2004). Role of eIF3 p170 in controlling synthesis of ribonucleotide reductase M2 and cell growth. *Oncogene* 23, 3790–3801. doi: 10.1038/sj.onc.1207465

Dong, Z., Liu, Z., Cui, P., Pincheira, R., Yang, Y., Liu, J., et al. (2009). Role of eIF3a in regulating cell cycle progression. *Exp. Cell Res.* 315, 1889–1894. doi: 10.1016/j.yexcr.2009.03.009

Dong, Z., Qi, J., Peng, H., Liu, J., and Zhang, J. T. (2013). Spectrin domain of eukaryotic initiation factor 3a is the docking site for formation of the a:b:i:g Subcomplex. *J. Biol. Chem.* 288, 27951–27959. doi: 10.1074/jbc.m113.483164

Dong, Z., and Zhang, J. T. (2003). EIF3 p170, a mediator of mimosine effect on protein synthesis and cell cycle progression. *Mol. Biol. Cell* 14, 3942–3951. doi: 10.1091/mbc.e02-12-0784

Dong, Z., and Zhang, J. T. (2006). Initiation factor eIF3 and regulation of mRNA translation, cell growth, and cancer. *Crit. Rev. Oncol. Hematol.* 59, 169–180. doi: 10.1016/j.critrevonc.2006.03.005

Gottlieb, T. M., and Jackson, S. P. (1993). The DNA-dependent protein kinase: requirement for DNA ends and association with Ku antigen. *Cell* 72, 131–142. doi: 10.1016/0092-8674(93)90057-w

Hartlerode, A. J., and Scully, R. (2009). Mechanisms of double-strand break repair in somatic mammalian cells. *Biochem. J.* 423, 157–168. doi: 10.1042/bj20090942

Helleday, T., Lo, J., Van Gent, D. C., and Engelward, B. P. (2007). DNA double-strand break repair: from mechanistic understanding to cancer treatment. *DNA Repair* 6, 923–935. doi: 10.1016/j.dnarep.2007.02.006

Hershey, J. W. (2015). The role of eIF3 and its individual subunits in cancer. *Biochim. Biophys. Acta* 1849, 792–800. doi: 10.1016/j.bbagrm.2014.10.005

Hoeijmakers, J. H. (2001). Genome maintenance mechanisms for preventing cancer. *Nature* 411, 366–374. doi: 10.1038/35077232

Kastan, M. B., and Bartek, J. (2004). Cell-cycle checkpoints and cancer. *Nature* 432, 316–323.

Kuo, L. J., and Yang, L. X. (2008). Gamma-H2AX - a novel biomarker for DNA double-strand breaks. *In Vivo* 22, 305–309.

Lanczky, A., Nagy, A., Bottai, G., Munkacsy, G., Szabo, A., Santarpia, L., et al. (2016). miRpower: a web-tool to validate survival-associated miRNAs utilizing expression data from 2178 breast cancer patients. *Breast Cancer Res. Treat.* 160, 439–446. doi: 10.1007/s10549-016-4013-7

Li, Z., Dong, Z., Myer, D., Yip-Schneider, M., Liu, J., Cui, P., et al. (2010). Role of 14-3-3sigma in poor prognosis and in radiation and drug resistance of human pancreatic cancers. *BMC Cancer* 10:598. doi: 10.1186/1471-2407-10-598

Lieber, M. R. (2010). The mechanism of double-strand DNA break repair by the nonhomologous DNA end-joining pathway. *Annu. Rev. Biochem.* 79, 181–211. doi: 10.1146/annurev.biochem.052308.093131

Liu, R. Y., Dong, Z., Liu, J., Yin, J. Y., Zhou, L., Wu, X., et al. (2011). Role of eIF3a in regulating cisplatin sensitivity and in translational control of nucleotide excision repair of nasopharyngeal carcinoma. *Oncogene* 30, 4814–4823. doi: 10.1038/onc.2011.189

Liu, Y., Liu, H., Han, B., and Zhang, J. T. (2006). Identification of 14-3-3sigma as a contributor to drug resistance in human breast cancer cells using functional proteomic analysis. *Cancer Res.* 66, 3248–3255. doi: 10.1158/0008-5472.can-05-3801

Lobrich, M., and Jeggo, P. A. (2007). The impact of a negligent G2/M checkpoint on genomic instability and cancer induction. *Nat. Rev. Cancer* 7, 861–869. doi: 10.1038/nrc2248

Mari, P. O., Florea, B. I., Persengiev, S. P., Verkaik, N. S., Bruggenwirth, H. T., Modesti, M., et al. (2006). Dynamic assembly of end-joining complexes requires interaction between Ku70/80 and XRCC4. *Proc. Natl. Acad. Sci. U.S.A.* 103, 18597–18602. doi: 10.1073/pnas.0609061103

Masutani, M., Sonenberg, N., Yokoyama, S., and Imataka, H. (2007). Reconstitution reveals the functional core of mammalian eIF3. *EMBO J.* 26, 3373–3383. doi: 10.1038/sj.emboj.7601765

Nemoto, N., Udagawa, T., Ohira, T., Jiang, L., Hirota, K., Wilkinson, C. R., et al. (2010). The roles of stress-activated Sty1 and Gcn2 kinases and of the protooncoprotein homologue Int6/eIF3e in responses to endogenous oxidative stress during histidine starvation. *J. Mol. Biol.* 404, 183–201. doi: 10.1016/j.jmb.2010.09.016

Pardo, B., Gomez-Gonzalez, B., and Aguilera, A. (2009). DNA repair in mammalian cells: DNA double-strand break repair: how to fix a broken relationship. *Cell Mol. Life Sci.* 66, 1039–1056. doi: 10.1007/s00018-009-8740-3

Pincheira, R., Chen, Q., and Zhang, J. T. (2001). Identification of a 170-kDa protein over-expressed in lung cancers. *Br. J. Cancer* 84, 1520–1527. doi: 10.1054/bjoc.2001.1828

Qi, J., Dong, Z., Liu, J., and Zhang, J. T. (2014). EIF3i promotes colon oncogenesis by regulating COX-2 protein synthesis and β-catenin activation. *Oncogene* 33, 4156–4163. doi: 10.1038/onc.2013.397

Reynolds, P., Anderson, J. A., Harper, J. V., Hill, M. A., Botchway, S. W., Parker, A. W., et al. (2012). The dynamics of Ku70/80 and DNA-PKcs at DSBs induced by ionizing radiation is dependent on the complexity of damage. *Nucleic Acids Res.* 40, 10821–10831. doi: 10.1093/nar/gks879

Rogakou, E. P., Pilch, D. R., Orr, A. H., Ivanova, V. S., and Bonner, W. M. (1998). DNA double-stranded breaks induce histone H2AX phosphorylation on serine 139. *J. Biol. Chem.* 273, 5858–5868. doi: 10.1074/jbc.273.10.5858

Rothkamm, K., Kruger, I., Thompson, L. H., and Lobrich, M. (2003). Pathways of DNA double-strand break repair during the mammalian cell cycle. *Mol. Cell Biol.* 23, 5706–5715. doi: 10.1128/mcb.23.16.5706-5715.2003

Spilka, R., Ernst, C., Bergler, H., Rainer, J., Flechsig, S., Vogetseder, A., et al. (2014). eIF3a is over-expressed in urinary bladder cancer and influences its phenotype independent of translation initiation. *Cell Oncol.* 37, 253–267. doi: 10.1007/s13402-014-0181-9

Stiff, T., O'driscoll, M., Rief, N., Iwabuchi, K., Lobrich, M., and Jeggo, P. A. (2004). ATM and DNA-PK function redundantly to phosphorylate H2AX after exposure to ionizing radiation. *Cancer Res.* 64, 2390–2396. doi: 10.1158/0008-5472.can-03-3207

Tumia, R. (2015). *Role of eIF3a Expression in Cellular Sensitivity to Ionizing Radiation Treatments by Regulating Synthesis of NHEJ Repair Proteins*. M.Sc Thesis, Indiana University, Bloomington, IN.

Udagawa, T., Nemoto, N., Wilkinson, C. R., Narashimhan, J., Jiang, L., Watt, S., et al. (2008). Int6/eIF3e promotes general translation and Atf1 abundance to modulate Sty1 MAPK-dependent stress response in fission yeast. *J. Biol. Chem.* 283, 22063–22075. doi: 10.1074/jbc.m710017200

Uematsu, N., Weterings, E., Yano, K., Morotomi-Yano, K., Jakob, B., Taucher-Scholz, G., et al. (2007). Autophosphorylation of DNA-PKCS regulates its dynamics at DNA double-strand breaks. *J. Cell Biol.* 177, 219–229. doi: 10.1083/jcb.200608077

van Gent, D. C., Hoeijmakers, J. H., and Kanaar, R. (2001). Chromosomal stability and the DNA double-stranded break connection. *Nat. Rev. Genet.* 2, 196–206. doi: 10.1038/35056049

Wu, X., Dong, Z., Wang, C. J., Barlow, L. J., Fako, V., Serrano, M. A., et al. (2016). FASN regulates cellular response to genotoxic treatments by increasing PARP-1 expression and DNA repair activity via NF-kappaB and SP1. *Proc. Natl. Acad. Sci. U.S.A.* 113, E6965–E6973.

Yaneva, M., Kowalewski, T., and Lieber, M. R. (1997). Interaction of DNA-dependent protein kinase with DNA and with Ku: biochemical and atomic-force microscopy studies. *EMBO J.* 16, 5098–5112. doi: 10.1093/emboj/16.16.5098

Yin, J. Y., Dong, Z., Liu, Z. Q., and Zhang, J. T. (2011a). Translational control gone awry: a new mechanism of tumorigenesis and novel targets of cancer treatments. *Biosci. Rep.* 31, 1–15. doi: 10.1042/bsr20100077

Yin, J. Y., Shen, J., Dong, Z. Z., Huang, Q., Zhong, M. Z., Feng, D. Y., et al. (2011b). Effect of eIF3a on response of lung cancer patients to platinum-based chemotherapy by regulating DNA repair. *Clin. Cancer Res.* 17, 4600–4609. doi: 10.1158/1078-0432.ccr-10-2591

Yin, J. Y., Dong, Z. Z., Liu, R. Y., Chen, J., Liu, Z. Q., and Zhang, J. T. (2013). Translational regulation of RPA2 via internal ribosomal entry site and by eIF3a. *Carcinogenesis* 34, 1224–1231. doi: 10.1093/carcin/bgt052

Zhang, L., Pan, X., and Hershey, J. W. (2007). Individual overexpression of five subunits of human translation initiation factor eIF3 promotes malignant transformation of immortal fibroblast cells. *J. Biol. Chem.* 282, 5790–5800. doi: 10.1074/jbc.m606284200

Zhou, M., Sandercock, A. M., Fraser, C. S., Ridlova, G., Stephens, E., Schenauer, M. R., et al. (2008). Mass spectrometry reveals modularity and a complete subunit interaction map of the eukaryotic translation factor eIF3. *Proc. Natl. Acad. Sci. U.S.A.* 105, 18139–18144. doi: 10.1073/pnas.0801313105

Conflict of Interest: The authors declare that the research was conducted in the absence of any commercial or financial relationships that could be construed as a potential conflict of interest.

frontiers in Cell and Developmental Biology

CORRECTION
published: 07 January 2021
doi: 10.3389/fcell.2020.629218

Corrigendum: eIF3a Regulation of NHEJ Repair Protein Synthesis and Cellular Response to Ionizing Radiation

Rima Tumia[1†], Chao J. Wang[1†], Tianhan Dong[1], Shijie Ma[2], Jenny Beebe[1], Juan Chen[1], Zizheng Dong[2], Jing-Yuan Liu[3] and Jian-Ting Zhang[1,2]*

[1] Department of Pharmacology and Toxicology, Indiana University School of Medicine, Indianapolis, IN, United States,
[2] Department of Cancer Biology, University of Toledo College of Medicine and Life Sciences, Toledo, OH, United States,
[3] Department of Medicine, University of Toledo College of Medicine and Life Sciences, Toledo, OH, United States

Keywords: eukaryotic initiation factor 3a (eIF3a), DNA repair, radiation, resistance, mRNA translation, protein synthesis, gamma-H2A histone family member X (γ-H2AX)

OPEN ACCESS

Edited and reviewed by:
Inna N. Lavrik,
University Hospital
Magdeburg, Germany

***Correspondence:**
Jian-Ting Zhang
jianting.zhang@utoledo.edu

[†] These authors have contributed equally to this work

Specialty section:
This article was submitted to Cell Death and Survival, a section of the journal Frontiers in Cell and Developmental Biology

Received: *13 November 2020*
Accepted: *15 December 2020*
Published: *07 January 2021*

Citation:
Tumia R, Wang CJ, Dong T, Ma S, Beebe J, Chen J, Dong Z, Liu J-Y and Zhang J-T (2021) Corrigendum: eIF3a Regulation of NHEJ Repair Protein Synthesis and Cellular Response to Ionizing Radiation. Front. Cell Dev. Biol. 8:629218. doi: 10.3389/fcell.2020.629218

A Corrigendum on

eIF3a Regulation of NHEJ Repair Protein Synthesis and Cellular Response to Ionizing Radiation

by Tumia, R., Wang, C. J., Dong, T., Ma, S., Beebe, J., Chen, J., et al. (2020). Front. Cell Dev. Biol. 8:753. doi: 10.3389/fcell.2020.00753

In the original article, there was a mistake in **Figure 1A** and **Figure 3A** as published. Wrong images for the Western blot of H1299 cells in **Figure 1A** and for the comet assay of the control un-irradiated H1299 cells in **Figure 3A** were accidently used for publication. The corrected **Figures 1** and **3** appear below.

The authors apologize for this error and state that this does not change the scientific conclusions of the article in any way. The original article has been updated.

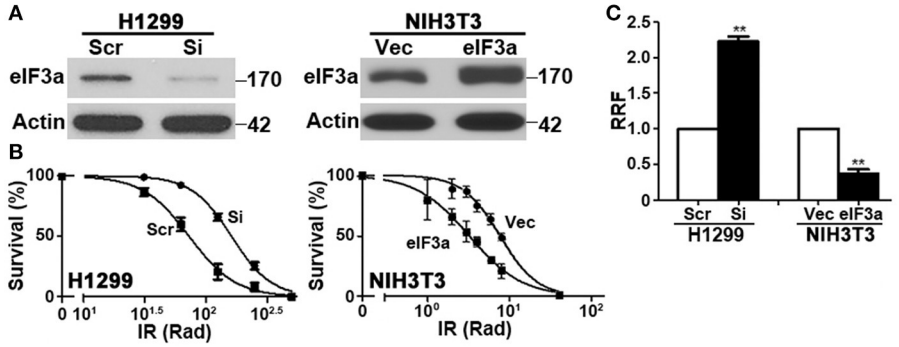

FIGURE 1 | Effect of eukaryotic initiation factor (eIF)3a expression on the cellular response to ionizing radiation (IR). Western blot analyses **(A)** and colony formation assay following IR treatment **(B)** of H1299 cells with transient eIF3a knockdown and NIH3T3 cells with stable eIF3a overexpression compared with their respective control cells. Actin was used as a loading control. Panel **(C)** shows a summary of eIF3a effects on cellular sensitivity to IR treatments. Relative resistance factor (RRF) was derived by dividing the IC_{50} of the test cells by that of their control cells ($n = 3$, $^{**}P < 0.01$).

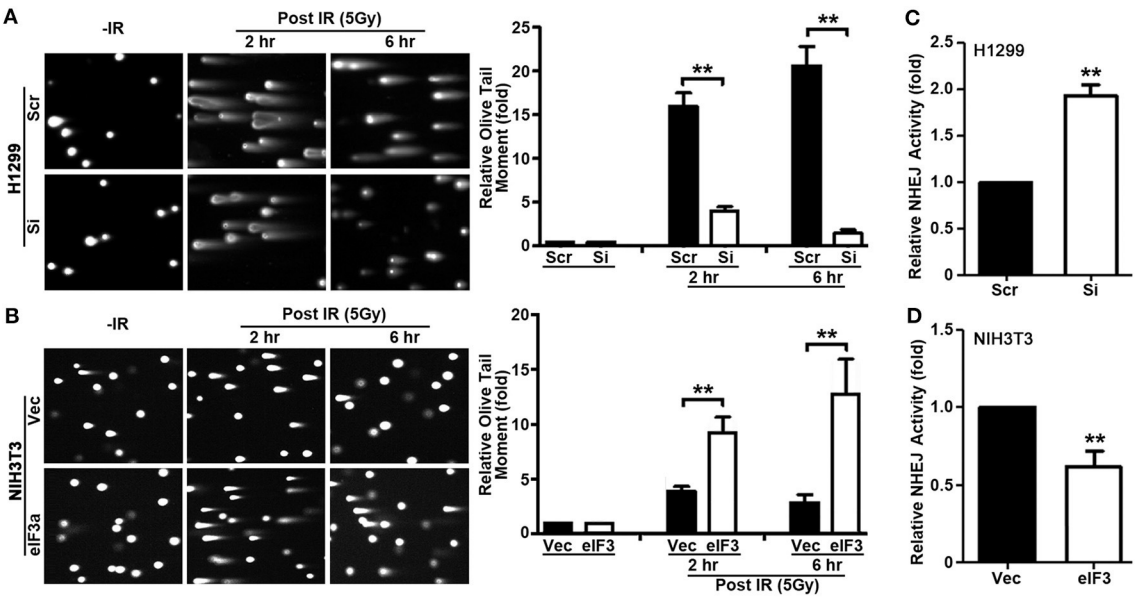

FIGURE 3 | Role of eukaryotic initiation factor (eIF)3a in non-homologous end joining (NHEJ) repair of ionizing radiation (IR)-induced double-strand breaks (DSBs). **(A,B)** Comet assay was used to determine eIF3a effects on the level of DSBs induced by IR in H1299 cells with transient eIF3a knockdown **(A)** and NIH3T3 cells with stable eIF3a overexpression **(B)** compared with their respective control cells. The histograms show the summary of quantitative analysis of Olive tail moment in these cells. **(C,D)** Host cell reactivation assays using reporter constructs were performed using H1299 cells with eIF3a knockdown **(C)** and NIH3T3 cells with eIF3a stable overexpression **(D)** compared with their respective control cells ($n = 3$; $^{**}P < 0.01$).

frontiers in Cell and Developmental Biology

ORIGINAL RESEARCH
published: 30 October 2020
doi: 10.3389/fcell.2020.590848

Activity of Human Apurinic/Apyrimidinic Endonuclease APE1 Toward Damaged DNA and Native RNA With Non-canonical Structures

Anastasia T. Davletgildeeva[1,2†], Alexandra A. Kuznetsova[1†], Olga S. Fedorova[1] and Nikita A. Kuznetsov[1*]*

[1] Institute of Chemical Biology and Fundamental Medicine of the SB RAS, Novosibirsk, Russia, [2] Department of Natural Sciences, Novosibirsk State University, Novosibirsk, Russia

OPEN ACCESS

Edited by:
Inna N. Lavrik,
University Hospital Magdeburg, Germany

Reviewed by:
Murat Saparbaev,
UMR 9019 Intégrité du génome et Cancers, France
Daniela Marasco,
University of Naples Federico II, Italy
Amangeldy Bissenbaev,
Al-Farabi Kazakh National University, Kazakhstan

***Correspondence:**
Olga S. Fedorova
fedorova@niboch.nsc.ru
Nikita A. Kuznetsov
nikita.kuznetsov@niboch.nsc.ru

† These authors have contributed equally to this work

Specialty section:
This article was submitted to Cell Death and Survival, a section of the journal Frontiers in Cell and Developmental Biology

Received: 03 August 2020
Accepted: 30 September 2020
Published: 30 October 2020

Citation:
Davletgildeeva AT, Kuznetsova AA, Fedorova OS and Kuznetsov NA (2020) Activity of Human Apurinic/Apyrimidinic Endonuclease APE1 Toward Damaged DNA and Native RNA With Non-canonical Structures. Front. Cell Dev. Biol. 8:590848. doi: 10.3389/fcell.2020.590848

The primary role of apurinic/apyrimidinic (AP) endonuclease APE1 in human cells is the cleavage of the sugar phosphate backbone 5′ to an AP site in DNA to produce a single-strand break with a 5′-deoxyribose phosphate and 3′-hydroxyl end groups. APE1 can also recognize and incise some damaged or modified nucleotides and possesses some minor activities: 3′–5′ exonuclease, 3′-phosphodiesterase, 3′-phosphatase, and RNase H. A molecular explanation for the discrimination of structurally different substrates by the single active site of the enzyme remains elusive. Here, we report a mechanism of target nucleotide recognition by APE1 as revealed by the results of an analysis of the APE1 process involving damaged DNA and native RNA substrates with non-canonical structures. The mechanism responsible for substrate specificity proved to be directly related to the ability of a target nucleotide to get into the active site of APE1 in response to an enzyme-induced DNA distortion.

Keywords: DNA repair, non-B-DNA, quadruplex, AP endonuclease, nucleotide recognition

INTRODUCTION

Human apurinic/apyrimidinic (AP) endonuclease APE1 is the key enzyme of the base excision repair pathway, which is responsible for processing AP sites in DNA (Wilson and Barsky, 2001; Demple and Sung, 2005). In the alternative nucleotide incision repair pathway, APE1 makes an incision of the phosphodiester bond on the 5′ side of a damaged nucleotide, resulting in the formation of a 3′-OH group and a 5′ dangling damaged nucleotide (Ischenko and Saparbaev, 2002; Gros et al., 2004; Guliaev et al., 2004; Daviet et al., 2007; Christov et al., 2010; Vrouwe et al., 2011; Prorok et al., 2012, 2013). In addition, the APE1 enzyme possesses endoribonuclease (Barzilay et al., 1995; Berquist et al., 2008; Barnes et al., 2009), 3′-phosphodiesterase, 3′-phosphatase (Chen et al., 1991), and 3′–5′-exonuclease activities (Chou and Cheng, 2002; Kuznetsova et al., 2018a). Of note, a comparison of all these DNA lesions and natural DNA and RNA nucleotides makes it clear that they significantly differ from one another in chemical nature. On the one hand, such a variety of

substrates indicates that the enzyme is indeed multifunctional; on the other hand, it raises the question of how APE1, which has a single active site, can control its substrate specificity and activity.

X-ray crystallographic studies of human APE1 in the free state (Gorman et al., 1997; Beernink et al., 2001; Manvilla et al., 2013) and in complex with nicked or abasic DNA (Mol et al., 2000a,b; Tsutakawa et al., 2013; Freudenthal et al., 2015) have revealed that this enzyme interacts preferentially with one of the duplex strands, usually to form hydrogen bonds and electrostatic contacts between DNA phosphate groups and amino acid side chains or amide groups of the peptide bonds of the protein. It has been shown that in a catalytically active complex with APE1, DNA is bent, and an abasic nucleotide is flipped out of the DNA double helix into the active site of the enzyme. As illustrated recently (Whitaker et al., 2018) in an elegant series of high-resolution APE1–DNA structural snapshots, APE1 removes 3′ nucleotides in the course of the 3′–5′-exonuclease reaction by placing the 3′ group within the intra-helical DNA cavity via a non–base-flipping mechanism. This process is facilitated by DNA structural disturbances caused by the presence of a mismatched or damaged base or nick formation as well as DNA bending. Nevertheless, the reality of this mechanism in endonuclease reactions is questionable due to significant restrictions on the nucleotide mobility in an unbroken DNA chain.

In our previous study (Kuznetsova et al., 2018b), we performed pulsed electron–electron double resonance (PELDOR) spectroscopy and pre–steady-state kinetic analysis with Forster resonance energy transfer (FRET) detection of DNA conformational changes during DNA binding and lesion recognition in model damaged duplex substrates containing 1,N^6-ethenoadenosine, α-adenosine, 5,6-dihydrouridine, or an abasic site. Equilibrium PELDOR and kinetic FRET data indicated that DNA binding by APE1 leads to noticeable damage-dependent bending of a DNA duplex. These data revealed that the DNA distortions induced by enzyme binding and initial-complex formation depend on the nature of the damaged nucleotide. Molecular dynamics simulations showed that the damaged nucleotide is everted from the DNA helix and placed into the enzyme's binding pocket. Nevertheless, no damage-specific contacts were detected between a damaged nucleotide and amino acid residues in the active site of the enzyme. It was suggested that the capacity of a damaged nucleotide to be everted from DNA and to be placed into the enzyme pocket could be the key factor behind the substrate specificity of APE1. This conclusion is in good agreement with the ability of APE1 to recognize many structurally unrelated nucleotides not only in DNA but also in RNA. According to the proposed model, one can conclude that the endoribonuclease activity of APE1 is linked with the structural features of RNA, which can facilitate the eversion of intact nucleotides in structurally distorted regions, such as a junction of stems and loops in hairpins, bulges, and bubbles. A plausible extrapolation of this model of substrate recognition suggests that APE1 can cleave not only RNA but also DNA in non-canonical B-forms. Therefore, the main objective of the present study was to obtain evidence for this supposition and to elucidate the key steps of the mechanism underlying APE1 interaction with model substrates that ensure specific recognition of a target nucleotide in DNA and RNA of non-canonical structures. To this end, we analyzed the efficacy of cleavage of a set of damaged DNA and native RNA substrates with non–B-form structures such as G-quadruplexes, hairpins, bulges, and bubbles that could facilitate the base eversion from the substrate into the APE1 active site.

MATERIALS AND METHODS

The Enzyme and DNA and RNA Substrates

The APE1 enzyme was isolated from *Escherichia coli* Rosetta 2 cells transformed with plasmid pET11a carrying the human *APE1* gene (Daviet et al., 2007). Briefly, to purify APE1 expressed as a recombinant protein, 1 L of culture [in Luria–Bertani (LB) broth] of *E. coli* strain Rosetta II (DE3) (Invitrogen, France) carrying the pET11a-APE1 construct was grown with 50 μg/ml ampicillin at 37°C until absorbance at 600 nm (A600) reached 0.6–0.7; APE1 expression was induced overnight with 0.2 mM isopropyl-β-*d*-thiogalactopyranoside. The method for isolation of wild-type APE1 has been described previously (Kuznetsova et al., 2014; Miroshnikova et al., 2016a). The protein concentration was measured by the Bradford method; the stock solution was stored at −20°C.

The synthesis of the oligonucleotides (**Table 1**) was carried out on an ASM-800 DNA/RNA synthesizer (Biosset, Russia) using standard commercial phosphoramidites and CPG solid supports from Glen Research (United States). The oligonucleotides were deprotected according to manufacturer's protocols and purified by HPLC. Oligonucleotide homogeneity was checked by denaturing 20% polyacrylamide gel electrophoresis (PAGE). Concentrations of oligonucleotides were calculated from their A_{260}. Oligonucleotide duplexes were prepared by annealing oligonucleotide strands at a 1:1 molar ratio.

Circular Dichroism (CD) Analysis

These spectra were recorded on a Jasco J-600 spectropolarimeter (Jasco, Japan), at 25°C in quartz cells with 1 cm path length. The concentration of DNA in the cell was 10 μM. The experiments were carried out in a buffer consisting of 50 mM Tris-HCl pH 7.5, 140 mM KCl, 1 mM EDTA, and 5 mM $MgCl_2$. The spectra were recorded at a bandwidth of 1.0 nm and a resolution of 1.0 nm at a scan speed of 50 nm/min.

PAGE Experiments

5′-6-carboxyfluorescein (FAM)–labeled or ^{32}P-labeled oligonucleotides were subjected to experiments on separation of cleavage products by PAGE. APE1 endonuclease assays with G-quadruplex DNA substrates were performed at 25°C in a reaction buffer consisting of 50 mM Tris-HCl pH 7.5, 5.0 mM $MgCl_2$, and 140 mM KCl, which is required for quadruplex structure formation. In case of bulged DNA substrates, the concentration of KCl was reduced to 50 mM. In case of RNA substrates, experiments were conducted at 25°C in a reaction buffer consisting of 50 mM Tris-HCl pH 7.5, 50 mM KCl, and

TABLE 1 | Oligonucleotide sequences forming non-canonical DNA and RNA substrates.

Folding type	Shorthand	Sequences
G-quadruplex	Q4	5′-FAM-TTAGGGTTAGGGTTAGGGTTAGGGTT-BHQ1-3′
	F14-Q4	5′-FAM-TTAGGGTTAGGGTFAGGGTTAGGGTT-BHQ1-3′
	F14-aPu13-Q4	5′-TTAGGGTTAGGG(aPu)FAGGGTTAGGGTT-3′
	F14-aPu15-Q4	5′-TTAGGGTTAGGGTF(aPu)GGGTTAGGGTT-3′
	F17-Q4	5′-FAM-TTAGGGTTAGGGTTAGFGTTAGGGTT-BHQ1-3′
	F17-aPu16-Q4	5′-TTAGGGTTAGGGTTA(aPu)FGTTAGGGTT-3′
	F17-aPu18-Q4	5′-TTAGGGTTAGGGTTAGF(aPu)TTAGGGTT-3′
	rQ4	5′-FAM-r(AGGGUUAGGGUUAGGGUUAGGGU)-3′
Duplex	dsF/G	5′-FAM-GCGCATACGGCATFATCAGGGAAGTGGG-BHQ1-3′/3′-CGCGTATGCCGTAGTAGTCCCTTCACCC-5′
	rAUA/UAU	5′-FAM-r(GCGCAUACGGAAUAAAAGGGAAGUGGG)-3′/3′-r(CGCGUAUGCCUUAUUUUCCCUUCACCC)-5′
Bulged structures	F/−Δ1	5′-FAM-GCGCATACGGCATFATCAGGGAAGTGGG-BHQ1-3′/3′-CGCGTATGCCGTA-TAGTCCCTTCACCC-5′
	F/−Δ2(5′)	5′-FAM-GCGCATACGGCATFATCAGGGAAGTGGG-BHQ1-3′/3′-CGCGTATGCCGT-TAGTCCCTTCACCC-5′
	F/−Δ2(3′)	5′-FAM-GCGCATACGGCATFATCAGGGAAGTGGG-BHQ1-3′/3′-CGCGTATGCCGTA-AGTCCCTTCACCC-5′
	F/−Δ3	5′-FAM-GCGCATACGGCATFATCAGGGAAGTGGG-BHQ1-3′/3′-CGCGTATGCCGT--AGTCCCTTCACCC-5′
	F/−Δ5	5′-FAM-GCGCATACGGCATFATCAGGGAAGTGGG-BHQ1-3′/3′-CGCGTATGCCG---GTCCCTTCACCC-5′
	F/ + Δ3	5′-FAM-GCGCATACGGCAT-F-ATCAGGGAAGTGGG-BHQ1-3′/3′-CGCGTATGCCGTAGGGTAGTCCCTTCACCC-5′
	F/ + Δ4	5′-FAM-GCGCATACGGCAT-F-ATCAGGGAAGTGGG-BHQ1-3′/3′-CGCGTATGCCGTACGGGTAGTCCCTTCACCC-5′
	F/ + Δ5	5′-FAM-GCGCATACGGCAT-F-ATCAGGGAAGTGGG-BHQ1-3′/3′-CGCGTATGCCGTACGGGCTAGTCCCTTCACCC-5′
	F/ + Δ7	5′-FAM-GCGCATACGGCAT--F--ATCAGGGAAGTGGG-BHQ1-3′/3′-CGCGTATGCCGTACCGGGCCTAGTCCCTTCACCC-5′
	rAUA/−Δ1	5′-FAM-r(GCGCAUACGGAAUAAAAGGGAAGUGGG)-3′/3′-r(CGCGUAUGCCUU-UUUUCCCUUCACCC)-5′
	rAUA/−Δ2	5′-FAM-r(GCGCAUACGGAAUAAAAGGGAAGUGGG)-3′/3′-r(CGCGUAUGCCUU-UUUCCCUUCACCC)-5′
	rAUA/−Δ3	5′-FAM-r(GCGCAUACGGAAUAAAAGGGAAGUGGG)-3′/3′-r(CGCGUAUGCCU--UUUCCCUUCACCC)-5′
Mismatch	rAUA/UCU	5′-FAM-r(GCGCAUACGGAAUAAAAGGGAAGUGGG)-3′/3′-r(CGCGUAUGCCUUCUUUUCCCUUCACCC)-5′
Bubbled structures	rAUA/CCC	5′-FAM-r(GCGCAUACGGAAUAAAAGGGAAGUGGG)-3′/3′-r(CGCGUAUGCCUCCCUUUCCCUUCACCC)-5′
Hairpin structure	rHP	5′-FAM-r(AUAUAACAUCAUUAUAU)-BHQ1-3′

1.0 mM EDTA to prevent 3′–5′ exonuclease degradation of substrates (Kuznetsova et al., 2020). The reaction was initiated by the addition of APE1. Aliquots of the reaction mixture were withdrawn, immediately quenched with a gel-loading dye containing 7 M urea and 25 mM EDTA, and loaded on a 20% (w/v) polyacrylamide/7 M urea gel. PAGE (gel concentration, 20%) was performed under denaturing conditions (7 Ì urea) at 55°C and a voltage of 200–300 V.

Partial hydrolysis of the model RNA substrates by RNase A was performed using the following procedure. The reaction mixture (20 μl) composed of a 3.0 μÌ substrate and 3.0 nM RNase A in a buffer [50 mM Tris-HCl (pH 8.5), 50 mM NaCl, 1 mM EDTA, 1 mM DTT, and 9% of glycerol] was incubated at 25°C for 5 min. The reaction mixture was then supplemented with 20 μl of a solution containing 7 M urea and 25 mM EDTA and incubated at 96°C for 5 min before gel loading.

Formation of the product was analyzed by autoradiography and quantified by scanning densitometry in the Gel-Pro Analyzer software, v.4.0 (Media Cybernetics, United States).

Kinetic traces of product accumulation, obtained in the PAGE analysis, were fitted to the single exponential curve by means of the Origin software (OriginLab Corp., United States; Eq. 1).

$$Product\ accumulation = A \times [1 - exp(-k_{obs} \times t)] \quad (1)$$

where A is the amplitude, k_{obs} (s^{-1}) denotes the observed rate constant, and t represents reaction time.

The dependence of observed rate constants k_{obs} on concentration of APE1 was fitted to Eq. 2:

$$k_{obs} = K_{bind} \times k_2 \times [APE1]/(K_{bind} \times [APE1] + 1) + k_{-2} \quad (2)$$

where K_{bind} is the equilibrium constant of the initial APE1–substrate complex (M^{-1}) and k_2 and k_{-2} are the rate constants (s^{-1}) of the second binding step.

In case of bulged DNA substrates, the initial rate of cleavage was estimated as the initial slope of the kinetic curve obtained under steady-state reaction conditions.

Stopped-Flow Fluorescence Measurements

These measurements with fluorescence detection were carried out using an SX.18MV stopped-flow spectrometer (Applied Photophysics Ltd., United Kingdom) equipped with a 150 W Xe arc lamp and an optical cell with 2 mm path length. The dead time of the instrument is 1.4 ms. The fluorescence of Trp was excited at λ_{ex} = 290 nm and monitored at λ_{em} > 320 nm as transmitted by filter WG-320 (Schott, Mainz, Germany). If 2-aminopurine (aPu) was present in an oligonucleotide, λ_{ex} of 310 nm was chosen to excite aPu fluorescence, and its emission was monitored at λ_{em} > 370 nm (Corion filter LG-370). Fluorescence of a FAM residue was excited at λ_{ex} = 494 nm and monitored at λ_{em} > 515 nm as transmitted by filter

OG-515 (Schott, Mainz, Germany). Stopped-flow fluorescence measurements were conducted with catalytically active APE1 at 25°C in a buffer consisting of 50 mM Tris-HCl pH 7.5, 140 mM KCl, and 5.0 mM $MgCl_2$.

APE1 was placed in one of the instrument's syringes and rapidly mixed in the reaction chamber with the DNA substrate from another syringe. The reported concentrations of reactants are those in the reaction chamber after the mixing. Typically, each trace shown in the figures is the average of four or more fluorescence traces recorded in individual experiments.

The sets of kinetic curves obtained at different concentrations of the reactants were analyzed in the DynaFit software (BioKin, Pullman, WA) (Kuzmic, 1996) as described elsewhere (Kladova et al., 2018b).

Molecular Interaction Assays by Microscale Thermophoresis (MST)

Substrate-binding constants were determined via the MST approach on Monolith NT.115 (NanoTemper Technologies, Germany). The concentration of an oligonucleotide in all titration experiments was 0.5 μM, and concentrations of APE1 were varied from 0.05 to 30.0 μM. The reaction mixtures were incubated at 25°C in a buffer consisting of 50 mM Tris-HCl pH 7.5, 140 mM KCl, and 5 mM EDTA in case of G-quadruplexes and in a buffer consisting of 50 mM Tris-HCl pH 7.5, 50 mM KCl, and 5 mM EDTA in case of bulged duplexes. The values of the binding constant were calculated by means of Eq. 3:

$$MST\ signal = F_{\text{nois}} + F_{\text{amp}} \times [APE1]/(1/K_{\text{bind}} + [APE1]) \quad (3)$$

where F_{nois} is a background signal, F_{amp} is amplitude of an MST signal change, and K_{bind} is the equilibrium binding constant (M^{-1}) for the formation of an enzyme–substrate complex.

In some cases, the signal-to-noise ratio was not sufficient for precise calculation of the binding constants. Therefore, all obtained values were used only as an evaluation of the ability of the enzyme to bind these structures.

RESULTS AND DISCUSSION

Design of Model Substrates

According to our previous findings (Kuznetsova et al., 2018b), the substrate specificity of APE1 to damaged nucleotides in the duplexes is controlled by the ability of a given damaged nucleotide to be everted from the DNA double chain in response to an enzyme-induced DNA distortion. Therefore, in the present study, several non–B-form DNA and RNA structures were designed that can affect the nucleotide eversion process (**Table 1**). All the DNA and RNA structures used belong to one of several groups: (1) duplexes, (2) G-quadruplexes, (3) bulge-containing structures, (4) mismatch and bubble-containing structures, and (5) hairpins (**Figure 1**). In the case of DNA substrates, a stable analog of a natural AP site (F-site), lacking the hydroxyl group on the C1′-atom of ribose was utilized as a damaged nucleotide. RNA substrates contained only native undamaged nucleotides. A set of undamaged DNA oligonucleotides served as controls of the endonuclease and 3′–5′ exonuclease activities of APE1 (**Table 1**). A FAM residue was introduced into the 5′ end of oligonucleotides to visualize cleavage products on the polyacrylamide gel. Some oligonucleotides contained 3′-terminal black hole quencher (BHQ1) to create a FRET pair with the FAM residue for the assay of substrate cleavage by the stopped-flow kinetic method.

Cleavage of Damaged DNA Substrates Having a Non–B-Form Structure

Cleavage of an F-Site in the DNA Forming G-Quadruplexes

The human telomeric G-quadruplex was employed as a model of a non-canonical DNA structure. Structural features of G-quadruplexes formed by undamaged oligonucleotides of the same sequence in both Na^+ and K^+ solutions have been reported elsewhere (Parkinson et al., 2002; Ambrus et al., 2006; Phan et al., 2007; Burra et al., 2019; Marzano et al., 2020). CD is usually used to study G-quadruplex DNA folding (Karsisiotis et al., 2011). There are three common topologies based on the directionality of neighboring strands, namely, parallel, antiparallel, and hybrid, each having a characteristic CD spectrum (Dai et al., 2007; Bugaut and Alberti, 2015).

Formation of the G-quadruplex structure by the Q4 sequence containing four TTAGGG telomeric repeats (**Table 1**) under the experimental conditions was confirmed by CD spectroscopy (**Supplementary Figure S1A**). The CD spectrum of unlabeled Q4 (**Supplementary Figure S1B**) reveals the hybrid type of its folding with a maximum at 295 nm. At the same time, the FAM-labeled Q4 quadruplex has greater amplitude at 265 nm in the CD spectra; this finding supports a parallel-type topology of the quadruplex. As expected, incorporation of an F-site into the loop region of the quadruplex (F14–Q4) does not cause significant changes in the CD spectrum. Furthermore, the CD spectrum of F17–Q4, which contains an F-site in the G-core region, also is very similar to the spectrum of Q4, thereby supporting the formation of the quadruplex structure by damaged oligonucleotides F14–Q4 and F17–Q4.

PAGE analysis of product accumulation during interactions of APE1 with FAM/BHQ1-labeled F17–Q4 and F14–Q4 uncovered F-site cleavage in both cases (**Figures 2A,B**). Moreover, the interaction of APE1 with both damaged quadruplexes and undamaged Q4 leads to slow 3′–5′ exonuclease degradation of DNA (**Figure 2C**). These data indicated that APE1 can recognize and process an F-site both at the core and in the loop of a G-quadruplex structure with parallel-type topology, and does it with fivefold different efficiency as estimated by exponential fitting using Eq. 1 (k_{obs} = 0.0044 ± 0.0004 s^{-1} in the loop and 0.021 ± 0.003 s^{-1} at the core, respectively, **Figure 2D**). These data are consistent with and complement the detailed research (Zhou et al., 2015), suggesting that APE1 cleaves an F-site in a Na^+-coordinated antiparallel topology (an F-site in the middle of the core GGG) but not in a K^+-coordinated hybrid topology (the F-site on the 5′ side of the core GGG) of a telomeric quadruplex. Moreover, in a recent study (Burra et al., 2019), it

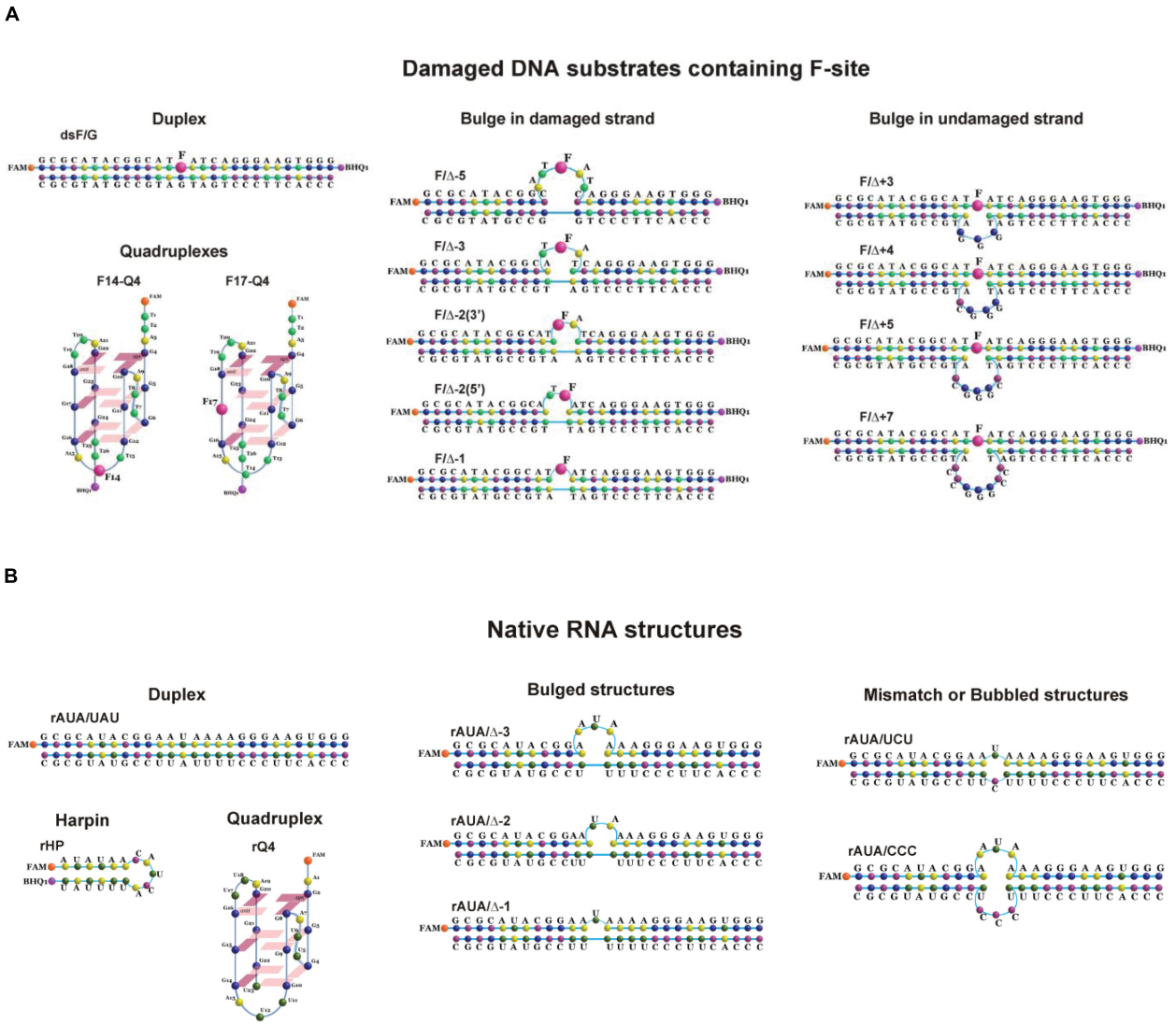

FIGURE 1 | Structures of DNA **(A)** and RNA **(B)** substrates: schematic structures of a control DNA duplex (containing an F-site) **(A)** or a native RNA duplex **(B)**; the unimolecular human telomeric G-quadruplex (containing an F-site) **(A)** or a native RNA quadruplex **(B)**; DNA duplexes containing an F-site with bulging of a damaged (1–5 nucleotides) or undamaged (3–7 nucleotides) strand **(A)**; native RNA with bulged or bubbled structures (1–3 nucleotides) **(B)**; short hairpin RNA structure with a 6-nucleotide stem pair and 5 nucleotides in the loop region **(B)**.

was clearly demonstrated that placement of an F-site at different positions of the core region of a telomeric quadruplex leads to a significant change in the native hybrid conformation. It was found that a damaged quadruplex with a predominant parallel conformation is preferable for enzymatic digestion (Burra et al., 2019). Taken together, our results lead to the conclusion that the efficacy of the F-site cleavage is dependent on the folding topology of a quadruplex; this topology can be associated with both the location of the F-site within the core GGG sequence and Na^+/K^+ experimental conditions. Moreover, F-site cleavage in the loop region is less efficient than that of the core sequence.

To rule out that this low cleavage efficiency of damaged quadruplexes is associated with insufficient complex formation under the experimental conditions used, an MST assay was carried out to evaluate the binding constant between APE1 and the quadruplex substrates (**Supplementary Figures S2, S3**). Of note, the titration curve for the F14–Q4 substrate recorded by MST did not allow us to determine K_{bind} by this method because of a low signal-to-noise ratio. Nevertheless, MST assay revealed binding of Q4 and F17–Q4 substrates by APE1 with very close affinity (0.4 ± 0.2 and 0.5 ± 0.2 μM^{-1} for Q4 and F17–Q4, respectively).

To further evaluate DNA binding and catalytic steps of APE1 interaction with F17–Q4, the observed rate constants at different APE1 concentrations were determined (**Figure 3A**). The observed rate constant k_{obs} indicated a hyperbolic type of dependence on the APE1 concentration (**Figure 3B**), which corresponds to a two-step kinetic scheme with fast equilibrium

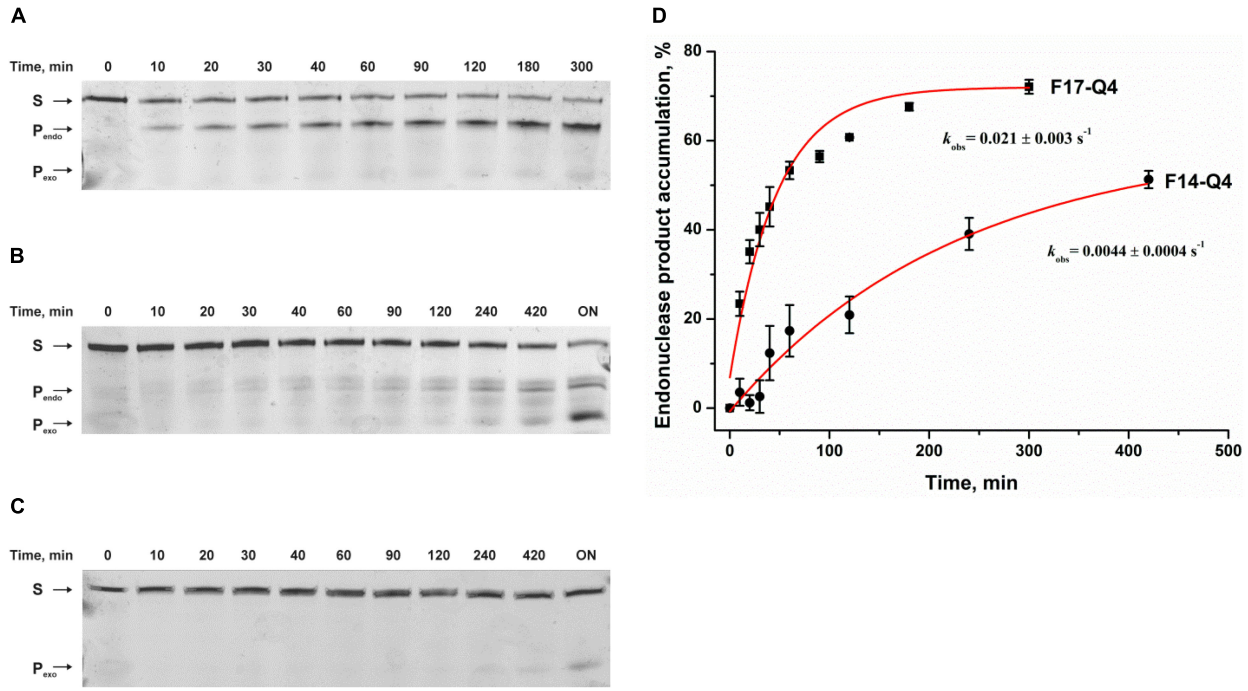

FIGURE 2 | Endonuclease activity of APE1 toward a damaged DNA quadruplex substrate. PAGE analysis of cleavage of F14–Q4 **(A)**, F17–Q4 **(B)**, or undamaged Q4 **(C)** by APE1. **(D)** Time course of product accumulation. Concentrations of the DNA substrate and APE1 were 1.0 and 3.0 μM, respectively. "ON" means overnight incubation. S corresponds to 26-nt oligonucleotide forming a quadruplex structure; P_{endo} is a 13-nt or 16-nt product of cleavage of F14–Q4 and F17–Q4, respectively; and P_{exo} is the short products of exonuclease degradation.

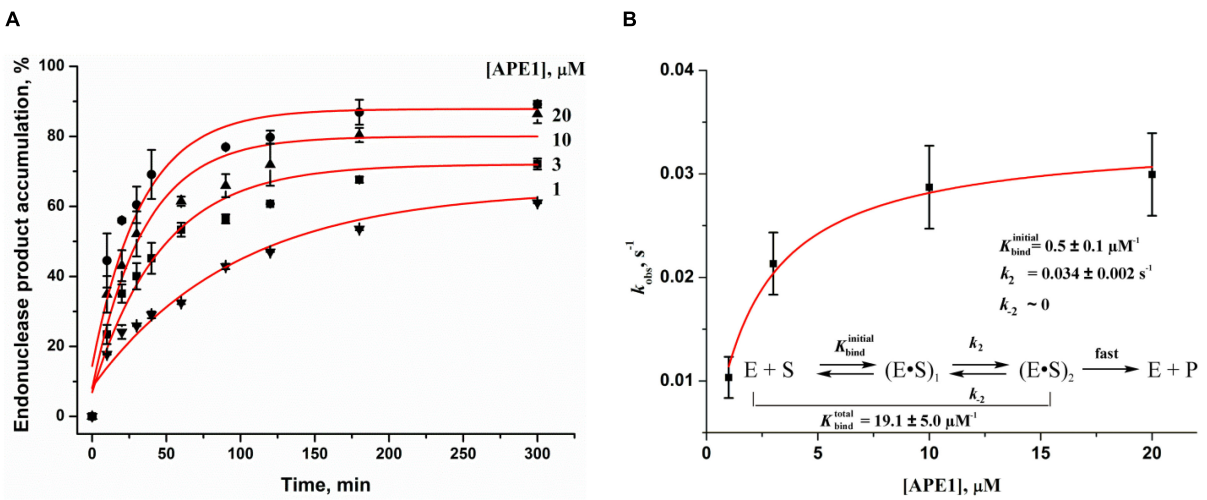

FIGURE 3 | Effects of APE1 concentration on the F17–Q4 cleavage. **(A)** Accumulation of the reaction product as determined by PAGE. [F17–Q4] = 1.0 μM, final concentrations of APE1 are shown near the kinetic trace. **(B)** Dependences of the observed rate constants k_{obs} on APE1 concentration. The data were fitted to a hyperbolic equation Eq. 2.

initial substrate binding and can be fitted to Eq. 2. The equilibrium constant of the initial enzyme–substrate complex K_{bind} was estimated to be 0.5 ± 0.1 μM^{-1}, indicating good binding of APE1 to the damaged quadruplex at the earliest stage of interaction. The rate constant of the second step, k_2, was equal to 0.034 ± 0.002 s^{-1}, whereas k_{-2} was near zero, revealing that the slow second step should increase the total binding constant. It is known that the rate constant of F-site cleavage in duplex substrates is fast and varies from 0.3 to 5.5 s^{-1} (Kanazhevskaya et al., 2010, 2012; Timofeyeva et al., 2011; Miroshnikova et al., 2016a,b), 68 to 97 s^{-1} (Timofeyeva et al., 2009), or even 700–850 s^{-1} (Maher and Bloom, 2007;

Schermerhorn and Delaney, 2013) depending on DNA duplex sequences, buffering conditions, and methods of cleavage detection. Therefore, the obtained rate constant of the second step is at least 10-fold less than the catalytic rate constant, suggesting that catalytic complex formation in the case of a quadruplex substrate is the rate-limiting step of the DNA cleavage (**Figure 3B**).

Because the recognition of a specific site in the substrate is accompanied by conformational adjustment of APE1 and DNA to optimize specific contacts in the enzyme–substrate complex, we performed a pre–steady-state kinetic analysis of conformational changes of APE1 and quadruplexes in the course of complex formation.

Real-time conformational rearrangements of APE1 and DNA during their interactions were visualized by stopped-flow kinetic assays with detection of intrinsic fluorescence from Trp residues of APE1 or fluorescence reporters incorporated into DNA, e.g., aPu and the FAM/BHQ1 FRET pair. The change in Trp fluorescence intensity in the reaction of APE1 with the DNA duplex containing an F-site consisted of characteristic phases (**Supplementary Figure S4A**) that have been identified earlier (Timofeyeva et al., 2009) as stages of DNA binding and catalysis. The decrease in fluorescence intensity in the initial part of the kinetic curves matches the formation of a catalytically competent complex. The catalytic stage of the process causes the formation of products and subsequent dissociation of the enzyme–product complex, which is accompanied by an increase in Trp fluorescence intensity at later time points (starting from approximately 0.1 s, **Supplementary Figure S4A**). As evidenced by the kinetic curves (**Supplementary Figure S4A**), the interaction of APE1 with a damaged or undamaged quadruplex does not result in any changes in the Trp fluorescence intensity, thereby strongly supporting the PAGE finding that the formation of the catalytic complex is slower than the cleavage reaction. In this case, detection of the catalytic complex by Trp fluorescence failed due to an insufficient concentration of this complex in the reaction mixture. On the other hand, these data can indicate that the type of binding of Q4 structures is different from the binding of DNA duplexes and therefore that the binding with quadruplex does not lead to Trp fluorescence quenching.

To analyze the substrate-binding process, a set of damaged quadruplexes was designed, containing an aPu residue (a fluorescent base analog) on the 3′ or 5′ side of an F-site in both substrates F14–Q4 and F17–Q4. Analysis of CD spectra revealed that the incorporation of aPu near the core F17 position (F17–aPu16–Q4 and F17–aPu18–Q4, **Supplementary Figure S1B**) results in preferable formation of a parallel type of quadruplex in comparison with the native hybrid fold of F14–aPu13–Q4 and F14–aPu15–Q4 structures, which contain modified nucleotides in the loop region. An analysis of fluorescence changes of aPu residues in all DNA substrates in the course of the interaction with APE1 (**Supplementary Figure S4B**) indicated that only F17–aPu16–Q4 was sensitive enough to detect enzyme–substrate complex formation. On the other hand, FRET detection allowed recording of the interaction of APE1 with either substrate F14–Q4 or F17–Q4 (**Supplementary Figure S4C**). A comparison of the profiles of fluorescence intensity among the interactions of APE1 with DNA quadruplexes containing an F-site allows us to select FAM/BHQ1-labeled F17–Q4 and F17–aPu16–Q4 as suitable models for further detailed analysis of the reaction with APE1 (**Figure 4**). Indeed, aPu fluorescence intensity is sensitive to the microenvironment of this residue and enabled registering of local conformational changes of a DNA substrate near the F-site (**Figure 4A**). On the other hand, the FAM/BHQ1-labeled F17–Q4 substrate helped to reveal "global" conformational changes that cause a change in the distance between the dye and quencher in the course of DNA substrate binding and cleavage (**Figure 4B**).

The rate constants of individual reaction steps (**Table 2**) were calculated via global fitting of the fluorescence data to **Scheme 1**, which contains the initial equilibrium binding step followed by the second rate-limiting transformation of the enzyme–substrate complex into the catalytic state in which a fast hydrolysis reaction takes place. The obtained data meant that different types of detection yield different values of initial substrate-binding constants $K_{\text{bind}}^{\text{initial}}$, indicating that initial transient complex ES detected by the different methods represents different "depths" of the damage recognition process. Nevertheless, all the methods of detection yielded equal rate constants k_2 of the slow second binding step, which leads to catalytic complex formation. Altogether, these data indicated that the molecular processes that proceed at the second step of catalytic complex formation are crucial for damaged nucleotide recognition and therefore that facilitation of this step will significantly increase enzyme efficacy. Moreover, this step could be affected by the secondary structure of DNA.

Cleavage of an F-Site in the Bulged DNA Structures

To facilitate the rate-limiting second binding step of non–B-form substrates and to evaluate the effect of target nucleotide eversion in different structures, we designed a set of F-site –containing DNA duplexes with bulging of a damaged (1–5 nucleotides) or undamaged (3–7 nucleotides) strand (**Table 1** and **Figure 1B**). The activity of APE1 was studied by direct PAGE analysis (**Supplementary Figure S5**), and the kinetics of accumulation of an endonucleolytic cleavage product were investigated (**Figures 5A,B**). The rate of DNA cleavage was estimated as the initial slope of the kinetic curve (**Figures 5C,D**).

It is noteworthy that the bulging of a single F-site (F/−Δ1) decreases the initial rate twofold in comparison with the full double-stranded substrate dsF/G (**Figure 5C**), suggesting that the substrate bending induced by the extra-helical position of the F-site slightly disturbs total interactions between the DNA-binding site of APE1 and the substrate. The constant of enzyme–substrate complex formation K_{bind} determined by MST (**Supplementary Figure S2B**) was also fourfold lower for F/−Δ1 in comparison with dsF/G. Moreover, an increase in bulging up to two F/−Δ2(5′) or three F/−Δ3 nucleotides does not have an additional effect on the enzymatic activity (**Figure 5C**) as well as substrate binding (**Supplementary Figure S2B**), keeping it at ∼50% of that of a fully complementary duplex. Therefore, expulsion of an abasic site from the double helix owing to bulge formation is not a key step in the process of F-site recognition.

Unexpectedly, the strongest effect on the enzymatic activity (**Figure 5C**), but not binding (**Supplementary Figure S2B**), was

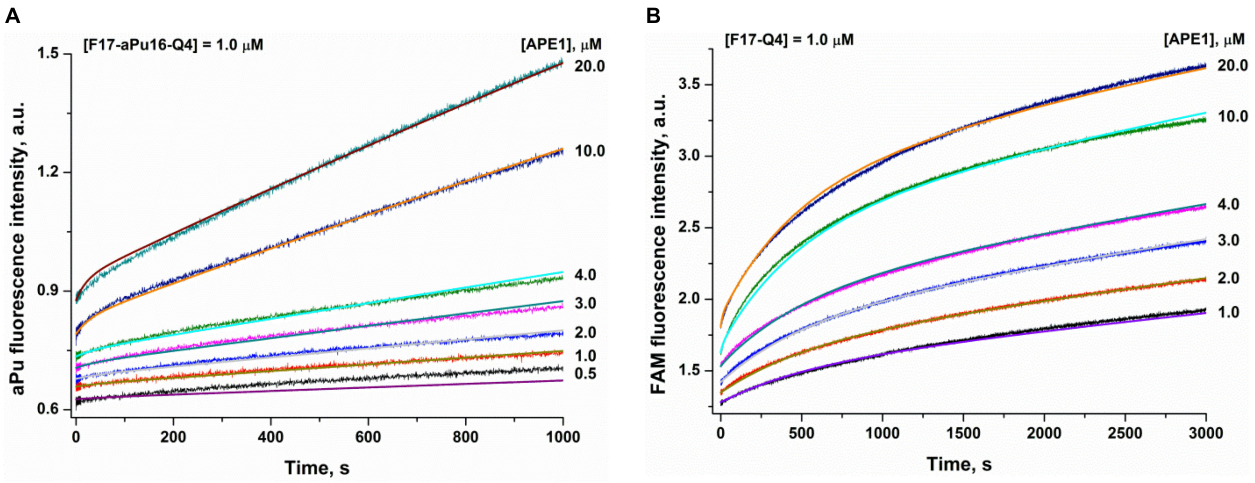

FIGURE 4 | Interaction of APE1 with a damaged quadruplex containing an F-site at the 17th position. **(A)** aPu fluorescence kinetic traces (substrate F17–aPu16–Q4). **(B)** FAM/BHQ1 FRET kinetic traces (substrate F17–Q4). Jagged traces represent experimental data; smooth curves are the results of fitting to **Scheme 1**.

observed in the case of bulging to two nucleotides [F/−Δ2(3′), which contains an F-site near the 3′ end of the duplex stem in the substrate], thus supporting the conclusion that this location of the damaged nucleotide blocks catalytic-state formation. Analysis of the literature data revealed that bulged DNA and RNA duplexes can adopt a variety of conformations depending on the bulge size (Gohlke et al., 1994; Schreck et al., 2015; Strom et al., 2015). Consequently, the efficacy of cleavage of bulged damaged DNA depends both on the ability of a particular structure to eject the damaged nucleotide and also on the topological arrangement of the damaged nucleotide in this structure.

As depicted in **Supplementary Figure S5G**, APE1 does not hydrolyze an F-site in the single-stranded oligonucleotide ssF, indicating that APE1 cannot form appropriate contacts with the single-stranded substrate to adjust the damaged nucleotide in the active site. Accordingly, the loss of activity on the F/−Δ5 structure means that 5 bulged nucleotides completely mimic a single strand and do not allow the enzyme to form appropriate contacts with the substrate, whereas binding constant K_{bind} for F/−Δ5 has the highest value among the tested substrates (**Supplementary Figure S2B**). The bulging of 3–7 nucleotides in the undamaged strand opposite the F-site (**Figure 5D**) decreases enzymatic activity to ∼50% in comparison with a fully complementary duplex regardless of loop size. This effect most likely is associated with an interaction of the enzyme predominantly with the damaged strand of the substrate.

Thus, it could be assumed that bulging of 5 nucleotides in the damaged strand is the critical size of a single-stranded region for the recognition of an F-site in the DNA and for the formation of a catalytic complex. By contrast, the loss of the activity in the case of F/−Δ2(3′) suggests that the position of the F-site in the 2-nucleotide bulging sequence TF [F/−Δ2(5′)] or FA [F/−Δ2(3′)] is also crucial for catalytic complex formation. Independence of DNA cleavage from the loop size in the undamaged strand confirms the ability of the enzyme to place large nucleotide moieties outside the active site. These findings also support the notion that F-site cleavage in the quadruplexes proceeds without significant distortion of the quadruplex structure, with no more than 5 single-stranded nucleotides near the F-site and placement of a large undamaged part of the quadruplex structure outside of the active site, as demonstrated for a 3- to 7-nucleotide bulge of the complementary strand in the duplexes.

TABLE 2 | The rate and equilibrium constants of the interaction of APE1 with a damaged quadruplex.

Constants	Type of detection		
	FRET	aPu	PAGE
$K_{bind}^{initial}$, μM^{-1}	0.08 ± 0.02	0.003 ± 0.001	0.5 ± 0.1
k_2, s^{-1}	0.03 ± 0.01	0.03 ± 0.01	0.034 ± 0.002

$$E + S \underset{}{\overset{K_{bind}}{\rightleftharpoons}} E{\bullet}S \xrightarrow{k_2} E + P$$

SCHEME 1 | The kinetic mechanism of the interaction of APE1 with a damaged quadruplex. E, enzyme; S, substrate; ES, enzyme-substrate complex; P, product.

Cleavage of Native RNA Substrates Having a Non–B-Form Structure

It has been reported earlier that APE1 has endoribonuclease activity (Barzilay and Hickson, 1995). As for the cleavage of undamaged RNA, APE1 preferentially catalyzes hydrolysis of the phosphodiester bond inside dinucleotides UA, UG, and CA in bulged sequences or weakly paired RNA regions (Berquist et al., 2008; Barnes et al., 2009; Kim et al., 2010), in good agreement with observed selectivity of APE1 toward damaged DNA substrates. A comparative analysis (Kuznetsova et al., 2020) of the cleavage efficiency of model RNA substrates containing

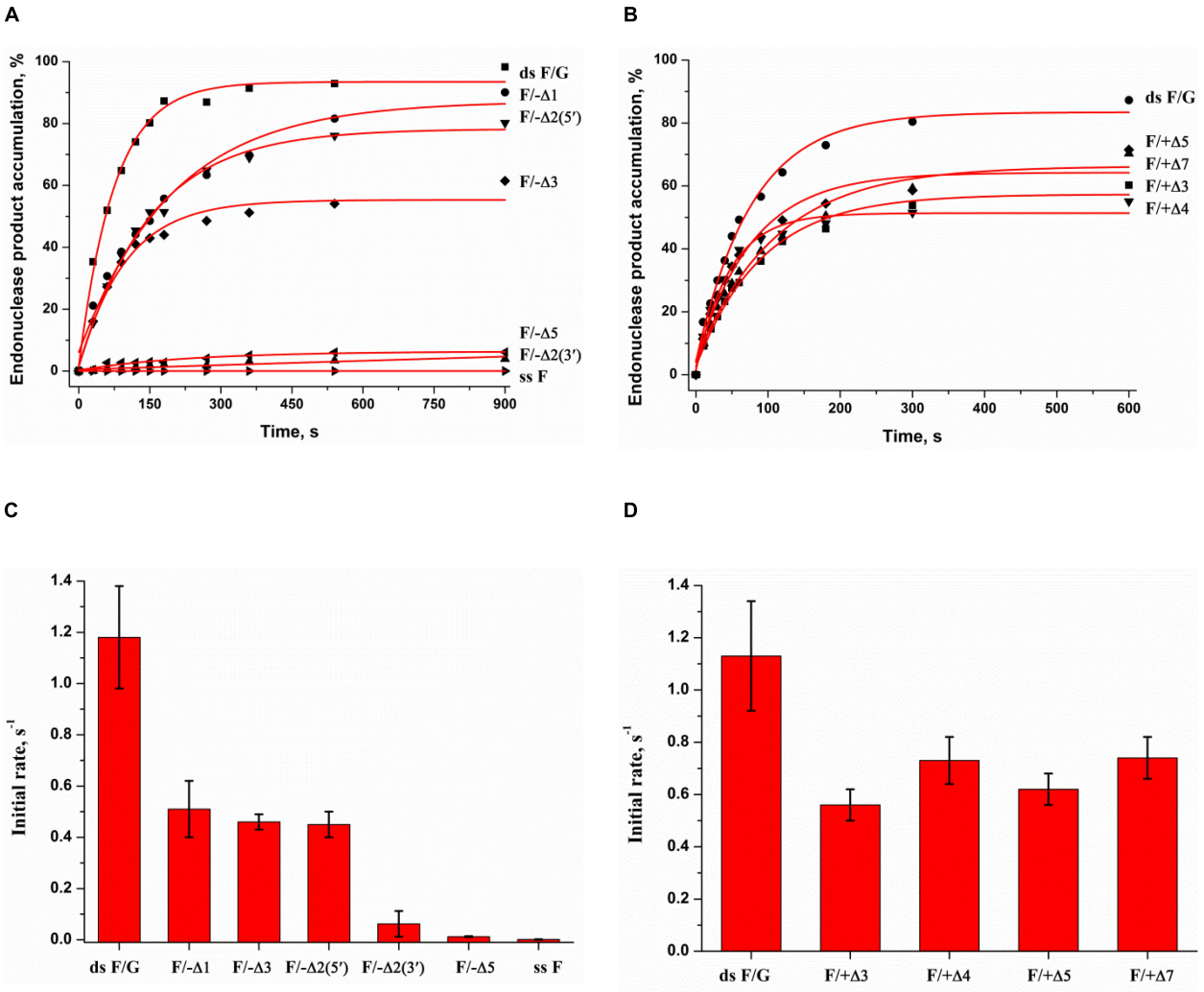

FIGURE 5 | Endonuclease activity of APE1 toward bulged DNA substrates. Time course of product accumulation revealed by PAGE analysis of DNA substrates containing an F-site with bulging in the damaged **(A)** or undamaged **(B)** strand. Comparison of the cleavage efficacy of DNA substrates containing an F-site with bulging in the damaged **(C)** or undamaged **(D)** strand. Concentrations of the DNA substrate and APE1 were 1.0 and 20.0 nM, respectively.

short-hairpin structures, in which the loop size was varied from 2 to 5 nucleotides, has revealed that the 5-nucleotide-long hairpin loop is more readily adapted to the substrate-binding site of the enzyme than shortened versions. Moreover, the position of the cleavage site in the 5-nucleotide loop also influenced the hydrolysis efficacy. Recent findings (Antoniali et al., 2017) revealed that endoribonuclease activity of APE1 could play an important role in RNA metabolism. It was shown (Antoniali et al., 2017) that APE1 is required for the processing of microRNAs miR-221/miR-222 (Garofalo et al., 2011) and miR-92b (Sun et al., 2019), which are considered to act as tumor suppressors.

To verify the mechanism of target nucleotide selection proposed in the present study, a series of native RNA substrates with a non–B-form structure was tested (**Figure 6**). To identify the cleavage site of APE1, all the tested RNA substrates were treated with RNase A, which selectively cleaves pyrimidine nucleotides. As illustrated in **Figure 6A**, a fully complementary stable RNA duplex, rAUA/UAU, was not cleaved by APE1, and even the formation of a single mismatch, rAUA/UCU, does not permit the formation of a catalytic complex with APE1. Nevertheless, bulging of a single uridine leads to slight product formation. Of note, an increase of the bulge from 1 to 3 nucleotides was accompanied by a stepwise increase of cleavage activity up to 15% (**Figure 6B**). Moreover, the efficacy of cleavage of a bubbled structure containing three mispaired nucleotides was also near 15%, again revealing the independence of the activity from the size of a non-target strand of the substrate. A short-hairpin structure was cleaved with the highest efficacy among the tested structures, indicating that a 5-nucleotide loop is sufficient for effective catalytic complex formation. Furthermore, it can be assumed that after cleavage in the loop region, the stability of a short RNA duplex is not sufficient to protect it from subsequent hydrolysis of all pyrimidine–purine sites in

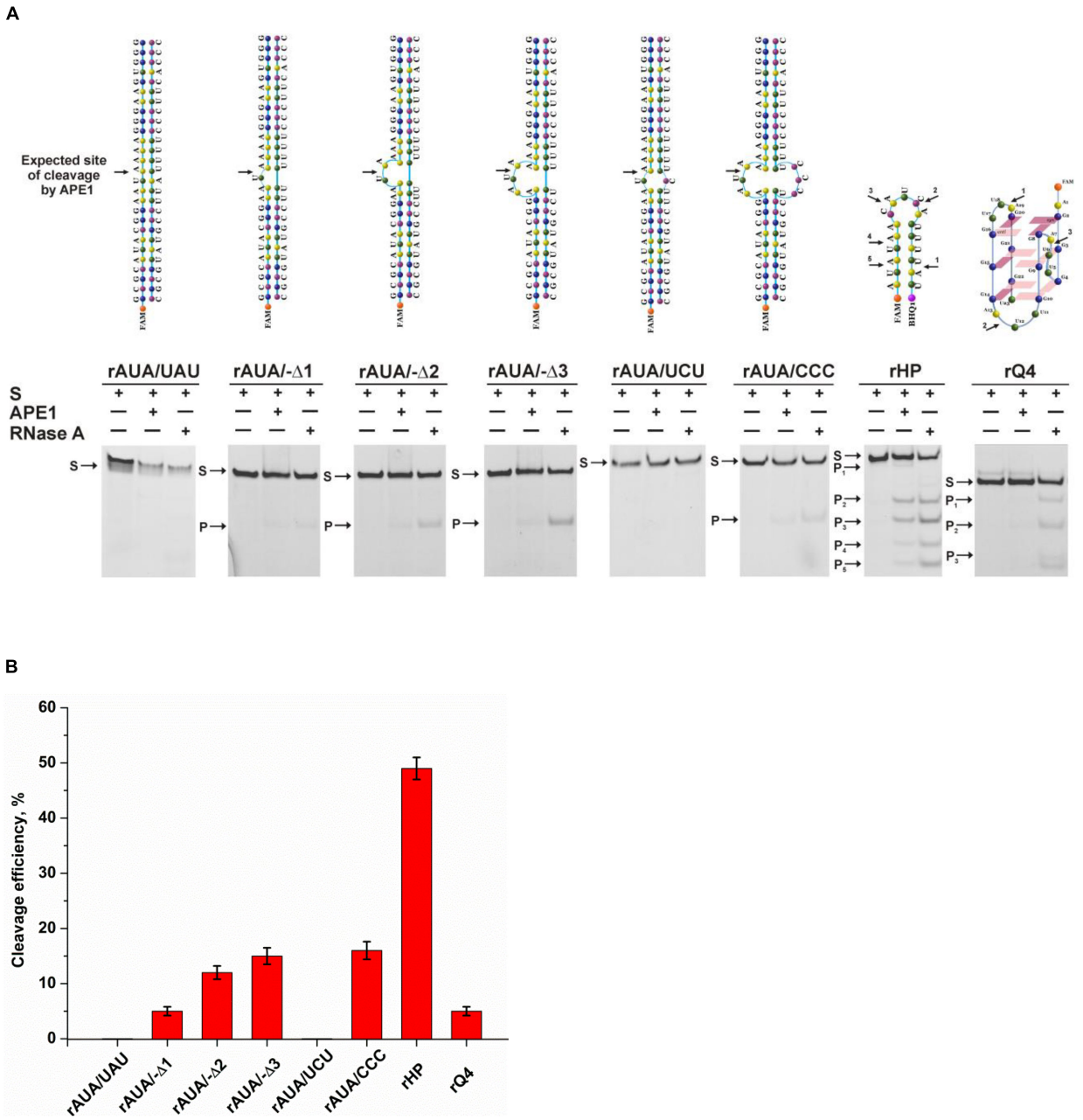

FIGURE 6 | The efficiency of cleavage of RNA substrates by APE1. **(A)** PAGE analysis of the reaction products. Positions of the hydrolyzed nucleotides are pointed out by arrows. **(B)** Comparison of the efficacy of cleavage of RNA substrates by APE1. [APE1] = 2 μM, [RNA] = 1 μM, reaction time = 1 h.

this sequence. Summarized hydrolysis of all five possible target sites leads to 50% cleavage of substrate rHP. It is worth noting that 3-nucleotide loops in the quadruplex structure rQ4, which contains a UA context, were very resistant to APE1 action with summary cleavage efficiency up to 5%. Taken together, it could be concluded that APE1 more efficiently cleaves RNA which contains single-stranded regions as a bulge or loop located near the duplex part, supporting the findings that the biological significance of the endoribonuclease activity is associated with processing of RNA in such non-canonical structures.

Considering our findings about the RNA substrates, it can be concluded that APE1 uses the same molecular mechanism of recognition of a target nucleotide in RNA substrates as the mechanism of F-site recognition in damaged DNA substrates. Moreover, the wide substrate specificity of APE1 toward an abasic site, some damaged bases [for example, etheno derivatives of DNA bases (Christov et al., 2010; Prorok et al., 2012), bulky photoproducts (Vrouwe et al., 2011), benzene-derived DNA adducts (Guliaev et al., 2004), α-anomers of 2′-deoxynucleosides (Gros et al., 2004), oxidatively damaged

pyrimidines (Daviet et al., 2007), or 2′-deoxyuridine (Prorok et al., 2013)], and native deoxyribonucleotides (3′–5′ exonuclease activity) and ribonucleotides (endoribonuclease activity) strongly supports the conclusion that the active site of APE1 does not form direct specific contacts with a damaged or native target nucleotide. Consequently, the common mechanism of target nucleotide recognition by APE1 (**Figure 7**) includes the formation of an initial enzyme–substrate complex in which sequential conformational changes of the substrate in response to enzyme-induced interactions is strongly needed for the formation of a catalytically active complex. The molecular processes that take place in the course of these rearrangements, such as substrate bending, local melting, target nucleotide eversion from the substrate and insertion into the enzyme active site, amino acid insertion, and the formation of a network of contacts, are important for the target nucleotide recognition and limit the rate of catalytic complex formation. Moreover, it is known that the unstructured N-terminal domain of APE1 is the key part of the enzyme, which is responsible for the redox function (Evans et al., 2000; Kelley et al., 2011; Bazlekowa-Karaban et al., 2019), plays an important role in the interaction with damaged DNA and RNA (Timofeyeva et al., 2009; Fantini et al., 2010), and also affects the protein–protein interactions of APE1 with nucleophosmin (Poletto et al., 2013) and other participants of the BER pathway (Kladova et al., 2018a; Moor et al., 2020). Therefore, it could be assumed that the N-terminal domain of APE1 also can affect the ability of the enzyme to bind non–B-form structures and participate in the recognition of the target nucleotide.

It is reasonable to suggest that facilitation of some of the molecular events during binding processes, for example, the eversion of the target nucleotide or the bending of the substrate, because of the features of the initial structure of the substrate with non–B-form components, may increase the rate of substrate cleavage. It should be mentioned that in addition to the eversion of a target nucleotide from the substrate structure, its insertion into the active site should be taken into account too. Of note, literature data available today about the APE1 activity on B-form damaged DNA duplexes enable a comparison of the efficacy of cleavage among different damaged DNA duplexes and thereby a comparison of the rates of the limiting step. The recognition and cleavage of an F-site in the complementary duplex proceed during a 1 s period (**Supplementary Figure S4A**), whereas the duration of recognition of damaged nucleotides in duplexes—e.g., 1,N^6-ethenoadenosine, α-adenosine, or 5,6-dihydrouridine (Kuznetsova et al., 2018b) – is longer, up to 1,000 s. Moreover, native ribonucleotides are processed by the enzyme within hours (**Figure 6**). It can be concluded that the nature of a target nucleotide that is inserted into the active site is also a very important factor for the formation of a catalytically active state of the APE1–substrate complex.

The obtained results mean that facilitation of F-site eversion in bulged structures decreases cleavage efficacy in comparison with a fully complementary duplex because of a decrease in the substrate-binding constant. During the eversion of a small abasic site and its insertion into the active site of the enzyme, the deoxyribose residue does not engage in any unfavorable interactions. By contrast, the insertion of any target nucleotide containing a damaged or native base into the active site of APE1 is much slower than the insertion of an abasic nucleotide because of steric hindrance. Indeed, in the case of bulged RNA, the cleavage efficacy clearly increased with the increasing bulge size, indicating that promotion of the eversion by the structure leads to skipping of some unfavorable contacts in the course of target base flipping out and insertion into the active site.

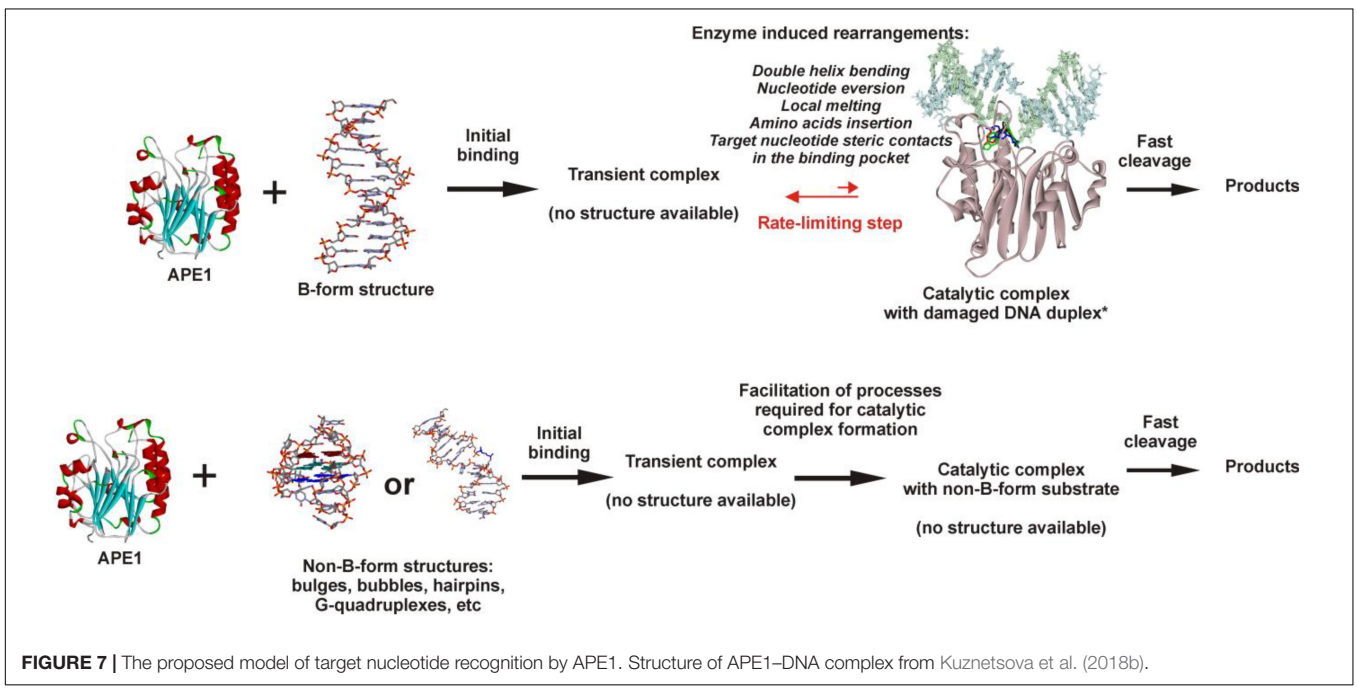

FIGURE 7 | The proposed model of target nucleotide recognition by APE1. Structure of APE1–DNA complex from Kuznetsova et al. (2018b).

CONCLUSION

Thus, a series of damaged DNA substrates and undamaged RNA substrates of a non–B-form structure was tested to evaluate the structural aberrations facilitating the process of target nucleotide recognition by APE1 and the formation of a catalytically competent complex. It was experimentally demonstrated that a human telomeric G-quadruplex containing an F-site, a native RNA quadruplex, and DNA duplexes containing an F-site with bulging of a damaged or undamaged strand as well as a native RNA having a bulged or bubbled structure and a short-hairpin RNA structure are processed during catalytic endonucleolytic cleavage by human AP endonuclease. It is important to note that in some specially designed DNA structures, a site-specific cleavage of a single-stranded DNA occurs as well. The mechanism of target nucleotide recognition is composed of two steps: initial transient complex formation and its subsequent rate-limiting transformation into a catalytically competent state. Facilitation of the eversion of a target nucleotide into the enzyme active site is mediated by some non–B-form regions in the substrate, which allows us to increase the formation rate of a catalytic complex, thereby enhancing the efficacy of the enzymatic catalysis. Thus, it is shown that the formation of non-canonical B-form structures by undamaged DNA is the key factor for the processing of a target nucleotide in the active site of the enzyme. In general, data obtained in the research on the specificity of AP endonuclease toward DNA and RNA substrates of various spatial structures expand our understanding of the molecular principles governing target nucleotide recognition by APE1.

DATA AVAILABILITY STATEMENT

All datasets presented in this study are included in the article/**Supplementary Material**.

AUTHOR CONTRIBUTIONS

AD and AK conducted the experiments. NK conceived and designed the experiments. AD, AK, NK, and OF analyzed the data. NK and OF contributed the reagents, materials, analytical tools, and wrote the manuscript. All authors contributed to the article and approved the submitted version.

FUNDING

The experimental part of the work was supported by the Russian Science Foundation grant 18-14-00135. Partial salary support was received from the Russian Ministry of Higher Education and Science project # AAAA-A17-117020210022-4.

SUPPLEMENTARY MATERIAL

The Supplementary Material for this article can be found online at: https://www.frontiersin.org/articles/10.3389/fcell.2020.590848/full#supplementary-material

REFERENCES

Ambrus, A., Chen, D., Dai, J., Bialis, T., Jones, R. A., and Yang, D. (2006). Human telomeric sequence forms a hybrid-type intramolecular G-quadruplex structure with mixed parallel/antiparallel strands in potassium solution. *Nucleic Acids Res.* 34, 2723–2735. doi: 10.1093/nar/gkl348

Antoniali, G., Serra, F., Lirussi, L., Tanaka, M., D'Ambrosio, C., Zhang, S., et al. (2017). Mammalian APE1 controls miRNA processing and its interactome is linked to cancer RNA metabolism. *Nat. Commun.* 8:797. doi: 10.1038/s41467-017-00842-848

Barnes, T., Kim, W. C., Mantha, A. K., Kim, S. E., Izumi, T., Mitra, S., et al. (2009). Identification of Apurinic/apyrimidinic endonuclease 1 (APE1) as the endoribonuclease that cleaves c-myc mRNA. *Nucleic Acids Res.* 37, 3946–3958. doi: 10.1093/nar/gkp275

Barzilay, G., and Hickson, I. D. (1995). Structure and function of apurinic/apyrimidinic endonucleases. *Bioessays* 17, 713–719. doi: 10.1002/bies.950170808

Barzilay, G., Walker, L. J., Robson, C. N., and Hickson, I. D. (1995). Site-directed mutagenesis of the human DNA repair enzyme HAP1: identification of residues important for AP endonuclease and RNase H activity. *Nucleic Acids Res.* 23, 1544–1550.

Bazlekowa-Karaban, M., Prorok, P., Baconnais, S., Taipakova, S., Akishev, Z., Zembrzuska, D., et al. (2019). Mechanism of stimulation of DNA binding of the transcription factors by human apurinic/apyrimidinic endonuclease 1, APE1. *DNA Repair.* 82:102698. doi: 10.1016/j.dnarep.2019.102698

Beernink, P. T., Segelke, B. W., Hadi, M. Z., Erzberger, J. P., Wilson, D. M. III, and Rupp, B. (2001). Two divalent metal ions in the active site of a new crystal form of human apurinic/apyrimidinic endonuclease, Ape1: implications for the catalytic mechanism. *J. Mol. Biol.* 307, 1023–1034. doi: 10.1006/jmbi.2001.4529

Berquist, B. R., McNeill, D. R., and Wilson, D. M. III (2008). Characterization of abasic endonuclease activity of human Ape1 on alternative substrates, as well as effects of ATP and sequence context on AP site incision. *J. Mol. Biol.* 379, 17–27. doi: 10.1016/j.jmb.2008.03.053

Bugaut, A., and Alberti, P. (2015). Understanding the stability of DNA G-quadruplex units in long human telomeric strands. *Biochimie* 113, 125–133. doi: 10.1016/j.biochi.2015.04.003

Burra, S., Marasco, D., Malfatti, M. C., Antoniali, G., Virgilio, A., Esposito, V., et al. (2019). Human AP-endonuclease (Ape1) activity on telomeric G4 structures is modulated by acetylatable lysine residues in the N-terminal sequence. *DNA Repair.* 73, 129–143. doi: 10.1016/j.dnarep.2018.11.010

Chen, D. S., Herman, T., and Demple, B. (1991). Two distinct human DNA diesterases that hydrolyze 3′-blocking deoxyribose fragments from oxidized DNA. *Nucleic Acids Res.* 19, 5907–5914.

Chou, K. M., and Cheng, Y. C. (2002). An exonucleolytic activity of human apurinic/apyrimidinic endonuclease on 3′ mispaired DNA. *Nature* 415, 655–659. doi: 10.1038/415655a

Christov, P. P., Banerjee, S., Stone, M. P., and Rizzo, C. J. (2010). Selective incision of the alpha-N-Methyl-formamidopyrimidine anomer by *Escherichia coli* endonuclease IV. *J. Nucleic Acids* 2010:850234. doi: 10.4061/2010/850234

Dai, J., Carver, M., Punchihewa, C., Jones, R. A., and Yang, D. (2007). Structure of the hybrid-2 type intramolecular human telomeric G-quadruplex in K+ solution: insights into structure polymorphism of the human telomeric sequence. *Nucleic Acids Res.* 35, 4927–4940. doi: 10.1093/nar/gkm522

Daviet, S., Couve-Privat, S., Gros, L., Shinozuka, K., Ide, H., Saparbaev, M., et al. (2007). Major oxidative products of cytosine are substrates for the nucleotide incision repair pathway. *DNA Repair.* 6, 8–18. doi: 10.1016/j.dnarep.2006.08.001

Demple, B., and Sung, J.-S. (2005). Molecular and biological roles of Ape1 protein in mammalian base excision repair. *DNA Repair.* 4, 1442–1449.

Evans, A. R., Limp-Foster, M., and Kelley, M. R. (2000). Going APE over ref-1. *Mutat. Res.* 461, 83–108.

Fantini, D., Vascotto, C., Marasco, D., D'Ambrosio, C., Romanello, M., Vitagliano, L., et al. (2010). Critical lysine residues within the overlooked N-terminal domain of human APE1 regulate its biological functions. *Nucleic Acids Res.* 38, 8239–8256. doi: 10.1093/nar/gkq691

Freudenthal, B. D., Beard, W. A., Cuneo, M. J., Dyrkheeva, N. S., and Wilson, S. H. (2015). Capturing snapshots of APE1 processing DNA damage. *Nat. Struct. Mol. Biol.* 22, 924–931. doi: 10.1038/nsmb.3105

Garofalo, M., Quintavalle, C., Romano, G., Croce, M. C., and Condorelli, G. (2011). miR221/222 in cancer: their role in tumor progression and response to therapy. *Curr. Mol. Med.* 12, 27–33. doi: 10.2174/156652412798376170

Gohlke, C., Murchie, A. I. H., Lilley, D. M. J., and Clegg, R. M. (1994). Kinking of DNA and RNA helices by bulged nucleotides observed by fluorescence resonance energy transfer. *Proc. Natl. Acad. Sci. U.S.A.* 91, 11660–11664. doi: 10.1073/pnas.91.24.11660

Gorman, M. A., Morera, S., Rothwell, D. G., de La Fortelle, E., Mol, C. D., Tainer, J. A., et al. (1997). The crystal structure of the human DNA repair endonuclease HAP1 suggests the recognition of extra-helical deoxyribose at DNA abasic sites. *EMBO J.* 16, 6548–6558. doi: 10.1093/emboj/16.21.6548

Gros, L., Ishchenko, A. A., Ide, H., Elder, R. H., and Saparbaev, M. K. (2004). The major human AP endonuclease (Ape1) is involved in the nucleotide incision repair pathway. *Nucleic Acids Res.* 32, 73–81. doi: 10.1093/nar/gkh165

Guliaev, A. B., Hang, B., and Singer, B. (2004). Structural insights by molecular dynamics simulations into specificity of the major human AP endonuclease toward the benzene-derived DNA adduct, pBQ-C. *Nucleic Acids Res.* 32, 2844–2852. doi: 10.1093/nar/gkh594

Ischenko, A. A., and Saparbaev, M. K. (2002). Alternative nucleotide incision repair pathway for oxidative DNA damage. *Nature* 415, 183–187. doi: 10.1038/415183a

Kanazhevskaya, L. Y., Koval, V. V., Vorobjev, Y. N., and Fedorova, O. S. (2012). Conformational dynamics of abasic DNA upon interactions with AP endonuclease 1 revealed by stopped-flow fluorescence analysis. *Biochemistry* 51, 1306–1321. doi: 10.1021/bi201444m

Kanazhevskaya, L. Y., Koval, V. V., Zharkov, D. O., Strauss, P. R., and Fedorova, O. S. (2010). Conformational transitions in human AP endonuclease 1 and its active site mutant during abasic site repair. *Biochemistry* 49, 6451–6461. doi: 10.1021/bi100769k

Karsisiotis, A. I., Hessari, N. M. A., Novellino, E., Spada, G. P., Randazzo, A., Webba, et al. (2011). Topological characterization of nucleic acid G-quadruplexes by UV absorption and circular dichroism. *Angew. Chem Int. Edn.* 50, 10645–10648. doi: 10.1002/anie.201105193

Kelley, R. M., Georgiadis, M. M., and Fishel, M. L. (2011). APE1/Ref-1role in redox signaling: translational applications of targeting the redox function of the DNA Repair/Redox protein APE1/Ref-1. *Curr. Mol. Pharmacol.* 5, 36–53. doi: 10.2174/1874467211205010036

Kim, W. C., King, D., and Lee, C. H. (2010). RNA-cleaving properties of human apurinic/apyrimidinic endonuclease 1 (APE1). *Int. J. Biochem. Mol. Biol.* 1, 12–25.

Kladova, O. A., Bazlekowa-Karaban, M., Baconnais, S., Piétrement, O., Ishchenko, A. A., Matkarimov, B. T., et al. (2018a). The role of the N-terminal domain of human apurinic/apyrimidinic endonuclease 1, APE1, in DNA glycosylase stimulation. *DNA Repair.* 64, 10–25. doi: 10.1016/j.dnarep.2018.02.001

Kladova, O. A., Krasnoperov, L. N., Kuznetsov, N. A., and Fedorova, O. S. (2018b). Kinetics and thermodynamics of DNA processing by wild type DNA-glycosylase endo III and its catalytically inactive mutant forms. *Genes* 9:190. doi: 10.3390/genes9040190

Kuzmic, P. (1996). Program DYNAFIT for the analysis of enzyme kinetic data: application to HIV proteinase. *Anal. Biochem.* 237, 260–273. doi: 10.1006/abio.1996.0238

Kuznetsova, A. A., Kuznetsov, N. A., Ishchenko, A. A., Saparbaev, M. K., and Fedorova, O. S. (2014). Pre-steady-state fluorescence analysis of damaged DNA transfer from human DNA glycosylases to AP endonuclease APE1. *Biochim. Biophys. Acta* 1840, 3042–3051. doi: 10.1016/j.bbagen.2014.07.016

Kuznetsova, A. A., Novopashina, D. S., Fedorova, O. S., and Kuznetsov, N. A. (2020). Effect of the substrate structure and metal ions on the hydrolysis of undamaged RNA by human AP endonuclease APE1. *Acta Nat.* 2, 33–44.

Kuznetsova, A. A., Fedorova, O. S.., and Kuznetsov, N. A. (2018a). Kinetic features of 3′-5′ exonuclease activity of human AP-endonuclease APE1. *Molecules* 23:2101. doi: 10.3390/molecules23092101

Kuznetsova, A. A., Matveeva, A. G., Milov, A. D., Vorobjev, Y. N., Dzuba, S. A., Fedorova, O. S., et al. (2018b). Substrate specificity of human apurinic/apyrimidinic endonuclease APE1 in the nucleotide incision repair pathway. *Nucleic Acids Res.* 46, 11454–11465. doi: 10.1093/nar/gky912

Maher, R. L., and Bloom, L. B. (2007). Pre-steady-state kinetic characterization of the AP endonuclease activity of human AP endonuclease 1. *J. Biol. Chem.* 282, 30577–30585. doi: 10.1074/jbc.M704341200

Manvilla, B. A., Pozharski, E., Toth, E. A., and Drohat, A. C. (2013). Structure of human apurinic/apyrimidinic endonuclease 1 with the essential Mg2+ cofactor. *Acta Crystallogr. D Biol. Crystallogr.* 69, 2555–2562. doi: 10.1107/S0907444913027042

Marzano, M., Falanga, A. P., Marasco, D., Borbone, N., D'Errico, S., Piccialli, G., et al. (2020). Evaluation of an analogue of the marine ε-PLL peptide as a ligand of G-quadruplex DNA structures. *Mar. Drugs* 18:49. doi: 10.3390/md18010049

Miroshnikova, A. D., Kuznetsova, A. A., Kuznetsov, N. A., and Fedorova, O. S. (2016a). Thermodynamics of damaged DNA binding and catalysis by human AP endonuclease 1. *Acta Nat.* 8, 103–110.

Miroshnikova, A. D., Kuznetsova, A. A., Vorobjev, Y. N., Kuznetsov, N. A., and Fedorova, O. S. (2016b). Effects of mono- and divalent metal ions on DNA binding and catalysis of human apurinic/apyrimidinic endonuclease 1. *Mol. Biosyst.* 12, 1527–1539. doi: 10.1039/c6mb00128a

Mol, C. D., Hosfield, D. J., and Tainer, J. A. (2000a). Abasic site recognition by two apurinic/apyrimidinic endonuclease families in DNA base excision repair: the 3′ ends justify the means. *Mutat. Res.* 460, 211–229.

Mol, C. D., Izumi, T., Mitra, S., and Tainer, J. A. (2000b). DNA-bound structures and mutants reveal abasic DNA binding by APE1 and DNA repair coordination. *Nature* 403, 451–456. doi: 10.1038/35000249

Moor, N., Vasil'eva, I., and Lavrik, O. (2020). Functional role of N-terminal extension of human ap endonuclease 1 in coordination of base excision dna repair via protein-protein interactions. *Int. J. Mol. Sci.* 21:3122. doi: 10.3390/ijms21093122

Parkinson, G. N., Lee, M. P. H., and Neidle, S. (2002). Crystal structure of parallel quadruplexes from human telomeric DNA. *Nature* 417, 876–880. doi: 10.1038/nature755

Phan, A. T., Kuryavyi, V., Luu, K. N., and Patel, D. J. (2007). Structure of two intramolecular G-quadruplexes formed by natural human telomere sequences in K+ solution. *Nucleic Acids Res.* 35, 6517–6525. doi: 10.1093/nar/gkm706

Poletto, M., Vascotto, C., Scognamiglio, P. L., Lirussi, L., Marascod, D., and Tell, G. (2013). Role of the unstructured N-terminal domain of the hAPE1 (human apurinic/apyrimidinic endonuclease 1) in the modulation of its interaction with nucleic acids and NPM1 (nucleophosmin). *Biochem. J.* 452, 545–557. doi: 10.1042/BJ20121277

Prorok, P., Alili, D., Saint-Pierre, C., Gasparutto, D., Zharkov, D. O., Ishchenko, A. A., et al. (2013). Uracil in duplex DNA is a substrate for the nucleotide incision repair pathway in human cells. *Proc. Natl. Acad. Sci. U.S.A.* 110, E3695–E3703. doi: 10.1073/pnas.1305624110

Prorok, P., Saint-Pierre, C., Gasparutto, D., Fedorova, O. S., Ishchenko, A. A., Leh, H., et al. (2012). Highly mutagenic exocyclic DNA adducts are substrates for the human nucleotide incision repair pathway. *PLoS One* 7:e51776. doi: 10.1371/journal.pone.0051776

Schermerhorn, K. M., and Delaney, S. (2013). Transient-state kinetics of apurinic/apyrimidinic (AP) endonuclease 1 acting on an authentic AP site and commonly used substrate analogs: the effect of diverse metal ions and base mismatches. *Biochemistry* 52, 7669–7677. doi: 10.1021/bi401218r

Schreck, J. S., Ouldridge, T. E., Romano, F., Louis, A. A., and Doye, J. P. K. (2015). Characterizing the bending and flexibility induced by bulges in DNA duplexes. *J. Chem. Phys.* 142:165101. doi: 10.1063/1.4917199

Strom, S., Shiskova, E., Hahm, Y., and Grover, N. (2015). Thermodynamic examination of 1- to 5-nt purine bulge loops in RNA and DNA constructs. *RNA* 21, 1313–1322. doi: 10.1261/rna.046631.114

Sun, Y., Feng, Y., Zhang, G., and Xu, Y. (2019). The endonuclease APE1 processes miR-92b formation, thereby regulating expression of the tumor suppressor LDLR in cervical cancer cells. *Ther. Adv. Med. Oncol.* 11:1758835919855859. doi: 10.1177/1758835919855859

Timofeyeva, N. A., Koval, V. V., Ishchenko, A. A., Saparbaev, M. K., and Fedorova, O. S. (2011). Lys98 substitution in human AP endonuclease 1 affects the kinetic

mechanism of enzyme action in base excision and nucleotide incision repair pathways. *PLoS One* 6:e24063. doi: 10.1371/journal.pone.0024063

Timofeyeva, N. A., Koval, V. V., Knorre, D. G., Zharkov, D. O., Saparbaev, M. K., Ishchenko, A. A., et al. (2009). Conformational dynamics of human AP endonuclease in base excision and nucleotide incision repair pathways. *J. Biomol. Struct. Dyn.* 26, 637–652. doi: 10.1080/07391102.2009.10507278

Tsutakawa, S. E., Shin, D. S., Mol, C. D., Izumi, T., Arvai, A. S., Mantha, A. K., et al. (2013). Conserved structural chemistry for incision activity in structurally non-homologous apurinic/apyrimidinic endonuclease APE1 and endonuclease IV DNA repair enzymes. *J. Biol. Chem.* 288, 8445–8455. doi: 10.1074/jbc.M112.422774

Vrouwe, M. G., Pines, A., Overmeer, R. M., Hanada, K., and Mullenders, L. H. (2011). UV-induced photolesions elicit ATR-kinase-dependent signaling in non-cycling cells through nucleotide excision repair-dependent and -independent pathways. *J. Cell Sci.* 124, 435–446. doi: 10.1242/jcs.075325

Whitaker, A. M., Flynn, T. S., and Freudenthal, B. D. (2018). Molecular snapshots of APE1 proofreading mismatches and removing DNA damage. *Nat. Commun.* 9:399. doi: 10.1038/s41467-017-02175-y

Wilson, D. M. III, and Barsky, D. (2001). The major human abasic endonuclease: formation, consequences and repair of abasic lesions in DNA. *Mutat. Res.* 485, 283–307.

Zhou, J., Fleming, A. M., Averill, A. M., Burrows, C. J., and Wallace, S. S. (2015). The NEIL glycosylases remove oxidized guanine lesions from telomeric and promoter quadruplex DNA structures. *Nucleic Acids Res.* 43, 4039–4054. doi: 10.1093/nar/gkv252

Conflict of Interest: The authors declare that the research was conducted in the absence of any commercial or financial relationships that could be construed as a potential conflict of interest.

frontiers in Cell and Developmental Biology

BRIEF RESEARCH REPORT
published: 09 November 2020
doi: 10.3389/fcell.2020.600868

Loss of *Drosophila* E3 Ubiquitin Ligase Hyd Promotes Extra Mitosis in Germline Cysts and Massive Cell Death During Oogenesis

Natalia V. Dorogova[1]†, Yuliya A. Galimova[2†], Elena Us. Bolobolova[1], Elina M. Baricheva[1] and Svetlana A. Fedorova[1]*

[1] Department of Cell Biology, Institute of Cytology and Genetics, SB RAS, Novosibirsk, Russia, [2] Department of the Regulation of Genetic Processes, Institute of Molecular and Cellular Biology, SB RAS, Novosibirsk, Russia

OPEN ACCESS

Edited by:
Inna N. Lavrik, University Hospital Magdeburg, Germany

Reviewed by:
Ribhav Mishra, Northwestern University, United States
Alexey Zamaraev, Lomonosov Moscow State University, Russia

***Correspondence:**
Natalia V. Dorogova
dorogova@bionet.nsc.ru

† These authors have contributed equally to this work

Specialty section:
This article was submitted to Cell Death and Survival, a section of the journal Frontiers in Cell and Developmental Biology

Received: *31 August 2020*
Accepted: *20 October 2020*
Published: *09 November 2020*

Citation:
Dorogova NV, Galimova YA, Bolobolova EU, Baricheva EM and Fedorova SA (2020) Loss of Drosophila E3 Ubiquitin Ligase Hyd Promotes Extra Mitosis in Germline Cysts and Massive Cell Death During Oogenesis. Front. Cell Dev. Biol. 8:600868. doi: 10.3389/fcell.2020.600868

The *Drosophila hyperplastic disc* (*hyd*) gene is the ortholog of mammalian tumor suppressor *EDD*, which is implicated in a wide variety of cellular processes, and its regulation is impaired in various tumors. It is a member of the highly conserved HECT family of E3 ubiquitin ligases, which directly attach ubiquitin to targeted substrates. In early works, it was shown that *Drosophila* Hyd may be a tumor suppressor because it is involved in the control of imaginal-disc cell proliferation and growth. In this study, we demonstrated that Hyd is also important for the regulation of female germ cell proliferation and that its depletion leads to additional germline cell mitoses. Furthermore, we revealed a previously unknown Hyd function associated with the maintenance of germ cells' viability. A reduction in *hyd* expression by either mutations or RNA interference resulted in large-scale germ cell death at different stages of oogenesis. Thus, the analysis of phenotypes arising from the *hyd* deficiency points to Hyd's role in the regulation of germline metabolic processes during oogenesis.

Keywords: oogenesis, cell death, E3 ubiquitin ligase, germ cells, *Drosophila*, *hyperplastic disc* gene

INTRODUCTION

The *Drosophila melanogaster hyperplastic disc* gene (*hyd*) has been classified as a tumor suppressor gene owing to the overgrowth phenotype of imaginal disc cells in mutant backgrounds (Mansfield et al., 1994; Shearer et al., 2015). It is an ortholog of mammalian *EDD*, which was originally identified as a progestin-regulated gene in human T47D breast cancer cells (*EDD* stands for 'E3 identified by differential display') (Callaghan et al., 1998; Clancy et al., 2003). Impaired regulation of *EDD* contributes to tumorigenesis, and various alterations of the *EDD* locus (mutations, deletions and especially amplifications) have been found in a number of common human cancers. The *hyd* gene, just as *EDD*, encodes a large protein (approximately 300 kDa) that is a member of the highly conserved family of E3 ubiquitin ligases containing the HECT domain, which mediates specific recognition of substrate proteins and their targeting by ubiquitin (Scheffner et al., 1995; Metzger et al., 2012). Ubiquitination affects the fate and properties of proteins: from proteasomal degradation to changes of a functional activity in such processes as DNA repair, transcription, immunity, autophagy and protein sorting and trafficking (Bhoj and Chen, 2009; Dikic et al., 2009). Through ubiquitination of a wide variety of substrate proteins, E3 ubiquitin ligases participate in

the regulation of diverse cellular processes. Dysregulation or dysfunction of E3 ubiquitin ligases gives rise to abnormalities in the ubiquitination system and causes serious pathologies, including neurodegeneration and cancer (Shearer et al., 2015).

E3 ubiquitin ligase Hyd is involved in numerous biological processes and is necessary at all stages of *Drosophila* development. Null-alleles of *hyd* are lethal at the larval stage, and temperature-sensitive alleles induce imaginal-disc hyperplasia and adult gonadal defects leading to sterility (Martin et al., 1977; Mansfield et al., 1994). A clone analysis has revealed that Hyd negatively regulates the expression of *Hedgehog (Hh)* and *Decapentaplegic (Dpp)* in the eye and wing discs. Loss of *hyd* function induces ectopic expression of both genes, resulting in disc cell overgrowth (Lee et al., 2002; Wang et al., 2014). These data have allowed researchers to conclude that Hyd is involved in the regulation of cell proliferation and cell cycle control through Hh signaling. In spermatogenesis, however, Hyd does not manifest the tumor suppressor properties; *hyd* mutants show substantial structural abnormalities in mitosis and meiosis, without excessive cell proliferation. On the contrary, testes of the mutant males are small and contain fewer germ cells as compared to the wild type (Pertceva et al., 2010). In the present work, we continued the study on the biological functions of *hyd* in *Drosophila* oogenesis. According to previous works, *hyd*-mutant females are sterile and have defects in ovary formation and germ tissue morphology. It remains unclear what cellular event or process in oogenesis is primarily affected by the Hyd deficiency.

The *Drosophila* ovary consists of 15–20 ovarioles, which represent a chain of progressively developing egg chambers (EChs). The anterior region of each ovariole is the germarium, which includes stem cells and early germline cells (GCs) going through a series of mitotic divisions. In the posterior of the germarium, 16 daughter GCs are surrounded by a monolayer of somatic follicle cells creating an ECh. After leaving the germarium, the ECh moves along the ovariole, gradually developing into a mature oocyte. According to the size and morphology of the ECh, oogenesis can be roughly divided into 14 stages (King, 1957; Spradling, 1993). Developmentally programmed cell death in the female germline occurs at three specific stages: in newly formed cysts (region 2 of the germarium), during mid-oogenesis (stages 7–8), and during late oogenesis (stages 12–13). Under normal nutritional conditions, cell death in the germarium and at stages 7–9 (called 'checkpoints' of cell death in oogenesis) takes place in response to developmental abnormalities and increases dramatically under the influence of various stressors. The death of nurse cells in late oogenesis occurs as part of normal development of each egg (Jenkins et al., 2013; Peterson et al., 2015; Bolobolova et al., 2020).

Here, we present a study of the Hyd function in *Drosophila* oogenesis. We showed that a reduction in *hyd* expression by mutations or RNA interference yields two main phenotypes of the germline. The first one is manifested as extra mitotic divisions that form EChs with 32 or 64 germ cells. Nonetheless, such an effect was observed only in *hyd*-mutant flies and at a low frequency. The second phenotype was large-scale germ cell death and ECh degradation. This phenotype was strong and highly penetrant and was observed both in the mutants and after a *hyd* knockdown via RNA interference (*hyd*-RNAi). We believe that the function of Hyd in oogenesis is not related to the regulation of cell death directly. Being an E3 ubiquitin ligase, it is involved in ubiquitination of the protein substrates responsible for the metabolism and biosynthetic activity of GCs. A dysfunction of this mechanism probably causes cell death due to a deficit of resources.

MATERIALS AND METHODS

Fly Stocks

All *Drosophila* stocks were raised at 25°C on standard cornmeal medium. We used Bloomington stocks: kni^{ri-1} hyd^{15} $e^1/TM3$, Sb^1 (3718) and y^1 w^{1118}; *PBac{3HPy + }*hyd^{C017}*/TM3,* Sb^1 Ser^1 (16256) as a source of mutant alleles, *w1118; P{w + mC = PTT-GA}Pabp2* GFP protein trap strain was used as a germline nuclei marker: (48-1) kindly provided by A. Debec (Université Pierre et Marie Curie, France).

We used the following strains for RNA interference: *hyd*-RNAi -y ^{1}sc*v^1;P{TRiP.HMS00343}attP2 (32352); *osk-GAL4* - w^{1118}; P{osk-GAL4:VP16}F/TM3, Sb^1 (44242); *nos-GAL4* - w^{1118}; P{w^{+mC} = GAL4:VP16-nos.UTR}CG6325^{MVD1} (4937); *7023-GAL4* – y^1 w*; P{GawB}109-30/CyO GAL4 (7023); *7024-GAL4* – y^1 w*; P{w + mW.hs = GawB}109-39/TM3,Sb^1 (7024); *36287-GAL4* 36287 w*; P{$w^{+mW.hs}$ = GawB}GR1.

RNA Isolation and Quantitative Real-Time PCR

Levels of *hyd* mRNA were assigned using method of qPCR. Total RNA preparation, reverse transcription (RT) and qPCR analyses were performed using Trizol (Invitrogen), Superscript III (Invitrogen), and SYBR green kits (Syntol) following the manufacturer's recommendations. The following primers were used: *hyd*-specific RT-HYD-Fw-5′-ACGCCAGGATTTGGTTTACTT and RT-HYD-Rev-5′-TTCGCAGTCGGTAGATGGGA, *RpL32*-specific RPL32-F-5′-TAAGCTGTCGCACAAATGG and RPL32-R-5′-AGGAACTTCTTGAATCCGGTG as a reference gene (Yang et al., 2013). The mean values ± standard deviation of the transcript abundance of three separate determinations.

Electron and Fluorescence Microscopy

Experimental procedures for electron and fluorescence microscopy were performed as described earlier (Pertceva et al., 2010). The primary antibodies were: monoclonal rabbit anti-VASA antibodies from Santa Cruz Biotechnology (1:300), rabbit anti-Dcp-1 (Asp216) from Cell Signaling Technology. The secondary antibodies were goat anti-rabbit conjugated to AlexaFluor-488 (1:500; Invitrogen #A-11001). TRITC-labeled phalloidin (Sigma-Aldrich #P1951) was used at 1:100 dilution to visualize F-actin as described previously (Guild et al., 1997). The LysoTracker assay was performed as described in Dorogova et al. (2014) (LysoTracker red DND-99 (Invitrogen, Molecular Probes, Basel, Switzerland). Ovaries were embedded with ProLong Gold anti-fade reagent with DAPI. Images were obtained using an AxioImager Z1 microscope with ApoTome

attachment (Zeiss), AxioCam MR and AxioVision software (Zeiss, Germany).

RESULTS

A Decrease in *hyd* Expression Leads to Both Ovary Atrophy and Extra Mitoses in Germline Cysts

To investigate the effect of the Hyd protein on oogenesis, we selected mutant alleles *hydC017* and *hyd15*, which have been described previously (Mansfield et al., 1994; Pertceva et al., 2010). The *hyd15* mutation, when homozygous, is lethal at the third instar larval stage, whereas *hydC017* homozygotes are viable but females exhibit a significant decline of fertility and of egg production. For cytological analysis of the effect of *hyd* mutation, viable females carrying hetero-allelic combination *hydC017/hyd15* were used. Wild-type strain—*Oregon R* and heterozygous siblings—hyd^{15} e^1/*TM3, Sb*^{1} *and* hyd^{C017}/*TM3, Sb*^{1} *Ser*^{1} were taken as control.

To determine how this hetero-allelic combination affects the level of *hyd* expression, we performed a real-time PCR analysis of adult *hydC017/hyd15* ovaries. Our data indicated that *hyd* mRNA expression was statistically significantly ∼2-fold lower in the mutants than in the control (wild type; **Figure 1**). Consequently, the oogenesis aberrations identified in *hydC017/hyd15* flies (as described below) could be associated with a deficiency in the *hyd* gene product.

The *hydC017/hyd15* females were found to be sterile and laid only a single egg, which did not develop. The gonads in such females mainly contained reduced ovarioles with a small number of EChs or without them at all (**Figures 2A–C**). Depending on the degree of the germ-line atrophy, we have identified 3 types of ovaries: completely reduced, significantly reduced and partially reduced. Completely reduced ones had no or a few GCs. Significantly reduced ovaries contained single GCs in germaria and single EChs in ovarioles. Partially reduced ovaries contained not only atrophied, but also normal ovarioles with EChs at different stages of oogenesis. In the wild type, ovaries with any of these phenotypes were not found (**Figure 2J**). Partially reduced ovaries also contained EChs with an excessive GC number: 2–3-fold higher than normal (**Figures 2C,D** and **Supplementary Table 1**).

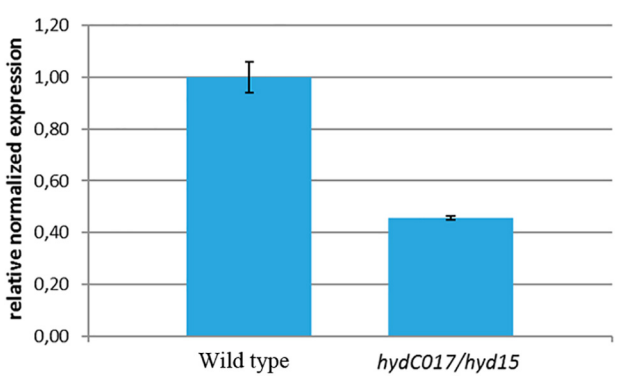

FIGURE 1 | Comparison of *hyd* mRNA expression levels between wild-type and *hydC017/hyd15* ovaries as estimated by real-time PCR. The *hyd* expression is ∼2-fold lower in the mutants than in the wild-type ovaries. The mean values ± standard deviation of the transcript abundance of three separate determinations.

Immunostaining of a GC marker, the Vasa protein, showed that most of the *hydC017/hyd15* ovaries were completely rudimentary (without GCs) or contained stand-alone germline cysts (**Figures 2E–G**). Mutant gonads formed normally in embryos and larvae, but their germline degraded at later stages; only some GCs gave rise to cysts that produced a normal ECh. Nevertheless, the formed EChs also degraded during mid-oogenesis: only 1% of them developed into eggs. Thus, the *hyd* mutation affected GC viability at different stages of GC development, thereby causing the death of both early GCs (including stem cells) in larval ovaries and germarium and differentiated GCs in mid-oogenesis.

Besides reduced EChs, a small number of *hydC017/hyd15* ovaries also contained multi-nuclear EChs (**Figure 2D** and **Supplementary Table 1**). To determine whether such EChs were a consequence of excessive cystoblast mitosis, we performed immunostaining with an antibody to phosphorylated histone H3. The serine phosphorylation of histone H3 marks the onset of mitosis; therefore, any cyst in normal germaria contains no more than eight metaphase groups (Kiger et al., 2000). The phospho-H3 histone staining revealed that the mutant germline cysts contained significantly larger than normal of mitotic chromosomes. In particular, the number of metaphase groups inside one cyst reached 16 and 32, and the number of anaphases reached 32 and 64 (**Figures 2H,I**). As a result, both germaria and EChs looked abnormally enlarged. This phenotype was a consequence of additional mitoses in germline cysts and indicated abnormal cell cycle control when *hyd* was mutated.

Germline-Specific Inhibition of *hyd* Expression Causes Massive Cell Death

The association of cell death with a decrease in the *hyd* activity was confirmed by our data from *hyd*-RNAi. For this experiment, we employed the *UAS/GAL4* system. To ectopically suppress the *hyd* gene expression in different ovary cells, we used the following tissue-specific drivers: *nanos*-GAL4 and *oskar*-GAL4 for GCs and *7023-GAL4*, *7024-GAL4* or *36287-GAL4* for somatic (follicular) cells. *UAS hyd*-RNAi strains and Oregon R were used as control.

Implementation of *hyd*-RNAi in follicular cells did not lead to any phenotypic changes in the ovaries, oogenesis abnormalities, or a decrease in fertility. Only a combination of *UAS-hyd*-RNAi with a germline-specific driver, *nanos-GAL4* or *oskar-GAL4*, resulted in massive cell death and ovarian atrophy, which were similar to the phenotypic manifestation of the *hyd* mutations under study.

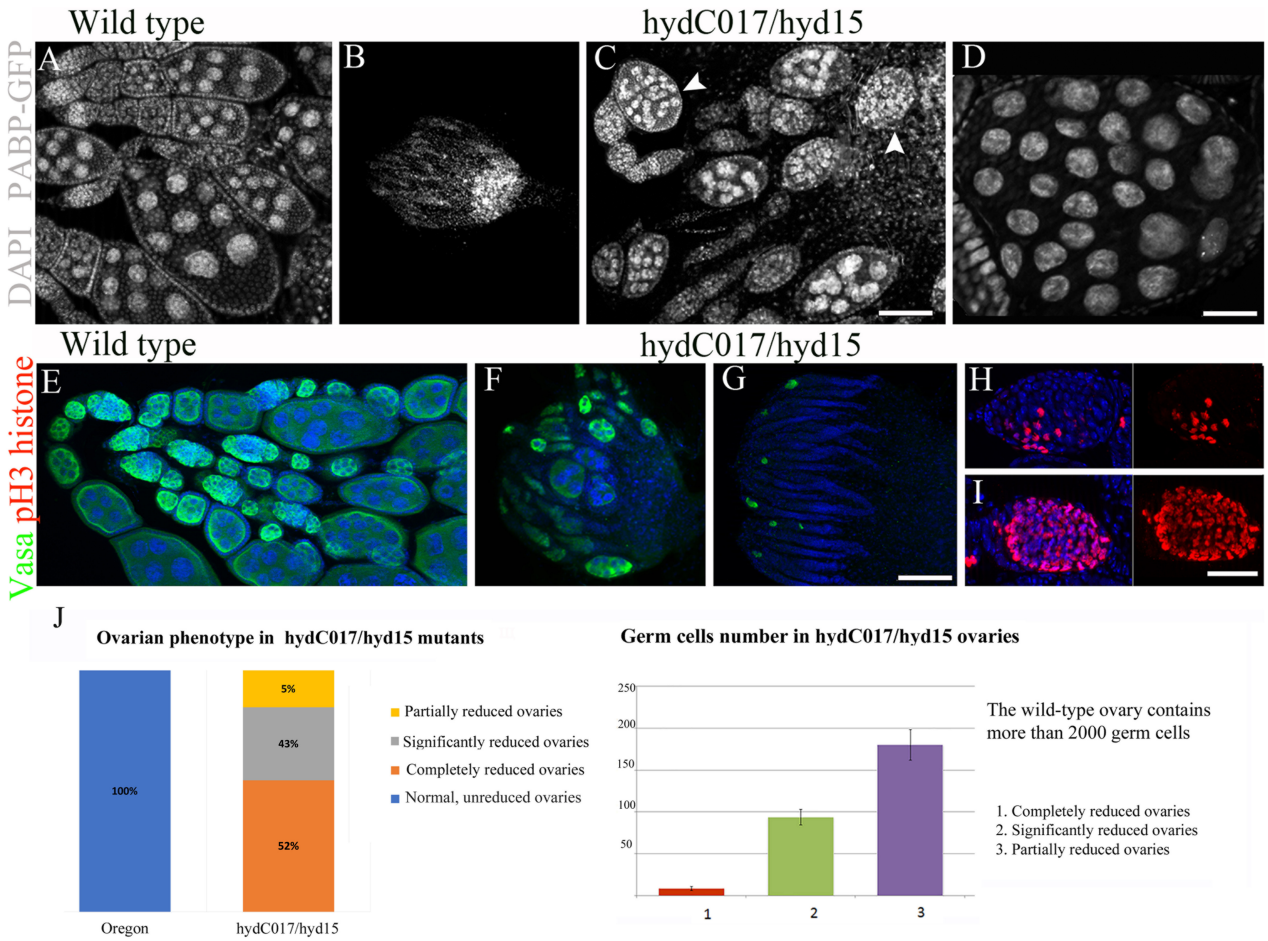

FIGURE 2 | Abnormalities of oogenesis and ovary formation in *hydC017/hyd15* females. **(A)** Normal ovarian morphology in wild-type females. **(B)** A reduced ovary of a *hydC017/hyd15* female without ovarioles and EChs. **(C)** A *hydC017/hyd15* female ovary with few ovarioles containing multi-nuclear EChs (arrowheads). **(D)** A multi-nuclear ECh in a *hydC017/hyd15* ovary. **(E–G)** Germ cell visualization by anti-Vasa staining in germaria and EChs. **(E)** Wild-type ovary. **(F,G)** Germline loss in a *hydC017/hyd15* female ovary. **(H,I)** Visualization of mitotic chromosomes in germline cysts using an anti-p-H3 histone antibody. Anaphase chromosomes in the wild type **(H)** and an excessive number of anaphase chromosomes in a *hydC017/hyd15* germline cyst **(I)**. (**J**) Phenotypic variability of reduced ovaries in *hydC017/hyd15* mutants and quantification of the germ cell numbers in the *hydC017/hyd15* ovaries. The number of germ cells per ovary was determined by counting VASA-positive cells from optical serial sections, 30 ovaries for each phenotype were examined. Data represent mean ± s.d., Student's *t*-test. For phenotypic analysis, the number of ovaries viewed—100. DNA: DAPI (blue), anti-Vasa staining: red, p-H3 histone staining: green. Scale bars: 10 μm **(A–C)**, 3 μm **(D)**, 10 μm **(E–G)**, 2 μm **(H,I)**

Early GC Death in Nanos-GAL4/UAS-*hyd*-RNAi Ovaries

Nanos-GAL4 is expressed in primordial GCs starting from embryogenesis. Accordingly, in *nanos-GAL4/UAS-hyd*-RNAi females, GC death occurred before the adult stage. In adult females, almost all the germline turned out to be atrophied, and the formed ovaries consisted only of somatic cells (**Figures 3A,B**).

The *nanos-GAL4/UAS-hyd*-RNAi ovaries formed normally until third instar larva and at this stage were indistinguishable from the control under a light microscope. In contrast, electron microscopy uncovered multiple signs of intracellular degradation. They included condensation of the nuclear matrix, nuclear-envelope invaginations, dilation of organelles and an increased number of various cytoplasm vesicles, including multi-vesicular and myelin bodies, lysosomes and stand-alone autophagosomes (**Figures 4A,B**). Such structural changes are suggestive of decreased functional activity of the cells. These processes extended to the entire germline of *nanos-GAL4/UAS-hyd*-RNAi ovaries, inducing their atrophy and somatic gonad formation.

Mid-Oogenesis GC Death in *oskar-GAL4/UAS-hyd*-RNAi Females

The *oskar-GAL4* driver is activated at stages 3–4 of oogenesis; accordingly, in *oskar-GAL4/UAS-hyd*-RNAi females, GC death occurred in mid-oogenesis (**Figure 3C**). Before dying, after stage 4 or 5, EChs failed to grow normally. Even though the *oskar-GAL4/UAS-hyd*-RNAi EChs continued developing, their size was much smaller than that in normal chambers at the same stage (**Figures 3D,E** and **Supplementary Figure 1**). EChs, growing slowly, accumulated in ovarioles, which consequently became abnormally long. In normal ovarioles, only 4–6 EChs

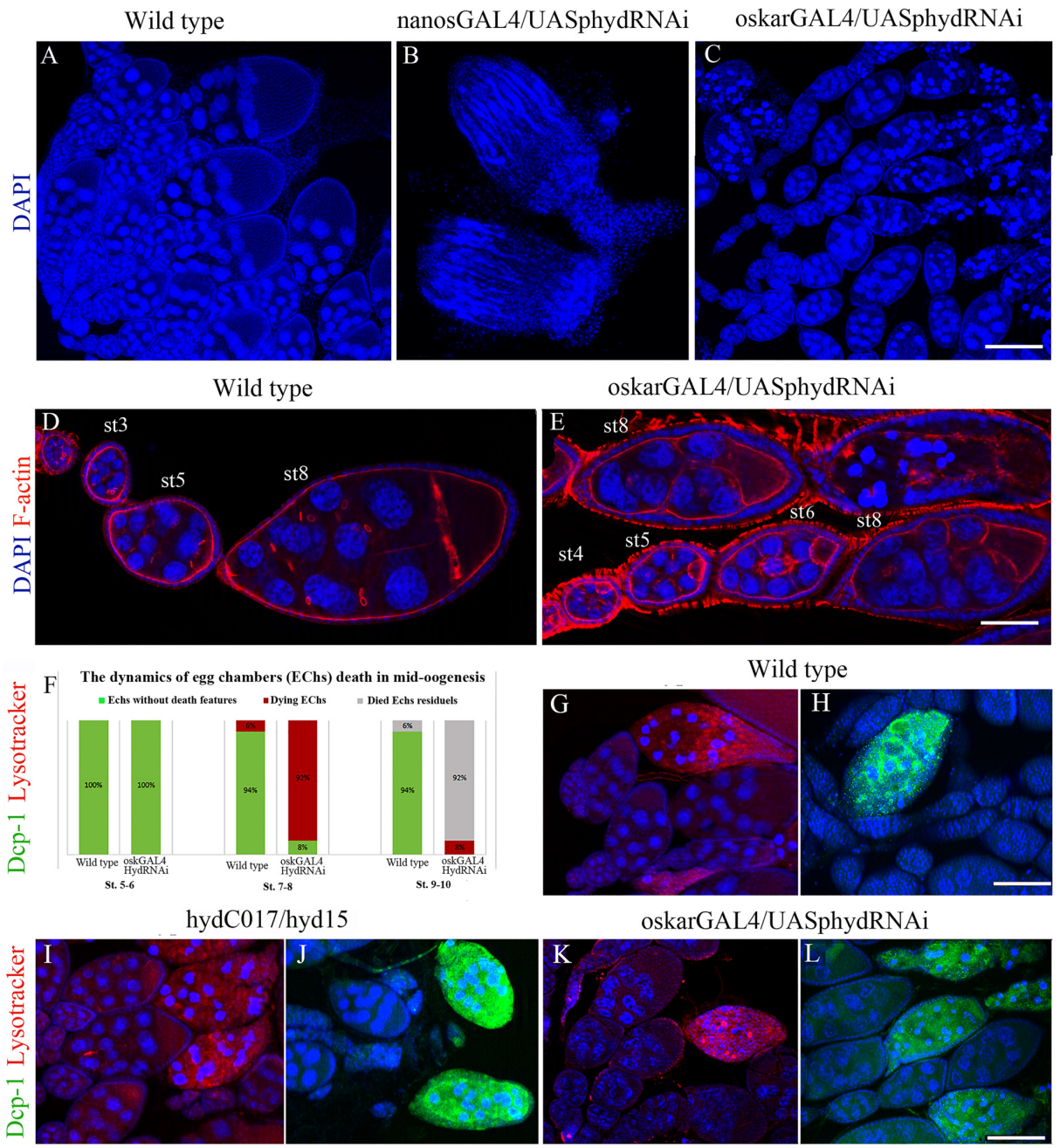

FIGURE 3 | Effects of the *hyd* RNAi knockdown on ovarian morphology and oogenesis. **(A)** Wild-type ovaries with normal ovarioles and EChs. **(B)** Reduced (somatic) ovaries of *nanos-GAL4/UAS-hyd*-RNAi females, lacking germ cells. **(C)** Mid-stage oogenesis arrest and massive ECh degradation in an *oskar-GAL4/UAS-hyd*-RNAi ovary. **(D,E)** Comparison of ovariole and ECh morphology at early oogenesis stages between a wild-type **(D)** and *oskar-GAL4/UAS-hyd*-RNAi ovary **(E)**. **(F)** Diagram representing a comparison of the number of dying egg chambers between the wild-type and *oskar-GAL4/UAS*-hyd-RNAi ovaries during the middle oogenesis. No. of examined ovaries – 50, for each type. **(G–H)** Cytological detection of lysosomal activity and effector caspase Dcp-1 in wild type, *hydC015/hyd15* and *oskar-GAL4/UAS-hyd*-RNAi degrading EChs. Dying egg chambers of all types of ovaries demonstrate similar patterns of LysoTracker and anti-Dcp-1 staining: wild-type (**G,H**), *hydC017/hyd15* (**I,J**), *oskar-GAL4/UAS*-hyd-RNAi (**K,L**). DNA: DAPI (blue), lysosomes: LysoTracker (red), Dcp-1 staining: Alexa 488 (green), F-actin staining: phalloidin (red). Scale bars: 15 μm **(A–C)**, 3 μm **(D,E)**, 12 μm **(G–L)**.

of different developmental stages, including late oogenesis, are usually observed. In *oskar-GAL4/UAS-hyd*-RNAi females, ovaries consisted of 6–9 EChs that slowly developed mainly up to the eighth stage. The delay in development ended with mid-oogenesis arrest and massive death of GCs. As a result, *oskar-GAL4/UAS-hyd*-RNAi ovaries contained, instead of vitellogenic EChs, a mass of degrading material. Only a small proportion, ∼8% of EChs, progressed to stages 9–10 but then died at the

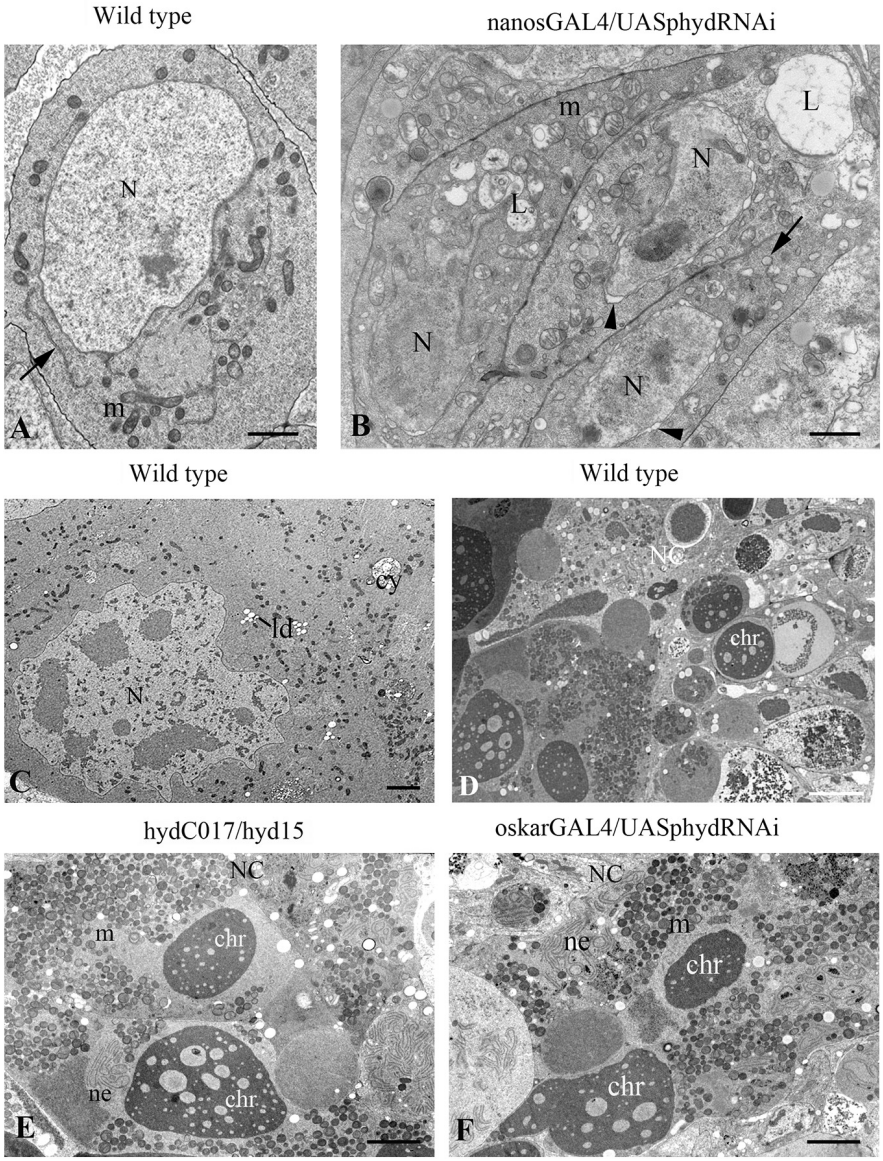

FIGURE 4 | Ultrastructural features of germ cell death in *hyd*-RNAi ovaries. **(A–B)** Electron micrographs of primordial GCs in wild-type and *nanos-GAL4/UAS-hyd*-RNAi ovaries at the third instar larva stage. **(A)** A wild-type GC with morphology typical of this stage: nuclei with smooth contours, evenly dispersed chromatin, and distinct nucleoli; the cytoplasm contains round or oval mitochondria, endoplasmic-reticulum cisterns (ER cisterns), Golgi complexes, and abundant ribosomes. **(B)** GCs with signs of intracellular degradation: condensation of the nuclear matrix, curvature of the nuclear outline, nuclear envelope dilation (arrowheads), mitochondrial swelling, ER vacuolization (arrows) and numerous lysosomes. N, nucleus; m, mitochondrion; L, lysosome. Scale bar: 1 μm. **(C–F)** Signs of mid-oogenesis cell death in a wild-type, *hydC015/hyd15* and *oskar-GAL4/UAS-hyd*-RNAi ECh. **(C)** A segment of a mid-oogenesis ECh before cell death. Nurse cell ultrastructure without structural anomalies or signs of degradation. **(D–F)** Morphology of a dying ECh in a wild-type **(D)**, *hydC015/hyd15* **(E)**, and *oskar-GAL4/UAS-hyd*-RNAi **(F)**. Nurse cell cytoplasm contains condensed chromatin material, aggregates of nuclear-envelope fragments and clusters of mitochondria, numerous lysosomes. In the nurse cell area, there are of varying content present in this layer. NC, nurse cell; N, nucleus; m, mitochondrion; chr, chromatin; ne, nuclear envelope. Scale bar: 5 μm.

beginning of late oogenesis. Therefore, the *hyd*-RNAi induced by the *oskar-GAL4* driver caused ECh growth retardation, which led to their complete degradation (100%).

Mid-stage death is a characteristic feature of *Drosophila* oogenesis and allows to save energy and resources eliminating defective or unnecessary EChs. Dying EChs are easily identified by abnormal condensation and subsequent fragmentation of chromatin, which are features of apoptotic cell death (Greenwood and Gautier, 2005; Sarkissian et al., 2014). In addition to apoptosis, autophagy is also involved in mid-oogenesis cell death (Bolobolova et al., 2020). Recent studies have convincingly shown that ubiquitin proteasomal machinery is important for the regulation of cell death pathways and that many E3 ubiquitin ligases take part in this process. To determine how E3 ligase Hyd

can be associated with mid-oogenesis death, we investigated this process in more detail by means of the main cytological markers of apoptosis and autophagy together with electron microscopy.

To detect autophagy, we utilized LysoTracker, an acidophilic dye that marks lysosomes and autophagosomes. A LysoTracker signal was detected in all *oskar-GAL4/UAS-hyd*-RNAi ovarioles, but its appearance coincided with the beginning of nuclear condensation, same as in the controls (**Figures 3F,G**). To verify the apoptotic events, we used an antibody recognizing effector caspase Dcp-1: a general apoptosis marker in *Drosophila* (Sarkissian et al., 2014). Immuno-fluorescence staining suggested that anti-Dcp-1 antibodies were incorporated into degenerating EChs of *hyd*-RNAi ovaries, and their pattern was indistinguishable from that in the control (**Figures 3H,I**).

We conducted an electron microscopic analysis to clarify the features of the cell death and to identify a possible pathological change in the germline before the death. Ultrastructural analysis of *oskar-GAL4/UAS-hyd*-RNAi imago ovaries showed that EChs underwent cell death at stages 7–8/9, as in the wild type. Moreover, some oocytes in the dying chambers contained stand-alone vitelline granules, which mean the onset of vitellogenesis. Before these stages, substantial abnormalities in GC ultrastructure were not detectable. The ECh degeneration was accompanied by specific structural transformations similar to those in the wild type (Giorgi and Deri, 1976). The nurse cell cytoplasm and nucleus featured increased electron density, and nuclear chromatin formed condensed masses. With further degeneration, the nuclear envelope in the nurse cells broke down, and nuclear material was released into the cytoplasm. Numerous fragments of nuclear membranes formed aggregates in the nurse cell cytoplasm with a specific parallel orientation in tracts. Most mitochondria combined into clusters. The cytoplasm contained large vacuoles of varying content and electron density (**Figures 4C,D,F**). The same cell death manifestations were observed in the *hydC017/hyd15* EChs (**Figure 4E**). All these events are characteristic signs of mid-oogenesis cell death, as described elsewhere (Giorgi and Deri, 1976).

Thus, the RNAi knockdown of the *hyd* gene did not cause anomalies in EChs' ultrastructure before their death. The ECh degradation occurred at the same stage of oogenesis as in the wild type, did not differ morphologically and had signs of both apoptosis and autophagy. This means that the GC death in *oskar-GAL4/UAS-hyd*-RNAi ovaries proceeds via the canonical *Drosophila* mid-oogenesis pathway.

DISCUSSION

This study showed that Hyd is critical for GCs' development and egg formation in *Drosophila*. The lack of this protein led to massive cell death and ECh degradation and, as a minor manifestation, to GC overproliferation as a consequence of additional mitoses. The observed effect was germline specific and independent of a somatic environment.

As an E3 ubiquitin ligase, Hyd is one of the key components of the ubiquitination system, which is important for the regulation of activities of proteins, their cellular functions and proteasomal degradation (Bhoj and Chen, 2009; Shearer et al., 2015) Analysis of protein–protein interactions by a yeast two-hybrid assay has allowed to identify more than 50 proteins that can potentially interact with Hyd in ovaries[1] (**Supplementary Table 1**). Hyd interactors can be both substrates for ubiquitination and proteins that cooperate with Hyd to form functional complexes. The variety of these proteins determines the multiple functions of Hyd in *Drosophila* oogenesis; therefore, its dysfunction or loss has dramatic downstream consequences.

Hyd Is Essential for the Maintenance of Germline Viability

Our findings indicate that Hyd is especially important for GC survival. Its lack induced the death of both early GCs in the larval ovaries and differentiated ones in mid-oogenesis.

According to our results, the death of Hyd-deficient GCs in *nanos-GAL4/UAS-hyd*-RNAi ovaries begins in late third instar larvae. The ovaries at this stage contain primordial germ cells (PGCs) that terminate to divide and specialize in two directions: several cells interact with a newly formed niche and become germline stem cells, whereas the remaining cells begin to differentiate and become cystoblasts (Gancz et al., 2011; Kahney et al., 2019; Hinnant et al., 2020). Germline differentiation factor Bam governs both stem cell maintenance and the differentiation of their progeny: Bam expression is inhibited in stem cells (where differentiation is prohibited) and activated in cystoblasts (where differentiation is promoted) (Ji et al., 2017; Mathieu and Huynh, 2017; Kahney et al., 2019). Bam over-expression in late third instar larva ovaries causes massive GC death and the formation of completely somatic gonads (Ohlstein and McKearin, 1997; Chen and McKearin, 2003). We noticed a similar phenotype when Hyd was either mutated or knocked down.

GC death at this stage of development is also associated with several intrinsic factors. It has been documented that such an effect is exerted by a strong mutation or knockout of any of the following genes: *ote* (coding for a nuclear lamina protein) (Barton et al., 2013), *mcm10* (its product acts in DNA replication) (Reubens et al., 2015), *γ-tubulin* (encodes the main component of the peri-centriolar material) (Tavosanis and Gonzalez, 2003) and *vasa* (its product has a multi-functional role in the germline) (Styhler et al., 1998). The same is true for over-expression of Dmp53, a homolog of mammalian p53 (Bakhrat et al., 2010). Nonetheless, almost all proteins encoded by these genes are important even before the late third instar stage. Only Ote has been shown to start functioning at this stage, and Ote is necessary for the progression of differentiation. In *ote* mutants, GCs are not able to differentiate and to die (Barton et al., 2013). On the other hand, stem cells are not susceptible to Ote loss and persist in adult ovaries (Barton et al., 2013), in contrast to the Hyd deficiency phenotype. Accordingly, we assume that Bam or components of Bam signaling are the most likely partners of Hyd at the very beginning of oogenesis, when the fate of PGCs is determined: to be stem cells or differentiate.

Massive death of germ cells also occurred in *oskar-GAL4/UAS-hyd*-RNAi ovaries through middle oogenesis. EChs containing

[1] http://www.flybase.org

Hyd-deficient GCs did not progress through the oogenesis mid-stage checkpoint and degraded completely in early vitellogenesis. It is known that this checkpoint is activated in response to adverse stimuli or physiological and developmental disorders (Pritchett et al., 2009; Jenkins et al., 2013; Peterson et al., 2015). GC death at this stage is tightly regulated both positively and negatively with the help of a genetic network that includes, in particular, genes responsible for the ubiquitination mechanism. Dysregulation or loss of function of these genes induces disturbances in cell death manifestations (Hou et al., 2008; Bergmann, 2010; Peterson et al., 2015). One of these abnormal manifestations is associated with cell death enhancement in mid-oogenesis. In particular, such a phenotype is observed when the genes encoding inhibitors of apoptosis (members of the IAP protein family) Bruce and Diap are suppressed (Rodriguez et al., 2002; Hay and Guo, 2006; Hou et al., 2008). However, the typical feature of the Hyd-deficient-ovary phenotype is not only mid-oogenesis arrest and increased cell death but also the preceding slowdown in ECh development and growth. Moreover, degrading EChs do not morphologically differ from the wild type and have signs of autophagy and apoptosis (these are normal).

These phenotypic features emerge in response to nutrient starvation or a reduction in insulin/TOR signaling (Drummond-Barbosa and Spradling, 2001; Barth et al., 2011; Pritchett and McCall, 2012). The insulin/TOR signaling network is a highly conserved mechanism responsible for cell and tissue growth. It acts as a sensor of nutrient availability to promote cell metabolism, growth and proliferation. In *Drosophila* oogenesis, the insulin/TOR axis is critical for GC development and oocyte maturation. In the presence of some disorders of this mechanism, EChs' growth is delayed, and they cannot enter energy-intensive vitellogenesis and hence degenerate (LaFever et al., 2010; Laws and Drummond-Barbosa, 2017; Jeong et al., 2019). We believe that Hyd either interacts with one of insulin/TOR targets or acts upstream by regulating the factors responsible for the biosynthesis in growing EChs.

Currently, there are no experimental data supporting the interaction of *Drosophila* Hyd with components of the insulin/TOR signaling network. Nonetheless, lately, it was reported that Hyd's human homolog, EDD, is involved in the regulation of mTOR (TORC1) via ubiquitination for proteasomal degradation of its target PP2Ac (TORC1-associated α4 phosphoprotein). Increased EDD expression in human breast cancer cells *in vitro* promotes TORC1 signaling, which activates the synthesis of an anti-apoptotic protein promoting drug resistance. On the contrary, a knockdown of EDD arrests cancer cell proliferation decreases their viability and increases apoptosis (MacDonald et al., 2019).

According to Flybase and DroID, the Hyd protein interacts with TOR signaling pathway proteins (Pdk1 and RagC) and with many factors necessary for the synthesis and modification of proteins and RNA and for Golgi and endoplasmic-reticulum functioning (**Supplementary Table 2**). Nonetheless, several studies should be conducted to determine which potential substrate interacts with E3 ubiquitin kinase Hyd *in vivo* to ensure germ cell survival.

One of Hyd Functions in Oogenesis Is Associated With the Control of Germ Cell Divisions

Some studies on the somatic tissue in imaginal discs have shown that Hyd is a negative regulator of Hh signaling. Hyd-deficient flies display eye disc overgrowth due to increased Hh activity (Mansfield et al., 1994; Lee et al., 2002; Hariharan and Bilder, 2006). In oogenesis, Hh participates in the control of germ cell proliferation through a somatic microenvironment: this protein is produced by a niche of stem germ cells to balance stem cell renewal and differentiation (Lu et al., 2015; Huang et al., 2017; Lai et al., 2017). One would expect that Hyd and Hh also interact in this context. According to our data, however, Hyd is necessary to control the number of cystoblast divisions, not stem cells, and unlike Hh, the Hyd protein can act autonomously in the germline. Therefore, we believe that the role of Hyd in female GC divisions is not mediated by Hh signaling either.

An extra round of cystoblasts' mitosis, as in *hyd* mutants, is also observed during dysregulation of the timely degradation of mitotic cyclins: cyclins A, B and E (Lilly et al., 2000; Wang and Lin, 2005; Chen et al., 2009). For instance, overexpression of genes encoding these proteins or a deletion of the CycA or CycB destruction box gives rise to one, less often two, extra rounds of mitotic division, resulting in 32- and 64-cell cysts (Jacobs et al., 1998; Doronkin et al., 2003). The degradation of cyclins is implemented mainly through ubiquitin-proteasome-dependent proteolysis; hence, its failures also prevent timely termination of mitosis (Ji et al., 2017; Chen et al., 2018; Hinnant et al., 2020). In *Drosophila* oogenesis, mutations of genes playing a part in the ubiquitination system induce an 'extra round of mitosis' phenotype, as in a *hyd*-deficient background. In particular, such a phenotype is observed after mutations of genes encoding subunits of the SCF complex (Skp1, Cullins, and F-box proteins), which is an E3 ubiquitin ligase. In these cases, cyclin E accumulation, entry into the S phase and doubling of the cell number are observed (Ohlmeyer and Schüpbach, 2003). The same phenotype is generated by mutations in the *effete* gene (encoding E2 ubiquitin-conjugating enzyme UbcD1) (Lilly et al., 2000), *encore* (coding for a protein interacting with the proteasome and Cyclin E) (Hawkins et al., 1996; Ohlmeyer and Schüpbach, 2003) or *slmb* (coding for an E3 ubiquitin ligase) (Muzzopappa and Wappner, 2005).

Recent research has shown that the stabilization of CycA expression during mitotic cystoblast divisions is controlled by Bam, which acts together with deubiquitinase Otu (Ji et al., 2017). Earlier in this article, we suggested that Hyd may be an antagonist of Bam signaling in early oogenesis, at the beginning of PGC differentiation. Perhaps their interplay continues during germline cyst divisions in the germarium, where Hyd, in contrast of Bam, is required for downregulation of cyclins and for timely ending of germ cell mitosis.

It is currently difficult to determine what other factors may be associated with Hyd in this context. The list of potential interactors contains several proteins responsible for cell cycle control (**Supplementary Table 2**). On the other hand, their participation in proliferation has not been demonstrated

experimentally. Therefore, additional original data are needed to resolve this issue.

In this article, we describe a previously unknown function of *Drosophila* Hyd in oogenesis and germ cell development. We demonstrated that Hyd is essential for timely regulation of germline cyst mitosis and for the maintenance of germ cell viability. Because Hyd is an E3 ubiquitin ligase, it contributes to cellular processes through ubiquitination of its substrate proteins. In the future, it is necessary to identify these proteins and determine their germline-specific functions in order to understand which signaling pathways and mechanisms mediate Hyd's involvement in oogenesis control.

DATA AVAILABILITY STATEMENT

The original contributions presented in the study are included in the article/**Supplementary Material**, further inquiries can be directed to the corresponding author.

AUTHOR CONTRIBUTIONS

ND, YG, and SF designed and conducted the experiments, analyzed the data, wrote and prepared the manuscript. EUB provided obtaining and analysis of electron microscopic data. EMB analyzed the data. All authors contributed to the article and approved the submitted version.

FUNDING

This work was supported by the ICG SB RAS budget project (No. 0324-2019-0042-C-01) and the grant from the Russian Foundation for Basic Research (No. 20-04-00496-a).

ACKNOWLEDGMENTS

Microscopic analyses were carried out at the Multiple-Access Center for Microscopy of Biological Subjects of the ICG SB RAS.

SUPPLEMENTARY MATERIAL

The Supplementary Material for this article can be found online at: https://www.frontiersin.org/articles/10.3389/fcell.2020.600868/full#supplementary-material

Supplementary Table 1 | 'Extra round of mitosis' phenotype manifestations.

Supplementary Table 2 | Hyd interacting proteins.

Supplementary Figure 1 | Egg chamber sizes reduction in *oskar-GAL4/UAS-hyd*-RNAi females. The measurement of the length and width of the egg chambers was carried out using LSM5 Image Browser (Zeiss). The length and width of the egg chambers in *oskar-GAL4/UAS-hyd*-RNAi ovaries are statistically valid less than in the wild type (Oregon). Data represent mean ± s.d., Student's *t*-test; $^{***}P < 0.001$; $n = 10$ egg chambers per condition. Diagrams were generated and statistical analyses performed in Prism (GraphPad).

REFERENCES

Bakhrat, A., Pritchett, T., Peretz, G., Mccall, K., and Abdu, U. (2010). *Drosophila* Chk2 and p53 proteins induce stage-specific cell death independently during oogenesis. *Apoptosis* 15, 1425–1434. doi: 10.1007/s10495-010-0539-z

Barth, J. M., Szabad, J., Hafen, E., and Köhler, K. (2011). Autophagy in *Drosophila ovaries* is induced by starvation and is required for oogenesis. *Cell Death Differ.* 18, 915–924. doi: 10.1038/cdd.2010.157

Barton, L. J., Pinto, B. S., Wallrath, L. L., and Geyer, P. K. (2013). The *Drosophila* nuclear lamina protein otefin is required for germline stem cell survival. *Dev. Cell.* 25, 645–654. doi: 10.1016/j.devcel.2013.05.023

Bergmann, A. (2010). The role of ubiquitylation for the control of cell death in *Drosophila*. *Cell Death Diff.* 17, 61–67. doi: 10.1038/cdd.2009.70

Bhoj, V. G., and Chen, Z. J. (2009). Ubiquitylation in innate and adaptive immunity. *Nature* 458, 430–437. doi: 10.1038/nature07959

Bolobolova, E. U., Dorogova, N. V., and Fedorova, S. A. (2020). Major scenarios of genetically regulated cell death during oogenesis in *Drosophila melanogaster*. *Rus. J. Genet.* 56, 655–665. doi: 10.1134/S1022795420060034

Callaghan, M. J., Russell, A. J., Woollatt, E., Sutherland, G. R., Sutherland, R. L., and Watts, C. K. (1998). Identification of a human HECT family protein with homology to the *Drosophila* tumor suppressor gene hyperplastic discs. *Oncogene* 17, 3479–3491. doi: 10.1038/sj.onc.1202249

Chen, D., and McKearin, D. M. (2003). A discrete transcriptional silencer in the bam gene determines asymmetric division of the *Drosophila* germline stem cell. *Development* 130, 1159–1170. doi: 10.1242/dev.00325

Chen, D., Wang, Q., Huang, H., Xia, L., Jiang, X., Kan, L., et al. (2009). Effete-mediated degradation of Cyclin A is essential for the maintenance of germline stem cells in *Drosophila*. *Development* 136, 4133–4142. doi: 10.1242/dev.039032

Chen, D., Zhou, L., Sun, F., Sun, M., and Tao, X. (2018). Cyclin B3 deficiency impairs germline stem cell maintenance and its overexpression delays cystoblast differentiation in *Drosophila ovary*. *Int. J. Mol. Sci.* 19:298. doi: 10.3390/ijms19010298

Clancy, J. L., Henderson, M. J., Russell, A. J., Anderson, D. W., Bova, R. J., Campbell, I. G., et al. (2003). EDD, the human orthologue of the hyperplastic discs tumour suppressor gene, is amplified and overexpressed in cancer. *Oncogene* 22, 5070–5081. doi: 10.1038/sj.onc.1206775

Dikic, I., Wakatsuki, S., and Walters, K. J. (2009). Ubiquitin-binding domains - from structures to functions. *Nat. Rev. Mol. Cell. Biol.* 10, 659–671. doi: 10.1038/nrm2767

Dorogova, N. V., Fedorova, E. V., Bolobolova, E. U., Ogienko, A. A., and Baricheva, E. M. (2014). GAGA protein is essential for male germ cell development in *Drosophila*. *Genesis* 52, 738–751. doi: 10.1002/dvg.22789

Doronkin, S., Djagaeva, I., and Beckendorf, S. K. (2003). The COP9 signalosome promotes degradation of Cyclin E during early *Drosophila oogenesis*. *Dev. Cell.* 4, 699–710. doi: 10.1016/s1534-5807(03)00121-7

Drummond-Barbosa, D., and Spradling, A. C. (2001). Stem cells and their progeny respond to nutritional changes during *Drosophila oogenesis*. *Dev. Biol.* 231, 265–278. doi: 10.1006/dbio.2000.0135

Gancz, D., Lengil, T., and Gilboa, L. (2011). Coordinated regulation of niche and stem cell precursors by hormonal signaling. *PLoS Biol.* 9:e1001202. doi: 10.1371/journal.pbio.1001202

Giorgi, F., and Deri, P. (1976). Cell death in ovarian chambers of *Drosophila melanogaster*. *J. Embryol. Exp. Morphol.* 35, 521–533.

Greenwood, J., and Gautier, J. (2005). From oogenesis through gastrulation: developmental regulation of apoptosis. *Semin. Cell. Dev. Biol.* 16, 215–224. doi: 10.1016/j.semcdb.2004.12.002

Guild, G. M., Connelly, P. S., Shaw, M. K., and Tilney, L. G. (1997). Actin filament cables in *Drosophila* nurse cells are composed of modules that slide passively past one another during dumping. *J. Cell Biol.* 138, 783–797. doi: 10.1083/jcb.138.4.783

Hariharan, I. K., and Bilder, D. (2006). Regulation of imaginal disc growth by tumor-suppressor genes in *Drosophila*. *Annu. Rev. Genet.* 40, 335–361. doi: 10.1146/annurev.genet.39.073003.100738

Hawkins, N. C., Thorpe, J., and Schüpbach, T. (1996). Encore, a gene required for the regulation of germ line mitosis and oocyte differentiation during *Drosophila oogenesis*. *Development* 122, 281–290.

Hay, B. A., and Guo, M. (2006). Caspase-dependent cell death in *Drosophila*. *Annu. Rev. Cell. Dev. Biol.* 22, 623–650. doi: 10.1146/annurev.cellbio.21.012804.093845

Hinnant, T. D., Merkle, J. A., and Ables, E. T. (2020). Coordinating proliferation, polarity, and cell fate. *Front. Cell. Dev. Biol.* 8:19. doi: 10.3389/fcell.2020.00019

Hou, Y. C., Chittaranjan, S., Barbosa, S. G., Mccall, K., and Gorski, S. M. (2008). Effector caspase Dcp-1 and IAP protein Bruce regulate starvation-induced autophagy during *Drosophila melanogaster* oogenesis. *J. Cell. Biol.* 182, 1127–1139. doi: 10.1083/jcb.200712091

Huang, J., Reilein, A., and Kalderon, D. (2017). Yorkie and Hedgehog independently restrict BMP production in escort cells to permit germline differentiation in the. *Development* 144, 2584–2594. doi: 10.1242/dev.147702

Jacobs, H. W., Knoblich, J. A., and Lehner, C. F. (1998). *Drosophila* Cyclin B3 is required for female fertility and is dispensable for mitosis like Cyclin B. *Genes Dev.* 12, 3741–3751. doi: 10.1101/gad.12.23.3741

Jenkins, V. K., Timmons, A. K., and Mccall, K. (2013). Diversity of cell death pathways: insight from the fly ovary. *Trends Cell. Biol.* 23, 567–574. doi: 10.1016/j.tcb.2013.07.005

Jeong, E. B., Jeong, S. S., Cho, E., and Kim, E. Y. (2019). Makorin 1 is required for *Drosophila oogenesis* by regulating insulin/Tor signaling. *PLoS One* 14:e0215688. doi: 10.1371/journal.pone.0215688

Ji, S., Li, C., Hu, L., Liu, K., Mei, J., Luo, Y., et al. (2017). Bam-dependent deubiquitinase complex can disrupt germ-line stem cell maintenance by targeting cyclin A. *Proc. Natl. Acad. Sci. U.S.A.* 114, 6316–6321. doi: 10.1073/pnas.1619188114

Kahney, E. W., Snedeker, J. C., and Chen, X. (2019). Regulation of *Drosophila* germline stem cells. *Curr. Opin. Cell Biol.* 60, 27–35. doi: 10.1016/j.ceb.2019.03.008

Kiger, A. A., White-Cooper, H., and Fuller, M. T. (2000). Somatic support cells restrict germline stem cell self-renewal and promote differentiation. *Nature* 407, 750–754. doi: 10.1038/35037606

King, R. C. (1957). Oogenesis in adult *Drosophila melanogaster*. II. Stage distribution as a function of age. *Growth* 21, 95–102.

LaFever, L., Feoktistov, A., Hsu, H. J., and Drummond-Barbosa, D. (2010). Specific roles of Target of rapamycin in the control of stem cells and their progeny in the *Drosophila ovary*. *Development* 137, 2117–2126. doi: 10.1242/dev.050351

Lai, C. M., Lin, K. Y., Kao, S. H., Chen, Y. N., Huang, F., and Hsu, H. J. (2017). Hedgehog signaling establishes precursors for germline stem cell niches by regulating cell adhesion. *J. Cell. Biol.* 216, 1439–1453. doi: 10.1083/jcb.201610063

Laws, K. M., and Drummond-Barbosa, D. (2017). Control of germline stem cell lineages by diet and physiology. *Results Probl. Cell Diff.* 59, 67–99. doi: 10.1007/978-3-319-44820-6_3

Lee, J. D., Amanai, K., Shearn, A., and Treisman, J. E. (2002). The ubiquitin ligase Hyperplastic discs negatively regulates hedgehog and decapentaplegic expression by independent mechanisms. *Development* 129, 5697–5706. doi: 10.1242/dev.00159

Lilly, M. A., De Cuevas, M., and Spradling, A. C. (2000). Cyclin A associates with the fusome during germline cyst formation in the *Drosophila ovary*. *Dev. Biol.* 218, 53–63. doi: 10.1006/dbio.1999.9570

Lu, T., Wang, S., Gao, Y., Mao, Y., Yang, Z., Liu, L., et al. (2015). COP9-Hedgehog axis regulates the function of the germline stem cell progeny differentiation niche in the *Drosophila ovary*. *Development* 142, 4242–4252. doi: 10.1242/dev.124768

MacDonald, T. M., Thomas, L. N., Daze, E., Marignani, P., Barnes, P. J., and Too, C. K. (2019). Prolactin-inducible EDD E3 ubiquitin ligase promotes TORC1 signalling, anti-apoptotic protein expression, and drug resistance in breast cancer cells. *Am. J. Cancer Res.* 9, 1484–1503.

Mansfield, E., Hersperger, E., Biggs, J., and Shearn, A. (1994). Genetic and molecular analysis of hyperplastic discs, a gene whose product is required for regulation of cell proliferation in *Drosophila melanogaster* imaginal discs and germ cells. *Dev. Biol.* 165, 507–526. doi: 10.1006/dbio.1994.1271

Martin, P., Martin, A., and Shearn, A. (1977). Studies of l(3)c43hs1 a polyphasic, temperature-sensitive mutant of *Drosophila melanogaster* with a variety of imaginal disc defects. *Dev. Biol.* 55, 213–232. doi: 10.1016/0012-1606(77)90168-3

Mathieu, J., and Huynh, J. R. (2017). Monitoring complete and incomplete abscission in the germ line stem cell lineage of *Drosophila ovaries*. *Methods Cell. Biol.* 137, 105–118. doi: 10.1016/bs.mcb.2016.03.033

Metzger, M. B., Hristova, V. A., and Weissman, A. M. (2012). HECT and RING finger families of E3 ubiquitin ligases at a glance. *J. Cell. Sci.* 125, 531–537. doi: 10.1242/jcs.091777

Muzzopappa, M., and Wappner, P. (2005). Multiple roles of the F-box protein Slimb in *Drosophila* egg chamber development. *Development* 132, 2561–2571. doi: 10.1242/dev.01839

Ohlmeyer, J. T., and Schüpbach, T. (2003). Encore facilitates SCF-Ubiquitin-proteasome-dependent proteolysis during *Drosophila oogenesis*. *Development* 130, 6339–6349. doi: 10.1242/dev.00855

Ohlstein, B., and McKearin, D. (1997). Ectopic expression of the *Drosophila* Bam protein eliminates oogenic germline stem cells. *Development* 124, 3651–3662.

Pertceva, J. A., Dorogova, N. V., Bolobolova, E. U., Nerusheva, O. O., Fedorova, S. A., and Omelyanchuk, L. V. (2010). The role of *Drosophila* hyperplastic discs gene in spermatogenesis. *Cell Biol. Int.* 34, 991–996. doi: 10.1042/CBI20100105

Peterson, J. S., Timmons, A. K., Mondragon, A. A., and Mccall, K. (2015). The end of the beginning: cell death in the germline. *Curr. Top. Dev. Biol.* 114, 93–119. doi: 10.1016/bs.ctdb.2015.07.025

Pritchett, T. L., and McCall, K. (2012). Role of the insulin/Tor signaling network in starvation-induced programmed cell death in *Drosophila oogenesis*. *Cell Death Diff.* 19, 1069–1079. doi: 10.1038/cdd.2011.200

Pritchett, T. L., Tanner, E. A., and Mccall, K. (2009). Cracking open cell death in the *Drosophila ovary*. *Apoptosis* 14, 969–979. doi: 10.1007/s10495-009-0369-z

Reubens, M. C., Biller, M. D., Bedsole, S. E., Hopkins, L. T., Ables, E. T., and Christensen, T. W. (2015). Mcm10 is required for oogenesis and early embryogenesis in *Drosophila*. *Mech. Dev.* 138(Pt 3), 291–299. doi: 10.1016/j.mod.2015.09.002

Rodriguez, A., Chen, P., Oliver, H., and Abrams, J. M. (2002). Unrestrained caspase-dependent cell death caused by loss of Diap1 function requires the *Drosophila* Apaf-1 homolog, Dark. *EMBO J.* 21, 2189–2197. doi: 10.1093/emboj/21.9.2189

Sarkissian, T., Timmons, A., Arya, R., Abdelwahid, E., and White, K. (2014). Detecting apoptosis in *Drosophila* tissues and cells. *Methods* 68, 89–96. doi: 10.1016/j.ymeth.2014.02.033

Scheffner, M., Nuber, U., and Huibregtse, J. M. (1995). Protein ubiquitination involving an E1-E2-E3 enzyme ubiquitin thioester cascade. *Nature* 373, 81–83. doi: 10.1038/373081a0

Shearer, R. F., Iconomou, M., Watts, C. K., and Saunders, D. N. (2015). Functional roles of the E3 ubiquitin ligase UBR5 in cancer. *Mol. Cancer Res.* 13, 1523–1532. doi: 10.1158/1541-7786.MCR-15-0383

Spradling, A. C. (1993). Germline cysts: communes that work. *Cell* 72, 649–651. doi: 10.1016/0092-8674(93)90393-5

Styhler, S., Nakamura, A., Swan, A., Suter, B., and Lasko, P. (1998). Vasa is required for GURKEN accumulation in the oocyte, and is involved in oocyte differentiation and germline cyst development. *Development* 125, 1569–1578.

Tavosanis, G., and Gonzalez, C. (2003). gamma-Tubulin function during female germ-cell development and oogenesis in *Drosophila*. *Proc. Natl. Acad. Sci. U.S.A.* 100, 10263–10268. doi: 10.1073/pnas.1731925100

Wang, G., Tang, X., Chen, Y., Cao, J., Huang, Q., Ling, X., et al. (2014). Hyperplastic discs differentially regulates the transcriptional outputs of hedgehog signaling. *Mech. Dev.* 133, 117–125. doi: 10.1016/j.mod.2014.05.002

Wang, Z., and Lin, H. (2005). The division of *Drosophila germline* stem cells and their precursors requires a specific cyclin. *Curr. Biol.* 15, 328–333. doi: 10.1016/j.cub.2005.02.016

Yang, S. A., Wang, W. D., Chen, C. T., Tseng, C. Y., Chen, Y. N., and Hsu, H. J. (2013). FOXO/Fringe is necessary for maintenance of the germline stem cell niche in response to insulin insufficiency. *Dev. Biol.* 382, 124–135. doi: 10.1016/j.ydbio.2013.07.018

Conflict of Interest: The authors declare that the research was conducted in the absence of any commercial or financial relationships that could be construed as a potential conflict of interest.

frontiers in Cell and Developmental Biology

ORIGINAL RESEARCH
published: 17 November 2020
doi: 10.3389/fcell.2020.581942

The Role of HDAC6 in TDP-43-Induced Neurotoxicity and UPS Impairment

Shinrye Lee[1†], Younghwi Kwon[1,2†], Seyeon Kim[1,2], Myungjin Jo[1], Yu-Mi Jeon[1], Mookyung Cheon[1], Seongsoo Lee[3], Sang Ryong Kim[4,5], Kiyoung Kim[6] and Hyung-Jun Kim[1*]*

[1] Dementia Research Group, Korea Brain Research Institute, Daegu, South Korea, [2] Department of Brain and Cognitive Sciences, DGIST, Daegu, South Korea, [3] Gwangju Center, Korea Basic Science Institute (KBSI), Gwangju, South Korea, [4] School of Life Sciences, BK21 Plus KNU Creative BioResearch Group, Institute of Life Science and Biotechnology, Kyungpook National University, Daegu, South Korea, [5] Brain Science and Engineering Institute, Kyungpook National University, Daegu, South Korea, [6] Department of Medical Biotechnology, Soonchunhyang University, Asan, South Korea

OPEN ACCESS

Edited by:
Inna N. Lavrik, University Hospital Magdeburg, Germany

Reviewed by:
Guanghui Wang, Soochow University, China
Shinsuke Ishigaki, Nagoya University, Japan

***Correspondence:**
Kiyoung Kim
kiyoung2@sch.ac.kr
Hyung-Jun Kim
kijang1@kbri.re.kr

[†] These authors have contributed equally to this work

Specialty section:
This article was submitted to Cell Death and Survival, a section of the journal Frontiers in Cell and Developmental Biology

Received: *10 July 2020*
Accepted: *30 October 2020*
Published: *17 November 2020*

Citation:
Lee SR, Kwon YH, Kim SY, Jo MJ, Jeon Y-M, Cheon MY, Lee SS, Kim SR, Kim KY and Kim H-J (2020) The Role of HDAC6 in TDP-43-Induced Neurotoxicity and UPS Impairment. Front. Cell Dev. Biol. 8:581942. doi: 10.3389/fcell.2020.581942

Transactive response DNA-binding protein 43 (TDP-43)-induced neurotoxicity is currently well recognized as a contributor to the pathology of amyotrophic lateral sclerosis (ALS), and the deposition of TDP-43 has been linked to other neurodegenerative diseases, such as frontotemporal lobar degeneration (FTLD) and Alzheimer's disease (AD). Recent studies also suggest that TDP-43-induced neurotoxicity is associated with ubiquitin-proteasome system (UPS) impairment. Histone deacetylase 6 (HDAC6) is a well-known cytosolic deacetylase enzyme that suppresses the toxicity of UPS impairment. However, the role of HDAC6 in TDP-43-induced neurodegeneration is largely unknown. In this study, we found that HDAC6 overexpression decreased the levels of insoluble and cytosolic TDP-43 protein in TDP-43-overexpressing N2a cells. In addition, TDP-43 overexpression upregulated HDAC6 protein and mRNA levels, and knockdown of *Hdac6* elevated the total protein level of TDP-43. We further found that HDAC6 modulates TDP-43-induced UPS impairment via the autophagy-lysosome pathway (ALP). We also showed that TDP-43 promoted a short lifespan in flies and that the accumulation of ubiquitin aggregates and climbing defects were significantly rescued by overexpression of HDAC6 in flies. Taken together, these findings suggest that HDAC6 overexpression can mitigate neuronal toxicity caused by TDP-43-induced UPS impairment, which may represent a novel therapeutic approach for ALS.

Keywords: tar DNA-binding protein 43, histone deacetylase 6, ubiquitin-proteasome system, amyotrophic lateral sclerosis, autophagy-lysosome pathway

INTRODUCTION

Transactive response DNA-binding protein 43 (TDP-43) is an evolutionarily conserved member of the heterogeneous nuclear ribonucleoprotein (hnRNP) family, and it is encoded by the *TARDBP* gene (Ou et al., 1995). Previous studies have revealed that TDP-43 regulates RNA metabolic processes, such as transcription, splicing, translation, and regulating stability of mRNA (Strong et al., 2007; Buratti and Baralle, 2008). TDP-43 is predominantly localized in the nucleus, but it can shuttle between the nucleus and the cytoplasm (Barmada et al., 2010). The accumulation

of misfolded or aggregated protein in affected neurons is a major pathological feature in most neurodegenerative diseases. It is already known that cytoplasmic accumulation of TDP-43 aggregates is one of the major characteristics of TDP-43 proteinopathy (Kim et al., 2014; Scotter et al., 2015; Shenouda et al., 2018), and this is a common pathological feature associated with many neurodegenerative diseases, such as Alzheimer's disease (AD), frontotemporal lobar degeneration (FTLD), and amyotrophic lateral sclerosis (ALS) (Neumann et al., 2006; Mackenzie et al., 2011; Tremblay et al., 2011). Many neuropathological mechanisms, such as oxidative stress, mitochondrial dysfunction, neuroinflammation, and ER stress, are linked to TDP-43 proteinopathy (Duan et al., 2010; Kim et al., 2014; Zhao et al., 2015; Wang et al., 2019). In particular, emerging clinical and experimental evidence suggests that dysfunctions in protein quality control, including problems with the ubiquitin-proteasome system (UPS) impairment, are the core pathological mechanism of TDP-43-mediated neurodegeneration (Scotter et al., 2014; Lee et al., 2019).

Histone acetyltransferases (HATs) and histone deacetylases (HDACs) are two classes of enzymes whose opposing activities regulate the dynamic levels of acetylation of specific lysine residues in histones and many other proteins (Yang and Seto, 2007). Histone deacetylase 6 (HDAC6) is a member of the class II HDAC family, and it contains a ubiquitin binding domain. Unlike other HDACs, HDAC6 targets non-histone substrates, such as α-tubulin, heat shock protein 90 (HSP90), and cortactin, to modulate widespread biological processes (Zhang et al., 2003, 2007; Kovacs et al., 2005). HDAC6 contains a ubiquitin-binding domain that binds to ubiquitinated proteins for degradation. In a previous study, HDAC6 rescued proteasome impairment in *Drosophila* (Pandey et al., 2007). Additionally, HDAC6 controls the autophagy-lysosome pathway (ALP). HDAC6 is not required for autophagy activation; rather, it leads to fusion of autophagosomes and lysosomes (Lee et al., 2010). Regarding interplay between autophagy and the UPS, HDAC6 was recently found to be a key molecule in many neurodegenerative diseases. Nevertheless, the functions of HDAC6 in neurodegenerative diseases are controversial. One study showed that deletion of HDAC6 postponed disease progression in a $SOD1^{G93A}$ ALS mouse model (Taes et al., 2013).

In this study, we investigated the potential role of HDAC6 in TDP-43-induced neurotoxicity using mammalian cell models as well as a *Drosophila* model of TDP-43 proteinopathy. We demonstrated that HDAC6 regulates the mislocalization and aggregation of TDP-43. Moreover, we determined that HDAC6 plays a critical role in the deposition of ubiquitinated aggregates and neurotoxicity induced by TDP-43 accumulation through regulation of the ALP pathway in TDP-43 proteinopathy.

MATERIALS AND METHODS

Reagents and Antibodies

The following reagents were purchased from the indicated providers: dimethyl sulfoxide (DMSO; Sigma, D8418) and mifepristone (RU-486; Sigma, M8046). The following antibodies were used for immunoblotting: mouse anti-TurboGFP (Origene, TA150041), rabbit anti-TDP-43 (Proteintech, 10782-2-AP), rabbit anti-LC3 (MBL, PM036), mouse anti-Polyubiquitin (Enzo Life Science, BML-PW8805), mouse anti-Flag (Cell Signaling Technology, 2044), rabbit anti-HDAC6 (Santa Cruz Biotechnology, sc-11420), mouse anti-Lamin A/C (EMD Millipore, 05-714), HRP-conjugated anti-alpha-tubulin (Cell Signaling Technology, 9099), HRP-conjugated anti-rabbit IgG (Santa Cruz Biotechnology, sc-2004), HRP-conjugated mouse IgM (Abcam, ab97230), and HRP-conjugated mouse IgG (Santa Cruz Biotechnology, sc-2005). The following antibodies were used for immunocytochemistry (ICC): rabbit anti-cleaved caspase-3 (CC3) antibody (Cell Signaling Technology, 9664) and Alexa 594-conjugated anti-rabbit IgG (Jackson ImmunoResearch, 111-585-144). The following antibodies were used for immunohistochemistry: rat anti-ELAV (DSHB, RAT-ELAV-7), mouse anti-Polyubiquitin (Enzo Life Science, BML-PW8805), Alexa-488 conjugated rat IgG (Jackson ImmunoResearch, 112-545-167), and Alexa-594 conjugated mouse IgM (Jackson ImmunoResearch, 115-587-020).

Cell Lines

The Neuro-2a (N2a) mouse neuroblastoma cell line was maintained in Dulbecco's modified Eagle's medium (DMEM, Gibco, 11995-065) supplemented with 10% heat-inactivated fetal bovine serum (FBS, Gibco, 16000-044) and 50 μg/ml penicillin-streptomycin (Gibco, 15140-122).

Transfection

Neuro-2a cells in six-well plates (40×10^4 cells/ml) were transfected with 4 μg of *Gfp* (*pCMV6-AC-Gfp*, Origene Technologies, PS100010) or human *TDP-43* (*pCMV6-AC-TDP-43-Gfp*, Origene Technologies, RG210639) vectors using Lipofectamine 3000 reagent (Invitrogen). Two days after transfection, the knockdown of target proteins was confirmed by immunoblot analysis. For siRNA transfection, N2a cells in six-well plates (40×10^4 cells/ml) were transfected with a control siRNA (Dharmacon; D-001810-10) or mouse *Hdac6* siRNA (Dharmacon; L-043456-02) using Lipofectamine RNAiMAX reagent (Invitrogen). Two days after transfection, the knockdown of target proteins was confirmed by RT-PCR.

Stable Transfection

Neuro-2a cells in six-well plates (40×10^4 cells/ml) were transfected with 4 μg of human *HDAC6* cDNA using Lipofectamine 3000 reagent (Invitrogen). An empty *pCMV6-Flag* vector was used as a negative control. Stable transfectants were selected in the presence of 800 μg/ml G418 (Gibco, 10131-027). The expression of transgenes was confirmed by immunoblot and ICC analysis.

Immunoblot Analysis

Cells were homogenized in Cell Lysis Buffer (Cell Signaling Technology, 9803) containing protease and phosphatase inhibitor cocktails. Protein concentrations of the cell lysates were determined by BCA protein assay (Thermo Fisher Scientific,

23225). Next, the protein extracts were mixed with 4× Bolt LDS sample buffer (Invitrogen) and 10× Bolt Sample Reducing Agent buffer (Invitrogen), and then they were boiled at 95°C for 5 min. An equal amount of protein from each sample was separated on Bolt 4–12% Bis-Tris gels (Invitrogen, NW04120BOX) or NuPAGE 3-8% Tris-Acetate gels (Invitrogen, EA0378BOX), and then it was transferred to polyvinylidene difluoride (PVDF, Invitrogen, LC2005) membranes. After blocking membranes with 5% skim milk in TBS with 0.025% Tween 20, blots were probed with antibodies as indicated and detected with an ECL prime kit (GE healthcare, RPN2232). Samples from three independent experiments were used, and the relative expression levels were determined using a Fusion-FX imaging system (Viber Lourmat).

Preparation of Soluble and Insoluble Cell Extracts

Cells were homogenized in RIPA buffer with protease and phosphatase inhibitor cocktails (Roche, 11836153001, 04906837001). Fractions that were soluble and insoluble in 1% Triton X-100 were obtained by centrifugation at 100,000 × *g* for 30 min at 4°C. Supernatants containing the soluble fractions were harvested, and the pellets for insoluble fractions were solubilized in 2% SDS detergent Cell Lysis Buffer (Cell Signaling Technology, 9803). After sonication, the cell lysates were mixed with 4× Bolt LDS Sample buffer (Invitrogen, B0007) and 10× Bolt Sample Reducing Agent buffer (Invitrogen, B0009), and then they were boiled at 95°C for 5 min.

Nuclear and Cytoplasmic Extraction

Cells were fractionated using NE-PER nuclear and cytosolic extraction reagents (Thermo Fisher Scientific, 78833). Nuclear and cytoplasmic fractions were obtained in ice-cold CER I and CER II buffer, respectively, by centrifugation at 16,000 × *g* for 5 min at 4°C. Supernatants containing the cytoplasmic extract were harvested, and the pellets were solubilized in ice-cold NER buffer. After vortexing, the extracts were centrifuged at 16,000 × *g* for 10 min at 4°C. Supernatants containing the nuclear extract were harvested. The extracts were mixed with 4× Bolt LDS sample buffer and 10× Bolt Sample Reducing Agent buffer, and then they were boiled at 95°C for 5 min.

Quantitative RT-PCR

RNA was extracted from cells by using a TRIzol plus RNA Purification Kit (Invitrogen, 12183-555) according to the manufacturer's instructions. cDNA synthesis was performed at 37°C for 120 min from 100 ng of RNA using a High Capacity cDNA Reverse Transcription kit (Applied Biosystems, 4368814). Quantitative RT-PCR was performed using a one-step SYBR® PrimeScript™ RT-PCR kit (Takara Bio Inc., RR420A) according to the manufacturer's instructions, which was followed by detection using an Applied Biosystems 7500 Real-Time PCR system (Applied Biosystems). *18S rRNA* and *Gapdh* were used as internal controls. The $2^{-\Delta\Delta Ct}$ method was used to calculate relative changes in gene expression, which were determined by real-time PCR experiments (Livak and Schmittgen, 2001).

Immunostaining

For ICC, cells were fixed in 4% paraformaldehyde (PFA) in PBS (Gibco, 70011-044) for 30 min at room temperature. The cells were then washed three times with PBS and permeabilized in PBS-T (0.3% Triton X-100) for 15 min at room temperature. After blocking with 5% BSA in PBS-T for 1 h, a rabbit anti-CC3 antibody (1:500 dilution) in 1% BSA in PBS-T was incubated with the cells overnight at 4°C. The cells were then washed three times with PBS and incubated with a secondary antibody [Alexa-594-conjugated rabbit IgG (Jackson ImmunoResearch, 111-585-144, 1:500 dilution)] for 1 h at room temperature. Then, samples were mounted and observed with a fluorescence microscope (Nikon). Photomicrographs from three randomly chosen fields were captured, and the number of $CC3^+$ cells was counted among total GFP^+ cells. For immunohistochemistry, adult flies were dissected in PBS and fixed in 4% PFA in PBS for 30 min at room temperature. The brains were then washed six times with PBS and preincubated in PBS-T for 15 min at room temperature. After blocking with 5% normal goat serum in PBS-T overnight at 4°C, primary antibodies [rat anti-ELAV (DSHB, RAT-ELAV-7, 1:100 dilution) and mouse anti-Polyubiquitin (Enzo Life Science, BML-PW8805, 1:500 dilution)] in 5% normal goat serum in PBS-T were incubated with the tissues for 2 days at 4°C. The brains were then washed six times with PBS and incubated with an Alexa-conjugated secondary antibody for 2 days at 4°C. Alexa 488-conjugated rat IgG (Jackson ImmunoResearch, 112-545-167, 1:500 dilution) and Alexa 594-conjugated mouse IgM (Jackson ImmunoResearch, 115-587-020, 1:500 dilution) were used as secondary antibodies as indicated. The samples were mounted and observed with a fluorescence confocal microscope (Leica). Photomicrographs from three randomly chosen fields were captured, and the number of polyubiquitin$^+$ cells was counted.

Mitochondrial Activity Assay

To assess neuronal mitochondrial dysfunction, *HDAC6-Flag* stable cells were cotransfected with *Gfp* or *TDP-43-Gfp* expression constructs. Two days after transfection, *Gfp*-transfected live cells were subjected to FACS. The sorted *Gfp*-transfected cells (8×10^4 cells/ml) were seeded into XF24-well culture plates (Seahorse Bioscience) and then were allowed to acclimate for 1 day in fresh DMEM. Cells were then washed twice with XF Base Medium supplemented with 2 mM L-glutamine, 10 mM D-glucose, and 1 mM sodium pyruvate (pH 7.4) before being incubated at 37°C in a non-CO_2 incubator for 1 h. Mitochondrial dysfunction was evaluated using a XF Cell Mito Stress Test Kit (Seahorse Bioscience) according to the manufacturer's instructions, which was followed by measurement using an XF24 Extracellular Flux Analyzer (Seahorse Bioscience). First, the 24-well utility plate was hydrated, treated with 2 μM oligomycin, 2 μM carbonyl cyanide 4-(trifluoromethoxy) phenylhydrazone (FCCP), 0.5 μM antimycin A/rotenone, and then calibrated by the analyzer. The basal oxygen consumption rate (OCR), ATP production, maximum reserve, and respiratory capacity were calculated as previously described (Dranka et al., 2011), with averages calculated from five wells per condition in each individual experiment. The OCR was

normalized to the total protein concentration (OD). After the seahorse analysis, the plate was centrifuged at 280 × *g* for 5 min. The media were aspirated, and the cells were washed twice with PBS. Then, cells were lyzed in RIPA buffer. Protein concentrations of cell lysates were determined using a BCA assay kit.

Fly Strains

Drosophila stocks were maintained on standard cornmeal agar media at 24°C unless otherwise noted. UAS-TDP-43 and UAS-ATXN2-32Q were described previously (Kim et al., 2014). UAS-HDAC6 has been described previously (Pandey et al., 2007). All other stocks were from The Bloomington Stock Center.

Climbing and Lifespan Assays

Adult males (0–1 day old) were separated and transferred into experimental vials containing fly media or paper mixed with or without RU-486 (in ethanol, 40 μg/ml) at a density of 25 flies per vial ($n > 100$). The number of dead flies was scored daily, and flies were transferred to fresh media or paper every other day. Adult locomotor function was assessed by a previously described method (Feany and Bender, 2000; Lee et al., 2019), and there were 125 flies per genotype for each time point in all experiments.

Statistical Analyses

Data were analyzed by Student's *t*-test (Vassar Stats[1]), one-way ANOVA, or two-way ANOVA test depending on comparison variables, and *post hoc* analysis was performed as indicated (GraphPad Prism Software). Differences were considered significant when $p < 0.05$ and are indicated as follows: $^{*}p < 0.05$; $^{**}p < 0.005$; $^{***}p < 0.001$; and *n.s.*, not significant.

RESULTS

HDAC6 Regulates the Aggregation and Mislocalization of TDP-43

To investigate the interaction between TDP-43 and HDAC6, we generated a stable N2a cell line expressing *Flag*-tagged *HDCA6*. The expression of HDAC6 was examined by western blotting (**Figure 1A**). Furthermore, to determine the effects of HDAC6 on TDP-43 aggregation, we separated cell extracts into insoluble and soluble fractions. Strikingly, HDAC6-overexpressing cells showed significantly decreased TDP-43 levels in both insoluble and soluble fractions (**Figure 1B**). Next, we transfected control *Gfp* or *Gfp*-tagged *TDP-43* into N2a cells that stably expressed either Flag or HDAC6. We found that HDAC6 overexpression clearly reduced total TDP-43-GFP protein levels compared to those of the control (**Figure 1C**). Moreover, we also observed that HDAC6 overexpression also significantly decreases the protein level of disease-associated TDP-43 mutant (TDP-43^{Q331K}-GFP) (**Supplementary Figure S1**).

The pathological features of TDP-43 proteinopathies are the cytoplasmic mislocalization of TDP-43 and the formation of insoluble TDP-43 aggregates. Indeed, cytoplasmic mislocalization of TDP-43 is a marker of TDP-43-induced toxicity (Kim et al., 2014; Scotter et al., 2015; Shenouda et al., 2018). Thus, to investigate whether HDAC6 regulates the mislocalization of TDP-43, we performed subcellular fractionation to measure the TDP-43 protein levels in both the cytoplasm and nucleus. The protein levels of both cytoplasmic and nuclear TDP-43 were significantly decreased in HDAC6-overexpressing cells (**Figure 1D**). These results indicate that HDAC6 overexpression mitigates the aggregation and cytoplasmic mislocalization of TDP-43.

A previous study showed that TDP-43 directly binds to *HDAC6* mRNA and acts as a regulator of HDAC6 expression (Fiesel et al., 2010; Kim et al., 2010). In line with this evidence, we also observed that TDP-43-overexpressing cells upregulated the expression of *HDAC6* mRNA (**Figure 2A**) compared to their levels in GFP-expressing cells. Flag-tagged HDAC6 expression did not affect the transcription level of *HDAC6* (**Supplementary Figure S2**). To further confirm that knockdown of *Hdac6* contributes to TDP-43 protein levels and mislocalization, we downregulated the expression of *Hdac6* by RNAi-mediated gene knockdown. Knockdown of *Hdac6* significantly increased the protein levels of TDP-43 in both insoluble and soluble fractions (**Figure 2B**). The mRNA level of *HDAC6* was also markedly decreased by *Hdac6* siRNA transfection in N2a cells (**Figure 2C**). To determine whether HDAC6 modulates TDP-43 pathology induced by TDP-43 overexpression, we measured the levels of TDP-43 protein by immunoblotting after inhibiting *Hdac6* in N2a cells expressing TDP-43. As expected, the levels of TDP-43 protein were significantly increased by *Hdac6* inhibition in TDP-43-overexpressing cells (**Figure 2D**). We also confirmed these results using a different *Hdac6* siRNA (**Supplementary Figure S3**). To investigate whether the deacetylase activity of HDAC6 is necessary for HDAC6 mediated TDP-43 regulation, we used tubacin as a specific inhibitor of HDAC6 (Lu et al., 2017). Tubacin treatment did not affect the level of TDP-43 protein in TDP-43-overexpressing neuronal cells. The HDAC6 mRNA level was also not altered in Tubacin-treated cells (**Supplementary Figure S4**). Taken together, these results suggest that the non-enzymatic function of HDAC6 is implicated in the regulation of TDP-43 pathology.

HDAC6 Modulates TD-43-Induced UPS Impairment via the Autophagy-Lysosome Pathway

Previous studies demonstrated that HDAC6 modulates the binding affinity of polyubiquitinated proteins, thereby regulating their autophagic degradation (Kawaguchi et al., 2003; Pandey et al., 2007). HDAC6 mediates the sequestration of polyubiquitinated proteins into the autophagosome (Pandey et al., 2007). To determine the effects of HDAC6 on TDP-43-induced UPS impairment, we examined the levels of polyubiquitinated proteins in HDAC6-coexpressing cells and compared them to the levels in cells expressing TDP-43 alone. Consistent with previous findings (Bendotti et al., 2012), TDP-43 overexpression markedly increased the level of polyubiquitinated

[1] www.vassarstats.net

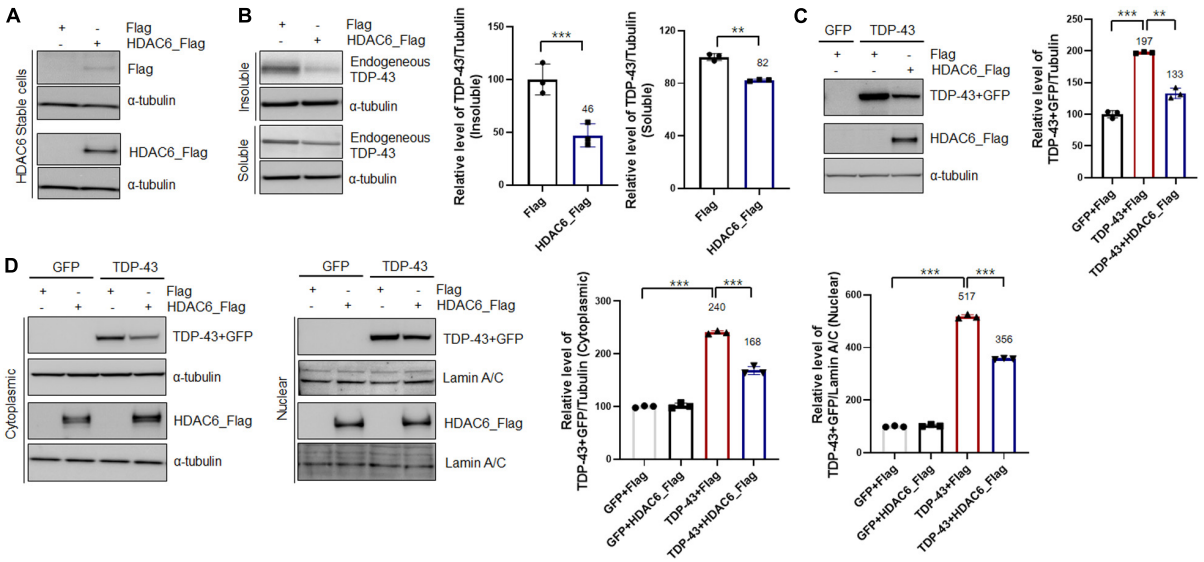

FIGURE 1 | Overexpression of HDAC6 suppresses the aggregation and mislocalization of TDP-43. **(A,B)** Stable Flag- or HDAC6-Flag-expressing cell lines were analyzed by immunoblotting. **(A)** Cell lysates were prepared, and samples were immunoblotted with an anti-Flag or HDAC6 antibody. **(B)** Protein levels of soluble and insoluble TDP-43 in HDAC6-Flag-expressing cells. Flag- or HDAC6-Flag-expressing cells were fractionated to generate a supernatant (the soluble fraction) and a pellet (the insoluble fraction) using lysis buffer containing 1% Triton X-100. Both soluble and insoluble TDP-43 protein levels were significantly decreased by HDAC6-Flag expression. Data are presented as the mean ± SD of three independent experiments. $^{**}p < 0.005$ and $^{***}p < 0.001$ (Student's *t*-test). **(C,D)** Stable Flag- or HDAC6-Flag-expressing cells were transiently transfected with a plasmid containing either *Gfp* or *TDP-43-Gfp* for 2 days. **(C)** Immunoblot analysis of an anti-TDP-43 or HDAC6 antibody. HDAC6 overexpression markedly decreased the level of TDP-43. Data are presented as the mean ± SD of three independent experiments. $^{**}p < 0.005$ and $^{***}p < 0.001$ (one-way ANOVA with Tukey's multiple comparison test). **(D)** Protein levels of nuclear and cytoplasmic TDP-43 or HDAC6. HDAC6 overexpression significantly reduced the protein levels of cytoplasmic and nuclear TDP-43 in TDP-43-GFP-expressing cells. Bar graph of the expression levels of cytoplasmic and nuclear TDP-43 normalized to that of tubulin or Lamin A/C. Data are presented as the mean ± SD of three independent experiments. $^{***}p < 0.001$ (one-way ANOVA with Tukey's multiple comparison test).

proteins in insoluble fractions. HDAC6 overexpression effectively decreased the insoluble polyubiquitinated protein levels induced by TDP-43 overexpression, whereas this level was mildly decreased in soluble fractions (**Figure 3A**). We also confirmed these results using MG132 as an inhibitor for the proteasome. Consistently, MG132 treatment also increased insoluble or soluble polyubiquitinated protein levels, and HDAC6 overexpression significantly suppressed MG132-induced accumulation of ubiquitinated proteins in N2a cells (**Supplementary Figure S5**). Moreover, HDAC6 overexpression decreased the endogenous TDP-43 protein in soluble and insoluble fraction (**Supplementary Figure S6**). Furthermore, knockdown of *Hdac6* increased the level of insoluble polyubiquitinated proteins in TDP-43-induced UPS impairment (**Figure 3B**). Moreover, *Hdac6* inhibition did not affect the level of soluble ubiquitinated proteins following TDP-43-induced UPS impairment (**Figure 3B**). We also showed that *Hdac6* knockdown clearly increased the endogenous TDP-43 protein in soluble and insoluble fraction (**Supplementary Figure S7**). Our data suggest that HDAC6 modulates TDP-43-induced UPS impairment in N2a cells.

We next investigated how HDAC6 regulates TDP-43-induced UPS impairment by monitoring the levels of LC3-I/II by western blotting. Interestingly, LC3-I/II levels in TDP-43-overexpressing cells were markedly increased compared to those of control cells. It is already known that the ALP is activated as a compensatory mechanism upon UPS impairment (Wang and Wang, 2015). HDAC6 expression in the TDP-43-expressing cells caused a further increase in LC3-I/II levels (**Figure 3C**). Moreover, knockdown of *Hdac6* completely abolished the levels of LC3-I/II in TDP-43-expressing cells, as opposed to what was observed in GFP-expressing cells (**Figure 3D**). We also confirmed TDP-43 protein levels in HDAC6 overexpressing or knock-down cells (**Supplementary Figure S8**). These results suggest that HDAC6 mediates TDP-43-induced UPS impairment via ALP. To further support this hypothesis, we used Bafilomycin A1 (Baf) as a specific inhibitor of autophagic degradation. We found that HDAC6 overexpression does not affect the level of TDP-43 protein under the condition of ALP inhibition (**Supplementary Figure S9**). These results indicate that HDAC6 overexpression mitigates TDP-43 induced toxicity via the ALP.

HDAC6 Attenuates TDP-43-Induced Mitochondrial Dysfunction and Neurotoxicity

Recent studies have suggested that mitochondrial damage and dysfunction are pathological features of many neurodegenerative diseases, such as ALS, AD, and Parkinson's disease (PD) (Shi et al., 2010; Gautier et al., 2014; Birnbaum et al., 2018). The TDP-43-induced mitochondrial defects could be a key characteristic of TDP-43 pathology. Therefore, to investigate

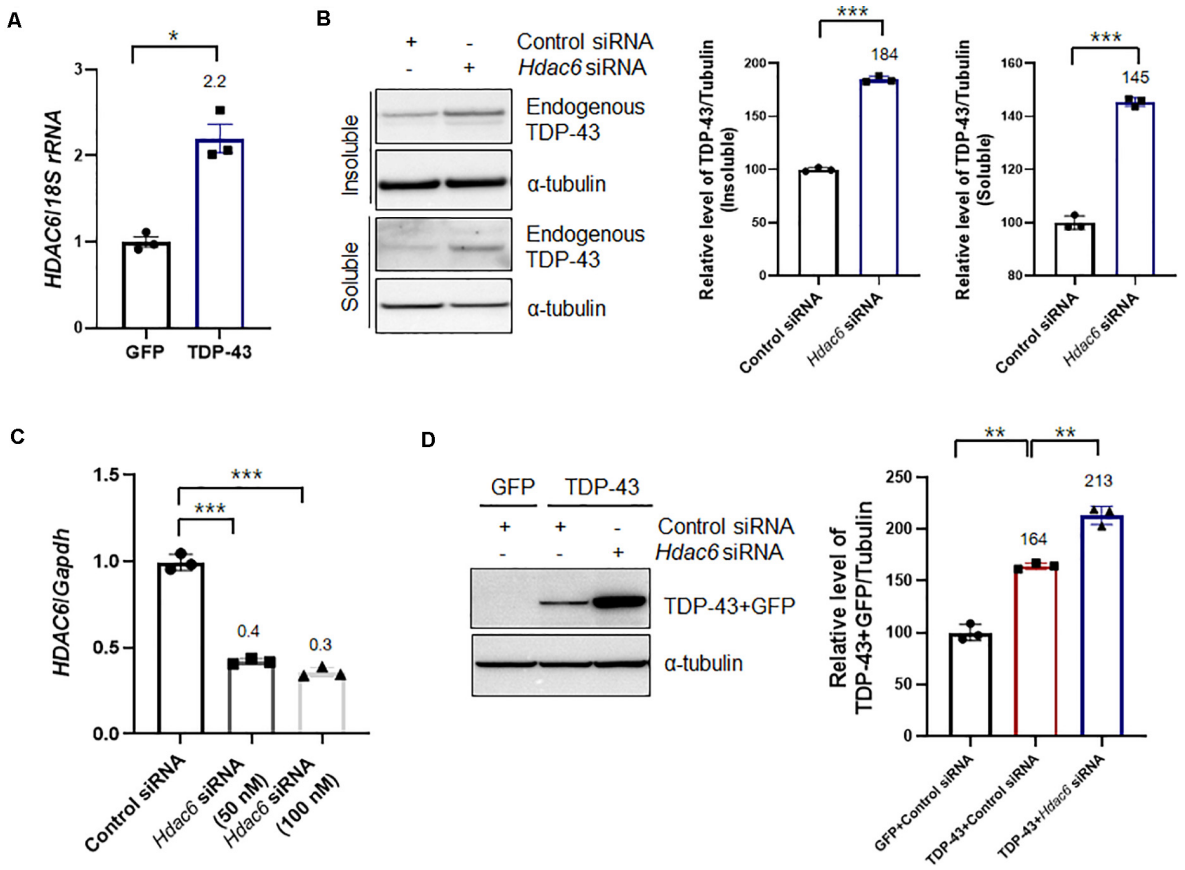

FIGURE 2 | Knockdown of *Hdac6* enhances the TDP-43 pathology in N2a cells. **(A)** N2a cells were transiently transfected with a plasmid containing either *Gfp* or *TDP43-Gfp* and were visualized after 2 days. **(A)** RT-PCR for *HDAC6* mRNA expression in GFP- or TDP-43-GFP-expressing cells. The quantification of *HDAC6* mRNA transcript levels is presented as the mean ± SEM from three independent real-time RT-PCR experiments. *18S rRNA* was used for normalization. $*p < 0.05$ (Student's *t*-test). **(B,C)** N2a cells were transfected with control siRNA (100 nM) or *Hdac6*-specific siRNA (50 or 100 nM) for 2 days. **(B)** Protein levels of soluble and insoluble TDP-43 in *Hdac6* knockdown cells. GFP- or TDP-43-GFP-expressing cells were fractionated into the supernatant (the soluble fraction) and the pellet (the insoluble fraction) using lysis buffer containing 1% Triton X-100. Both soluble and insoluble TDP-43 protein levels were significantly increased by TDP-43-GFP expression. Data are presented as the mean ± SD of three independent experiments. $***p < 0.001$ (Student's *t*-test). **(C)** Transfection with an *Hdac6* siRNA efficiently downregulated the mRNA level of *HDAC6* in N2a cells. Data are presented as the mean ± SD of three independent experiments. *Gapdh* was used for normalization. $***p < 0.001$ (Student's *t*-test). **(D)** Control or *Hdac6* knockdown cells were transiently transfected with a plasmid containing either *Gfp* or *TDP-43-Gfp* and were then grown for 2 days. Immunoblot analysis of an anti-TDP-43 antibody. *Hdac6* knockdown markedly increased the level of TDP-43. Data are presented as the mean ± SD of three independent experiments. $**p < 0.005$ (one-way ANOVA with Tukey's multiple comparison test).

whether HDAC6 is implicated in mitochondrial dysfunction caused by TDP-43 expression, we monitored the cellular OCR in real time as a measure of mitochondrial respiration and glycolysis using a Seahorse XF24 Extracellular Flux Analyzer. Sequential injections of oligomycin, FCCP, antimycin A, and rotenone measure basal respiration, ATP production, maximal respiration, and spare respiratory capacity. Notably, we found that basal respiration, ATP production, maximal respiration, and spare respiratory capacity parameters were markedly decreased by TDP-43-expressing cells compared to GFP-expressing cells. The reductions in basal respiration, ATP production, and maximal respiration parameters induced by TDP-43 were greatly ameliorated by HDAC6 overexpression, but spare respiratory capacity was not altered (**Figures 4A,B**). We next investigated whether HDAC6 regulates TDP-43-induced neurotoxicity, and we measured the levels of CC3 by immunostaining. CC3 is a standard marker for apoptotic cell death (Bressenot et al., 2009). As expected, the CC3-positive cells were greatly increased in the N2a cells expressing TDP-43 compared with the positive cells in the controls. Importantly, TDP-43-induced cell death was more strongly suppressed in HDAC6-expressing cells than it was in Flag-expressing cells (**Figure 4C**). These findings reveal the possibility that HDAC6 attenuates TDP-43-induced neurotoxicity and UPS impairment via ALP.

Overexpression of HDAC6 Ameliorates UPS Impairment and Behavioral Deficits in the *Drosophila* Model of TDP-43 Proteinopathy

Given the strong *in vitro* evidence that HDAC6 regulates TDP-43-induced UPS impairment and toxicity in N2a cells, we next

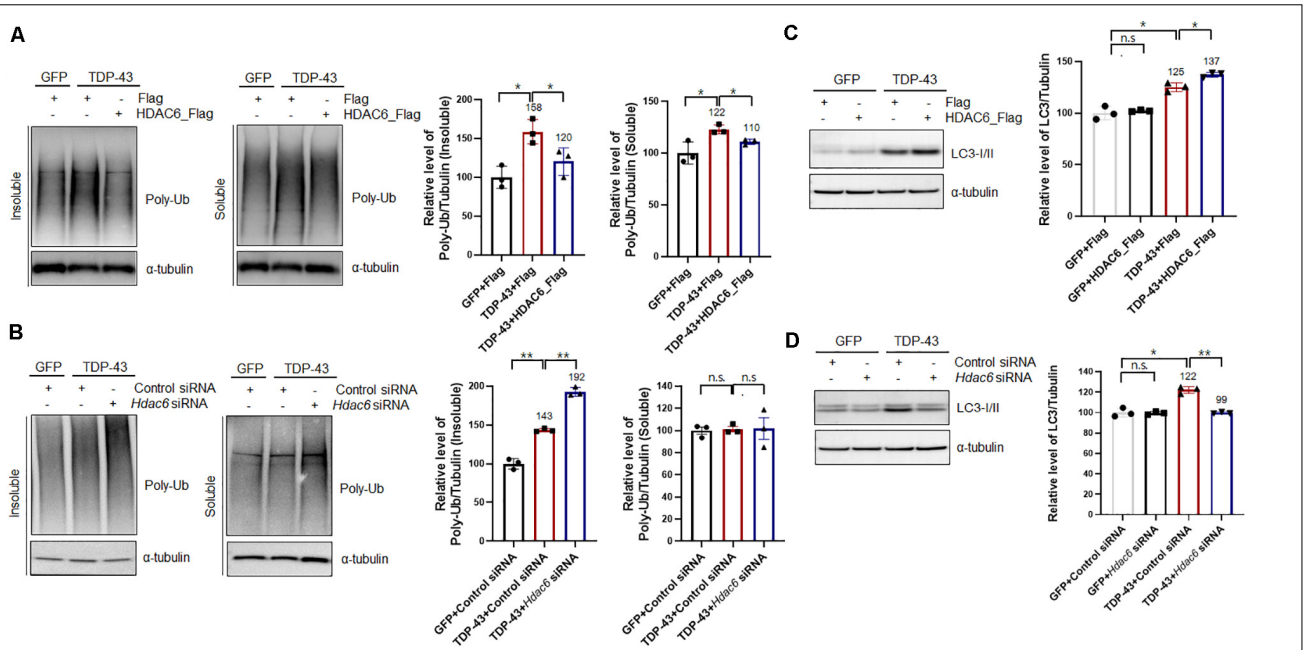

FIGURE 3 | HDAC6 mitigates TDP-43-induced UPS impairment via the autophagy-lysosome pathway. **(A,C)** Stable Flag- or HDAC6-Flag-expressing cells were transiently transfected with a plasmid containing either *Gfp* or *TDP-43-Gfp* and were then grown for 2 days. **(A)** Soluble and insoluble polyubiquitinated protein levels were significantly increased by TDP-43-GFP expression. HDAC6 overexpression significantly reduced TDP-43-induced polyubiquitinated protein levels. Cells were fractionated into the supernatant (the soluble fraction) and the pellet (the insoluble fraction) using lysis buffer containing 1% Triton X-100. Data are presented as the mean ± SD of three independent experiments. $^{*}p < 0.05$ (one-way ANOVA with Tukey's multiple comparison test). **(C)** Immunoblot analysis of an anti-LC3 antibody. HDAC6 overexpression markedly increased the level of TDP-43 in TDP-43-GFP-expressing cells. Data are presented as the mean ± SD of three independent experiments. $^{*}p < 0.05$, *n.s.*, not significant (one-way ANOVA with Tukey's multiple comparison test). **(B,D)** Control or *Hdac6* knockdown cells were transiently transfected with a plasmid containing either *Gfp* or *TDP-43-Gfp* and were then grown for 2 days. **(B)** Soluble and insoluble polyubiquitinated protein levels were significantly increased by TDP-43-GFP expression. *Hdac6* knockdown significantly increased TDP-43-induced polyubiquitinated protein levels. Cells were fractionated into the supernatant (the soluble fraction) and the pellet (the insoluble fraction) using lysis buffer containing 1% Triton X-100. Data are presented as the mean ± SD of three independent experiments. $^{**}p < 0.005$, *n.s.*, not significant (one-way ANOVA with Tukey's multiple comparison test). **(D)** Immunoblot analysis of an anti-LC3 antibody. *Hdac6* knockdown markedly decreased the level of LC3 in TDP-43-GFP-expressing cells. Data are presented as the mean ± SD of three independent experiments. $^{*}p < 0.05$, $^{**}p < 0.005$, *n.s.*, not significant (one-way ANOVA with Tukey's multiple comparison test).

examined whether overexpressing HDAC6 could suppress TDP-43-induced toxicity *in vivo* using a *Drosophila* model of TDP-43 proteinopathy that expresses human TDP-43 and ATXN2-32Q (Elden et al., 2010; Kim et al., 2014). To test the effect of HDAC6 overexpression on TDP-43/ATXN2 toxicity, we next investigated whether HDAC6 contributes to the restoration of neuronal defects induced by TDP-43/ATXN2 expression in flies. Previously, we showed that flies expressing TDP-43/ATXN2 showed a markedly reduced climbing ability compared to controls (Lee et al., 2019). This climbing deficit and shortened life span were significantly rescued by overexpression of human HDAC6 (**Figures 5A,B**). These results indicate that TDP-43/ATXN2-induced neuronal toxicity can be suppressed by HDAC6 expression. Furthermore, we also found that HDAC6 expression decreased polyubiquitinated aggregates in brain tissues of TDP-43/ATXN2-expressing flies (**Figure 5C**). Taken together, we concluded that overexpression of HDAC6 attenuates UPS impairment in TDP-43/ATXN2 flies, which is similar to what was found in the cell-based TDP-43 proteinopathy model. Our data suggest that HDAC6 overexpression ameliorates UPS impairment and behavioral deficits in a *Drosophila* model of TDP-43 proteinopathy.

DISCUSSION

Understanding HDAC6 function in TDP-43 proteinopathy is crucial for the development of effective treatments for ALS. In this study, we identified HDAC6 as a modulator of cytoplasmic mislocalization and aggregation of TDP-43 in N2a cells. We also found that TDP-43 overexpression increased HDAC6 protein levels. Previously, we revealed that TDP-43-overexpression in neuronal cells dramatically increases the co-localization of polyubiquitinated aggregates and p62 proteins (Lee et al., 2019). Moreover, level of 20S beta5 subunit incorporated into proteasome complex was markedly decreased in TDP-43-expressing cells (Lee et al., 2019). Furthermore, we observed that HDAC6 overexpression mitigates TDP-43-induced UPS impairment via ALP. Importantly, HDAC6 overexpression represses the accumulation of ubiquitinated aggregates in cell models and *Drosophila* models of TDP-43 proteinopathy. Polyubiquitinated proteins can be degraded by ALP under conditions of UPS dysfunction (Korolchuk et al., 2010). Previous studies reported that HDAC6 is a cytoplasmic microtubule-associated deacetylase that mediates the degradation of polyubiquitinated proteins in an ALP-dependent

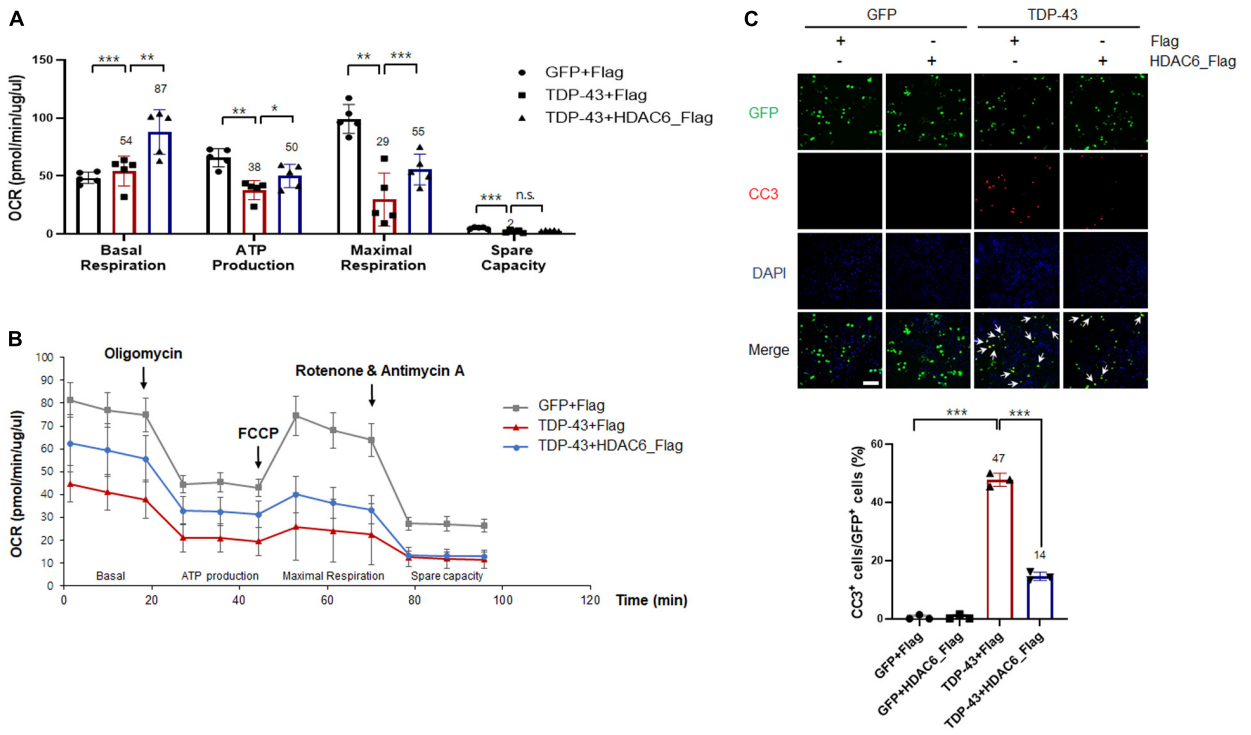

FIGURE 4 | HDAC6 attenuates TDP-43-induced mitochondrial dysfunction and neurotoxicity in N2a cells. **(A,B)** Stable Flag- or HDAC6-Flag-expressing cells were transfected with either *Gfp* or *TDP-43-Gfp* expression constructs, grown for 2 days, and then analyzed. **(A)** Mitochondrial dysfunction analysis of *Gfp*-transfected sorted cells to detect the basal OCR, ATP production, maximum reserve, and respiratory capacity by a Seahorse XF Analyzer. The OCR was normalized to the total protein concentration. **(B)** Quantification of the basal respiration, ATP production, maximum respiration, and spare respiratory capacity is shown as a percentage of the basal values. Data are presented as the mean ± SEM. $*p < 0.05$, $**p < 0.005$, $***p < 0.001$, and *n.s.*, not significant (two-way ANOVA with Tukey's multiple comparison test). **(C)** Stable Flag- or HDAC6-Flag-expressing cells were transfected with either *Gfp* or *TDP-43-Gfp* vector were stained for cleaved caspase-3 (CC3; red) or DAPI (nuclei; blue). Arrowheads indicate the colocalization of CC3 with TDP-43-GFP-positive cells. Data are presented as the mean ± SD of three independent experiments. $***p < 0.001$ (one-way ANOVA with Tukey's multiple comparison test). Scale bars, 50 μm.

manner (Pandey et al., 2007; Lee et al., 2010). HDAC6 suppresses the toxicity of UPS impairment in *Drosophila* models in an autophagy-dependent manner (Pandey et al., 2007). Moreover, ALP induction enhances the TDP-43 turnover rate and reduces TDP-43-induced neurotoxicity (Wang et al., 2012; Cheng et al., 2015; Leibiger et al., 2018; Nguyen et al., 2018). These results present the possibility that HDAC6 plays an important role in TDP-43 proteinopathy.

Autophagy is a common, major pathway for protein degradation via autophagosome-lysosome fusion in many neurodegenerative diseases. Several studies have shown that HDAC6 plays an important role in autophagosome-lysosome fusion during autophagy. Notably, deletion of HDAC6 resulted in autophagosome maturation failure in an *in vitro* model, resulting in enhanced neurodegeneration (Lee et al., 2010). HDAC6 binds to ubiquitinated proteins via its BUZ domain in an association similar to that of p62/SQSTM1, and the binding occurs under conditions of proteasome impairment (Bjorkoy et al., 2006; Liu et al., 2016). Moreover, HDAC6 interacts with dynein motor protein for transport to aggresomes, a process that is required for autophagic degradation of aggregated proteins (Kawaguchi et al., 2003). To investigate whether HDAC6 regulates autophagic degradation of insoluble ubiquitinated proteins, we examined the levels of polyubiquitinated proteins in insoluble fractions of HDAC6- and TDP-43-coexpressing cells. Intriguingly, overexpression of HDAC6 reduces the accumulation of insoluble polyubiquitinated proteins under conditions of UPS impairment. We also found that HDAC6 overexpression significantly increased the LC3-I/II levels induced by TDP-43 overexpression in N2a cells. Furthermore, we showed that neurospecific expression of HDAC6 decreased the amount of polyubiquitinated aggregates in TDP-43/ATXN2-expressing flies *in vivo*. These results also suggest that HDAC6 facilitates the autophagic degradation of insoluble ubiquitinated proteins in TDP-43 proteinopathy.

Mitochondrial dysfunction is a key pathological feature of ALS pathology. Although TDP-43 accumulation in neurons causes abnormalities in mitochondrial morphology, dynamics, and function in *in vivo* and *in vitro* models (Shan et al., 2010; Xu et al., 2010; Lu et al., 2012; Khalil et al., 2017; Davis et al., 2018), the physiological role of TDP-43 in maintaining mitochondrial function is still unclear. In this study, we observed that HDAC6 attenuates TDP-43-induced mitochondrial dysfunction in N2a cells. TDP-43-induced neurotoxicity is currently a well-known contributor to the pathology of ALS and other neurodegenerative diseases.

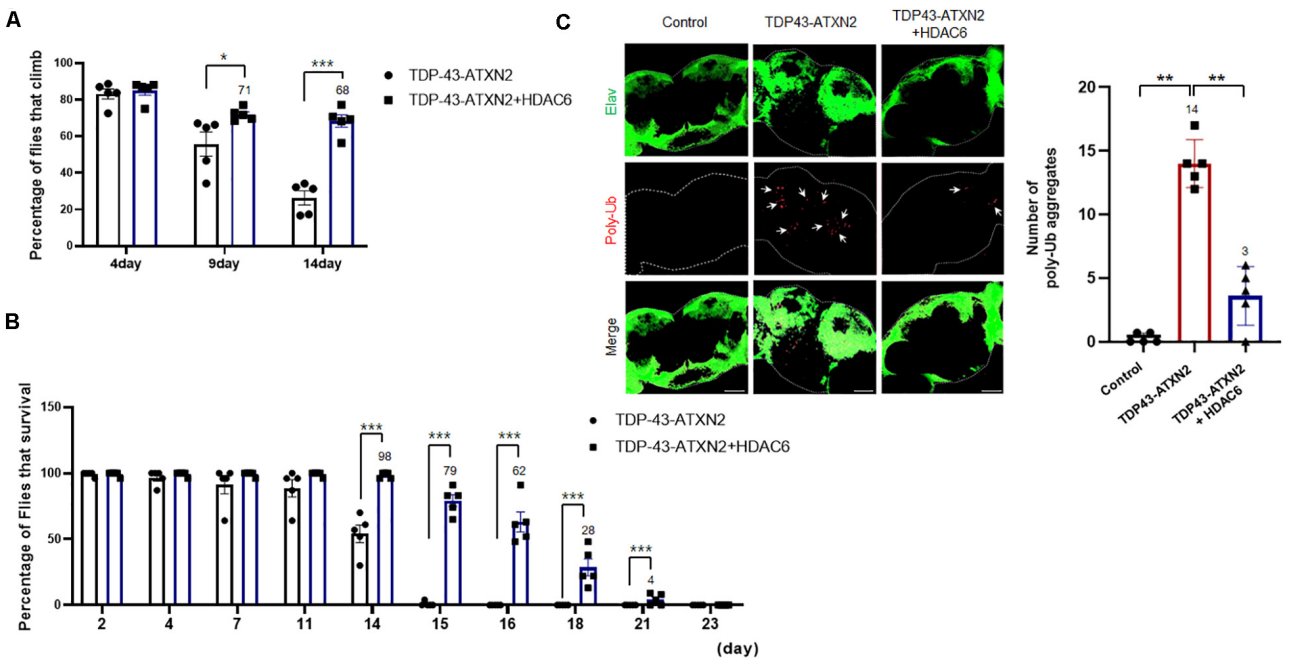

FIGURE 5 | HDAC6 overexpression mitigates neuronal toxicity and ubiquitin aggregates in a fly model of TDP-43 proteinopathies. **(A,B)** Climbing ability and shortened lifespan of TDP-43/ATXN2 or TDP-43/ATXN2+HDAC6 flies at the indicated time-points. The TDP-43/ATXN2-induced motility deficit was significantly rescued by overexpression of HDAC6. Quantification of the percentage of flies that climbed and survived. Data are presented as the mean ± SEM of four independent experiments. $^{*}p < 0.05$, and $^{***}p < 0.001$ (Student's *t*-test). **(C)** The brains of TDP-43/ATXN2 or TDP-43/ATXN2+HDAC6 flies were immunostained for polyubiquitin (red) and Elav (green). Overexpression of HDAC6 significantly reduced the accumulation of ubiquitinated inclusions in the brains of TDP-43/ATXN2+HDAC6 flies. Elav is a marker of most differentiated neuronal cells in the central and peripheral nervous systems of *Drosophila*. The quantification of the number of polyubiquitin-positive inclusions per brain is shown (*right*). Arrowheads indicate polyubiquitin-positive inclusions. Data are presented as the mean ± SEM of four independent experiments. $^{**}p < 0.001$ (one-way ANOVA with Bonferroni multiple comparison test). Scale bars, 50 μm. Genotypes: Control is *elavGS/+*, TDP-43/ATXN2 is *UAS-ATXN2-32Q/+; elavGS,UAS-TDP-43/+*, TDP-43/ATXN2+HDAC6 is *UAS-ATXN2-32Q/UAS-HDAC6; elavGS,UAS-TDP-43/+*.

Cytoplasmic aggregates of TDP-43 have been linked to ALS, FTLD, and AD (Scotter et al., 2015; James et al., 2016; Meriggioli and Kordower, 2016). We showed that TDP-43-induced apoptotic cell death was significantly reduced when TDP-43 was coexpressed with HDAC6. Furthermore, TDP-43-induced neurotoxicity is greatly attenuated by autophagy stimulators in rat cortical neurons (Barmada et al., 2014). Therefore, we concluded that HDAC6 overexpression suppresses TDP-43-induced mitochondrial defects and neurotoxicity via ALP.

CONCLUSION

In summary, we demonstrated the following: (1) HDAC6 overexpression decreased the insoluble TDP-43 protein levels in N2a cells; (2) HDAC6 regulates the cytoplasmic mislocalization and aggregation of TDP-43 in N2a cells; (3) HDAC6 mediates TDP-43-induced UPS impairment via ALP; (4) HDAC6 modulates TDP-43-induced mitochondrial dysfunction and neurotoxicity; and (5) HDAC6 overexpression ameliorates UPS impairment and behavioral deficits in a *Drosophila* TDP-43 model. We identified that HDAC6 modulates TDP-43-induced UPS impairment and neurotoxicity via ALP by analyzing TDP-43 overexpression models. Therefore, our results suggest that targeting HDAC6 may represent a novel therapeutic intervention for neurodegenerative diseases with TDP-43 proteinopathy.

DATA AVAILABILITY STATEMENT

The original contributions presented in the study are included in the article/**Supplementary Material**. Further inquiries can be directed to the corresponding author/s.

AUTHOR CONTRIBUTIONS

SrL, YhK, SyK, MJ, and Y-MJ planned and performed the experiments. SrL, MC, SL, SRK, and KK provided ideas for the project and participated in writing the manuscript. SrL, YhK, KK, and H-JK wrote the manuscript. All authors read and approved the final manuscript.

FUNDING

This work was supported by the KBRI Research Program of the Ministry of Science, ICT and Future Planning (20-BR-02-08 and

-BR-02-10); the Basic Science Research Program through the National Research Foundation of Korea (NRF), funded by the Ministry of Science, ICT and Future Planning (NRF-2020R1A2C4002366 and NRF-2019R1F1A1045639); and the Korea Health Technology R&D Project through the Korea Health Industry Development Institute (KHIDI), funded by the Ministry of Health and Welfare, South Korea (Grant No. HI14C1135); the Soonchunhyang University Research Fund. Confocal microscopy data were acquired in the Advanced Neural Imaging Center in KBRI.

SUPPLEMENTARY MATERIAL

The Supplementary Material for this article can be found online at: https://www.frontiersin.org/articles/10.3389/fcell.2020.581942/full#supplementary-material

REFERENCES

Barmada, S. J., Serio, A., Arjun, A., Bilican, B., Daub, A., Ando, D. M., et al. (2014). Autophagy induction enhances TDP43 turnover and survival in neuronal ALS models. *Nat. Chem. Biol.* 10, 677–685. doi: 10.1038/nchembio.1563

Barmada, S. J., Skibinski, G., Korb, E., Rao, E. J., Wu, J. Y., and Finkbeiner, S. (2010). Cytoplasmic mislocalization of TDP-43 is toxic to neurons and enhanced by a mutation associated with familial amyotrophic lateral sclerosis. *J. Neurosci.* 30, 639–649. doi: 10.1523/JNEUROSCI.4988-09.2010

Bendotti, C., Marino, M., Cheroni, C., Fontana, E., Crippa, V., Poletti, A., et al. (2012). Dysfunction of constitutive and inducible ubiquitin-proteasome system in amyotrophic lateral sclerosis: implication for protein aggregation and immune response. *Prog. Neurobiol.* 97, 101–126. doi: 10.1016/j.pneurobio.2011.10.001

Birnbaum, J. H., Wanner, D., Gietl, A. F., Saake, A., Kundig, T. M., Hock, C., et al. (2018). Oxidative stress and altered mitochondrial protein expression in the absence of amyloid-beta and tau pathology in iPSC-derived neurons from sporadic Alzheimer's disease patients. *Stem Cell Res.* 27, 121–130. doi: 10.1016/j.scr.2018.01.019

Bjorkoy, G., Lamark, T., and Johansen, T. (2006). p62/SQSTM1: a missing link between protein aggregates and the autophagy machinery. *Autophagy* 2, 138–139. doi: 10.4161/auto.2.2.2405

Bressenot, A., Marchal, S., Bezdetnaya, L., Garrier, J., Guillemin, F., and Plenat, F. (2009). Assessment of apoptosis by immunohistochemistry to active caspase-3, active caspase-7, or cleaved PARP in monolayer cells and spheroid and subcutaneous xenografts of human carcinoma. *J. Histochem. Cytochem.* 57, 289–300. doi: 10.1369/jhc.2008.952044

Buratti, E., and Baralle, F. E. (2008). Multiple roles of TDP-43 in gene expression, splicing regulation, and human disease. *Front. Biosci.* 13:867–878. doi: 10.2741/2727

Cheng, C. W., Lin, M. J., and Shen, C. K. (2015). Rapamycin alleviates pathogenesis of a new Drosophila model of ALS-TDP. *J. Neurogenet.* 29, 59–68. doi: 10.3109/01677063.2015.1077832

Davis, S. A., Itaman, S., Khalid-Janney, C. M., Sherard, J. A., Dowell, J. A., Cairns, N. J., et al. (2018). TDP-43 interacts with mitochondrial proteins critical for mitophagy and mitochondrial dynamics. *Neurosci. Lett.* 678, 8–15. doi: 10.1016/j.neulet.2018.04.053

Dranka, B. P., Benavides, G. A., Diers, A. R., Giordano, S., Zelickson, B. R., Reily, C., et al. (2011). Assessing bioenergetic function in response to oxidative stress by metabolic profiling. *Free Radic. Biol. Med.* 51, 1621–1635. doi: 10.1016/j.freeradbiomed.2011.08.005

Duan, W., Li, X., Shi, J., Guo, Y., Li, Z., and Li, C. (2010). Mutant TAR DNA-binding protein-43 induces oxidative injury in motor neuron-like cell. *Neuroscience* 169, 1621–1629. doi: 10.1016/j.neuroscience.2010.06.018

Elden, A. C., Kim, H. J., Hart, M. P., Chen-Plotkin, A. S., Johnson, B. S., Fang, X., et al. (2010). Ataxin-2 intermediate-length polyglutamine expansions are associated with increased risk for ALS. *Nature* 466, 1069–1075. doi: 10.1038/nature09320

Feany, M. B., and Bender, W. W. (2000). A Drosophila model of Parkinson's disease. *Nature* 404, 394–398. doi: 10.1038/35006074

Fiesel, F. C., Voigt, A., Weber, S. S., Van Den Haute, C., Waldenmaier, A., Gorner, K., et al. (2010). Knockdown of transactive response DNA-binding protein (TDP-43) downregulates histone deacetylase 6. *EMBO J.* 29, 209–221. doi: 10.1038/emboj.2009.324

Gautier, C. A., Corti, O., and Brice, A. (2014). Mitochondrial dysfunctions in Parkinson's disease. *Rev. Neurol.* 170, 339–343. doi: 10.1016/j.neurol.2013.06.003

James, B. D., Wilson, R. S., Boyle, P. A., Trojanowski, J. Q., Bennett, D. A., and Schneider, J. A. (2016). TDP-43 stage, mixed pathologies, and clinical Alzheimer's-type dementia. *Brain* 139, 2983–2993. doi: 10.1093/brain/aww224

Kawaguchi, Y., Kovacs, J. J., Mclaurin, A., Vance, J. M., Ito, A., and Yao, T. P. (2003). The deacetylase HDAC6 regulates aggresome formation and cell viability in response to misfolded protein stress. *Cell* 115, 727–738. doi: 10.1016/S0092-8674(03)00939-5

Khalil, B., Cabirol-Pol, M. J., Miguel, L., Whitworth, A. J., Lecourtois, M., and Lievens, J. C. (2017). Enhancing Mitofusin/Marf ameliorates neuromuscular dysfunction in Drosophila models of TDP-43 proteinopathies. *Neurobiol. Aging* 54, 71–83. doi: 10.1016/j.neurobiolaging.2017.02.016

Kim, H. J., Raphael, A. R., Ladow, E. S., Mcgurk, L., Weber, R. A., Trojanowski, J. Q., et al. (2014). Therapeutic modulation of eIF2alpha phosphorylation rescues TDP-43 toxicity in amyotrophic lateral sclerosis disease models. *Nat. Genet.* 46, 152–160. doi: 10.1038/ng.2853

Kim, S. H., Shanware, N. P., Bowler, M. J., and Tibbetts, R. S. (2010). Amyotrophic lateral sclerosis-associated proteins TDP-43 and FUS/TLS function in a common biochemical complex to co-regulate HDAC6 mRNA. *J. Biol. Chem.* 285, 34097–34105. doi: 10.1074/jbc.M110.154831

Korolchuk, V. I., Menzies, F. M., and Rubinsztein, D. C. (2010). Mechanisms of cross-talk between the ubiquitin-proteasome and autophagy-lysosome systems. *FEBS Lett.* 584, 1393–1398. doi: 10.1016/j.febslet.2009.12.047

Kovacs, J. J., Murphy, P. J., Gaillard, S., Zhao, X., Wu, J. T., Nicchitta, C. V., et al. (2005). HDAC6 regulates Hsp90 acetylation and chaperone-dependent activation of glucocorticoid receptor. *Mol. Cell.* 18, 601–607. doi: 10.1016/j.molcel.2005.04.021

Lee, J. Y., Koga, H., Kawaguchi, Y., Tang, W., Wong, E., Gao, Y. S., et al. (2010). HDAC6 controls autophagosome maturation essential for ubiquitin-selective quality-control autophagy. *EMBO J.* 29, 969–980. doi: 10.1038/emboj.2009.405

Lee, S., Jeon, Y. M., Cha, S. J., Kim, S., Kwon, Y., Jo, M., et al. (2019). PTK2/FAK regulates UPS impairment via SQSTM1/p62 phosphorylation in TARDBP/TDP-43 proteinopathies. *Autophagy* 16, 1396-1412. doi: 10.1080/15548627.2019.1686729

Leibiger, C., Deisel, J., Aufschnaiter, A., Ambros, S., Tereshchenko, M., Verheijen, B. M., et al. (2018). TDP-43 controls lysosomal pathways thereby determining its own clearance and cytotoxicity. *Hum. Mol. Genet.* 27, 1593–1607. doi: 10.1093/hmg/ddy066

Liu, W. J., Ye, L., Huang, W. F., Guo, L. J., Xu, Z. G., Wu, H. L., et al. (2016). p62 links the autophagy pathway and the ubiqutin-proteasome system upon ubiquitinated protein degradation. *Cell Mol. Biol. Lett.* 21:29. doi: 10.1186/s11658-016-0031-z

Livak, K. J., and Schmittgen, T. D. (2001). Analysis of relative gene expression data using real-time quantitative PCR and the 2(-Delta Delta C(T)) Method. *Methods* 25, 402–408. doi: 10.1006/meth.2001.1262

Lu, C. Y., Chang, Y. C., Hua, C. H., Chuang, C., Huang, S. H., Kung, S. H., et al. (2017). Tubacin, an HDAC6 Selective Inhibitor, Reduces the Replication of the Japanese Encephalitis Virus via the Decrease of Viral RNA Synthesis. *Int. J. Mol. Sci.* 18:954. doi: 10.3390/ijms18050954

Lu, J., Duan, W., Guo, Y., Jiang, H., Li, Z., Huang, J., et al. (2012). Mitochondrial dysfunction in human TDP-43 transfected NSC34 cell lines and the protective effect of dimethoxy curcumin. *Brain Res. Bull.* 89, 185–190. doi: 10.1016/j.brainresbull.2012.09.005

Mackenzie, I. R., Neumann, M., Baborie, A., Sampathu, D. M., Du Plessis, D., Jaros, E., et al. (2011). A harmonized classification system for FTLD-TDP pathology. *Acta Neuropathol.* 122, 111–113. doi: 10.1007/s00401-011-0845-8

Meriggioli, M. N., and Kordower, J. H. (2016). TDP-43 Proteinopathy: Aggregation and Propagation in the Pathogenesis of Amyotrophic Lateral Sclerosis. *Mov. Disord.* 31:1139. doi: 10.1002/mds.26645

Neumann, M., Sampathu, D. M., Kwong, L. K., Truax, A. C., Micsenyi, M. C., Chou, T. T., et al. (2006). Ubiquitinated TDP-43 in frontotemporal lobar degeneration and amyotrophic lateral sclerosis. *Science* 314, 130–133. doi: 10.1126/science.1134108

Nguyen, D. K. H., Thombre, R., and Wang, J. (2018). Autophagy as a common pathway in amyotrophic lateral sclerosis. *Neurosci. Lett.* 697:34-48. doi: 10.1016/j.neulet.2018.04.006

Ou, S. H., Wu, F., Harrich, D., Garcia-Martinez, L. F., and Gaynor, R. B. (1995). Cloning and characterization of a novel cellular protein. TDP-43, that binds to human immunodeficiency virus type 1 TAR DNA sequence motifs. *J. Virol.* 69, 3584–3596. doi: 10.1128/JVI.69.6.3584-3596.1995

Pandey, U. B., Nie, Z., Batlevi, Y., Mccray, B. A., Ritson, G. P., Nedelsky, N. B., et al. (2007). HDAC6 rescues neurodegeneration and provides an essential link between autophagy and the UPS. *Nature* 447, 859–863. doi: 10.1038/nature05853

Scotter, E. L., Chen, H. J., and Shaw, C. E. (2015). TDP-43 Proteinopathy and ALS: Insights into Disease Mechanisms and Therapeutic Targets. *Neurotherapeutics* 12, 352–363. doi: 10.1007/s13311-015-0338-x

Scotter, E. L., Vance, C., Nishimura, A. L., Lee, Y. B., Chen, H. J., Urwin, H., et al. (2014). Differential roles of the ubiquitin proteasome system and autophagy in the clearance of soluble and aggregated TDP-43 species. *J. Cell Sci.* 127, 1263–1278. doi: 10.1242/jcs.140087

Shan, X., Chiang, P. M., Price, D. L., and Wong, P. C. (2010). Altered distributions of Gemini of coiled bodies and mitochondria in motor neurons of TDP-43 transgenic mice. *Proc. Natl. Acad. Sci. U S A.* 107, 16325–16330. doi: 10.1073/pnas.1003459107

Shenouda, M., Zhang, A. B., Weichert, A., and Robertson, J. (2018). Mechanisms Associated with TDP-43 Neurotoxicity in ALS/FTLD. *Adv. Neurobiol.* 20, 239–263. doi: 10.1007/978-3-319-89689-2_9

Shi, P., Gal, J., Kwinter, D. M., Liu, X., and Zhu, H. (2010). Mitochondrial dysfunction in amyotrophic lateral sclerosis. *Biochim. Biophys. Acta* 1802, 45–51. doi: 10.1016/j.bbadis.2009.08.012

Strong, M. J., Volkening, K., Hammond, R., Yang, W., Strong, W., Leystra-Lantz, C., et al. (2007). TDP43 is a human low molecular weight neurofilament (hNFL) mRNA-binding protein. *Mol. Cell. Neurosci.* 35, 320–327. doi: 10.1016/j.mcn.2007.03.007

Taes, I., Timmers, M., Hersmus, N., Bento-Abreu, A., Van Den Bosch, L., Van Damme, P., et al. (2013). Hdac6 deletion delays disease progression in the SOD1G93A mouse model of ALS. *Hum. Mol. Genet.* 22, 1783–1790. doi: 10.1093/hmg/ddt028

Tremblay, C., St-Amour, I., Schneider, J., Bennett, D. A., and Calon, F. (2011). Accumulation of transactive response DNA binding protein 43 in mild cognitive impairment and Alzheimer disease. *J. Neuropathol. Exp. Neurol.* 70, 788–798. doi: 10.1097/NEN.0b013e31822c62cf

Wang, C., and Wang, X. (2015). The interplay between autophagy and the ubiquitin-proteasome system in cardiac proteotoxicity. *Biochim. Biophys. Acta* 1852, 188–194. doi: 10.1016/j.bbadis.2014.07.028

Wang, I. F., Guo, B. S., Liu, Y. C., Wu, C. C., Yang, C. H., Tsai, K. J., et al. (2012). Autophagy activators rescue and alleviate pathogenesis of a mouse model with proteinopathies of the TAR DNA-binding protein 43. *Proc. Natl. Acad. Sci. U S A.* 109, 15024–15029. doi: 10.1073/pnas.1206362109

Wang, P., Deng, J., Dong, J., Liu, J., Bigio, E. H., Mesulam, M., et al. (2019). TDP-43 induces mitochondrial damage and activates the mitochondrial unfolded protein response. *PLoS Genet.* 15:e1007947. doi: 10.1371/journal.pgen.1007947

Xu, Y. F., Gendron, T. F., Zhang, Y. J., Lin, W. L., D'alton, S., Sheng, H., et al. (2010). Wild-type human TDP-43 expression causes TDP-43 phosphorylation, mitochondrial aggregation, motor deficits, and early mortality in transgenic mice. *J. Neurosci.* 30, 10851–10859. doi: 10.1523/JNEUROSCI.1630-10.2010

Yang, X. J., and Seto, E. (2007). HATs and HDACs: from structure, function and regulation to novel strategies for therapy and prevention. *Oncogene* 26, 5310–5318. doi: 10.1038/sj.onc.1210599

Zhang, X., Yuan, Z., Zhang, Y., Yong, S., Salas-Burgos, A., Koomen, J., et al. (2007). HDAC6 modulates cell motility by altering the acetylation level of cortactin. *Mol. Cell.* 27, 197–213. doi: 10.1016/j.molcel.2007.05.033

Zhang, Y., Li, N., Caron, C., Matthias, G., Hess, D., Khochbin, S., et al. (2003). HDAC-6 interacts with and deacetylates tubulin and microtubules in vivo. *EMBO J.* 22, 1168–1179. doi: 10.1093/emboj/cdg115

Zhao, W., Beers, D. R., Bell, S., Wang, J., Wen, S., Baloh, R. H., et al. (2015). TDP-43 activates microglia through NF-kappaB and NLRP3 inflammasome. *Exp. Neurol.* 273, 24–35. doi: 10.1016/j.expneurol.2015.07.019

Conflict of Interest: The authors declare that the research was conducted in the absence of any commercial or financial relationships that could be construed as a potential conflict of interest.

frontiers in Cell and Developmental Biology

ORIGINAL RESEARCH
published: 23 November 2020
doi: 10.3389/fcell.2020.606685

Wheat Germination Is Dependent on Plant Target of Rapamycin Signaling

Bauyrzhan Smailov[1,2], Sanzhar Alybayev[1,2], Izat Smekenov[1,2], Aibek Mursalimov[1,2], Murat Saparbaev[1,3], Dos Sarbassov[4]* and Amangeldy Bissenbaev[1,2]**

[1] Department of Molecular Biology and Genetics, Faculty of Biology and Biotechnology, Al-Farabi Kazakh National University, Almaty, Kazakhstan, [2] Scientific Research Institute of Biology and Biotechnology Problems, Al-Farabi Kazakh National University, Almaty, Kazakhstan, [3] Groupe «Mechanisms of DNA Repair and Carcinogenesis», Equipe Labellisée LIGUE 2016, CNRS UMR 9019, Université Paris-Sud, Gustave Roussy Cancer Campus, Villejuif, France, [4] Department of Biology, Nazarbayev University, Nur-Sultan, Kazakhstan

OPEN ACCESS

Edited by:
Nikita Kuznetsov, Institute of Chemical Biology and Fundamental Medicine (RAS), Russia

Reviewed by:
Rustem Omarov, L.N. Gumilyov Eurasian National University, Kazakhstan
Yegor S. Vassetzky, UMR 8126 Signalisation, Noyaux et Innovations en Cancérologie, France
Dindial Ramotar, Hamad bin Khalifa University, Qatar

***Correspondence:**
Amangeldy Bissenbaev
amangeldy.bisenbaev@kaznu.kz
Dos Sarbassov
dos.sarbassov@nu.edu.kz
Murat Saparbaev
murat.saparbaev@gustaveroussy.fr

Specialty section:
This article was submitted to Cell Death and Survival, a section of the journal Frontiers in Cell and Developmental Biology

Received: *15 September 2020*
Accepted: *21 October 2020*
Published: *23 November 2020*

Citation:
Smailov B, Alybayev S, Smekenov I, Mursalimov A, Saparbaev M, Sarbassov D and Bissenbaev A (2020) Wheat Germination Is Dependent on Plant Target of Rapamycin Signaling. Front. Cell Dev. Biol. 8:606685. doi: 10.3389/fcell.2020.606685

Germination is a process of seed sprouting that facilitates embryo growth. The breakdown of reserved starch in the endosperm into simple sugars is essential for seed germination and subsequent seedling growth. At the early stage of germination, gibberellic acid (GA) activates transcription factor GAMYB to promote *de novo* synthesis of isoforms of α-amylase in the aleurone layer and scutellar epithelium of the embryo. Here, we demonstrate that wheat germination is regulated by plant target of rapamycin (TOR) signaling. TOR is a central component of the essential-nutrient–dependent pathway controlling cell growth in all eukaryotes. It is known that rapamycin, a highly specific allosteric inhibitor of TOR, is effective in yeast and animal cells but ineffective in most of higher plants likely owing to structural differences in ubiquitous rapamycin receptor FKBP12. The action of rapamycin on wheat growth has not been studied. Our data show that rapamycin inhibits germination of wheat seeds and of their isolated embryos in a dose-dependent manner. The involvement of *Triticum aestivum* TOR (TaTOR) in wheat germination was consistent with the suppression of wheat embryo growth by specific inhibitors of the TOR kinase: pp242 or torin1. Rapamycin or torin1 interfered with GA function in germination because of a potent inhibitory effect on α-amylase and *GAMYB* gene expression. The TOR inhibitors selectively targeted the GA-dependent gene expression, whereas expression of the abscisic acid-dependent *ABI5* gene was not affected by either rapamycin or torin1. To determine whether the TaTOR kinase activation takes place during wheat germination, we examined phosphorylation of a ribosomal protein, *T. aestivum* S6 kinase 1 (TaS6K1; a substrate of TOR). The phosphorylation of serine 467 (S467) in a hydrophobic motif on TaS6K1 was induced in a process of germination triggered by GA. Moreover, the germination-induced phosphorylation of TaS6K1 on S467 was dependent on TaTOR and was inhibited by rapamycin or torin1. Besides, a gibberellin biosynthesis inhibitor (paclobutrazol; PBZ)

blocked not only α-amylase gene expression but also TaS6K1 phosphorylation in wheat embryos. Thus, a hormonal action of GA turns on the synthesis of α-amylase in wheat germination via activation of the TaTOR–S6K1 signaling pathway.

Keywords: target of rapamycin pathway, gibberellic acid, abscisic acid, α-amylase, ribosomal protein S6 kinase 1, rapamycin, torin1, wheat seed

HIGHLIGHTS

- Rapamycin or ATP-competitive TOR inhibitors effectively inhibit germination of wheat whole seeds and isolated embryos dose-dependently.
- TOR-S6K1 signaling is important for regulation of GA-induced mobilization of starch and for seedling growth.

INTRODUCTION

The breakdown of reserved starch in the endosperm into simple sugars is an essential step for seed germination and subsequent seedling growth. At the early stage of germination, gibberellic acid (GA) activates the myb-like transcription factor (GAMYB) that promotes *de novo* synthesis of α-amylase in the aleurone layer and embryo. α-Amylase expression in the embryo is localized to the scutellar epithelium (Kaneko et al., 2002). Furthermore, GA stimulates *de novo* synthesis of proteases and peptidases and ∼50% of total protein synthesis during germination (Bak-Jensen et al., 2007). Among hydrolases, abundant α-amylases play a central role in the metabolizing of starch that determines the rate of germination and seedling growth. Abscisic acid (ABA) represses most effects of GA including α-amylase expression in aleurone and embryonic tissues (Gomez-Cadenas et al., 2001). GA induces α-amylase expression in rice (Gomi et al., 2004) and barley (Fu et al., 2002) aleurone cells through proteasome-dependent degradation of DELLA proteins (SLR1, slender rice-1 in rice and SLN, slender 1 in barley) mediated by receptor GID1. Furthermore, it has been shown that prior to the establishment of the GID1–DELLA and GA perception system, the effect of GA on α-amylase mRNA expression is preceded by increases in cytosolic free Ca^{2+} concentration and changes in cytosolic pH and in the concentrations of calmodulin and cyclic GMP (Bethke et al., 1997). Experiments with an agonist and inhibitor of heterotrimeric G proteins point to their involvement in the oat aleurone response to GA (Jones et al., 1998). Recently, it was reported that reactive oxygen species perform a key function in the regulation of α-amylase production in barley aleurone cells (Aoki et al., 2014). Nonetheless, how GA regulates α-amylase synthesis in wheat germination remains poorly characterized.

Target of rapamycin (TOR) is a central regulator of cell proliferation and growth in eukaryotic cells. TOR integrates signals from multitude inputs such as growth factors, stress, nutrients, and energy to regulate protein synthesis, energy metabolism, cell cycle progression, and autophagy (Saxton and Sabatini, 2017). In animals and yeast, TOR is present in at least two structurally and functionally distinct multiprotein complexes: TORC1 and TORC2 (Loewith and Hall, 2011; Laplante and Sabatini, 2012). TORC2 does not exist in plants (Shi et al., 2018). The core components of mammalian TORC1 are mammalian TOR (mTOR), RAPTOR (regulatory-associated protein of mTOR), and mLST8 (mammalian lethal with SEC13 protein 8). The stability of interactions among mTOR, RAPTOR, and mLST8 is sensitive to nutrient and energy levels (Saxton and Sabatini, 2017). The best-characterized effector of TORC1 is a translational regulator (a 40S ribosomal protein) called S6 kinase 1 (S6K1) (Pearce et al., 2010). It regulates translation initiation by phosphorylating the S6 protein of the 40S ribosomal subunit and by stimulating eIF-4A helicase activity (Holz et al., 2005). Some studies indicate that animal S6K participates in regulation of fundamental cellular processes, including transcription, translation, protein and lipid synthesis, cell growth, cell size determination, and cell metabolism (Saxton and Sabatini, 2017). In contrast to animal S6Ks, there are a few studies characterizing plant S6Ks despite the importance of their function. A key role of S6K in chromosome stability and regulation of cell proliferation was shown in *Arabidopsis* (Henriques et al., 2010; Schepetilnikov et al., 2011). In addition, *Arabidopsis* S6K1 activation by TOR is important for reinitiating the translation of an mRNA that contains upstream open reading frames in 5′-untranslated regions (Schepetilnikov et al., 2013). The TOR–RAPTOR2–S6K1 complex is critical for the modulation of thylakoid membrane lipid biosynthesis and homeostasis in rice (Sun et al., 2016). Elucidation of TOR signaling has been advanced by studies on the mechanism of action of rapamycin. Rapamycin is a bacterially produced macrolide that inhibits TOR and has a variety of clinical applications such as antifungal, immunosuppressant, and anticancer treatments. In mammalian systems, most of the known mTOR substrates were discovered and validated using rapamycin as a pharmacological probe (Thoreen et al., 2009). Rapamycin forms a complex with its intracellular receptor FK506-binding protein 12 kDa (FKBP12), and the complex binds to a specific region of TOR (defined as the FKBP12–rapamycin binding domain; FRB) and thereby inhibits the kinase activity of TOR. Although rapamycin is a highly specific allosteric inhibitor of mTOR, it is only a partial inhibitor of this enzyme. Rapamycin targets mTORC1 but not mTORC2 (Sarbassov et al., 2004, 2006). Torin1 is a synthetic mTOR inhibitor that blocks ATP binding

Abbreviations: ABA, abscisic acid; FKBP12, FK506-binding protein 12 kDa; GA, gibberellic acid; GAMYB, GA-induced myb-like transcription factor; mTOR, mammalian TOR; PBZ, paclobutrazol; TaABI5, *Triticum aestivum* ABA response element-binding factor; TaS6K1, *Triticum aestivum* ribosomal protein S6 kinase 1; TOR, target of rapamycin.

to mTOR and thus inactivates both mTORC1 and mTORC2. Torin1 and rapamycin each inhibits overall protein synthesis, induces autophagosome formation, and thus mimics the effects of starvation (Thoreen et al., 2009; Zhao et al., 2015). Despite the connections of mTORC1 to translational machinery, the effects of rapamycin on mammalian cell growth and proliferation are much less dramatic than the effects on yeast growth and proliferation and are highly dependent on the cell type (Barbet et al., 1996; Thoreen et al., 2009).

Plant TOR may be poorly sensitive to rapamycin as a result of mutations in the *Arabidopsis thaliana* FKBP12 protein that prevent the assembly of inhibitory complex TOR–rapamycin–FKBP12 (Ren et al., 2011, 2012). On the other hand, some studies have shown that tomato (Xiong et al., 2016) and *A. thaliana* seedlings are sensitive to micromolar doses of rapamycin (Xiong and Sheen, 2012; Xiong et al., 2013). The phosphorylation of S6K1 threonine 449 (T449) was shown to be inhibited when 100 nM torin1 was added for a 30-min incubation to transfected protoplasts transiently expressing *A. thaliana* S6K1 (AtS6K1) tagged with FLAG (Xiong et al., 2013). In a yeast reconstitution model, it was shown that rice S6Ks restore ribosomal-protein S6's phosphorylation in a rapamycin-sensitive manner in yeast cells lacking Ypk3, an ortholog of mammalian S6Ks (Yaguchi and Kozaki, 2018). Furthermore, transcriptome analysis of rice cells revealed that rapamycin treatment significantly suppress expression of 120 genes encoding histones, chromatin modulators, ribosomal proteins, and protein synthesis machineries (De Vleesschauwer et al., 2018). These observations suggest that plant TOR plays an important part in the regulation of transcriptional and translational processes just as in other eukaryotes.

A loss-of-function mutation of *Raptor1b* leads to a substantial delay in *Arabidopsis* seed germination; delayed germination and seedling growth in Raptor1b-null seeds are partially restored by an exogenous supply of GA (Salem et al., 2018). In the present study, we examined the effects of mTOR inhibitors (rapamycin or torin1) on the germination of wheat seeds and on α-amylase gene expression in the wheat embryos.

MATERIALS AND METHODS

Wheat Growth Conditions

The wheat (*Triticum aestivum*, variety Kazakhstanskaya 19) seeds were sterilized in 2% (v/v) NaOCl for 20 min and washed twice with sterile water, once with 0.01 M HCl, and thoroughly with sterile distilled water. The surface-sterilized seeds were germinated under long-daylight conditions at room temperature on filter paper soaked with sterile water supplemented with 1 μM GA and with or without various concentrations of rapamycin or torin1 (0.5, 1.0, 5.0, or 10.0 μM). Primary roots, shoots, and seedlings were photographed, and shoot length and fresh weight of seedlings were measured at 4 days after germination (DAG). In addition, the embryos isolated from 1-DAG seeds were transferred to the 0.5× MS medium in Petri dishes with 1 μM GA or 10 μM ABA and different inhibitors (rapamycin, torin1, or pp242) for 4-day incubation, unless specified otherwise.

Wheat Embryo Incubation Conditions

Embryos were dissected from 1-DAG seeds by means of a scalpel. Only intact embryos with no starch or aleurone tissue adhering to the scutellar tissue were studied. Twenty embryos were incubated in each well of six-well plastic plates in 2 ml of 10 mM $CaCl_2$ with 2.5 μg/ml of chloramphenicol. Embryos were incubated up to 24 h at room temperature in the dark with constant shaking at 125 rpm. GA and ABA were purchased from Sigma-Aldrich (Germany). GA was applied at 1 μM and ABA at 10 μM. Assays were carried out in the presence or absence of various concentrations of rapamycin (LC Laboratories, Woburn, MA, United States) or torin1 (Cayman Chemical Company, Ann Arbor, MI, United States) or 100 μM PBZ (Sigma-Aldrich, Germany). Rapamycin and torin1 were dissolved in DMSO and stored at −20°C according to the manufacturer's instructions. The rapamycin solution was preheated to 37°C prior to its application.

RNA Isolation and cDNA Synthesis

The *T. aestivum* cDNA encoding putative ribosomal protein S6 kinases (*tas6k1*) was identified by its homology to rice S6K1 (GenBank accession No. AK451448.1). TaS6K1 cDNA was prepared by reverse-transcription polymerase chain reaction (RT-PCR) with gene-specific primers (**Table 1**). Total RNA was isolated from young leaves of *T. aestivum* variety Kazakhstanskaya 19 by the TRIzol method. The yield and purity of RNA were determined spectrophotometrically, and the quality of RNA was evaluated by electrophoresis in a 1% formaldehyde agarose gel. First-strand cDNA was synthesized by reverse transcription from 5 μg of total RNA as a template under the following conditions: 200 U of RevertAid M-MuLV reverse transcriptase (Thermo Scientific, Lithuania), 0.5 μg of the oligo-dT_{18} primer, and 1 μM dNTPs in a final volume of 20 μl. An aliquot of the first-strand cDNA served as a template in the PCR for the synthesis of second-strand cDNA, and subsequent amplification of double-stranded cDNA was performed with designed gene-specific primers. The amplicons were separated by electrophoresis in a 1% agarose gel, and the product of expected size was extracted from the gel using the Silica Bead DNA Gel

TABLE 1 | Primers employed in this study.

Primers	DNA sequence (5′-3′)	Amplicon length (bp)
TaS6K_Fw	TATCGAATTCACATGGTTTCCTCTGAG	1,475
TaS6K_Rev	ATCACCCGGGGGATCCTTAGCCTAGAG	
Amy1–3a_Fw	ATGTGGCCCTTCCCTTCCGA	409
Amy1–3a_rev	TGGATGTCCCTCATCCTCACTTTTACA	
TaGamyB_Fw	GGTGGACTACGTGAAGAAGC	369
TaGamyB_Rev	GATTTTCGCCGCAGTTGAAATCGC	
TaABI5 _Fw	TGACGCTGGAGCAGTTTCTT	332
TaABI5_Rev	TCGCCCATGCAGTTCATCAT	
α-Tubilin_Fw	ATCTCCAACTCCACCAGTGTCG	219
α-Tubilin_Rev	TCATCGCCCTCATCACCGTC	
RHT_SmaI_Fw	ATTATCCCGGGATGAAGCGGGAGTACCA	1,895
RHT_HindIII_Rev	TATTCAAGCTTTCACGGCCCGGCCAGG	

Extraction Kit (Thermo Scientific, Lithuania). The fragment was cloned into the pBluescript II SK (+) vector at *Eco*RI and *Bam*HI restriction sites by means of the Rapid DNA Ligation Kit (Thermo Scientific, Lithuania), and the ligation product was transfected into competent *Escherichia coli* DH5α cells. Colonies of *E. coli* carrying the plasmid with an insert were screened out by complementation of the *lacZ* gene, and the plasmid DNAs were isolated with the GeneJET Plasmid Miniprep Kit (Thermo Scientific, Lithuania). The presence of the insert in the isolated plasmids was confirmed by PCR with gene-specific primers, and its sequence was confirmed by sequencing in both directions with forward and reverse M13 primers.

Primers used for RT-PCR (PCR) are listed in **Table 1**. RT-PCR amplification of a 409 bp fragment of α-amylase cDNA was performed using Amy1-3a_Fw and Amy1-3a_Rev as a forward and reverse primer, respectively. RT-PCR amplification of the 369-bp fragment representing cDNA of *GAMYB* was performed with TaGamyB_Fw and TaGamyB_Rev as a forward and reverse primer, respectively. RT-PCR amplification of *T. aestivum* ABA response element-binding factor (*TaABI5*) cDNA (332 bp) was performed with TaABI5_Fw and TaABI5_Rev as a forward and reverse primer, respectively. All amplifications were carried out with Taq DNA polymerase (Promega, Madison, WI 53711, United States). The resulting PCR products were resolved by electrophoresis in a 2% agarose gel and visualized by ethidium bromide staining.

Expression and Purification of 6xHis-Tagged TaS6K1

The cDNA encoding TaS6K1 was subcloned into the pET28c vector at *Eco*RI and *Not*I sites resulting in expression plasmid pET28c-TaS6K1, which carries an N-terminal 6xHis-tag sequence. The wheat recombinant TaS6K1 (rTaS6K1) protein was expressed in (and purified from) the *E. coli* Rosetta (DE3) strain. Briefly, *E. coli* cells were electroporated with pET28c-TaS6K1, the resultant kanamycin-resistant transformants were grown to optical density at 600 nm of 0.6 at 37°C, and protein expression was then induced by 0.1 mM isopropyl β-D-1-thiogalactopyranoside (IPTG) overnight at 30°C. Due to high expression in the Rosetta strain, it was possible to purify rTaS6K1 to homogeneity via only two chromatographic steps. All the purification procedures were carried out at 4°C. The bacteria were harvested by centrifugation, and the cell pellets were lysed using a French press at 18,000 psi in a buffer consisting of 20 mM HEPES-KOH (pH 7.6), 50 mM KCl, and a Complete Protease Inhibitor Cocktail (Roche Diagnostics, Switzerland). The lysates were cleared by centrifugation at 40,000 × *g* for 30 min at 4°C, and the buffer in the resulting supernatant was adjusted to 500 mM NaCl and 20 mM imidazole. The protein sample was loaded onto a HiTrap Chelating HP column (GE Healthcare) charged with Ni^{2+}. The eluted fractions containing rTaS6K1 were pooled and loaded onto a 1-ml HiTrap-Heparin column (GE Healthcare). The bound proteins were eluted in a 50–600 mM KCl gradient. The purified protein samples were stored at −20°C in 50% glycerol. The homogeneity of the protein preparations was verified by SDS-PAGE (**Supplementary Figure S1A**).

Preparation of an Anti-TaS6K1 Antibody

The anti-TaS6K1 polyclonal antibody was raised against the full-length 6xHis-tagged rTaS6K1 protein. Approximately 0.5 mg of the purified rTaS6K1 was mixed with an equal volume of Freund's complete adjuvant (F5881, Sigma-Aldrich, Canada) and injected at five spots on the back of each rabbit. Three additional injections were made at 2-week intervals. 1 week after the last injection, blood was collected, and ammonium sulfate was added to 3 ml of the obtained rabbit antiserum to achieve 50% saturation. The precipitate was collected by centrifugation, and the pellet was dissolved in purified water and dialyzed against 10 mM potassium phosphate buffer (pH 7.0). The obtained immunoglobulin fraction was loaded on a column with protein A agarose beads equilibrated with the abovementioned buffer. After a wash with the same buffer, antibodies were eluted with 100 mM glycine buffer (pH 3.0). The IgG-containing fractions were pooled, and pH was adjusted to 7.0 with 1.0 M Tris base. The resulting suspension was kept at 4°C. This antibody was evaluated in an optimized Western blot assay, and the obtained signal was very strong even when the antibody was diluted 1:20,000.

Antiserum Titer Determination by an ELISA

The titers of antisera were determined by an indirect ELISA. Each well of a 96-well ELISA plate (Corning Inc., United States) was coated with 1 μg of rTaS6K1 dissolved in 100 μl of 50 mM carbonate-bicarbonate buffer (pH 9.6) via overnight incubation at 4°C. After three washes with phosphate-buffered saline (PBS) Tween buffer (PBST; 0.05% of Tween 20 in PBS, pH 7.4), the wells were blocked with 100 μl of 3% BSA in PBST for 1 h at 37°C and then washed again twice with PBST. After blocking, 100 μl of serially diluted anti-TaS6K1 serum (1:1,000 to 1:128,000) was added into the antigen-coated wells. The plate was covered with an adhesive plastic and incubated for 2 h at room temperature and then washed four times with PBST. At the next step, a 1:30,000-diluted alkaline phosphatase-conjugated goat anti-rabbit IgG antibody (Sigma, Canada) was added at 100 μl/well and incubated for 1 h at 37°C. After a wash, 100 μl of a freshly prepared p-nitrophenyl phosphate (substrate) solution was added into each well, and the plate was incubated at room temperature in a dark place. Finally, absorbance was measured at 405 nm (A_{405}) on a Multiskan FC plate reader (Thermo Scientific, Waltham, MA, United States). The antibody titer is defined as the highest dilution of antiserum at which the ratio of A_{405} (A_{405} of post-immunization serum/A_{405} of preimmunization serum) is >2:1. All samples were tested in triplicate, with each plate containing control wells with positive serum samples and control wells with negative reference serum.

Plant Protein Extraction and Western Blotting

Wheat embryos were ground in liquid nitrogen and then resuspended in lysis buffer A consisting of 50 mM Tris–HCl, 50 mM sodium β-glycerophosphate (pH 7.6), 25 mM EDTA, 25 mM EGTA, 50 mM NaF, 5 mM Na_3VO_4, 10% of glycerol, 1% of

Triton X-100, 1 mM phenylmethylsulfonyl fluoride, and EDTA-free protease inhibitors (Roche Applied Science). The cell debris was pelleted, and the protein concentration was determined using the Bradford Protein Assay Kit (Bio-Rad, France). Total protein samples (25 μg) from each extract were fractionated by SDS-PAGE in a 10% gel and then electroblotted onto a polyvinylidene difluoride (PVDF) membrane (Pierce) by means of a Bio-Rad Mini-Trans-blot Cell. After that, the membrane was gently shaken in a blocking solution consisting of 5% milk and 0.1% Tween 20 in 1× TBS [Tris-buffered saline: 50 mM Tris–HCl (pH 7.5) and 20 mM NaCl] for 1 h at room temperature. After removal of the blocking solution, the membrane was incubated in 10 ml of a 20,000-fold dilution of either the anti-α-amylase polyclonal antibody or anti-TaS6K1 polyclonal antibody overnight at 4°C. The membrane was washed five times in 10 ml of wash buffer (1× TBS with 0.1% of Tween 20) for 5 min each time. Next, the membrane was incubated in 10 ml of a secondary antibody (1:30,000 dilution in the blocking solution with 0.1% of Tween 20) for 1 h at room temperature. Then, the membrane was washed five times in 10 ml of wash buffer, for 5 min each time. The working substrate solution was prepared by mixing an equal volume of a peroxide solution and luminal/enhancer solution and was used at 0.1 ml/(cm^2 of the blot area). The membrane was incubated in the working solution for 2 min in darkness, and Kodak X-Omat was exposed to the film. The polyclonal antibody to wheat α-amylase was kindly provided by Dr. A. Khakimzhanov (Aitkhozhin Institute of Molecular Biology and Biochemistry, Kazakhstan).

For analyses of phosphorylation of TaS6K1 in cell-free extracts, the embryos were dissected from 1-DAG seeds pre-treated with 100 μM PBZ for 20 h and then were incubated with 10 mM $CaCl_2$ and 1 μM GA in the absence or presence of 10 μM rapamycin. The wheat embryos were ground in liquid nitrogen and then resuspended in lysis buffer B consisting of 50 mM Tris–HCl (pH 7.6), 150 mM NaCl, an EDTA-free phosphatase inhibitor cocktail, 1 mM phenylmethylsulfonyl fluoride, 10 μg/ml of leupeptin, and 1 μg/ml of aprotinin. Samples of cell lysates containing 10 μg of protein were separated by SDS-PAGE in a 10% gel and transferred to a 0.2-μm PVDF membrane (Pierce). Membranes were blocked with 5% BSA for 2 h in TBS with 0.02% of Tween 20 and probed overnight with an anti-phospho-p70 S6 kinase (T389) antibody (1:1,000; Cell Signaling Technology, Danvers, MA, United States) and the anti-TaS6K1 antibody (1:20,000), followed by 1 h incubation with secondary antibodies coupled to peroxidase (1:10,000 and 1:30,000, respectively).

Zymogram Analysis of α-Amylase

Non-denaturing polyacrylamide gel electrophoresis (native PAGE) was performed according to the standard method (Laemmli, 1970) to obtain a zymogram of α-amylase. Wheat embryos were ground in liquid nitrogen and then resuspended in 10 mM $CaCl_2$. The samples were mixed with 50% saccharose and loaded onto a polyacrylamide gel (4 and 10% polyacrylamide for the stacking and resolving gels, respectively). Electrophoresis was carried out at 100 V and 4°C. After that, the gel was incubated in 10 mM $CaCl_2$ for 30 min at room temperature. Then, the gel was incubated in a 1% (w/v) starch solution at 30°C and shaken for 60 min. After the gel was washed with distilled water, it was stained with the Lugol solution (1.3% I_2 and 3% KI). The bands of α-amylase activity appeared as bright bands on a dark background and were photographed.

Immunoprecipitation of TaS6K1

Wheat embryos were ground in liquid nitrogen and then resuspended in lysis buffer A. After centrifugation at 13,000 × *g* for 10 min, 4 μg of the anti-TaS6K1 polyclonal antibody was added to the cleared supernatant and incubated with rotation for 6 h. Then, 20 μl of a 50% slurry of protein G-Sepharose was added, and the incubation was continued for 4 h. Captured immunoprecipitates were washed three times with lysis buffer. Samples were resolved by SDS-PAGE, and proteins were transferred to a PVDF membrane and visualized by immunoblotting with either the anti-TaS6K1 polyclonal antibody or phospho-AtS6K antibody (p-T449; Abcam, Cambridge, United Kingdom). A goat anti-rabbit IgG (Abcam, Cambridge, United Kingdom) or mouse anti-rabbit IgG (Conformation Specific; Cell Signaling Technology, Danvers, MA, United States) antibody, respectively, was used to detect the primary antibodies.

Statistical Analysis

Data were analyzed for statistical significance by the application of complete randomized design with three replicates. The two-tailed *t* test, assuming equal variances, was conducted to determine whether the differences were statistically significant. Data with a value of $P < 0.05$ were deemed significant.

RESULTS

Effects of Rapamycin or Another mTOR Kinase Inhibitor on the Growth of Wheat Whole Seeds and of Isolated Wheat Embryos

In initial experiments, we assessed the effects of rapamycin on the germination capacity of intact wheat seeds. Germination of wheat seeds was tested in the presence of various concentrations of rapamycin. The effects of rapamycin on seed growth were observed after 2 and 4 days (**Figure 1A**). Rapamycin at 0.1–1.0 μM caused a relatively weak inhibition of the germination of caryopses. Significant retardation of radicle emergence was observed in the presence of 5 or 10 μM rapamycin following 2 days of treatment. Although the rapamycin-treated seeds were able to germinate after 4 days, we observed potent retardation of seedling growth by 10 μM rapamycin leading to a substantial reduction in fresh weight of seedlings and in root and shoot length ($P < 0.01$). **Figures 2A,B** shows that rapamycin at 10 μM caused a reduction in the length of shoots by 49.17%, length of roots by 67.47%, and fresh weight of seedlings by 64% when compared with the control (DMSO-treated) seeds.

In yeasts and animals, rapamycin has been used extensively to dissect the TOR pathway because of the ability to specifically inhibit TOR activity (Thoreen et al., 2009). Nonetheless, in

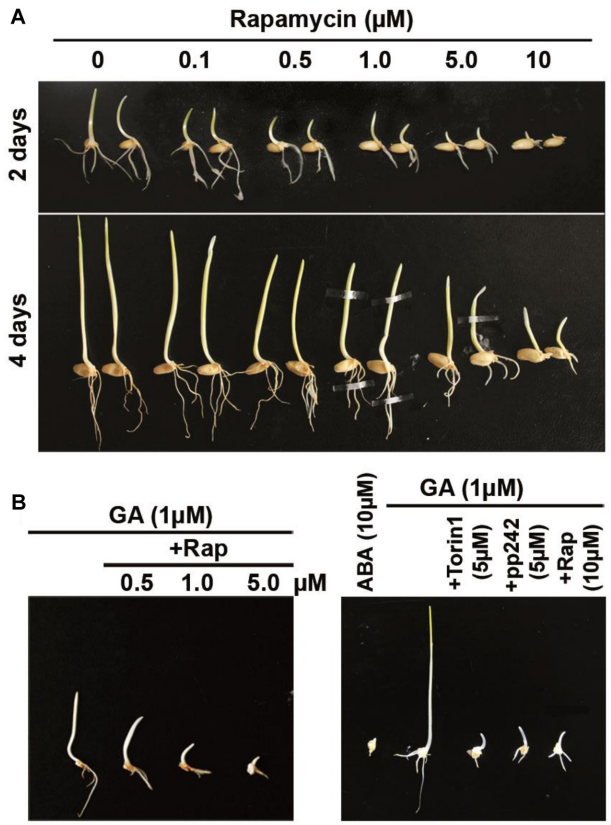

FIGURE 1 | Rapamycin and ATP-competitive target of rapamycin (TOR) inhibitors exert inhibitory effects on the growth of wheat whole seeds and of isolated wheat embryos. **(A)** The phenotype of seedlings after 2 and 4 days of germination in the presence of rapamycin. The surface-sterilized seeds were germinated under long-daylight conditions at room temperature on filter paper soaked with sterile water supplemented with rapamycin at different concentrations for 2 and 4 days. **(B)** Effects of rapamycin and ATP-competitive TOR inhibitors on isolated wheat embryos. The embryos were incubated on a 0.5× MS medium with 10 μM ABA or 1 μM GA alone and in combination with rapamycin, torin1, or pp242 for 4 days.

comparison with yeast or mammalian cells growth inhibition of wheat seeds requires much higher concentrations of rapamycin (Vezina et al., 1975; Kuo et al., 1992). Recently, new mTOR kinase inhibitors were developed that are more effective than rapamycin in cancer therapy (Zhang et al., 2011). The new TOR kinase inhibitors are ATP-competitive compounds targeting the ATP-binding pocket within the mTOR kinase domain (Zhou et al., 2010). The mTOR kinase inhibitors have been successfully applied to inhibit TOR signaling in plants (Montane and Menand, 2013; Dong et al., 2015; Xiong and Sheen, 2015; Xiong et al., 2016). We found that the suppressive effect of torin1 on wheat germination was more potent compared to the effects of rapamycin, namely, the torin1-treated wheat seedlings contained a smaller cotyledon with a significant concentration-dependent reduction in seedling growth. A substantial decrease in shoot (91%) and root length (86.76%) compared to the control was observed after 5 μM torin1 treatment. At the 1 μM concentration, its inhibitory effect decreased to 41.64 and 24%, respectively, and only a weak effect of torin1 was detectable at 0.5 μM indicating only a 9.1 and 5% decrease, respectively. The strong inhibitory impact of torin1 at 5 μM was consistent with a dramatic 95% decrease in fresh weight of seedlings, which was only 56.7% at 1 μM torin1 (**Figures 2C,D**).

The germination of isolated wheat embryos also indicated sensitivity to the mTOR inhibitors. To investigate the sensitivity of embryo growth to rapamycin, the isolated embryos were transferred to the 0.5× MS medium with 10 μM ABA or 1 μM GA alone and in combination with rapamycin, torin1, or pp242 (**Figure 1B**). Naturally occurring growth inhibitor ABA was very effective at repressing embryo growth judging by the growth of untreated control embryos. We found that rapamycin at 0.5 μM inhibited embryo growth even after 4 days of incubation, meaning its more potent impact on isolated wheat embryos. The inhibitory influence of rapamycin on embryo growth was more pronounced at its higher concentrations (5 and 10 μM). Besides, the embryo growth was significantly inhibited by mTOR kinase inhibitor torin1 or pp242 (**Figure 1B**). In the absence of GA, mTOR kinase inhibitors also strongly inhibited the embryo growth (**Supplementary Figure S2**).

Taken together, these results strongly indicated that the growth of wheat seeds is dependent on *T. aestivum* TOR (TaTOR) signaling.

Rapamycin and Torin1 Each Inhibits the Expression of GA-Induced α-Amylase and *GAMYB* Genes but Not the ABA-Induced *TaABI5* Gene

The analysis of wheat embryo extracts uncovered a significant increase in α-amylase levels in embryos treated with 1 μM GA_3 for 24 h compared with the extract obtained from the untreated (control) embryos. The addition of 10 μM ABA to the incubation medium abrogated α-amylase production (**Figure 3A**). A dose-dependent effect of rapamycin on the GA-induced α-amylase production meant that rapamycin was effective at concentrations between 1 and 10 μM. Rapamycin at the 1 or 5 μM concentration had a weak effect on α-amylase production, whereas 10 μM rapamycin completely blocked the GA-induced α-amylase synthesis. We also examined the influence of torin1. As shown in **Figure 3A**, the incubation of embryos with torin1 prevented the GA-induced α-amylase accumulation in the concentration range from 1 to 10 μM.

The observation that the mTOR inhibitors were sufficient to block GA-induced α-amylase production in wheat embryos suggested that the TOR kinase activity is required for GA signaling. To determine whether TOR kinase activation is required for α-amylase mRNA accumulation, wheat embryos were incubated with 1 μM GA, 10 μM ABA, 1 μM GA + rapamycin (1–10 μM), or 1 μM GA + torin1 (1–10 μM) for 24 h, and relative levels of α-amylase gene expression were examined by RT-PCR. We found that GA induced a high level of α-amylase mRNA accumulation compared with untreated embryos (**Figure 3B**). The influence of rapamycin and of torin1 on α-amylase mRNA accumulation was concentration dependent. Their dose–response pattern was almost identical

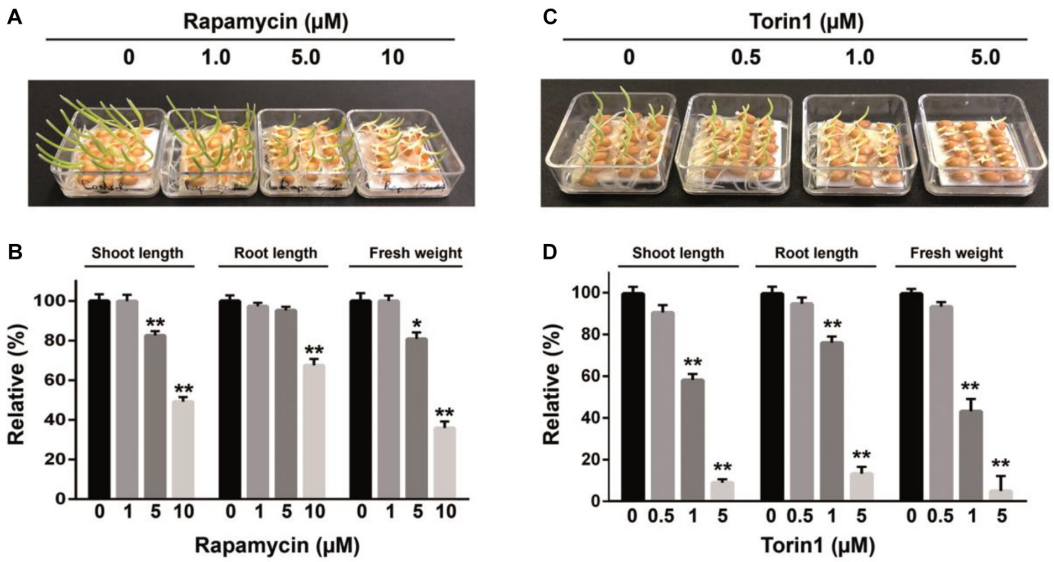

FIGURE 2 | The inhibitory effects of rapamycin and torin1 on growth of wheat whole seeds. The phenotype of seedlings after 4 days of germination in the presence rapamycin **(A)** or torin1 **(C)**; the fresh weight of seedlings and primary root and shoot lengths shown in panels **(A,C)** were measured and presented in panels **(B,D)** accordingly. The surface-sterilized seeds were germinated under long-daylight conditions at room temperature on filter paper soaked with sterile water supplemented with rapamycin or torin1 at different concentrations for 4 days. Values represent mean ± SEM. Asterisks indicate significant differences from the DMSO treatment (0.1%), according to Student's *t* test (*$P < 0.05$, **$P < 0.01$). Each studied drug concentration corresponds to three biological replicates.

to that noted for the α-amylase protein production in wheat embryos, as presented in **Figure 3A**. The expression profile of the α-tubulin gene was not altered by rapamycin or torin1 treatment. Therefore, the expression data are consistent with the above observations where rapamycin or torin1 inhibited the GA-induced α-amylase production, suggesting that the mTOR inhibitors suppress the induction of α-amylase gene expression and prevent the α-amylase enzyme synthesis (**Figure 3A**).

The major α-amylases in wheat (*T. aestivum*) are the high- and low-isoelectric point (pI) α-amylases encoded by two multigene families (α-Amy-1 and α-Amy-2 genes) located on chromosomes 6 and 7, respectively. Interestingly, the α-amylase isoenzymes in wheat cultivars differ in their pI but not in molecular weight (∼43 kDa) (Cheng et al., 2014). During wheat seed germination, high-pI α-amylase is produced at a higher concentration than low-pI α-amylase (Amy2) (Ju et al., 2019). In our study, the effect of GA was accompanied by the appearance of strong distinct bands corresponding to high-pI α-amylase on the electropherogram. Rapamycin and ATP-competitive inhibitors of TOR kinase abrogated this effect of GA (**Figure 3C**).

Because we observed a decrease in α-amylase gene expression and α-amylase activity after the inhibition of TOR, we tested whether the GA-induced *GAMYB* mRNA accumulation is sensitive to rapamycin or torin1. In cereals, GA regulates α-amylase synthesis in the aleurone and scutellar epithelium via induction of transcription factor GAMYB, which binds to a highly conserved GA-responsive element (GARE) in the promoters of α-amylase genes (Gubler et al., 1995; Washio, 2003). To assess the impact of TOR signaling on the GA-dependent GAMYB expression, we measured levels of *GAMYB* and α-amylase mRNAs in wheat embryos incubated with or without GA and an mTOR inhibitor. As depicted in **Supplementary Figure S3**, the levels of *GAMYB* and α-amylase mRNAs were induced dramatically by GA following 24 h of incubation. ABA caused an opposite effect by reducing the levels of *GAMYB* and α-amylase mRNAs that were associated with the induction of *TaABI5* mRNA expression. Although the rapamycin or torin1 treatment led to a substantial reduction of α-amylase and *GAMYB* mRNAs levels in GA-treated wheat embryos, neither mTOR inhibitor abolished ABA-dependent expression of TaABI5. This finding showed that the mTOR inhibitors selectively targeted the GA-dependent gene expression without turning on the ABA-dependent suppression of wheat embryo growth.

Taken together, these data suggested that the activation of TOR signaling takes place in the wheat scutellar epithelium and switches on critical steps of germination by inducing GAMYB and α-amylase synthesis.

GA-Dependent Phosphorylation TaS6K Is Sensitive to Inhibitors of the TOR Kinase and GA Biosynthesis Inhibitor Paclobutrazol

A well-validated substrate of the mTOR kinase is a p70 ribosomal protein: S6K1. The phosphorylation state of this protein represents the TORC1 activity in animal and plant cells (Mahfouz et al., 2006; Meyuhas and Dreazen, 2009; Fenton and Gout, 2011; Xiong and Sheen, 2015). Using a tBLASTn search, we identified a *T. aestivum* cDNA encoding putative wheat S6K1 by searching for an AtS6K1 ortholog within the wheat genome.

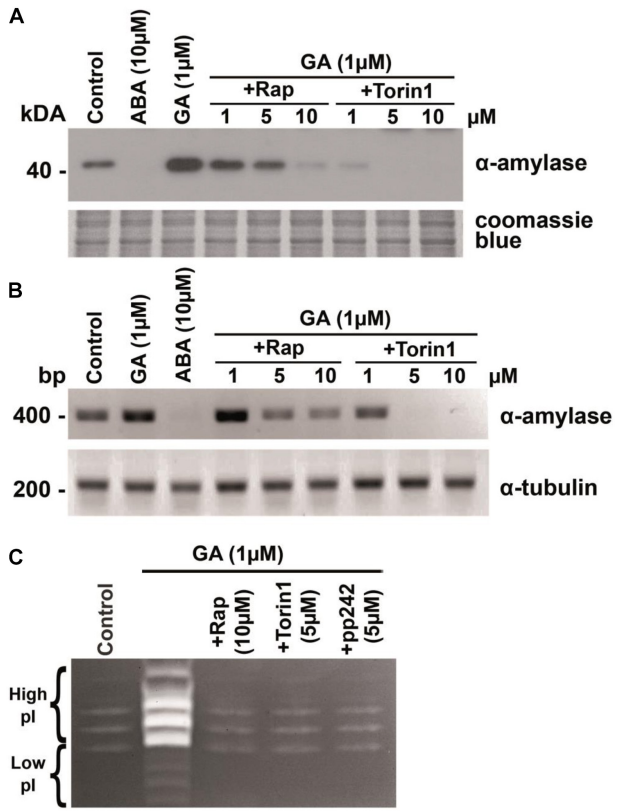

FIGURE 3 | Gibberellic acid (GA)-induced expression of the α-amylase gene is attenuated in the presence of TOR kinase inhibitors.
(A) Concentration-dependent influence of rapamycin or torin1 on GA-induced production of α-amylase. The wheat embryos dissected from 1-DAG seeds were incubated for 24 h in the presence 10 mM $CaCl_2$ (control) with or without 10 μM abscisic acid (ABA), or 1 μM GA, or 1 μM GA with different concentrations of rapamycin or torin1. The embryos were then lysed and subjected to immunoblotting. Rap, rapamycin. **(B)** Concentration-dependent effects of rapamycin and torin1 on GA-induced accumulation of α-amylase mRNA. The wheat embryos were incubated as described in panel **(A)**. A 409-bp fragment of α-amylase cDNA was amplified by RT-PCR with gene-specific primers. α-Tubulin expression served as an internal loading control. **(C)** Detection of α-amylase activity by staining. The wheat embryos were incubated for 24 h in the presence of 1 μM GA and 10 mM $CaCl_2$ with or without rapamycin, torin1, or pp242. The embryos were then lysed and subjected to staining for the activity of α-amylases following partition in a polyacrylamide gel electrophoresis (native PAGE).

An alignment of the TaS6K1 protein sequence revealed a high similarity to human S6K1 (47% sequence identity, GenBank accession No. NP_001258989.1), AtS6K (63% sequence identity, GenBank accession No. NC_003074.8), and *Oryza sativa* S6K1 (89% sequence identity, GenBank accession No. ABF95793.1; **Supplementary Figure S4**).

The wheat S6K protein sequence consists of 481 amino acid residues with a predicted molecular mass of 53.6 kDa. N- and C-terminal sequences are least conserved between TaS6K1 and animal S6K1 proteins in contrast to their highly conserved kinase domains. Analysis of the kinase domain structure of TaS6K1 revealed an activation loop (T-loop) motif, turn motif (TM), and hydrophobic motif (HM) with their phosphorylation sites conserved in all S6 kinases belonging to the AGC kinase family (**Figure 4**). In *T. aestivum*, sites T-loop serine 309 (S309), TM S451, and HM serine 467 (S467) correspond to sites threonine 229 (T229), S371, and T389 in human S6K1 (Magnuson et al., 2012; **Figures 4A,B**). TaS6K1 resembles AtS6K and also lacks the TOR signaling (TOS) motif within its N terminus and the autoinhibitory loop at the C terminus.

Next, to determine the possible involvement of TaS6K1 in the GA signaling pathway, we prepared a cDNA encoding TaS6K1 from the wheat young leaves by RT-PCR. Sequencing results indicated that the CDS sequence of TaS6K1 is identical to the NCBI version of TaS6K1 (GenBank accession No. AK451448.1). To study the TaS6K1 protein, we developed a specific antibody. To this end, the 6xHis-tagged form of the rTaS6K1 protein was expressed in *E. coli* strain Rosetta (DE3) and purified by affinity chromatography. The purified rTaS6K1 protein was injected into rabbits to produce the antibody. Coomassie-stained gels revealed that the purified rTaS6K1 protein represented the main protein band and did not contain other contaminating proteins that migrated slightly below a 70-kDa protein marker (**Supplementary Figure S1A**). In an immunoblotting analysis, the affinity-purified polyclonal anti-TaS6K1 antibody detected a single protein band corresponding to a purified 6xHis-tagged rTaS6K1 protein (**Supplementary Figure S1B**) but not another 6xHis-tagged recombinant protein, *T. aestivum* Ape1L (TaApe1L) (Joldybayeva et al., 2014; **Supplementary Figure S1B**). The ELISA results indicated that the purified polyclonal antibody has high sensitivity to TaS6K1 (**Supplementary Figure S5**).

The site of TORC1-mediated phosphorylation in S6K1 is conserved between yeast and humans. In wheat, the hydrophobic-motif S467 site corresponds to the T389 site in the human S6K1 protein and to the T449 site in the *Arabidopsis* S6K1 protein (**Figures 4A,B**). The phosphorylation of S6K1 on T389 or T449 represents TORC1 activity in animal or *Arabidopsis* cells, respectively. Therefore, we analyzed the TORC1-dependent phosphorylation of TaS6K1 in wheat embryos after initial enrichment of the TaS6K1 protein by immunoprecipitation with the specific affinity-purified antibody. The immunopurified TaS6K1 protein from cell extracts of wheat embryos treated with GA alone, GA + rapamycin (10 μM), or GA + torin1 (10 μM) for 24 h was analyzed by immunoblotting with the phospho-specific S6K1 antibody recognizing the phosphorylated HM site on *A. thaliana* S6K1 (Cao et al., 2019). As shown in **Figure 5A**, TaS6K1 phosphorylation was clearly detectable in the cell extracts of wheat embryos exposed to GA. Rapamycin reduced the phosphorylation of TaS6K1 on S467 at the concentrations preventing the GA-induced α-amylase synthesis.

Our study suggests that the GA-dependent TOR activity initiates germination through induction of α-amylase expression in wheat embryos. To test whether the TOR activity is dependent on *de novo* GA biosynthesis, we incubated wheat embryos with 100 μM PBZ known as a potent inhibitor of GA biosynthesis (Takahashi et al., 1991). As shown in **Figure 5B**, the presence of 1 μM GA substantially increased the α-amylase level in the embryos when compared with control embryos. The inhibition

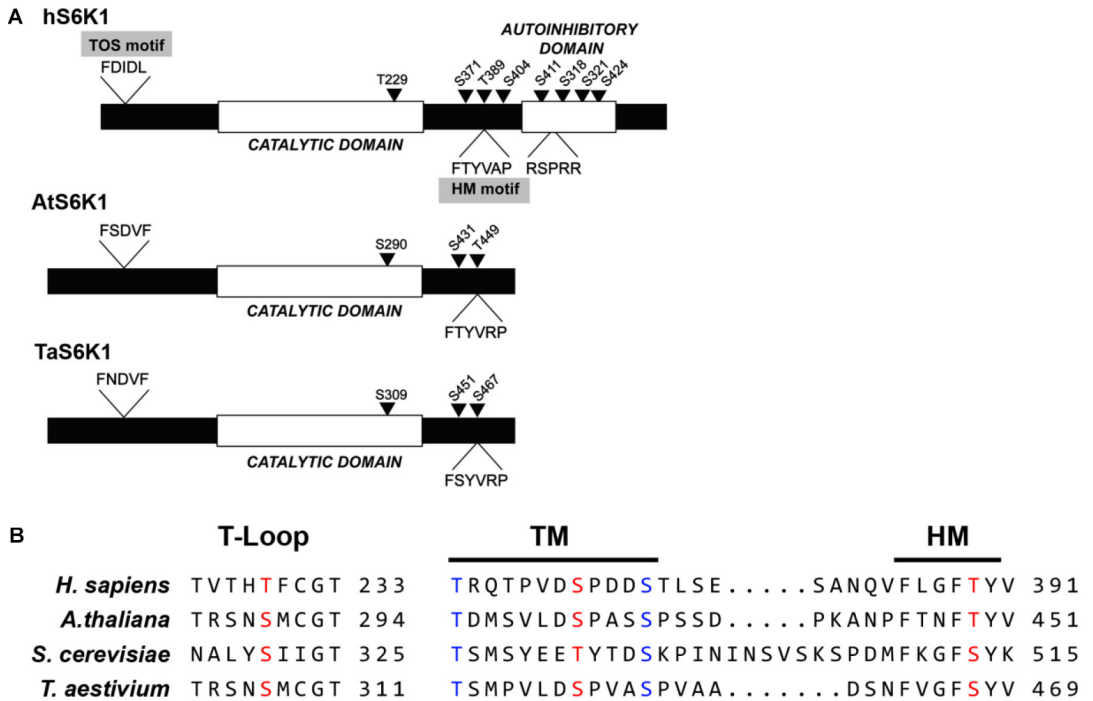

FIGURE 4 | The protein kinase sequence analysis of *Triticum aestivum* ribosomal protein S6 kinase 1 (TaS6K1) and its alignment with the orthologs. **(A)** Comparison of human S6K1 (hS6K1), *A. thaliana* S6K1 (AtS6K1), and *T. aestivum* S6K1 (TaS6K1). hS6K1 contains a TOS-motif, catalytic domain, and autoinhibitory domain, whereas TaS6K1 and AtS6K1 have a putative catalytic domain. Possible phosphorylation sites in TaS6K1 were predicted based on the comparison with phosphorylation sites of hS6K1. Conserved and important serine (S) and threonine (T) residues are marked with arrows. **(B)** Sequence alignment of the T-loop, turn motif (TM), and hydrophobic motif (HM) of hS6K1, AtS6K1, TaS6K1, and *Saccharomyces cerevisiae* Ypk3.

of GA synthesis completely blocked the α-amylase production, suggesting that the inhibitor was effective in repressing the synthesis of gibberellins. The addition of GA reversed the PBZ effect by restoring the α-amylase production. The expression level of TaS6K1 in the GA-treated wheat embryos was similar to that in the control or PBZ-treated embryos (**Figure 5B**). High phosphorylation of TaS6K1 was detected in GA-treated wheat embryos but not in PBZ-treated embryos (**Figure 5B**).

The phospho-specific antibody recognizing the T389 site on S6K1 was also effective at monitoring the phosphorylation of TaS6K1 in cell-free extracts of the wheat embryos treated with GA (**Figure 5C**). In the presence of GA, the phosphorylation of TaS6K1 increased following 3 h of incubation. The addition of rapamycin along with GA resulted in a significant decrease in the TaS6K1 phosphorylation.

DISCUSSION

Our study reveals a role of TOR signaling in wheat embryo growth. This conclusion is based on our finding that mTOR inhibitors were effective in suppressing wheat germination.

The inhibitory impact of rapamycin on wheat germination in isolated embryos was more pronounced compared with its effect in whole seeds. The dose response implies that the rapamycin concentration was 10-fold higher in intact seeds than in isolated embryos. This finding suggests that the drug permeability is hindered substantially in intact seeds, and the isolated wheat embryo is more accessible to the treatment with rapamycin. Of note, in our study, a significant reduction in wheat seed growth was observed at 10 μM rapamycin. This concentration range is at least 100 times the concentration that inhibits yeast proliferation (Heitman et al., 1991) or that reduces the size and proliferation of mouse embryonic fibroblasts (Wicker et al., 1990; Sarbassov et al., 2006; Thoreen and Sabatini, 2009). It is likely that a high concentration of rapamycin is required because of poor penetration of rapamycin through the thick hemicellulosic wall of plant cells. Indeed, this notion is supported by the observation that rapamycin at 100 nM is effective at inhibiting an endogenous TOR protein kinase activity as revealed by phosphorylation of the T449 site of AtS6K1 and the T455 site of AtS6K2 in an isolated protoplast (Xiong and Sheen, 2012). Besides, rapamycin causes only weak growth inhibition of most higher plant species including *Arabidopsis*, *Nicotiana tabacum*, *Brassica napus*, cotton, and potato (Menand et al., 2002; Mahfouz et al., 2006; Sormani et al., 2007; Ren et al., 2012; Montane and Menand, 2013; Deng et al., 2016, 2017; Song et al., 2017). The insensitivity or low sensitivity to rapamycin can be attributed to a limited ability of plant FKBP12 proteins to form an inhibitory ternary complex with rapamycin owing to a lack of the critical amino acids mediating the interaction with rapamycin (Choi et al., 1996; Xu et al., 1998; Sormani et al., 2007). On the other hand, it has been reported that the growth of *Zea mays* and tomato [variety *Solanum lycopersicum* (SI)] is sensitive to rapamycin (Agredano-Moreno et al., 2007; Xiong et al., 2016). A functional

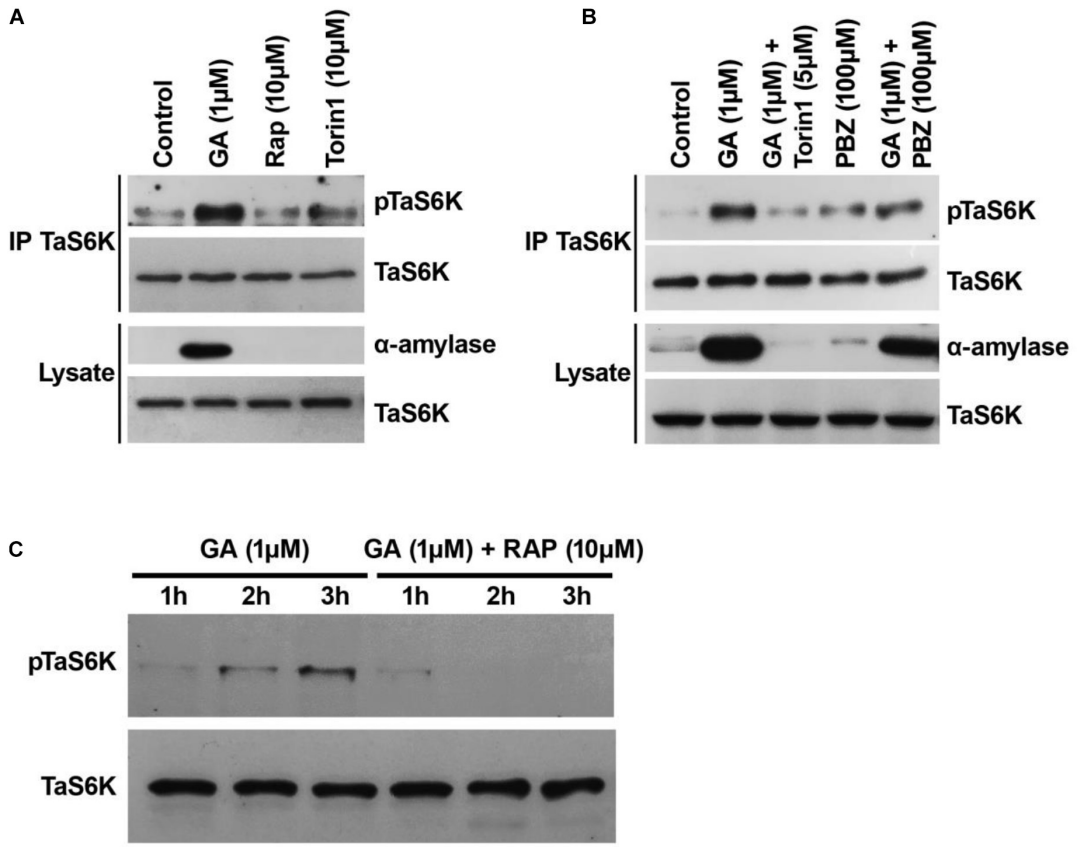

FIGURE 5 | *Triticum aestivum* TOR (TaTOR) activity of isolated wheat embryos sensitive to TOR inhibitors and GA biosynthesis inhibitor paclobutrazol (PBZ). **(A)** The TaS6K1 phosphorylation is sensitive to the mTOR inhibitors. The wheat embryos dissected from 1-DAG seeds were incubated in 10 mM $CaCl_2$ (control) with or without 1 μM GA or rapamycin or torin1 for 24 h. Rap, rapamycin. **(B)** The S467 phosphorylation level of TaS6K1 sensitive to the presence of paclobutrazol. The experiment was performed as in panel **(A)** using torin1 and PBZ as indicated. After 24 h, the embryos were lysed, TaS6K1 was immunoprecipitated, and the lysates and TaS6K1 immunoprecipitates were analyzed by immunoblotting for the indicated proteins or TaS6K phosphorylation. **(C)** Time course analyses of phosphorylation of TaS6K1 in wheat embryo cell-free extracts. Embryos were pre-treated with 100 μM PBZ for 20 h and were incubated with 1 μM GA and 10 mM $CaCl_2$ in the absence or presence of 10 μM rapamycin for the indicated periods. After the incubation time was over, the embryos were lysed and analyzed for phosphorylation states of TaS6K1 by immunoblotting.

study indicates that heterologous expression of tomato FKBP12 in *Arabidopsis* restores sensitivity to rapamycin (Xiong et al., 2016). It can be assumed that the rapamycin sensitivity in plants is species dependent, and more detailed studies are needed to determine why plants show different responses to the drug. Our study expands the list of rapamycin-sensitive plants by showing that rapamycin-dependent TaTOR signaling is launched during wheat seed germination.

Recent studies indicate that ATP-competitive inhibitors of the TOR kinase, including TORIN2, AZD-8055, WYE-132, and KU-63794, are more potent than rapamycin in inhibiting plant growth (Montane and Menand, 2013), and this phenomenon is linked to direct inhibition of the mTOR kinase activity. In our study, torin1 was ∼10-fold more effective than rapamycin at inhibiting the growth of the wheat seeds and of their isolated embryos. Indeed, torin1 exerted strong inhibition of root and shoot growth at 1 μM and caused a growth reduction in a concentration-dependent manner (**Figures 2C,D**). Altogether, the data indicate that rapamycin and torin1 most likely inhibit wheat seed growth by targeting the TaTOR protein.

The *Arabidopsis* genome contains one *TOR* gene (*AtTOR*) (Menand et al., 2002), two *RAPTOR* genes (Anderson et al., 2005; Deprost et al., 2005; Mahfouz et al., 2006; Rexin et al., 2015; Salem et al., 2018), and two *LST8* genes (Moreau et al., 2012). A loss-of-function mutation in *Raptor1b* leads to a significant delay in *Arabidopsis* seed germination (Salem et al., 2018). GA plays a crucial part in the regulation of early seed germination and breaking of dormancy (Weitbrecht et al., 2011). The breakdown of stored starch in the endosperm to support early seedling growth is an essential step for seed germination and subsequent seedling growth. At the early stage of germination, GA activates transcription factor GAMYB, which promotes *de novo* synthesis of α-amylases and an array of other hydrolases in the aleurone layer and embryo (Bethke et al., 1997). We hypothesized that the GA-dependent synthesis of α-amylase and consequent seed germination are mediated by the triggering of the TaTOR signaling pathway. We found that rapamycin specifically blocked

GA-induced α-amylase gene expression in wheat embryos. In this experiment, the effective range of rapamycin was between 1 to 10 μM for inhibition, and complete inhibition was reached in a 10 μM range (**Figure 3**). Torin1 was more effective than rapamycin and inhibited α-amylase gene expression at 1 μM. The dose-dependent effects of rapamycin and torin1 on the GA-induced α-amylase gene expression are consistent with those seen in the germination experiment.

It is noteworthy that the TOR inhibitors selectively targeted the GA-dependent gene expression without affecting ABA-dependent *TaABI5* gene expression. The finding that the mTOR inhibitors suppressed GA-regulated transcription factor GAMYB (implicated in the induction of α-amylase genes) indicates that TOR signaling performs a function upstream of the GA-dependent transcription of *GAMYB* gene. These results point out that TOR signaling plays an important role in the GA-inducible expression of α-amylase.

A key substrate and mediator of the TOR protein kinase is S6K1, which is evolutionarily conserved between plants and humans (Fenton and Gout, 2011; Xiong and Sheen, 2012, 2014). To investigate the involvement of S6K1 (a key substrate and mediator of the TOR protein kinase) in GA signaling, we isolated the cDNA gene of TaS6K1, an uncharacterized substrate of TOR in wheat. Sequence homology indicates that *tas6k1* is the human *p70 s6k* gene ortholog, and its product is likely to be a direct target of the TOR kinase activity in wheat plants (**Figure 4A,B**). Western blotting with the antibody generated against TaS6K1 revealed that TaS6K1 was present in the control wheat embryos,

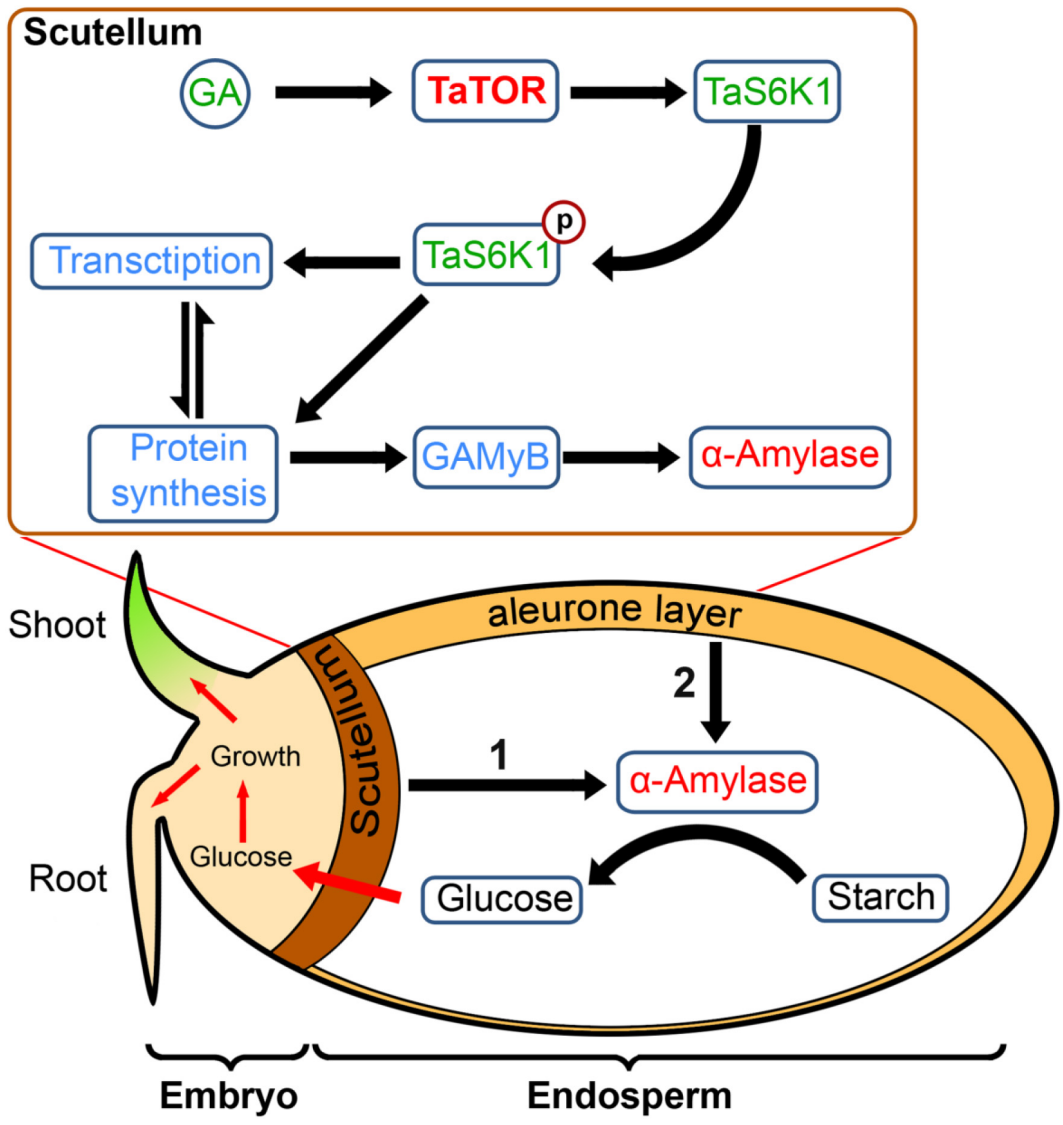

FIGURE 6 | The model: a role of pTOR signaling in wheat germination. At the initial triggering stage of germination, GA by activating the TaTOR–TaS6K1 signaling induces the synthesis of GA-induced myb-like transcription factor (GAMYB) and α-amylase in wheat embryo scutella cells required for turning on the germination and seedling growth. An intensive α-amylase synthesis takes place later in aleurone cells following an initial stage of germination.

and its expression was not induced by GA. By contrast, we detected increased TaS6K1 phosphorylation only in the presence of GA. Moreover, the TOR-dependent phosphorylation of a hydrophobic motif of TaS6K1 was sensitive to rapamycin and torin1 (**Figure 5A**).

The data presented here mean that GA switches on wheat germination processes by activating TaTOR signaling. Nonetheless, considering the antagonistic functions of ABA and GA, one could assume that the inhibition of the TOR kinase activity suppresses a GA response by decreasing the synthesis of ABA not by interfering with GA signaling.

Indeed, ABA, which induces polysome disassembly, inhibits cytokinin-induced phosphorylation of the 40S ribosomal S6 protein (Yakovleva and Kulaeva, 1987). More recently, it was demonstrated that the inhibition of TOR complex activity causes a significant decrease in ABA concentration and in the expression of genes *ZEP*, *NCED3*, and *AAO3* involved in ABA biosynthesis, in contrast to ABA-catabolic genes *CYP707A2* and *CYP707A3* (Kravchenko et al., 2015).

One way to examine the role of endogenous GA is to use an inhibitor of GA biosynthesis: PBZ. The latter inhibits GA biosynthesis by blocking cytochrome P450-dependent monooxygenases, thereby inhibiting oxidation of ent-kaurene into ent-kaurenoic acid (Rademacher, 2000).

In our study, gibberellin biosynthesis inhibitor PBZ blocked not only the α-amylase gene expression but also phosphorylation of TaS6K1 in wheat embryos. Exogenously applied GA reversed the PBZ effect by restoring the α-amylase production and phosphorylation of TaS6K1 (**Figure 5B**). Of note, in the presence of GA, the phosphorylation of TaS6K1 increased following 3 h of incubation (**Figure 5C**) and persisted over the course of 24 h (**Figures 5A,B**) in the PBZ-pre-treated embryos.

Thus, the data on gibberellin biosynthesis inhibitor support our theoretical model suggesting that GA regulates TOR–S6K1 signaling by launching the TaTOR kinase activity.

Dry seeds are heterotrophic; hence, germination depends on the energy accumulated in storage materials until the seedling reaches the autotrophic state. However, for starch in the endosperm to be converted to sugars, the embryonic scutellum and aleurone cell must synthesize secretory proteins such as α-amylase (**Figure 6**). In cereals, the α-amylase synthesis first initiated in the scutellum of embryos and followed by the aleurone layer (Subbarao et al., 1998). Synthesis of α-amylase requires a large pool of available amino acids, which is likely to come from the protein storage vacuoles (Bethke et al., 1997). From our results, we propose that, in wheat embryo scutella cells, the effect of GA directly or indirectly can mediate TOR activation, triggering phosphorylation of TaS6K1 at the TOR-specific hydrophobic motif residue S467, which promotes the induction of synthesis of α-amylase and therefore the initiation of germination and subsequent seedling growth (**Figure 6**).

How GA can activate TaTOR signaling is an attractive puzzle to pursue. Activation of mTORC1 in animal cells by amino acids depends on the small GTPase RagA/B or RagC/D or small GTPase Rheb by growth factor signaling (Shen et al., 2017). In plant *A. thaliana*, auxin can activate TOR via Rho-like small GTPase 2 (ROP2) (Schepetilnikov et al., 2017). Of note, two putative Rho GTPase genes were found to be upregulated 17- to 40-fold in response to GA in barley (Chen and An, 2006). It will be interesting to determine whether high expression of GA-dependent Rho GTPases is sufficient to trigger TaTOR kinase activity. Most likely, a biochemical characterization of the TaTOR complex will be a most informative study in identifying a GA-dependent regulatory component of Ta-TOR complex that has been critical in identifying a role of the Rag GTPases in a nutrient-dependent regulation of mTORC1.

CONCLUSION

In conclusion, the presented data indicate that GA-dependent activation of TOR–S6K1 signaling turns on active synthesis of α-amylase required for wheat embryo growth.

DATA AVAILABILITY STATEMENT

The raw data supporting the conclusions of this article will be made available by the authors, without undue reservation.

ETHICS STATEMENT

The animal study protocol was reviewed and approved by the Ethics Committee on the Bioethics of the Scientific Center for Anti-Infectious Drugs (SCAID), Almaty, Kazakhstan.

AUTHOR CONTRIBUTIONS

BS, SA, IS, and AM conducted the experiments. AB, DS, and MS wrote the manuscript and analyzed the data. All authors contributed to the critical review of the manuscript and approved the submitted version.

FUNDING

This work was funded by the Ministry of Education and Science of the Republic of Kazakhstan (KZ) (grants Nos. AP05131569 and AP05131478).

SUPPLEMENTARY MATERIAL

The Supplementary Material for this article can be found online at: https://www.frontiersin.org/articles/10.3389/fcell.2020.606685/full#supplementary-material

REFERENCES

Agredano-Moreno, L. T., Reyesdela Cruz, H., Martinez-Castilla, L. P., and Sánchez de Jiménez, E. (2007). Distinctive expression and functional regulation of the maize (*Zea mays* L.) TOR kinase ortholog. *Mol. Biosyst.* 3, 794–802. doi: 10.1039/b705803a

Anderson, G. H., Veit, B., and Hanson, M. R. (2005). The Arabidopsis *AtRaptor* genes are essential for post-embryonic plant growth. *BMC Biol.* 3:12. doi: 10.1186/1741-7007-3-12

Aoki, N., Ishibashi, Y., Kai, K., Tomokiyo, R., Yuasa, T., and Iwaya-Inoue, M. (2014). Programmed cell death in barley aleurone cells is not directly stimulated by reactive oxygen species produced in response to gibberellin. *J. Plant Physiol.* 171, 615–618. doi: 10.1016/j.jplph.2014.01.005

Bak-Jensen, K. S., Laugesen, S., Ostergaard, O., Finnie, C., Roepstorff, P., and Svensson, B. (2007). Spatio-temporal profiling and degradation of α-amylase isozymes during barley seed germination. *FEBS J.* 274, 2552–2565. doi: 10.1111/j.1742-4658.2007.05790.x

Barbet, N. C., Schneider, U., Helliwell, S. B., Stansfield, I., Tuite, M. F., and Hall, M. N. (1996). TOR controls translation initiation and early G1 progression in yeast. *Mol. Biol. Cell* 7, 25–42. doi: 10.1091/mbc.7.1.25

Bethke, P. C., Schuurink, R. C., and Jones, R. L. (1997). Hormonal signaling in cereal aleurone. *J. Exp. Bot.* 48, 1337–1356. doi: 10.1093/jxb/48.7.1337

Cao, P., Kim, S. J., Xing, A., Schenck, C. A., Liu, L., Jiang, N., et al. (2019). Homeostasis of branched-chain amino acids is critical for the activity of TOR signaling in *Arabidopsis*. *eLife* 8:e50747.

Chen, K., and An, Y. Q. C. (2006). Transcriptional responses to gibberellin and abscisic acid in barley aleurone. *J. Integr. Plant Biol.* 48, 591–612. doi: 10.1111/j.1744-7909.2006.00270.x

Cheng, C. R., Oldach, K., Mrva, K., and Mares, D. (2014). Analysis of high pI α-Amy-1 gene family members expressed in late maturity α-amylase in wheat (*Triticum aestivum* L.). *Mol. Breed.* 33, 519–529. doi: 10.1007/s11032-013-9968-z

Choi, J., Chen, J., Schreiber, S. L., and Clardy, J. (1996). Structure of the FKBP12-rapamycin complex interacting with the binding domain of human FRAP. *Science* 273, 239–242. doi: 10.2307/2890420

De Vleesschauwer, D., Filipe, O., Hoffman, G., Seifi, H. S., Haeck, A., Canlas, P., et al. (2018). Target of rapamycin signaling orchestrates growth-defense trade-offs in plants. *New Phytol.* 217, 305–319. doi: 10.1111/nph.14785

Deng, K., Dong, P., Wang, W., Feng, L., Xiong, F., Wang, K., et al. (2017). The TOR pathway is involved in adventitious root formation in *Arabidopsis* and potato. *Front. Plant Sci.* 8:784. doi: 10.3389/fpls.2017.00784

Deng, K., Yu, L., Zheng, X., Zhang, K., Wang, W., Dong, P., et al. (2016). Target of rapamycin is a key player for auxin signaling transduction in *Arabidopsis*. *Front. Plant Sci.* 7:291. doi: 10.3389/fpls.2016.00291

Deprost, D., Truong, H. N., Robaglia, C., and Meyer, C. (2005). An *Arabidopsis* homolog of RAPTOR/KOG1 is essential for early embryo development. *Biochem. Biophys. Res. Commun.* 326, 844–850. doi: 10.1016/j.bbrc.2004.11.117

Dong, P., Xiong, F., Que, Y., Wang, K., Yu, L., Li, Z., et al. (2015). Expression profiling and functional analysis reveals that TOR is a key player in regulating photosynthesis and phytohormone signaling pathways in *Arabidopsis*. *Front. Plant Sci.* 6:677. doi: 10.3389/fpls.2015.00677

Fenton, T. R., and Gout, I. T. (2011). Functions and regulation of the 70 kDa ribosomal S6 kinases. *Int. J. Biochem. Cell Biol.* 43, 47–59. doi: 10.1016/j.biocel.2010.09.018

Fu, X., Richards, D. E., Ait-ali, T., Hynes, L. W., Ougham, H., Peng, J., et al. (2002). Gibberellin-mediated proteasome-dependent degradation of the barley DELLA protein SLN1 repressor. *Plant Cell* 14, 3191–3200. doi: 10.1105/tpc.006197

Gomez-Cadenas, A., Zentella, R., Walker-Simmons, M. K., and Ho, T. H. (2001). Gibberellin/abscisic acid antagonism in barley aleurone cells: site of action of the protein kinase PKABA1 in relation to gibberellin signaling molecules. *Plant Cell* 13, 667–679. doi: 10.1105/tpc.13.3.667

Gomi, K., Sasaki, A., Itoh, H., Ueguchi-Tanaka, M., Ashikari, M., Kitano, H., et al. (2004). GID2, an F-box subunit of the SCF E3 complex, specifically interacts with phosphorylated SLR1 protein and regulates the gibberellin-dependent degradation of SLR1 in rice. *Plant J.* 37, 626–634. doi: 10.1111/j.1365-313x.2003.01990.x

Gubler, F., Kalla, R., Robert, J. K., and Jacobsen, J. V. (1995). Gibberellin-regulated expression of a *myb* gene in barley aleurone cells: evidence for MYB transactivation of a high-pI α-amylase gene promoter. *Plant Cell* 7, 1879–1891. doi: 10.1105/tpc.7.11.1879

Heitman, J., Movva, N. R., and Hall, M. N. (1991). Targets for cell cycle arrest by the immunosuppressant rapamycin in yeast. *Science* 253, 905–909. doi: 10.1126/science.1715094

Henriques, R., Magyar, Z., Monardes, A., Khan, S., Zalejski, C., Orellana, J., et al. (2010). *Arabidopsis* S6 kinase mutants display chromosome instability and altered RBR1-E2F pathway activity. *EMBO J.* 29, 2979–2993. doi: 10.1038/emboj.2010.164

Holz, M. K., Ballif, B. A., Gygi, S. P., and Blenis, J. (2005). mTOR and S6K1 mediate assembly of the translation preinitiation complex through dynamic protein interchange and ordered phosphorylation events. *Cell* 123, 569–580. doi: 10.1016/j.cell.2005.10.024

Joldybayeva, B., Prorok, P., Grin, I. R., Zharkov, D. O., Ishenko, A. A., Tudek, B., et al. (2014). Cloning and characterization of a wheat homologue of apurinic/apyrimidinic endonuclease APE1L. *PLoS One* 9:e92963. doi: 10.1371/journal.pone.0092963

Jones, H. D., Smith, S. J., Desikan, R., Plakidou-Dymock, S., Lovegrove, A., and Hooley, R. (1998). Heterotrimeric G proteins are implicated in gibberellin induction of amylase gene expression in wild oat aleurone. *Plant Cell* 10, 245–254. doi: 10.1105/tpc.10.2.245

Ju, L., Deng, G., Liang, J., Zhang, H., Li, Q., Pan, Z., et al. (2019). Structural organization and functional divergence of high isoelectric point α-amylase genes in bread wheat (*Triticum aestivum* L.) and barley (*Hordeum vulgare* L.). *BMC Genet.* 20:25. doi: 10.1186/s12863-019-0732-1

Kaneko, M., Itoh, H., Ueguchi-Tanaka, M., Ashikari, M., and Matsuoka, M. (2002). The -amylase induction in endosperm during rice seed germination is caused by gibberellin synthesis in epithelium. *Plant Physiol.* 128, 1264–1270. doi: 10.1104/pp.010785

Kravchenko, A., Citerne, S., Jehanno, I., Bersimbaev, R. I., Veit, B., Meyer, C., et al. (2015). Mutations in the Arabidopsis *Lst8* and *Raptor* genes encoding partners of the TOR complex, or inhibition of TOR activity decrease abscisic acid (ABA) synthesis. *Biochem. Biophys. Res. Commun.* 467, 992–997. doi: 10.1016/j.bbrc.2015.10.028

Kuo, C. J., Chung, J., Fiorentino, D. F., Flanagan, W. M., Blenis, J., and Crabtree, G. R. (1992). Rapamycin selectively inhibits interleukin-2 activation of p70 S6 kinase. *Nature* 358, 70–73. doi: 10.1038/358070a0

Laemmli, U. K. (1970). Cleavage of structural proteins during the assembly of the head of bacteriophage T4. *Nature* 227, 680–685. doi: 10.1038/227680a0

Laplante, M., and Sabatini, D. M. (2012). mTOR signaling in growth control and disease. *Cell* 149, 274–293. doi: 10.1016/j.cell.2012.03.017

Loewith, R., and Hall, M. N. (2011). Target of rapamycin (TOR) in nutrient signaling and growth control. *Genetics* 189, 1177–1201. doi: 10.1534/genetics.111.133363

Magnuson, B., Ekim, B., and Fingar, D. C. (2012). Regulation and function of ribosomal protein S6 kinase (S6K) within mTOR signalling networks. *Biochem. J.* 441, 1–21. doi: 10.1042/BJ20110892

Mahfouz, M. M., Kim, S., Delauney, A. J., and Verma, D. P. (2006). *Arabidopsis* TARGET OF RAPAMYCIN interacts with RAPTOR, which regulates the activity of S6 kinase in response to osmotic stress signals. *Plant Cell* 18, 477–490. doi: 10.1105/tpc.105.035931

Menand, B., Desnos, T., Nussaume, L., Berger, F., Bouchez, D., Meyer, C., et al. (2002). Expression and disruption of the *Arabidopsis TOR* (target of rapamycin) gene. *Proc. Natl. Acad. Sci. U.S.A.* 99, 6422–6427. doi: 10.1073/pnas.092141899

Meyuhas, O., and Dreazen, A. (2009). Ribosomal protein S6 kinase from TOP mRNAs to cell size. *Prog. Mol. Biol. Transl. Sci.* 90, 109–153. doi: 10.1016/S1877-1173(09)90003-5

Montane, M. H., and Menand, B. (2013). ATP-competitive mTOR kinase inhibitors delay plant growth by triggering early differentiation of meristematic cells but no developmental patterning change. *J. Exp. Bot.* 64, 4361–4374. doi: 10.1093/jxb/ert242

Moreau, M., Azzopardi, M., Clément, G., Dobrenel, T., Marchive, C., Renne, C., et al. (2012). Mutations in the *Arabidopsis* homolog of LST8/GβL, a partner of the target of rapamycin kinase, impair plant growth, flowering, and metabolic adaptation to long days. *Plant Cell* 24, 463–481. doi: 10.1105/tpc.111.091306

Pearce, L. R., Komander, D., and Alessi, D. R. (2010). The nuts and bolts of AGC protein kinases. *Nat. Rev. Mol. Cell Biol.* 11, 9–22. doi: 10.1038/nrm2822

Rademacher, W. (2000). Growth retardants: effects on gibberellin biosynthesis and other metabolic pathways. *Annu. Rev. Plant Biol.* 51, 501–531. doi: 10.1146/annurev.arplant.51.1.501

Ren, M., Qiu, S., Venglat, P., Xiang, D., Feng, L., Selvaraj, G., et al. (2011). Target of rapamycin regulates development and ribosomal RNA expression through kinase domain in Arabidopsis. *Plant Physiol.* 155, 1367–1382. doi: 10.1104/pp.110.169045

Ren, M., Venglat, P., Qiu, S., Feng, L., Cao, Y., Wang, E., et al. (2012). Target of rapamycin signaling regulates metabolism, growth, and life span in *Arabidopsis*. *Plant Cell* 24, 4850–4874. doi: 10.1105/tpc.112.107144

Rexin, D., Meyer, C., Robaglia, C., and Veit, B. (2015). TOR signalling in plants. *Biochem. J.* 470, 1–14. doi: 10.1042/BJ20150505

Salem, M. A., Li, Y., Bajdzienko, K., Fisahn, J., Watanabe, M., Hoefgen, R., et al. (2018). RAPTOR controls developmental growth transitions by altering the hormonal and metabolic balance. *Plant Physiol.* 177, 565–593. doi: 10.1104/pp.17.01711

Sarbassov, D. D., Ali, S. M., Kim, D.-H., Guertin, D. A., Latek, R. R., Erdjument-Bromage, H., et al. (2004). Rictor, a novel binding partner of mTOR, defines a rapamycin-insensitive and raptor-independent pathway that regulates the cytoskeleton. *Curr. Biol.* 14, 1296–1302. doi: 10.1016/j.cub.2004.06.054

Sarbassov, D. D., Ali, S. M., Sengupta, S., Sheen, J.-H., Hsu, P. P., Bagley, A. F., et al. (2006). Prolonged rapamycin treatment inhibits mTORC2 assembly and Akt/PKB. *Mol. Cell* 22, 159–168. doi: 10.1016/j.molcel.2006.03.029

Saxton, R. A., and Sabatini, D. M. (2017). mTOR signaling in growth, metabolism, and disease. *Cell* 169, 361–371. doi: 10.1016/j.cell.2017.02.004

Schepetilnikov, M., Dimitrova, M., Mancera-Martı nez, E., Geldreich, A., Keller, M., and Ryabova, L. A. (2013). TOR and S6K1 promote translation reinitiation of uORF containing mRNAs via phosphorylation of eIF3h. *EMBO J.* 32, 1087–1102. doi: 10.1038/emboj.2013.61

Schepetilnikov, M., Kobayashi, K., Geldreich, A., Caranta, C., Robaglia, C., Keller, M., et al. (2011). Viral factor TAV recruits TOR/S6K1 signalling to activate reinitiation after long ORF translation. *EMBO J.* 30, 1343–1356. doi: 10.1038/emboj.2011.39

Schepetilnikov, M., Makarian, J., Srour, O., Geldreich, A., Yang, Z., Chicher, J., et al. (2017). GTPase ROP2 binds and promotes activation of target of rapamycin, TOR, in response to auxin. *EMBO J.* 36, 886–903. doi: 10.15252/embj.201694816

Shen, K., Choe, A., and Sabatini, D. M. (2017). Intersubunit crosstalk in the Rag GTPase heterodimer enables mTORC1 to respond rapidly to amino acid availability. *Mol. Cell* 68, 552–565. doi: 10.1016/j.molcel.2017.09.026

Shi, L., Wu, Y., and Sheen, J. (2018). TOR signaling in plants: conservation and innovation. *Development* 145:dev160887. doi: 10.1242/dev.160887

Song, Y., Zhao, G., Zhang, X., Li, L., Xiong, F., Zhuo, F., et al. (2017). The crosstalk between Target of Rapamycin (TOR) and Jasmonic Acid (JA) signaling existing in *Arabidopsis* and cotton. *Sci. Rep.* 7:45830. doi: 10.1038/srep45830

Sormani, R., Yao, L., Menand, B., Ennar, N., Lecampion, C., Meyer, C., et al. (2007). *Saccharomyces cerevisiae* FKBP12 binds *Arabidopsis thaliana* TOR and its expression in plants leads to rapamycin susceptibility. *BMC Plant Biol.* 7:26. doi: 10.1186/1471-2229-7-26

Subbarao, K. V., Datta, R., and Sharma, R. (1998). Amylases synthesis in scutellum and aleurone layer of maize seeds. *Phytochemistry* 49, 657–666. doi: 10.1016/s0031-9422(97)00964-3

Sun, L., Yu, Y., Hu, W., Min, Q., Kang, H., Li, Y., et al. (2016). Ribosomal protein S6 kinase1 coordinates with TOR-Raptor2 to regulate thylakoid membrane biosynthesis in rice. *Biochim. Biophys. Acta* 1861, 639–649. doi: 10.1016/j.bbalip.2016.04.009

Takahashi, N., Phinney, B. O., MacMillan, J., and Rademacher, W. (1991). "Inhibitors of gibberellin biosynthesis: applications in agriculture and horticulture," in *Gibberellins*, eds N. Takahashi, B. O. Phinney, and J. MacMillan (New York, NY: Springer-Verlag), 296–310. doi: 10.1007/978-1-4612-3002-1_29

Thoreen, C. C., Kang, S. A., Chang, J. W., Liu, Q., Zhang, J., Gao, Y., et al. (2009). An ATP-competitive mammalian target of rapamycin inhibitor reveals rapamycin-resistant functions of mTORC1. *J. Biol. Chem.* 284, 8023–8032. doi: 10.1074/jbc.M900301200

Thoreen, C. C., and Sabatini, D. M. (2009). Rapamycin inhibits mTORC1, but not completely. *Autophagy* 5, 725–726. doi: 10.4161/auto.5.5.8504

Vezina, C., Kudelski, A., and Sehgal, S. N. (1975). Rapamycin (AY-22,989), a new antifungal antibiotic: taxonomy of the producing streptomycete and isolation of the active principle. *J. Antibiot.* 28, 721–726. doi: 10.7164/antibiotics.28.721

Washio, K. (2003). Functional dissections between GAMYB and Dof transcription factors suggest a role for protein–protein associations in the gibberellin-mediated expression of the RAmy1A gene in the rice aleurone. *Plant Physiol.* 133, 850–863. doi: 10.1104/pp.103.027334

Weitbrecht, K., Müller, K., and Leubnermetzger, G. (2011). First off the mark: early seed germination. *J. Exp. Bot.* 62, 3289–3309. doi: 10.1093/jxb/err030

Wicker, L. S., Boltz, R. C. Jr., Matt, V., Nichols, E. A., Peterson, L. B., and Sigal, N. H. (1990). Suppression of B cell activation by cyclosporin A, FK506 and rapamycin. *Eur. J. Immunol.* 20, 2277–2283. doi: 10.1002/eji.1830201017

Xiong, F., Dong, P., Liu, M., Xie, G., Wang, K., Zhuo, F., et al. (2016). Tomato FK506 binding protein 12KD (FKBP12) mediates the interaction between rapamycin and Target of Rapamycin (TOR). *Front. Plant Sci.* 7:1746. doi: 10.3389/fpls.2016.01746

Xiong, Y., McCormack, M., Li, L., Hall, Q., Xiang, C., and Sheen, J. (2013). Glucose-TOR signalling reprograms the transcriptome and activates meristems. *Nature* 496, 181–186. doi: 10.1038/nature12030

Xiong, Y., and Sheen, J. (2012). Rapamycin and glucose-target of rapamycin (TOR) protein signaling in plants. *J. Biol. Chem.* 287, 2836–2842. doi: 10.1074/jbc.M111.300749

Xiong, Y., and Sheen, J. (2014). The role of target of rapamycin signaling Networks in plant growth and metabolism. *Plant Physiol.* 164, 499–512. doi: 10.1104/pp.113.229948

Xiong, Y., and Sheen, J. (2015). Novel links in the plant TOR kinase signaling network. *Curr. Opin. Plant Biol.* 28, 83–91. doi: 10.1016/j.pbi.2015.09.006

Xu, Q., Liang, S., Kudla, J., and Luan, S. (1998). Molecular characterization of a plant FKBP12 that does not mediate action of FK506 and rapamycin. *Plant J.* 15, 511–519. doi: 10.1046/j.1365-313X.1998.00232x

Yaguchi, M., and Kozaki, A. (2018). Plant S6 kinases do not require hydrophobic motif phosphorylation for activity in yeast lacking Ypk3. *FEBS Lett.* 592, 610–620. doi: 10.1002/1873-3468.12980

Yakovleva, L. A., and Kulaeva, O. N. (1987). The effect of phytohormones on phosphorylation of ribosomal proteins in detached pumpkin cotyledons. *Biochem. Physiol. Pflanz.* 182, 359–365. doi: 10.1016/S0015-3796(87)80002-1

Zhang, Y. J., Duan, Y., and Zheng, X. F. (2011). Targeting the mTOR kinase domain: the second generation of mTOR inhibitors. *Drug Discov. Today* 16, 325–331. doi: 10.1016/j.drudis.2011.02.008

Zhao, J., Zhai, B., Gygi, S. P., and Goldberg, A. L. (2015). mTOR inhibition activates overall protein degradation by the ubiquitin proteasome system as well as by autophagy. *Proc. Natl. Acad. Sci. U.S.A.* 112, 15790–15797. doi: 10.1073/pnas.1521919112

Zhou, H., Luo, Y., and Huang, S. (2010). Updates of mTOR inhibitors. *Anticancer Agents Med. Chem.* 10, 571–581. doi: 10.2174/187152010793498663

Conflict of Interest: The authors declare that the research was conducted in the absence of any commercial or financial relationships that could be construed as a potential conflict of interest.

frontiers in Cell and Developmental Biology

ORIGINAL RESEARCH
published: 26 November 2020
doi: 10.3389/fcell.2020.606596

The *Arabidopsis thaliana* Poly(ADP-Ribose) Polymerases 1 and 2 Modify DNA by ADP-Ribosylating Terminal Phosphate Residues

Sabira Taipakova[1], Aigerim Kuanbay[1,2], Christine Saint-Pierre[3], Didier Gasparutto[3], Yeldar Baiken[4,5], Regina Groisman[2], Alexander A. Ishchenko[2], Murat Saparbaev[1,2]* and Amangeldy K. Bissenbaev[1]**

[1] Department of Molecular Biology and Genetics, Faculty of Biology and Biotechnology, Al-Farabi Kazakh National University, Almaty, Kazakhstan, [2] Groupe «Mechanisms of DNA Repair and Carcinogenesis«, Equipe Labellisée LIGUE 2016, CNRS UMR9019, Université Paris-Saclay, Villejuif, France, [3] CEA, CNRS, IRIG/SyMMES-UMR5819/CREAB, Université Grenoble Alpes, Grenoble, France, [4] National Laboratory Astana, Nazarbayev University, Nur-Sultan, Kazakhstan, [5] School of Engineering and Digital Sciences, Nazarbayev University, Nur-Sultan, Kazakhstan

OPEN ACCESS

Edited by:
Nikita Kuznetsov, Institute of Chemical Biology and Fundamental Medicine (RAS), Russia

Reviewed by:
Modesto Redrejo-Rodríguez, Autonomous University of Madrid, Spain
Luca Palazzo, National Research Council (CNR), Italy

***Correspondence:**
Alexander A. Ishchenko
alexander.ishchenko@gustaveroussy.fr
Murat Saparbaev
murat.saparbaev@gustaveroussy.fr
Amangeldy K. Bissenbaev
Amangeldy.Bisenbaev@kaznu.kz

Specialty section:
This article was submitted to Cell Death and Survival, a section of the journal Frontiers in Cell and Developmental Biology

Received: *15 September 2020*
Accepted: *22 October 2020*
Published: *26 November 2020*

Citation:
Taipakova S, Kuanbay A, Saint-Pierre C, Gasparutto D, Baiken Y, Groisman R, Ishchenko AA, Saparbaev M and Bissenbaev AK (2020) The Arabidopsis thaliana Poly(ADP-Ribose) Polymerases 1 and 2 Modify DNA by ADP-Ribosylating Terminal Phosphate Residues. Front. Cell Dev. Biol. 8:606596. doi: 10.3389/fcell.2020.606596

Proteins from the poly(ADP-ribose) polymerase (PARP) family, such as PARP1 and PARP2, use NAD^+ as a substrate to catalyze the synthesis of polymeric chains consisting of ADP-ribose units covalently attached to an acceptor molecule. PARP1 and PARP2 are viewed as DNA damage sensors that, upon binding to strand breaks, poly(ADP-ribosyl)ate themselves and nuclear acceptor proteins. The flowering plant *Arabidopsis thaliana* contains three genes encoding homologs of mammalian PARPs: *atPARP1*, *atPARP2*, and *atPARP3*. Both atPARP1 and atPARP2 contain poly(ADP-ribosyl)ating activity; however, it is unknown whether they could covalently modify DNA by ADP-ribosylating the strand break termini. Here, we report that similar to their mammalian counterparts, the plant atPARP1 and atPARP2 proteins ADP-ribosylate 5′-terminal phosphate residues in duplex DNA oligonucleotides and plasmid containing at least two closely spaced DNA strand breaks. AtPARP1 preferentially catalyzes covalent attachment of ADP-ribose units to the ends of recessed DNA duplexes containing 5′-phosphate, whereas atPARP2 preferentially ADP-ribosylates the nicked and gapped DNA duplexes containing the terminal 5′-phosphate. Similar to their mammalian counterparts, the plant PARP-catalyzed DNA ADP-ribosylation is particularly sensitive to the distance that separates two strand breaks in the same DNA molecule, 1.5 and 1 or 2 turns of helix for atPARP1 and atPARP2, respectively. PAR glycohydrolase (PARG) restored native DNA structure by hydrolyzing the PAR–DNA adducts generated by atPARPs. Biochemical and mass spectrometry analyses of the PAR–DNA adducts showed that atPARPs utilize phosphorylated DNA termini as an alternative to protein acceptor residues to catalyze PAR chain synthesis *via* phosphodiester bond formation between C1′ of ADP-ribose and a phosphate residue of the terminal nucleotide in

DNA fragment. Taken together, these data establish the presence of a new type of DNA-modifying activity in *Arabidopsis* PARPs, suggesting a possible role of DNA ADP-ribosylation in DNA damage signaling and repair of terrestrial plants.

Keywords: plant DNA repair, *Arabidopsis thaliana*, DNA strand break, nicotinamide adenine dinucleotide (NAD) +, poly(ADP-ribose) polymerase (PARP), ADP-ribosylation

INTRODUCTION

Land plants are under constant exposition to a variety of abiotic stresses including UV radiation, droughts, temperature variation, salinity, and other environmental extremes that can extensively damage cellular DNA. In addition to that, plants experience endogenous oxidative stress because of reactive oxygen species (ROS) generated during respiration in mitochondria, photorespiration in chloroplasts, and various biotic stresses. Oxidative damage to DNA caused by ROS is believed to be a major source of genome instability and aging (Cadet and Wagner, 2013). Importantly, direct attack of ROS on DNA abstracts hydrogen from deoxyribose carbons leading to single- and double-strand DNA breaks (SSBs and DSBs, respectively) (Balasubramanian et al., 1998). In addition, DNA strand breaks can be generated indirectly during DNA excision repair of modified bases, replication fork collapse, and topoisomerase action (Pommier et al., 2010). If left undetected and unrepaired, DNA strand breaks have detrimental consequences, such as gross chromosomal rearrangements, persistent genome instability, and cell death. The poly(ADP-ribose) polymerase (PARP) superfamily of proteins, also referred to as the diphtheria toxin-like ADP-ribosyltransferase (ARTD) family, is widespread in eukaryotes and has been identified by homology search in all six major eukaryotic supergroups (Perina et al., 2014). The well-characterized PARP enzymes, mammalian PARP1 and PARP2, catalyze the synthesis of long chains of ADP-ribose (PAR) covalently attached to acceptor proteins using nicotinamide adenine dinucleotide (NAD^+) as a substrate (Kim et al., 2005; Schreiber et al., 2006; Hottiger et al., 2010). It is agreed that PARP1, PARP2, and PARP3 are sensors of DNA damage that are activated by binding to DNA strand discontinuities. After activation of the catalytic domain, PARPs poly/mono-ADP-ribosylate (PARylate/MARylate) themselves and different nuclear proteins, these in turn regulate the functions of ADP-ribosylated proteins. The ADP-ribose polymer synthesized by PARPs has a complex branched structure, which confers a negative charge and thus stimulates electrostatic repulsion of PARylated proteins from DNA (Tanaka et al., 1984; Satoh et al., 1994). It should be stressed that the PARP-catalyzed covalent protein posttranslational modification is a reversible process since PAR is rapidly degraded by poly(ADP-ribose) glycohydrolase (PARG) which specifically hydrolyze the ribose–ribose bonds in the polymer. Hence, the activation of PARP-catalyzed auto-ADP-ribosylation and modification of nuclear proteins such as histones is one of the common cellular responses to DNA damage (De Murcia and Menissier De Murcia, 1994).

From the past, molecular characterization of DNA repair mechanisms has been mainly focused on bacterial, yeast, and animal cells (Friedberg et al., 2006), with much less attention paid to the mechanisms that maintain the genome stability in plants. The genome of *Arabidopsis thaliana*, a widely used model plant of the dicot group, contains three genes encoding homologs of mammalian poly(ADP-ribose) polymerases (PARPs): *atPARP1*, *atPARP2*, and *atPARP3*. Previously, it was shown that plant PARP1 and PARP2 contain poly(ADP-ribosyl)-transferase activity (Chen et al., 1994; Lepiniec et al., 1995; Babiychuk et al., 1998). Sequence analysis revealed that atPARP1 has a very similar domain architecture to that of human PARP1 (Babiychuk et al., 1998), and it consists of five domains of known functions: three N-terminal zinc finger domains implicated in DNA damage detection, the BRCA1 C-terminus (BRCT) domain for automodification, the WGR domain with the conserved Trp-Gly-Arg (WGR) motif for DNA binding, and the highly conserved catalytic (CAT) domain consisting of two subdomains, ADP-ribosyltransferase catalytic subdomain (ART) and helical subdomain (HD) which is an autoinhibitory domain that blocks productive NAD(+) binding regulating PARP catalytic activity (Eustermann et al., 2015) (**Figure 1**). The atPARP2 protein contains highly conserved ART subdomain and is structurally most similar to human PARP2 (**Figure 1**). AtPARP2 has no zinc fingers and BRCT domains like human PARP1, but contains two N-terminal SAF/Acinus/PIAS motif (SAP) domains that confer DNA-binding activity (Aravind and Koonin, 2000; Lamb et al., 2012). Expression of atPARP2 in yeast revealed poly(ADP-ribosyl)ating activity generating mainly short polymers with the size of 10–15 residues; however, longer polymers up to 40 ADP-ribosyl units were also observed (Babiychuk et al., 1998). AtPARP1 and atPARP2 contain a typical histidine-tyrosine-glutamic acid H-Y-E catalytic triad in their conserved ART subdomains, whereas atPARP3 and orthologous plant proteins have an alternative cysteine-valine-glutamic acid (C_{653}-V_{687}-E_{782} and C_N-V_N-E_N, respectively) triad in their catalytic domain (Citarelli et al., 2010; Stolarek et al., 2015). Noteworthy, a recent study demonstrated that atPARP3 lost NAD(+)-binding capability and poly(ADP-ribose) polymerase activity and may play different biological roles from those of atPARP1 and atPARP2 enzymes in plants (Gu et al., 2019).

The atPARP1 and atPARP2 proteins have nuclear localization and ADP-ribosylate themselves (automodification) and acceptor proteins in the presence of nicked DNA *in vitro* and *in vivo* (Babiychuk et al., 1998; Doucet-Chabeaud et al., 2001; Feng et al., 2015; Liu et al., 2017; Chen et al., 2018). The treatment of *Arabidopsis* with ionizing radiation, zeocin, and DNA cross-linking agent such as cisplatin activates the expression of atPARP1 and atPARP2, but not that of atPARP3 (Doucet-Chabeaud et al., 2001; Boltz et al., 2014; Yuan et al., 2014). In agreement with these observations, *Arabidopsis parp1* and

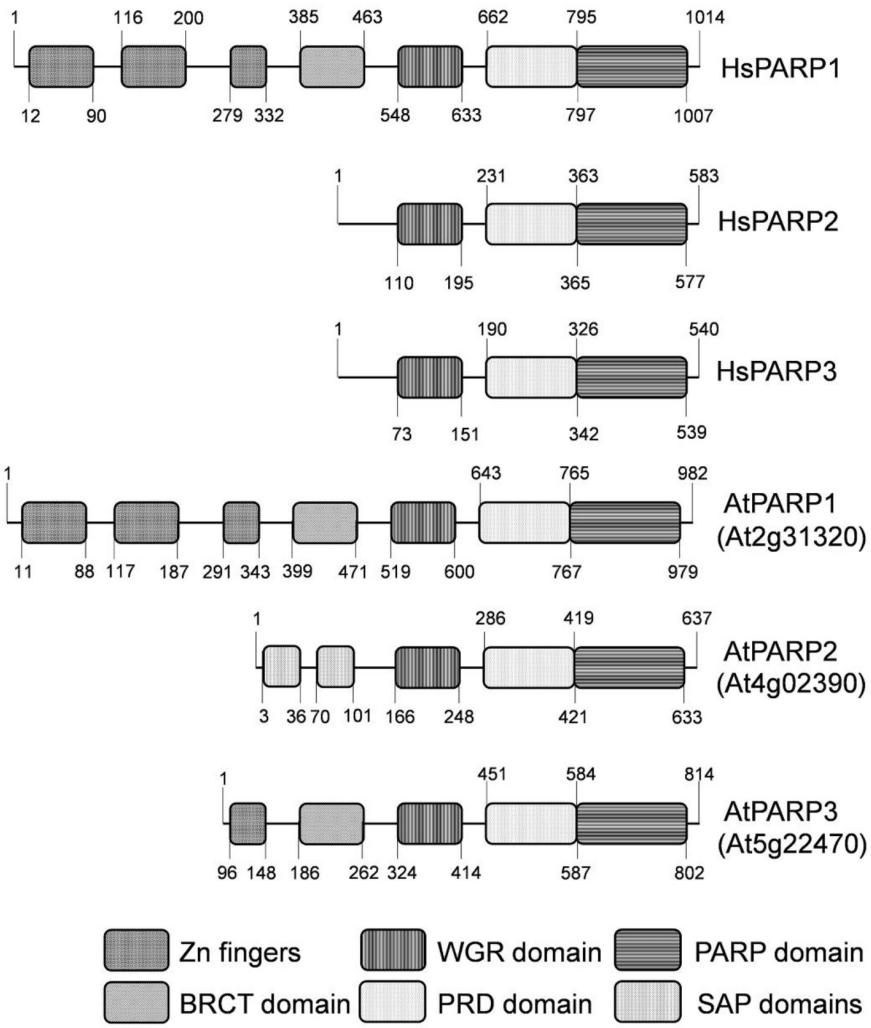

FIGURE 1 | Schematic representation of domain structures of human and *Arabidopsis thaliana* PARP proteins. Zn1, Zn2, and Zn3—three zinc-binding domains; BRCT: BRCA-1 C-terminal domain for phospho-protein binding. WGR—conserved Trp-Gly-Arg motif for putative nucleic acid binding; PRD—PARP regulatory domain; PARP—PARP catalytic domain; SAP—SAF-A/B, Acinus and PIAS motif for putative DNA/RNA binding.

parp2 single mutant plants exhibit enhanced sensitivity to the alkylating agent methyl methane sulfonate (MMS) and the radiomimetic agent bleomycin (Jia et al., 2013; Boltz et al., 2014; Zhang et al., 2015; Klemm et al., 2017). Interestingly, the *Arabidopsis parp2* single mutants exhibited a stronger decrease in poly(ADP-ribosyl)ation and were more sensitive to bleomycin and mitomycin, as compared with *parp1* single ones (Boltz et al., 2014; Song et al., 2015). Nevertheless, both atPARPs participate in the responses to DNA damage since Arabidopsis *parp1 parp2* double mutants showed increased sensitivity to genotoxic stress, as compared with single *parp* mutants (Jia et al., 2013; Song et al., 2015; Zhang et al., 2015). Additionally, atPARP1 mRNA was induced in *parp2* mutants, and conversely, atPARP2 mRNA was induced in *parp1* mutants (Boltz et al., 2014). Interestingly, atPARP1 and atPARP2 proteins similar to their human counterparts can interact with each other (Song et al., 2015; Liu et al., 2017). Surprisingly, *A. thaliana parp1 parp2 parp3* triple mutants did not exhibit higher sensitivity to DNA damage, as compared with double *parp1 parp2* mutant, suggesting that atPARP3 plays a minor role in DNA damage response and repair in seedlings (Zhang et al., 2015). Nevertheless, mutation in barley PARP3 homolog (HvPARP3) resulted in an altered root growth in response to bleomycin (Stolarek et al., 2015). In contrast to studies on animal models, the plant *Arabidopsis* mutant lines for PARP genes including double and a triple mutant *parp1 parp2 parp3* did not exhibit significant phenotypic abnormalities under normal non-stressed growth conditions (Song et al., 2015; Zhang et al., 2015; Rissel et al., 2017). Nevertheless, plant PARP activity controls cell cycle progression and redox status, suggesting a regulatory function of atPARPs in plant development. In agreement with this, the seed germination is altered in *parp1*, *parp2*, and *parp3* single mutant plants. Under normal non-stressed conditions, parp3 mutant plants germinated faster than the wild type, whereas *parp1* and *parp2* showed reduced

germination rates (Pham et al., 2015). Noteworthy, the double *parp1 parp2* mutant of *Arabidopsis* showed more rapid primary and lateral root growth, suggesting that plant PARPs inhibit mitosis and promote cell differentiation (Liu et al., 2017). Based on these observations, it was proposed that PARPs influence plant development only under specific conditions the nature of which requires further investigations (Rissel and Peiter, 2019).

The fact that protein ADP-ribosylation has been increased in the Arabidopsis *parp* triple mutant suggests the presence of supplementary PARP-like enzymes in plants. Indeed, in addition to the canonical PARP proteins, higher plants have a plant-specific family of proteins containing PARP-like domains, called the SRO (Similar to RCD One) proteins. The SRO family possesses a central catalytic PARP domain with an unusual catalytic triad motif (L-H-N) which is flanked by an N-terminal WWE domain [poly(ADP-ribose) binding domain] and a C-terminal RST domain (RCD1-SRO-TAF4—plant-specific protein–protein interaction domain) (Ahlfors et al., 2004; Jaspers et al., 2010). In *Arabidopsis*, the family includes the proteins Radical-induced Cell Death1 (RCD1) and its five homologs SRO1–SRO5 (Belles-Boix et al., 2000; Jaspers et al., 2010). Bioinformatics and biochemical data suggest that the SRO proteins do not have PARP activity; however, mutant analyses have shown that these proteins play a significant role in stress response (Ahlfors et al., 2004; Jaspers et al., 2009; Teotia and Lamb, 2009; Teotia and Lamb, 2011).

At variance to mammals, plants possess two genes atPARG1 (At2g31870) and atPARG2 (At2g31865) encoding for the poly(ADP-ribose) glycohydrolase (Zhang et al., 2015). Under the same conditions, atPARG1 plays an essential role and atPARG2 a minor one. Interestingly, the atPARG1 deficiency results in more DNA damage and enhanced cell death in plants after bleomycin treatment, than the lack of AtPARPs, possibly due to a high toxicity of free poly(ADP-ribose) polymer (Zhang et al., 2015).

Recent studies have demonstrated a new phenomenon of postreplicative DNA ADP-ribosylation of strand break termini in synthetic duplex DNA oligonucleotides; this reaction is catalyzed by mammalian PARP1, PARP2, and PARP3 (Talhaoui et al., 2016; Munnur and Ahel, 2017; Belousova et al., 2018; Zarkovic et al., 2018). PARP1 and PARP2 catalyze the covalent addition of ADP-ribose units to 5′- and 3′-terminal phosphates and to 2′-OH termini of modified nucleotides at DNA strand breaks, producing covalent PAR–DNA adducts (Talhaoui et al., 2016). PARP1 preferentially ADP-ribosylates DNA strand break termini containing terminal phosphates or 2′-OH group in gapped, recessed DNA duplexes, whereas PARP2 preferentially acts on 5′-terminal phosphates at DSB termini of nicked DNA (Talhaoui et al., 2016; Zarkovic et al., 2018). Also, PARP3 can effectively generate mono-(ADP-ribosyl)ated DNA (MAR–DNA) in which ADP-ribose moiety is covalently linked to 5′-terminal phosphate residues at DSB and SSB in DNA substrate (Munnur and Ahel, 2017; Belousova et al., 2018), thus sharing its substrate specificity with PARP2.

Here, we examined the interactions of plant PARP proteins with various DNA substrates using *in vitro* approaches. Our results reveal that both purified *Arabidopsis* atPARP1 and atPARP2 proteins can covalently modify DNA oligonucleotide duplexes by the addition of multiple poly(ADP-ribose) units to 3′ and 5′ extremities of DNA strand breaks. The atPARP-catalyzed covalent DNA ADP-ribosylation is reversible since PARG can efficiently remove the PAR polymer from DNA and restore initial DNA structure. The mechanistic characteristics and possible functional role of the new activity of plant atPARPs are discussed.

MATERIALS AND METHODS

Bacterial Strains, Plasmids, and Reagents

Cell culture media were from Invitrogen (Life Technologies SAS, Saint Aubin, France). The *Escherichia coli* Rosetta 2(DE3) cells, used for the recombinant protein expression, were from Novagen-EMD4 Biosciences (Merck Chemicals, Nottingham, United Kingdom). Restriction enzymes, T4 DNA ligase, RPROTKSOL-RO: recombinant PCR grade Proteinase K were from Roche (Basel, Swiss), deoxyribonuclease I from bovine pancreas (DNAse I) was from ThermoFisher Scientific (Lithuania), and calf-intestinal alkaline phosphatase (CIP) was from New England Biolabs France (Evry, France). Snake venom phosphodiesterase 1 from *Crotalus adamanteus* (SVPDE1) was from Worthington (Biochemical Corporation). The purified human Nudix (nucleoside diphosphate-linked moiety X)-type motif 16 (NUDT16) protein was prepared as described (Palazzo et al., 2015). Bovine PARG was from Trevigen (Gaithersburg, United States). Bleomycin was from Sanofi-Aventis (France).

Oligonucleotides

Sequences of the oligonucleotides and their duplexes used in the present work are shown in **Supplementary Table S1**. All oligonucleotides were purchased from Eurogentec (Seraing, Belgium) including modified oligonucleotides. Prior to enzymatic assays, the oligonucleotides were labeled either at the 5′ end using T4 polynucleotide kinase (New England Biolabs-OZYME, France) in the presence of [γ-^{32}P]ATP (3,000 Ci mmol^{-1}) (PerkinElmer) or at the 3′ end by means of terminal deoxynucleotidyl transferase (New England Biolabs) in the presence of [α-^{32}P]-3′-dATP (cordycepin 5′-triphosphate, 5,000 Ci mmol^{-1}; PerkinElmer) according to the manufacturer's protocol. Cold ATP at 1 mM was added to phosphorylate the remaining non-labeled oligonucleotides. After the reactions, radioactively labeled oligonucleotides were desalted on a Sephadex G-25 column equilibrated with water and then annealed with a corresponding complementary strand for 3 min at 65°C in the buffer containing 20 mM HEPES-KOH (pH 7.6) and 50 mM KCl. In addition, the radioactive labeling of DNA and proteins was performed using [adenylate-^{32}P] NAD^+ (800 Ci mmol^{-1}) (PerkinElmer) in the presence of atPARPs, oligonucleotides, and 1 mM cold NAD^+. To prepare a 5′-[^{32}P]labeled linearized nicked plasmid DNA substrate, 50 μM pML2 plasmid (same as pBluescript but contains insertion of a unique *Pml*I site) was linearized with 30 U of *Pml*I for 1 h at 37°C in 1 × CutSmart buffer (New England Biolabs, France), then nicked with 15 U of Nb.BsmI for 1 h at 65°C. The ^{32}P label

was introduced by reannealing of the linearized pML2 with 5′-[^{32}P]-labeled ExoA d(GTGGTTGTAAAACCTCAGCCAG) oligonucleotide corresponding to the 22-nt fragment spanning the region between the 5′ end of DSB and Nb.BsmI-induced nick. The nicked, gapped, or recessed DNA duplexes ExoA•RexT$^{nick/gap/rec}$ composed of RexT d(GGAATTCCCCGCGCCAAATTTCTCTAAGTCTCCGCGCCAC), ExoA d(GTGGCGCGGAGACTTAGAGAA), and either 5P-Exo19 d(pATTTGGCGCGGGGAATTCC) or 5P-Exo18, d(pTTTGGCGCGGGGAATTCC), where 5P is a 5′-terminal phosphate (**Supplementary Table S1**), were mostly used to quantify PARylation of DNA ends by atPARPs.

Plant Material, Cell-Free Extracts, and Genomic DNA Extraction

The *A. thaliana* wild-type (WT) Col-0 strain and mutant lines, harboring T-DNA insertions in the atPARP genes, were obtained from the Arabidopsis Biological Resource Center[1]. For all plants, seeds were sown on 1/2 Murashige–Skoog (MS) agar plates containing 1% sucrose and 1% agar, stratified for 48 h at 4°C and grown under long day conditions at 22°C under 16 h light/8 h dark cycles. They were collected at 18 days and transplanted to soil for seed harvest. The *A. thaliana* wild-type Col-0 strain and mutant line seeds were stratified and then grown for 14 days on MS agar plate. Two-week-old *Arabidopsis* seedlings were treated with 50 μg•ml^{-1} bleomycin (MS plates with plants were covered with 5 ml PBS containing the drug) and plants were collected after 24 h.

Cell-Free Extract Preparation

Extracts were prepared from 100 mg fresh untreated or treated with bleomycin 14-day-old seedlings (whole plant) in extraction buffer (20 mM HEPES-KOH, pH 7.6, 50 mM KCl, 5 mM $MgCl_2$, 1 mM DTT, 10% glycerol, 0.1% NP-40 and protease inhibitor cocktail at 1:100).

Genomic DNA Preparation

The plant genomic DNA (gDNA) was extracted from 100 mg fresh untreated or treated with bleomycin 14-day-old seedlings (whole plant) in liquid nitrogen using the CTAB method. Extracted gDNA were purified further by RNase A and proteinase K treatments, followed by phenol/chloroform extraction and ethanol precipitation of DNA.

RNA Analysis and cDNA Synthesis

Total RNA was extracted from 100 mg of fresh leaf tissues of *A. thaliana* in liquid nitrogen using the TRIzol reagent (Invitrogen) according to the manufacturer's instructions. Intact, high-quality RNA samples were confirmed by the presence of two bright 28S and 18S rRNA bands in ethidium bromide-stained agarose gels visualized under UV light. Five micrograms of DNA-free total RNA was converted into single-stranded DNA using a mix of oligo-dT_{20} primers and the First Strand cDNA Synthesis Kit (Thermo Scientific). PCR was performed using 2 μl of a 20-fold dilution of cDNA, 15 pmol of each primer, and 1 U of Taq polymerase in a 25-μl reaction volume. To generate the cDNA for full-length atPARP1 (corresponds to the gene At2g31320) and atPARP2 (corresponds to the gene At4g02390), the coding sequences were PCR-amplified using primers atPARP1*Nde*I_F/atPARP1*Bam*HI_R for atPARP1 and atPARP2*Nde*I_F/atPARP2*Bam*HI_R for atPARP2 (**Table 1**). The PCR fragments of atPARP1 and atPARP2 were cloned into the pBluescriptII SK(+) vector at *Nde*I/*Bam*HI restriction sites, respectively, using the Rapid DNA ligation kit (Thermo Scientific). Colonies of transformed *E. coli* DH5α cells carrying plasmids with an insert were screened by *lacZ* complementation, and the plasmid DNA was isolated with the GeneJET Plasmid Miniprep kit (Thermo Scientific). The DNA inserts were sequenced in both directions with M13 forward and reverse primers.

TABLE 1 | List of PCR primers used for cloning and site-directed mutagenesis.

atPARP1*Nde*I_F	**CAGCCATATGGCAAGCCCTCATAAGC**
atPARP1*Bam*HI_R	AGGCGGATCCTTAGCGTTTGTGTTTAAAGC
atPARP2*Nde*I_F	CAGCCATATGGCAAACAAGCTGAAGG
atPARP2*Bam*HI_R	AGGCGGATCCTTAATGTTTGTAGTTG
atPARP1_E960K_F	CGAACTGATGTATAACAAATATATTGTATATGATAC
atPARP1_E960K_R	GTATCATATACAATATATTTGTTATACATCAGTTCG
atPARP1_E960Q_F	CGAACTGATGTATAACCAATATATTGTATATGATAC
atPARP1_E960Q_R	GTATCATATACAATATATTGGTTATACATCAGTTCG
atPARP2_E614K_F	GCATGCTGCTGTATAACAAATATATTGTTTATAAC
atPARP2_E614K_R	GTTATAAACAATATATTTGTTATACAGCAGCATGC

Expression and Purification of atPARP1 and atPARP2 Proteins

The cDNA fragments encoding atPARP1 and atPARP2 were subcloned into the *Nde*I and *Bam*HI restriction sites of the pET28c vector. The resulting plasmids pET28c-atPARP1 and pET28c-atPARP2 can express the recombinant proteins containing an N-terminal His-tag in an *E. coli* (DE3) strain. The following mutants atPARP1^{E960K}, atPARP1^{E960Q}, and atPARP2^{E614K} were constructed using the QuikChange site-directed mutagenesis kit (Stratagene) and the oligonucleotide primers are shown in **Table 1**. The WT and mutant atPARP proteins were purified from *E. coli* Rosetta 2 (DE3) strain (Merck). Briefly, the transformed *E. coli* cells were grown to OD_{600} ∼ 0.6 at 37°C in LB medium and then induced by incubating with 50 μM isopropyl β-D-1-thiogalactopyranoside overnight at 25°C. Owing to strong expression in the Rosetta strain, it was possible to purify the atPARP1 and atPARP2 proteins to near homogeneity using only two chromatographic steps. All purification procedures were carried out at 4°C. Bacteria were harvested by centrifugation, and cell pellets were lysed using a French press at 18,000 psi in a buffer containing 50 mM Tris-HCl pH 8.0, 100 mM NaCl, 1 mM EDTA, 5% glycerol, 1 mM DTT, and 0.5% NP-40 supplemented with Complete Protease Inhibitor Cocktail (Roche Diagnostics, Switzerland). The lysates were cleared by centrifugation at 40,000 × *g* for 60 min at 4°C, and the resulting supernatant

[1]http://www.arabidopsis.org

was adjusted to 500 mM NaCl and 20 mM imidazole and loaded onto a HiTrap Chelating HP column (GE Healthcare) charged with Ni^{2+}. The eluted fractions containing the recombinant proteins were pooled and loaded onto a 1-ml HiTrap-Heparin column (GE Healthcare). The bound proteins were eluted in a 50–1,500-mM NaCl gradient. The homogeneity of the purified proteins were assessed by using the SDS-PAGE method (**Supplementary Figure S1**). The purified protein samples were stored at -20°C in 50% glycerol.

Preparation of Anti-atPARP2 Antibodies and Western Blotting

The anti-atPARP2 polyclonal antibodies were raised against the full-length recombinant His-tagged *Arabidopsis* atPARP2 protein. Approximately 1 mg of the purified recombinant atPARP2 protein was mixed with Freund's complete adjuvant and injected into rabbits. Three additional injections were made at 2-week intervals. One week after the last injection, the blood was collected and the immune serum was affinity purified using protein A agarose fast flow resin (Sigma). The purified rabbit anti-atPARP2 polyclonal antibodies were used as primary antibodies, and the horseradish peroxidase-conjugated goat anti-rabbit IgG was used as a secondary antibody. Plant cell-free extracts (∼12 μg of protein) were separated in a 10% SDS-polyacrylamide gel and then electroblotted onto a polyvinyl difluoride membrane (Pierce) using a Bio-Rad Mini-transblot cell according to the manufacturer's instructions. After the transfer of proteins, the membrane was gently shaken in blocking solution containing 5% milk and 0.1% Tween-20 in 1 × TBS (Tris-buffered saline: 50 mM Tris-HCl pH 7.5, 20 mM NaCl) for 1 h at room temperature. After removing the blocking solution, the membrane was incubated in 10 ml of the affinity-purified anti-atPARP2 antibodies (1:30,000 dilution in the blocking solution with 0.1% Tween-20) overnight at 4°C. The membrane was washed five times in 10 ml of the wash buffer (1 × TBS supplemented with 0.1% Tween-20), for 5 min each time. After washing, the membrane was incubated with the secondary antibody (1:60,000 dilution in the blocking solution with 0.1% Tween-20) in 10 ml for 1 h at room temperature. Then the membrane washed five times in 10 ml of the wash buffer, for 5 min each time. The working substrate solution was prepared by mixing an equal volume of peroxide solution and luminal/enhancer solution and used at 0.1 ml cm^{-2} per blot area. The membrane was incubated in the working solution for 2 min in the dark and exposed to Kodak X-Omat film.

Activity Assay for Poly(ADP-Ribose) Polymerase

The standard DNA PARylation assay (10 μl) was performed by incubating 20 nM [^{32}P]-labeled oligonucleotide, 250 nM atPARP1 or atPARP2, and 1 mM NAD^+, in ADPR buffer [20 mM HEPES-KOH pH 7.6, 50 mM KCl, 5 mM $MgCl_2$, 1 mM DTT, and μg•ml^{-1} bovine serum albumin (BSA)], for 30 min at 37°C, unless otherwise stated. After the reaction, the samples were incubated in the presence of 50 μg•ml^{-1} proteinase K and 0.15% SDS for 30 min at 50°C followed by incubation for 3 min at 95°C. The samples were desalted on a Sephadex G-25 column (Amersham Biosciences) equilibrated in 7.5 M urea, and then the products were analyzed by electrophoresis in the denaturing 20% (w/v) polyacrylamide gel (PAGE, 7 M urea, 0.5 × TBE, 42°C). A wet gel was wrapped in a plastic drape, then exposed to a Storage Fuji FLA-3000 Phosphor Screen, which was then scanned using Typhoon FLA 9500, and digital images were obtained and quantified using FUJI Image Gauge V3.12 software.

Hydrolysis of the ADP-Ribosylated DNA Adducts by PARG and DNA-Modifying Enzymes

The hydrolysis of PAR–DNA and MAR–DNA adducts with PARG was performed after denaturing of the atPARP proteins by heating a sample for 20 min at 80°C, then 50 pg•μl^{-1} PARG was added to the reaction mixtures, and samples were incubated for 30 min at 37°C. The reaction products were analyzed as described above. The dephosphorylation assay with CIP was performed using 10 U of the enzyme in the CIP buffer (provided by New England Biolabs) for 1 h at 37°C. The hydrolysis of the PAR–DNA polymers by SVPDE1 was performed in two steps: first, incubation of 20 nM DNA substrate with 250 nM atPARP2 and 1 mM NAD^+ in the PARP buffer (see above) for 30 min at 37°C, and then the second step was incubation with 100 mU SVPDE1 in the reaction mixture supplemented with 10 mM $MgCl_2$ and 75 mM Tris-HCl pH 8.9, for 1 h at 37°C. In addition, the SVPDE1 reaction products were treated with 10 U CIP in the CIP buffer for 40 min at 37°C, unless otherwise stated. The reaction products were analyzed as described above. Hydrolysis of the PAR–DNA polymer by the Nudix hydrolase was performed using 2–20 μM NUDT16 in the DNA PARylation assay buffer supplemented with 10 mM $MgCl_2$ for 18 h at 30°C, unless otherwise stated.

Identification of the ADP-Ribosylated DNA Adducts by Matrix-Assisted Laser Desorption Ionization Time-of-Flight Mass Spectrometry

Mass spectrometry measurements were performed as described previously (Talhaoui et al., 2016). Briefly, 5 μM of cold non-radioactive 5′-phosphorylated 30-mer nicked duplex oligonucleotide [referred to here as p10•RT-A^{Nick} or S18 and composed of a 30-mer (RT-A) template strand and two 5′-phosphorylated complementary strands: 10-mer (p10) and 20-mer (pT19)] (**Supplementary Table S1**) was incubated with 2.5 μM atPARP2 in the presence of 1 mM NAD^+ at 37°C for 1 h. After incubation, the reaction was stopped by heating the samples for 20 min at 80°C. Then, the reaction products were precipitated with 2% lithium perchlorate in acetone, desalted, and used for the matrix-assisted laser desorption ionization time-of-flight (MALDI-TOF) mass spectrometry (MS) measurements. MALDI-TOF mass spectra were obtained in the negative mode on a Microflex mass spectrometer (Bruker, Wissembourg, France), equipped with a 337-nm nitrogen laser and pulsed delay source extraction. The matrix was prepared by dissolving 3-hydroxypicolinic acid in 10 mM ammonium citrate buffer and a small amount of Dowex-50W 50 × 8-200 cation exchange resin (Sigma). The matrix (1 μl) was added

to the sample (1 μl) on the target plate and allowed to dry. The spectra were calibrated using reference oligonucleotides of known masses.

Analysis of the Efficiency of atPARP2-Catalyzed Auto- and DNA ADP-Ribosylation

The efficiency of atPARP2-catalyzed auto- and DNA ADP-ribosylation was measured using a cold ExoA●RexT^{Nick} duplex phosphorylated at the 5′ end of the nick and with or without a phosphate at the 5′ DSB terminus. The assay was performed in the ADPR buffer without BSA. One micromolar atPARP2 was incubated in the presence of 10 μM oligonucleotide duplex and 1 μM [adenylate-^{32}P]NAD$^+$ for 30 min at 37°C. The reactions were terminated by the addition of the stop solution (7.5 M urea, 0.33% SDS, 10 mM EDTA, and 0.25% bromophenol blue) at 1:1 (v/v) and heating at 95°C for 10 s, after which the products of the reactions were analyzed on denaturing PAGE as described above.

Analysis of Plant Genomic DNA for the Presence of PAR–DNA Adducts

Isolation of gDNA was described above in the *Plant Material, Cell-Free Extracts, and Genomic DNA Extraction* section. To examine the presence of ADP-ribosylated DNA adducts in plant, 1,000 ng of gDNA extracted from the control and treated 14-day-old seedlings (whole plant) were dot blotted on a Hybond N$^+$ nylon membrane (GE Healthcare). DNA and PAR were fixed to the membrane by heating at 80°C for 2 h and then analyzed with the mouse monoclonal anti-poly(ADP-ribose) antibody 10H (1:2,000, Enzo Life Sciences Inc., United States) and the rabbit monoclonal *anti-pan-ADP-ribose* binding reagent MABE1016 (1:2,000, Millipore, United States). Immunodetection of poly(ADP-ribose) on the blot strips has been performed by using the ECL method, followed by a scan with Amersham® Imager 600 instrument (GE Healthcare) and by short exposure to blue-light-sensitive autoradiography film.

RESULTS

Plant atPARP1 and atPARP2 Modify DNA Oligonucleotide Duplexes in the Presence of NAD$^+$

In our previous work, we have demonstrated that *in vitro* mammalian PARP1 and PARP2 proteins can poly(ADP-ribosyl)ate duplex oligonucleotides containing multiple closely spaced DNA strand breaks and phosphorylated termini. *A. thaliana* atPARP1 and atPARP2 proteins share homology with mammalian PARP1 and PARP2 proteins, respectively, suggesting that the plant proteins might also exhibit DNA modification activities. To verify this, we examined the biochemical activities of the purified atPARP1 and atPARP2 proteins using DNA substrates containing more than two strand breaks to mimic clustered DNA damage and repair intermediates: ExoA●RexT^{Nick} (referred to as S13) and ExoA●RexT^{gap} (referred to as S10), which are 40-mer oligonucleotide duplexes containing a nick and one-nucleotide gap, respectively, composed of a 40-mer (RexT, also referred to as S1) template strand and two complementary strands: 21-mer (ExoA) and phosphorylated 18-mer (5′pExo18) or 19-mer (5′pExo19) strands (**Supplementary Table S1**). In addition, we prepared ExoA●RexT^{rec} (referred to as S3, S5, and S6) and Exo20●RexT^{rec} (referred to as S4), which are recessed duplexes with a 5′ single-stranded tail, composed of RexT and ExoA or Exo20, respectively. In ExoA●RexT^{rec} duplex, either ExoA or RexT was [^{32}P]-labeled at the 5′ end, and in Exo20●RexT^{rec}, Exo20 was [^{32}P]-labeled at the 3′ end. The 5′-[^{32}P] labeled oligonucleotide duplexes were incubated with the atPARP proteins in the presence of 1 mM NAD$^+$; the reactions were stopped by adding 0.15% SDS and 50 μg●ml^{-1} proteinase K and incubating for 30 min at 55°C. After this, the samples were desalted and then heat treated (5 min at 95°C) in a gel loading buffer, and the products were separated by electrophoresis on a denaturing polyacrylamide gel. Analysis of the reaction products revealed that 3–60% of the [^{32}P]-labeled oligonucleotides are converted to slowly migrating DNA products which run on the gel above the non-modified 21-mer fragment (**Figure 2A**, lanes 2, 4, 6, 8, 10, and 12), suggesting that the PAR polymer synthesized by atPARPs generated a complex with DNA. Importantly, these slowly migrating PAR–DNA products were resistant to proteinase K, SDS, and heat treatment pointing to a possible covalent nature of the atPARP-induced DNA modifications. Noteworthy, atPARP2 modifies DNA more efficiently as compared with atPARP1 (**Figures 2A,B**). Particularly, atPARP1 generated mainly high-molecular-weight (HMW) PAR–DNA products, which were unable to enter the gel (**Figure 2A**, lanes 2, 4, and 6), whereas atPARP2 produced, in addition to HMW, low-molecular-weight (LMW) PAR–DNA products which were able to enter the gel and migrated as a ladder of distinct DNA fragments above the free 21-mer fragment (lanes 8, 10, and 12). As shown in **Figure 2B**, the relative efficiency levels of the atPARP1- and atPARP2-catalyzed formation of PAR–DNA products were strongly dependent on DNA duplex structures. AtPARP1 preferentially modifies the recessed duplex ExoA●RexT^{rec} (S5) (20% of HMW PAR–DNA products) and to a lesser extent the gapped and nicked DNA duplexes (3 and 10% of HMW PAR–DNA products, respectively), whereas atPARP2 prefers gapped and nicked duplexes (30 and 60% of LMW and HMW PAR–DNA products, respectively) as compared with a recessed DNA (14% of PAR–DNA products). It should be noted that atPARP1, but not atPARP2, induces limited non-specific 3′ →5′ exonuclease degradation of the 21-mer fragment (**Figure 2A**, lanes 2, 4, and 6), suggesting a non-specific DNA exonuclease contamination in recombinant atPARP1 preparation. Furthermore, the incubation of atPARP1 with ExoA●RexT^{Nick} (S13) and, to a much lesser extent, with ExoA●RexT^{gap} (S10) produces a discrete band migrating at the position of the 40-mer fragment (lanes 4 and 6), suggesting the presence of a DNA ligase activity in the purified plant protein. These observations suggest that the recombinant atPARP1 protein, despite extensive purifications, is contaminated by the

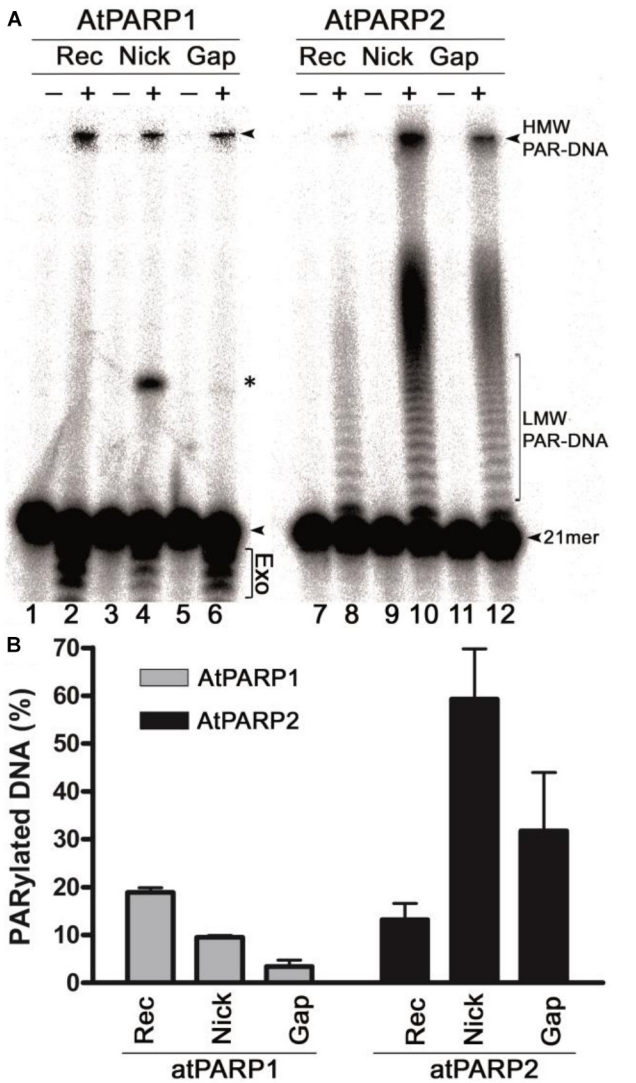

FIGURE 2 | AtPARP-catalyzed formation of radioactively labeled high-molecular-weight (HMW) DNA products. **(A)** Denaturing PAGE analysis of atPARP1- and atPARP2-generated HMW products after incubation with 5′-[^{32}P]-labeled 40-mer nicked, gapped, and recessed DNA duplexes. Arrows indicate the 21-mer free oligonucleotide, HMW and LMW PAR–DNA products. Asterisk indicates a nonspecific ligation product generated by NAD^+-dependent *E. coli* DNA ligase A. "Exo" indicates exonuclease degradation products of 21-mer fragment. For details, see section "Materials and Methods." **(B)** Graphic representation of the formation of HMW and LMW products by atPARPs when acting upon gapped, nicked, and recessed DNA duplexes. Each bar represents atPARP activity as mean ± SD from three independent experiments.

host NAD^+-dependent *E. coli* DNA ligase A and non-specific DNA exonucleases.

Next, we examined time, NAD^+, and protein concentration dependence of the PAR–DNA product formation by the atPARP proteins. For this, we incubated atPARP1 and atPARP2 with their preferred substrates 5′-[^{32}P]-labeled ExoA●RexT^{rec} (S5) and ExoA●RexT^{Nick} (S13), respectively, under varying concentrations of NAD^+ and protein. For atPARP1, the PAR–DNA products were not formed in the absence or at very low concentrations of NAD^+ (0–10 μM) and protein (5–50 nM) (**Figures 3A,B**), but the level of DNA modification steadily increased at higher concentrations of NAD^+ (from 25 μM to 1 mM) and protein (100–250 nM) (**Figures 3A,B** and **Supplementary Figure S2**). Noteworthy, the DNA PARylation activity of atPARP1 quickly reached the plateau level after only 1 min incubation and increased very little following 30 min incubation (**Figure 3C**). Similarly for atPARP2, the DNA PARylation was very low or absent at low concentrations of NAD^+ (0–25 μM) (**Figure 3A**) and protein (5–10 nM) (**Figure 3B**), but the activity steadily increased at higher concentrations of NAD^+ (0.1–1 mM) and protein (25–250 nM) (**Figure 3** and **Supplementary Figure S2**). Noteworthy, when the protein concentration was below 250 nM, atPARP2 was not able to generate the HMW PAR–DNA products, but only LMW products (**Supplementary Figure S2**). It should be noted that atPARP2, but not atPARP1, generated LMW PAR–DNA products that migrate as a ladder of distinct DNA fragments above the 21-mer free oligonucleotide which becomes a smear at the distance of 1/3 from the start of the gel (**Supplementary Figure S2**). The appearance of the DNA ladder implies distributive synthesis of PAR polymer by atPARP2, whereas the formation of HMW PAR–DNA fragments by both atPARP enzymes suggests a high processivity of the synthesis of PAR polymer by plant PARP enzymes (**Supplementary Figure S2**). Taken together, these results suggest that the plant PARPs, similar to their mammalian counterparts, can synthesize long PAR polymers covalently attached to DNA.

Characterization of the DNA Substrate Specificity of atPARP-Catalyzed PARylation

Next, we assessed in more detail the influence of the different DNA structures [nick, gap, recessed duplexes and single-stranded (ss) DNA] and nature of DNA termini on the atPARP-catalyzed formation of PAR–DNA adducts. For this purpose, we incubated [^{32}P]-labeled DNA oligonucleotides of various configurations and terminus structures in the presence of atPARPs and NAD^+. After incubation, the reaction products were analyzed on the denaturing PAGE and the formation of the PAR–DNA adducts was quantified (**Figure 4A**). Quantification of the results shown in **Figure 4B** revealed that (i) overall, atPARP2 was more active as compared with atPARP1 on the majority of DNA substrates tested; (ii) atPARP1 was more active on the recessed DNA duplex (^{32}pExo15●Rex12T^{rec} or S7) which contains the 15-mer fragment, as compared with ^{32}pExoA●RexT^{rec} duplex (S5) with longer 21-mer strand; and (iii) the substrate preference of atPARP2 was opposite to that of atPARP1, since atPARP2 was active on the latter DNA substrate (^{32}pExoA●RexT^{rec} or S5), but lost its activity on the former one (^{32}pExo15●Rex12T^{rec} or S7). Interestingly, the presence of two 5′-terminal phosphates in ExoA●RexT$^{nick/gap}$ duplexes (S10 and S13) was necessary for a more efficient DNA PARylation, whereas

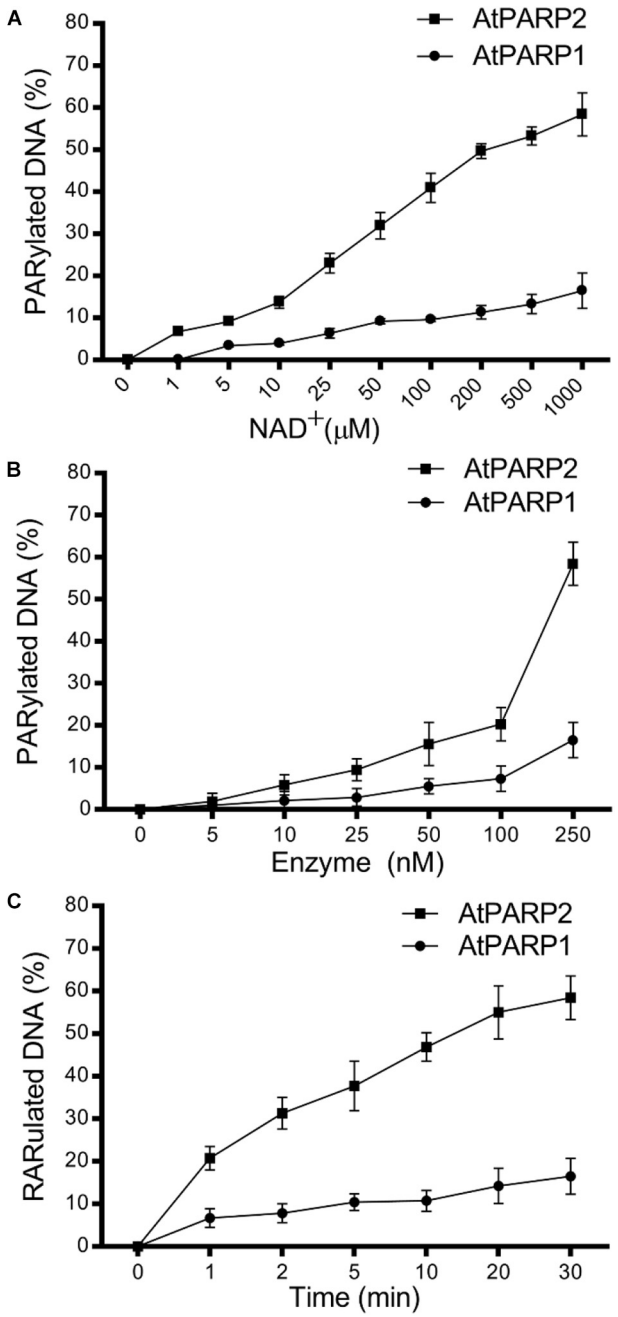

FIGURE 3 | Dependence of the atPARP-catalyzed PAR–DNA formation on reaction conditions; 250 nM atPARP1 and atPARP2 incubated with 20 nM DNA duplex for 30 min at 37°C. **(A)** atPARP1- and atPARP2-catalyzed DNA PARylation in the presence of varying concentrations of NAD^+ (1–1,000 μM). **(B)** The dependence of DNA PARylation on atPARP protein concentrations (0–250 nM). **(C)** Time dependence of DNA PARylation by atPARPs (0–30 min). For details, see section "Materials and Methods."

the presence of the 3′-terminal phosphate and cordycepin (3′-dAMP) in S12 and S4, respectively, strongly inhibited DNA modification (**Figure 4**). Taken together, these results suggest that the substrate specificities of plant atPARP1 and atPARP2 proteins resemble to their mammalian counterparts PARP1 and PARP2, respectively.

Construction and Characterization of Catalytic Site atPARP1^{E960K,E960Q} and atPARP2^{E614K} Mutants

The catalytic domain of PARP1, also referred to as ADP-ribosyltransferase (ART) domain, is highly conserved in all PARP family members and shares structural similarity with the plant ADP-ribosylating enzymes. Active mammalian PARPs share a conserved histidine-tyrosine-glutamic acid (H-Y-E) triad (PARP signature) in their catalytic domains (Hassa and Hottiger, 2008). This evolutionary conserved "H-Y-E" triad is essential for the positioning of NAD^+ during ADP-ribosylation: in PARP1, H862 and Y896 participate in the binding of NAD^+, while E988 is critical for catalysis and substrate positioning. Y896 stacks with the nicotinamide ring (Steffen et al., 2013), H862 binds to the 2′-OH of NAD^+ adenine-ribose, and E988 makes a hydrogen bond with the 2′-OH of the nicotinamide-ribose and polarizes the NAD^+ molecule for nucleophilic attack (Ruf et al., 1998). Alignment of amino acid sequences of ART domains of PARPs revealed a significant homology between human and plant enzymes: PARP1 shared 49.6 and 45.6% homology with atPARP1 and atPARP2, respectively. Noteworthy, human and plant PARPs shared conserved catalytic triad H-Y-E: the catalytic triad of human PARP1 H862-Y896-E988 corresponds to that of atPARP1 consisting of H833-Y867-E960 and atPARP2 consisting of H486-Y520-E614 residues.

To ensure that the observed DNA repair activities of recombinant atPARPs are not due to trace contamination by either bacterial host proteins or other unknown factors, we have constructed site-directed mutants of atPARP1 and atPARP2 and then purified them using the same scheme as for the wild-type proteins. The highly conserved catalytic E960 in atPARP1 and E614 in atPARP2 were replaced by either lysine (K) or glutamine (Q) resulting in single substitution mutants: atPARP1^{E960K}, atPARP1^{E960Q}, and atPARP2^{E614K}. It should be noted that in the human PARP1 protein, the corresponding mutations E988Q and E988K strongly reduce > 40-fold the enzyme activity and convert PARP1 into a mono-ADP-ribosyl-transferase (Marsischky et al., 1995; Rolli et al., 1997). The purified atPARP1^{E960K}, atPARP1^{E960Q}, and atPARP2^{E614K} mutant proteins were incubated with the 5′-^{32}P-labeled Exo15•Rex12T^{Rec} (S7) and p10•RT-A^{Nick} (S18) duplexes, respectively, to measure the DNA ADP-ribosylation activity. The results revealed that the atPARP1^{E960K} mutant protein completely lost DNA ADP-ribosylation activities (**Figure 5A**, lanes 8–11), whereas, as expected, the atPARP1^{E960Q} mutant exhibited robust DNA MARylation activity (lanes 12–14). Noteworthy, at higher protein concentration, the atPARP1^{E960Q} mutant was able to synthesize short ADP-ribose oligomers, but rather in a distributive manner (lane 15). In control reactions, human PARP1 and WT atPARP1 synthesized mainly HMW PAR–DNA products (**Figure 5A**, lanes 1 and 6–7, respectively). The atPARP2^{E614K} mutant

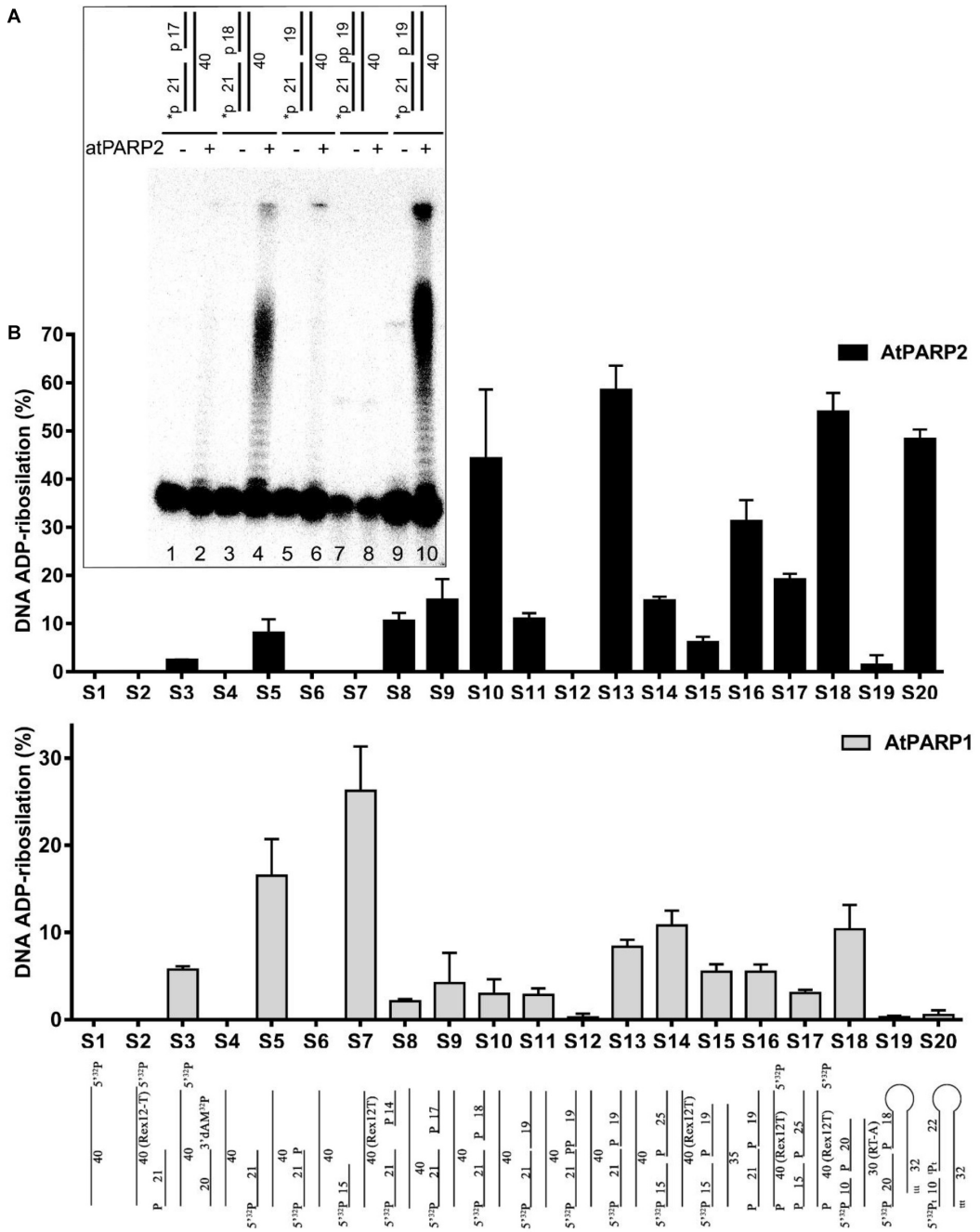

FIGURE 4 | Effect of the DNA structure and nature of termini on the atPARP1- and atPARP2-catalyzed formation of PAR–DNA adducts; 250 nM atPARP proteins were incubated with 20 nM [^{32}P]-labeled oligonucleotide in the presence of 1 mM NAD$^+$ for 30 min at 37°C. The products of the reaction were separated using denaturing PAGE and the relative amounts of the PAR–DNA products were measured. **(A)** Denaturing gel showing the influence of terminal DNA phosphate residues on atPARP2-catalyzed DNA PARylation. **(B)** Graphic representation of the effects of various DNA structures on atPARP1- and atPARP2-catalyzed DNA PARylation. The data on PARP-catalyzed formation of PAR–DNA products are presented as mean ± SD from three independent experiments. For details, see section "Materials and Methods."

at low protein concentration did not show detectable DNA PARylation activity (**Figure 5B**, lanes 7–8), but exhibited a very weak DNA mono-ADP-ribosylation (MARylation) activity at higher protein concentration (lanes 9–10). In control reactions, human PARP2 and WT atPARP2 showed efficient DNA PARylation activity (**Figure 5B**, lane 2 and lanes 3–6, respectively). Altogether, these results indicate that the highly conserved E960 of atPARP1 and E614 of atPARP2 are essential for DNA PARylation activities of plant enzymes and that the preparations of plant proteins used in this

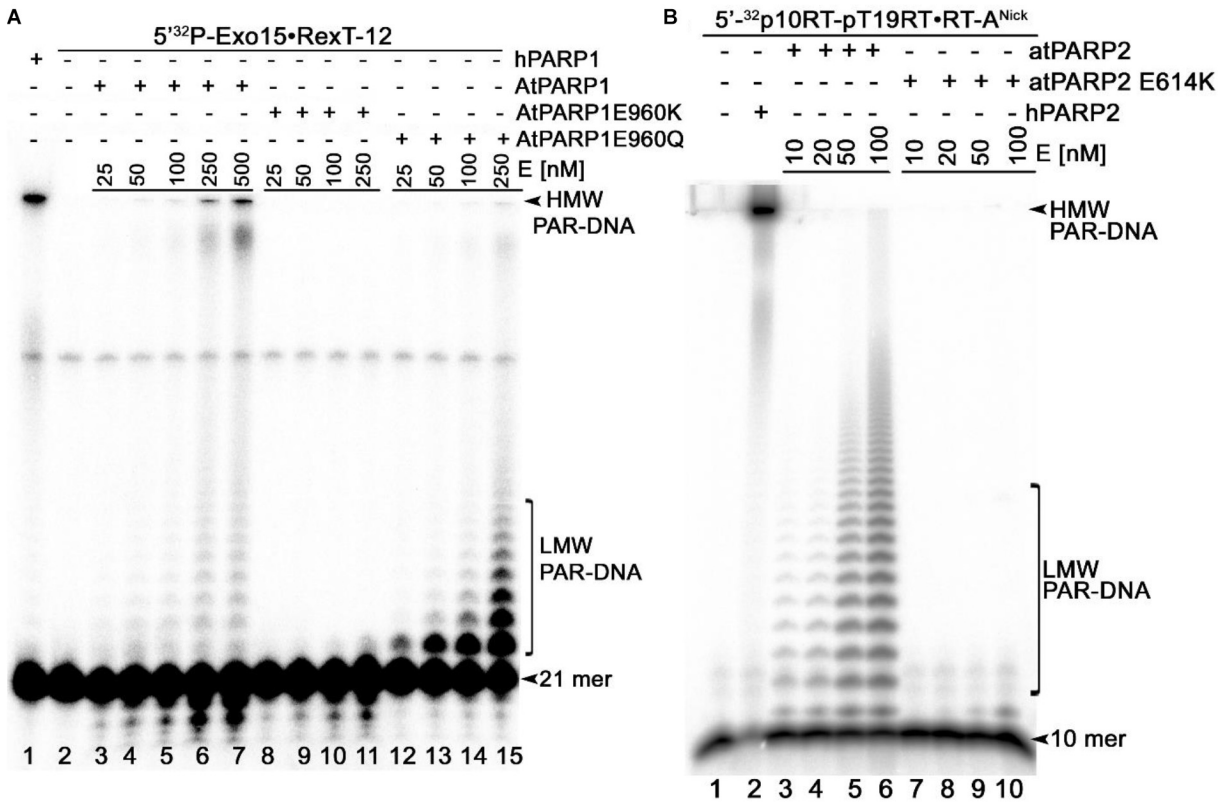

FIGURE 5 | Denaturing PAGE analysis of the PAR–DNA adducts generated by atPARP mutants; 25–500 nM atPARP1 variants and human PARP1 were incubated with 20 nM 5′-[^{32}P]-labeled Exo15•Rex12T^{Rec} duplex (S7) and 1 mM NAD$^+$ at 37°C for 30 min. On the other hand, 10–100 nM atPARP2 variants and human PARP2 were incubated with 20 nM 5′-[^{32}P]-labeled 10RT pT19RT•RT-A^{Nick} duplex (S18) and 1 mM NAD$^+$ at 37°C for 30 min. **(A)** Analysis of the PAR-DNA products generated by atPARP1-WT and atPARP1-E960K and atPARP1-E960Q mutants. **(B)** Analysis of the PAR-DNA products generated by atPARP2-WT and atPARP2-E614K mutant. Arrows indicate HMW and LMW PAR–DNA products and free oligonucleotides. For more details, see section "Materials and Methods."

study are not contaminated by some unknown bacterial ADP-ribose transferases.

Analysis of the Structure and Composition of PAR–DNA Adducts

The mammalian PARPs use DNA strand break termini containing either the terminal phosphate residues or the 3′-terminal cordycepin moiety with 2′ hydroxyl group as acceptor residues for ADP-ribose chain synthesis. To verify whether plant PARPs employ the same mechanisms to modify DNA, we incubated 5′-[^{32}P]-labeled DNA duplexes with atPARPs and then treated the reaction products with various enzymes including (i) PAR glycohydrolase (PARG) that hydrolyzes ribose–ribose *O*-glycosidic (1″ →2′) bonds in PAR polymers to produce monomeric ADP-ribose (**Figure 6A**); (ii) CIP that removes phosphate groups from the 5′ and 3′ ends of DNA strand breaks; (iii) snake venom phosphodiesterase 1 (SVPDE1), which digests DNA in the 3′ →5′ direction producing dNMPs and cleaves pyrophosphate bonds in a PAR polymer to generate the 2′-(5″-phosphoribosyl)-5′-adenosine monophosphate (pRib-AMP) compound as an end product (**Figure 6A**); (iv) deoxyribonuclease I from bovine pancreas (DNAse I) that non-specifically cleaves ssDNA and dsDNA to produce di, tri, and oligomer DNA fragments; and (v) proteinase K, a highly efficient non-specific serine protease that can efficiently digest majority of proteins.

Incubation of the 5′-[^{32}P]-labeled ExoA•RexT^{Nick} (S13) duplex with atPARP2 resulted in the formation of LMW and HMW PAR–DNA complexes (**Figure 6B**, lanes 4 and 9). As expected, the treatment of PAR–DNA complexes with PARG resulted in complete disappearance of the ADP-ribosylated DNA and restoration of the original 21-mer fragment (lane 6), indicating that PARG can completely remove ADP-ribose moieties attached to DNA. However, these PAR–DNA complexes were resistant to proteinase K, SDS, and heat treatment (lane 10), suggesting that the PAR polymer is not attached to the atPARP2 protein. Indeed, the DNAse I treatment of PAR–DNA complexes resulted in a faster mobility of LMW and HMW products (**Figure 6C**, lane 10), indicating that PAR polymers are linked to the labeled 21-mer fragment. Noteworthy, CIP dephosphorylates free 5′-[^{32}P]-labeled ExoA•RexT^{Nick} duplex (**Figure 6B**, lane 2 and **Figure 6C**, lane 3), but not the [^{32}P]-labeled LMW and HMW PAR–DNA adducts generated by atPARP2 (**Figure 6B**, lane 5 and **Figure 6C**, lane 6), indicating that the 5′-terminal P of PARylated oligonucleotides is not

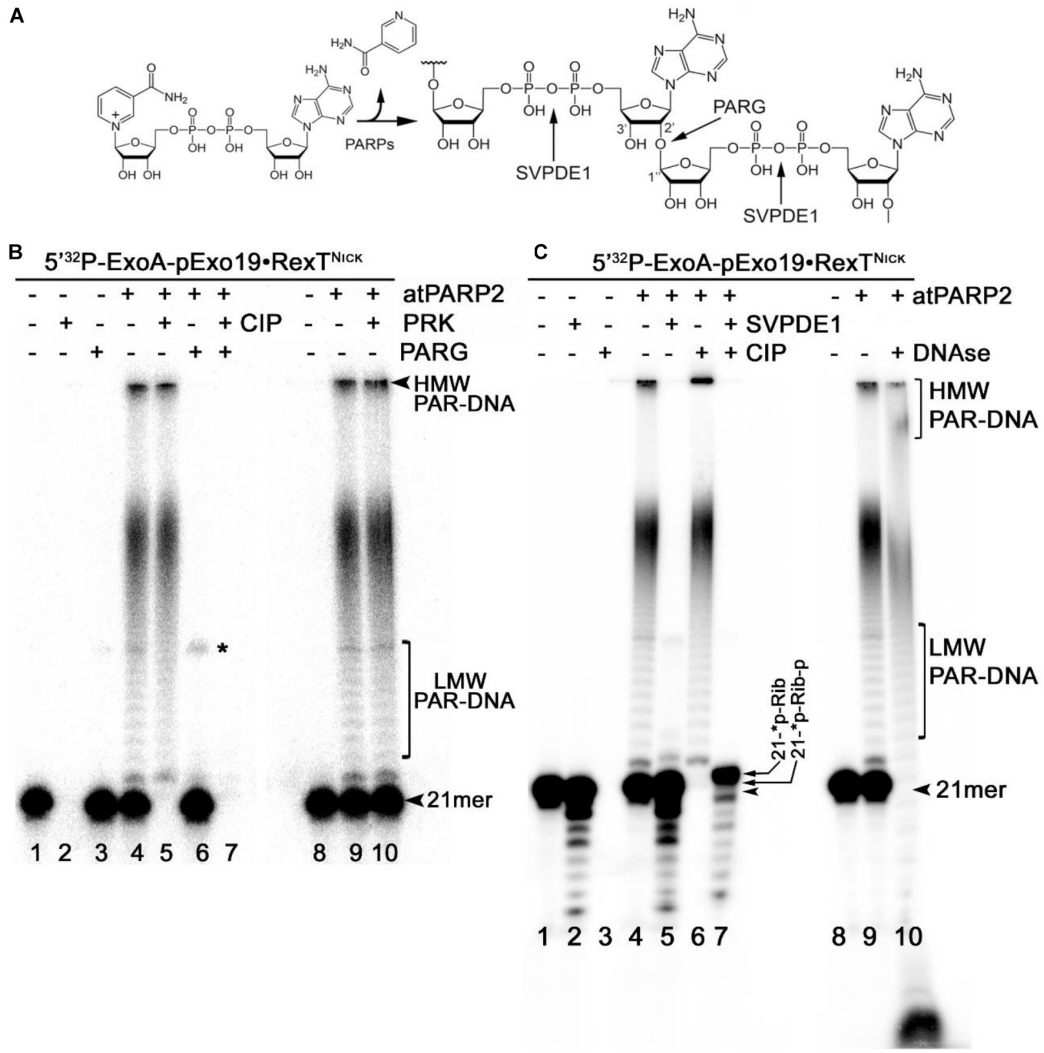

FIGURE 6 | Analysis of the products of enzymatic digestion of the PAR–DNA adducts. PAR–DNA products were generated by incubation of 20 nM 5′-[^{32}P]-ExoA pExo19•RexT^{Nick} oligonucleotide duplex (S13) with 250 nM atPARP2 in the presence of 1 mM NAD$^+$ for 30 min at 37°C. After reactions, the samples were heated for 20 min at 80°C and then incubated in the presence of either 50 pg•μl^{-1} PARG (in ADPR buffer), or 50 μg•ml^{-1} proteinase K, or 0.1 U SVPDE1 (in SVPDE1 buffer) or 10 U CIP (in CIP buffer) for 60 or 30 min at 37°C, respectively. **(A)** Graphical representation of the formation of poly(ADP-ribose) polymer and enzyme cleavage sites. **(B)** Denaturing PAGE analysis of the products of PARG- and proteinase-catalyzed digestion of the 5′-[^{32}P]-labeled PAR–DNA products. **(C)** Denaturing PAGE analysis of the products of SVPDE-, CIP-, and DNase-catalyzed digestion of the 5′-[^{32}P]-labeled PAR–DNA products. Arrows indicate HMW and LMW PAR–DNA products and the 21-mer free oligonucleotide. Asterisk indicates a non-specific ligation product produced by *E. coli* NAD$^+$-dependent DNA ligase A.

accessible to the phosphatase. Moreover, the efficient shielding of 5′-[^{32}P] groups from CIP, by the short ADP-ribose oligomers attached to ExoA oligonucleotide in LMW PAR–DNA products (**Figure 6B**, lane 5 and **Figure 6C**, lane 6), suggests that these DNA 5′-phosphates are protected *via* covalent phosphodiester bond between 5′P and C1′ of ADP-ribose.

Under the reaction conditions used, SVPDE1 degrades the free 5′-[^{32}P]-labeled ExoA•RexT^{Nick} duplex in the 3′ → 5′ direction, resulting in the appearance of a fast migrating ladder with bands below the 21-mer fragment (**Figure 6C**, lane 2). Incubation of the PARylated ExoA•RexT^{Nick} duplex with SVPDE1 resulted in a disappearance of LMW and HMW PAR–DNA complexes (lane 5), indicating that the enzyme degrades PAR by cleaving the pyrophosphate bonds within a polymer chain. The SVPDE1-catalyzed hydrolysis of [^{32}P]-labeled PAR–DNA products converted the LMW and HMW complexes back to a free DNA fragment, which migrates somewhat similar to a free 21-mer (lane 5). We propose that this SVPDE1-generated 21-mer fragment still contains the phosphoribosyl moiety left after the hydrolysis of the last ADP-ribose monomer linked to the terminal DNA phosphate residue at the 5′ end of ExoA. In agreement with this, the combined treatment of 5′-[^{32}P]-labeled PAR–DNA products with SVPDE1 and CIP resulted in the appearance of a band (lane 7) that

migrated more slowly than free 21-mer 5′-[^{32}P]-labeled ExoA (lane 1). This result strongly suggests the presence of a protecting ribose moiety at the 5′ end of the ADP-ribosylated ExoA that remains after the removal of PAR and phosphate residue by SVPDE1 and CIP, respectively.

Next, we examined the structure and composition of PAR–DNA adducts generated by atPARP1. For this, the 5′-[^{32}P]-labeled PARylated Exo15●Rex12T^{Rec} (S7) oligonucleotide duplexes were incubated with PARG, CIP, DNAse I, and PRK. As expected, PARG treatment of PARylated DNA, but not that of PRK, completely restored the native structure of the 15-mer oligonucleotide (**Supplementary Figure S3**). PARylated Exo15●Rex12T^{Rec} duplexes, contrary to free oligonucleotides, were resistant to CIP and DNAse I treatments (**Supplementary Figure S3**). These results indicate that both atPARPs ADP-ribosylate DNA oligonucleotides in a similar manner by generating structurally similar PAR–DNA adducts. Thus, we can conclude that plant PARPs, similar to their mammalian counterparts, catalyze covalent attachment of an ADP-ribose unit to DNA termini *via* a phosphodiester bond between DNA terminal phosphate residue and C1′ of ADP-ribose.

Nucleoside Diphosphate-Linked Moiety X Hydrolase Cleaves the PAR–DNA Complexes to Generate the Phosphoribosylated DNA Adducts

Previously, it was demonstrated that nucleoside diphosphate-linked moiety X (Nudix) hydrolases can act on a free ADP-ribose residue (and on a PAR polymer attached to a protein) by hydrolyzing the pyrophosphate bonds (Mildvan et al., 2005). In addition, Nudix hydrolases can cleave a long PAR polymer attached to DNA (Palazzo et al., 2015; Talhaoui et al., 2016; Belousova et al., 2018); here, this property was exploited to further characterize DNA ADP-ribosylation catalyzed by plant PARPs. For this, the 5′-[^{32}P]-labeled ExoA●RexT^{Nick} (S13) and Exo15●Rex12T^{Rec} (S7) duplexes were ADP-ribosylated by atPARP1 and atPARP2, respectively, and the resulting PAR–DNA complexes were incubated with an excess amount of the human Nudix hydrolase, NUDT16, and the products of reaction were analyzed by denaturing PAGE.

Incubation of the 5′-[^{32}P]-labeled free oligonucleotide duplexes with an excess amount of NUDT16 resulted only in slight degradation of the 21-mer oligonucleotide, whereas the shorter 15-mer oligonucleotide degraded more strongly (**Figure 7**, lanes 2 and 9, respectively), suggesting that the human Nudix hydrolase contains a weak non-specific nucleolytic cleavage activity. NUDT16 completely degraded the PAR–DNA adducts and generated distinct DNA fragments that migrated similar to free 21-mer and 15-mer oligonucleotides (lanes 5 and 12). The mechanism of action of NUDT16 on PAR suggests that a phosphoribosyl (pRib) moiety attached to the 5′-terminal [^{32}P] residue at DNA termini (21-*p-Rib-p and 15-*p-Rib-p, where the asterisk denotes a radioactive ^{32}P residue) should remain after NUDT16-catalyzed hydrolysis of pyrophosphate bonds of the ADP-ribose unit was covalently linked to DNA. As expected, the treatment of NUDT16-derived DNA oligonucleotides with CIP resulted in the appearance of the distinct 5′-monoribosylated 21- and 15-mer DNA fragments (lanes 7 and 14, respectively), which migrated more slowly than free 21- and 15-mer DNA oligonucleotides (lanes 1 and 8, respectively) and the 5′-monophosphoribosylated 21- and 15-mer NUTD16 products (lanes 5 and 12, respectively). These results suggest that NUTD16 generated the 21-*p-Rib-p and 15-*p-Rib-p fragments by hydrolysis of the PARylated 21- and 15-mer oligonucleotides, respectively. After that, CIP dephosphorylated NUTD16 products to generate monoribosylated 21-*p-Rib and 15-*p-Rib fragments which still contain ^{32}P residue. Noteworthy, CIP did not remove the 5′-[^{32}P] residue in PARylated DNA fragments, even after hydrolysis of the PAR polymer by NUDT16 (lanes 5–12), indicating that the remaining ribose sugar moiety protects 5′P in the 5′-[^{32}P]-ExoA(Exo15)-p*-Rib oligonucleotide. These results further confirms that the plant PARPs catalyze covalent attachment of an ADP-ribose unit to DNA *via* a phosphodiester bond between DNA 5′P and C1′ of ADP-ribose.

Identification of the ADP-Ribose–DNA Adducts by Matrix-Assisted Laser Desorption Ionization Time-of-Flight Mass Spectrometry

In the above data, a putative molecular mechanism of *Arabidopsis* atPARP-catalyzed DNA PARylation is revealed from the migration pattern of end-labeled DNA fragments in a denaturing PAGE (**Figures 6**, **7**). To further substantiate the mechanism of action of atPARP enzymes on duplex oligonucleotides, we characterized the nature of PAR–DNA adducts by MALDI-TOF MS analysis of the PARylated DNA products. For this purpose, we selected atPARP2 as the most efficient enzyme and constructed cold non-radioactive 30-mer nicked duplex oligonucleotide (referred to here as p10●RT-A^{Nick} or S18), composed of a 30-mer (RT-A) template strand and two 5′-phosphorylated complementary strands: 10-mer (p10) and 19-mer (p19), as DNA substrate (**Supplementary Table S1**). It should be noted that, when acting upon p10●RT-A^{Nick}, atPARP2 generates mainly LMW PAR–DNA products, which migrate as DNA ladders in the denaturing gel, indicating the presence of short ADP-ribose oligomers (1–20 units) linked to the 10-mer fragment (**Supplementary Figure S4**). Furthermore, short, low-molecular-weight oligonucleotides (such as 10-mer in p10●RT-A^{Nick}) have in general higher probability of detection by MALDI-TOF MS as compared with their long, high-molecular-weight oligonucleotide analogs (such as 21-mer in ExoA●RexT^{Nick}, or S13) (Nordhoff et al., 1996); thus, the employment of p10●RT-A^{Nick} allowed us to significantly increase the sensitivity of mass spectrometry.

MALDI-TOF analysis of the mock-treated p10●RT-A^{Nick} duplex showed the presence of two major peaks at [M-H]$^-$ = 3,105.6 Da and [M-H]$^-$ = 5,949.5 Da corresponding to the phosphorylated 10-mer and 19-mer oligonucleotides, as well as a minor peak corresponding to 30-mer RT-A oligonucleotide (**Figure 8A**). Analysis of the mass spectra of the atPARP2 ADP-ribosylated p10●RT-A^{Nick} duplex oligonucleotide

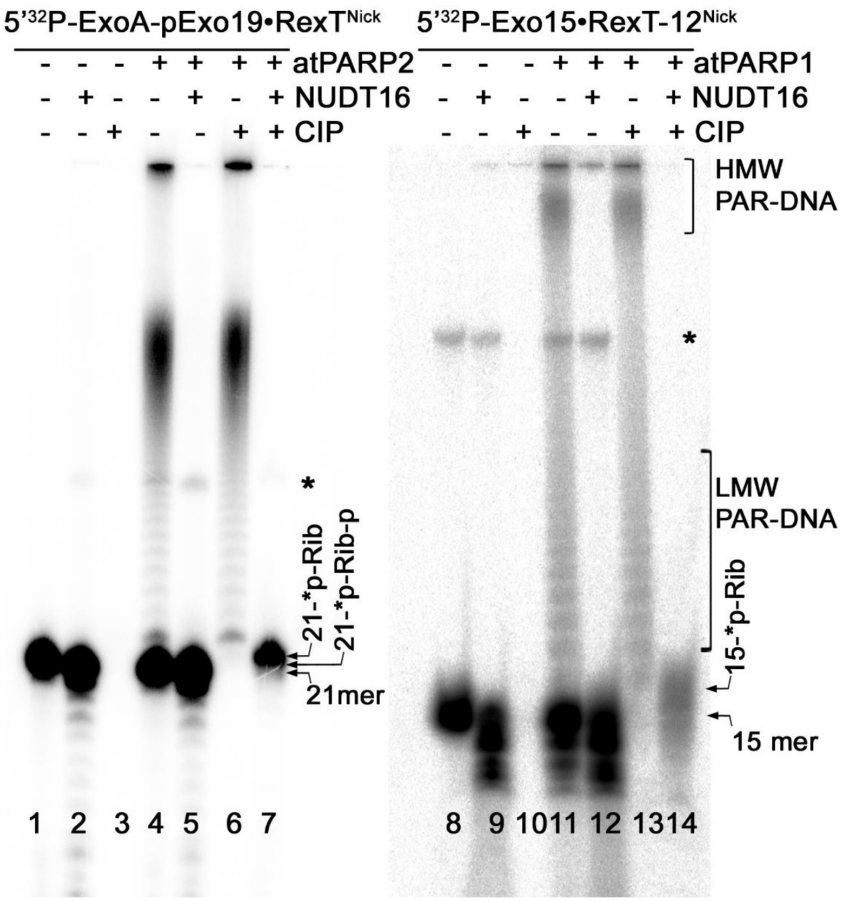

FIGURE 7 | Denaturing PAGE analysis of the products of NUDT16- and CIP-catalyzed hydrolysis of the PAR–DNA adducts generated by atPARP1 and atPARP2. The 20-nM 5′-[^{32}P]-labeled ExoA pExo19•RexT^{Nick} duplex (S13) was incubated with 250 nM atPARP2 and 1 mM NAD$^+$, and the 20-nM 5′-[^{32}P]-labeled Exo15•Rex12T^{Rec} duplex (S7) was incubated with 250 nM atPARP1 and 1 mM NAD$^+$ at 37°C for 30 min. After incubation with atPARPs, the samples were heated for 20 min at 80°C and the resulting [^{32}P]-labeled HMW products were further incubated with 20 μM NUDIX16. Arrows indicate phosphoribosylated (Rib-p), ribosylated (Rib), and native [^{32}P]-labeled 21-mer and 25-mer oligonucleotides, "*p" stands for a labeled phosphate residue. Asterisk indicates a nonspecific ligation product produced by *E. coli* NAD$^+$-dependent DNA ligase A. For more details, see section "Materials and Methods."

revealed two monocharged peaks at $[M\text{-}H]^-$ = 3,647.9 and 4,189.5 Da corresponding to the 5′-phosphorylated 10-mers that contain one and two ADP-ribose residues, respectively (calculated mass, 3,647 and 4,187 Da) (**Figure 8B**). These results indicate that atPARP2 catalyzes covalent attachment of ADP-ribose residues to the 5′-phosphorylated 10-mer (p10) oligonucleotide. In conclusion, these data are in good agreement with those obtained through the analysis of the PAR–DNA products on denaturing PAGE (**Figures 6**, **7**) and unambiguously confirm the formation of the covalent PAR–DNA adducts by plant PARPs.

The Switch of atPARP2 Substrate Specificity Depends on the Presence of Terminal Phosphates and DNA Duplex Configuration

Depending on the specific configurations of multiple closely spaced DNA strand breaks, mammalian PARP1–3 can switch their substrate specificity from protein to DNA only ADP-ribosylation (Zarkovic et al., 2018; Matta et al., 2020). In order to assess the relative efficiency of atPARP2-catalyzed auto- (protein) versus DNA ADP-ribosylation activities, we used non-radioactive (cold), non-phosphorylated, nicked 40-mer ExoA•RexT^{Nick} duplex as a cofactor and cold phosphorylated pExoA•RexT^{Nick} duplex (S13) as a DNA substrate. It should be noted that the pExoA•RexT^{Nick} duplex containing 5′-phosphorylated 21-mer fragment is prone to covalent ADP-ribosylation by human and plant PARPs at the 5′-terminal phosphate residue, whereas the ExoA•RexT^{Nick} duplex containing non-phosphorylated 21-mer fragment is not a substrate for ADP-ribosylation by PARPs. Importantly, both DNA duplexes can activate auto-ADP-ribosylation of mammalian and plant PARPs. To avoid the formation of long PAR polymers, we incubated 10-fold the molar excess of DNA duplexes (10 μM) over atPARP2 (1 μM) in the presence of limited amount of radioactively labeled [adenylate-^{32}P]NAD$^+$ (1 μM). We expected that under this particular

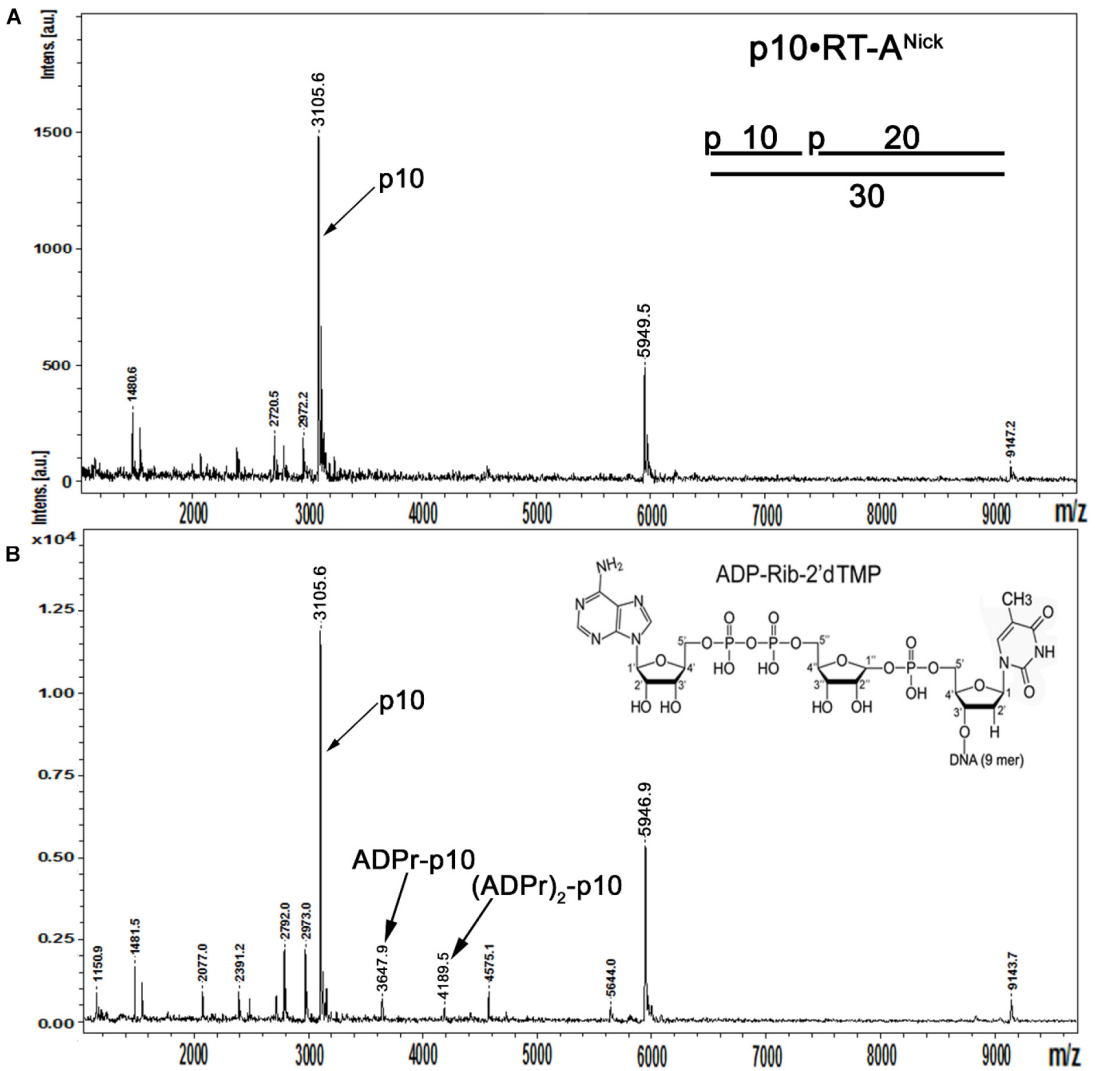

FIGURE 8 | MALDI-TOF MS analysis of the mono- and poly-ADP-ribosylated oligonucleotides generated by atPARP2. Five micromolars of the cold 5′-phosphorylated non-radioactive p10•RT-A^{Nick} duplex (S18) was ADP-ribosylated in the presence of 2.5 μM of atPARP2 and 1 mM NAD$^+$ at 37°C for 1 h. **(A)** MALDI-TOF spectrum of the control mock-treated cold 5′-phosphorylated RT^{Nick} duplex. **(B)** MALDI-TOF spectrum of the unpurified atPARP2 reaction products supplemented with the purified 10-mer p-10-RT-poly-ADP-ribose fragment as a size marker. For more details, see section "Materials and Methods."

reaction conditions, atPARP2 and other PARPs would favor the MARylation, rather than PARylation, of proteins and DNA. Human PARP3 was used as a control, because when acting upon pExoA•RexT^{Nick} duplex, this enzyme switches its substrate specificity from auto- to only DNA MARylation (Zarkovic et al., 2018). However, if PARP3 acts upon the non-phosphorylated ExoA•RexT^{Nick} duplex as DNA cofactor, it switches to auto-MARylation.

As shown in **Figure 9**, human PARP3 incubated with cold pExoA•RexT^{Nick} duplex (S13) and [adenylate-^{32}P]NAD$^+$ generated MARylated 21-mer pExoA fragment (lane 7), which migrated slower than the 21-mer size marker (lane 13), whereas no DNA MARylation occurred when PARP3 was incubated with the non-phosphorylated 40-mer nicked duplex (lane 12). On the other hand, incubation of atPARP2 with cold phosphorylated pExoA•RexT^{Nick} and radioactive NAD$^+$ resulted in the generation of a major band at the top of the gel, smears, and a minor band migrating similar to MARylated 21-mer pExoA fragment (lane 3). Formation of the major band at the top of the gel suggests auto-ADP-ribosylation of atPARP2, whereas the appearance of the smearing and modified 21-mer pExoA fragment suggests PARylation and MARylation of DNA, respectively. In agreement with these, treatment of the atPARP2 reaction products by proteinase K resulted in the disappearance of a major band and a dramatic decrease in smearing, but not the minor band (lane 4). As expected, DNAse I and PARG treatments resulted in the complete disappearance of the minor MARylated 21-mer pExoA fragment, but not the major band (lanes 5 and 6).

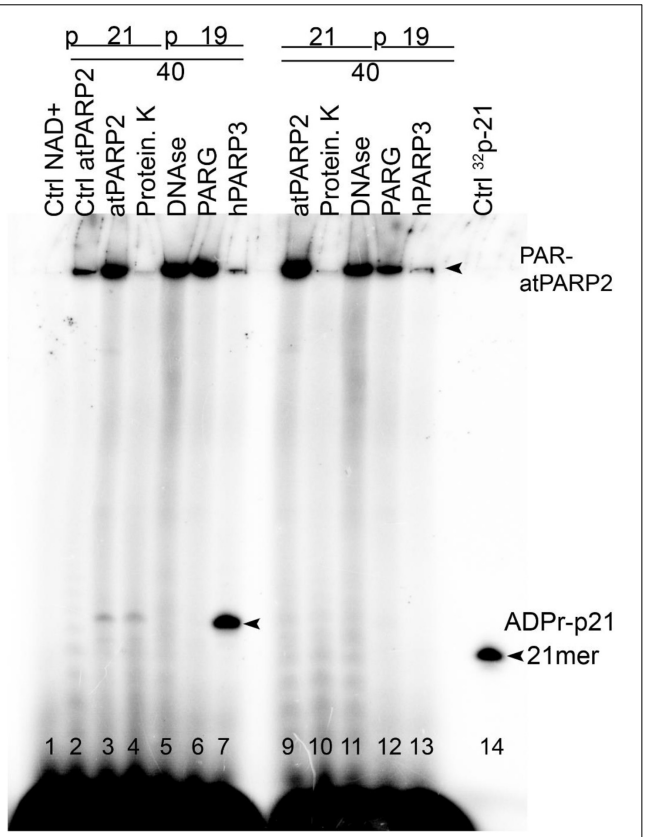

FIGURE 9 | Comparison of the relative efficiency of atPARP2-catalyzed auto- and DNA ADP-ribosylation; 1 μM atPARP2 and 50 nM human PARP3 were incubated with 10 μM cold oligonucleotide duplexes in the presence of 1 μM [adenylate-^{32}P]-NAD^{+} for 30 min at 37°C. The reaction products were analyzed by denaturing PAGE. Arrows indicate PAR–DNA, mono-ADPr-p21 mer products and free 21-mer oligonucleotide. For more details, see section "Materials and Methods."

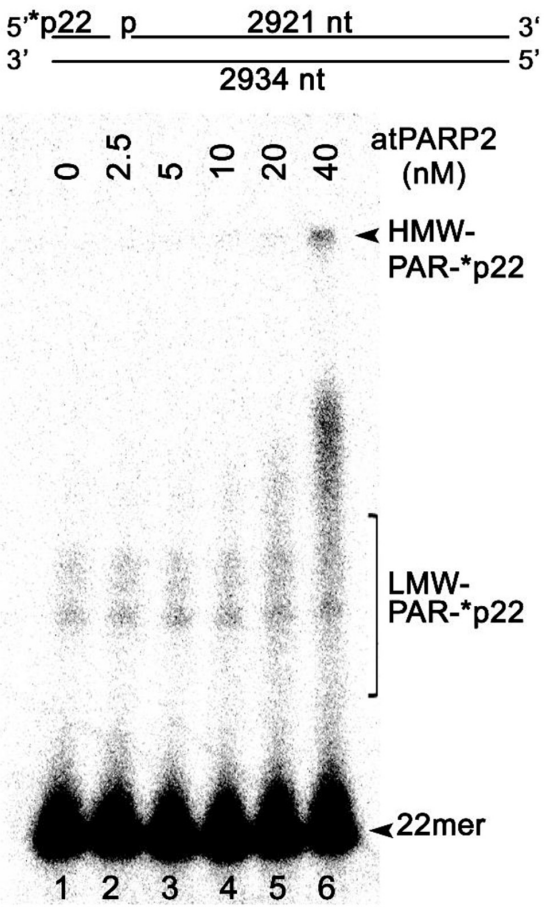

FIGURE 10 | AtPARP2 poly-ADP-ribosylates linear plasmid 2.3 kb DNA fragment; 1 nM 5′-[^{32}P]-labeled linearized nicked pML2 plasmid DNA was incubated with 2.5–40 nM atPARP2 under the standard reaction conditions. After incubation, the reaction products analyzed by denaturing PAGE. Arrows indicate HMW and LMW PAR–DNA products and free oligonucleotides. For more details, see section "Materials and Methods."

These results suggest that atPARP2 when acting upon phosphorylated nicked duplex can partially switch its substrate specificity from protein to DNA, but keeps its preference for auto-ADP-ribosylation.

Incubation of atPARP2 with cold non-phosphorylated ExoA•RexT^{Nick} duplex and radioactive NAD^{+} resulted in the generation of a major band at the top of the gel and some smearing, and no discrete bands migrating between 21-mer pExoA fragment and the top of the gel were observed (**Figure 9**, lane 8). Proteinase K treatment, but not that of DNAse I and PARG, resulted in the complete loss of a major band, suggesting auto-ADP-ribosylation of atPARP2 (lane 9 versus lanes 10–11). Noteworthy, the PARG treatment resulted in a significant decrease of the top band and smearing, suggesting the presence of PARylated atPARP2 protein and free PAR polymer (lane 11). Taken together, these results strongly suggest that DNA fragments containing multiple closely spaced phosphorylated strand break termini are prone to covalent modifications by plant PARP proteins.

Previously, it has been demonstrated that mammalian PARPs can ADP-ribosylate with high efficiency long plasmid DNA fragments containing an SSB in close proximity to DSB termini (Zarkovic et al., 2018). To examine whether atPARP2 could ADP-ribosylate high-molecular-weight DNA fragments, we constructed a linear 2,934-bp plasmid-based DNA fragment containing a single nick 22 nt away from the 5′-[^{32}P]-labeled blunt-ended DSB (**Figure 10**). The 40-nM atPARP2 protein exhibited robust ADP-ribosylation of the 5′-phosphorylated 22-mer fragment which positioned between nick and DSB end (lane 6), suggesting that the DNA ADP-ribosylation activity of *Arabidopsis* PARPs is not limited to short oligonucleotide duplexes, but extends to high-molecular-weight DNA structures. Taken together, these data showed that plant PARPs have broad DNA substrate specificities similar to that of mammalian counterparts, although atPARP2 has more efficient DNA ADP-ribosylation activity as compared with that of atPARP1.

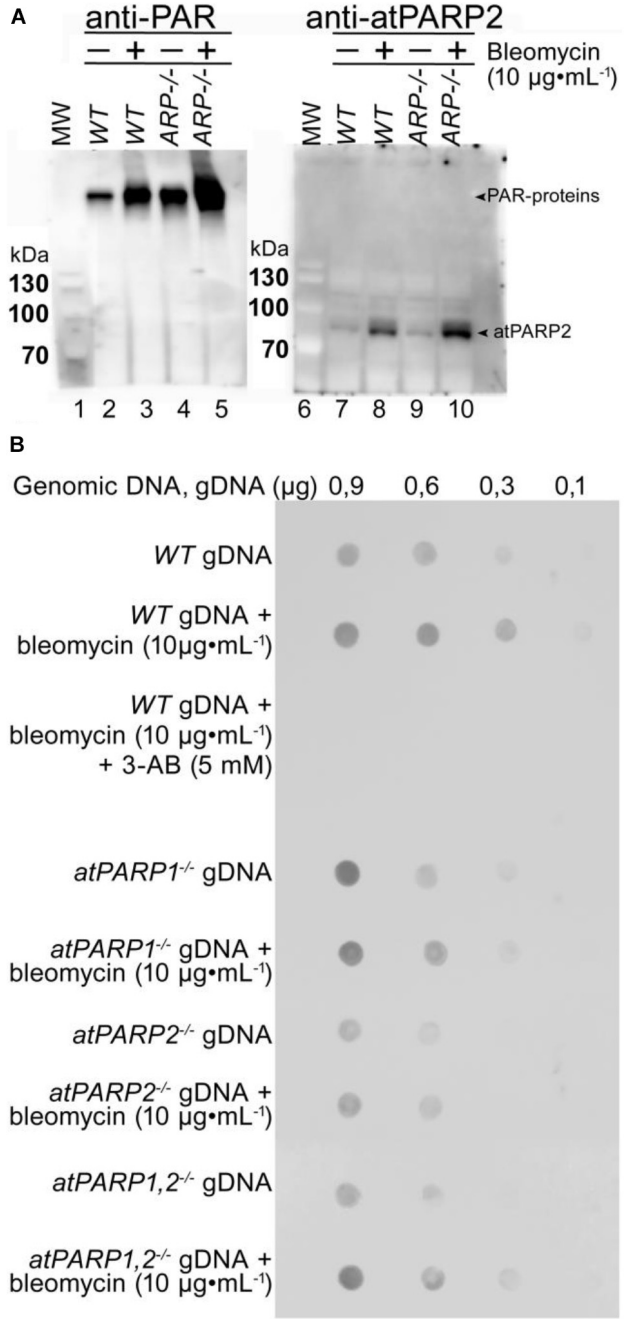

FIGURE 11 | Detection of ADP-ribosylation in plant cells. **(A)** Western blot analysis of protein ADP-ribosylation in WT and mutant plant extracts. Wild-type Col-0 and AP endonuclease-deficient *ARP*$^{-/-}$ mutant seeds were grown on MS agar medium. Two-week-old *Arabidopsis* plants were transferred to 10 µg•ml^{-1} of bleomycin for 18 h. Total proteins were extracted from whole plants, separated by SDS-PAGE, and analyzed by immunoblotting using anti-PAR and anti-atPARP2 antibodies. Arrows indicate PARylated proteins and atPARP2 protein. **(B)** Detection of PAR–DNA adducts in gDNA extracted from 14-day-old seedlings grown under either normal conditions or genotoxic stress. Different quantities of gDNA in TE buffer (10 mM Tris-Cl pH 8.0, 1 mM EDTA) were spotted onto a nylon membrane, followed by mouse monoclonal anti-poly(ADP-ribose) antibody 10H dot blotting. For more details, see section "Materials and Methods."

Search for PAR–DNA Adducts in Plant Genomic DNA After a Genotoxic Treatment

To measure ADP-ribosylation *in vivo*, cell-free extracts and cellular DNA from *Arabidopsis* were analyzed by immunoblotting using the homemade polyclonal rabbit antibodies against atPARP2 and commercial anti-PAR monoclonal antibody. The *Arabidopsis* PARPs were activated by plant exposure to bleomycin (10 µg•ml^{-1}). To measure protein ADP-ribosylation, soluble cell-free extracts form *A. thaliana WT* and *arp*$^{-/-}$ (AP endonuclease-deficient) mutant were separated on SDS-PAGE gel, and then Western blotted using anti-PAR and anti-atPARP2 antibodies (**Figure 11A**). Anti-PAR antibody detected a weak PARylation activity in non-treated WT plants, which strongly increased after exposure of the plants to bleomycin (lanes 1 and 2, respectively), suggesting that DNA strand breaks induced by bleomycin activate PARP-catalyzed ADP-ribosylation. Noteworthy, the level of PARylation in non-treated *arp*$^{-/-}$ mutant plants (lane 3) was significantly higher as compared with *WT* (lane 1), suggesting the accumulation of unrepaired DNA strand breaks in the absence of major plant AP endonuclease and activation of the DNA damage signaling pathway. As expected, the exposure to bleomycin of the *arp*$^{-/-}$ mutant leads to a significantly higher level of PARylation (lane 4) as compared with both control non-treated *arp*$^{-/-}$ plants (lane 3) and even treated *WT* plants (lane 2), suggesting that ARP participates in the repair of bleomycin-induced DNA strand breaks. Western blot using anti-atPARP2 antibodies showed bleomycin-induced overexpression of the atPARP2 protein in *WT* and *arp*$^{-/-}$ mutant plants (lanes 8 and 10) as compared with non-treated controls (lanes 7 and 9). Again, the overexpression of atPARP2 in response to DNA damage was significantly higher in *arp*$^{-/-}$ mutant plants as compared with *WT* ones (lane 10 versus 8). Overall, these results suggest that in the response to DNA damage, plants activate protein ADP-ribosylation and overexpress the atPARP2 protein.

To examine a putative DNA ADP-ribosylation activity in living cells, gDNA were isolated from *WT* and *atPARP*-deficient plants treated or not with bleomycin and examined for the presence of PAR. The gDNA were repeatedly purified, including extensive RNAse A and proteinase K treatments followed by phenol/chloroform extraction, and then analyzed by the dot blotting technique using the mouse anti-PAR monoclonal antibody and the rabbit monoclonal anti-pan-ADP-ribose binding reagent (MABE1016). Immunodot blot analysis of 0.9 and 0.6 µg of the gDNA isolated from control non-treated *WT*, *atPARP1*$^{-/-}$, *atPARP2*$^{-/-}$, and double mutant *atPARP1*$^{-/-}$ *atPARP2*$^{-/-}$ revealed the presence of PAR in all samples (**Figure 11B** and **Supplementary Figure S5**). The gDNA purified from bleomycin-treated plants showed increased presence of PAR, as compared with non-treated controls. Nevertheless, the presence of gDNA-associated PAR in control non-treated *WT* and *atPARPs*$^{-/-}$ mutant plant suggest two possibilities: (i) contamination of the purified gDNA with PARylated peptides that are tightly bound or cross-linked to DNA and highly resistant to proteinase K treatments or with

free ADP-ribose oligomers which may exist in non-covalent intertwined complexes with gDNA and (ii) cross-reactivity or non-specific recognition of some DNA structures present in plant gDNA by monoclonal anti-PAR antibodies. Taken together, these results demonstrate that the PAR-specific antibodies, although good to detect PARylated proteins, have very limited use to detect covalent PAR–DNA adducts because they are not able to specifically recognize DNA nucleotide linked to ADP-ribose. Thus, new types of antibodies are required to detect ADP-ribosylated DNA in living cells that can recognize both ADP-ribose and DNA nucleotide with high specificity.

DISCUSSION

In the present work, by using *in vitro* approaches, we demonstrated that plant *A. thaliana* poly(ADP-ribose) polymerases atPARP1 and atPARP2, similar to their mammalian counterparts, ADP-ribosylate DNA strand break termini harboring terminal phosphate residues. Particularly, atPARP1, like human PARP1, preferentially PARylates recessed DNA duplex and exhibits the following order of preference: Rec > Nick > Gap duplexes. On the other hand, atPARP2, like mammalian PARP2, PARylates Nick and Gap duplexes more efficiently than recessed duplex and displays the following order of preference: Nick > Gap > Rec duplexes (**Figure 2**). Kinetics of DNA PARylation and optimal concentrations of NAD^+ and enzymes were determined (**Figure 3** and **Supplementary Figure S2**). We further substantiated the DNA substrate requirements for the efficient ADP-ribosylation of DNA strand breaks by plant PARPs (**Figure 4**). Noteworthy, contrary to mammalian enzymes, atPARP2 exhibited higher DNA PARylation activity, than atPARP1, on the majority of DNA substrates tested. Nevertheless, the atPARP1, but not atPARP2, was able to PARylate recessed DNA duplex containing short 15-mer oligonucleotide with 5′-terminal phosphate, suggesting that these plant enzymes have non-overlapping DNA substrate specificities. It should be stressed that the plant PARPs were particularly sensitive to the distance that separate DSB and SSB (presented in the form of nick, gap, or ssDNA tail) in a DNA duplex. For example, atPARP1 exhibited preference for DNA substrates containing two strand breaks separated by 1.5 turns of helix, whereas atPARP2 preferred the distance of 1 or 2 turns of helix (**Figure 4**). Thus, the presence of multiple closely spaced DNA strand breaks, their comparative positioning, and the nature of 5′ and 3′ termini in the DNA substrate are essential for the atPARP-catalyzed DNA ADP-ribosylation. Overall, except higher activity of atPARP2, the substrate specificities of plant atPARP1 and atPARP2 proteins were very similar to that of their mammalian counterparts PARP1 and PARP2, respectively.

The plant atPARPs share structural similarity with other PARP family members and contain a highly conserved catalytic triad "H-Y-E" in their ART domains. In this study, single substitution mutants—atPARP1^{E960K}, atPARP1^{E960Q}, and atPARP2^{E614K}—in which a highly conserved glutamic acid residue in the catalytic triad was replaced by lysine or glutamine, were characterized for DNA ADP-ribosylation activity. As expected, all plant mutant atPARPs, similar to the corresponding mammalian mutants, have greatly reduced DNA PARylation activities (**Figure 5**). Nevertheless, atPARP1^{E960Q} and atPARP2^{E614K} mutants exhibited from robust to very weak DNA MARylation activity, respectively. Thus, these results demonstrate that highly conserved glutamic acid residue in the catalytic triad of plant atPARPs is required for DNA PARylation activities and that the preparations of recombinant PARP proteins are not contaminated by some uncharacterized host ADP-ribose transferases.

Biochemical analysis of the structure and composition of PAR–DNA adducts generated by plant PARPs, using the following enzymes: PARG, CIP, SVPDE1, DNAse I and PRK, revealed that similar to their mammalian counterparts, atPARPs utilize the 5′-terminal DNA phosphates as acceptor residue to covalently attach the ADP-ribose unit to synthesize the PAR polymer (**Figure 6** and **Supplementary Figure S3**). We further substantiated the molecular mechanism of the plant atPARP-catalyzed DNA ADP-ribosylation by identifying the products of PAR–DNA degradation with human Nudix hydrolase, NUDT16. NUDT16 cleaves the PAR polymer attached to [^{32}P]-labeled oligonucleotide duplex and generates ribosylated DNA fragment, in which the terminal phosphate residue is protected from dephosphorylation by CIP (**Figure 7**). These results indicate that atPARPs transfer ADP-ribose unit to terminal DNA phosphate residue at the strand break termini to generate a phosphodiester bond between DNA 5′P and C1′ of ADP-ribose. The putative molecular structure of ADP-ribose–p-DNA adduct was further confirmed by MALDI-TOF MS analysis of the ADP-ribosylated DNA fragments (**Figure 8** and **Supplementary Figure S4**). The mass spectra of the atPARP2 ADP-ribosylated p10•RT-A^{Nick} duplex oligonucleotide (S18) showed the presence of two new peaks corresponding to the 5′-phosphorylated 10-mers containing one and two ADP-ribose residues (**Figure 8B**). Thus, the mass spectrometry data and biochemical analysis demonstrate that the structure of the covalent PAR–DNA adducts generated by plant atPARPs is the same as that synthesized by mammalian PARP enzymes.

Depending on the structure of DNA, mammalian PARPs can switch their mode of action from auto-ADP-ribosylation to DNA ADP-ribosylation (Zarkovic et al., 2018; Matta et al., 2020). Here, we demonstrate that plant atPARP2 can acquire additional substrate specificity when acting on 5′-phosphorylated nicked DNA duplex (**Figure 9**). Contrary to human PARP3, atPARP2 did not completely switch from auto- to DNA ADP-ribosylation when acting on its preferred DNA substrate, but continue to act on both substrates: protein and DNA, with the preference for the former one. Under the experimental conditions used, the non-phosphorylated nicked DNA duplex activates atPARP2-catalyzed auto-ADP-ribosylation to a similar extent as the phosphorylated one. It is possible that a certain configuration of the phosphorylated strand break termini in a DNA substrate, not examined in this work, would enable more pronounced switch from auto- to DNA ADP-ribosylation in plant atPARP2. Importantly, similar to mammalian PARPs, the DNA ADP-ribosylation activity of plant atPARP2 is not limited to short duplex oligonucleotides, but is also efficient toward strand breaks within high-molecular-weight linear plasmid DNA (**Figure 10**),

suggesting that in plants, covalent modification of DNA may occur in chromosomal context.

We attempt to examine a possible biological role of atPARP-dependent DNA ADP-ribosylation by immunoblotting of the purified genomic DNA from plants to detect PAR–DNA adducts. The results revealed that two commercial monoclonal anti-PAR antibodies recognize gDNA isolated from both control non-treated and bleomycin-treated plants and also wild-type and PARP-deficient plants (**Figure 11** and **Supplementary Figure S5**), suggesting that the approach used in the present study lacks sufficient specificity to detect PAR–DNA adducts in gDNA. New more advanced tools are required to reliably distinguish the ADP-ribosylated DNA products from the ADP-ribosylated proteins and free PAR polymers in living cells.

Overall, the plant atPARP1 and atPARP2 contain less efficient DNA ADP-ribosylation activity as compared with their mammalian homologs PARP1 and PARP2. In addition, contrary to mammalian PARPs, atPARP2 is a major poly(ADP-ribose) polymerase in *Arabidopsis* and has higher activity than atPARP1. AtPARP-catalyzed DNA ADP-ribosylation strongly depends on the presence of closely spaced multiple DNA strand breaks, which are located within either 1.5 or 1.0 and 2.0 turns of helix. In summary, the finding that plant poly(ADP-ribose) polymerases can covalently modify the termini of DNA strand breaks by covalent attachment of PAR chains *in vitro* suggests that this property is universally conserved among eukaryotic PARPs and that in plants cellular DNA may undergo postreplicative modification in response to DNA damage.

DATA AVAILABILITY STATEMENT

The original contributions presented in the study are included in the article/**Supplementary Materials**, further inquiries can be directed to the corresponding author/s.

AUTHOR CONTRIBUTIONS

ST, AK, RG, YB, and AI performed all the biochemical experiments. ST and AK performed all the plant experiments. AI, MS, and AB designed all the experiments. CS-P and DG performed the mass spectrometry analysis. ST, AI, MS, and AB wrote the manuscript.

FUNDING

This work was supported by grants from the Committee of Science of the Ministry of Education and Science of the Republic of Kazakhstan: grant nos. AP05131478 to ST, and AP05131569 to AB, and from la Ligue Nationale Française Contre le Cancer « Equipe LNCC 2016 » (https://www.ligue-cancer.net) and Electricité de France RB 2020-02 (http://www.edf.fr) to MS, from the French National Research Agency (grant ANR-18-CE44-0008) and Fondation ARC (PJA-20181208015) to AI, from the French National Research Agency (grant ANR-18-CE44-0008-03), Labex ARCANE and CBH-EUR-GS (ANR-17-EURE-0003) to DG, from Oak Ridge Associated Universities (ORAU) grant 091019CRP2111, national grant AP08053387 from The Ministry of Education & Science of the Republic of Kazakhstan to YB, ST, and YB were supported by Postdoctoral fellowship from Al-Farabi Kazakh National University and by Doctoral fellowship from Nazarbayev University, respectively.

ACKNOWLEDGMENTS

We are grateful to Dr. Sylvia de Pater (Leiden University, Netherlands) for providing *Arabidopsis thaliana* atPARP-deficient mutants.

SUPPLEMENTARY MATERIAL

The Supplementary Material for this article can be found online at: https://www.frontiersin.org/articles/10.3389/fcell.2020.606596/full#supplementary-material

REFERENCES

Ahlfors, R., Lang, S., Overmyer, K., Jaspers, P., Brosche, M., Tauriainen, A., et al. (2004). *Arabidopsis* radical-induced cell death1 belongs to the wwe protein-protein interaction domain protein family and modulates abscisic acid, ethylene, and methyl jasmonate responses. *Plant Cell* 16, 1925–1937. doi: 10.1105/tpc.021832

Aravind, L., and Koonin, E. V. (2000). Sap - a putative DNA-binding motif involved in chromosomal organization. *Trends Biochem. Sci.* 25, 112–114. doi: 10.1016/s0968-0004(99)01537-6

Babiychuk, E., Cottrill, P. B., Storozhenko, S., Fuangthong, M., Chen, Y., O'farrell, M. K., et al. (1998). Higher plants possess two structurally different poly(adp-ribose) polymerases. *Plant J.* 15, 635–645. doi: 10.1046/j.1365-313x.1998.00240.x

Balasubramanian, B., Pogozelski, W. K., and Tullius, T. D. (1998). DNA strand breaking by the hydroxyl radical is governed by the accessible surface areas of the hydrogen atoms of the DNA backbone. *Proc. Natl. Acad. Sci. U.S.A.* 95, 9738–9743. doi: 10.1073/pnas.95.17.9738

Belles-Boix, E., Babiychuk, E., Van Montagu, M., Inze, D., and Kushnir, S. (2000). Ceo1, a new protein from *Arabidopsis thaliana*, protects yeast against oxidative damage. *FEBS Lett.* 482, 19–24. doi: 10.1016/s0014-5793(00)02016-0

Belousova, E. A., Ishchenko, A. A., and Lavrik, O. I (2018). Dna is a new target of parp3. *Sci. Rep.* 8:4176. doi: 10.1038/s41598-018-22673-3

Boltz, K. A., Jasti, M., Townley, J. M., and Shippen, D. E. (2014). Analysis of poly(adp-ribose) polymerases in *Arabidopsis* telomere biology. *PLoS One* 9:e88872. doi: 10.1371/journal.pone.0088872

Cadet, J., and Wagner, J. R. (2013). DNA base damage by reactive oxygen species, oxidizing agents, and uv radiation. *Cold Spring Harb. Perspect. Biol.* 5:a012559. doi: 10.1101/cshperspect.a012559

Chen, C., Masi, R., Lintermann, R., and Wirthmueller, L. (2018). Nuclear import of *Arabidopsis* poly(adp-ribose) polymerase 2 is mediated by importin-alpha and a nuclear localization sequence located between the predicted sap domains. *Front. Plant Sci.* 9:1581. doi: 10.3389/fpls.2018.01581

Chen, Y. M., Shall, S., and O'farrell, M. (1994). Poly(adp-ribose) polymerase in plant nuclei. *Eur. J. Biochem.* 224, 135–142. doi: 10.1111/j.1432-1033.1994.tb20004.x

Citarelli, M., Teotia, S., and Lamb, R. S. (2010). Evolutionary history of the poly(adp-ribose) polymerase gene family in eukaryotes. *BMC Evol. Biol.* 10:308. doi: 10.1186/1471-2148-10-308

De Murcia, G., and Menissier De Murcia, J. (1994). Poly(adp-ribose) polymerase: a molecular nick-sensor. *Trends Biochem. Sci.* 19, 172–176. doi: 10.1016/0968-0004(94)90280-1

Doucet-Chabeaud, G., Godon, C., Brutesco, C., De Murcia, G., and Kazmaier, M. (2001). Ionising radiation induces the expression of parp-1 and parp-2 genes in *Arabidopsis*. *Mol. Genet. Genomics* 265, 954–963. doi: 10.1007/s004380100506

Eustermann, S., Wu, W. F., Langelier, M. F., Yang, J. C., Easton, L. E., Riccio, A. A., et al. (2015). Structural basis of detection and signaling of DNA single-strand breaks by human parp-1. *Mol. Cell.* 60, 742–754. doi: 10.1016/j.molcel.2015.10.032

Feng, B., Liu, C., De Oliveira, M. V., Intorne, A. C., Li, B., Babilonia, K., et al. (2015). Protein poly(adp-ribosyl)ation regulates *Arabidopsis* immune gene expression and defense responses. *PLoS Genet.* 11:e1004936. doi: 10.1371/journal.pgen.1004936

Friedberg, E. C., Walker, G. C., Siede, W., Wood, R. D., Schultz, R. A., and Ellenberger, T. (2006). *DNA Repair and Mutagenesis*. Washington, DC: ASM Press.

Gu, Z., Pan, W., Chen, W., Lian, Q., Wu, Q., Lv, Z., et al. (2019). New perspectives on the plant parp family: *Arabidopsis* parp3 is inactive, and parp1 exhibits predominant poly (adp-ribose) polymerase activity in response to DNA damage. *BMC Plant Biol.* 19:364. doi: 10.1186/s12870-019-1958-9

Hassa, P. O., and Hottiger, M. O. (2008). The diverse biological roles of mammalian parps, a small but powerful family of poly-adp-ribose polymerases. *Front. Biosci.* 13, 3046–3082. doi: 10.2741/2909

Hottiger, M. O., Hassa, P. O., Luscher, B., Schuler, H., and Koch-Nolte, F. (2010). Toward a unified nomenclature for mammalian adp-ribosyltransferases. *Trends Biochem. Sci.* 35, 208–219. doi: 10.1016/j.tibs.2009.12.003

Jaspers, P., Blomster, T., Brosche, M., Salojarvi, J., Ahlfors, R., Vainonen, J. P., et al. (2009). Unequally redundant rcd1 and sro1 mediate stress and developmental responses and interact with transcription factors. *Plant J.* 60, 268–279. doi: 10.1111/j.1365-313X.2009.03951.x

Jaspers, P., Overmyer, K., Wrzaczek, M., Vainonen, J. P., Blomster, T., Salojarvi, J., et al. (2010). The rst and parp-like domain containing sro protein family: analysis of protein structure, function and conservation in land plants. *BMC Genomics* 11:170. doi: 10.1186/1471-2164-11-170

Jia, Q., Den Dulk-Ras, A., Shen, H., Hooykaas, P. J., and De Pater, S. (2013). Poly(adp-ribose)polymerases are involved in microhomology mediated back-up non-homologous end joining in *Arabidopsis thaliana*. *Plant Mol. Biol.* 82, 339–351. doi: 10.1007/s11103-013-0065-9

Kim, M. Y., Zhang, T., and Kraus, W. L. (2005). Poly(adp-ribosyl)ation by parp-1: 'Par-laying' nad+ into a nuclear signal. *Genes Dev.* 19, 1951–1967. doi: 10.1101/gad.1331805

Klemm, T., Mannuss, A., Kobbe, D., Knoll, A., Trapp, O., Dorn, A., et al. (2017). The DNA translocase rad5a acts independently of the other main DNA repair pathways, and requires both its atpase and ring domain for activity in *Arabidopsis thaliana*. *Plant J.* 91, 725–740. doi: 10.1111/tpj.13602

Lamb, R. S., Citarelli, M., and Teotia, S. (2012). Functions of the poly(adp-ribose) polymerase superfamily in plants. *Cell Mol. Life Sci.* 69, 175–189. doi: 10.1007/s00018-011-0793-4

Lepiniec, L., Babiychuk, E., Kushnir, S., Van Montagu, M., and Inze, D. (1995). Characterization of an *Arabidopsis thaliana* cdna homologue to animal poly(adp-ribose) polymerase. *FEBS Lett.* 364, 103–108. doi: 10.1016/0014-5793(95)00335-7

Liu, C., Wu, Q., Liu, W., Gu, Z., Wang, W., Xu, P., et al. (2017). Poly(adp-ribose) polymerases regulate cell division and development in *Arabidopsis* roots. *J. Integr. Plant Biol.* 59, 459–474. doi: 10.1111/jipb.12530

Marsischky, G. T., Wilson, B. A., and Collier, R. J. (1995). Role of glutamic acid 988 of human poly-adp-ribose polymerase in polymer formation. Evidence for active site similarities to the adp-ribosylating toxins. *J. Biol. Chem.* 270, 3247–3254. doi: 10.1074/jbc.270.7.3247

Matta, E., Kiribayeva, A., Khassenov, B., Matkarimov, B. T., and Ishchenko, A. A. (2020). Insight into DNA substrate specificity of parp1-catalysed DNA poly(adp-ribosyl)ation. *Sci. Rep.* 10:3699. doi: 10.1038/s41598-020-60631-0

Mildvan, A. S., Xia, Z., Azurmendi, H. F., Saraswat, V., Legler, P. M., Massiah, M. A., et al. (2005). Structures and mechanisms of nudix hydrolases. *Arch. Biochem. Biophys.* 433, 129–143. doi: 10.1016/j.abb.2004.08.017

Munnur, D., and Ahel, I. (2017). Reversible mono-adp-ribosylation of DNA breaks. *FEBS J.* 284, 4002–4016. doi: 10.1111/febs.14297

Nordhoff, E., Kirpekar, F., and Roepstorff, P. (1996). Mass spectrometry of nucleic acids. *Mass Spectrom. Rev.* 15, 67–138. doi: 10.1002/(sici)1098-2787(1996)15:2<67::aid-mas1>3.0.co;2-8

Palazzo, L., Thomas, B., Jemth, A. S., Colby, T., Leidecker, O., Feijs, K. L., et al. (2015). Processing of protein adp-ribosylation by nudix hydrolases. *Biochem. J.* 468, 293–301. doi: 10.1042/BJ20141554

Perina, D., Mikoc, A., Ahel, J., Cetkovic, H., Zaja, R., and Ahel, I. (2014). Distribution of protein poly(adp-ribosyl)ation systems across all domains of life. *DNA Repair* 23, 4–16. doi: 10.1016/j.dnarep.2014.05.003

Pham, P. A., Wahl, V., Tohge, T., De Souza, L. R., Zhang, Y., Do, P. T., et al. (2015). Analysis of knockout mutants reveals non-redundant functions of poly(adp-ribose)polymerase isoforms in *Arabidopsis*. *Plant Mol. Biol.* 89, 319–338. doi: 10.1007/s11103-015-0363-5

Pommier, Y., Leo, E., Zhang, H., and Marchand, C. (2010). DNA topoisomerases and their poisoning by anticancer and antibacterial drugs. *Chem. Biol.* 17, 421–433. doi: 10.1016/j.chembiol.2010.04.012

Rissel, D., Heym, P. P., Thor, K., Brandt, W., Wessjohann, L. A., and Peiter, E. (2017). No silver bullet - canonical poly(adp-ribose) polymerases (parps) are no universal factors of abiotic and biotic stress resistance of *Arabidopsis thaliana*. *Front. Plant Sci.* 8:59. doi: 10.3389/fpls.2017.00059

Rissel, D., and Peiter, E. (2019). Poly(adp-ribose) polymerases in plants and their human counterparts: parallels and peculiarities. *Int. J. Mol. Sci.* 20:1638. doi: 10.3390/ijms20071638

Rolli, V., O'farrell, M., Menissier-De Murcia, J., and De Murcia, G. (1997). Random mutagenesis of the poly(adp-ribose) polymerase catalytic domain reveals amino acids involved in polymer branching. *Biochemistry* 36, 12147–12154. doi: 10.1021/bi971055p

Ruf, A., Rolli, V., De Murcia, G., and Schulz, G. E. (1998). The mechanism of the elongation and branching reaction of poly(adp-ribose) polymerase as derived from crystal structures and mutagenesis. *J. Mol. Biol.* 278, 57–65. doi: 10.1006/jmbi.1998.1673

Satoh, M. S., Poirier, G. G., and Lindahl, T. (1994). Dual function for poly(adp-ribose) synthesis in response to DNA strand breakage. *Biochemistry* 33, 7099–7106. doi: 10.1021/bi00189a012

Schreiber, V., Dantzer, F., Ame, J. C., and De Murcia, G. (2006). Poly(adp-ribose): novel functions for an old molecule. *Nat. Rev. Mol. Cell. Biol.* 7, 517–528. doi: 10.1038/nrm1963

Song, J., Keppler, B. D., Wise, R. R., and Bent, A. F. (2015). Parp2 is the predominant poly(adp-ribose) polymerase in *Arabidopsis* DNA damage and immune responses. *PLoS Genet.* 11:e1005200. doi: 10.1371/journal.pgen.1005200

Steffen, J. D., Brody, J. R., Armen, R. S., and Pascal, J. M. (2013). Structural implications for selective targeting of parps. *Front. Oncol.* 3:301. doi: 10.3389/fonc.2013.00301

Stolarek, M., Gruszka, D., Braszewska-Zalewska, A., and Maluszynski, M. (2015). Alleles of newly identified barley gene hvparp3 exhibit changes in efficiency of DNA repair. *DNA Repair* 28, 116–130. doi: 10.1016/j.dnarep.2015.02.018

Talhaoui, I., Lebedeva, N. A., Zarkovic, G., Saint-Pierre, C., Kutuzov, M. M., Sukhanova, M. V., et al. (2016). Poly(adp-ribose) polymerases covalently modify strand break termini in DNA fragments in vitro. *Nucleic Acids Res.* 44, 9279–9295. doi: 10.1093/nar/gkw675

Tanaka, Y., Yoshihara, K., Itaya, A., Kamiya, T., and Koide, S. S. (1984). Mechanism of the inhibition of ca2+, mg2+-dependent endonuclease of bull seminal plasma induced by adp-ribosylation. *J. Biol. Chem.* 259, 6579–6585.

Teotia, S., and Lamb, R. S. (2009). The paralogous genes radical-induced cell death1 and similar to rcd one1 have partially redundant functions during *Arabidopsis* development. *Plant Physiol.* 151, 180–198. doi: 10.1104/pp.109.142786

Teotia, S., and Lamb, R. S. (2011). Rcd1 and sro1 are necessary to maintain meristematic fate in *Arabidopsis thaliana*. *J. Exp. Bot.* 62, 1271–1284. doi: 10.1093/jxb/erq363

Yuan, D., Lai, J., Xu, P., Zhang, S., Zhang, J., Li, C., et al. (2014). Atmms21 regulates DNA damage response and homologous recombination

repair in *Arabidopsis*. *DNA Repair* 21, 140–147. doi: 10.1016/j.dnarep.2014.04.006

Zarkovic, G., Belousova, E. A., Talhaoui, I., Saint-Pierre, C., Kutuzov, M. M., Matkarimov, B. T., et al. (2018). Characterization of DNA adp-ribosyltransferase activities of parp2 and parp3: new insights into DNA adp-ribosylation. *Nucleic Acids Res.* 46, 2417–2431. doi: 10.1093/nar/gkx1318

Zhang, H., Gu, Z., Wu, Q., Yang, L., Liu, C., Ma, H., et al. (2015). *Arabidopsis* parg1 is the key factor promoting cell survival among the enzymes regulating post-translational poly(adp-ribosyl)ation. *Sci. Rep.* 5:15892. doi: 10.1038/srep15892

Conflict of Interest: The authors declare that the research was conducted in the absence of any commercial or financial relationships that could be construed as a potential conflict of interest.

frontiers in Cell and Developmental Biology

ORIGINAL RESEARCH
published: 30 November 2020
doi: 10.3389/fcell.2020.595687

Lesion Recognition and Cleavage of Damage-Containing Quadruplexes and Bulged Structures by DNA Glycosylases

Alexandra A. Kuznetsova[1], Olga S. Fedorova[1,2]* and Nikita A. Kuznetsov[1,2]**

[1] *Institute of Chemical Biology and Fundamental Medicine of SB RAS, Novosibirsk, Russia,* [2] *Department of Natural Sciences, Novosibirsk State University, Novosibirsk, Russia*

Human telomeres as well as more than 40% of human genes near the promoter regions have been found to contain the sequence that may form a G-quadruplex structure. Other non-canonical DNA structures comprising bulges, hairpins, or bubbles may have a functionally important role during transcription, replication, or recombination. The guanine-rich regions of DNA are hotspots of oxidation that forms 7,8-dihydro-8-oxoguanine, thymine glycol, and abasic sites: the lesions that are handled by the base excision repair pathway. Nonetheless, the features of DNA repair processes in non-canonical DNA structures are still poorly understood. Therefore, in this work, a comparative analysis of the efficiency of the removal of a damaged nucleotide from various G-quadruplexes and bulged structures was performed using endonuclease VIII-like 1 (NEIL1), human 8-oxoguanine-DNA glycosylase (OGG1), endonuclease III (NTH1), and prokaryotic formamidopyrimidine-DNA glycosylase (Fpg), and endonuclease VIII (Nei). All the tested enzymes were able to cleave damage-containing bulged DNA structures, indicating their important role in the repair process when single-stranded DNA and intermediate non–B-form structures such as bubbles and bulges are formed. Nevertheless, our results suggest that the ability to cleave damaged quadruplexes is an intrinsic feature of members of the H2tH structural family, suggesting that these enzymes can participate in the modulation of processes controlled by the formation of quadruplex structures in genomic DNA.

Keywords: base excision repair, DNA glycosylase, G-quadruplex, DNA bulge, pre-steady-state kinetics, fluorescence

OPEN ACCESS

Edited by:
You-Wen He,
Duke University, United States

Reviewed by:
Istvan Boldogh,
University of Texas, United States
Lyudmila Rachek,
University of South Alabama, United States

****Correspondence:***
Alexandra A. Kuznetsova
sandra-k@niboch.nsc.ru
Olga S. Fedorova
fedorova@niboch.nsc.ru
Nikita A. Kuznetsov
nikita.kuznetsov@niboch.nsc.ru

Specialty section:
This article was submitted to Cell Death and Survival, a section of the journal Frontiers in Cell and Developmental Biology

Received: *17 August 2020*
Accepted: *10 November 2020*
Published: *30 November 2020*

Citation:
Kuznetsova AA, Fedorova OS and Kuznetsov NA (2020) Lesion Recognition and Cleavage of Damage-Containing Quadruplexes and Bulged Structures by DNA Glycosylases. Front. Cell Dev. Biol. 8:595687. doi: 10.3389/fcell.2020.595687

INTRODUCTION

Exogenous and endogenous agents such as very reactive cell metabolites, external environmental compounds, and ionizing or UV irradiation constantly damage cellular DNA. The main sources of endogenous damage to DNA are reactive oxygen species (ROS). The latter give rise to various DNA base lesions, including thymine glycol (Tg), 7,8-dihydro-8-oxoguanine (8-oxoguanine, oxoG), 4,6-diamino-5-formamidopyrimidine (Fapy-A), and 2,6-diamino-4-hydroxy-5-formamidopyrimidine (Fapy-G; Wallace, 2002; Evans et al., 2004). Damages to DNA bases can be mutagenic and when unrepaired may result in blockage of DNA polymerases, base mispairing, and finally genomic

instability (Wallace, 2002). The bulk of this endogenous burden is managed by base excision DNA repair (BER). The latter involves a few DNA *N*-glycosylases specific to the removal of a large spectrum of alkylated, oxidized, or deaminated bases, and sometimes normal mispaired bases; this process generates abasic (apurinic/apyrimidinic; AP) sites in DNA (Friedman and Stivers, 2010; Svilar et al., 2011).

Aside from the canonical duplex structure, DNA can populate a large variety of states, from four-stranded arrangements to single-stranded conformations. Guanine-rich nucleic acid molecules can fold into non-B form RNA or DNA structures called G-quadruplexes. These are secondary structures formed by four strands of certain G-rich sequences of nucleic acids. They are a consequence of stacking of multiple stable "G-quartets," i.e., planar arrangements of four guanines held together by Hoogsteen hydrogen bonds and additionally stabilized by monovalent cations (usually Na^+ or K^+; Sen and Gilbert, 1988, 1990). G-quadruplex topologies can be categorized into several types, such as parallel, antiparallel, and hybrid (Wang and Patel, 1993; Parkinson et al., 2002; Ambrus et al., 2006; Phan et al., 2006, 2007; Dai et al., 2007). Typically, the syn/anti-glycosidic conformation of guanines is regarded as a major factor for the folding of the G-quadruplex structure. There is specific nomenclature for G4 folds in the repeat sequence of the telomere, where the parallel fold is termed the propeller, and the antiparallel fold coordinately bound to potassium ions is termed the hybrid and can have two conformations (Xu, 2011). In the parallel folds, loops are double-strand reversals, and in antiparallel folds, loops are edgewise, diagonal, and/or double-strand reversals.

The structure and function of G-quadruplexes have aroused much interest. Recently, they were implicated in some human genetic neurodegenerative diseases (Haeusler et al., 2014; Brčić and Plavec, 2015). G-quadruplexes are thought to be also crucial for DNA replication (Besnard et al., 2012; Valton et al., 2014), telomere maintenance (Paeschke et al., 2005, 2008; Xu, 2011), genome rearrangements (Ribeyre et al., 2009; Lemmens et al., 2015), the DNA damage response (Rodriguez et al., 2012; Lopez et al., 2017), chromatin structure (Hänsel-Hertsch et al., 2016; Mao et al., 2018), RNA processing (Kwok et al., 2016), and transcriptional (Fernando et al., 2009; David et al., 2016), or translational regulation (Kumari et al., 2007; Kwok et al., 2015). Human telomeres consist of a 100–200 bp 3' single-stranded overhang with 5'-TTAGGG-3' repeats (McElligott and Wellinger, 1997).

It should be mentioned that the most important oxidative damaged bases in the 5'-TTAGGG-3' context are Tg and oxoG: the major oxidation products of DNA thymine and guanine, respectively. It is known that Tg is an effective block for DNA polymerases and consequently a lesion lethal to the cell, whereas oxoG is a premutagenic lesion causing a mispairing with adenine (Wallace, 2002; Fleming and Burrows, 2017).

It has been shown previously that guanine-to-8-oxoguanine (Vorlícková et al., 2012b) or guanine-to-adenine (Tomaško et al., 2009) substitutions and guanine abasic lesions (Školáková et al., 2010) in the telomeric quadruplex support a noticeable tendency: it is not the lesion type but the position of the modification that determines the impact on the stability and conformation of the quadruplex. It has been found that most sensitive sites are located in the middle tetrad. Owing to the preference of oxoG for the *syn* conformation, distinct responses have been registered when guanines were replaced with various glycosidic conformations. OxoG accommodation at sites that were originally in an *anti* or *syn* conformation in a unsubstituted telomeric G-quadruplex requires, respectively, a slight structural rearrangement or a large conformational shift (Bielskutė et al., 2019). Nonetheless, the resulting structures still conform to a hybrid-type topology and are stable at physiological temperatures.

Despite the important functions that G-quadruplexes perform in gene transcription and telomere biology, the features of initiation of base excision processes by DNA glycosylases in non-canonical structures, including quadruplexes, are still poorly understood. In humans, 11 DNA glycosylases have been identified that specialize in the recognition and removal of various damaged bases. A comparison of the known structures of DNA glycosylases has uncovered six structural families having common structural domains: HhH-GPD, H2tH, UDG, AAG, ALK, and T4 Endo V (Brooks et al., 2013).

There are a few biochemical works (Zhou et al., 2013, 2015; Makasheva et al., 2020) showing how DNA glycosylases of two structural families H2tH (NEIL1, NEIL2, and mNeil3) and HhH-GPD (OGG1 and NTH1) remove oxidized lesions from a telomeric quadruplex or DNA bubble structures. It was shown that only mNeil3 exerts an excision activity on Tg in a quadruplex DNA. Nonetheless, guanidinohydantoin, and spiroiminodihydantoin, which are further oxidation products of oxoG, in quadruplex DNA, are good substrates for both mNeil3 and NEIL1 (Zhou et al., 2013). It was revealed that none of the glycosylases has an activity toward quadruplex DNA containing oxoG. Of note, a recently published (Brázda et al., 2018) detailed analysis of amino acid composition of all the known human G-quadruplex–binding proteins revealed a conserved RG-rich domain as a common feature of human G-quadruplex–binding proteins. Unexpectedly, this motif was identified in human enzymes NEIL1–NEIL3, which belong to the H2tH structural family.

To further evaluate the ability of DNA glycosylases that belong to different structural families to hydrolyze the *N*-glycosidic bond of damaged bases in G-quadruplexes and bulged structures, in this work, we performed a comparative analysis of the efficiency of damage removal by human DNA glycosylases NEIL1, OGG1, and NTH1. As a control, two prokaryotic enzymes from the H2tH structural family were examined: formamidopyrimidine-DNA glycosylase (Fpg) and endonuclease VIII (Nei), which are responsible for the removal of oxoG and Tg, respectively. Direct registration of product formation by polyacrylamide gel electrophoresis (PAGE) helped us to estimate the effectiveness of enzymatic hydrolysis of damaged G-quadruplexes under the same experimental conditions. The recognition of a specific site in the substrate is accompanied by a conformational adjustment (of the enzyme and DNA) optimizing specific contacts in the enzyme–substrate complex; therefore, we performed a kinetic pre–steady-state analysis of conformational changes in enzymes and damaged quadruplexes during their interaction. Conformational real-time rearrangements of DNA

during the interaction with DNA glycosylases were visualized by detection of fluorescence reporters incorporated into DNA, e.g., the FAM/BHQ1 Förster resonance energy transfer (FRET) pair or a 2-aminopurine (aPu) residue on the 3' or 5' side of Tg or oxoG. aPu fluorescence intensity is sensitive to the microenvironment of this residue and enabled registering local conformational changes of a DNA substrate near the damaged nucleotide. On the other hand, the FAM/BHQ1-labeled damaged quadruplexes help to reveal "global" conformational changes that cause a change in the distance between the quencher and dye in the course of DNA substrate binding and cleavage.

MATERIALS AND METHODS

Oligodeoxyribonucleotides

Sequences of the Oligodeoxyribonucleotides (ODNs) used in this study are listed in **Table 1**. The ODNs were synthesized by the standard phosphoramidite method on an ASM-700 synthesizer (BIOSSET, Novosibirsk, Russia) from phosphoramidites purchased from Glen Research (Sterling, VA, United States). Synthetic oligonucleotides were unloaded from the solid support with ammonium hydroxide, according to manufacturer protocols. Deprotected oligonucleotides were purified by high-performance liquid chromatography. Concentrations of the ODNs were calculated from their absorbance at 260 nm. ODN duplexes were prepared by annealing modified and complementary strands at a 1:1 molar ratio.

Circular Dichroism Analysis

G-quadruplex folding was characterized by Circular dichroism (CD) spectroscopy using a JASCO spectrometer. The G-quadruplex samples were annealed at a 10 μM concentration in a buffer (50 mM Tris–HCl pH 7.5, 140 or 50 mM KCl, 1 mM EDTA) via heating of the samples at 90°C for 5 min followed by slow cooling down to room temperature. For each annealed G-quadruplex, CD analysis of each sample was performed by averaging of 16 CD scans at 25°C. Representative spectra of quadruplexes are shown in figures.

Enzyme Purification

The human OGG1 protein was purified as described previously (Kuznetsov et al., 2014). The purification of full-length human endonuclease VIII-like NEIL1 was performed as reported before (Katafuchi et al., 2004). Formamidopyrimidine-DNA glycosylase (Fpg) and endonuclease VIII (Nei) from *Escherichia coli* were purified in their native form without tags or other modifications according to (Kuznetsova et al., 2019) and (Kladova et al., 2019), respectively.

Wild-type human endonuclease III NTH1 was isolated from *E. coli* Rosetta 2 cells transformed with plasmid pET28c-NTH1. Cells of *E. coli* Rosetta 2 were grown in the Luria–Bertani (LB) medium (1 L) containing 50 μg/mL kanamycin at 37°C to an optical density of 0.6–0.7 at 600 nm. After that, the temperature was lowered to 20°C, and transcription was induced by the addition of isopropyl-β-D-thiogalactopyranoside to 0.2 mM. Next, the cells were incubated for 16 h and then centrifuged (10,000 × *g*, 10 min). A cell suspension was prepared in 30 mL of buffer I (20 mM HEPES-NaOH pH 7.8) containing 40 mM NaCl and a protease inhibitor cocktail (Complete, Germany). The cells were lysed by means of a Thermo French Pressure Cell Press. All the subsequent procedures were conducted at 4°C. The cell lysate was centrifuged (40,000 × *g*, 40 min), and NaCl in the supernatant was adjusted to 200 mM; then the supernatant loaded onto column I (Q-Sepharose Fast Flow, Amersham Biosciences, Sweden) with subsequent washing with buffer I (20 mM HEPES-NaOH pH 7.8) containing 200 mM NaCl. Fractions containing the protein were collected and loaded onto column II (HiTrap-Chelating™, Amersham Biosciences, Sweden) in buffer II (20 mM HEPES-NaOH pH 7.8, 500 mM NaCl, and 20 mM imidazole). Chromatography was performed in buffer II with a linear gradient of imidazole 20→500 mM. The solution's absorbance was detected at a wavelength of 280 nm. The protein purity was determined by gel electrophoresis. Fractions containing the NTH1 protein were dialyzed against a buffer (20 mM HEPES-NaOH pH 7.5, 1 mM EDÒÀ, 1 mM dithiothreitol, 250 mM NaCl, and 50% of glycerol) and stored at –20°C.

Concentrations of all the enzymes were determined via the absorbance at 280 nm and an appropriate extinction coefficient. The activity of various proteins was tested by means of their classic substrates and was checked just before use.

Microscale Thermophoresis Measurements

These measurements were carried out using Monolith NT.115 (NanoTemper Technologies). Monolith™ NT.115 Standard Treated Capillaries were used. Each point on the fluorescence titration curves was obtained by measurement of the fluorescence intensity of separate solutions (10 μl) containing an oligonucleotide ligand (0.5 μM) and an enzyme at the required concentration in binding buffer (50 mM Tris–HCl pH 7.5, 50 mM KCl, 1 mM EDTA, 1 mM DTT, and 7% of glycerol). The mixtures were incubated at 25°C for 10 min. All titration experiments were repeated at least twice.

Assays of Glycosylase Activity by PAGE

Single-turnover enzyme assays were performed in reaction buffer composed of 50 mM Tris–HCl pH 7.5, 50, or 140 mM KCl, 1.0 mM EDTA, 1.0 mM dithiothreitol, and 7% of glycerol (v/v). The reaction solution contained 2.0 μM enzyme and 1.0 μM DNA substrate. The reactions with damaged quadruplexes and duplexes were carried out at 25°C for 1 h or 5 min, respectively, and quenched by a gel-loading dye containing 7 M urea and 50 mM EDTA. Then, the reaction solutions were loaded on a 20% (w/v) polyacrylamide gel containing 7 M urea. The reactions with bulged substrates were carried out at 25°C for 5 min (Fpg and Nei) or 30 min (OGG1, NEIL1, and NTH1). The electrophoresis was run in 1 × TBE at 50 V/cm and 55°C. The gel was visualized using an E-Box CX.5 TS gel documentation system (Vilber Lourman, France). All the experiments were repeated at least twice. The degree of cleavage was calculated as the ratio of the peak area of the cleavage product to the sum of the peak areas of

TABLE 1 | Sequences of the ODNs, and structure of the modified residue[a].

Name	Sequence	Description
Q4	5′-TTAGGGTTAGGGTTAGGGTTAGGGTT-3′	Control undamaged G-quadruplex
Q4-Tg	5′-FAM-TTAGGGTTAGGGT(Tg)AGGGTTAGGGTT-BHQ1-3′	G-quadruplex with Tg at 14th position (loop region)
Q4-aPu-Tg	5′-TTAGGGTTAGGG(aPu)(Tg)AGGGTTAGGGTT-3′	G-quadruplex with Tg at 14th position and aPu located on 3′ or 5′ side of damage
Q4-Tg-aPu	5′-TTAGGGTTAGGGT(Tg)(aPu)GGGTTAGGGTT-3′	
Q4-oxoG	5′-FAM-TTAGGGTTAGGGTTAG(oxoG)GTTAGGGTT-BHQ1-3′	G-quadruplex with oxoG at 17th position (in middle of GGG)
Q4-aPu-oxoG	5′-TTAGGGTTAGGGTTA(aPu)(oxoG)GTTAGGGTT-3′	G-quadruplex with oxoG at 17th position and aPu located on 3′ or 5′ side of damage
Q4-oxoG-aPu	5′-TTAGGGTTAGGGTTAG(oxoG)(aPu)TTAGGGTT-3′	
Type I Tg/A	5′-FAM- GCTCA(Tg)GTACAGAGCTG-3′ 3′-BHQ1-CGAGT A CATGTCTCGAC-5′	Control duplex with Tg; FAM and BHQ1 are located on one side of duplex
Type II Tg/A	5′-FAM-GCTCA(Tg)GTACAGAGCTG-3′ 3′- CGAGT A CATGTCTCGAC-BHQ1-5′	Control duplex with Tg; FAM and BHQ1 are located on opposite sides of duplex
Type I oxoG/C	5′-FAM- GCTCA(oxoG)GTACAGAGCTG-3′ 3′-BHQ1-CGAGT C CATGTCTCGAC-5′	Control duplex with oxoG; FAM and BHQ1 are located on one side of duplex
Type II oxoG/C	5′-FAM-GCTCA(oxoG)GTACAGAGCTG-3′ 3′- CGAGT C CATGTCTCGAC-BHQ1-5′	Control duplex with oxoG; FAM and BHQ1 are located on opposite sides of duplex
C/G	5′-GCTCACGTACAGAGCTG-3′ 3′-CGAGTGCATGTCTCGAC-FAM-5′	Control duplex without damage
F/G	5′-GCTCA(F)GTACAGAGCTG-3′ 3′-CGAGT G CATGTCTCGAC-FAM-5′	Control duplex containing tetrahydrofuran (F) residue resembling abasic site, uncleavable by DNA glycosylases
X/G	5′-FAM-GCGCATACGGCAT**X**ATCAGGGAAGTGGG-BHQ1-3′ 3′- CGCGTATGCCGTA**G**TAGTCCCTTCACCC-5′	Duplexes, X = oxoG or Tg
X/-Δ1	5′-FAM-GCGCATACGGCAT**X**ATCAGGGAAGTGGG-BHQ1-3′ 3′- CGCGTATGCCGTA**-**TAGTCCCTTCACCC-5′	Bulge in damaged strand, X = oxoG or Tg
X/-Δ2(5′)	5′-FAM-GCGCATACGGCAT**X**ATCAGGGAAGTGGG-BHQ1-3′ 3′- CGCGTATGCCGT**–**TAGTCCCTTCACCC-5′	
X/-Δ2(3′)	5′-FAM-GCGCATACGGCAT**X**ATCAGGGAAGTGGG-BHQ1-3′ 3′- CGCGTATGCCGTA**–**AGTCCCTTCACCC-5′	
X/-Δ3	5′-FAM-GCGCATACGGCAT**X**ATCAGGGAAGTGGG-BHQ1-3′ 3′- CGCGTATGCCGT**—**AGTCCCTTCACCC-5′	
X/-Δ5	5′-FAM-GCGCATACGGCAT**X**ATCAGGGAAGTGGG-BHQ1-3′ 3′- CGCGTATGCCG**—–**GTCCCTTCACCC-5′	
X/+Δ3	5′-FAM-GCGCATACGGCAT**-X-**ATCAGGGAAGTGGG-BHQ1-3′ 3′- CGCGTATGCCGTA**GGG**TAGTCCCTTCACCC-5′	Bulge in undamaged strand, X = oxoG or Tg
X/+Δ4(5′)	5′-FAM-GCGCATACGGCAT**-X–**ATCAGGGAAGTGGG-BHQ1-3′ 3′- CGCGTATGCCGTA**GGGC**TAGTCCCTTCACCC-5′	
X/+Δ4(3′)	5′-FAM-GCGCATACGGCAT**-X–**ATCAGGGAAGTGGG-BHQ1-3′ 3′- CGCGTATGCCGTA**CGGG**TAGTCCCTTCACCC-5′	
X/+Δ5	5′-FAM-GCGCATACGGCAT**–X–**ATCAGGGAAGTGGG-BHQ1-3′ 3′- CGCGTATGCCGTA**CGGGC**TAGTCCCTTCACCC-5′	
X/+Δ7	5′-FAM-GCGCATACGGCAT**—X—**ATCAGGGAAGTGGG-BHQ1-3′ 3′- CGCGTATGCCGTA**CCGGGCC**TAGTCCCTTCACCC-5′	

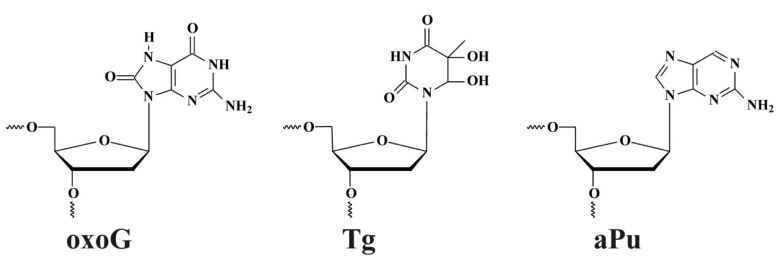

[a] *aPu is fluorescent base 2-aminopurine, BHQ1 is black hole quencher, FAM is 6-carboxyfluorescein, oxoG is 8-oxoguanine, and Tg is thymine glycol.*

the product and the initial substrate. Error in the evaluation of the degree of cleavage did not exceed 20% usually.

Stopped-Flow Experiments

We employed a SX20 stopped-flow spectrometer (Applied Photophysics Ltd., United Kingdom) equipped with a 150 W Xe arc lamp and an optical cell with 2 mm path length. The dead time of the instrument is 1.4 ms. The fluorescence of aPu was excited at λ_{ex} = 310 nm and monitored at λ_{em} > 370 nm as transmitted by filter WG-370 (Schott, Mainz, Germany). Fluorescence of a 6-carboxyfluorescein (FAM) residue was excited at λ_{ex} = 494 nm and monitored at λ_{em} > 515 nm as transmitted by filter OG-515 (Schott, Mainz, Germany). All experiments were carried out at 25°C in a buffer consisting of 50 mM Tris–HCl pH 7.5, 50, or 140 mM KCl, 1 mM EDTA, 1 mM DDT, and 7% of glycerol (v/v). The concentration of the enzyme in the reaction chamber after mixing in all experiments was 2.0 μM, and concentrations of a substrate were 1.0 μM. Typically, each trace shown is the average of four or more individual experiments; reported rate constants represent the mean (with standard deviation) of such datasets.

RESULTS AND DISCUSSION

Structural Analysis of Quadruplexes Containing oxoG and Tg by CD Spectroscopy

Structural features of undamaged telomeric G-quadruplexes are well known (Parkinson et al., 2002; Ambrus et al., 2006; Phan et al., 2007; Burra et al., 2019). There are three conformational topologies, namely, a parallel, antiparallel, and hybrid fold. To obtain structural insights, we analyzed the ODNs under study by CD spectroscopy, under several buffering conditions. The ODNs were folded in a buffer containing 140 mM KCl, in which undamaged Q4 folds into a hybrid quadruplex structure (**Figure 1A**; Ambrus et al., 2006). Because high salt concentration can disrupt ionic enzyme–DNA contacts, we also utilized a buffer with 50 mM KCl, which is typically used for DNA glycosylase assays (Tchou et al., 1994; Jiang et al., 1997; Radicella et al., 1997; Hazra et al., 2002). Additionally, incorporation of Tg or oxoG as the damaged nucleotide in the loop region or at the core, respectively, can destabilize the quadruplex structure (**Figure 1B**). Moreover, the use of an aPu residue as a fluorescent reporter also leads to a loss of two hydrogen bonds in the G-tetrad.

The CD spectrum of undamaged quadruplex Q4 in the buffer containing 140 mM KCl contains two pronounced maxima at 290 and 265 nm, supporting the hybrid-fold conformation (**Figure 2A**). Moreover, the CD spectrum profile of undamaged Q4 in the buffer with 50 mM KCl was very similar (data not shown), indicating that the changes of KCl concentration do not affect the G-quadruplex folding topology. Obtained CD spectra at both salt concentrations confirmed the hybrid-type structure, which appeared to be a stabler and thus predominant conformation of undamaged Q4 (Ambrus et al., 2006; Vorlíčková et al., 2012a).

It should be noted, that all quadruplexes containing Tg and aPu nucleotides in the loop region (**Figure 1A, Q4-Tg, Q4-aPu-Tg,** and **Q4**-Tg-aPu, respectively) yielded CD spectra similar to those of control undamaged Q4 (**Figure 2A**), indicating that these modifications of the loop region did not lead to a change of the hybrid-type folding.

In contrast, the ODN with oxoG in the middle position of GGG (Q4-oxoG) as well as ODNs additionally containing an aPu nucleotide on the 3' or 5' side of oxoG showed a drastic change in the CD spectra as compared with the native hybrid fold of undamaged Q4 (**Figure 2B**). Placement of the damage in the center of the GGG sequence gave a maximum peak at 263 nm and a minimum at 245 nm, which are typical of parallel G-quadruplex structures assumed by telomeric sequences under molecular-crowding conditions (Heddi and Phan, 2011). These data suggest that the oxoG modification of Q4 structure leads to obvious prevalence of a parallel conformation in the case of oxoG-containing substrates (Vorlíčková et al., 2005).

Cleavage of Quadruplexes Containing oxoG and Tg

The model random non-telomeric 17-nt duplexes containing specific damage, oxoG or Tg, were used to estimate the reference level of the glycosylase activity. As presented in **Figure 3A**, the cleavage of damaged nucleotides, oxoG or Tg, was performed by a specific DNA glycosylase. Nei, Fpg, and NEIL1 led to the formation of the reaction product corresponding to β,δ-elimination, whereas OGG1 and NTH1 generated the product corresponding only to β-elimination.

To measure the activity of DNA glycosylases toward quadruplex structures, Q4-oxoG, and Q4-Tg (**Figure 3B**) were used. The reaction mixture containing 2.0 μM enzyme and 1.0 μM DNA substrate was incubated at 25°C for 5 min or 1 h for duplex or quadruplex structures, respectively. The interaction of Fpg with Q4-oxoG led to the cleavage of the substrate at the oxoG position with ∼60% cleavage extent (**Figure 3C**). It should be noted that the interaction of OGG1 with Q4-oxoG did not cause substrate cleavage at all. The interaction of Nei with Q4-Tg resulted in the formation of both cleavage products corresponding to β-elimination and β,δ-elimination reactions with summarized efficiency of ∼25%. Nonetheless, the cleavage of Q4-Tg by NTH1 and NEIL1 was much less efficient and did not exceed 10% (**Figure 3C**).

Binding of Quadruplexes Containing oxoG and Tg

Because low efficiency of cleavage of damaged quadruplexes can be associated with insufficient complex formation under the experimental conditions, we performed the Microscale thermophoresis (MST) assay to evaluate the binding constant corresponding to the interaction between DNA glycosylases and the quadruplex substrates. The MST technique allows to quickly measure the strength of the interaction between two molecules in solution by detecting a variation in the fluorescence signal of a fluorescently labeled DNA in a free state and in the complex with an enzyme. Therefore, the low

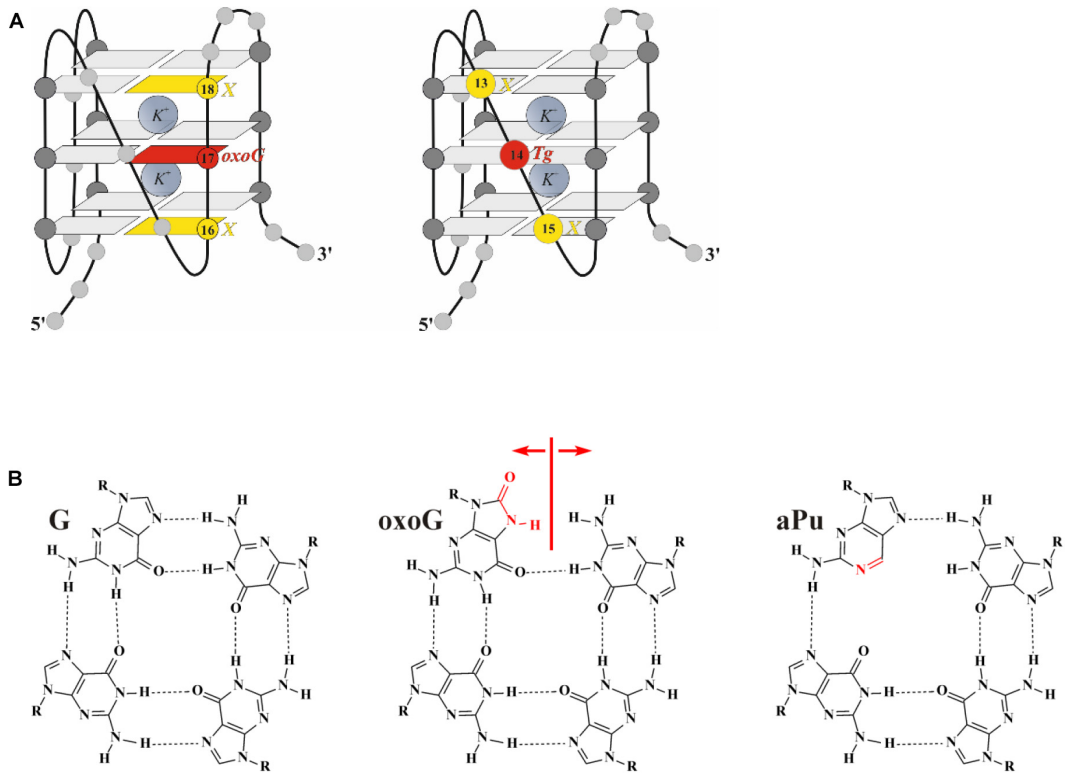

FIGURE 1 | (A) The hybrid type of quadruplex folding. **(B)** Chemical structures of guanine (G), 2-aminopurine (aPu), and 8-oxoguanine (oxoG) in a G-quartet context. Positions 14 and 17, highlighted in red, were chosen to incorporate damaged nucleotide Tg and oxoG, respectively; positions 13, 15, 16, and 18, highlighted in yellow, were chosen to incorporate fluorescent nucleotide X.

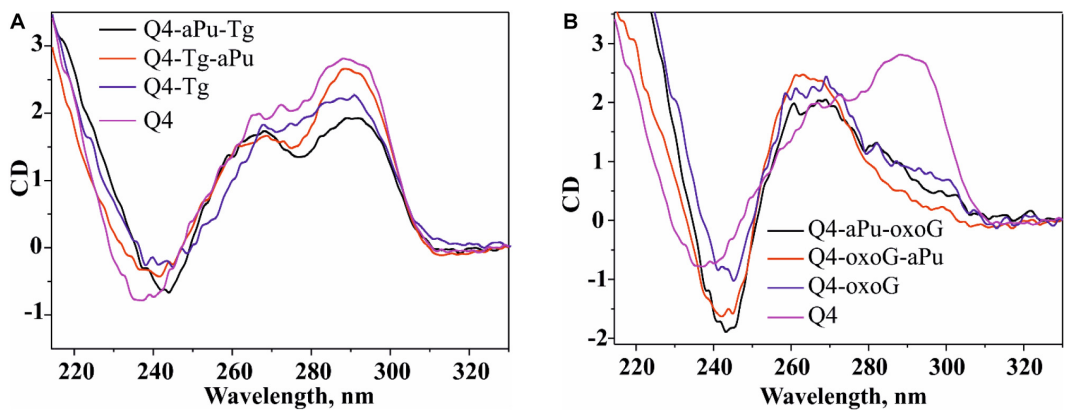

FIGURE 2 | The CD spectra of the G-quadruplex containing Tg **(A)** or oxoG **(B)**. Concentration of G-quadruplexes was 10 μM. CD spectra were recorded at 25°C in the following buffer: 50 mM Tris–HCl pH 7.5, 140 mM KCl, 1 mM EDTA. Representative spectra of quadruplexes are given.

efficiency of cleavage of quadruplex substrates during 1 h reaction time (**Figure 3B**) enabled us to carry out MST experiments without an influence of the DNA cleavage reaction. In the titration experiments (**Figure 4**), four types of DNA were tested: the control native duplex without damage (C/G), the control duplex containing an F-site (an uncleavable-by-DNA-glycosylases analog of an AP-site, F/G), the control G-quadruplex without damage (Q4), and G-quadruplexes with Tg or oxoG (Q4-Tg or Q4-oxoG). In some cases, the ratio of the signal to noise in the MST assay was not sufficient for precise calculation of dissociation constants K_d. Therefore, all the obtained values were used only as estimates of the ability of enzymes to bind these structures. The obtained data are summarized in **Table 2**.

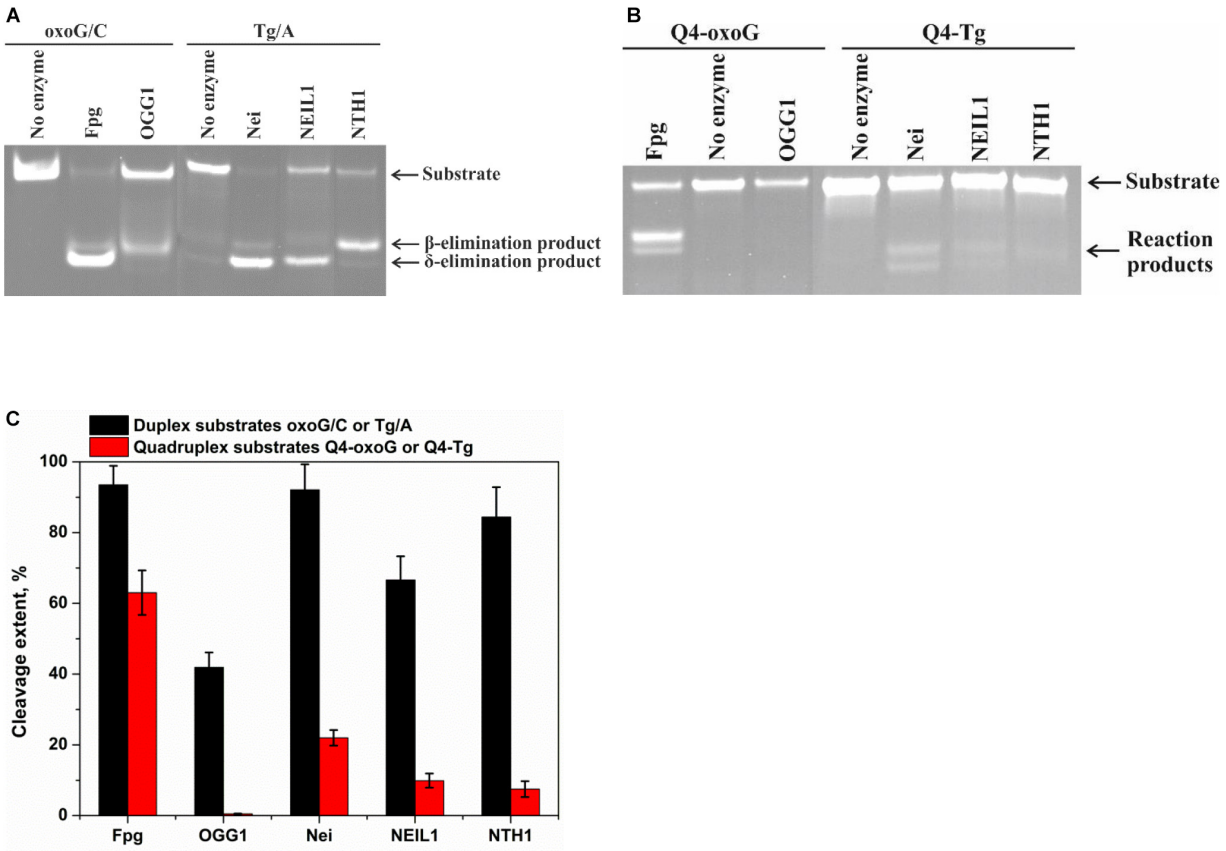

FIGURE 3 | PAGE analysis of glycosylase activities toward the lesion-containing 17-nt DNA duplexes oxoG/C and Tg/A **(A)** and quadruplex DNA Q4-oxoG and Q4-Tg **(B)**. Comparison of the efficiency of cleavage of the tested substrates by DNA glycosylases **(C)**. [Enzyme] = 2 μM, [DNA] = 1 μM, Ô = 25°C, and reaction time = 5 min for duplexes or 1 h for quadruplexes. Experiments were repeated twice. Representative gels are shown.

A comparison of dissociation constants K_d revealed good binding of DNA glycosylases to all the tested ODNs. Moreover, the values of constants were slightly dependent on both the structure of DNA and the presence of the lesion. These data indicate that the formation of even a non-specific complex between a DNA glycosylase and damaged DNA yielded sufficient changes of the signal in the MST assay. Nevertheless, the formation of such "primary" complexes was not enough to achieve a catalytic competent state with damaged quadruplexes. Indeed, similar DNA binding by different DNA glycosylases led to significantly different efficiency of cleavage of quadruplexes. Therefore, to further elucidate the features of DNA glycosylase interaction with Q4-DNA substrates, stopped-flow fluorescence measurements of real-time conformational transitions in substrates were conducted.

Conformational Rearrangements in the Course of Interaction of OGG1 or Fpg With oxoG-Substrates Forming Quadruplexes

It has been previously shown by pre–steady-state analyses that the recognition of a damaged nucleotide in a duplex substrate is accompanied by a conformational adjustment of the damaged DNA; this process optimizes specific contacts in the enzyme–substrate complex in the case of either Fpg (Kuznetsov et al., 2007b, 2011, 2012) or OGG1 (Kuznetsov et al., 2007a, 2014; Kuznetsova et al., 2014; Lukina et al., 2017). The results of the kinetic analysis clearly indicated that Fpg and OGG1 can control substrate specificity via a multi-stage mechanism of recognition of a specific site, accompanied by conformational changes both in the DNA substrate and in the enzyme. The kinetic scheme of oxoG recognition includes a primary non-specific encounter, initial destabilization of the DNA around the damaged nucleotide, emergence of a kink in the DNA, eversion of the oxoG base from the duplex into the active site of the enzyme, filling of the consequent void in the DNA duplex, and finally, fine tuning of the enzyme and DNA resulting in a catalytically active conformation.

The kinetic pre–steady-state analysis of conformational changes of oxoG-containing quadruplexes in the course of interaction with OGG1 or Fpg was performed. Real-time conformational rearrangements of quadruplexes during the interactions with the enzymes were visualized via the detection of fluorescence of fluorescence reporters incorporated into DNA, e.g., the FAM/BHQ1 FRET pair or the aPu residue placed on

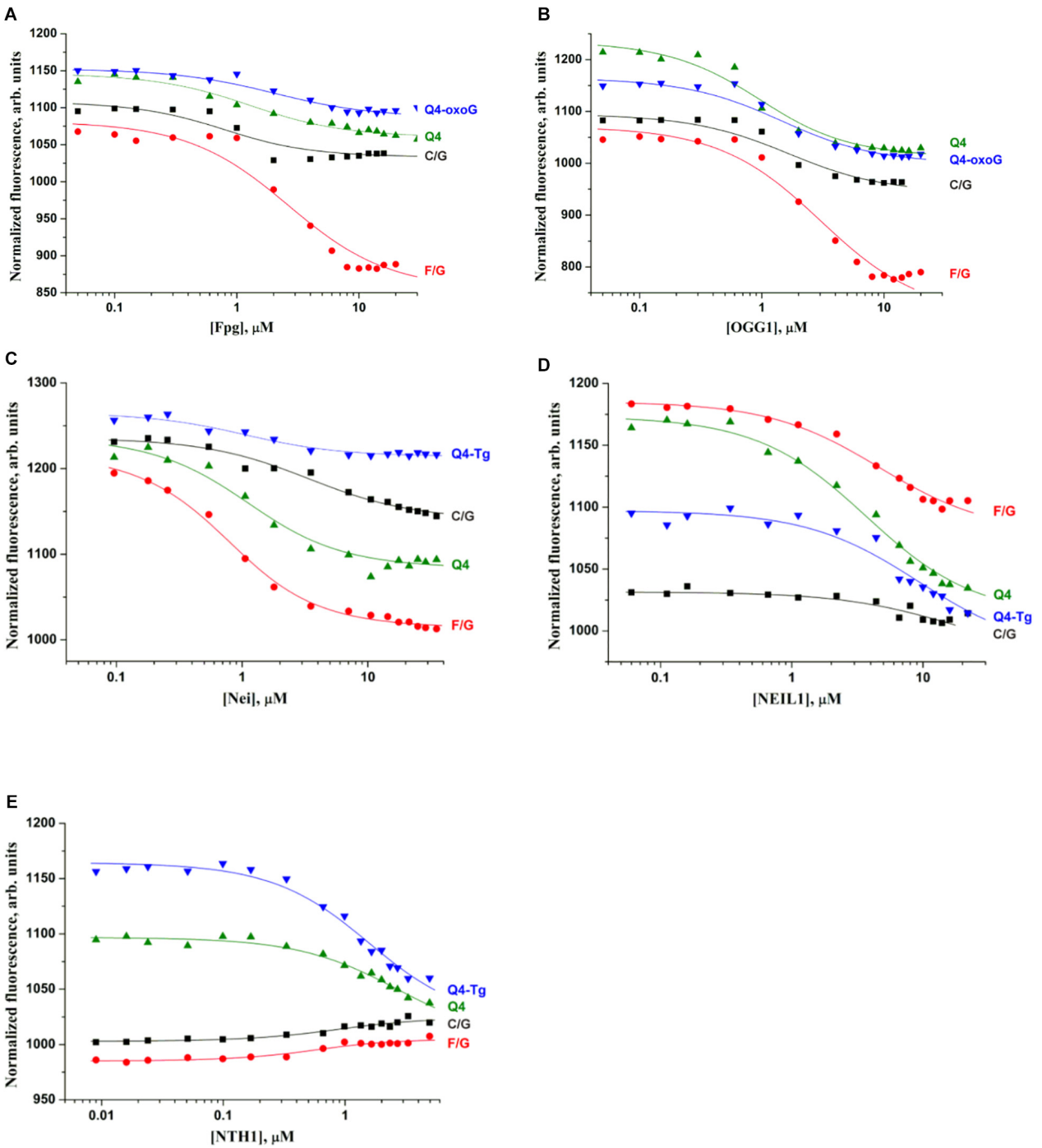

FIGURE 4 | Titration curves characterizing the interaction of Fpg **(A)**, OGG1 **(B)**, Nei **(C)**, NEIL1 **(D)**, and NTH1 **(E)** with a native duplex without damage (C/G), a duplex containing an F-site (F/G), an undamaged G-quadruplex (Q4), and G-quadruplexes with Tg or oxoG (Q4-Tg or Q4-oxoG). Concentration of DNA was 0.5 μM. Titration was performed in the following buffer: 50 mM Tris–HCl pH 7.5, 50 mM KCl, 1 mM EDTA, 1 mM DTT, and 7% of glycerol.

the 3' or 5' side of oxoG. The FRET-labeled duplex substrates containing an oxoG lesion served as the control of substrate-binding and cleavage processes. For this purpose, two types of FRET-labeled duplexes were designed: type I duplex substrates (**Figure 5A**) contained FAM and BHQ1 at the 5' ends of the ODNs; type II DNA substrates (**Figure 5B**) contained FAM at the 5' end and BHQ1 at the 3' end of the duplex-forming ODNs. The interaction of an enzyme with a model oxoG-containing DNA duplex (**Figures 6A,B**) led to DNA bending in the enzyme–substrate complex and thereby was accompanied by a decline

TABLE 2 | The values of the dissociation constant K_d (μM) measured by MST.

Enzyme	Type of DNA				
	C/G	F/G	Q4	Q4-oxoG	Q4-Tg
Fpg	1.6 ± 1.1	1.9 ± 0.7	1.0 ± 0.3	1.2 ± 0.4	–
OGG1	1.4 ± 0.5	2.8 ± 0.7	0.7 ± 0.2	1.2 ± 0.3	–
Nei	3.1 ± 0.7	0.5 ± 0.06	0.9 ± 0.2	–	0.8 ± 0.2
NEIL1	17 ± 15	4.4 ± 0.9	3.4 ± 0.5	–	9.1 ± 3.0
NTH1	0.7 ± 0.4	0.3 ± 0.2	2.5 ± 0.8	–	1.3 ± 0.3

in the FRET signal owing to shrinkage of the distance between FAM and quenching BHQ1 placed at the 5' ends of the duplex-forming oligonucleotides (type I duplex). The emergence of the increase in the FRET signal at the end of kinetic traces for both types of duplex denotes the catalytic reaction and product release resulting in the growth of the distance between FAM and BHQ1. Moreover, expectedly, the type II DNA substrate containing FRET labels at the same end of the DNA duplex showed a greater change in the amplitude of the FRET signal.

The interaction of Fpg with type II oxoG/C led to strong growth of FAM fluorescence up to second 100 (**Figure 6A**), whereas the interaction of Fpg with type I oxoG/C duplex caused a FAM fluorescence decrease up to second 5 and then a FAM fluorescence increase up to second 100. The same FAM fluorescence changes were observed for the interaction of OGG1 with either type of oxoG/C duplex (**Figure 6B**). Therefore, the analysis of kinetic curves obtained for DNA duplexes allowed to clearly associate the changes of the FRET signal with different steps of the interaction of the enzymes with the substrate.

The interaction of Fpg with Q4-oxoG led to a fast initial decrease in FAM fluorescence with a subsequent increase up to millisecond 100 and a decrease up to second 2, indicating that the quadruplex-binding process is consistent with more complicated molecular events than the binding of duplex substrates. The slow two-phase increase in the FRET signal in the time range > 2 s denotes slow cleavage of the quadruplex and dissociation of the product (**Figure 6A**). On the other hand, the interaction of OGG1 with Q4-oxoG had no effect on FAM fluorescence (**Figure 6B**), suggesting that the binding of OGG1 to the quadruplex does not cause any changes in the distance between FAM and BHQ1.

Additionally, we used oxoG-containing duplexes and quadruplexes with aPu located on the 3′ or 5′ side of a damaged nucleotide (**Figures 6C,D**). The intensity of emission by aPu is strongly affected by its environment; for instance, it is quenched partially when aPu is stacked (Rachofsky et al., 2001). Detection of aPu fluorescence intensity in the course of the interaction of each enzyme with a duplex substrate revealed an increase of the intensity in the initial portion of the kinetic trace. According to previous reports on Fpg and OGG1 (Kuznetsov et al., 2007a,b; Kuznetsova et al., 2014), in this time interval, the oxoG residue flips out of the double helix, thereby leaving a void in the DNA helix. The subsequent introduction of amino acid residues of the active site into this void caused a subsequent decrease in aPu fluorescence intensity. The catalytic steps and dissociation of the enzyme–product complex caused the second increase in aPu fluorescence intensity owing to the transfer of this aPu to a more hydrophilic environment.

The interaction of Fpg with Q4-aPu-oxoG or Q4-oxoG-aPu did not lead to significant changes of fluorescence intensity in the initial portion of the kinetic curve. Nevertheless, at the end of the kinetic curve, an increase in aPu fluorescence intensity was observed (**Figure 6C**), pointing to a shift of aPu into more hydrophilic surroundings, possibly owing to destabilization of the quadruplex structure after the cleavage by the enzyme. These data suggest that oxoG eversion and catalytic-complex formation in the case of a quadruplex substrate is the rate-limiting step of DNA cleavage by Fpg. In this case, detection of the catalytic complex via aPu fluorescence failed due to an insufficient concentration of this complex in the reaction mixture. The interaction of OGG1 with Q4-oxoG-aPu had no effect on aPu fluorescence intensity (**Figure 6D**), supporting the notion that the enzyme cannot form appropriate contacts with the substrate and induce eversion of the oxoG base. Nevertheless, in the course of the interaction of OGG1 with Q4-aPu-oxoG, an increase in aPu fluorescence intensity was recorded, which suggests that the enzyme induces conformational changes in the quadruplex, and there are attempts of local melting and eversion of the damaged nucleotide into the enzyme active site.

Therefore, our findings imply that OGG1 cannot recognize the oxoG base located in the core of a quadruplex structure, whereas Fpg manages to form specific contacts with oxoG and to catalyze base removal and DNA cleavage.

Kinetic Analysis of Interactions of Nei, NEIL1, or NTH1 With Each Tg-Containing Substrate Forming a Quadruplex

The same set of experiments was conducted with substrates containing Tg as a damaged nucleotide in the loop part of a quadruplex substrate. Two types of FRET-labeled Tg/A duplexes were used to assign the changes in the FRET signal to substrate-binding and catalysis steps. As depicted in **Figure 7A**, the interaction of Nei with type I Tg/A led to an increase in FAM fluorescence up to time point 300 s, whereas the interaction of Nei with type II Tg/A resulted in a fast FAM fluorescence decrease up to time point 0.1 s owing to the duplex bending and then to an increase of FAM fluorescence in the course of substrate cleavage. The same FAM fluorescence behavior was observed for the interaction of NEIL1 with either type of Tg/A duplex (**Figure 7B**). Of note, the interaction of NTH1

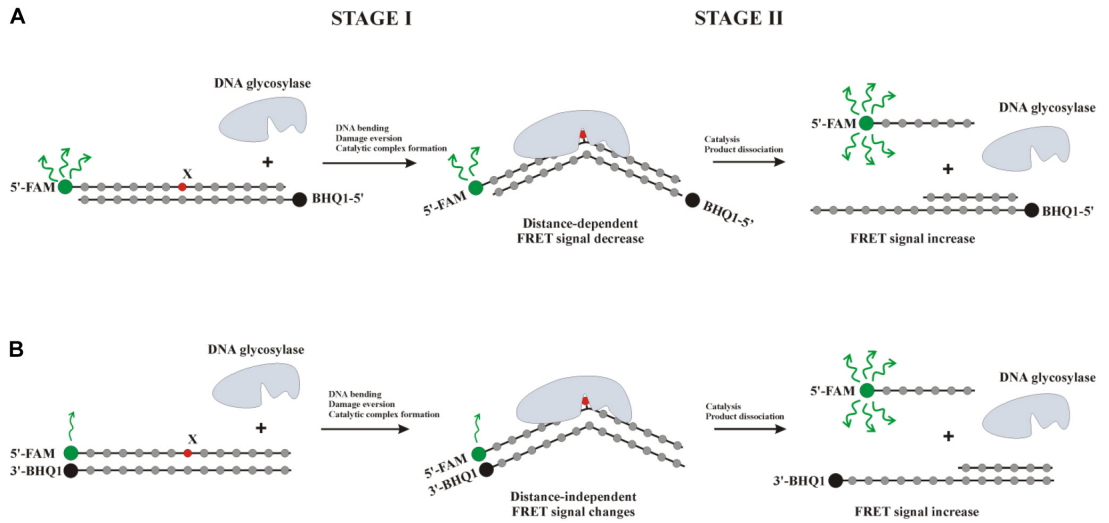

FIGURE 5 | Interaction of DNA glycosylases with a type I **(A)** or type II **(B)** FRET-labeled substrate. Stage 1: the formation of an enzyme–substrate complex, accompanied by DNA duplex bending and damaged-nucleotide eversion; stage 2: elimination of the damaged base and cleavage of the AP-site, thus leading to the release of a short oligonucleotide fragment and an increase in the distance between FAM (fluorophore) and BHQ1 (quencher) accompanied by a significant increase in the FRET signal.

with these substrates caused a decrease in FAM fluorescence followed by an increase even in the case of the type I duplex substrate (**Figure 7C**).

The interaction of Nei or NEIL1 with Q4-Tg led to a decrease of FAM fluorescence in the initial part of kinetic curves (300 ms and 7 s for Nei and NEIL1, respectively), revealing the formation of an enzyme–substrate complex in which FAM/BHQ1 residues became closer to each other. The subsequent increase in the FRET signal indicates slow cleavage of the G-quadruplex (**Figures 7A,B**). The interaction of NTH1 with Q4-Tg led to an initial decrease phase of FAM fluorescence up to second 100, suggesting that the rate of substrate binding and damage recognition by NTH1 is much slower than that of Nei and NEIL1 (**Figure 7C**).

The interaction of Nei, NEIL1, or NTH1 with Q4-aPu-Tg or Q4-Tg-aPu did not cause significant changes in aPu fluorescence for all the enzymes (**Figure 7D**) regardless of the ability to be cleaved by these enzymes. These data uncovered low sensitivity of aPu fluorescence—when this residue is located in the single-stranded loop region of the quadruplex—to the processes of substrate binding and DNA cleavage.

Cleavage of oxoG and Tg in the Bulged DNA Structures

To further elucidate the mechanism of damaged nucleotide recognition in non–B-form DNA structures by DNA glycosylases, we designed a set of oxoG- and Tg-containing DNA duplexes with bulging of a damaged or undamaged strand having a bulge size of 1 to 5 or 3 to 7 nucleotides, respectively, (**Figure 8**). We analyzed by PAGE the efficacy of cleavage of a set of damaged DNA substrates that could facilitate DNA bending and the base eversion from the substrate into an enzyme's active site.

The findings indicated that Fpg recognizes and removes oxoG from the oxoG/G pair with slightly lower efficiency as compared with the oxoG/C pair (**Figure 9A**, PAGE oxoG/C data are not shown). It is known that Fpg (Kuznetsov et al., 2007b) has opposite base specificity toward the oxoG/C pair as compared to oxoG/G, oxoG/T, and oxoG/A. It is noteworthy that the bulging of a single oxoG nucleotide (oxoG/-Δ1) or two nucleotides [oxoG/-Δ2(5')] also slightly decreased the efficiency of DNA cleavage in comparison with the oxoG/C substrate. On the other hand, the strongest effect on the Fpg activity (**Figure 9A**) was observed in the case of bulging of 2 nucleotides in oxoG/-Δ2(3'), which contains an oxoG near the 3' end of the duplex stem in the substrate, or 5 nucleotides (oxoG/-Δ5), which mimic single-stranded DNA. The bulge in the undamaged strand opposite oxoG reduced oxoG cleavage efficacy by approximately twofold regardless of the bulge size, suggesting that Fpg can place large nucleotide moieties outside the active site.

Of note, cleavage efficiency of OGG1 toward bulged DNA structures had features similar to those observed for Fpg (**Figure 9B**, PAGE oxoG/C data are not shown). Moreover, the two types of OGG1 activities, the cleavage of the *N*-glycosidic linkage and β-elimination, had similar profiles, indicating that recognition of oxoG limits the enzymatic activity. It was found that in the case of OGG1, just as the worst substrates—which contained the bulge of 2 [oxoG/-Δ2(3')] or 5 nucleotides (oxoG/-Δ5)—the mismatched oxoG/G duplex was also a very poor substrate in comparison with oxoG/C. The strong preferential excision of oxoG from the oxoG/C pair in comparison with the oxoG/G pair is associated with stabilization of the cytosine base by many hydrogen bonds

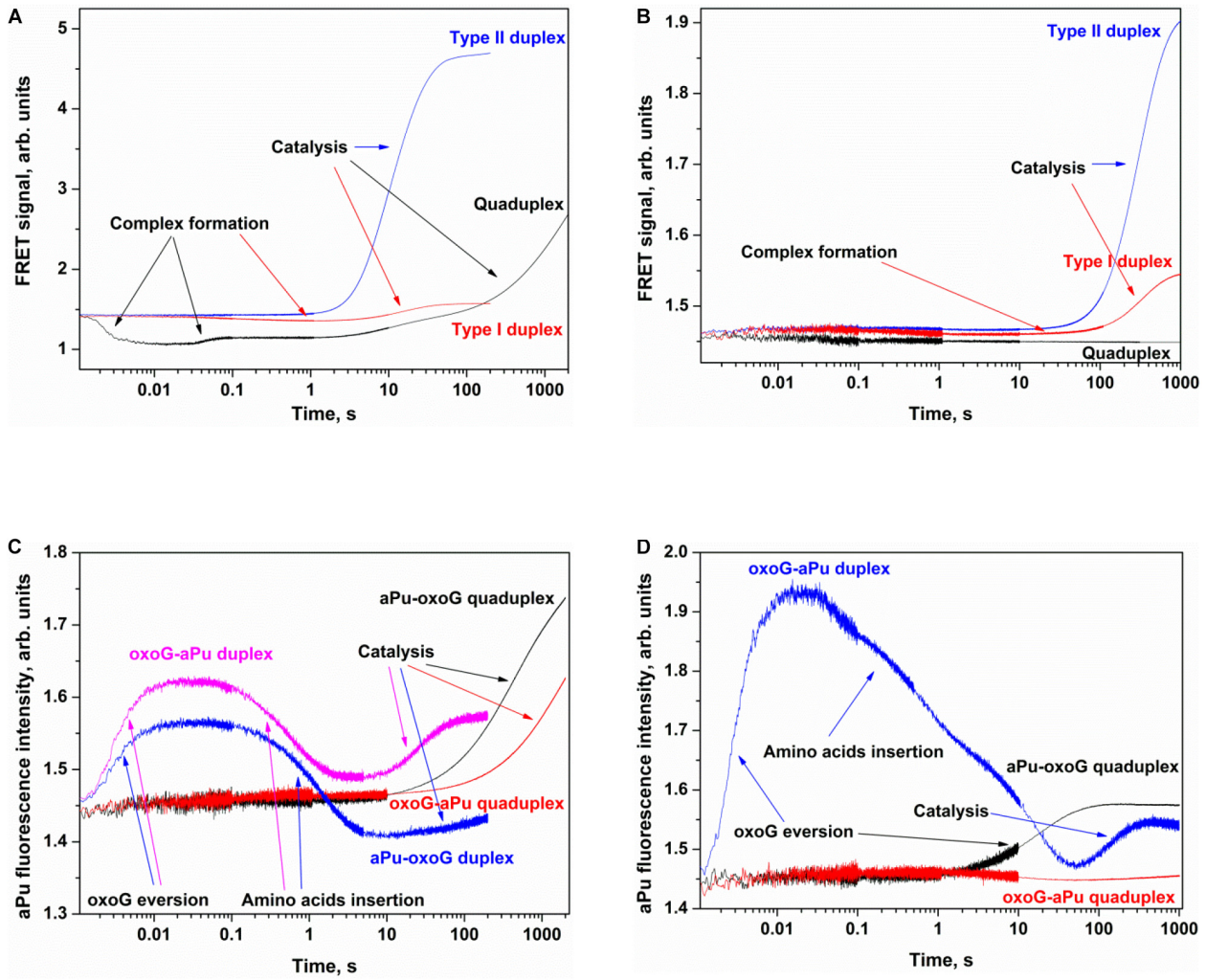

FIGURE 6 | Processing of oxoG-containing duplexes and quadruplexes by Fpg **(A,C)** or OGG1 **(B,D)** as detected by means of changes in a FRET signal **(A,B)** or aPu fluorescence intensity **(C,D)**. Concentration of DNA substrates = 1 μM, and concentration of enzymes = 2 μM.

with Arg-154, Asn-149, and Arg-204 and van der Waals bonding to Tyr-203 (Bruner et al., 2000). The common mechanism of the damaged-nucleotide recognition by OGG1 was analyzed in detail elsewhere (Kuznetsova et al., 2014) and includes the formation of an initial transient enzyme–substrate complex in which sequential conformational changes of the enzyme and substrate are strongly needed for the formation of a catalytically active complex. The molecular processes that take place during these rearrangements include substrate bending, local melting of the duplex, damaged-nucleotide eversion from the substrate and insertion into the enzyme active site, amino acid residue insertion, and the formation of a network of contacts. There was high activity of OGG1 toward DNA substrates containing a bulge in the undamaged strand, just as in some cases of a bulge in a damaged strand [oxoG/-Δ1, oxoG/-Δ2(5'), and oxoG/-Δ3]. This observation suggests that facilitation of some of these processes (for example, the eversion of the damaged nucleotide or the bending of the substrate) may contribute the catalytic-complex formation because of the features of the initial structure of the duplex with the bulge.

A comparison of the efficiency of cleavage of Tg-containing duplexes by Nei (**Figure 9C**) and most clearly by NEIL1 (**Figure 9D**) uncovered a slight dependence on the location of the Tg nucleotide and on the size of the bulge. Indeed, in the case of Nei, the bulging in the undamaged or damaged strand decreased the enzymatic activity to ∼50% in comparison with a Tg/G duplex only in the cases of maximal bulge size (Tg/+Δ7 and Tg/−Δ5, respectively). At the same time, NEIL1 can efficiently cleave DNA regardless of the structure of the substrate. By contrast, NTH1 (**Figure 9E**), which belongs to the HhH structural family, manifested a significant decrease in cleavage efficiency toward structures with a 2–5-nucleotide bulge in the damaged strand but was mostly active toward structures with the bulge in the undamaged strand.

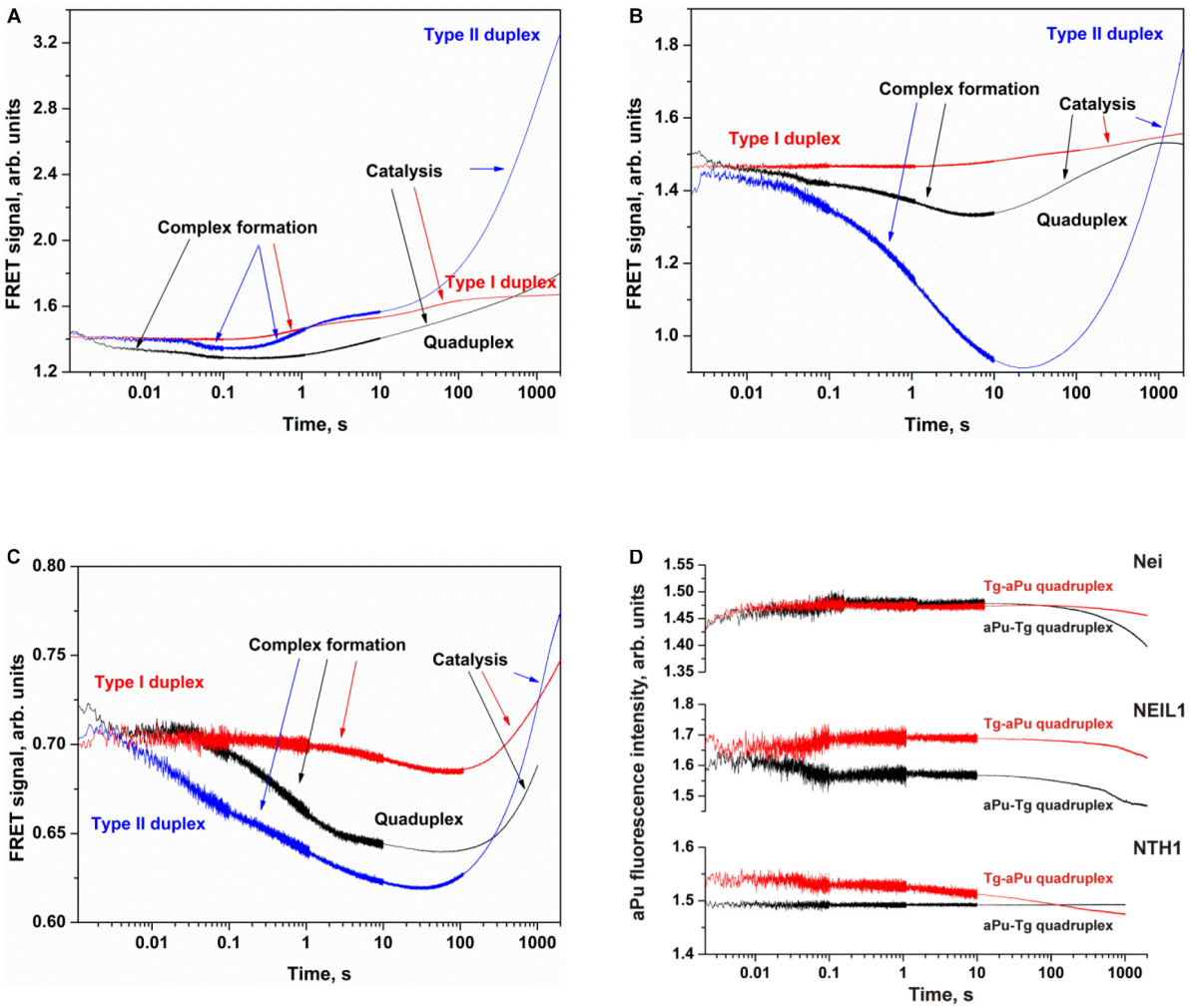

FIGURE 7 | Processing of Tg-containing duplexes and quadruplexes by Nei **(A)**, NEIL1 **(B)**, and NTH1 **(C)** as detected by means of changes in a FRET signal or aPu fluorescence intensity **(D)**. Concentration of DNA substrates = 1 μM, and concentration of enzymes = 2 μM.

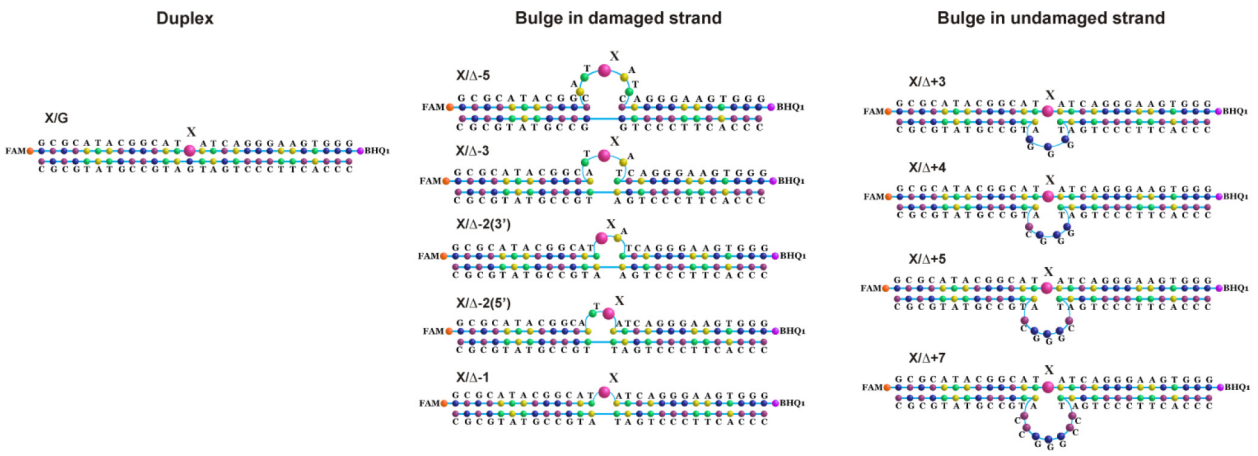

FIGURE 8 | Schematic structures of X-containing DNA duplexes (X = oxoG or Tg) with bulging of a damaged (1–5 nucleotides) or undamaged (3–7 nucleotides) strand.

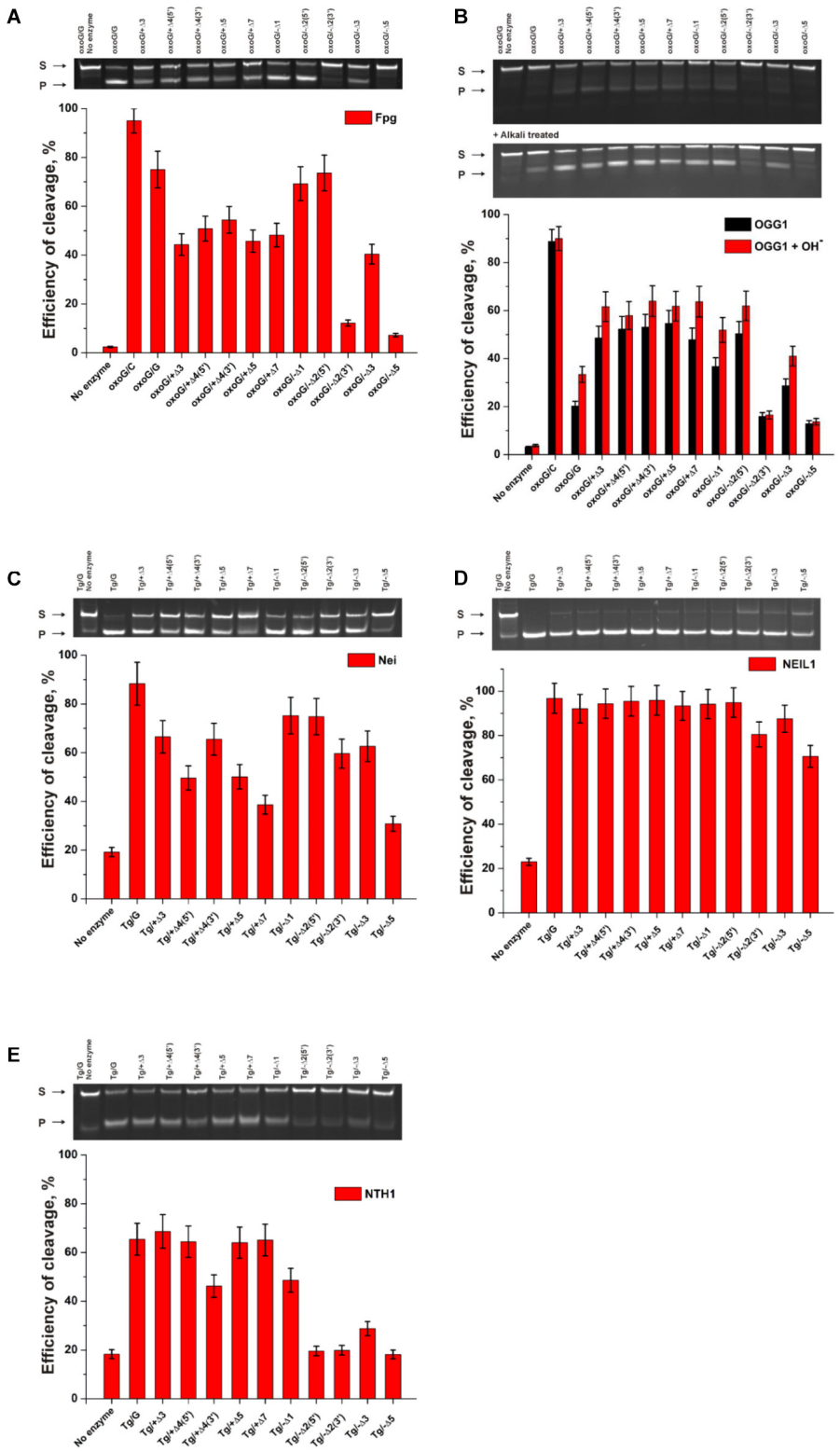

FIGURE 9 | The efficiency of cleavage of oxoG-containing bulged DNA structures [by Fpg **(A)** or OGG1 **(B)**] and of Tg-containing bulged DNA structures by Nei **(C)**, NEIL1 **(D)**, and NTH1 **(E)**. [Enzyme] = 2 μM, [DNA] = 1 μM, Ò = 25°C, and reaction time = 5 min for Fpg, Nei, and NEIL1 or 30 min for OGG1 and NTH1. Experiments were repeated twice. Representative gels are shown.

CONCLUSION

One of the most important problems in studies on DNA glycosylases is elucidation of the enzymatic mechanisms that ensure precise recognition of a damaged base and its effective removal from DNA. Many DNA glycosylases have been structurally characterized to understand how damaged DNA bases are found and detected among numerous unmodified bases (Brooks et al., 2013). To solve this problem, we have performed pre–steady-state kinetic analyses of conformational changes in DNA glycosylases and in DNA substrates during their interactions (Kuznetsov and Fedorova, 2016, 2020).

DNA glycosylases of different structural families form completely different contacts in the substrate-binding site and in the active pocket, and different amino acid residues participate in specific recognition of the damaged nucleotide and in catalysis. Nonetheless, almost all DNA glycosylases have common features of interaction with substrates. Structural studies show that all DNA glycosylases bend the DNA molecule and flip out the damaged nucleotide from the DNA duplex. Moreover, as a rule, the damaged nucleotide is placed in the pocket of the active site, in which it is finally verified via formation of specific contacts with a damaged base, and some amino acid residues of the enzymes are inserted into the DNA void formed after base eversion. The sequence of these stages leads to the formation of the catalytic complex, in which the damaged nucleotide is optimally located in the active site of the enzyme for interactions with catalytic amino acid residues.

Our data indicate that the capacity for catalytic-complex formation with a non–B-form substrate depends on the structural family of the tested DNA glycosylases. Indeed, all these DNA glycosylases were able to form a complex with quadruplex DNA as revealed by MST, but pre–steady-state fluorescent analysis showed that OGG1 cannot form appropriate contacts with a quadruplex to induce oxoG eversion. Another enzyme of the same HhH structural family, NTH1, also has a barely noticeable activity toward a quadruplex containing Tg. On the other hand, all members of the H2tH structural family, i.e., Fpg, Nei, and NEIL1, can recognize a known cognate damaged nucleotide whether it is located in the loop or at the core of the quadruplex. From our findings about the bulged substrates, it can be concluded that DNA glycosylases OGG1 and NTH1 of the HhH structural family have much lower efficiency toward DNA substrates containing a bulge in the damaged strand. Nonetheless, some positions of a damaged nucleotide are poor substrates for members of both structural families, for example, the location near the 3' end of the duplex stem in X/-Δ2(3') substrates (X = oxoG or Tg), which contains a 2-nucleotide bulge, or the location in the 5-nucleotide bulge (X/-Δ5, X = oxoG or Tg), which mimics single-stranded DNA. It was found that NEIL1 can cleave Tg in all the tested bulged substrates as effectively as in the quadruplex. These results reveal that the biological function of this enzyme may be associated with the repair of non–B-form structures in DNA. Indeed, the ability of the tested enzymes to cleave damage-containing bulged DNA structures implies that these enzymes are important for the repair during transcription, replication, or recombination when single-stranded DNA and intermediate non–B-form structures, such as bubbles and bulges, can be formed. Nevertheless, our results suggest that the ability to cleave damaged quadruplexes is an intrinsic feature of members of the H2tH structural family, thus supporting the notion that these enzymes can participate in the modulation of processes controlled by the formation of quadruplex structures in genomic DNA.

DATA AVAILABILITY STATEMENT

The original contributions presented in the study are included in the article/supplementary material, further inquiries can be directed to the corresponding author/s.

AUTHOR CONTRIBUTIONS

AK conducted the experiments. NK conceived and designed the experiments. AK, NK, and OF analyzed the data. NK and OF contributed reagents, materials, and/or analytical tools. AK, NK, and OF wrote the manuscript. All authors contributed to the article and approved the submitted version.

FUNDING

This work was supported by the Russian Foundation for Basic Research (19-04-00012) and in part by budget financing for routine maintenance of the equipment used (project No. AAAA-A17-117020210022-4).

REFERENCES

Ambrus, A., Chen, D., Dai, J., Bialis, T., Jones, R. A., and Yang, D. (2006). Human telomeric sequence forms a hybrid-type intramolecular G-quadruplex structure with mixed parallel/antiparallel strands in potassium solution. *Nucl. Acids Res.* 34, 2723–2735. doi: 10.1093/nar/gkl348

Besnard, E., Babled, A., Lapasset, L., Milhavet, O., Parrinello, H., Dantec, C., et al. (2012). Unraveling cell type-specific and reprogrammable human replication origin signatures associated with G-quadruplex consensus motifs. *Nat. Struct. Mol. Biol.* 19, 837–844. doi: 10.1038/nsmb.2339

Bielskuteľ, S., Plavec, J., and Podbevšek, P. (2019). Impact of Oxidative Lesions on the Human Telomeric G-Quadruplex. *J. Am. Chem. Soc.* 141, 2594-2603. doi: 10.1021/jacs.8b12748

Brázda, V., Cerveò, J., Bartas, M., Mikysková, N., Coufal, J., and Pečinka, P. (2018). The amino acid composition of quadruplex binding proteins reveals a shared motif and predicts new potential quadruplex interactors. *Molecules* 23:2341. doi: 10.3390/molecules23092341

Brčić, J., and Plavec, J. (2015). Solution structure of a DNA quadruplex containing ALS and FTD related GGGGCC repeat stabilized by 8-bromodeoxyguanosine substitution. *Nucl. Acids Res.* 43, 8590–8600. doi: 10.1093/nar/gkv815

Brooks, S. C., Adhikary, S., Rubinson, E. H., and Eichman, B. F. (2013). Recent advances in the structural mechanisms of DNA glycosylases. *Biochim. Biophys. Acta* 1834, 247–271. doi: 10.1016/j.bbapap.2012.10.005

Bruner, S. D., Norman, D. P., and Verdine, G. L. (2000). Structural basis for recognition and repair of the endogenous mutagen 8-oxoguanine in DNA. *Nature* 403, 859–866. doi: 10.1038/35002510

Burra, S., Marasco, D., Malfatti, M. C., Antoniali, G., Virgilio, A., Esposito, V., et al. (2019). Human AP-endonuclease (Ape1) activity on telomeric G4 structures is modulated by acetylatable lysine residues in the N-terminal sequence. *DNA Repair* 73, 129–143. doi: 10.1016/j.dnarep.2018.11.010

Dai, J., Carver, M., Punchihewa, C., Jones, R. A., and Yang, D. (2007). Structure of the hybrid-2 type intramolecular human telomeric G-quadruplex in K+ solution: insights into structure polymorphism of the human telomeric sequence. *Nucl. Acids Res.* 35, 4927–4940. doi: 10.1093/nar/gkm522

David, A. P., Margarit, E., Domizi, P., Banchio, C., Armas, P., and Calcaterra, N. B. (2016). G-quadruplexes as novel cis-elements controlling transcription during embryonic development. *Nucl. Acids Res.* 44, 4163–4173. doi: 10.1093/nar/gkw011

Evans, M. D., Dizdaroglu, M., and Cooke, M. S. (2004). Oxidative DNA damage and disease: induction, repair and significance. *Mutat. Res.* 567, 1–61. doi: 10.1016/j.mrrev.2003.11.001

Fernando, H., Sewitz, S., Darot, J., Tavaré, S., Huppert, J. L., and Balasubramanian, S. (2009). Genome-wide analysis of a G-quadruplex-specific single-chain antibody that regulates gene expression. *Nucl. Acids Res.* 37, 6716–6722. doi: 10.1093/nar/gkp740

Fleming, A. M., and Burrows, C. J. (2017). Formation and processing of DNA damage substrates for the hNEIL enzymes. *Free Radic. Biol. Med.* 107, 35–52. doi: 10.1016/j.freeradbiomed.2016.11.030

Friedman, J. I., and Stivers, J. T. (2010). Detection of damaged DNA bases by DNA glycosylase enzymes. *Biochemistry* 49, 4957–4967. doi: 10.1021/bi100593a

Haeusler, A. R., Donnelly, C. J., Periz, G., Simko, E. A. J., Shaw, P. G., Kim, M. S., et al. (2014). C9orf72 nucleotide repeat structures initiate molecular cascades of disease. *Nature* 507:195. doi: 10.1038/nature13124

Hänsel-Hertsch, R., Beraldi, D., Lensing, S. V., Marsico, G., Zyner, K., Parry, A., et al. (2016). G-quadruplex structures mark human regulatory chromatin. *Nat. Genet.* 48, 1267–1272. doi: 10.1038/ng.3662

Hazra, T. K., Izumi, T., Boldogh, I., Imhoff, B., Kow, Y. W., Jaruga, P., et al. (2002). Identification and characterization of a human DNA glycosylase for repair of modified bases in oxidatively damaged DNA. *Proc. Natl. Acad. Sci. U.S.A.* 99, 3523–3528. doi: 10.1073/pnas.062053799

Heddi, B., and Phan, A. T. (2011). Structure of human telomeric DNA in crowded solution. *J. Am. Chem. Soc.* 133, 9824–9833. doi: 10.1021/ja200786q

Jiang, D., Hatahet, Z., Melamede, R. J., Kow, Y. W., and Wallace, S. S. (1997). Characterization of *Escherichia coli* endonuclease VIII. *J. Biol. Chem* 272, 32230–32239.

Katafuchi, A., Nakano, T., Masaoka, A., Terato, H., Iwai, S., Hanaoka, F., et al. (2004). Differential specificity of human and *Escherichia coli* endonuclease III and VIII homologues for oxidative base lesions. *J. Biol. Chem.* 279, 14464–14471. doi: 10.1074/jbc.M400393200

Kladova, O. A., Kuznetsov, N. A., and Fedorova, O. S. (2019). Thermodynamics of the DNA repair process by endonuclease VIII. *Acta Nat.* 11, 29–37. doi: 10.32607/20758251-2019-11-1-29-37

Kumari, S., Bugaut, A., Huppert, J. L., and Balasubramanian, S. (2007). An RNA G-quadruplex in the 5′ UTR of the NRAS proto-oncogene modulates translation. *Nat. Chem. Biol.* 3, 218–221. doi: 10.1038/nchembio864

Kuznetsov, N. A., and Fedorova, O. S. (2016). Thermodynamic analysis of fast stages of specific lesion recognition by DNA repair enzymes. *Biochemistry* 81, 1136–1152. doi: 10.1134/S0006297916100114

Kuznetsov, N. A., and Fedorova, O. S. (2020). Kinetic milestones of damage recognition by DNA glycosylases of the Helix-hairpin-Helix structural superfamily. *Adv. Exp. Biol. Med* 1241, 1-18.

Kuznetsov, N. A., Koval, V. V., Nevinsky, G. A., Douglas, K. T., Zharkov, D. O., and Fedorova, O. S. (2007a). Kinetic conformational analysis of human 8-oxoguanine-DNA glycosylase. *J. Biol. Chem.* 282, 1029–1038. doi: 10.1074/jbc.M605788200

Kuznetsov, N. A., Koval, V. V., Zharkov, D. O., Vorobjev, Y. N., Nevinsky, G. A., Douglas, K. T., et al. (2007b). Pre-steady-state kinetic study of substrate specificity of *Escherichia coli* formamidopyrimidine-DNA glycosylase. *Biochemistry* 46, 424–435. doi: 10.1021/bi060787r

Kuznetsov, N. A., Kuznetsova, A. A., Vorobjev, Y. N., Krasnoperov, L. N., and Fedorova, O. S. (2014). Thermodynamics of the DNA damage repair steps of human 8-oxoguanine DNA glycosylase. *PLoS One* 9:e98495. doi: 10.1371/journal.pone.0098495

Kuznetsov, N. A., Milov, A. D., Isaev, N. P., Vorobjev, Y. N., Koval, V. V., Dzuba, S. A., et al. (2011). PELDOR analysis of enzyme-induced structural changes in damaged DNA duplexes. *Mol. Biosyst.* 7, 2670–2680. doi: 10.1039/c1mb05189j

Kuznetsov, N. A., Vorobjev, Y. N., Krasnoperov, L. N., and Fedorova, O. S. (2012). Thermodynamics of the multi-stage DNA lesion recognition and repair by formamidopyrimidine-DNA glycosylase using pyrrolocytosine fluorescence–stopped-flow pre-steady-state kinetics. *Nucl. Acids Res.* 40, 7384–7392. doi: 10.1093/nar/gks423

Kuznetsova, A. A., Kladova, O. A., Barthes, N. P. F., Michel, B. Y., Burger, A., Fedorova, O. S., et al. (2019). Comparative Analysis of Nucleotide Fluorescent Analogs for Registration of DNA Conformational Changes Induced by Interaction with Formamidopyrimidine-DNA Glycosylase Fpg. *Russ. J. Bioorganic Chem.* 45, 591-598. doi: 10.1134/S1068162019060256

Kuznetsova, A. A., Kuznetsov, N. A., Ishchenko, A. A., Saparbaev, M. K., and Fedorova, O. S. (2014). Step-by-Step Mechanism of DNA Damage Recognition by Human 8-Oxoguanine DNA Glycosylase. *Biochim. Biophys. Acta* 1840, 387–395. doi: 10.1016/j.bbagen.2013.09.035

Kwok, C. K., Ding, Y., Shahid, S., Assmann, S. M., and Bevilacqua, P. C. (2015). A stable RNA G-quadruplex within the 5'-UTR of Arabidopsis thaliana ATR mRNA inhibits translation. *Biochem. J.* 467, 91–102. doi: 10.1042/BJ20141063

Kwok, C. K., Sahakyan, A. B., and Balasubramanian, S. (2016). Structural analysis using SHALiPE to reveal RNA G-quadruplex formation in human precursor MicroRNA. *Angew. Chem. Int. Ed.* 55, 8958-8961. doi: 10.1002/anie.201603562

Lemmens, B., Van Schendel, R., and Tijsterman, M. (2015). Mutagenic consequences of a single G-quadruplex demonstrate mitotic inheritance of DNA replication fork barriers. *Nat. Commun.* 6:8909. doi: 10.1038/ncomms9909

Lopez, C. R., Singh, S., Hambarde, S., Griffin, W. C., Gao, J., Chib, S., et al. (2017). Yeast Sub1 and human PC4 are G-quadruplex binding proteins that suppress genome instability at co-transcriptionally formed G4 DNA. *Nucl. Acids Res.* 45, 5850–5862. doi: 10.1093/nar/gkx201

Lukina, M. V., Kuznetsova, A. A., Kuznetsov, N. A., and Fedorova, O. S. (2017). The kinetic analysis of recognition of the damaged nucleotides by mutant forms of the 8-Oxoguanine DNA Glycosylase hOGG1. *Russ. J. Bioorg. Chem.* 43, 1–12. doi: 10.1134/S1068162017010058

Makasheva, K. A., Endutkin, A. V., and Zharkov, D. O. (2020). Requirements for dna bubble structure for efficient cleavage by helix-two-turn-helix dna glycosylases. *Mutagenesis* 35, 119-128. doi: 10.1093/mutage/gez047

Mao, S. Q., Ghanbarian, A. T., Spiegel, J., Martínez Cuesta, S., Beraldi, D., Di Antonio, M., et al. (2018). DNA G-quadruplex structures mold the DNA methylome. *Nat. Struct. Mol. Biol.* 25, 951–957. doi: 10.1038/s41594-018-0131-8

McElligott, R., and Wellinger, R. J. (1997). The terminal DNA structure of mammalian chromosomes. *EMBO J.* 16, 3705–3714. doi: 10.1093/emboj/16.12.3705

Paeschke, K., Juranek, S., Simonsson, T., Hempel, A., Rhodes, D., and Lipps, H. J. (2008). Telomerase recruitment by the telomere end binding protein-β facilitates G-quadruplex DNA unfolding in ciliates. *Nat. Struct. Mol. Biol.* 15, 598–604. doi: 10.1038/nsmb.1422

Paeschke, K., Simonsson, T., Postberg, J., Rhodes, D., and Lipps, H. J. (2005). Telomere end-binding proteins control the formation of G-quadruplex DNA structures in vivo. *Nat. Struct. Mol. Biol.* 12, 847–854. doi: 10.1038/nsmb982

Parkinson, G. N., Lee, M. P. H., and Neidle, S. (2002). Crystal structure of parallel quadruplexes from human telomeric DNA. *Nature* 417, 876–880. doi: 10.1038/nature755

Phan, A. T., Kuryavyi, V., Luu, K. N., and Patel, D. J. (2007). Structure of two intramolecular G-quadruplexes formed by natural human telomere sequences in K+ solution. *Nucl. Acids Res.* 35, 6517–6525. doi: 10.1093/nar/gkm706

Phan, A. T., Luu, K. N., and Patel, D. J. (2006). Different loop arrangements of intramolecular human telomeric (3+1) G-quadruplexes in K+ solution. *Nucl. Acids Res.* 34, 5715–5719. doi: 10.1093/nar/gkl726

Rachofsky, E. L., Osman, R., and Ross, J. B. A. (2001). Probing structure and dynamics of DNA with 2-aminopurine: effects of local environment on fluorescence. *Biochemistry* 40, 946–956. doi: 10.1021/bi001664o

Radicella, J. P., Dherin, C., Desmaze, C., Fox, M. S., and Boiteux, S. (1997). Cloning and characterization of hOGG1, a human homolog of the OGG1 gene of Saccharomyces cerevisiae. *Proc. Natl. Acad. Sci. U.S.A.* 94, 8010–8015. doi: 10.1073/pnas.94.15.8010

Ribeyre, C., Lopes, J., Boulé, J. B., Piazza, A., Guédin, A., Zakian, V. A., et al. (2009). The yeast Pif1 helicase prevents genomic instability caused by G-quadruplex-forming CEB1 sequences in vivo. *PLoS Genet.* 5:e1000475. doi: 10.1371/journal.pgen.1000475

Rodriguez, R., Miller, K. M., Forment, J. V., Bradshaw, C. R., Nikan, M., Britton, S., et al. (2012). Small-molecule-induced DNA damage identifies alternative DNA structures in human genes. *Nat. Chem. Biol.* 8, 301–310. doi: 10.1038/nchembio.780

Sen, D., and Gilbert, W. (1988). Formation of parallel four-stranded complexes by guanine-rich motifs in DNA and its implications for meiosis. *Nature* 334, 364-366. doi: 10.1038/334364a0

Sen, D., and Gilbert, W. (1990). A sodium-potassium switch in the formation of four-stranded G4-DNA. *Nature* 344, 410–414. doi: 10.1038/344410a0

Školáková, P., Bednáøová, K., Vorlíčková, M., and Sagi, J. (2010). Quadruplexes of human telomere dG3(TTAG3)3 sequences containing guanine abasic sites. *Biochem. Biophys. Res. Commun.* 399, 203–208. doi: 10.1016/j.bbrc.2010.07.055

Svilar, D., Goellner, E. M., Almeida, K. H., and Sobol, R. W. (2011). Base excision repair and lesion-dependent subpathways for repair of oxidative DNA damage. *Antioxidants Redox Signal.* 14, 2491–2507. doi: 10.1089/ars.2010.3466

Tchou, J., Bodepudi, V., Shibutani, S., Antoshechkin, I., Miller, J., Grollman, A. P., et al. (1994). Substrate specificity of Fpg protein. recognition and cleavage of oxidatively damaged DNA. *J. Biol. Chem.* 269, 15318–15324.

Tomaško, M., Vorlíčková, M., and Sagi, J. (2009). Substitution of adenine for guanine in the quadruplex-forming human telomere DNA sequence G3(T2AG3)3. *Biochimie* 91, 171-179. doi: 10.1016/j.biochi.2008.07.012

Valton, A. L., Hassan-Zadeh, V., Lema, I., Boggetto, N., Alberti, P., Saintomé, C., et al. (2014). G4 motifs affect origin positioning and efficiency in two vertebrate replicators. *EMBO J.* 33, 732-746. doi: 10.1002/embj.201387506

Vorlíčková, M., Chládková, J., Kejnovská, I., Fialová, M., and Kypr, J. (2005). Guanine tetraplex topology of human telomere DNA is governed by the number of (TTAGGG) repeats. *Nucl. Acids Res.* 33, 5851–5860. doi: 10.1093/nar/gki898

Vorlíčková, M., Kejnovská, I., Bednáøová, K., Renčiuk, D., and Kypr, J. (2012a). Circular dichroism spectroscopy of DNA: from duplexes to quadruplexes. *Chirality* 24, 691–698. doi: 10.1002/chir.22064

Vorlícková, M., Tomasko, M., Sagi, A. J., Bednarova, K., and Sagi, J. (2012b). 8-Oxoguanine in a quadruplex of the human telomere DNA sequence. *FEBS J.* 279, 29–39. doi: 10.1111/j.1742-4658.2011.08396.x

Wallace, S. S. (2002). Biological consequences of free radical-damaged DNA bases. *Free Radic. Biol. Med.* 33, 1–14. doi: 10.1016/s0891-5849(02)00827-4

Wang, Y., and Patel, D. J. (1993). Solution structure of the human telomeric repeat d[AG3(T2AG3)3] G-tetraplex. *Structure* 1, 263–282. doi: 10.1016/0969-2126(93)9001

Xu, Y. (2011). Chemistry in human telomere biology: structure, function and targeting of telomere DNA/RNA. *Chem. Soc. Rev.* 40, 2719–2740. doi: 10.1039/c0cs00134a

Zhou, J., Fleming, A. M., Averill, A. M., Burrows, C. J., and Wallace, S. S. (2015). The NEIL glycosylases remove oxidized guanine lesions from telomeric and promoter quadruplex DNA structures. *Nucl. Acids Res.* 43, 4039–4054. doi: 10.1093/nar/gkv252

Zhou, J., Liu, M., Fleming, A. M., Burrows, C. J., and Wallace, S. S. (2013). Neil3 and NEIL1 DNA glycosylases remove oxidative damages from quadruplex DNA and exhibit preferences for lesions in the telomeric sequence context. *J. Biol. Chem.* 288, 27263–27272. doi: 10.1074/jbc.M113.479055

Conflict of Interest: The authors declare that the research was conducted in the absence of any commercial or financial relationships that could be construed as a potential conflict of interest.

frontiers in Cell and Developmental Biology

REVIEW
published: 03 December 2020
doi: 10.3389/fcell.2020.598860

The Base Excision Repair Pathway in the Nematode *Caenorhabditis elegans*

*Noha Elsakrmy[1], Qiu-Mei Zhang-Akiyama[2] and Dindial Ramotar[1]**

[1] Division of Biological and Biomedical Sciences, College of Health and Life Sciences, Hamad Bin Khalifa University, Education City, Qatar, [2] Laboratory of Stress Response Biology, Graduate School of Science, Kyoto University, Kyoto, Japan

Exogenous and endogenous damage to the DNA is inevitable. Several DNA repair pathways including base excision, nucleotide excision, mismatch, homologous and non-homologous recombinations are conserved across all organisms to faithfully maintain the integrity of the genome. The base excision repair (BER) pathway functions to repair single-base DNA lesions and during the process creates the premutagenic apurinic/apyrimidinic (AP) sites. In this review, we discuss the components of the BER pathway in the nematode *Caenorhabditis elegans* and delineate the different phenotypes caused by the deletion or the knockdown of the respective DNA repair gene, as well as the implications. To date, two DNA glycosylases have been identified in *C. elegans*, the monofunctional uracil DNA glycosylase-1 (UNG-1) and the bifunctional endonuclease III-1 (NTH-1) with associated AP lyase activity. In addition, the animal possesses two AP endonucleases belonging to the exonuclease-3 and endonuclease IV families and in *C. elegans* these enzymes are called EXO-3 and APN-1, respectively. In mammalian cells, the DNA polymerase, Pol beta, that is required to reinsert the correct bases for DNA repair synthesis is not found in the genome of *C. elegans* and the evidence indicates that this role could be substituted by DNA polymerase theta (POLQ), which is known to perform a function in the microhomology-mediated end-joining pathway in human cells. The phenotypes observed by the *C. elegans* mutant strains of the BER pathway raised many challenging questions including the possibility that the DNA glycosylases may have broader functional roles, as discuss in this review.

Keywords: *C. elegans*, base excision repair pathway, DNA glycosylases and AP endonucleases, germ cells, survival, phenotypes, DNA damaging agents

OPEN ACCESS

Edited by:
Brian C. Schaefer, Uniformed Services University of the Health Sciences, United States

Reviewed by:
Murat Saparbaev, UMR 9019 Intégrité du Génome et Cancers, France
Robert W. Sobol, University of South Alabama Mitchell Cancer Institute, United States

****Correspondence:***
Dindial Ramotar
dramotar@hbku.edu.qa

Specialty section:
This article was submitted to Cell Death and Survival, a section of the journal Frontiers in Cell and Developmental Biology

Received: *25 August 2020*
Accepted: *09 November 2020*
Published: *03 December 2020*

Citation:
Elsakrmy N, Zhang-Akiyama Q-M and Ramotar D (2020) The Base Excision Repair Pathway in the Nematode Caenorhabditis elegans. Front. Cell Dev. Biol. 8:598860. doi: 10.3389/fcell.2020.598860

INTRODUCTION

Damage to the DNA is an inevitable process occurring persistently within a living cell. Various exogenous and endogenous insults induce oxidation, deamination, alkylation, depurination, and other premutagenic changes on the DNA bases that threaten the integrity of the genome. Oxidative base damage alone is estimated to be 10,000 per human cell per day (Lindahl and Barnes, 2000). Several DNA repair mechanisms such as the base excision repair (BER), nucleotide excision repair (NER), mismatch excision repair, and recombinational DNA repair have evolved to function faithfully to evade the toxic and mutagenic consequences of various DNA lesions. The BER pathway primarily repairs endogenously generated DNA lesions and it is. initiated by a DNA

glycosylase recognizing the damaged base (**Figure 1**; Krokan and Bjørås, 2013). Although most DNA glycosylases are substrate-specific, some display redundancy and broad substrate specificity (Katafuchi et al., 2004). For instance, of the eleven BER DNA glycosylases conserved in humans, four are able to recognize uracil bases in the DNA, which can arise through cytosine deamination or as a result of misincorporation by a DNA polymerase (Whitaker et al., 2017). Once an aberrant base is recognized by a monofunctional DNA glycosylase, the enzyme cleaves the N-glycosidic bond between the base and the deoxyribose sugar. This creates an apurinic/apyrimidinic (AP) or also refer to as an abasic site. These non-instructional AP sites are premutagenic as they can lead to the misincorporation of the incorrect base by DNA polymerases, and thus must be removed by an AP endonuclease. The AP endonuclease cleaves the DNA backbone 5′ to the AP site, leaving behind a 3′-hydroxyl and a 5′-deoxyribophosphate (dRP) residue. The gap created by the removal of the damaged base is filled by the single insertion of the correct nucleotide through the action of a DNA polymerase. The same DNA polymerase has a deoxyribophosphodiesterase activity that removes the 5′-dRP, enabling DNA ligase to enter and seal the nick to complete the pathway that is referred to as "Short Patch" BER. In mammalian cells, the ligation step requires the formation of a complex that includes DNA ligase I or III and the scaffolding protein X-ray Repair Cross-Complementing protein 1 (XRCC1) (Tomkinson et al., 2001).

Processing of the damaged base can be initiated by a bifunctional, instead of a monofunctional DNA glycosylase. In addition to the N-glycosylic activity, bifunctional DNA glycosylases such as endonuclease III (NTH) are capable of also cleaving the DNA backbone 3′ to the AP site in a β-elimination reaction. This creates a 5′-phosphate group and a 3′-blocking group such as the 3′-α, β-unsaturated aldehyde residue created by NTH1. This 3′-blocking group must be removed to allow the insertion of the new nucleotide. The 3′-blocking group is removed by the 3′-phosphodiesterase activity that is endowed by AP endonucleases, thereby generating a 3′-hydroxyl group to enable nucleotide insertion and ligation by DNA polymerase and DNA ligase, respectively. It is believed that when the BER pathway is initiated by a bifunctional DNA glycosylase to remove oxidatively damaged bases, the "Long Patch" BER serves as an alternative repair process (Klungland and Lindahl, 1997). In the Long Patch BER a stretch of several nucleotides, often 2–15, is inserted and at the same time the 5′-end is displaced by the newly synthesized complementary strand. The displaced strand forms what is known as a 5′-flap, which is then removed by a Flap structure specific endonuclease FEN-1, a specialized nuclease that removes the 5′-overhanging flap, thus preparing the nick to be sealed by a DNA ligase. Apparently, directing the cell machinery toward Long Patch BER depends on several factors such as existence of cluster base damage, the abundance of certain replication factors including the proliferating cell nuclear antigen, as well as the interaction with downstream enzymes such as polymerase β or the flap endonuclease (Klungland and Lindahl, 1997).

Base excision repair plays an essential role in maintaining the integrity of the genome and proper functioning of cells. Defects in BER are linked to the development of several diseases [reviewed in Wallace et al. (2012) and Wallace (2014)]. For instance, mutations in polymerase β are found in nearly 30% of human cancers (Starcevic et al., 2004), whereas mutations in UNG-1 have been linked to colorectal cancer and glioblastoma (Moon et al., 1998; Broderick et al., 2006) and recently, mutations in XRCC-1 have been linked to the development of hepatocellular carcinoma (Mattar et al., 2018). Moreover, mutations in BER have been linked to neurodegenerative diseases such as Alzheimer's and Parkinson's diseases (Kwiatkowski et al., 2016; Sanders et al., 2017), as well as the established contribution of a deteriorating BER system to the process of aging (Vijg and Suh, 2013). Thus, it is of essence that researchers delineate the components of the BER pathway and its interaction with genomic lesions and other cellular components.

The redundancy of DNA glycosylases, as well as the essentiality of downstream enzymes in early life stages have made it challenging to create nullizygous animal models that are viable and to demonstrate a clear phenotype. *Caenorhabditis elegans* is a powerful animal model for studying base excision repair for several reasons. While it has a short life span, high number of progenies and convenient for growth in the laboratory, it possesses fewer BER enzymes exhibiting minimal redundancy to explore the specific phenotypic effects of single BER gene. In addition, many viable nullizygous knockout and knockdown of *C. elegans* BER genes are available or can be created to study this pathway. In this review, we aim to discuss the components of BER and the resulting mutant phenotypes in *C. elegans*. We will highlight the gaps in understanding the BER system in *C. elegans* and to tackle the longstanding question as to why this organism has only two DNA glycosylases, while several of these enzymes can be found in bacteria, yeast and human cells.

FIRST EVIDENCE OF BER IN *C. elegans*

The use of *C. elegans* as a model for studying DNA repair first captured the attention of scientists in the late 1990's – early 2000's when *C. elegans* was shown to resist irradiation-induced DNA damage (Chin and Villeneuve, 2001). Later, the existence of a BER pathway in *C. elegans* was first reported when two AP endonuclease genes *apn-1* and *exo-3* were isolated from *C. elegans* and the predicted amino acid sequences were shown to share nearly 40% identity with the functionally established counterparts from *Saccharomyces cerevisiae,* Apn1 and Apn2, and *Escherichia coli*, Nfo (endonuclease IV) and Xth (exonuclease III), respectively (Masson et al., 1996; Shatilla et al., 2005b). Subsequent studies defined that APN-1 and EXO-3 from *C. elegans* were indeed AP endonucleases (Shatilla et al., 2005a; Yang et al., 2012). As further discoveries came along that include the identification of two DNA glycosylases, UNG-1 and NTH-1, *C. elegans* formed a unique model for the study of BER as it became clear from rigorous homology searches and biochemical analyses that this organism possesses fewer enzymes as compared to the human complements of BER enzymes. This made *C. elegans* a simpler model to study the much more complex

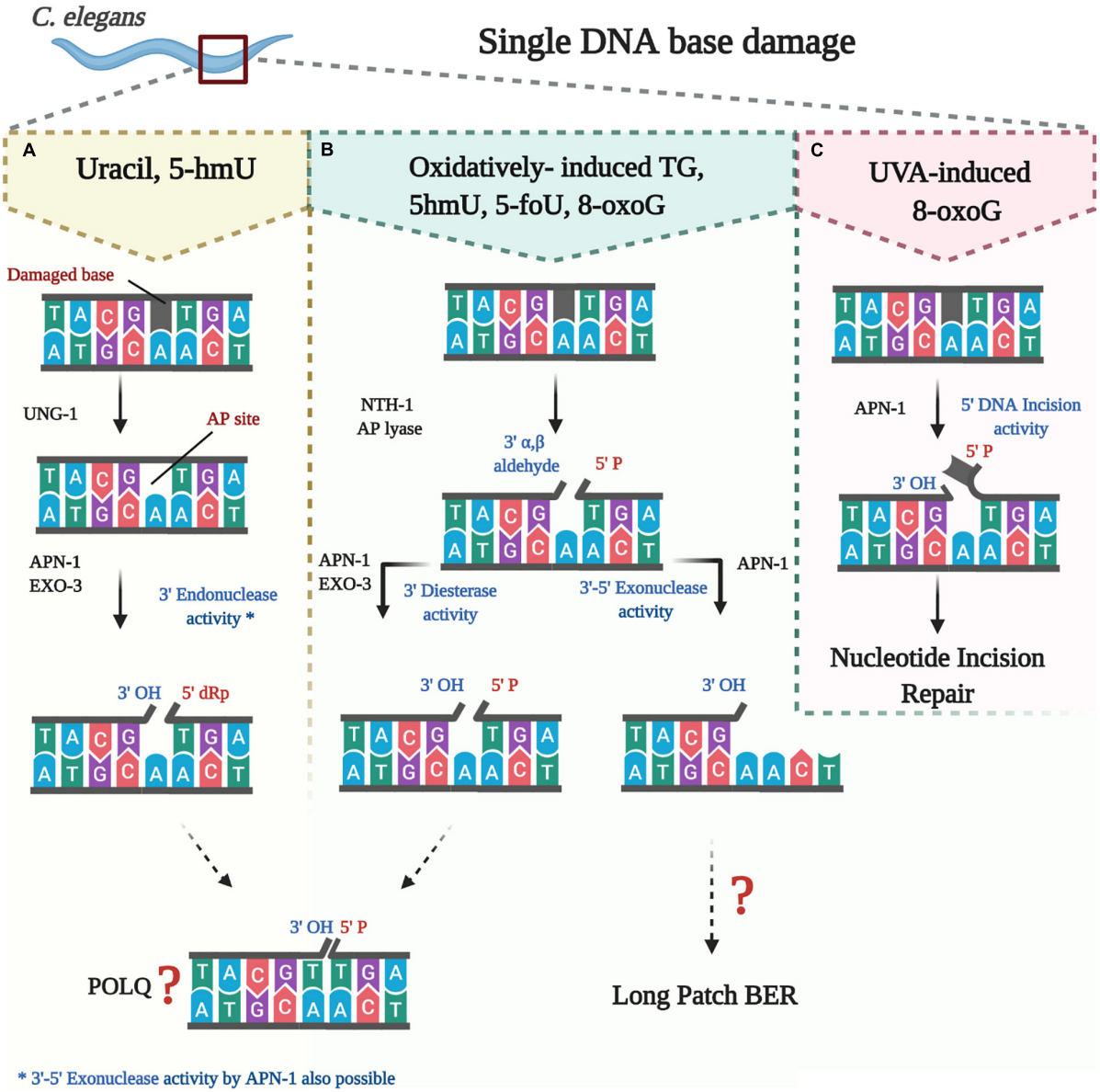

FIGURE 1 | Processing of oxidatively damaged bases by the BER pathway in *C. elegans*. **(A)** uracil and likely 5-hmU are removed by UNG-1 to create an AP site that is processed by either APN-1 or EXO-3 or both. **(B)** oxidatively damaged bases are removed by NTH-1, which then nicks the resulting AP site to create a blocked 3 end that needs further processing by either APN-1 or EXO-3 or both. **(C)** direct nicking of oxidatively damaged base by APN-1.

system in humans. In addition, identifying phenotype of DNA-repair deficient worms, forms a plausible solution to uncover corresponding phenotype in humans, which is often masked by the overlapping activity of the different enzymes constituting the BER pathway. **Figure 1** summarizes the BER pathway in *C. elegans*.

DNA GLYCOSYLASES IN *C. elegans*

The first DNA glycosylase to be discovered was a uracil DNA glycosylase of *E. coli* in the laboratory of Tomas Lindahl in 1974, setting the stage to show that a DNA glycosylase initiates the BER pathway by recognizing the uracil base as a lesion in the DNA (Friedberg and Lindahl, 2004). This seminal work was followed by many discoveries establishing that DNA glycosylases are well defined across several organisms (Denver et al., 2003; Wallace, 2014). The *C. elegans* uracil DNA glycosylase was initially described in early 2000's using an *in vitro* BER repair assay, which monitored the removal of an installed uracil opposite guanine (U·G) in a 42-mer double stranded oligonucleotide substrate (Shatilla and Ramotar, 2002). Several years later, the *ung-1* and *nth*-1 genes encoding Uracil DNA Glycosylase UNG-1 and Endonuclease III NTH-1, respectively, were identified and

characterized in *C. elegans* (Nakamura et al., 2008; Morinaga et al., 2009). Despite several attempts, including extensive homology searches and most importantly enzymatic assays designed to remove specific DNA lesions such as 8-oxoGuanine, no other DNA glycosylases have been found in *C. elegans* besides UNG-1 and NTH-1 (Denver et al., 2003; Papaluca et al., 2018). It seems puzzling that this multicellular organism conserved only two DNA glycosylases when the unicellular *E. coli*, the budding yeast *S. cerevisiae* and human cells have conserved eight, five and eleven DNA glycosylases, respectively (Denver et al., 2003; Wallace, 2014). Assuming that there are indeed only two DNA glycosylases in *C. elegans*, this raises an important question of the substrate specificity and the multifunctionality of CeUNG-1 and CeNTH-1, as compared to other organisms and making *C. elegans* an interesting model for the study of BER pathway.

The Enzymatic Activities of *C. elegans* UNG-1 and NTH-1

Uracil in DNA arises *in vivo* through the incorporation of dUTP opposite adenine by DNA polymerases during DNA replication and via spontaneous deamination of cytosine to give rise to a U·G mispair that leads to a C·T transition mutation (Tye et al., 1978; Friedberg and Lindahl, 2004). In humans, four enzymes are capable of recognizing mispaired uracil bases and initiate its excision repair. These enzymes are Uracil DNA glycosylase (UNG), single-strand-selective monofunctional uracil glycosylase 1 (SMUG-1), thymine DNA glycosylase (TDG), and methyl CpG binding domain protein 4 (MBD4). UNG removes uracil from both double and single stranded DNA, as well as possesses the ability to process other substrates such as 5-fluorouracil (5-FU) and cytosine oxidation products including alloxane, isodialuric acid, and 5′, 6′-dihydrouracil (Dizdaroglu et al., 1996; Fischer et al., 2007). SMUG-1, not only excises U, but it is also capable of processing other uracil derivatives such as 5-hydroxyuracil (5-hU) and 5-hydroxymethyl uracil (5-hmU), which can arise as a result of oxidation of thymine. TDG, on the other hand, removes T, U, and 5-hmU when mispaired with G in double stranded DNA. Similarly, the glycosylase domain of MBD4 functions to remove T, U, and 5-hmU opposite a G, but mainly in CpG-rich regions of the DNA.

The genome of *C. elegans*, however, encodes only a homologous sequence to the human uracil DNA glycosylase with 58.2% similarity (Nakamura et al., 2008); none of the other three enzymes (SMUG-1, TDG, and MBD4) appear to be encoded by the organism (Denver et al., 2003; Nakamura et al., 2008). In 2008, using BLAST search Nakamura et al. (2008) were able to identify the sequence of CeUNG-1, consistent with the initial observation made in 2000 for the presence of UNG-1 in *C. elegans*. The authors reported that UNG-1 is a homolog of the *E. coli ung* gene product, with 49% shared identity. *C. elegans ung-1* is located on chromosome III, containing three exons, and its product is ∼ 32 kDa in size (Nakamura et al., 2008). Similar to DNA glycosylases present in *E. coli* and mammalian cells, the structure of CeUNG-1 contains two active sites A and B, where the former is present between residues 116 and 137 and the latter is present between residues 247 and 253 (Pearl, 2000; Denver et al., 2003; Nakamura et al., 2008). Cloning of *C. elegans ung-1* into *E. coli* strain BL21 enabled the purification of UNG-1. The glycosylase demonstrated efficient removal of U·A and U·G mismatches from dsDNA, although with a stronger affinity toward the U·G mismatched base pairs (Nakamura et al., 2008). This is confirmed in another study, where UNG-1 demonstrated two-fold increase in processing of U·G lesions (Skjeldam et al., 2010). CeUNG-1 can also remove uracil from ssDNA (Nakamura et al., 2008; Skjeldam et al., 2010). Inhibition of CeUNG-1 by the *lactobacillus* uracil glycosylase inhibitor Ugi strongly supported that UNG-1 belongs to the UNG family 1 group (Karran et al., 1981; Nakamura et al., 2008; Skjeldam et al., 2010).

Recently, it has been reported that UNG-1 may possess the ability to process the oxidized base lesion 5-hmU. This is based on phenotypic analysis of *C. elegans ung-1* mutant showing decreased survival upon exposure to the nucleoside form of 5-hmU (Papaluca et al., 2018). We propose that *C. elegans* UNG-1, unlike Ung from other organisms, may have evolved to acquire a broader substrate specificity and thus could act as the dominant DNA glycosylase *in vivo* to remove various modified forms of uracil such as the 5-hmU lesion. Because *C. elegans* lacks the related human SMUG1 DNA glycosylase, which has been shown to remove 5-hmU (Boorstein et al., 2001), supports the notion that UNG-1 may have a role in 5hmU removal. *C. elegans* UNG-1 shares a modest 12.6% identity with SMUG1 (Zauri et al., 2015). A closer examination of the identity revealed that *C. elegans* UNG-1 shares five amino acid residues Ser58, Pro218, Gly226, Glu233, and Leu234 that are unique to human SMUG1 residues Ser48, Pro166, Gly174, Glu181 and Leu182 and which are absent in human UNG1 (Papaluca et al., 2018). Whether these five amino acid residues are involved in conferring upon *C. elegans* UNG-1 the ability to recognize and process 5-hmU in a manner similar to human SMUG1 will need to be investigated.

The second DNA glycosylase found to initiate BER pathway in *C. elegans* is NTH-1. NTH-1 belong to the helix-hairpin-helix (HhH) superfamily of DNA glycosylases (Endonuclease III, Nth) that are conserved in almost all forms of life (Denver et al., 2003). Members of the NTH-1 family share enzymatic activities that recognize and remove oxidatively damaged pyrimidine bases such as thymine glycol (Tg), 5-formyluracil (5-foU), and 5-hmU in DNA. Unlike the monofunctional UNG-1, NTH-1 is a dual function enzyme that has an AP lyase in addition to its DNA glycosylase activity. Following removal of the oxidized damage pyrimidine base, the resulting AP site left by NTH-1 can be cleaved by its AP lyase activity. NTH-1 cuts the DNA backbone 3′- to the AP site in a β-elimination reaction, and generates a 3′-α, β-unsaturated aldehyde group that is removed by the 3′-diesterase activity of either APN-1 or EXO-3 to create a 3′-OH allowing for nucleotide insertion by DNA polymerase (**Figure 1**; Mazumder et al., 1991; Shatilla et al., 2005a; Yang et al., 2012).

It is noteworthy that although the major domain is well conserved amongst the family of Nth proteins, the sequences of amino acid in the N-terminal region are different between CeNTH-1 and *E. coli* Nth-1 (Morinaga et al., 2009). This is reminiscent of the long N-terminal found in *C. elegans* APN-1, but not *E. coli* Nfo (see below). Interestingly, expressing only the portion of *C. elegans nth-1* sequence reported in phylogenetic

studies as the NTH-1 ortholog in *E. coli* produced a protein that is unable to perform NTH-1-like activities (Morinaga et al., 2009). However, modification of the *nth-1* sequence by inclusion of the 117 bp corresponding to the missing N-terminal restored the DNA glycosylase activity (Morinaga et al., 2009). This full length CeNTH-1 shared 67.4% similarity to the human NTH-1, and catalyzed the removal of oxidized pyrimidine bases, particularly thymine glycol (Tg), 5-formyl uracil (5-foU), 5-hmU, and to a weaker extent, 8-oxoguanine (8-oxoG) (Morinaga et al., 2009). *In vivo* measurement of DNA repair revealed that NTH-1 is capable of restoring nuclear DNA integrity within 24 h of exposure to the oxidizing agent H_2O_2 that creates various oxidized bases such as thymine glycol (Hunter et al., 2012). Repair in mitochondrial genome is also seen, although less efficiently (Hunter et al., 2012). The most compelling evidence that NTH-1 functions as a DNA glycosylase *in vivo* came from a study whereby the *C. elegans nth-1* gene was expressed in the *E. coli* double mutant strain deficient for both Nth and Nei; the two DNA glycosylases known to repair oxidized pyrimidine bases in the bacterium. Expression of the *C. elegans nth-1* gene in the *E. coli nth;nei* double mutant strain rescued it from the genotoxic effects of H_2O_2, consistent with a direct role for NTH-1 in the repair of oxidative DNA lesions (Morinaga et al., 2009).

Phenotype of *ung-1* and *nth-1* Deficient *C. elegans*

The phenotypic and physiologic consequences of *C. elegans ung-1* knockdown were assessed in several reports (**Figure 2**; Nakamura et al., 2008; Skjeldam et al., 2010; Papaluca et al., 2018). Despite deletion of the *ung-1* gene, the resulting mutant strain demonstrated a normal egg-laying rate and larval development, in addition to a normal life span compared to N2 strain (Nakamura et al., 2008). Interestingly, the *C. elegans ung-1* mutant was no more sensitive than the wild type (WT) upon exposure to sodium hydrogen sulfite ($NaHSO_3$); a DNA damaging agent that induces cytosine base deamination and creates U·G lesion (Burgers and Klein, 1986; Nakamura et al., 2008; Miyaji et al., 2018). These findings are unique to *C. elegans* as *S. cerevisiae* and *E. coli* cells lacking Ung activity showed high sensitivity to $NaHSO_3$ (Simmons and Friedberg, 1979; Burgers and Klein, 1986). One possibility for the lack of sensitivity of the *C. elegans ung-1* mutant toward $NaHSO_3$ could be due to efficient bypass of the U·G lesion, which may not occur in *E. coli* or yeast *ung1* mutants. As such, we postulate that the deficiency of UNG-1 may lead to the recruitment of a translesion polymerase to bypass the U·G lesion, thereby avoiding toxic AP sites and single strand breaks that would be ordinarily created by the presence of UNG-1 and the subsequent processing by an AP endonuclease.

Recently, UNG-1 was implicated to process the thymine oxidation product 5-hmU (Papaluca et al., 2018). This was detected through *in vivo* survival analysis where u*ng-1* mutant worms were shown to be sensitive to the genotoxic effects of 5-hmU, but not the *nth-1* mutant strain, indicating that UNG-1 could be the main DNA glycosylase to process 5-hmU bases in the nematode genome. This observation is also consistent with a previous finding that the germ cells of *ung-1* mutants might be sensitive to ionizing radiation underscoring the role of UNG-1 in repairing oxidized DNA lesions induced by this agent (Skjeldam et al., 2010). If indeed the above observations are correct, then it would be the first time a substrate other than uracil has been postulated for UNG-1 in *C. elegans*.

In *C. elegans*, germ cell apoptosis is a natural and very sensitive response to excessive endogenous or exogenous DNA damage, as opposed to monitoring progeny survival. Different genotoxic agents induce apoptosis through different pathways (**Figure 3**). For example, ionizing radiation provokes oxidative DNA damage in a CEP-1 dependent apoptotic pathway in wild type *C. elegans* (Hoffman et al., 2014). CEP-1, the *C. elegans* ortholog of the mammalian proapoptotic transcription factor p53, is required to induce CED-1 that forms a ring around apoptotic cells and is easily visualized as CED-1:GFP (Hoffman et al., 2014; Papaluca et al., 2018). In contrast, the oxidant paraquat (Methyl Viologen) induces germline apoptosis through a different mechanism that involves the p38 MAPK-dependent pathway (Salinas et al., 2006). Congruent to these reports, Skjeldam et al. (2010) observed that CEP-1-dependent apoptotic pathway is not induced by paraquat treatment in the wild-type, nor in the *ung-1* deficient worms. Furthermore, the authors showed that CEP-1 induced germ cell apoptosis increased in *ung-1* deficient nematode compared with the wild-type N2 after exposure to ionizing radiation and thus established a role for UNG-1 in DNA repair following exposure to ionizing radiation (Skjeldam et al., 2010). Upon exposure to paraquat, cell death increased in the wild-type worms, but not in the *ung-1* deficient worms. This unexpected finding is due to alteration in transcriptional regulation where it has been observed that the p38 MAPK pathway and other response pathways to oxidative stress have been suppressed in the *ung-1* deficient nematode thereby impairing apoptosis (Skjeldam et al., 2010).

Studies for identification of phenotypic changes in *nth-1* deficient *C. elegans* were also conducted. As indicated in **Figure 2**, *nth-1* mutants show normal life span, embryonic viability, and brood size (Morinaga et al., 2009; Hunter et al., 2012; Kassahun et al., 2018). These phenotypes were not affected by exposure to H_2O_2 or paraquat (Morinaga et al., 2009). Similar to the wild type strain N2, *nth-1* deficient strain also exhibits effective repair of its nuclear and mitochondrial DNA (mtDNA) upon exposure to H_2O_2 (Hunter et al., 2012; Volkova et al., 2020). However, these *nth-1* knockout strains compared to wild type do undergo chronic oxidative stress and mitochondrial dysfunction, as reflected by elevated steady state levels of ROS (Kassahun et al., 2018). This is congruent with an observed transcriptional upregulation of cellular proteins involved in activation of SKN-1 (Fensgard et al., 2010; Kassahun et al., 2018) a transcription factor that mediates transcriptional responses to oxidative stress (Kahn et al., 2008). Downregulation of insulin/IGF-1 (IIS) pathway is also seen in *nth-1* mutants (Fensgard et al., 2010). Apparently, suppression of the IIS pathway is shown to induce longevity in *C. elegans* (Rusyn et al., 2007). These alterations could represent a defense mechanism against oxidative DNA damage and explain the normal lifespan seen in NTH-1 deficient strain.

It is interesting to note that both UNG-1 and NTH-1 deficient mutants show a similar morphology of impaired CEP-1

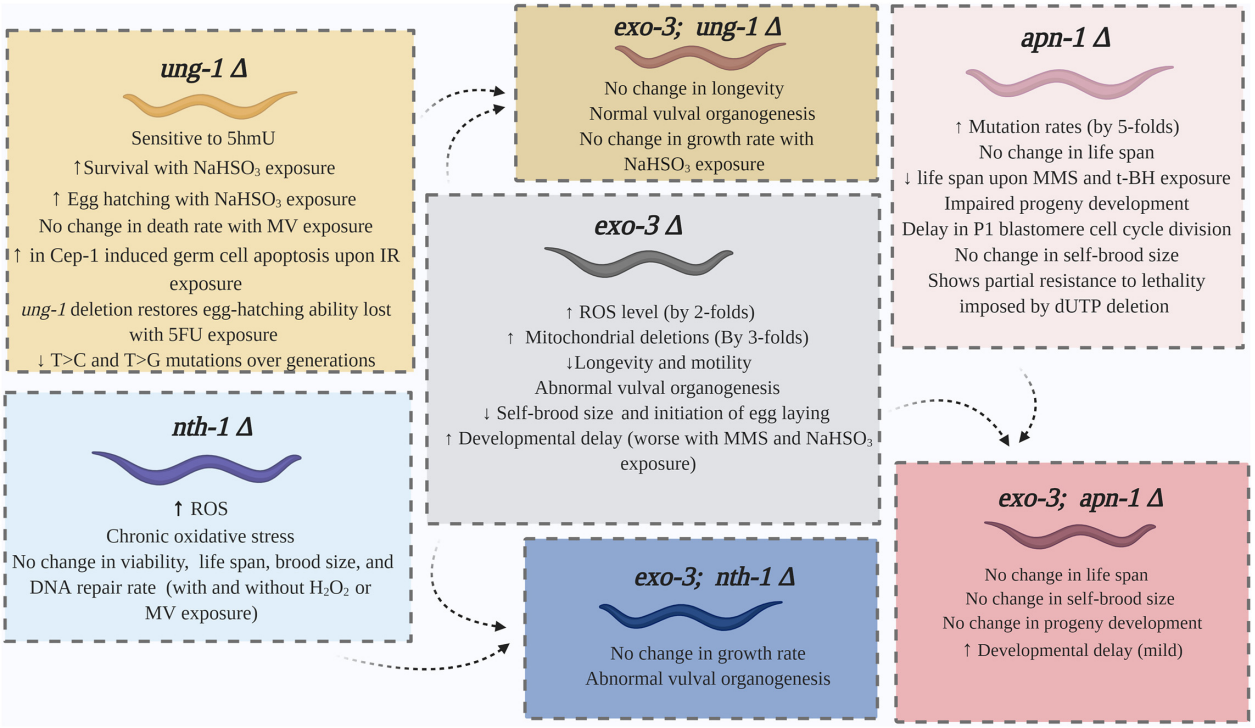

FIGURE 2 | Summary of the phenotypes displayed by the single and double mutants of the BER pathway of *C. elegans*.

independent apoptotic response to oxidative damage, although NTH-1 is the main DNA glycosylase involved in oxidative damage repair in BER pathway (Skjeldam et al., 2010; Kassahun et al., 2018). This has been explained by the identification of compensatory transcriptional changes that attenuate p38-MAPK-stress activated pathways, and not due to loss of DNA repair from the deleted DNA glycosylase (Fensgard et al., 2010; Skjeldam et al., 2010; Kassahun et al., 2018).

AP ENDONUCLEASES IN *C. elegans*

Following the initiation of base excision repair by a monofunctional DNA glycosylase to generate an AP site or by a bifunctional DNA glycosylase that subsequently creates 3′-blocking group, an AP endonuclease is recruited to process the secondary lesion to produce a 3′-hydroxyl group for DNA repair synthesis. AP endonuclease enzymes are multifunctional proteins that are conserved in all organisms (Li and Wilson, 2014). In addition to their endonuclease function to cleave AP sites, AP endonucleases possess 3′-diesterase activity, 3′-5′-exonuclease activity, as well as 5′-DNA incision activity that contributes to nucleotide incision repair (Hosfield et al., 1999; Daley et al., 2010; Redrejo-Rodriguez et al., 2016). The AP endonucleases belong to one of two families, the exonuclease III family (Exo III) or the endonuclease IV (Endo IV) family. While both families are metal-dependent, a distinct feature of Endo IV enzymes is the presence of tightly bound Zn^{+2} ions to perform cleavage of the phosphodiester bond, while EXO III enzymes require the addition of Mg^{+2} ions to exert its functions (Hosfield et al., 1999; Daley et al., 2010; Redrejo-Rodriguez et al., 2016).

It is important to highlight that in human cells two AP endonucleases have been identified, APE1 and APE2. APE-1 is the major AP endonuclease as it is responsible for about 95% of DNA repair activity (Demple et al., 1991; Li and Wilson, 2014). APE-1, sometimes referred to as redox effector factor-1 (Ref-1), is capable of performing other cellular functions related to redox regulation of ubiquitous and tissue specific transcription factors (Kelley et al., 2012). In humans, inappropriate APE1 expression or function are associated with several cancerous and neurodegenerative diseases (Xanthoudakis et al., 1996; Whitaker et al., 2017). This renders APE1 an attractive target for the diagnosis and treatment of cancer as well as other diseases (Park et al., 2014; Ayyildiz et al., 2020). Dual deletion of the *APE1* alleles in mice causes early embryonic lethality that led to a set of challenging experiments to study the enzyme-phenotype correlations. Because of the conserved enzymatic functions as well as the viability of *apn-1* or *exo-3* null mutants, attracted the interest of many scientists to use *C. elegans* as a suitable animal model for the study of AP endonuclease enzymes in BER and to deduce possible impact on health and disease.

Structural and Functional Analysis of *C. elegans* EXO-3 and APN-1

The first report of an AP endonuclease existing in *C. elegans* was published in 1996 (Masson et al., 1996). The gene identified through cDNA library screening encoded a 30 kDa protein with

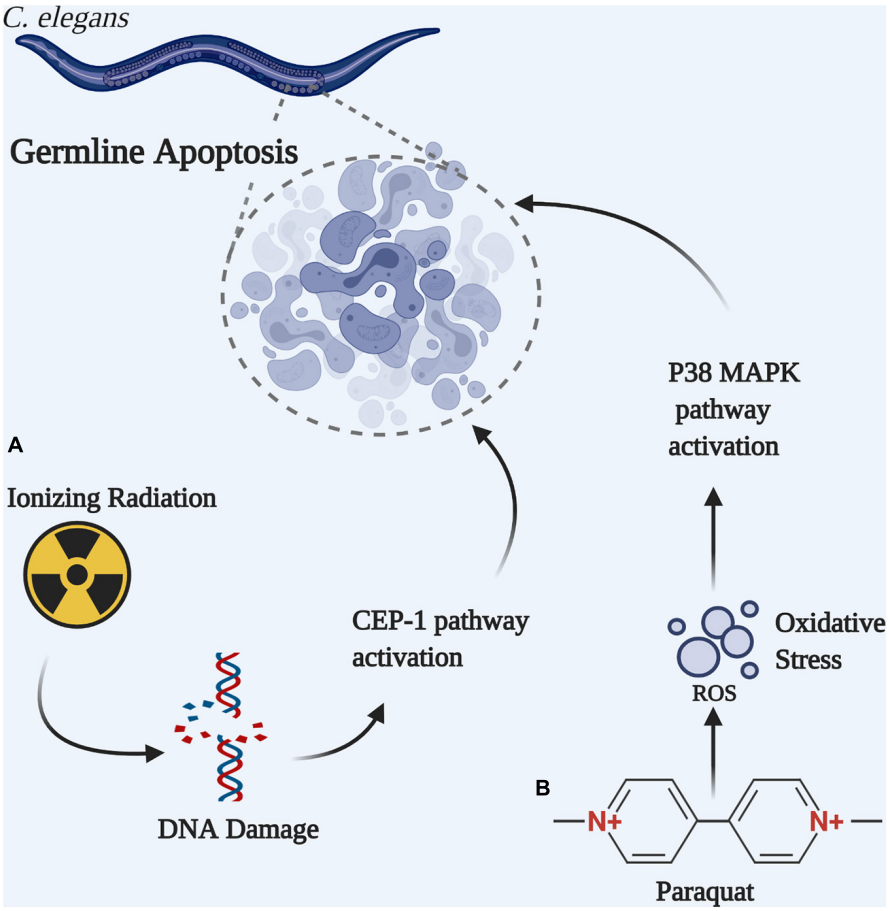

FIGURE 3 | Germline apoptosis can be initiated by different pathways in *C. elegans*. **(A)** Ionizing radiation-induced DNA double strand break activates the CEP-1-dependent apoptotic pathway. **(B)** Paraquat-induced oxidative DNA damage activates the P38 MAPK-dependent apoptotic pathway.

278 amino acids that shared homology with *E. coli* Endo IV and was called CeAPN-1. Expression of CeAPN-1 in *E. coli* mutants deficient in AP endonuclease activities to test for cross-species complementation failed to produce a functional protein, as the protein was degraded (Masson et al., 1996). However, it was confirmed that an active AP endonuclease activity was present in crude extracts of *C. elegans*, but the activity could not be attributed exclusively to the identified CeAPN-1 (Masson et al., 1996). Further investigations revealed that embryonic extract derived from *C. elegans* contained an AP endonuclease activity with high similarity to that displayed by the *E. coli* exonuclease III (Xth), particularly in its resultant nicked product and in addition to its Mg^{+2}-dependence (Shatilla and Ramotar, 2002). This finding raised the possibility there must be at least two AP endonuclease genes in *C. elegans*, *Ceapn-1,* and *Ceexo-3*. Indeed, a *C. elegans* exonuclease-3 (EXO-3) was later identified by using cross-species complementation analysis whereby a mutant *S. cerevisiae* strain YW778, lacking three genes including *APN1* and *APN2* encoding the two AP endonucleases, was exploited to isolate the *C. elegans* AP endonuclease genes (Shatilla et al., 2005a,b). The YW778 mutant strain is sensitive to DNA damaging agents such as MMS that induces formation of AP sites (Vance and Wilson, 2001). Expression of *C. elegans* APN-1 or EXO-3 successfully rescued the yeast DNA repair capabilities and recovered its resistance to MMS (Shatilla et al., 2005b).

Exonuclease-3 of *C. elegans* shares 44% and 64% homology with *E. coli* Xth (exo III) and human APE1, respectively (Shatilla et al., 2005b). *In vitro* DNA repair assays demonstrate that EXO-3 is a strong AP endonuclease that cleaves AP sites to produce a 3′-OH and 5′-dRp ends in the presence of very low Mg^{+2} concentration (Shatilla et al., 2005b). Addition of 5 mM EDTA, a metal chelating agent, completely abolishes the enzymatic endonuclease activity. EXO-3 also possesses a 3′-diesterase activity capable of excising 3′-α, β-unsaturated aldehyde residues on DNA oligonucleotides that are generated by the action of NTH-1 AP lyase on AP sites. However, it seems this enzymatic activity has a more stringent requirement for Mg^{+2} ions and requires a minimum of 1 mM $MgCl_2$ to be added to the *in vitro* reaction mixture for the 3′-diesterase activity to be evident (Shatilla et al., 2005a). Despite its name, *C. elegans* EXO-3 does not display a 3′-5′-exonuclease

activity. This is contrary to human APE1 or Xth of *E. coli*, however, the 3′-5′-exonuclease activity is harbored by the *C. elegans* APN-1 instead, in a manner similar to the yeast Apn1 (Vance and Wilson, 2001). *In vitro* assays also failed to detect any activity of a direct 5′-DNA incision toward oxidized bases such as 5,6-dihydroxyuridine, suggesting that *C. elegans* EXO-3 is not directly involved in nucleotide incision repair pathway as human APE1 (Shatilla et al., 2005a; Li and Wilson, 2014). In contrast, *C. elegans* APN-1, and not EXO-3, appears to share more functions with human APE1 (see below) (Yang et al., 2012).

Structural analysis of EXO-3 revealed that substitution of the amino acid His at 279 with Ala or replacing Asp at 190 with Ala completely diminishes the DNA repair capability of EXO-3, and these variants can no longer rescue the AP endonuclease deficient yeast YW778 strain from the genotoxic effects of MMS or agents that create DNA single strand breaks with blocked 3′-ends (Shatilla et al., 2005a). Indeed, *in vitro* experiments with H279A and D190A variants confirm loss of EXO-3 function. Nevertheless, substitution of Glu68 with Ala results in a variant (E68A) that performs AP endonuclease and 3′-diesterase activity *in vitro* in the presence of additional Mg^{2+}, but these activities are lost *in vivo*, possibly due to an impaired process beyond the AP endonuclease step (Shatilla et al., 2005a). Interestingly, band-shift experiment revealed that purified native EXO-3 does not stay bound to the AP site substrate in either the absence or the presence of embryonic extract derived from *C. elegans*. In contrast, the purified EXO-3 variant E68A retards the mobility of the AP site substrate only in the presence of the extract. Since purified E68A alone has no effect on the mobility of the AP site substrate, it is assumed that dissociation of the variant from the substrate is a slow process thereby trapping a protein from the extract (Shatilla et al., 2005a). The identity of this protein is under investigation and it is likely a component of the BER pathway.

The second AP endonuclease functioning in the BER pathway in *C. elegans* is APN-1. Although the *apn-1* gene was identified in 1996, the encoded APN-1 protein was only characterized many years later, even after EXO-3, as explained below (Yang et al., 2012). RNA interference studies indicated that knock down of APN-1 caused the animal to lose its resistance to DNA damage induced by MMS (Zakaria et al., 2010). This suggests a unique function for APN-1 that is not substituted by EXO-3 even though both enzymes have the ability to process MMS-induced AP sites (Shatilla and Ramotar, 2002). This prompted the isolation and characterization of APN-1 even though this brought along many new challenges (Yang et al., 2012).

The *apn-1* gene, which is located on chromosome 2 encodes a 396 amino acid-long APN-1 polypeptide (UniProt database) (APN-1, 2020). The APN-1 amino acid sequence from 119 to 396 shared 63% homology with both *S. cerevisiae* Apn1 and *E. coli* Nfo (Shatilla et al., 2005b). The N-terminal amino acid stretch (1–63) of the protein is not directly related to the nuclease activities of the protein, however, this segment is essential for APN-1 localization into the nucleus (Wang et al., 2014). This was evident from an APN-1 variant (1–63Δ) that retained cytoplasmic distribution compared to the nuclear localization of the full-length APN-1 when tested in a yeast system (Wang et al., 2014). Isolation of the *apn-1* gene from a *C. elegans* library designed for yeast two-hybrid screening did not contain the full-length APN-1, and instead carried only a portion of APN-1 from amino acid 119 to 396 (Shatilla et al., 2005b; Wang et al., 2014). Expression of this truncated APN-1 (119–396), which included the region essential for endonuclease activity, to test for cross specie complementation in the yeast AP endonuclease deficient strain YW778 showed no ability to rescue this yeast YW778 mutant strain from MMS-induced AP sites, and thus this strain remained very sensitivity to MMS. Interestingly, the inclusion of a nuclear localization signal to the APN-1 (119–396) caused its localization to the nucleus and which restored full MMS resistance to the YW778 strain to the level of the wild type yeast strain YW465 (Yang et al., 2012; Wang et al., 2014). This approach has allowed the purification and characterization of APN-1, and like yeast Apn1 and *E. coli* endo IV, the CeAPN-1 required no additional metal ions for enzymatic activities. Similar to other endo IV family members, APN-1 of *C. elegans* performs four DNA repair functions with the following enzymatic activities, AP endonuclease, 3′-diesterase, NIR and 3′-5′-exonuclease (Yang et al., 2012). It is noteworthy that the diesterase activity of APN-1 requires relatively higher protein concentrations to be evident, suggesting that APN-1 preferentially cleaves abasic sites to generate a 3′-OH at higher rates than cleaving 3′-blocking groups generated by AP lyases (Yang et al., 2012; Wang et al., 2014). As stated earlier, APN-1 incorporated the 3′-5′-exonuclease activity, which is lacking in the EXO-3 enzyme suggesting that APN-1 could have a broader function in *C. elegans* (Yang et al., 2012; Wang et al., 2014). It is worth noting that CeAPN-1 possesses all the same activity of human APE1, except the ability to serve as a redox factor whereby APE1 has a key cysteine C65 that can reduce a number of transcription factors such as p53 (Nassour et al., 2016). While APE1 is essential in mammalian cells, deletion of either *apn-1* or *exo-3* or both genes in *C. elegans* do not cause lethality, raising the possibility of the importance of the redox function of APE1. So far, no homolog of CeAPN-1 (endo IV member) has been found in human cells, although a second APE1 like enzyme, APE2, with limited function has been isolated and partially characterized (Hadi et al., 2002; Guikema et al., 2007; Burkovics et al., 2009).

Site-directed mutagenesis allowed for the creation of two APN-1 variants, the E261G and the E215G (Yang et al., 2012). Based on the ribbon structure of APN-1 alone and in contact with damaged DNA, it appears that glutamate at position 261 is located within the metal binding pocket and comes in direct contact with the DNA strand, while the glutamate residue at 215 is not directly involved in metal binding (Yang et al., 2012). Although neither substitutions affected the expressed protein size or structure, the variant E215G, and not E261G, was capable of preventing spontaneous DNA mutations as well as rescuing the mutant YW778 strain from bleomycin-induced lesions, suggesting that Glu215 does not play a role in DNA repair (Yang et al., 2012). It appears that replacing the glutamic acid residue at position 261 with a glycine reduced the size of the ion-binding pocket as indicated by the provisional structure of the

protein, thus blocking the metal from making contact with the DNA (Yang et al., 2012).

Phenotypic Changes of EXO3 and APN-1 Mutant Strains

Caenorhabditis elegans knockout and knockdown for the APN-1 and EXO-3 AP endonucleases do not lead to inviable phenotypes. The *exo-3* mutant strains often demonstrate a more severe phenotype compared to *apn-1* mutants (**Figure 2**; Schlotterer et al., 2010; Zakaria et al., 2010; Kato et al., 2015; Miyaji et al., 2018). RNA interference (RNAi) studies indicate that *exo-3* knockdown does not terminate growth completely, rather it results in developmental delay by an average of 6 h from the wild type strain; a delay that is aggravated by exposure to toxic agents such as MMS and $NaHSO_3$ (Miyaji et al., 2018). Deletion of *apn-1* in addition to *exo-3* did not alter the observed phenotype as *exo-3;apn-1* double mutants were reported to demonstrate developmental delay as well (Miyaji et al., 2018). In addition, *exo-3* deletion reduced *C. elegans* motility (head and overall body), and induces abnormal vulval organogenesis (Schlotterer et al., 2010; Miyaji et al., 2018). Furthermore, *exo-3* knockdown compromises longevity and reduces life span by an average of 3.1 days, compared to wild type (Schlotterer et al., 2010). Knockout studies conducted later supported this finding, although a wider mean difference of 5.4 days was reported (Kato et al., 2015). This is also accompanied by about 30% reduction of self-brood size than N2 worms (Kato et al., 2015). These impaired phenotypes indicate that *exo-3* is vital to the development of *C. elegans*.

On a cellular level, *exo-3* mutants (RNAi) display 2-fold increase in ROS generation, particularly colocalized with the neuronal system, as well as a 3-fold increase in mtDNA deletions, which is thought to contribute to aging (Harman, 1972; Schlotterer et al., 2010). These effects are thought to be mediated through *cep-1*-dependent mechanism. It appears that wild type *C. elegans* strain with suppressed *cep-1* (RNAi) expression, as well as *cep-1* knockout strain (VC172) show elevated EXO-3 levels (Schlotterer et al., 2010). A similar finding is observed in human cells where p53, the human *cep-1* ortholog, is believed to downregulate the human *exo-3* ortholog APE1 through inhibition of S1 and S1-mediated APE1 transcription (Zaky et al., 2008). However, it is noteworthy that the observed *exo-3* upregulation induced by *cep-1* inhibition may not grant the animal additional resistance to oxidative damage. An RNAi *cep-1* knockout (GK138) strain was shown to be as sensitive as wild type strains to oxidative DNA damage upon placement in a hyperbaric O_2 chamber (Arum and Johnson, 2007). Although *exo-3* expression levels were not assessed in this particular study nonetheless, the GK138 mutant strain showed an increase in life span that is similar to that observed in wild type *cep-1* RNAi-treated animals created by Schlotterer et al. (2010) which had shown a confirmed increase in *exo-3* levels. Interestingly, knockdown of *cep-1* expression in *exo-3* (RNAi) wild type strains rescued the phenotype with a preserved neuronal function, normalized ROS levels, as well as increased animal motility compared to *exo-3* (RNAi) treated worms alone (Schlotterer et al., 2010). We reasoned that *cep-1* inhibition probably elicits an antioxidant response in the *exo-3* mutant. This can be discerned from the inability to detect changes in oxidative DNA damage levels in *cep-1* mutant NC172 or GK138 strains, as well as a failure to detect a significant change in ROS levels in *cep-1* silenced (RNAi) N2 worms (Arum and Johnson, 2007; Schlotterer et al., 2010). It is likely that EXO-3 may execute other functions that are not DNA repair-related, as in the case of the human APE1 that is involved also in transcription regulation besides a role in BER (Tell et al., 2009).

As in the case of *exo-3* mutants, several distinct phenotypes are observed in *apn-1* knockout and knockdown models. *C. elegans* strains mutated for *apn-1* showed up to 5-fold increase in mutation rates as discerned by a *gfp-lacZ* reporter, which has an insertion that sets *lacZ* out of frame and when mutated brings *lacZ* in frame (Zakaria et al., 2010). Under normal growth conditions, these *apn-1* mutants show no reduction in life span despite the increase burden of mutations (Zakaria et al., 2010; Miyaji et al., 2018). However, upon exposure to DNA damaging agents such as MMS and *tert*-butylhydroperoxide (*t*-BH), the *apn-1* mutants displayed a reduction in life span by 3–4 days (Zakaria et al., 2010). In contrast, exposure of the *apn-1* mutant to UVC radiation did not decrease its lifespan compared to the wild type, implying that APN-1 is not essential for mitigating the genotoxicity of ultraviolet radiation as it is for MMS and *t*-BH (Zakaria et al., 2010). Diminishing APN-1 activity in *C. elegans* is also accompanied by an impaired progeny development. Compared to wild type, *apn-1* mutants (RNAi) show a striking difference of 30% lower egg-hatching rate at 24 h of incubation. The difference in egg-hatching rate is significantly minimized to 10% at 36 h and beyond, indicating an impaired developmental rate in *apn-1* strains compared to wild type (Zakaria et al., 2010). It appears that *apn-1* deletion impacts progeny development at the very early stages of embryogenesis, likely due to the accumulation of lethal mutations in the germ cells.

The first cell to give rise to *C. elegans* is P0 cell which divides into an AB cell and a P1 cell (Brauchle et al., 2003). While AB cell is not affected by DNA damage occurring during this stage, the P1 cell division decreased in response to a DNA damage-activated checkpoint signaling pathway (Brauchle et al., 2003). Time-lapse microscopy revealed that *apn-1* knockdown strains exhibited a delayed P1 cell cycle division by about 39 s (P value < 0.003) compared to wild type strains (Zakaria et al., 2010). This delay was specific to P1 cells as no difference in AB cell cycle length was noted between wild type and *apn-1* mutated cells (Zakaria et al., 2010). Nevertheless, impairment of progeny development in *apn-1* mutants was not necessarily associated with altered progeny production; *apn-1* mutants laid eggs in a similar pattern to that of wild type, as evident in an unaffected self-brood size (Zakaria et al., 2010; Kato et al., 2015). Lastly, APN-1 appears to contribute significantly to the animal lethality resulting from knockdown of the *dut-1* gene encoding the deoxyuridine 5′-triphosphate nucleotidohydrolase (DUT-1). DUT-1 converts dUTP into dUMP, which is the precursor for the synthesis of dTTP, and in the absence of DUT-1 there is an increased in dUTP levels that can be used efficiently by DNA polymerase for incorporation opposite adenine in the genome.

DUT-1 inhibition increased uracil incorporation in the DNA and following removal by UNG-1 resulted in an increased level of toxic AP sites that diminished *C. elegans* survival (Dengg et al., 2006). Downregulation of *apn-1* (RNAi) in the *dut-1* mutant partially resolved the imposed lethality as evident by nearly 7% of broods reaching adulthood, in contrast to *exo-3* mutants where only 0.2% successfully reached adult stages (Zakaria et al., 2010). One interpretation of these findings is that UNG-1 removal of uracil is followed by recruitment of APN-1, and not EXO-3, to process the AP sites to create an accumulation of toxic single strand DNA breaks that could further lead to double strand breaks (Zakaria et al., 2010). Under this condition, the downregulation of *apn-1* may not be efficient to suppress the cleavage of the AP sites left by UNG-1. Alternatively, we cannot exclude the possibility that the AP sites left by UNG-1 action are rapidly cleaved *via* competition by the AP lyase activity of NTH-1 to create toxic DNA single strand breaks with 3′-blocked ends (Papaluca et al., 2018). As such, it would be important to test whether knockdown of *nth-1* will completely rescue the lethality caused by *dut-1* mutation in *C. elegans*. In the case of *E. coli* or yeast, the *dut1* or *DUT1* gene, respectively, is essential and an allele of *dut1-1* with compromised activity in yeast is lethal in the absence of *APN1* (Guillet et al., 2006). It is possible that the lethality of the *dut1-1*; *apn1* double mutant may be the result of AP lyases, such as Ntg1 and Ntg2, acting on the accumulated AP sites to generate toxic single strand breaks with 3′-blocked ends. In both model systems, *C. elegans* and yeast, it seems that processing of *dut1*-mediated AP sites by AP lyases may lead to lethality due to accumulation of toxic DNA single strand breaks.

AP Endonucleases During Life Span of *C. elegans*

The life cycle *of C. elegans* constitutes several stages that can be described as embryogenesis, four larval stages L1-L4, and two adult stages: the young adult, and the gravid adult stage (Altun and Hall, 2009). Articulating findings scattered across several reports of AP endonuclease expression helps draw a general notion of the roles APN-1 and EXO-3 execute throughout *C. elegans* lifespan. *In situ* hybridization of *exo-3* and *apn-1* mRNA identifies that both genes are expressed in the gonads of male and hermaphrodite worms, and that AP sites are efficiently repaired in the gonads of *C. elegans* (Kato et al., 2015). In contrast to *apn-1*, deletion of *exo-3* is accompanied by reduced self-brood size in an *nth-1* dependent manner (∼30% less than the N2 strain) in addition to a delayed initiation of egg-laying, suggesting that exo-3 plays a vital role in the progeny development or gonad maturation phase by processing endogenous lesions that must be processed by NTH-1 and channel to EXO-3 (Kato et al., 2015). During embryogenesis, APN-1 is needed to overcome a DNA damage checkpoint and aid cell cycle progression of the P1 blastomere (Zakaria et al., 2010). Following hatching, expression levels of both APN-1 and EXO-3, as indicated by mRNA transcripts, remains the same throughout the egg and larval stages. Interestingly, at 60 h, corresponding to young adult stage, *apn-1* expression is increased to 2.3 times its levels at 0 h (i.e., egg stage), while to a more extensive level *exo-3* levels increased by 13-fold its levels at the egg stage (Miyaji et al., 2018). Moreover, expression remains at such levels with subsequent progression into the gravid adult stage at 72 h (Miyaji et al., 2018). Upon aging, *exo-3* expression started to decline to reach a level of 45% reduction at 6 days of age, compared to day 1, and remain at such level for the remainder of the nematode life span (Schlotterer et al., 2010). As expected, the declining *exo-3* levels by day 6 correlated with increased mtDNA deletions by day 5. Taken together, there is an essential need for functional AP endonucleases in all of the *C. elegans* life stages, particularly, at adult stages. Moreover, it appears that EXO-3 plays a vital role in the animal development, as evident by a more severe phenotype in *exo-3* mutants compared to *apn-1* (Schlotterer et al., 2010; Zakaria et al., 2010; Kato et al., 2015; Miyaji et al., 2018).

DNA POLYMERASE AND LIGASE IN *C. elegans*

Polymerase Q and Polymerase H

Despite clear evidence of a full BER pathway in *C. elegans,* a homologous sequence for polymerase B (POLB), the X-family DNA polymerase primarily active in base excision repair in human cells was not found (Loeb and Monnat, 2008). Computer-based sequence analysis successfully located 11 putative DNA polymerase sequences, but this approach failed to identify a conserved sequence for POLB or any other X family members (Asagoshi et al., 2012). Furthermore, DNA polymerase assay failed to detect POLB-like activity in the cellular extracts of the nematode (Asagoshi et al., 2012). Notably, several studies suggest that a DNA polymerase theta [or polymerase Q (POLQ) or a polymerase eta polymerase H (POLH)] is involved in DNA repair in *C. elegans*. Both POLQ and POLH belong to the A-family of DNA polymerases and are considered translesion synthesis (TLS) polymerases (also known as bypass polymerases) (Loeb and Monnat, 2008). TLS polymerases catalyze insertion of nucleotides opposite damage site and are error-prone when synthesizing DNA in the absence of a template strand, as in non-homologous end joining (NHEJ) (Loeb and Monnat, 2008). Indeed, POLQ is an essential component of alternative NHEJ in mammalian cells (Mateos-Gomez et al., 2015). Likewise, experiments on *C. elegans* identified that alt-NHEJ was shown to be completely dependent on POLQ, particularly in the germline and is considered the main source of insertion/deletion mutations and thus essential for genetic diversification in *C. elegans* (Roerink et al., 2014; van Schendel et al., 2015). Nonetheless, endeavors to explore a potential role for POLQ in BER pathway led Asagoshi et al. (2012) to identify the presence of a POLQ-like activity in the cellular extracts of *C. elegans* contributing to gap-filling synthesis. Knockout experiments confirmed the involvement of POLQ-1 in the pathway (Asagoshi et al., 2012). More recently, it has been shown that the knockdown of *polq-1* sensitized the animals upon exposure to 5hmU, suggesting a role for POLQ-1 in processing this oxidative DNA lesion via the BER pathway (Papaluca et al., 2018). So far, it would appear that processing, for example, of the oxidized base lesion 5hmU would require the sequential actions of UNG-1, APN-1, and POLQ-1 (Papaluca et al., 2018).

Two additional DNA polymerases, POLH and POLK of *C. elegans* are also implicated in DNA repair (Ohkumo et al., 2006; Akagi et al., 2009; Roerink et al., 2012). Both *C. elegans* POLH and POLK are unique as they do not share homologous recombination repair functions with their human orthologs (Roerink et al., 2012). *polh* and *polk* mutant strains are sensitive to MMS, while the double mutants are even more sensitive to MMS. Since MMS exerts DNA damage through alkylating guanine and adenine bases, which can be repaired by BER, it remains possible that both of these polymerases could participate in the BER pathway in *C. elegans* (Lundin et al., 2005; Roerink et al., 2012).

It remains unclear which of the two possible DNA ligases, LIG-1, and LIG-4, are involved in mending the final step of the BER pathway and which protein would serve the function of coordinating the single strand break repair, if no potential XRCC1 scaffold protein exists in *C. elegans* to orchestrate the recruitments of the various DNA repair proteins in the pathway (Wilson et al., 2017).

Poly(ADP-ribose)polymerases

Poly(ADP-ribose) polymerases are a group of conserved enzymes involved in apoptotic pathways, post translational modifications, and chromatin remodeling (Hassa and Hottiger, 2008). Notably, PARPs play a role in DNA repair and were proven to be involved in base excision repair (Trucco et al., 1998; Beneke et al., 2000; Le Page et al., 2003). Two homologs sequences were identified in *C. elegans*, namely *pme-1* and *pme-2* (also known as *parp-1* and *parp-2*) (Gagnon et al., 2002). *C. elegans pme-1* encodes a 108 kDa PARP with an N-terminal that contains two Zn^{+2} finger motifs, and a catalytic C-terminal with the canonical PARP motif (Gagnon et al., 2002). PME-1 shares 31% amino acid identity and 78% PARP motif similarity to its human ortholog (Gagnon et al., 2002). PME-2, with a 24% amino acid similarity, is also an active PARP, albeit its shorter primary structure that shared fewer motifs compared to human PARP-2 (Gagnon et al., 2002). Enzymatic inhibition of PME-1 and PME-2 in *C. elegans* was associated with a reduced progeny survival rate after exposure to ionizing radiation, likely due to impaired DNA repair response (Dequen et al., 2005). Knockout worms also demonstrate increased sensitivity to cisplatin treatment reflected in reduced brood size and viability (Crone et al., 2015). Interestingly, BER and transcription-coupled NER were recently shown to be involved in protecting against cisplatin-induced cytotoxicity (Slyskova et al., 2018). Furthermore, *pme-1* and *pme-2* mutants do not experience reduced viability upon exposure to high doses of Manganese (Mn^{+2}) (Neumann et al., 2020). This is interesting given that Mn^{+2} exposure was correlated with an impaired poly(ADP-ribosyl)ation-mediated DNA damage response, which is thought to enhance sensitivity to genotoxic drugs (Bornhorst et al., 2010, 2013).

Poly(ADP) ribose polymers are subsequently degraded by poly(ADP-ribose) glycohydrolase (PARG) (St-Laurent and Desnoyers, 2011). *C. elegans* genome encodes two PARGs: *pme-3* and *pme-4*, which share 18% and 22% overall identity, and 42% and 40% PARG motif similarity to human PARG, respectively (St-Laurent et al., 2007). Knockdown (RNAi) of both genes results in enhanced sensitivity to ionizing radiation (St-Laurent et al., 2007), which can be suppressed by an impaired TLS pathway via mutational deactivation of POLQ (Bae et al., 2020). Despite the presence of these enzymes in *C. elegans*, there is no direct evidence to link the PARPs and PARGs to the BER pathway.

MUTATIONAL SIGNATURES IN *C. elegans*

Recently, *C. elegans* has been acquiring increasing attention as an animal model for the study of mutational signatures (Meier et al., 2014, 2020a; Volkova et al., 2020). Particularly due to the conservation of key DNA repair pathways, as well as the affordability and feasibility of sequencing successive generations of this short-lived nematode. Genome sequencing of 17 DNA repair deficient mutants indicated that on average, a single mutation per generation is observed not only in wild type, but also in DNA repair defective mutants (Meier et al., 2014; Volkova et al., 2020). With such low mutation rate, animals need to be propagated for at least 20–40 generations to allow rigorous comparison and statistical analysis (Meier et al., 2020a). Generally, base substitutions are the most frequent DNA mutations encountered in WT and mutant strains (Meier et al., 2014). It is interesting that except for MMR mutants, the mutation rates of *C. elegans* DNA repair mutants do not exceed 2 to 5-fold that of baseline (Volkova et al., 2020). BER impaired *exo-3* and *ung-1*, but not *apn-1, pme-1, or pme-2* mutants show a significant increase in base substitution per generation as compared to the WT strain (Meier et al., 2020b). As expected, *ung-1* mutants experience less T > C and T > G mutations (Meier et al., 2014). However, no significant difference in structural variants or insertion/deletion mutations was reported for BER mutants (Meier et al., 2020b). Overall, the maintenance of genomic integrity is surprisingly robust despite knockout of the various DNA repair pathways, accentuating the redundancy of DNA repair mechanisms in *C. elegans* (Volkova et al., 2020).

BER ENZYMES IN RELATION TO OTHER DNA REPAIR PATHWAYS

Besides the BER pathway, *C. elegans* also conserved the additional major DNA repair pathways including nucleotide excision, mismatch, non-homologous and homologous recombination pathways. As in the BER pathway, not all the components of the various DNA repair pathways have been found in *C. elegans* when compared to the proteins found in the human DNA repair pathways (Wilson et al., 2017). It is not clear whether *C. elegans* lacks these components, and which are fulfilled by the roles of other unrelated proteins. However, this would require a more in-depth discussion that is not within the scope of this review.

It is noteworthy that *C. elegans* has the ability to recruit components from one DNA repair pathway to execute a function in another pathway. For example, the enzymes of the BER pathway do not necessarily work in isolation, they can show redundancy and overlap with other pathways. In this section,

we provide a brief overview of some of the links to other DNA repair pathways.

Link to MMR

Depletion of *apn-1* (RNAi) in *exo-3* mutant TM4374 strain resulted in increased sensitivity to 5-FU, suggesting that APN-1 is involved in the process that removes 5-FU (SenGupta et al., 2013). Further analysis indicated that 5-FU induced toxicity was not UNG-1 dependent, but EXO-3 and APN-1 dependent, suggesting that an alternative pathway is acting upstream of the AP endonucleases role in nicking of the DNA (SenGupta et al., 2013). Indeed, epistasis analysis indicates that APN-1 and EXO-3 function in cooperation with other Mismatch repair (MMR) pathway enzymes leading to 5-FU induced toxicity. It appears that EXO-3 is required for DNA nicking and subsequent MMR activation, whereas APN-1 induces DNA damage checkpoint activation to allow the repair process (SenGupta et al., 2013).

Link to NER

As discussed earlier, deletion of *nth-1* does not change the life span of *C. elegans*. On the other hand, if the nucleotide excision repair (NER) gene *xpa-1* is lost, the life span is shortened (Fensgard et al., 2010). The double mutations in the *nth -1* and *xpa-1* genes are expected to further shorten the life span, however, it was reported that the loss of NTH-1 activity restores the life span of short-lived *xpa-1* mutant to the same level as the wild-type worms (Fensgard et al., 2010). Furthermore, the authors have found that depletion of both NTH-1 and XPA-1 induced an oxidative stress response, as well as changes in global expression profiles that involved the upregulation of genes responding to endogenous stress and downregulation of IIS (Fensgard et al., 2010). It is possible that NTH-1 may serve to recognize certain DNA damage that it cannot repair and forming transcription blocking lesion, which may then recruit XPA (Fensgard et al., 2010). Alternatively, NTH-1 may produce toxic single strand breaks requiring XPA-1 function via the NER pathway.

PERSPECTIVES

We initially believed that *C. elegans* would provide a simpler system to study the BER pathway in multicellular organisms, but the findings to date led us to suggest that this model is more complex and raises a number of questions that need to be resolved. The complexity lies in the fact that deleting, for example, the *nth-1* gene triggers a complex regulation of genes to combat oxidative stress thereby dampening any severe phenotypes that might be caused as a consequence of NTH-1 deficiency. Establishing this link might be important to find ways to activate similar systems in human cells to bypass NTH1 defects. Of note, CeNTH-1 has an extended N-terminal that is crucial for the DNA glycosylase activity, although it remains unclear what is the exact function of this region of the enzyme. One tenable possibility is that the N-terminal of NTH-1 might serve to scan the genome and recognize damaged bases to activate the DNA glycosylase activity.

Besides the above challenges, several additional aspects remain unresolved regarding the BER system in *C. elegans*, for example (i) it is unclear whether a second uracil DNA glycosylase exists in *C. elegans* as raised by earlier reports While extracts derived from UNG-1 deficient strain suggest the existence of a second uracil DNA glycosylase activity in *C. elegans*, its genome does not appear to encode another homolog, (ii) there is no biochemical evidence to show that UNG-1 can process the oxidized base lesion 5hmU, although this is strongly supported by phenotypic data, (iii) it remains uncertain whether UNG-1 and NTH-1 might recognize a broad range of DNA lesions and or serve as sensors to channel the lesions to other DNA repair pathways, and (iv) whether there are distinct complexes involving the DNA glycosylases and AP endonucleases to process oxidative DNA lesions.

We expect that the *C. elegans* model will continue to provide new challenges and uncover novel mechanisms by which this organism uses a limited number of proteins to combat oxidative DNA lesions. It would be interesting to determine whether the *ung-1;nth-1;apn-1;exo-3* quadruple deletion mutant would survive, or other DNA repair pathways would be exploited to repair the accumulated oxidative DNA lesions.

AUTHOR CONTRIBUTIONS

NE wrote the entire manuscript. NE and DR revised and edited the final version. Q-MZ-A verified the accuracy of the final version. All authors contributed to the article and approved the submitted version.

FUNDING

This work was supported by Qatar Foundation.

REFERENCES

Akagi, J., Masutani, C., Kataoka, Y., Kan, T., Ohashi, E., Mori, T., et al. (2009). Interaction with DNA polymerase eta is required for nuclear accumulation of REV1 and suppression of spontaneous mutations in human cells. *DNA Repair.* 8, 585–599. doi: 10.1016/j.dnarep.2008.12.006

APN-1 (2020). *UniProtKB - Q10002 (APN1_CAEEL).* Bethesda, MA: National Institutes of Health.

Altun, Z. F., and Hall, D. H. (2020). Handbook of *C. elegans* Anatomy. *In WormAtla*.

Arum, O., and Johnson, T. E. (2007). Reduced expression of the *Caenorhabditis elegans* p53 ortholog cep-1 results in increased longevity. *J. Gerontol. A Biol. Sci. Med. Sci.* 62, 951–959. doi: 10.1093/gerona/62.9.951

Asagoshi, K., Lehmann, W., Braithwaite, E. K., Santana-Santos, L., Prasad, R., Freedman, J. H., et al. (2012). Single-nucleotide base excision repair DNA polymerase activity in *C. elegans* in the absence of DNA polymerase β. *Nucleic Acids Res.* 40, 670–681. doi: 10.1093/nar/gkr727

Ayyildiz, D., Antoniali, G., D'Ambrosio, C., Mangiapane, G., Dalla, E., Scaloni, A., et al. (2020). Architecture of the human Ape1 interactome defines novel cancers signatures. *Sci. Rep.* 10:28. doi: 10.1038/s41598-019-56981-z

Bae, W., Park, J. H., Lee, M. H., Park, H. W., and Koo, H. S. (2020). Hypersensitivity to DNA double-strand breaks associated with PARG deficiency is suppressed by exo-1 and polq-1 mutations in *Caenorhabditis elegans*. *FEBS J,* 287, 1101–1115. doi: 10.1111/febs.15082

Beneke, R., Geisen, C., Zevnik, B., Bauch, T., Muller, W. U., Kupper, J. H., et al. (2000). DNA excision repair and DNA damage-induced apoptosis are linked to Poly(ADP-ribosyl)ation but have different requirements for p53. *Mol. Cell Biol.* 20, 6695–6703. doi: 10.1128/mcb.20.18.6695-6703.2000

Boorstein, R. J., Cummings, A. Jr., Marenstein, D. R., Chan, M. K., Ma, Y., Neubert, T. A., et al. (2001). Definitive identification of mammalian 5-hydroxymethyluracil DNA N-glycosylase activity as SMUG1. *J. Biol. Chem.* 276, 41991–41997. doi: 10.1074/jbc.M106953200

Bornhorst, J., Ebert, F., Hartwig, A., Michalke, B., and Schwerdtle, T. (2010). Manganese inhibits poly(ADP-ribosyl)ation in human cells: a possible mechanism behind manganese-induced toxicity? *J. Environ. Monit.* 12, 2062–2069. doi: 10.1039/c0em00252f

Bornhorst, J., Meyer, S., Weber, T., Böker, C., Marschall, T., Mangerich, A., et al. (2013). Molecular mechanisms of Mn induced neurotoxicity: RONS generation, genotoxicity, and DNA-damage response. *Mol. Nutr. Food Res.* 57, 1255–1269. doi: 10.1002/mnfr.201200758

Brauchle, M., Baumer, K., and Gonczy, P. (2003). Differential activation of the DNA replication checkpoint contributes to asynchrony of cell division in *C. elegans* embryos. *Curr. Biol.* 13, 819–827. doi: 10.1016/s0960-9822(03)00295-1

Broderick, P., Bagratuni, T., Vijayakrishnan, J., Lubbe, S., Chandler, I., and Houlston, R. S. (2006). Evaluation of NTHL1, NEIL1, NEIL2, MPG, TDG, UNG and SMUG1 genes in familial colorectal cancer predisposition. *BMC Cancer* 6:243. doi: 10.1186/1471-2407-6-243

Burgers, P. M., and Klein, M. B. (1986). Selection by genetic transformation of a *Saccharomyces cerevisiae* mutant defective for the nuclear uracil-DNA-glycosylase. *J. Bacteriol.* 166, 905–913. doi: 10.1128/jb.166.3.905-913.1986

Burkovics, P., Hajdú, I., Szukacsov, V., Unk, I., and Haracska, L. (2009). Role of PCNA-dependent stimulation of 3'-phosphodiesterase and 3'-5' exonuclease activities of human Ape2 in repair of oxidative DNA damage. *Nucleic Acids Res.* 37, 4247–4255. doi: 10.1093/nar/gkp357

Chin, G. M., and Villeneuve, A. M. (2001). *C. elegans* mre-11 is required for meiotic recombination and DNA repair but is dispensable for the meiotic G(2) DNA damage checkpoint. *Genes Dev.* 15, 522–534. doi: 10.1101/gad.864101

Crone, B., Aschner, M., Schwerdtle, T., Karst, U., and Bornhorst, J. (2015). Elemental bioimaging of Cisplatin in *Caenorhabditis elegans* by LA-ICP-MS. *Metallomics* 7, 1189–1195. doi: 10.1039/c5mt00096c

Daley, J. M., Zakaria, C., and Ramotar, D. (2010). The endonuclease IV family of apurinic/apyrimidinic endonucleases. *Mutat. Res.* 705, 217–227. doi: 10.1016/j.mrrev.2010.07.003

Demple, B., Herman, T., and Chen, D. S. (1991). Cloning and expression of APE, the cDNA encoding the major human apurinic endonuclease: definition of a family of DNA repair enzymes. *Proc. Natl. Acad. Sci. U.S.A.* 88, 11450–11454. doi: 10.1073/pnas.88.24.11450

Dengg, M., Garcia-Muse, T., Gill, S. G., Ashcroft, N., Boulton, S. J., and Nilsen, H. (2006). Abrogation of the CLK-2 checkpoint leads to tolerance to base-excision repair intermediates. *EMBO Rep.* 7, 1046–1051. doi: 10.1038/sj.embor.7400782

Denver, D. R., Swenson, S. L., and Lynch, M. (2003). An evolutionary analysis of the helix-hairpin-helix superfamily of DNA repair glycosylases. *Mol. Biol. Evol.* 20, 1603–1611. doi: 10.1093/molbev/msg177

Dequen, F., Gagnon, S. N., and Desnoyers, S. (2005). Ionizing radiations in *Caenorhabditis elegans* induce poly(ADP-ribosyl)ation, a conserved DNA-damage response essential for survival. *DNA Repair.* 4, 814–825. doi: 10.1016/j.dnarep.2005.04.015

Dizdaroglu, M., Karakaya, A., Jaruga, P., Slupphaug, G., and Krokan, H. E. (1996). Novel activities of human uracil DNA N-glycosylase for cytosine-derived products of oxidative DNA damage. *Nucleic Acids Res.* 24, 418–422. doi: 10.1093/nar/24.3.418

Fensgard, O., Kassahun, H., Bombik, I., Rognes, T., Lindvall, J. M., and Nilsen, H. (2010). A two-tiered compensatory response to loss of DNA repair modulates aging and stress response pathways. *Aging* 2, 133–159. doi: 10.18632/aging.100127

Fischer, F., Baerenfaller, K., and Jiricny, J. (2007). 5-Fluorouracil is efficiently removed from DNA by the base excision and mismatch repair systems. *Gastroenterology* 133, 1858–1868. doi: 10.1053/j.gastro.2007.09.003

Friedberg, E. C., and Lindahl, T. (2004). Inroads into base excision repair II. The discovery of DNA glycosylases. "An N-glycosidase from Escherichia coli that releases free uracil from DNA containing deaminated cytosine residues,". *Proc. Nat. Acad. Sci. U.S.A.* 3, 1532–1536. doi: 10.1016/j.dnarep.2004.05.014 discussion 1531-1532.

Gagnon, S. N., Hengartner, M. O., and Desnoyers, S. (2002). The genes pme-1 and pme-2 encode two poly(ADP-ribose) polymerases in *Caenorhabditis elegans*. *Biochem. J.* 368(Pt 1), 263–271. doi: 10.1042/BJ20020669

Guikema, J. E., Linehan, E. K., Tsuchimoto, D., Nakabeppu, Y., Strauss, P. R., Stavnezer, J., et al. (2007). APE1- and APE2-dependent DNA breaks in immunoglobulin class switch recombination. *J. Exp. Med.* 204, 3017–3026. doi: 10.1084/jem.20071289

Guillet, M., Van Der Kemp, P. A., and Boiteux, S. (2006). dUTPase activity is critical to maintain genetic stability in *Saccharomyces cerevisiae*. *Nucleic Acids Res.* 34, 2056–2066. doi: 10.1093/nar/gkl139

Hadi, M. Z., Ginalski, K., Nguyen, L. H., and Wilson, D. M. III (2002). Determinants in nuclease specificity of Ape1 and Ape2, human homologues of *Escherichia coli* exonuclease III. *J. Mol. Biol.* 316, 853–866. doi: 10.1006/jmbi.2001.5382

Harman, D. (1972). The biologic clock: the mitochondria? *J. Am. Geriatr. Soc.* 20, 145–147. doi: 10.1111/j.1532-5415.1972.tb00787.x

Hassa, P. O., and Hottiger, M. O. (2008). The diverse biological roles of mammalian PARPS, a small but powerful family of poly-ADP-ribose polymerases. *Front. Biosci.* 13:3046–3082. doi: 10.2741/2909

Hoffman, S., Martin, D., Melendez, A., and Bargonetti, J. (2014). *C. elegans* CEP-1/p53 and BEC-1 are involved in DNA repair. *PLoS One* 9:e88828. doi: 10.1371/journal.pone.0088828

Hosfield, D. J., Guan, Y., Haas, B. J., Cunningham, R. P., and Tainer, J. A. (1999). Structure of the DNA repair enzyme endonuclease IV and its DNA complex: double-nucleotide flipping at abasic sites and three-metal-ion catalysis. *Cell* 98, 397–408. doi: 10.1016/s0092-8674(00)81968-6

Hunter, S. E., Gustafson, M. A., Margillo, K. M., Lee, S. A., Ryde, I. T., and Meyer, J. N. (2012). In vivo repair of alkylating and oxidative DNA damage in the mitochondrial and nuclear genomes of wild-type and glycosylase-deficient *Caenorhabditis elegans*. *DNA Repair.* 11, 857–863. doi: 10.1016/j.dnarep.2012.08.002

Kahn, N. W., Rea, S. L., Moyle, S., Kell, A., and Johnson, T. E. (2008). Proteasomal dysfunction activates the transcription factor SKN-1 and produces a selective oxidative-stress response in *Caenorhabditis elegans*. *Biochem. J.* 409, 205–213. doi: 10.1042/bj20070521

Karran, P., Cone, R., and Friedberg, E. C. (1981). Specificity of the bacteriophage PBS2 induced inhibitor of uracil-DNA glycosylase. *Biochemistry* 20, 6092–6096. doi: 10.1021/bi00524a027

Kassahun, H., SenGupta, T., Schiavi, A., Maglioni, S., Skjeldam, H. K., Arczewska, K., et al. (2018). Constitutive MAP-kinase activation suppresses germline apoptosis in NTH-1 DNA glycosylase deficient *C. elegans*. *DNA Repair.* 61, 46–55. doi: 10.1016/j.dnarep.2017.11.009

Katafuchi, A., Matsubara, M., Terato, H., Iwai, S., Hanaoka, F., and Ide, H. (2004). Damage specificity of human DNA glycosylases for oxidative pyrimidine lesions. *Nucleic Acids Symp. Ser.* 48, 175–176. doi: 10.1093/nass/48.1.175

Kato, Y., Moriwaki, T., Funakoshi, M., and Zhang-Akiyama, Q.-M. (2015). *Caenorhabditis elegans* EXO-3 contributes to longevity and reproduction: differential roles in somatic cells and germ cells. *Mutation Res.* 772, 46–54. doi: 10.1016/j.mrfmmm.2015.01.001

Kelley, M. R., Georgiadis, M. M., and Fishel, M. L. (2012). APE1/Ref-1 role in redox signaling: translational applications of targeting the redox function of the DNA repair/redox protein APE1/Ref-1. *Curr. Mol. Pharmacol.* 5, 36–53. doi: 10.2174/1874467211205010036

Klungland, A., and Lindahl, T. (1997). Second pathway for completion of human DNA base excision-repair: reconstitution with purified proteins and requirement for DNase IV (FEN1). *EMBO J.* 16, 3341–3348. doi: 10.1093/emboj/16.11.3341

Krokan, H. E., and Bjørås, M. (2013). Base excision repair. *Cold Spring Harb. Perspect. Biol.* 5:a012583. doi: 10.1101/cshperspect.a012583

Kwiatkowski, D., Czarny, P., Toma, M., Jurkowska, N., Sliwinska, A., Drzewoski, J., et al. (2016). Associations between DNA Damage, DNA base excision repair gene variability and Alzheimer's Disease risk. *Dement Geriatr. Cogn. Disord.* 41, 152–171. doi: 10.1159/000443953

Le Page, F., Schreiber, V., Dherin, C., De Murcia, G., and Boiteux, S. (2003). Poly(ADP-ribose) polymerase-1 (PARP-1) is required in murine cell lines for base excision repair of oxidative DNA damage in the absence of DNA polymerase beta. *J. Biol. Chem.* 278, 18471–18477. doi: 10.1074/jbc.M212905200

Li, M., and Wilson, D. M. III (2014). Human apurinic/apyrimidinic endonuclease 1. *Antioxid Redox Signal.* 20, 678–707. doi: 10.1089/ars.2013.5492

Lindahl, T., and Barnes, D. E. (2000). Repair of endogenous DNA damage. *Cold Spring Harb. Symp. Quant Biol.* 65, 127–133. doi: 10.1101/sqb.2000.65.127

Loeb, L. A., and Monnat, R. J. Jr. (2008). DNA polymerases and human disease. *Nat. Rev. Genet.* 9, 594–604. doi: 10.1038/nrg2345

Lundin, C., North, M., Erixon, K., Walters, K., Jenssen, D., Goldman, A. S., et al. (2005). Methyl methanesulfonate (MMS) produces heat-labile DNA damage but no detectable in vivo DNA double-strand breaks. *Nucleic Acids Res.* 33, 3799–3811. doi: 10.1093/nar/gki681

Masson, J. Y., Tremblay, S., and Ramotar, D. (1996). The *Caenorhabditis elegans* gene CeAPN1 encodes a homolog of *Escherichia coli* and yeast apurinic/apyrimidinic endonuclease. *Gene* 179, 291–293. doi: 10.1016/s0378-1119(96)00375-7

Mateos-Gomez, P. A., Gong, F., Nair, N., Miller, K. M., Lazzerini-Denchi, E., and Sfeir, A. (2015). Mammalian polymerase theta promotes alternative NHEJ and suppresses recombination. *Nature* 518, 254–257. doi: 10.1038/nature14157

Mattar, M. M., Zekri, A. N., Hussein, N., Morsy, H., Esmat, G., and Amin, M. A. (2018). Polymorphisms of base-excision repair genes and the hepatocarcinogenesis. *Gene* 675, 62–68. doi: 10.1016/j.gene.2018.06.056

Mazumder, A., Gerlt, J. A., Absalon, M. J., Stubbe, J., Cunningham, R. P., Withka, J., et al. (1991). Stereochemical studies of the .beta.-elimination reactions at aldehydic abasic sites in DNA: endonuclease III from *Escherichia coli*, sodium hydroxide, and Lys-Trp-Lys. *Biochemistry* 30, 1119–1126. doi: 10.1021/bi00218a033

Meier, B., Cooke, S. L., Weiss, J., Bailly, A. P., Alexandrov, L. B., Marshall, J., et al. (2014). *C. elegans* whole-genome sequencing reveals mutational signatures related to carcinogens and DNA repair deficiency. *Genome Res.* 24, 1624–1636. doi: 10.1101/gr.175547.114

Meier, B., Volkova, N. V., Gerstung, M., and Gartner, A. (2020a). Analysis of mutational signatures in *C. elegans*: implications for cancer genome analysis. *DNA Repair.* 95:102957. doi: 10.1016/j.dnarep.2020.102957

Meier, B., Volkova, N. V., Hong, Y., Bertolini, S., González-Huici, V., Petrova, T., et al. (2020b). Systematic analysis of mutational spectra associated with DNA repair deficiency in ⁢em>*C. elegans*⁢/em&gt. *bioRxiv* [Preprint]. doi: 10.1101/2020.06.04.133306

Miyaji, M., Hayashi, Y., Funakoshi, M., Tanaka, A., and Zhang-Akiyama, Q. M. (2018). AP endonuclease EXO-3 deficiency causes developmental delay and abnormal vulval organogenesis, Pvl, through DNA glycosylase-initiated checkpoint activation in *Caenorhabditis elegans*. *Sci. Rep.* 8:16736. doi: 10.1038/s41598-018-35063-6

Moon, Y. W., Park, W. S., Vortmeyer, A. O., Weil, R. J., Lee, Y. S., Winters, T. A., et al. (1998). Mutation of the uracil DNA glycosylase gene detected in glioblastoma. *Mutat. Res.* 421, 191–196. doi: 10.1016/s0027-5107(98)00165-1

Morinaga, H., Yonekura, S., Nakamura, N., Sugiyama, H., Yonei, S., and Zhang-Akiyama, Q. M. (2009). Purification and characterization of *Caenorhabditis elegans* NTH, a homolog of human endonuclease III: essential role of N-terminal region. *DNA Repair.* 8, 844–851. doi: 10.1016/j.dnarep.2009.04.020

Nakamura, N., Morinaga, H., Kikuchi, M., Yonekura, S., Ishii, N., Yamamoto, K., et al. (2008). Cloning and characterization of uracil-DNA glycosylase and the biological consequences of the loss of its function in the nematode *Caenorhabditis elegans*. *Mutagenesis* 23, 407–413. doi: 10.1093/mutage/gen030

Nassour, H., Wang, Z., Saad, A., Papaluca, A., Brosseau, N., Affar el, B., et al. (2016). Peroxiredoxin 1 interacts with and blocks the redox factor APE1 from activating interleukin-8 expression. *Sci. Rep.* 6:29389. doi: 10.1038/srep29389

Neumann, C., Baesler, J., Steffen, G., Nicolai, M. M., Zubel, T., Aschner, M., et al. (2020). The role of poly(ADP-ribose) polymerases in manganese exposed *Caenorhabditis elegans*. *J. Trace Elem. Med. Biol.* 57, 21–27. doi: 10.1016/j.jtemb.2019.09.001

Ohkumo, T., Masutani, C., Eki, T., and Hanaoka, F. (2006). Deficiency of the *Caenorhabditis elegans* DNA polymerase eta homologue increases sensitivity to UV radiation during germ-line development. *Cell Struct. Funct.* 31, 29–37. doi: 10.1247/csf.31.29

Papaluca, A., Wagner, J. R., Saragovi, H. U., and Ramotar, D. (2018). UNG-1 and APN-1 are the major enzymes to efficiently repair 5-hydroxymethyluracil DNA lesions in *C. elegans*. *Sci. Rep.* 8:6860. doi: 10.1038/s41598-018-25124-1

Park, J. S., Kim, H. L., Kim, Y. J., Weon, J.-I., Sung, M.-K., Chung, H. W., et al. (2014). Human AP endonuclease 1: a potential marker for the prediction of environmental carcinogenesis risk. *Oxid, Med.Cell. Longev.* 2014:730301. doi: 10.1155/2014/730301

Pearl, L. H. (2000). Structure and function in the uracil-DNA glycosylase superfamily. *Mutat. Res.* 460, 165–181. doi: 10.1016/s0921-8777(00)00025-2

Redrejo-Rodriguez, M., Vigouroux, A., Mursalimov, A., Grin, I., Alili, D., Koshenov, Z., et al. (2016). Structural comparison of AP endonucleases from the exonuclease III family reveals new amino acid residues in human AP endonuclease 1 that are involved in incision of damaged DNA. *Biochimie* 128-129, 20–33. doi: 10.1016/j.biochi.2016.06.011

Roerink, S. F., Koole, W., Stapel, L. C., Romeijn, R. J., and Tijsterman, M. (2012). A broad requirement for TLS polymerases eta and kappa, and interacting sumoylation and nuclear pore proteins, in lesion bypass during *C. elegans* embryogenesis. *PLoS Genet.* 8:e1002800. doi: 10.1371/journal.pgen.1002800

Roerink, S. F., van Schendel, R., and Tijsterman, M. (2014). Polymerase theta-mediated end joining of replication-associated DNA breaks in *C. elegans*. *Genome Res.* 24, 954–962. doi: 10.1101/gr.170431.113

Rusyn, I., Fry, R. C., Begley, T. J., Klapacz, J., Svensson, J. P., Ambrose, M., et al. (2007). Transcriptional networks in *S. cerevisiae* linked to an accumulation of base excision repair intermediates. *PLoS One* 2:e1252. doi: 10.1371/journal.pone.0001252

Salinas, L. S., Maldonado, E., and Navarro, R. E. (2006). Stress-induced germ cell apoptosis by a p53 independent pathway in *Caenorhabditis elegans*. *Cell Death Differ.* 13, 2129–2139. doi: 10.1038/sj.cdd.4401976

Sanders, L. H., Paul, K. C., Howlett, E. H., Lawal, H., Boppana, S., Bronstein, J. M., et al. (2017). Editor's highlight: base excision repair variants and pesticide exposure increase Parkinson's Disease Risk. *Toxicol. Sci.* 158, 188–198. doi: 10.1093/toxsci/kfx086

Schlotterer, A., Hamann, A., Kukudov, G., Ibrahim, Y., Heckmann, B., Bozorgmehr, F., et al. (2010). Apurinic/apyrimidinic endonuclease 1, p53, and thioredoxin are linked in control of aging in *C. elegans*. *Aging Cell* 9, 420–432. doi: 10.1111/j.1474-9726.2010.00572.x

SenGupta, T., Torgersen, M. L., Kassahun, H., Vellai, T., Simonsen, A., and Nilsen, H. (2013). Base excision repair AP endonucleases and mismatch repair act together to induce checkpoint-mediated autophagy. *Nat. Commun.* 4:2674. doi: 10.1038/ncomms3674

Shatilla, A., Ishchenko, A. A., Saparbaev, M., and Ramotar, D. (2005a). Characterization of *Caenorhabditis elegans* exonuclease-3 and evidence that a Mg2+-dependent variant exhibits a distinct mode of action on damaged DNA. *Biochemistry* 44, 12835–12848. doi: 10.1021/bi050195t

Shatilla, A., Leduc, A., Yang, X., and Ramotar, D. (2005b). Identification of two apurinic/apyrimidinic endonucleases from *Caenorhabditis elegans* by cross-species complementation. *DNA Repair.* 4, 655–670. doi: 10.1016/j.dnarep.2005.02.005

Shatilla, A., and Ramotar, D. (2002). Embryonic extracts derived from the nematode *Caenorhabditis elegans* remove uracil from DNA by the sequential action of uracil-DNA glycosylase and AP (apurinic/apyrimidinic) endonuclease. *Biochem. J.* 365(Pt 2), 547–553. doi: 10.1042/BJ20020375

Simmons, R. R., and Friedberg, E. C. (1979). Enzymatic degradation of uracil-containing deoxyribonucleic acid. V. Survival of *Escherichia coli* and coliphages treated with sodium bisulfite. *J. Bacteriol.* 137, 1243–1252.

Skjeldam, H. K., Kassahun, H., Fensgard, O., SenGupta, T., Babaie, E., Lindvall, J. M., et al. (2010). Loss of *Caenorhabditis elegans* UNG-1 uracil-DNA glycosylase affects apoptosis in response to DNA damaging agents. *DNA Repair.* 9, 861–870. doi: 10.1016/j.dnarep.2010.04.009

Slyskova, J., Sabatella, M., Ribeiro-Silva, C., Stok, C., Theil, A. F., Vermeulen, W., et al. (2018). Base and nucleotide excision repair facilitate resolution of platinum drugs-induced transcription blockage. *Nucleic Acids Res.* 46, 9537–9549. doi: 10.1093/nar/gky764

Starcevic, D., Dalal, S., and Sweasy, J. B. (2004). Is there a link between DNA polymerase beta and cancer? *Cell Cycle* 3, 998–1001.

St-Laurent, J. F., and Desnoyers, S. (2011). Poly(ADP-ribose) metabolism analysis in the nematode *Caenorhabditis elegans*. *Methods Mol. Biol.* 780, 413–425. doi: 10.1007/978-1-61779-270-0_25

St-Laurent, J. F., Gagnon, S. N., Dequen, F., Hardy, I., and Desnoyers, S. (2007). Altered DNA damage response in *Caenorhabditis elegans* with impaired poly(ADP-ribose) glycohydrolases genes expression. *DNA Repair.* 6, 329–343. doi: 10.1016/j.dnarep.2006.10.027

Tell, G., Quadrifoglio, F., Tiribelli, C., and Kelley, M. R. (2009). The many functions of APE1/Ref-1: not only a DNA repair enzyme. *Antioxid Redox Signal.* 11, 601–620. doi: 10.1089/ars.2008.2194

Tomkinson, A. E., Chen, L., Dong, Z., Leppard, J. B., Levin, D. S., Mackey, Z. B., et al. (2001). Completion of base excision repair by mammalian DNA ligases. *Prog. Nucleic Acid Res. Mol. Biol.* 68, 151–164. doi: 10.1016/s0079-6603(01)68097-8

Trucco, C., Oliver, F. J., de Murcia, G., and Menissier-de Murcia, J. (1998). DNA repair defect in poly(ADP-ribose) polymerase-deficient cell lines. *Nucleic Acids Res.* 26, 2644–2649. doi: 10.1093/nar/26.11.2644

Tye, B. K., Chien, J., Lehman, I. R., Duncan, B. K., and Warner, H. R. (1978). Uracil incorporation: a source of pulse-labeled DNA fragments in the replication of the *Escherichia coli* chromosome. *Proc. Natl. Acad. Sci. U.S.A.* 75, 233–237. doi: 10.1073/pnas.75.1.233

van Schendel, R., Roerink, S. F., Portegijs, V., van den Heuvel, S., and Tijsterman, M. (2015). Polymerase Theta is a key driver of genome evolution and of CRISPR/Cas9-mediated mutagenesis. *Nat. Commun.* 6:7394. doi: 10.1038/ncomms8394

Vance, J. R., and Wilson, T. E. (2001). Repair of DNA strand breaks by the overlapping functions of lesion-specific and non-lesion-specific DNA 3' phosphatases. *Mol. Cell Biol.* 21, 7191–7198. doi: 10.1128/MCB.21.21.7191-7198.2001

Vijg, J., and Suh, Y. (2013). Genome instability and aging. *Annu. Rev. Physiol.* 75, 645–668. doi: 10.1146/annurev-physiol-030212-183715

Volkova, N. V., Meier, B., González-Huici, V., Bertolini, S., Gonzalez, S., Vöhringer, H., et al. (2020). Mutational signatures are jointly shaped by DNA damage and repair. *Nat. Commun.* 11, 2169–2169. doi: 10.1038/s41467-020-15912-7

Wallace, S. S. (2014). Base excision repair: a critical player in many games. *DNA Repair.* 19, 14–26. doi: 10.1016/j.dnarep.2014.03.030

Wallace, S. S., Murphy, D. L., and Sweasy, J. B. (2012). Base excision repair and cancer. *Cancer Lett.* 327, 73–89. doi: 10.1016/j.canlet.2011.12.038

Wang, Z., Yang, X., Mazouzi, A., and Ramotar, D. (2014). The long N-terminus of the *C. elegans* DNA repair enzyme APN-1 targets the protein to the nucleus of a heterologous system. *Gene* 553, 151–157. doi: 10.1016/j.gene.2014.10.016

Whitaker, A. M., Schaich, M. A., Smith, M. R., Flynn, T. S., and Freudenthal, B. D. (2017). Base excision repair of oxidative DNA damage: from mechanism to disease. *Front. Biosci.* 22:1493–1522. doi: 10.2741/4555

Wilson, D. M. III, Rieckher, M., Williams, A. B., and Schumacher, B. (2017). Systematic analysis of DNA crosslink repair pathways during development and aging in *Caenorhabditis elegans*. *Nucleic Acids Res.* 45, 9467–9480. doi: 10.1093/nar/gkx660

Xanthoudakis, S., Smeyne, R. J., Wallace, J. D., and Curran, T. (1996). The redox/DNA repair protein, Ref-1, is essential for early embryonic development in mice. *Proc. Natl. Acad. Sci. U.S.A.* 93, 8919–8923. doi: 10.1073/pnas.93.17.8919

Yang, X., Fan, J., Ishchenko, A. A., Patel, D., Saparbaev, M. K., and Ramotar, D. (2012). Functional characterization of the *Caenorhabditis elegans* DNA repair enzyme APN-1. *DNA Repair.* 11, 811–822. doi: 10.1016/j.dnarep.2012.06.009

Zakaria, C., Kassahun, H., Yang, X., Labbe, J. C., Nilsen, H., and Ramotar, D. (2010). *Caenorhabditis elegans* APN-1 plays a vital role in maintaining genome stability. *DNA Repair.* 9, 169–176. doi: 10.1016/j.dnarep.2009.11.007

Zaky, A., Busso, C., Izumi, T., Chattopadhyay, R., Bassiouny, A., Mitra, S., et al. (2008). Regulation of the human AP-endonuclease (APE1/Ref-1) expression by the tumor suppressor p53 in response to DNA damage. *Nucleic Acids Res.* 36, 1555–1566. doi: 10.1093/nar/gkm1173

Zauri, M., Berridge, G., Thezenas, M. L., Pugh, K. M., Goldin, R., Kessler, B. M., et al. (2015). CDA directs metabolism of epigenetic nucleosides revealing a therapeutic window in cancer. *Nature* 524, 114–118. doi: 10.1038/nature14948

Conflict of Interest: The authors declare that the research was conducted in the absence of any commercial or financial relationships that could be construed as a potential conflict of interest.

frontiers in Cell and Developmental Biology

REVIEW
published: 21 December 2020
doi: 10.3389/fcell.2020.607045

DNA-Histone Cross-Links: Formation and Repair

Manideep C. Pachva[1], Alexei F. Kisselev[2], Bakhyt T. Matkarimov[3], Murat Saparbaev[4] and Regina Groisman[4]**

[1] Department of Molecular Oncology, British Columbia Cancer Research Centre, Vancouver, BC, Canada, [2] Department Drug Discovery and Development, Harrison School of Pharmacy, Auburn University, Auburn, AL, United States, [3] National Laboratory Astana, Nazarbayev University, Nur-Sultan, Kazakhstan, [4] Groupe "Mechanisms of DNA Repair and Carcinogenesis", Equipe Labellisée LIGUE 2016, CNRS UMR 9019, Université Paris-Saclay, Villejuif, France

OPEN ACCESS

Edited by:
Nikita Kuznetsov, Institute of Chemical Biology and Fundamental Medicine (RAS), Russia

Reviewed by:
Anna Yudkina, Institute of Chemical Biology and Fundamental Medicine (RAS), Russia
Chunying Li, Georgia State University, United States

***Correspondence:**
Murat Saparbaev
murat.saparbaev@gustaveroussy.fr
Regina Groisman
regina.groisman@gustaveroussy.fr

Specialty section:
This article was submitted to Cell Death and Survival, a section of the journal Frontiers in Cell and Developmental Biology

Received: *16 September 2020*
Accepted: *30 November 2020*
Published: *21 December 2020*

Citation:
Pachva MC, Kisselev AF, Matkarimov BT, Saparbaev M and Groisman R (2020) DNA-Histone Cross-Links: Formation and Repair. Front. Cell Dev. Biol. 8:607045. doi: 10.3389/fcell.2020.607045

The nucleosome is a stretch of DNA wrapped around a histone octamer. Electrostatic interactions and hydrogen bonds between histones and DNA are vital for the stable organization of nucleosome core particles, and for the folding of chromatin into more compact structures, which regulate gene expression via controlled access to DNA. As a drawback of tight association, under genotoxic stress, DNA can accidentally cross-link to histone in a covalent manner, generating a highly toxic DNA-histone cross-link (DHC). DHC is a bulky lesion that can impede DNA transcription, replication, and repair, often with lethal consequences. The chemotherapeutic agent cisplatin, as well as ionizing and ultraviolet irradiations and endogenously occurring reactive aldehydes, generate DHCs by forming either stable or transient covalent bonds between DNA and side-chain amino groups of histone lysine residues. The mechanisms of DHC repair start to unravel, and certain common principles of DNA-protein cross-link (DPC) repair mechanisms that participate in the removal of cross-linked histones from DNA have been described. In general, DPC is removed via a two-step repair mechanism. First, cross-linked proteins are degraded by specific DPC proteases or by the proteasome, relieving steric hindrance. Second, the remaining DNA-peptide cross-links are eliminated in various DNA repair pathways. Delineating the molecular mechanisms of DHC repair would help target specific DNA repair proteins for therapeutic intervention to combat tumor resistance to chemotherapy and radiotherapy.

Keywords: DNA-histone cross-link, nucleosome core particle, chromatin, genome instability, spartan protease, proteasome, DNA repair

INTRODUCTION

Cellular DNA is constantly altered by endogenous and exogenous factors, resulting in tens of thousands of lesions in a human cell every day (Lindahl, 1993). This damage may be classified into two types according to size: non-bulky DNA and bulky DNA. Non-bulky DNA lesions include base mismatches, abasic sites, and small base modifications, which in general are repaired by mismatch repair (MMR), base excision repair (BER), nucleotide incision repair (NIR), direct reversal

repair (DRR), and translesion DNA synthesis (TLS) (Gros et al., 2004; Fortini and Dogliotti, 2007; Sharma et al., 2013; Yi and He, 2013; Ignatov et al., 2017). Bulky DNA lesions include, among other types of damage: double-strand breaks, DNA-protein cross-links (DPCs), and intra- and inter-strand DNA cross-links. The structural complexity of certain bulky DNA lesions requires the use of several DNA repair pathways acting in a coordinated manner, including homologous recombination (HR), non-homologous DNA end-joining (NHEJ), nucleotide excision repair (NER), TLS and BER; Fanconi anemia (FA) signaling system and complex proteolytic machinery (Ishchenko et al., 2006; Ho and Schärer, 2010; Duxin et al., 2014; Tretyakova et al., 2015; Martin et al., 2017). Non-bulky DNA lesions cause limited and local DNA perturbations, whereas bulky ones induce significant distortions in the overall DNA helix structure (Ide et al., 2011). DNA-protein cross-links (DPCs) are formed when a protein covalently binds to DNA (Tretyakova et al., 2015). They are difficult to repair because of their super-bulky character compared with known voluminous, helix-distorting DNA lesions, such as UV-induced pyrimidine dimers. These super-bulky adducts can be generated by exposure of cells to endogenous and exogenous cross-linking agents (Stingele et al., 2017; Zhang et al., 2020). The presence of protein covalently attached to DNA strongly interferes with DNA replication, transcription, repair, and chromatin remodeling (Kuo et al., 2007; Klages-Mundt and Li, 2017; Yudkina et al., 2018; Ji et al., 2019). DPCs may be classified into five types, according to the nature of the covalent link in the DNA-protein complex and the presence of DNA strand breaks (Ide et al., 2015, 2018; Nakano et al., 2017). Type 1, the most common type of DPC, is formed when proteins covalently link to a nitrogenous base in undisrupted DNA. Type 2-4 cross-links occur when DNA-cleaving enzymes are trapped in a covalent intermediate with a DNA strand (Ide et al., 2015, 2018; Nakano et al., 2017). Type 2 is formed when bi-functional DNA glycosylases and repair enzymes containing β-lyase activity such as DNA polymerase β and Parp1 irreversibly bind to a cleaved apurinic/apyrimidinic (AP) site (Ide et al., 2015, 2018; Nakano et al., 2017). Type 3 is generated during abortive DNA strand cleavage by topoisomerase 1 (Top1) and formation of a covalent tyrosinyl–phosphodiester bond between the protein and the 3′-terminal DNA phosphate moiety of SSB (Ide et al., 2015, 2018; Nakano et al., 2017). The abortive action of topoisomerase 2 (Top2) generates type 4 DPC, in which tyrosine is linked to the 5′-terminal phosphates of double-strand breaks (DSB) (Ide et al., 2015, 2018; Nakano et al., 2017). Recently, a new type of DPC emerged after the discovery of HMCES, a 5-hydroxymethylcytosine (5hmC) binding protein which can recognize abasic sites in single stranded DNA (ssDNA) and form a covalent ssDNA-HMCES crosslink to prevent error-prone translesion synthesis past the lesion (Mohni et al., 2019). Because of the differences in structure and composition between these five groups, each type of DPC is processed by a distinct repair mechanism. It seems difficult to remove super-bulky Type 1 DPC in the canonical linear DNA excision repair pathways because the presence of a protein molecule blocks access to DNA. Nevertheless, recent studies have revealed that nucleotide excision repair (NER) and homologous recombination (HR) can remove certain types of DPCs in a nuclease-dependent manner (Zhang et al., 2020). However, it is still not clear whether these repair pathways could deal with other types of DPC. Stingele et al. (2017) have proposed that each constituent of DPC: DNA, protein, and the covalent linkage between them might be processed by three different repair mechanisms. A recent paper by Kühbacher and Duxin (2020) provides comprehensive review on the formation and repair of DPCs. In this review, we summarize the current knowledge regarding the repair mechanisms involved in removal of DHCs induced by various genotoxic agents. Covalent cross-linking to DNA occurs more often with DNA binding proteins, such as histones, transcription factors, and DNA metabolizing enzymes including repair factors and topoisomerases (Klages-Mundt and Li, 2017). In the cell nucleus, histones are assembled into an octamer forming the nucleosome core with 147 bp of DNA wrapped around and tightly bound to it (Luger et al., 1997, 2012). This basic chromatin structure makes histones primary targets of DNA cross-linking agents, leading to the formation of DNA-histone cross-links (DHC) (Solomon and Varshavsky, 1985). Currently, the repair mechanisms counteracting DHCs generated by various factors only started to unravel.

DNA-HISTONE CROSS-LINKS (DHCs)

Nucleosomal DNA is packaged into compact units referred as chromosomes, in which core nucleosome particles are connected by stretches of linker DNA up to 80 bp length. A nucleosome core particle (NCP) is composed of two copies each of histones H2A, H2B, H3, and H4. The molecular weight of individual histones range from 11 to 22 KDa, whereas the molecular weight of histone octamer in NCP is 210 KDa (Eickbush and Moudrianakis, 1978; Luger et al., 1997). The stability of the nucleosome is based on various protein-protein interactions, and numerous non-covalent electrostatic and hydrogen bonds between histones and the DNA duplex (Luger et al., 1997, 2012; Davey et al., 2002; Rohs et al., 2009). The primary structure of chromatin can be depicted as a beads-on-a-string organization of individual nucleosomes, which can be further folded into compact secondary and tertiary structures, with the help of histone variants present in certain nucleosomes and post-translational modifications (PTMs) situated in disordered histone tails (Woodcock and Dimitrov, 2001; Luger et al., 2012). The folding of chromatin into primary, secondary, and tertiary structures is crucial for regulating the accessibility of DNA to complex multi-protein machinery involved in DNA replication, transcription, and repair. Non-covalent interactions between DNA and histones enable chromatin dynamics to switch between the closed and open conformations. DHCs impair chromatin flexibility, which may subsequently affect long-distance interactions in chromatin that would indirectly disturb DNA replication, transcription, and repair within a topologically associating domain (TAD) (Hinz et al., 2010; Todd and Lippard, 2010; Tretyakova et al., 2015; Hauer and Gasser, 2017; Nakano et al., 2017). DHCs belong to type 1, a non-enzymatic form of DPC, in which a protein is covalently attached to an undisrupted DNA (Ide et al., 2011). Several comprehensive studies describing the mechanisms of formation of DHCs have

been published recently (Ming et al., 2017; Shang et al., 2019; Yang and Greenberg, 2019), nevertheless, it is not known whether specific repair mechanisms for the removal of DHCs exist. In this review, we focus mainly on the repair pathways of DHCs and briefly describe their formation.

Formation of DHCs

A water-soluble covalent complex of DNA and histones (H2A and H2B) was first identified in a UV cross-linking assay (Smith, 1966; Sperling and Sperling, 1978). With this finding, it became evident that UV irradiation can induce DHCs in addition to well-known pyrimidine dimers. It was then discovered that exogenous and endogenous aldehydes could also form DHCs in cells (Lam et al., 1985; Kuykendall and Bogdanffy, 1992). More than 10% of amino acid residues in histones are lysines, whereas, aldehydes preferentially react with ε-amino groups of lysine side-chains with the formation of a Schiff base, which further reacts with exocyclic amino groups of guanine, adenine, and cytosine DNA bases, creating methylene linkage. Many cross-linking agents, such as chromate, metal ions, and cisplatin (*cis*-diaminedichloroplatinum-II), also induce DHCs in cells (Zhitkovich and Costa, 1992). Platinum compounds not only cause DNA-DNA cross-links but also covalently link DNA-protein complexes. In the case of histones (**Figure 1A**), these compounds cross-link ε-amino-groups of lysines and N^7 atoms of guanosines (Tretyakova et al., 2015; Ming et al., 2017). Cross-links between DNA and methionine residues were also observed in an X-ray structure of nucleosomes treated with platinum compounds (Wu et al., 2008). Exposure of purified nucleosome to bi-functional alkylating agents (e.g., nitrogen mustards) also cross-links histones to guanosines in DNA (Shang et al., 2019); however, these types of cross-links in cells are much less abundant than DNA cross-links with cysteines and histidines of non-histone proteins (Loeber et al., 2009).

Histones can also directly react with 5-formylcytosine, a naturally occurring modified DNA base, and 8-oxoguanine, a major oxidative DNA damage product. Lysine amino groups react with 5-formylcytosine (**Figure 1B**), with the formation of a reversible Schiff base (Li et al., 2017; Raiber et al., 2018). The reaction of lysine side-chains with 8-oxoguanosine produced a stable protein cross-linked spiroiminodihydantoin (Sp) adduct (Xu et al., 2008).

Finally, the majority of DHCs are produced by a reaction between histone lysines and an aldehyde form of the 2′-deoxyribose at apurinic/apyrimidinic (AP) sites (**Figure 1C**) that are either directly formed upon damage or generated during excision of damaged bases in the base excision repair pathway (Solomon and Varshavsky, 1985; Sczepanski et al., 2010). The resulting Schiff base often undergoes strand-breaking ß-elimination, followed by a reversal of a histone-DNA cross-link. Since histone emerges unaltered from the reaction, the whole process is sometimes referred to as histone-catalyzed strand cleavage at AP sites (Ren et al., 2019). It should be noted that histone PTMs and the chromatin state could have a significant impact on DHC formation at abasic sites and with DNA bases (Sczepanski et al., 2010; Bowman and Poirier, 2015).

Mechanisms of Repair of DHC

Although DPCs, especially DHCs, often occur in cells and present a constant threat to genome stability, it is presumed that, except for tyrosyl-DNA phosphodiesterases, there is no specialized DNA repair pathway dedicated to meet these super-bulky challenges. Instead, the cell employs several distinct DNA repair and protein degradation mechanisms to target cross-linked DNA and protein/histone components in a given DPC/DHC. The covalently bound protein could be detected and degraded to a small peptide by cell proteolytic machinery, such as the specialized proteases SPRTN/Wss1, Ddi1, and GCNA1, or by proteasome, an ATP-dependent multi-subunit protease complex, whereas the damaged DNA component is detected and repaired in the NER, BER, HR, NHEJ, and FA pathways.

Proteasome-Dependent Proteolysis of Histones Cross-Linked to DNA

Proteasome-mediated proteolysis is the major pathway for the degradation of damaged proteins in a cell. A 26S proteasome consists of a cylindrical 20S core particle and one or two 19S regulatory particles (Ciechanover, 1998; Lecker et al., 2006). Although 20S core can bind to different regulatory particles, only the 19S particle confers the ability to degrade ubiquitylated proteins (Coux et al., 1996; Adams, 2004; Stadtmueller and Hill, 2011). Considering the vital role of the proteasome in the degradation of damaged protein, proteasome and ubiquitin involvement in the proteolysis of DHCs or DPCs remains a topic of debate. Inhibition of proteasome in *Xenopus* egg extracts did not stabilize the DPCs (Nakano et al., 2007; Duxin et al., 2014). However, many studies of the repair of DPCs in mammalian cells suggest proteasome participation (Adams, 2004; Baker et al., 2007; Zecevic et al., 2010; Larsen et al., 2019). Proteasome involvement in DHC removal surfaced for the first time in the research of Quievryn and Zhitkovich (2000), who discovered that proteasome inhibitors prevent the removal of DHCs and sensitize human cells to lower levels of formaldehyde. A study in *Xenopus* egg extracts found that DPCs are ubiquitylated by TRAIP E3 ubiquitin ligase and are subsequently degraded by the proteasome (Duxin et al., 2014; Larsen et al., 2019). However, an earlier study clearly demonstrated that DPCs are not marked with polyubiquitin chains, but are nevertheless subjected to proteasomal degradation by a mechanism that is not well understood (Nakano et al., 2009). The 26S proteasome can degrade purified non-ubiquitylated histones (Kisselev et al., 2006), raising the possibility of proteasomal degradation of non-ubiquitylated damaged histones in cells. A couple of studies have demonstrated that during replication stress induced by genotoxic agents, histones are hyperacetylated, and then specifically degraded in a ubiquitin-independent manner by a complex of 20S proteasome with PA200 proteasome activator, a distinct regulatory particle (Qian et al., 2013; Mandemaker et al., 2018). Although these studies have demonstrated that the ubiquitin-independent degradation of acetylated histones alleviates replication stress, the additional function of PA200-20S

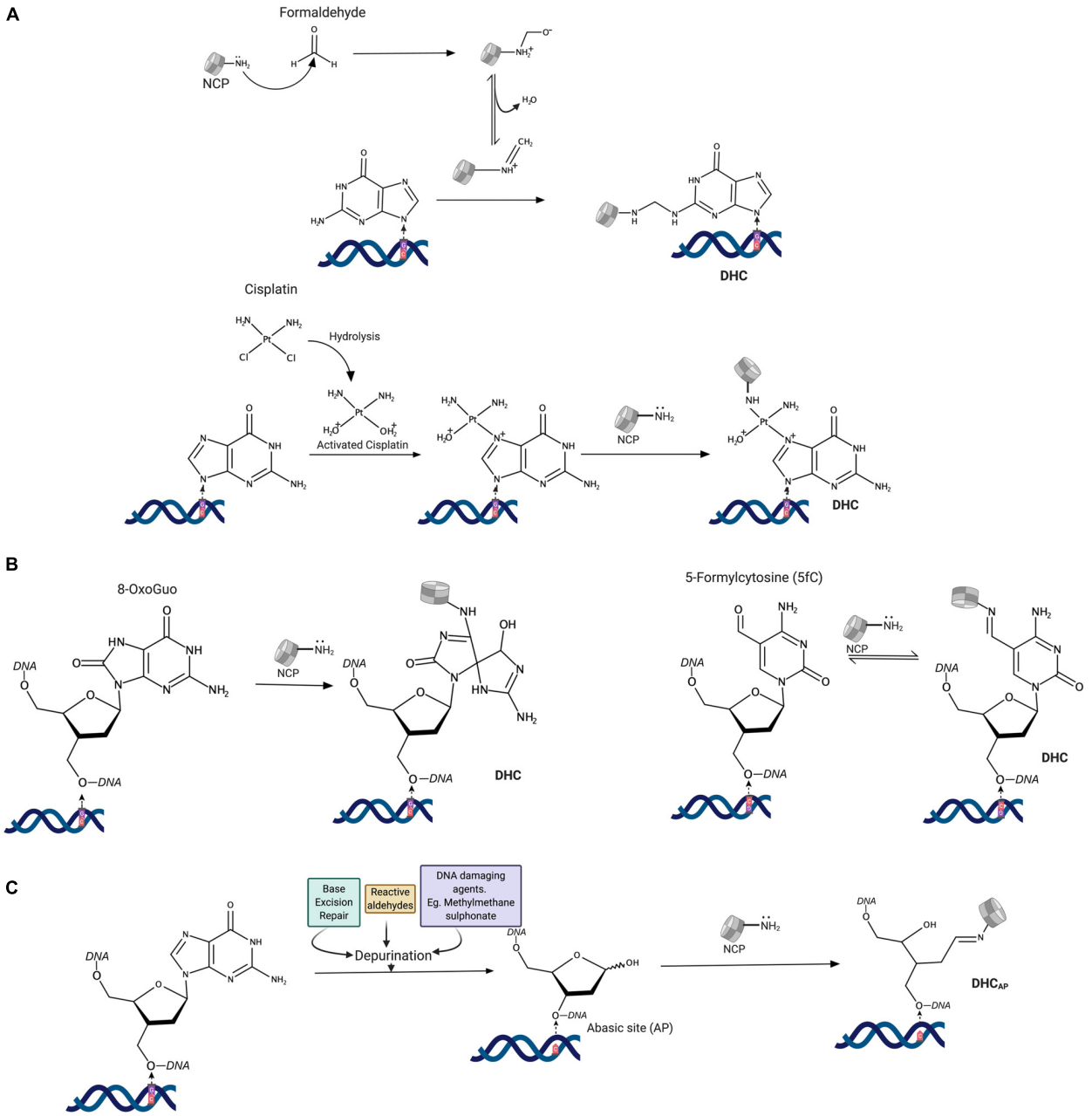

FIGURE 1 | Mechanisms of histone-DNA cross-links formation. **(A)** Reaction mechanisms of DNA cross-linking agents. **(B)** Direct cross-linking of histones to modified DNA bases. **(C)** Abasic site mediated cross-linking of histones to DNA. NCP-NH_2: *N*-terminal amine (Lysine) of histones in the nucleosome core.

proteasome in DHC repair cannot be excluded. Moreover, PA200 was detected in nuclear speckles, and its role in DNA repair has been proposed (Ustrell et al., 2002). Thus, more detailed understanding of the role of proteasome in DHC repair requires further investigation.

The 20S proteasome is a hollow, barrel-shaped particle composed of 28 non-identical subunits arranged into four stacked rings. The active sites are sequestered inside an internal cavity separated from regulatory 19S and PA200 complexes by a gated channel. This 13Å channel is too narrow for a folded protein to enter (Löwe et al., 1995; Groll et al., 1997). For complete degradation of a DNA-cross-linked protein, the cross-linked DNA nucleotide itself would have to enter the proteolytic chamber, pulling a DNA strand inside. However, the DNA component of a DPC might be too bulky to enter the channel. Therefore, proteasome can remove only part of a cross-linked protein, converting DHC into a smaller DNA-peptide cross-link. Alternatively, traditional proteases, in which an active site is located in a cleft on the enzyme surface, could be involved in excision of the bulk of the non-cross-linked polypeptide chain,

which can then be degraded by any of these proteases and by the proteasome.

METALLOPROTEASE-BASED PROTEOLYSIS OF HISTONES CROSS-LINKED TO DNA

Wss1 (weak suppressor of smt3) is a DNA-dependent metalloprotease, whose role in DPC removal was unraveled in a study in which treatment of yeast cells lacking Wss1 and TDP1 with formaldehyde resulted in a synthetic sickness (Stingele et al., 2014). It was also demonstrated that SUMOylation of both enzymatic and non-enzymatic DPCs by DNA-bound SUMO ligases targets them to Wss1 (Psakhye and Jentsch, 2012; Jentsch and Psakhye, 2013; Stingele et al., 2014; Balakirev et al., 2015). Search for an ortholog of Wss1 in higher eukaryotes revealed another metalloprotease, Dvc1/Spartan, of the SprT protease family, whose function was initially thought to be a removal of Polη from chromatin during translesion DNA repair synthesis. (Davis et al., 2012; Mosbech et al., 2012). Spartan/Dvc1 has a similar domain organization and shares a common evolutionary origin with Wss1. Like Wss1, Dvc1/Spartan also repairs DPCs in *Xenopus* egg extracts (Duxin et al., 2014; Stingele et al., 2014, 2015). A detailed study of DPC removal by Spartan/Dvc1 in *Xenopus* levis revealed stepwise proteolysis of DPC during DNA replication (Larsen et al., 2019). During replication, on both the leading and lagging strands, CMG helicase bypasses the DPC lesion, followed by the stalling of DNA polymerase (Duxin et al., 2014; Larsen et al., 2019; Sparks et al., 2019). Replicative DNA polymerase stalled at DPC triggers the recruitment of Spartan protease (**Figure 2A**), which then degrades the DPC protein component (Larsen et al., 2019; Reinking et al., 2020). However, in the case of DHCs, CMG helicase bypass would depend on the complexity of nucleosomal damage. If the crosslink involves just a single histone within NCP, then CMG helicase can bypass the DHC due to small size of protein residue. If multiple histones within NCP are cross-linked, then the large nucleosome-size DHC should stall CMG helicase, triggering the ubiquitination of crosslinked histones by TRAIP E3 ubiquitin ligase and their subsequent degradation by 26S proteasome (Nakano et al., 2013; Larsen et al., 2019; Sparks et al., 2019). In contrast to Wss1, targeting of DPCs by Spartan/Dvc1 does not require SUMOylation of DPC (Duxin et al., 2014; Larsen et al., 2019). Several studies have demonstrated that proteasome and Spartan might work in concert to attain efficient DPC proteolysis. For proteolysis of DPC by proteasome, the active site topology in the 20S core particle makes it arduous for efficient proteolysis, leaving a larger peptide adduct, which could be further degraded by Spartan (Larsen et al., 2019; Sparks et al., 2019). The above observations support a hypothesis proposed by the Walter laboratory (Larsen et al., 2019) that initial proteolysis of DPC by proteasome may help reduce the size of a DPC for the CMG helicase bypass. This stepwise process applies for most type 1 DPCs when histones cross-linked to DNA are initially degraded either by 26S proteasome or PA200-20S proteasome, and in a second step by Spartan (**Figure 2A**). Validation of this hypothetical order of steps in proteolysis of DHC by the proteasome and Spartan requires more research. However, a recent study proved that Wss1 is actively involved in histone proteolysis in a NCP during replication stress (Maddi et al., 2020). Although this study showed that Wss1 removes histones non-covalently bound to DNA, it is very likely that this protease can also remove histones covalently cross-linked to DNA. Initially, it was thought that Spartan/Dvc1 could only execute DPC proteolysis in a replication-dependent manner, but later it was demonstrated that Spartan/Dvc1 could act on a single-stranded DNA to degrade DPC independently of replisome (Larsen et al., 2019). A couple of other studies have also demonstrated that in fly embryos Spartan is recruited to chromatin before replication and that its absence greatly sensitized the arrested, non-replicating L1 worm larvae to formaldehyde (Delabaere et al., 2014; Stingele et al., 2016; Reinking et al., 2020). This evidence clearly defines a role for Spartan in the replication-independent repair of DPCs, which may be required for chromatin-based transactions associated with transcription. More data are required to confirm the existence of transcription-coupled DPC repair in cells.

Germ cell nuclear acidic peptidase (GCNA), also known as germ cell nuclear antigen or acidic repeat containing (ACRC), is a metalloprotease that contains an SprT domain, such as Spartan/Dvc1 (Carmell et al., 2016; Dokshin et al., 2020). It has recently been demonstrated in *Caenorhabditis elegans* that GCNA/ACRC, with its C-terminal Spartan (SprT)-domain, can also be involved in the removal of formaldehyde-induced DPCs in exposed cells (Borgermann et al., 2019). Recently, another study of Drosophila embryos clearly established that the loss of GCNA resulted in the accumulation of DPCs that included histones, confirming the role of GCNA in the removal of DHCs (Bhargava et al., 2020). Like Wss1, it was proved that SUMOylation of DPC triggers the recruitment of GCNA/ACRC protease, but in a replication-independent manner (Borgermann et al., 2019). Noteworthy, the chromatin-associated proteins were highly SUMOylated (Borgermann et al., 2019) (**Figure 2B**), suggesting that formaldehyde induces DHCs, which are then SUMOylated to recruit GCNA/ACRC SprT protease. However, the detailed mechanism of GCNA/ACRC-mediated repair of DHC requires further investigation.

Ddi1 PROTEASE-BASED PROTEOLYSIS OF HISTONES CROSS-LINKED TO DNA

It was recently shown that a novel protease, Ddi1 (DNA-damage inducible-1), is involved in DPC repair (Serbyn et al., 2020). Ddi1 is an aspartic protease. Its protease domain is structurally similar to that of retroviral aspartic proteases (Krylov and Koonin, 2001; Sirkis et al., 2006). Ddi1 is involved in response to hydroxyurea (HU)-induced replication stress by facilitating the removal of replication termination factor RTF2, restarting stalled replication forks (Kottemann et al., 2018). In addition, it is well documented that *Saccharomyces cerevisiae* Ddi1 contains a ubiquitin-like (UBL)-ubiquitin associated (UBA) domain, which enables the protein to act as a shuttle delivering ubiquitylated proteins to the

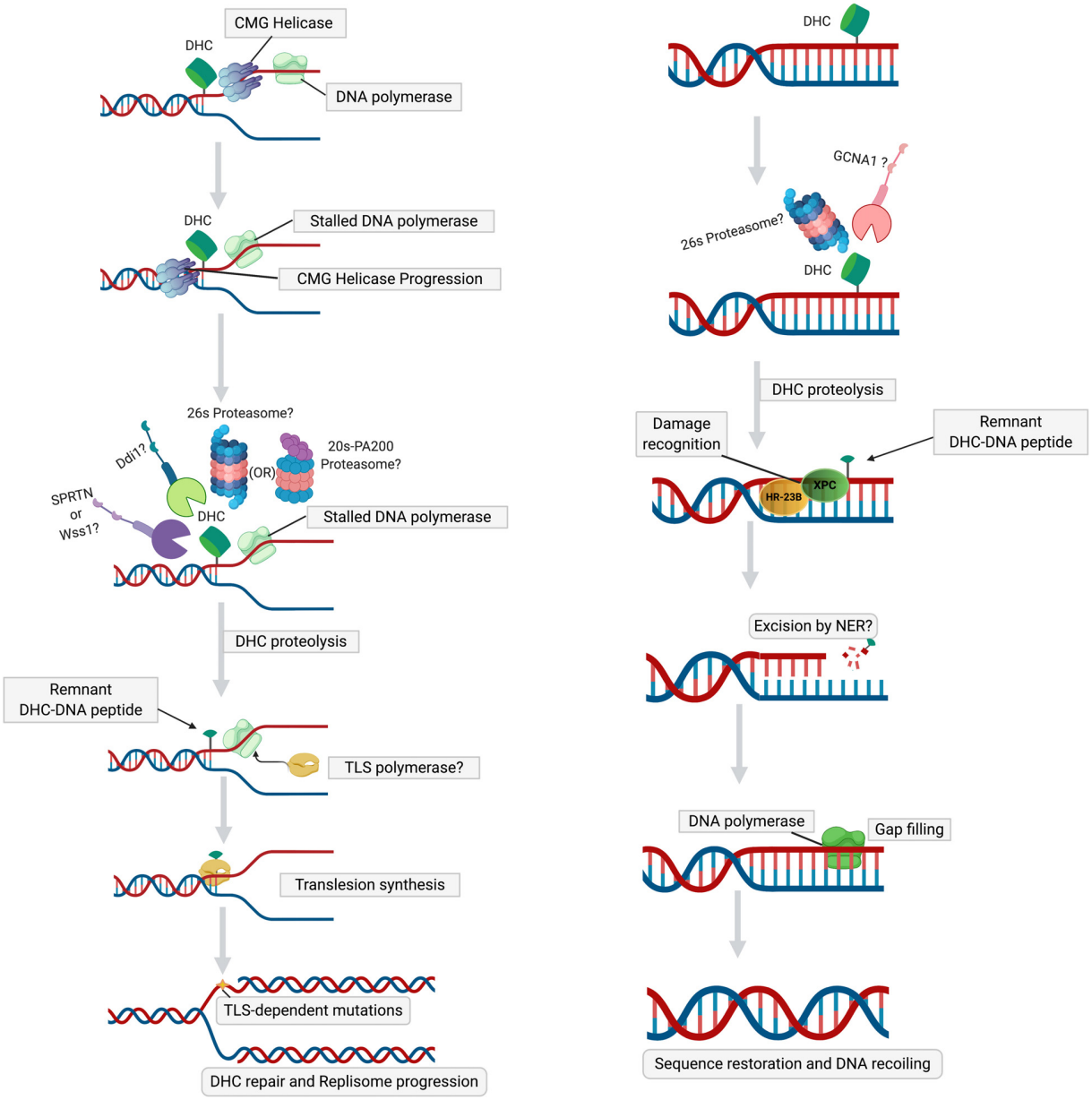

FIGURE 2 | Mechanisms of DHC repair. **(A)** Replication-dependent DHC removal. Stalling of DNA polymerase at DHC during replication triggers proteolysis of DHC by the proteasome (26S or PA200), followed either by the SPRTN or Ddi1 proteases. The peptide-DNA crosslink, a product of proteolyzed DHC, is bypassed by translesion synthesis (TLS) DNA polymerases, resuming the replisome progression. **(B)** Replication-independent DHC removal. In non-dividing cells, when histones are cross-linked to DNA, distortion of the DNA helix induces histone PTMs (acetylation or SUMOylation) and chromatin opening, thus permitting the proteolysis of DHC by 26S proteasome or GCNA1 protease. The peptide-DNA crosslink, a remnant of proteolyzed DHC, is then excised by NER, followed by gap-filling by DNA polymerase and ligation, which lead to the restoration of primary DNA sequence and chromatin.

proteasome (Dantuma et al., 2009). However, a genetic screen using the *tdp1wss1* mutant defective in the processing of DNA-Top1 covalent cross-link (Top1cc), revealed that Ddi1 could rescue mutant cells treated with Top1cc trapping and other genotoxic agents (Serbyn et al., 2020). Retention of Flp-Nick-Induced DPC in Ddi1-depleted cells confirmed a direct role of Ddi1 in DPC repair, due to proteolysis catalyzed by its retroviral-like protease domain (Krylov and Koonin, 2001; Serbyn et al., 2020). Previous evidence supports the idea that the proteolytic function of Ddi1 in DNA repair is replisome-dependent (Clarke et al., 2001; Kottemann et al., 2018) (**Figure 2A**). However, Ddi1-dependent proteolysis of stalled RNA polymerase II (Pol II)

on chromatin suggests an additional function of this protease (Serbyn et al., 2020). Interestingly, it has been demonstrated that Ddi1-mediated proteolysis of DPCs can be a proteasome-independent compensatory mechanism in the case of Wss1 dysfunction (Serbyn et al., 2020). Yeast Ddi1, and the human ortholog DDI2, are more dependent on poly-ubiquitination as compared to proteasome; these proteases cannot cleave non-ubiquitylated proteins and prefer substrates bearing extra-long ubiquitin chains (Sivá et al., 2016; Dirac-Svejstrup et al., 2020; Yip et al., 2020). Serbyn et al. (2020) found that depletion of Ddi1 makes cells hypersensitive to formaldehyde, suggesting that DHC can be a major substrate of aspartyl protease-catalyzed proteolysis. However, the extension of this function of yeast Ddi1 to its human DDI2 ortholog remains unclear, since certain structural domains of Ddi1 and human DDI2 are not evolutionarily conserved (Sivá et al., 2016; Trempe et al., 2016). In conclusion, the respective roles of Ddi1 and DDI2 in the removal of DHCs in higher eukaryotes remain to be investigated.

DNA REPAIR PATHWAYS IN DHC REMOVAL

As mentioned earlier, protein components (histones) of DHC are mainly targeted by specific proteases; however, partial proteolysis of cross-linked histones will still leave a small peptide covalently attached to DNA, requiring the coupling of proteases with classical DNA repair pathways to ensure complete removal of DHC and restoration of the primary DNA structure. In absence of studies on the DHC specific repair mechanisms, in this review we tried to infer the knowledge available on specific type 1 DPC repair mechanisms that are applicable to DHCs.

Nucleotide Excision Repair

Several biochemical and genetic studies showed that NER-deficient cells are sensitive to formaldehyde, suggesting direct involvement of NER in DHC removal (Nishioka, 1973; Takahashi et al., 1985). However, other studies have revealed that NER defective cells are not sensitive to 5-aza-2′-deoxycytidine (5-azadC)-based treatment, which induces cross-linking of DNA cytosine residues to DNA methyltransferase 1 (Dnmt1). This implies that NER can excise DPCs with smaller proteins (<8–12 kDa) induced by formaldehyde, but does not excise DPCs that contain proteins of larger size (>15 kDa), induced by 5-azaC (Bhagwat and Roberts, 1987; Lal et al., 1988; Nakano et al., 2007). This size limitation for excision of DPCs by bacterial NER may be attributed to the strong dependence of UvrB loading efficiency on DPC size, which subsequently influences the overall incision efficiency of the UvrABC nuclease complex. Thus, bacterial NER machinery can make bracketed incisions on DNA strands containing DPC with a small peptide, but not with a large one (Minko et al., 2002, 2005; Nakano et al., 2007). Histones are relatively small proteins ranging in size from 11 to 16 kDa; it was therefore proposed that DHCs could be removed in the NER pathway without preceding proteolysis step. Based on these observations, one may also propose that DHCs/DPCs induced by AP sites in DNA might be removed by NER (Torres-Ramos et al., 2000; Sczepanski et al., 2010). However, the role of NER in repair of AP sites induced DHCs remains to be established. A few studies have demonstrated that NER is implicated in DPC repair in mammalian cells (Fornace, 1982; Baker et al., 2007). Each histone is very small in size; they are assembled into a large NCP, which may sterically inhibit the loading of XPC/Rad23B and XPA/RPA complexes onto the DHC site (Ide et al., 2011). When the XPA/RPA complex fails to bind to the damage site, TFIIH cannot access and open up the DNA duplex around DHC to discriminate between intact and damaged DNA strands. All these render subsequent cleavage of this strand by XPG and XPF-ERCC1 nucleases unfeasible. Thus, proteolysis of DNA-cross-linked NCP might be required for efficient removal of a histone trapped on DNA by the NER machinery (Nakano et al., 2009). A study using mammalian cells has demonstrated that XPF/ERCC1 nuclease requires pre-processing of the cross-linked protein adduct by the proteasome and proteases before its removal (Nakano et al., 2009; Zhang et al., 2011; Stingele et al., 2017). In *uvrA* cells, plasmid cross-linked to the partially digested histone H1 (peptide sizes: 4.5 kDa and 1.8–3.5 kDa) was more efficiently repaired than a DPC containing a full-length histone (22 kDa) (Nakano et al., 2007) (**Figure 2A**). It is also worth noting that chromatin remodeling at a DNA damage site is required to provide access to NER machinery (Dinant et al., 2012). Covalent cross-linking of histones will impede this process, strongly suggesting that shrinkage of the bulky protein component must precede repair of the DNA component by the NER pathway. Further studies are required to understand the involvement of specific repair pathway(s) that precede and succeed NER and the sequence of steps involved in the removal of DPC/DHC (involving NER).

Homologous Recombination

The role of homologous recombination in DPC repair has been addressed in bacterial genetic studies, where it was found that *Escherichia coli recA* and *recB* mutants defective for homologous recombination (HR) are sensitized to formaldehyde and 5-azadC-induced DPCs (Nishioka, 1973; Takahashi et al., 1985). Further studies revealed that the role of HR in DPC repair is highly conserved in mammalian cells, and that clipping of DPC by the conventional MRN complex leads to strong resistance to DPC-inducing agents (Connelly et al., 2003; Neale et al., 2005; Ridpath et al., 2007; de Graaf et al., 2009; Orta et al., 2013). MRN, a heterotrimeric protein complex, is a DNA nuclease involved in the resection of a double-strand break (DSB) that initiates the HR pathway (Neale et al., 2005; Rothenberg et al., 2009). Increased sister chromatid exchange rates and accumulation of DSBs and RAD51 foci near DPC in formaldehyde-treated mammalian cells further support involvement of HR pathway in DPC removal (Shaham et al., 1997). However, the molecular mechanism of HR-mediated DPC removal is still poorly understood. The repair of DPC in *E. coli* is dependent on the RecBCD nuclease that initiates the HR pathway (Bidnenko et al., 2002; Nakano et al., 2007). DSB adjacent to DPC and stalled replisome could be generated by re-replication of incomplete nascent DNA strands, with the subsequent collapse of the replication fork. They can also be generated by RecG helicase-mediated fork reversal, leading to

the formation of a Holliday junction, which is then processed by RecBCD nuclease to generate DSB (McGlynn and Lloyd, 2001; Michel et al., 2004; Payne et al., 2006; Nakano et al., 2007, 2009). Certain studies suggest that replisome stalling at DPC does not lead to fork collapse, because template switching via fork reversal may allow DNA synthesis (Nakano et al., 2007; Stingele et al., 2015; Klages-Mundt and Li, 2017). In addition, other studies showed that DSB formation is not observed during the replication-dependent repair of DPCs in *Xenopus* egg extracts and hamster cells treated with DPC-inducing agents (Speit et al., 2000; Duxin et al., 2014). Thus, studies regarding the induction of DSBs near DPC have provided conflicting results, necessitating further studies of the mechanisms of HR-mediated DPCs repair. Differences in the sensitivity of *E. coli recA* and *uvrA* mutants, deficient for HR and NER respectively, to large DPCs inducing 5-azadC, revealed that unlike NER, HR could repair large DPCs (Santi et al., 1984; Bhagwat and Roberts, 1987; Ide et al., 2011; Zhang et al., 2020). Since histones are small proteins (11–16 kDa), their size should not be an obstacle to DHC repair in the HR-pathway. However, HR may not directly repair the DHC lesion in the chromatin context until access is provided to DNA damage-sensing factors. Thus, pre-processing of NCP containing a DHC or a repair pathway that precedes HR must be required to repair DHC by HR. Further research is needed to validate this model.

Fanconi Anemia Pathway

The Fanconi anemia (FA) pathway is involved in the repair of inter-strand DNA cross-links (ICLs) and plays a pivotal role in cellular defense against reactive aldehydes (Ridpath et al., 2007; Rosado et al., 2011; Kottemann and Smogorzewska, 2013; Ceccaldi et al., 2016). However, the role of the FA pathway in DPCs repair is currently under debate (Duxin and Walter, 2015). A study conducted by Orta et al. (2013) suggests that Fanconi anemia-dependent HR is required for DPC removal in cells treated with 5-azadC. In addition, several studies have shown that cells depleted in FANC2, FANCQ/XPF, and FANCG proteins are sensitive to DPC-inducing agents, such as acetaldehyde, formaldehyde, and 5-azadC (Ridpath et al., 2007; Mechilli et al., 2008; Lorenti Garcia et al., 2009; Langevin et al., 2011; Rosado et al., 2011; Orta et al., 2013). The majority of DPCs induced by reactive aldehydes are DHCs (Solomon and Varshavsky, 1985). These results are in stark contrast to an *in vitro* study by Duxin et al. (2014), who demonstrated that depletion of FANCI-FANCD2 from *Xenopus* egg extracts inhibited ICL repair, but not DPC repair or TLS-mediated bypass. In agreement with latter observations, studies using *C. elegans* and mouse embryonic fibroblasts showed that depletion of FANCD2 did not affect the cells' sensitivity to formaldehyde (Stingele et al., 2016). Despite these conflicting reports, the potential role of FA pathway components in the removal of DHCs should not be overlooked. A conserved FANCM-MHF DNA remodeling complex that recognizes a DNA lesion at the stalled replication fork, contains histone-binding sites (Yan et al., 2010). Therefore, it is possible that the FANCM-MHF complex, which recruits downstream Fanconi proteins to excise DHC, could readily recognize DNA cross-linked histones. Future studies are necessary to confirm and delineate the role of the FA pathway in DHC removal, and to determine whether the FA pathway requires pre-processing of DHC/DPC for their removal.

Base Excision Repair

DNA glycosylase-initiated base excision repair (BER) is a major pathway for removing small non-bulky base lesions resulting from deamination, oxidation, and alkylation which do not significantly distort the DNA helix (Krokan and Bjørås, 2013). However, the DNA glycosylases NEIL1 and NEIL3 can also resolve psoralen-induced bulky ICLs in three- and four-stranded DNA structures (Couvé-Privat et al., 2007; Couvé et al., 2009; Martin et al., 2017). NEIL1, a bi-functional DNA glycosylase, can also repair Sp-amine adduct-containing DN-protein cross-links (McKibbin et al., 2013). Furthermore, another study demonstrated that a DPC generated as repair intermediate of PARP1, could be processed by BER machinery (Prasad et al., 2019). Thus, the role of BER may not be limited to small non-bulky DNA lesions.

Interestingly, it has been found that an oxidized AP site formed by a reactive oxygen species (ROS) can trap DNA polymerase β (Polβ) to form a stable DNA- Polβ cross-link (Polβ-DPC) (DeMott et al., 2002). It was later found that DNA glycosylase-generated AP sites can also trap several DNA repair proteins, such as PARP1, Ku proteins, DNA polymerase λ (Polλ), and other factors (Prasad et al., 2019; Quiñones et al., 2020). Thus, under certain circumstances, instead of repairing the lesion, BER can act as a source of a DPC lesion.

It is unknown whether impairment of BER machinery affects cells' sensitivity to various DPC inducing agents. Also, it is not clear whether BER, like NER, has a size limit for processing of DPCs. As mentioned earlier, histones in a NCP can cross-link to abasic sites. In fact, the AP site generated by a DNA glycosylase may trap histones to form a covalent DHC. A Schiff base at an AP site can lead to DNA strand scission, thus contributing to major nucleosomal DNA damage. Although detailed information on the role of BER in formation of DHC is available, at present, little is known about the role of DNA glycosylases and AP endonucleases in the repair of this chromatin damage. Past evidence suggests that NEIL1 DNA glycosylase has a flexible active site that can accommodate bulky modifications of DNA bases and efficiently remove them (Couvé et al., 2009; McKibbin et al., 2013). Thus, it is predicted that NEIL1, and possibly NEIL3, may play a role in the processing of DHC, but that remains to be confirmed. Also, several studies suggest that BER coupled to proteolysis could participate in the efficient removal of DPC/DHC (Hauer et al., 2017; Prasad et al., 2019; Quiñones et al., 2020). Hence, further studies are required to gather information on the role of BER proteins in DHC removal.

Translesion Synthesis

When a DNA replication fork stalls at unrepaired DNA damage, the cell can circumvent the obstacle through tolerance pathways, such as an HR-mediated template switch mechanism and translesion DNA synthesis (TLS). TLS is a lesion bypass mechanism that tolerates DNA damage and allows for DNA replication to proceed through unrepaired bulky nucleobase adducts (Woodgate, 1999; Friedberg et al., 2005; Lehmann et al.,

2007; Sale, 2013). DPCs are super-bulky lesions that can stall replication forks and lead to their collapse. These lesions require a collaborative network of several cellular repair systems to remove them. However, removal of DPC in a stalled replication fork could provoke fork collapse and generation of DSB, with detrimental consequences to a cell, depending on the DNA repair mechanism used. On the other hand, the TLS pathway initiated by specific DNA polymerases replicates over and past the lesion in the damaged DNA template, thus providing a form of DNA damage tolerance, which avoids fork collapse and DSB. Therefore, TLS can play an important role in the management of DPCs in cells. Indeed, several studies have reported that specialized TLS DNA polymerases can bypass DPCs (Duxin et al., 2014; Wickramaratne et al., 2016; Pande et al., 2017; Larsen et al., 2019). Nevertheless, these studies demonstrated that large non-processed DPCs require the degradation of large protein adducts to smaller peptides cross-linked to DNA to allow bypass by TLS DNA polymerases. Thus, partial proteolysis of DPCs is necessary for efficient TLS bypass (**Figure 2A**). Larsen et al. (2019) study in *Xenopus* egg extracts clearly established that DPC proteolysis by Spartan/Dvc1 ensures efficient bypass by TLS-specific DNA polymerases REV1-Polζ. Although TLS DNA polymerases help bypass the DPC lesion, the extension of DNA past the lesion by the same DNA polymerases is error-prone and can lead to mutagenesis. Hence, DNA repair pathways, such as mismatch repair (MMR) and NER, could be coupled with TLS to prevent DPC-induced mutations. A study by Wickramaratne et al. (2016) demonstrated that partially digested DHC (histones H4 and H2A) can be bypassed by human TLS DNA polymerases η and κ. However, the authors did not investigate proteolysis of DHCs and the specific proteases involved in their digestion and of the DNA repair pathways that follow TLS. Thus, understanding the role of TLS and associated repair systems in counteracting the genotoxic effects of DHCs requires further investigation.

THE INTERPLAY OF DHC REPAIR PATHWAYS

Due to the heterogeneity and super-bulky size of DHCs, several distinct DNA repair pathways may work in concert to remove them. Although cells lack DHC-specific damage sensors, these lesions can be detected and processed by well-known classic DNA repair pathways with the help of various proteases. When a replication fork is stalled at a DHC, the cross-linked histone could be digested by Spartan/Dvc1 protease and proteasome. Proteolysis of DHC by Spartan and proteasome could be backed up with Ddi1 protease in yeast, or with DDI2 in higher eukaryotes. After proteolysis, the remnant peptide could be bypassed by TLS DNA polymerases to avoid replication fork collapse (**Figure 2A**). Previous evidence also suggested that partial proteolysis of a DPC/DHC coupled with TLS could be a way to repair these complex DNA lesions (Duxin et al., 2014). However, to avoid TLS induced mutations, proteolysis of DPC/DHC could be coupled to NER and HR. Data from several studies support the idea that the combination of proteolysis and NER could be a convenient error-free mechanism for cells to remove the majority of DPCs. Nonetheless, proteolytic degradation of the protein component may also be coupled with BER during removal of DHC/DPC if NER cannot remove the remnant adduct after proteolysis. Considering that most histone cross-links are formed at abasic sites, the BER pathway may have a specific role in removal of AP site-induced DPCs. This leads us to hypothesize that for the efficient removal of AP site-induced DHCs, proteolysis coupled with BER could be one of the most preferred in cells under genotoxic stress conditions that promote DNA base loss (McKibbin et al., 2013; Prasad et al., 2019; Quiñones et al., 2020). One could speculate that HR proceeds after proteolysis. However, Stingele et al. (2014) have demonstrated that HR and proteolysis are two distinct means of resolving DPCs during the S phase of the cell cycle. When there is a DNA strand incision next to a DPC, or when the DPC load is high, the FA-dependent HR or MRN complex-dependent HR, respectively, may take over the protease-mediated repair. Certain aldehyde-induced DPCs require a DNA strand incision near the lesion, which is further processed by FA-dependent HR. Since reactive aldehydes preferentially induce DHCs, it is proposed that FA-dependent HR (ICL-like repair) may serve as a back-up mechanism when proteolysis coupled TLS/NER/BER is inactive or dysfunctional.

Replication-independent repair of DHCs may involve the 26S proteasome-mediated degradation of DHC, followed by removal of the remnant peptide by the global genome or transcription-coupled (TC) NER (Quievryn and Zhitkovich, 2000; de Graaf et al., 2009) (**Figure 2A**). Considering that Spartan/Dvc1 protease can play a role outside DNA replication, it may mediate DHC proteolysis that blocks transcription, and the remnants are then removed in the TC-NER sub-pathway. In germ and certain quiescent cells, the GCNA1/ACRC protease may be involved in degradation of DHCs, whereas remnants of the proteolysis could be removed by NER (**Figure 2B**). In the absence of NER, replication-independent proteolysis by proteasome 26S/Spartan/GCNA1 may be coupled with BER to remove DHCs. These hypothetical models of the interplay of different repair pathways in DHC removal require further studies to test them.

CONCLUDING REMARKS

DNA-protein cross-links occur frequently and are the most bulky DNA lesions in living cells. Among various DPCs, DHCs occupy a special place, because histones, the most abundant DNA-binding proteins, constitute the nucleosome, a basic structural unit of chromatin. Therefore, we propose to classify DNA-histone covalent complexes as a special DHC group of DPCs. Histones cross-link either to DNA bases, mostly guanines and 5-formylcytosines, or to the AP site sugar (Ren et al., 2019). With more than 10,000 abasic sites generated every day in a cell far exceeding the number of oxidized bases (Lindahl, 1993), this lesion is the most abundant type of endogenous DNA damage.

Indeed, around 10% of AP sites catalyze the formation of DPCs, among which the majority are likely to be DHCs (Ren et al., 2019). Therefore, it seems that hundreds, and perhaps even thousands of histone cross-links to abasic sites in DNA are formed every day in a cell. Even greater production of DHCs is expected in cells exposed to certain genotoxic stress, leading to significant biological consequences, such as sensitization of cancer cell to chemotherapeutic agents. It is difficult to delineate a single repair pathway for various types of DHCs. Similar to DPCs, the repair of super-bulky DHC lesions requires two steps: partial proteolysis of histone and repair of remaining cross-linked peptide via DNA excision. Cells utilize several proteases and DNA repair pathways for these purposes. Assuming that active BER can generate an excess number of AP sites as repair intermediates of DNA glycosylases, this repair pathway might be one of the major factors in the formation of DHCs in cells. A recent discovery of the role of DNA glycosylases of the Nei-family in repair of bulky ICLs suggests that the BER pathway may participate in removal of AP site-induced DHCs (Couvé-Privat et al., 2007; Semlow et al., 2016; Martin et al., 2017). In eukaryotic cells, chromatin dynamics plays an essential role in DHC removal by various DNA repair pathways. For example, it is well documented that partial and transient nucleosomal DNA unwrapping is indispensable for DNA repair and for transcription initiation. Indeed, several studies have indicated that on average, DNA unwrapping events occur several times per second (Li and Widom, 2004). DHCs should strongly interfere with natural nucleosome unwrapping, and hence with DNA lesion detection, signaling, and repair. Moreover, several laboratories have detected inter-nucleosomal cross-links, including DHCs mediated by histone tail domains. These structures should further impede accessibility of DNA lesions for the DNA repair machinery (Banerjee et al., 2018; Yang and Greenberg, 2019). This implies that PTMs of histone tails via lysine acetylation and methylation, and recruitment of chromatin remodeling complexes, may also influence DHC formation and repair (Yang et al., 2019). Blocking chromatin remodeling and DNA repair pathways involved in DHC removal should lead to the persistence of these DNA lesions and further impede chromatin-based transactions and chromatin organization. However, current knowledge regarding DNA repair pathways involved in DHC removal is far from complete. Further studies are required to delineate the mechanisms involved in the repair of DHCs.

AUTHOR CONTRIBUTIONS

MP, BM, MS, and RG wrote the DNA repair part of the review. MP, RG, and AK wrote the proteasome part of the review and prepared figures. All authors discussed and contributed to analysis of published literature and to writing the manuscript. All authors contributed to the article and approved the submitted version.

FUNDING

This work was supported by grants from la Ligue Nationale Française Contre le Cancer "Equipe LNCC 2016" (https://www.ligue-cancer.net) and Electricité de France RB 2020-02 (http://www.edf.fr) to MS, by Nazarbayev University Oak Ridge Associated Universities (ORAU) grant 091019CRP2111 to BM and by grant 1R01CA213223 from the National Cancer Institute to AK. MP is supported by a U54 Moonshot grant from the National Institutes of Health (NIH) and the SBF-SU2C grant from American Association of Cancer Research/Sub-Children's Hospital of Philadelphia to Dr. Poul Sorensen.

ACKNOWLEDGMENTS

We thank Biorender.com and Marvin Sketch for their assistance in preparation of the figures. We are grateful to Dr. Noah Horowitz for editing assistance.

REFERENCES

Adams, J. (2004). The development of proteasome inhibitors as anticancer drugs. *Cancer Cell* 5, 417–421. doi: 10.1016/S1535-6108(04)00120-5

Baker, D. J., Wuenschell, G., Xia, L., Termini, J., Bates, S. E., and Riggs, A. D. (2007). Nucleotide excision repair eliminates unique dna-protein cross-links from mammalian cells. *J. Biol. Chem.* 282, 22592–22604. doi: 10.1074/jbc.M702856200

Balakirev, M. Y., Mullally, J. E., Favier, A., Assard, N., Sulpice, E., and Lindsey, D. F. (2015). Wss1 metalloprotease partners with Cdc48/Doa1 in processing genotoxic SUMO conjugates. *eLife* 4:e06763. doi: 10.7554/eLife.06763

Banerjee, D. R., Deckard, C. E., Elinski, M. B., Buzbee, M. L., Wang, W. W., and Batteas, J. D. (2018). Plug-and-play approach for preparing chromatin containing site-specific DNA modifications: the influence of chromatin structure on base excision repair. *J. Am. Chem. Soc.* 140, 8260–8267. doi: 10.1021/jacs.8b04063

Bhagwat, A. S., and Roberts, R. J. (1987). Genetic analysis of the 5-azacytidine sensitivity of *Escherichia coli* K-12. *J. Bacteriol.* 169, 1537–1546. doi: 10.1128/jb.169.4.1537-1546.1987

Bhargava, V., Goldstein, C. D., Russell, L., Xu, L., Ahmed, M., Li, W., et al. (2020). GCNA preserves genome integrity and fertility across species. *Dev. Cell* 52, 38.e10–52.e10. doi: 10.1016/j.devcel.2019.11.007

Bidnenko, V., Ehrlich, S. D., and Michel, B. (2002). Replication fork collapse at replication terminator sequences. *EMBO J.* 21, 3898–3907. doi: 10.1093/emboj/cdf369

Borgermann, N., Ackermann, L., Schwertman, P., Hendriks, I. A., Thijssen, K., Liu, J. C., et al. (2019). SUMOylation promotes protective responses to DNA-protein crosslinks. *EMBO J.* 38:e101496. doi: 10.15252/embj.2019101496

Bowman, G. D., and Poirier, M. G. (2015). Post-translational modifications of histones that influence nucleosome dynamics. *Chem. Rev.* 115, 2274–2295. doi: 10.1021/cr500350x

Carmell, M. A., Dokshin, G. A., Skaletsky, H., Hu, Y.-C., van Wolfswinkel, J. C., Igarashi, K. J., et al. (2016). A widely employed germ cell marker is an ancient disordered protein with reproductive functions in diverse eukaryotes. *eLife* 5:e19993. doi: 10.7554/eLife.19993

Ceccaldi, R., Sarangi, P., and D'Andrea, A. D. (2016). The Fanconi anaemia pathway: new players and new functions. *Nat. Rev. Mol. Cell Biol.* 17, 337–349. doi: 10.1038/nrm.2016.48

Ciechanover, A. (1998). The ubiquitin-proteasome pathway: on protein death and cell life. *EMBO J.* 17, 7151–7160. doi: 10.1093/emboj/17.24.7151

Clarke, D. J., Mondesert, G., Segal, M., Bertolaet, B. L., Jensen, S., Wolff, M., et al. (2001). Dosage suppressors of pds1 implicate ubiquitin-associated domains in checkpoint control. *Mol. Cell. Biol.* 21, 1997–2007. doi: 10.1128/MCB.21.6.1997-2007.2001

Connelly, J. C., de Leau, E. S., and Leach, D. R. F. (2003). Nucleolytic processing of a protein-bound DNA end by the *E. coli* SbcCD (MR) complex. *DNA Repair.* 2, 795–807. doi: 10.1016/S1568-7864(03)00063-6

Couvé, S., Macé-Aimé, G., Rosselli, F., and Saparbaev, M. K. (2009). The human oxidative DNA Glycosylase NEIL1 excises psoralen-induced interstrand DNA cross-links in a three-stranded DNA structure. *J. Biol. Chem.* 284, 11963–11970. doi: 10.1074/jbc.M900746200

Couvé-Privat, S., Macé, G., Rosselli, F., and Saparbaev, M. K. (2007). Psoralen-induced DNA adducts are substrates for the base excision repair pathway in human cells. *Nucleic Acids Res* 35, 5672–5682. doi: 10.1093/nar/gkm592

Coux, O., Tanaka, K., and Goldberg, A. L. (1996). Structure and functions of the 20S and 26S proteasomes. *Annu. Rev. Biochem.* 65, 801–847. doi: 10.1146/annurev.bi.65.070196.004101

Dantuma, N. P., Heinen, C., and Hoogstraten, D. (2009). The ubiquitin receptor Rad23: at the crossroads of nucleotide excision repair and proteasomal degradation. *DNA Repair.* 8, 449–460. doi: 10.1016/j.dnarep.2009.01.005

Davey, C. A., Sargent, D. F., Luger, K., Maeder, A. W., and Richmond, T. J. (2002). Solvent mediated interactions in the structure of the nucleosome core particle at 1.9 a resolution. *J. Mol. Biol.* 319, 1097–1113. doi: 10.1016/S0022-2836(02)00386-8

Davis, E. J., Lachaud, C., Appleton, P., Macartney, T. J., Näthke, I., and Rouse, J. (2012). DVC1 (C1orf124) recruits the p97 protein segregase to sites of DNA damage. *Nat. Struct. Mol. Biol.* 19, 1093–1100. doi: 10.1038/nsmb.2394

de Graaf, B., Clore, A., and McCullough, A. K. (2009). Cellular pathways for DNA repair and damage tolerance of formaldehyde-induced DNA-protein crosslinks. *DNA Repair.* 8, 1207–1214. doi: 10.1016/j.dnarep.2009.06.007

Delabaere, L., Orsi, G. A., Sapey-Triomphe, L., Horard, B., Couble, P., and Loppin, B. (2014). The spartan ortholog maternal haploid is required for paternal chromosome integrity in the drosophila zygote. *Curr. Biol,* 24, 2281–2287. doi: 10.1016/j.cub.2014.08.010

DeMott, M. S., Beyret, E., Wong, D., Bales, B. C., Hwang, J.-T., Greenberg, M. M., et al. (2002). Covalent trapping of human DNA Polymerase β by the Oxidative DNA Lesion 2-deoxyribonolactone. *J. Biol. Chem.* 277, 7637–7640. doi: 10.1074/jbc.C100577200

Dinant, C., Bartek, J., and Bekker-Jensen, S. (2012). Histone displacement during nucleotide excision repair. *Int. J. Mol. Sci.* 13, 13322–13337. doi: 10.3390/ijms131013322

Dirac-Svejstrup, A. B., Walker, J., Faull, P., Encheva, V., Akimov, V., Puglia, M., et al. (2020). DDI2 is a ubiquitin-directed endoprotease responsible for cleavage of transcription factor NRF1. *Mol. Cell* 79, 332.e7–341.e7. doi: 10.1016/j.molcel.2020.05.035

Dokshin, G. A., Davis, G. M., Sawle, A. D., Eldridge, M. D., Nicholls, P. K., Gourley, T. E., et al. (2020). GCNA interacts with spartan and topoisomerase II to regulate genome stability. *Dev. Cell* 52, 53.e6–68.e6. doi: 10.1016/j.devcel.2019.11.006

Duxin, J. P., Dewar, J. M., Yardimci, H., and Walter, J. C. (2014). Repair of a DNA-protein crosslink by replication-coupled proteolysis. *Cell* 159, 346–357. doi: 10.1016/j.cell.2014.09.024

Duxin, J. P., and Walter, J. C. (2015). What is the DNA repair defect underlying Fanconi anemia? *Curr. Opin. Cell Biol.* 37, 49–60. doi: 10.1016/j.ceb.2015.09.002

Eickbush, T. H., and Moudrianakis, E. N. (1978). The histone core complex: an octamer assembled by two sets of protein-protein interactions. *Biochemistry* 17, 4955–4964. doi: 10.1021/bi00616a016

Fornace, A. J. (1982). Detection of DNA single-strand breaks produced during the repair of damage by DNA-protein cross-linking agents. *Cancer Res.* 42, 145–149.

Fortini, P., and Dogliotti, E. (2007). Base damage and single-strand break repair: mechanisms and functional significance of short- and long-patch repair subpathways. *DNA Repair.* 6, 398–409. doi: 10.1016/j.dnarep.2006.10.008

Friedberg, E. C., Lehmann, A. R., and Fuchs, R. P. P. (2005). Trading places: how do DNA polymerases switch during translesion DNA synthesis? *Mol. Cell* 18, 499–505. doi: 10.1016/j.molcel.2005.03.032

Groll, M., Ditzel, L., Löwe, J., Stock, D., Bochtler, M., Bartunik, H. D., et al. (1997). Structure of 20S proteasome from yeast at 2.4Å resolution. *Nature* 386, 463–471. doi: 10.1038/386463a0

Gros, L., Ishchenko, A. A., Ide, H., Elder, R. H., and Saparbaev, M. K. (2004). The major human AP endonuclease (Ape1) is involved in the nucleotide incision repair pathway. *Nucleic Acids Res.* 32, 73–81. doi: 10.1093/nar/gkh165

Hauer, M. H., and Gasser, S. M. (2017). Chromatin and nucleosome dynamics in DNA damage and repair. *Genes Dev.* 31, 2204–2221. doi: 10.1101/gad.307702.117

Hauer, M. H., Seeber, A., Singh, V., Thierry, R., Sack, R., Amitai, A., et al. (2017). Histone degradation in response to DNA damage enhances chromatin dynamics and recombination rates. *Nat. Struct. Mol. Biol.* 24, 99–107. doi: 10.1038/nsmb.3347

Hinz, J. M., Rodriguez, Y., and Smerdon, M. J. (2010). Rotational dynamics of DNA on the nucleosome surface markedly impact accessibility to a DNA repair enzyme. *PNAS* 107, 4646–4651. doi: 10.1073/pnas.0914443107

Ho, T. V., and Schärer, O. D. (2010). Translesion DNA synthesis polymerases in DNA interstrand crosslink repair. *Environ. Mol. Mutagen.* 51, 552–566. doi: 10.1002/em.20573

Ide, H., Nakano, T., Salem, A. M. H., and Shoulkamy, M. I. (2018). DNA–protein cross-links: formidable challenges to maintaining genome integrity. *DNA Repair.* 71, 190–197. doi: 10.1016/j.dnarep.2018.08.024

Ide, H., Shoulkamy, M. I., Nakano, T., Miyamoto-Matsubara, M., and Salem, A. M. H. (2011). Repair and biochemical effects of DNA–protein crosslinks. *Mutat. Res. Fund.Mol. Mech. Mutagen.* 711, 113–122. doi: 10.1016/j.mrfmmm.2010.12.007

Ide, H., Nakano, T., Shoulkamy, M. I., and Salem, A. M. H. (2015). "Formation, repair, and biological effects of DNA–protein cross-link damage," *Adv. DNA Repair*. ed C. C. Chen (INTECH), 43–80. doi: 10.5772/59683

Ignatov, A. V., Bondarenko, K. A., and Makarova, A. V. (2017). Non-bulky lesions in human DNA: the ways of formation, repair, and replication. *Acta Nat.* 9, 12–26. doi: 10.32607/20758251-2017-9-3-12-26

Ishchenko, A. A., Deprez, E., Maksimenko, A., Brochon, J.-C., Tauc, P., and Saparbaev, M. K. (2006). Uncoupling of the base excision and nucleotide incision repair pathways reveals their respective biological roles. *PNAS* 103, 2564–2569. doi: 10.1073/pnas.0508582103

Jentsch, S., and Psakhye, I. (2013). Control of nuclear activities by substrate-selective and protein-group SUMOylation. *Annu. Rev. Genet.* 47, 167–186. doi: 10.1146/annurev-genet-111212-133453

Ji, S., Thomforde, J., Rogers, C., Fu, I., Broyde, S., and Tretyakova, N. Y. (2019). Transcriptional bypass of DNA–protein and DNA–Peptide conjugates by T7 RNA polymerase. *ACS Chem. Biol.* 14, 2564–2575. doi: 10.1021/acschembio.9b00365

Kisselev, A. F., Callard, A., and Goldberg, A. L. (2006). Importance of the different proteolytic sites of the proteasome and the efficacy of inhibitors varies with the protein substrate. *J. Biol. Chem.* 281, 8582–8590. doi: 10.1074/jbc.M509043200

Klages-Mundt, N. L., and Li, L. (2017). Formation and repair of DNA-protein crosslink damage. *Sci. China Life Sci.* 60, 1065–1076. doi: 10.1007/s11427-017-9183-4

Kottemann, M. C., Conti, B. A., Lach, F. P., and Smogorzewska, A. (2018). Removal of RTF2 from Stalled Replisomes Promotes Maintenance of Genome Integrity. *Mol. Cell* 69, 24.e5–35.e5. doi: 10.1016/j.molcel.2017.11.035

Kottemann, M. C., and Smogorzewska, A. (2013). Fanconi anaemia and the repair of Watson and Crick DNA crosslinks. *Nature* 493, 356–363. doi: 10.1038/nature11863

Krokan, H. E., and Bjørås, M. (2013). Base excision repair. *Cold Spring Harb. Perspect. Biol.* 5:a012583. doi: 10.1101/cshperspect.a012583

Krylov, D. M., and Koonin, E. V. (2001). Correspondence: a novel family of predicted retroviral-like aspartyl proteases with a possible key role in eukaryotic cell cycle control. *Curr. Biol.* 11, R584–R587. doi: 10.1016/S0960-9822(01)00357-8

Kühbacher, U., and Duxin, J. P. (2020). How to fix DNA-protein crosslinks. *DNA Repair* 94:102924. doi: 10.1016/j.dnarep.2020.102924

Kuo, H. K., Griffith, J. D., and Kreuzer, K. N. (2007). 5-azacytidine–induced methyltransferase-DNA adducts block DNA replication in vivo. *Cancer Res.* 67, 8248–8254. doi: 10.1158/0008-5472.CAN-07-1038

Kuykendall, J. R., and Bogdanffy, M. S. (1992). Efficiency of DNA-histone crosslinking induced by saturated and unsaturated aldehydes in vitro. *Mutat. Res.* 283, 131–136. doi: 10.1016/0165-7992(92)90145-8

Lal, D., Som, S., and Friedman, S. (1988). Survival and mutagenic effects of 5-azacytidine in *Escherichia coli*. *Mutat. Res. DNA Repair Rep.* 193, 229–236. doi: 10.1016/0167-8817(88)90033-8

Lam, C. W., Casanova, M., and Heck, H. D. (1985). Depletion of nasal mucosal glutathione by acrolein and enhancement of formaldehyde-induced DNA-protein cross-linking by simultaneous exposure to acrolein. *Arch. Toxicol.* 58, 67–71. doi: 10.1007/BF00348311

Langevin, F., Crossan, G. P., Rosado, I. V., Arends, M. J., and Patel, K. J. (2011). Fancd2 counteracts the toxic effects of naturally produced aldehydes in mice. *Nature* 475, 53–58. doi: 10.1038/nature10192

Larsen, N. B., Gao, A. O., Sparks, J. L., Gallina, I., Wu, R. A., Mann, M., et al. (2019). Replication-coupled dna-protein crosslink repair by SPRTN and the proteasome in xenopus egg extracts. *Mol. Cell* 73, 574.e7–588.e7. doi: 10.1016/j.molcel.2018.11.024

Lecker, S. H., Goldberg, A. L., and Mitch, W. E. (2006). Protein degradation by the ubiquitin–proteasome pathway in normal and disease states. *JASN* 17, 1807–1819. doi: 10.1681/ASN.2006010083

Lehmann, A. R., Niimi, A., Ogi, T., Brown, S., Sabbioneda, S., Wing, J. F., et al. (2007). Translesion synthesis: Y-family polymerases and the polymerase switch. *DNA Repair* 6, 891–899. doi: 10.1016/j.dnarep.2007.02.003

Li, F., Zhang, Y., Bai, J., Greenberg, M. M., Xi, Z., and Zhou, C. (2017). 5-Formylcytosine Yields DNA–protein cross-links in nucleosome core particles. *J. Am. Chem. Soc.* 139, 10617–10620. doi: 10.1021/jacs.7b05495

Li, G., and Widom, J. (2004). Nucleosomes facilitate their own invasion. *Nat. Struct. Mol. Biol.* 11, 763–769. doi: 10.1038/nsmb801

Lindahl, T. (1993). Instability and decay of the primary structure of DNA. *Nature* 362, 709–715. doi: 10.1038/362709a0

Loeber, R. L., Michaelson-Richie, E. D., Codreanu, S. G., Liebler, D. C., Campbell, C. R., and Tretyakova, N. Y. (2009). Proteomic analysis of DNA-Protein cross-linking by antitumor nitrogen Mustards. *Chem. Res. Toxicol.* 22, 1151–1162. doi: 10.1021/tx900078y

Lorenti Garcia, C., Mechilli, M., Proietti De Santis, L., Schinoppi, A., Katarzyna, K., and Palitti, F. (2009). Relationship between DNA lesions, DNA repair and chromosomal damage induced by acetaldehyde. *Mutat. Res. Fund. Mol. Mech. Mutagen.* 662, 3–9. doi: 10.1016/j.mrfmmm.2008.11.008

Löwe, J., Stock, D., Jap, B., Zwickl, P., Baumeister, W., and Huber, R. (1995). Crystal structure of the 20S proteasome from the archaeon *T. acidophilum* at 3.4 A resolution. *Science* 268, 533–539. doi: 10.1126/science.7725097

Luger, K., Dechassa, M. L., and Tremethick, D. J. (2012). New insights into nucleosome and chromatin structure: an ordered state or a disordered affair? *Nat, Rev. Mol. Cell Biol.* 13, 436–447. doi: 10.1038/nrm3382

Luger, K., Mäder, A. W., Richmond, R. K., Sargent, D. F., and Richmond, T. J. (1997). Crystal structure of the nucleosome core particle at 2.8 A resolution. *Nature* 389, 251–260. doi: 10.1038/38444

Maddi, K., Sam, D. K., Bonn, F., Prgomet, S., Tulowetzke, E., Akutsu, M., et al. (2020). Wss1 promotes replication stress tolerance by degrading histones. *Cell Rep.* 30, 3117.e4–3126.e4. doi: 10.1016/j.celrep.2020.02.018

Mandemaker, I. K., Geijer, M. E., Kik, I., Bezstarosti, K., Rijkers, E., Raams, A., et al. (2018). DNA damage-induced replication stress results in PA200-proteasome-mediated degradation of acetylated histones. *EMBO Rep.* 19:e45566. doi: 10.15252/embr.201745566

Martin, P. R., Couvé, S., Zutterling, C., Albelazi, M. S., Groisman, R., Matkarimov, B. T., et al. (2017). The human DNA glycosylases NEIL1 and NEIL3 Excise Psoralen-Induced DNA-DNA cross-links in a four-stranded DNA structure. *Sci. Rep.* 7:17438. doi: 10.1038/s41598-017-17693-4

McGlynn, P., and Lloyd, R. G. (2001). Rescue of stalled replication forks by RecG: simultaneous translocation on the leading and lagging strand templates supports an active DNA unwinding model of fork reversal and Holliday junction formation. *PNAS* 98, 8227–8234. doi: 10.1073/pnas.111008698

McKibbin, P. L., Fleming, A. M., Towheed, M. A., Van Houten, B., Burrows, C. J., and David, S. S. (2013). Repair of hydantoin lesions and their amine adducts in DNA by base and nucleotide excision repair. *J. Am. Chem. Soc.* 135, 13851–13861. doi: 10.1021/ja4059469

Mechilli, M., Schinoppi, A., Kobos, K., Natarajan, A. T., and Palitti, F. (2008). DNA repair deficiency and acetaldehyde-induced chromosomal alterations in CHO cells. *Mutagenesis* 23, 51–56. doi: 10.1093/mutage/gem042

Michel, B., Grompone, G., Florès, M.-J., and Bidnenko, V. (2004). Multiple pathways process stalled replication forks. *PNAS* 101, 12783–12788. doi: 10.1073/pnas.0401586101

Ming, X., Groehler, A., Michaelson-Richie, E. D., Villalta, P. W., Campbell, C., and Tretyakova, N. Y. (2017). Mass spectrometry based proteomics study of cisplatin-induced DNA–Protein cross-linking in human fibrosarcoma (HT1080) cells. *Chem. Res. Toxicol.* 30, 980–995. doi: 10.1021/acs.chemrestox.6b00389

Minko, I. G., Kurtz, A. J., Croteau, D. L., Van Houten, B., Harris, T. M., and Lloyd, R. S. (2005). Initiation of repair of DNA–polypeptide cross-links by the UvrABC nuclease. *Biochemistry* 44, 3000–3009. doi: 10.1021/bi0478805

Minko, I. G., Zou, Y., and Lloyd, R. S. (2002). Incision of DNA–protein crosslinks by UvrABC nuclease suggests a potential repair pathway involving nucleotide excision repair. *PNAS* 99, 1905–1909. doi: 10.1073/pnas.042700399

Mohni, K. N., Wessel, S. R., Zhao, R., Wojciechowski, A. C., Luzwick, J. W., Layden, H., et al. (2019). HMCES maintains genome integrity by shielding abasic sites in single-strand DNA. *Cell* 176, 144.e13–153.e13. doi: 10.1016/j.cell.2018.10.055

Mosbech, A., Gibbs-Seymour, I., Kagias, K., Thorslund, T., Beli, P., Povlsen, L., et al. (2012). DVC1 (C1orf124) is a DNA damage–targeting p97 adaptor that promotes ubiquitin-dependent responses to replication blocks. *Nat. Struct. Mol. Biol.* 19, 1084–1092. doi: 10.1038/nsmb.2395

Nakano, T., Katafuchi, A., Matsubara, M., Terato, H., Tsuboi, T., Masuda, T., et al. (2009). Homologous recombination but not nucleotide excision repair plays a pivotal role in tolerance of DNA-protein cross-links in mammalian cells. *J. Biol. Chem.* 284, 27065–27076. doi: 10.1074/jbc.M109.019174

Nakano, T., Miyamoto-Matsubara, M., Shoulkamy, M. I., Salem, A. M. H., Pack, S. P., Ishimi, Y., et al. (2013). Translocation and stability of replicative DNA helicases upon encountering DNA-protein cross-links. *J. Biol. Chem.* 288, 4649–4658. doi: 10.1074/jbc.M112.419358

Nakano, T., Morishita, S., Katafuchi, A., Matsubara, M., Horikawa, Y., Terato, H., et al. (2007). Nucleotide excision repair and homologous recombination systems commit differentially to the repair of DNA-protein crosslinks. *Mol. Cell* 28, 147–158. doi: 10.1016/j.molcel.2007.07.029

Nakano, T., Xu, X., Salem, A. M. H., Shoulkamy, M. I., and Ide, H. (2017). Radiation-induced DNA–protein cross-links: mechanisms and biological significance. *Free Radic. Biol. Med.* 107, 136–145. doi: 10.1016/j.freeradbiomed.2016.11.041

Neale, M. J., Pan, J., and Keeney, S. (2005). Endonucleolytic processing of covalent protein-linked DNA double-strand breaks. *Nature* 436, 1053–1057. doi: 10.1038/nature03872

Nishioka, H. (1973). Lethal and mutagenic action of formaldehyde in Hcr+ and Hcr− strains of *Escherichiacoli*. *Mutat. Res. Fund. Mol. Mech. Mutag.* 17, 261–265. doi: 10.1016/0027-5107(73)90175-9

Orta, M. L., Calderón-Montaño, J. M., Domínguez, I., Pastor, N., Burgos-Morón, E., López-Lázaro, M., et al. (2013). 5-Aza-2′-deoxycytidine causes replication lesions that require Fanconi anemia-dependent homologous recombination for repair. *Nucleic Acids Res.* 41, 5827–5836. doi: 10.1093/nar/gkt270

Pande, P., Ji, S., Mukherjee, S., Schärer, O. D., Tretyakova, N. Y., and Basu, A. K. (2017). Mutagenicity of a model DNA-Peptide cross-link in human cells: roles of translesion synthesis DNA polymerases. *Chem. Res. Toxicol.* 30, 669–677. doi: 10.1021/acs.chemrestox.6b00397

Payne, B. T. I., van Knippenberg, I. C., Bell, H., Filipe, S. R., Sherratt, D. J., and McGlynn, P. (2006). Replication fork blockage by transcription factor-DNA complexes in *Escherichia coli*. *Nucleic Acids Res.* 34, 5194–5202. doi: 10.1093/nar/gkl682

Prasad, R., Horton, J. K., Dai, D.-P., and Wilson, S. H. (2019). Repair pathway for PARP-1 DNA-protein crosslinks. *DNA Repair* 73, 71–77. doi: 10.1016/j.dnarep.2018.11.004

Psakhye, I., and Jentsch, S. (2012). Protein group modification and synergy in the SUMO pathway as exemplified in DNA Repair. *Cell* 151, 807–820. doi: 10.1016/j.cell.2012.10.021

Qian, M.-X., Pang, Y., Liu, C. H., Haratake, K., Du, B.-Y., Ji, D.-Y., et al. (2013). Acetylation-mediated proteasomal degradation of core histones during DNA repair and spermatogenesis. *Cell* 153, 1012–1024. doi: 10.1016/j.cell.2013.04.032

Quievryn, G., and Zhitkovich, A. (2000). Loss of DNA–protein crosslinks from formaldehyde-exposed cells occurs through spontaneous hydrolysis and an active repair process linked to proteosome function. *Carcinogenesis* 21, 1573–1580. doi: 10.1093/carcin/21.8.1573

Quiñones, J. L., Thapar, U., Wilson, S. H., Ramsden, D. A., and Demple, B. (2020). Oxidative DNA-protein crosslinks formed in mammalian cells by abasic site lyases involved in DNA repair. *DNA Repair* 87:102773. doi: 10.1016/j.dnarep.2019.102773

Raiber, E.-A., Portella, G., Martínez Cuesta, S., Hardisty, R., Murat, P., Li, Z., et al. (2018). 5-Formylcytosine organizes nucleosomes and forms Schiff base interactions with histones in mouse embryonic stem cells. *Nat. Chem.* 10, 1258–1266. doi: 10.1038/s41557-018-0149-x

Reinking, H. K., Hofmann, K., and Stingele, J. (2020). Function and evolution of the DNA-protein crosslink proteases Wss1 and SPRTN. *DNA Repair* 88:102822. doi: 10.1016/j.dnarep.2020.102822

Ren, M., Bai, J., Xi, Z., and Zhou, C. (2019). DNA damage in nucleosomes. *Sci. China Chem.* 62, 561–570. doi: 10.1007/s11426-018-9421-5

Ridpath, J. R., Nakamura, A., Tano, K., Luke, A. M., Sonoda, E., Arakawa, H., et al. (2007). Csells deficient in the FANC/BRCA pathway are hypersensitive to plasma levels of formaldehyde. *Cancer Res.* 67, 11117–11122. doi: 10.1158/0008-5472.CAN-07-3028

Rohs, R., West, S. M., Sosinsky, A., Liu, P., Mann, R. S., and Honig, B. (2009). The role of DNA shape in protein-DNA recognition. *Nature* 461, 1248–1253. doi: 10.1038/nature08473

Rosado, I. V., Langevin, F., Crossan, G. P., Takata, M., and Patel, K. J. (2011). Formaldehyde catabolism is essential in cells deficient for the Fanconi anemia DNA-repair pathway. *Nat. Struct. Mol. Biolo.* 18, 1432–1434. doi: 10.1038/nsmb.2173

Rothenberg, M., Kohli, J., and Ludin, K. (2009). Ctp1 and the MRN-complex are required for endonucleolytic Rec12 removal with release of a single class of oligonucleotides in fission yeast. *PLoS Genet.* 5:e1000722. doi: 10.1371/journal.pgen.1000722

Sale, J. E. (2013). Translesion DNA synthesis and mutagenesis in eukaryotes. *Cold Spring Harb. Perspect. Biol.* 5:a012708. doi: 10.1101/cshperspect.a012708

Santi, D. V., Norment, A., and Garrett, C. E. (1984). Covalent bond formation between a DNA-cytosine methyltransferase and DNA containing 5-azacytosine. *PNAS* 81, 6993–6997. doi: 10.1073/pnas.81.22.6993

Sczepanski, J. T., Wong, R. S., McKnight, J. N., Bowman, G. D., and Greenberg, M. M. (2010). Rapid DNA–protein cross-linking and strand scission by an abasic site in a nucleosome core particle. *PNAS* 107, 22475–22480. doi: 10.1073/pnas.1012860108

Semlow, D. R., Zhang, J., Budzowska, M., Drohat, A. C., and Walter, J. C. (2016). Replication-dependent unhooking of DNA interstrand cross-links by the NEIL3 glycosylase. *Cell* 167, 498.e14–511.e14. doi: 10.1016/j.cell.2016.09.008

Serbyn, N., Noireterre, A., Bagdiul, I., Plank, M., Michel, A. H., Loewith, R., et al. (2020). The aspartic protease Ddi1 contributes to DNA-Protein crosslink repair in yeast. *Mol. Cell* 77, 1066.e9–1079.e9. doi: 10.1016/j.molcel.2019.12.007

Shaham, J., Bomstein, Y., Melzer, A., and Ribak, J. (1997). DNA–Protein crosslinks and sister chromatid exchanges as biomarkers of exposure to formaldehyde. *Int. J. Occup. Environ. Health* 3, 95–104. doi: 10.1179/10773529780400 7695

Shang, M., Ren, M., and Zhou, C. (2019). Nitrogen mustard induces formation of DNA–histone cross-links in nucleosome core particles. *Chem. Res. Toxicol.* 32, 2517–2525. doi: 10.1021/acs.chemrestox.9b00354

Sharma, S., Helchowski, C. M., and Canman, C. E. (2013). The roles of DNA polymerase ζ and the Y family DNA polymerases in promoting or preventing genome instability. *Mutat. Res. Fund. Mol. Mech. Mutagen.* 74, 97–110. doi: 10.1016/j.mrfmmm.2012.11.002

Sirkis, R., Gerst, J. E., and Fass, D. (2006). Ddi1, a eukaryotic protein with the retroviral protease fold. *J. Mol. Biol.* 364, 376–387. doi: 10.1016/j.jmb.2006.08.086

Sivá, M., Svoboda, M., Veverka, V., Trempe, J.-F., Hofmann, K., Kožíšek, M., et al. (2016). Human DNA-damage-inducible 2 protein is structurally and functionally distinct from its yeast Ortholog. *Sci. Rep.* 6:30443. doi: 10.1038/srep30443

Smith, K. C. (1966). Physical and chemical changes induced in nucleic acids by ultraviolet light. *Radiat. Res. Suppl.* 6, 54–79. doi: 10.2307/3583551

Solomon, M. J., and Varshavsky, A. (1985). Formaldehyde-mediated DNA-protein crosslinking: a probe for in vivo chromatin structures. *PNAS* 82, 6470–6474. doi: 10.1073/pnas.82.19.6470

Sparks, J. L., Chistol, G., Gao, A. O., Räschle, M., Larsen, N. B., Mann, M., et al. (2019). The CMG helicase bypasses DNA-Protein cross-links to facilitate their repair. *Cell* 176, 167.e21–181.e21. doi: 10.1016/j.cell.2018.10.053

Speit, G., Schütz, P., and Merk, O. (2000). Induction and repair of formaldehyde-induced DNA–protein crosslinks in repair-deficient human cell lines. *Mutagenesis* 15, 85–90. doi: 10.1093/mutage/15.1.85

Sperling, J., and Sperling, R. (1978). Photochemical cross-linking of histones to DNA nucleosomes. *Nucleic Acids Res.* 5, 2755–2773. doi: 10.1093/nar/5.8.2755

Stadtmueller, B. M., and Hill, C. P. (2011). Proteasome activators. *Mol. Cell* 41, 8–19. doi: 10.1016/j.molcel.2010.12.020

Stingele, J., Bellelli, R., Alte, F., Hewitt, G., Sarek, G., Maslen, S. L., et al. (2016). Mechanism and regulation of DNA-protein crosslink repair by the DNA-Dependent metalloprotease SPRTN. *Mol. Cell* 64, 688–703. doi: 10.1016/j.molcel.2016.09.031

Stingele, J., Bellelli, R., and Boulton, S. J. (2017). Mechanisms of DNA–protein crosslink repair. *Nat. Rev. Mol. Cell Biol.* 18, 563–573. doi: 10.1038/nrm.2017.56

Stingele, J., Habermann, B., and Jentsch, S. (2015). DNA–protein crosslink repair: proteases as DNA repair enzymes. *Trends Biochem. Sci.* 40, 67–71. doi: 10.1016/j.tibs.2014.10.012

Stingele, J., Schwarz, M. S., Bloemeke, N., Wolf, P. G., and Jentsch, S. (2014). A DNA-dependent protease involved in DNA-Protein crosslink repair. *Cell* 158, 327–338. doi: 10.1016/j.cell.2014.04.053

Takahashi, K., Morita, T., and Kawazoe, Y. (1985). Mutagenic characteristics of formaldehyde on bacterial systems. *Mutat. Res. Genet. Toxicol.* 156, 153–161. doi: 10.1016/0165-1218(85)90058-8

Todd, R. C., and Lippard, S. J. (2010). Consequences of cisplatin binding on nucleosome structure and dynamics. *Chem. Biol.* 17, 1334–1343. doi: 10.1016/j.chembiol.2010.10.018

Torres-Ramos, C. A., Johnson, R. E., Prakash, L., and Prakash, S. (2000). Evidence for the involvement of nucleotide excision repair in the removal of abasic sites in yeast. *Mol. Cell. Biol.* 20, 3522–3528. doi: 10.1128/MCB.20.10.3522-3528.2000

Trempe, J.-F., Šašková, K. G., Sivá, M., Ratcliffe, C. D. H., Veverka, V., Hoegl, A., et al. (2016). Structural studies of the yeast DNA damage-inducible protein Ddi1 reveal domain architecture of this eukaryotic protein family. *Sci. Rep.* 6:33671. doi: 10.1038/srep33671

Tretyakova, N. Y., Groehler, A., and Ji, S. (2015). DNA-protein cross-links: formation. structural identities, and biological outcomes. *Acc. Chem. Res.* 48, 1631–1644. doi: 10.1021/acs.accounts.5b00056

Ustrell, V., Hoffman, L., Pratt, G., and Rechsteiner, M. (2002). PA200, a nuclear proteasome activator involved in DNA repair. *EMBO J.* 21, 3516–3525. doi: 10.1093/emboj/cdf333

Wickramaratne, S., Ji, S., Mukherjee, S., Su, Y., Pence, M. G., Lior-Hoffmann, L., et al. (2016). Bypass of DNA-protein cross-links conjugated to the 7-Deazaguanine Position of DNA by translesion synthesis polymerases. *J. Biol. Chem.* 291, 23589–23603. doi: 10.1074/jbc.M116.745257

Woodcock, C. L., and Dimitrov, S. (2001). Higher-order structure of chromatin and chromosomes. *Curr. Opin. Genet. Dev.* 11, 130–135. doi: 10.1016/s0959-437x(00)00169-6

Woodgate, R. (1999). A plethora of lesion-replicating DNA polymerases. *Genes Dev.* 13, 2191–2195. doi: 10.1101/gad.13.17.2191

Wu, B., Dröge, P., and Davey, C. A. (2008). Site selectivity of platinum anticancer therapeutics. *Nat. Chem. Biol.* 4, 110–112. doi: 10.1038/nchembio.2007.58

Xu, X., Muller, J. G., Ye, Y., and Burrows, C. J. (2008). DNA–protein cross-links between guanine and lysine depend on the mechanism of oxidation for formation of C5 Vs C8 guanosine adducts. *J. Am. Chem. Soc.* 130, 703–709. doi: 10.1021/ja077102a

Yan, Z., Delannoy, M., Ling, C., Daee, D., Osman, F., Muniandy, P. A., et al. (2010). A histone-fold complex and FANCM form a conserved DNA-remodeling complex to maintain genome stability. *Mol. Cell* 37, 865–878. doi: 10.1016/j.molcel.2010.01.039

Yang, K., and Greenberg, M. M. (2019). DNA–protein cross-link formation in nucleosome core particles treated with methyl methanesulfonate. *Chem. Res. Toxicol.* 32, 2144–2151. doi: 10.1021/acs.chemrestox.9b00314

Yang, K., Prasse, C., and Greenberg, M. M. (2019). Effect of histone lysine methylation on DNA lesion reactivity in nucleosome core particles. *Chem. Res. Toxicol.* 32, 910–916. doi: 10.1021/acs.chemrestox.9b00049

Yi, C., and He, C. (2013). DNA repair by reversal of DNA damage. *Cold Spring Harb. Perspect. Biol.* 5:a012575. doi: 10.1101/cshperspect.a012575

Yip, M. C. J., Bodnar, N. O., and Rapoport, T. A. (2020). Ddi1 is a ubiquitin-dependent protease. *PNAS* 117, 7776–7781. doi: 10.1073/pnas.1902298117

Yudkina, A. V., Dvornikova, A. P., and Zharkov, D. O. (2018). Variable termination sites of DNA polymerases encountering a DNA–protein cross-link. *PLoS One* 13:e0198480. doi: 10.1371/journal.pone.0198480

Zecevic, A., Hagan, E., Reynolds, M., Poage, G., Johnston, T., and Zhitkovich, A. (2010). XPA impacts formation but not proteasome-sensitive repair of DNA–protein cross-links induced by chromate. *Mutagenesis* 25, 381–388. doi: 10.1093/mutage/geq017

Zhang, H., Xiong, Y., and Chen, J. (2020). DNA–protein cross-link repair: what do we know now? *Cell Biosci.* 10:3. doi: 10.1186/s13578-019-0366-z

Zhang, Y.-W., Regairaz, M., Seiler, J. A., Agama, K. K., Doroshow, J. H., and Pommier, Y. (2011). Poly(ADP-ribose) polymerase and XPF–ERCC1 participate in distinct pathways for the repair of topoisomerase I-induced DNA damage in mammalian cells. *Nucleic Acids Res.* 39, 3607–3620. doi: 10.1093/nar/gkq1304

Zhitkovich, A., and Costa, M. (1992). A simple, sensitive assay to detect DNA-protein crosslinks in intact cells and in vivo. *Carcinogenesis* 13, 1485–1489. doi: 10.1093/carcin/13.8.1485

Conflict of Interest: AK is the founder and Chief Scientific Officer of InhiProt LLC.

The authors declare that the research was conducted in the absence of any commercial or financial relationships that could be construed as a potential conflict of interest.

frontiers in Cell and Developmental Biology

ORIGINAL RESEARCH
published: 23 December 2020
doi: 10.3389/fcell.2020.604732

Human Tyrosyl-DNA Phosphodiesterase 1 Possesses Transphosphooligonucleotidation Activity With Primary Alcohols

Nadezhda Dyrkheeva[1†], Rashid Anarbaev[1,2†], Natalia Lebedeva[1†], Maxim Kuprushkin[1], Alexandra Kuznetsova[1], Nikita Kuznetsov[1], Nadejda Rechkunova[1] and Olga Lavrik[1,2]*

[1] Institute of Chemical Biology and Fundamental Medicine, Siberian Branch of the Russian Academy of Sciences, Novosibirsk, Russia, [2] Department of Natural Sciences, Novosibirsk State University, Novosibirsk, Russia

OPEN ACCESS

Edited by:
Jiyan Zhang, Independent Researcher, Beijing, China

Reviewed by:
Yuriy L. Orlov, I.M. Sechenov First Moscow State Medical University, Russia
Elizaveta Gromova, Lomonosov Moscow State University, Russia

***Correspondence:**
Olga Lavrik
lavrik@niboch.nsc.ru

† These authors have contributed equally to this work and share first authorship

Specialty section:
This article was submitted to Cell Death and Survival, a section of the journal Frontiers in Cell and Developmental Biology

Received: *10 September 2020*
Accepted: *05 November 2020*
Published: *23 December 2020*

Citation:
Dyrkheeva N, Anarbaev R, Lebedeva N, Kuprushkin M, Kuznetsova A, Kuznetsov N, Rechkunova N and Lavrik O (2020) Human Tyrosyl-DNA Phosphodiesterase 1 Possesses Transphosphooligonucleotidation Activity With Primary Alcohols. Front. Cell Dev. Biol. 8:604732. doi: 10.3389/fcell.2020.604732

Human tyrosyl-DNA phosphodiesterase 1 (TDP1) belongs to the phospholipase D superfamily, whose members contain paired catalytic histidine and lysine residues within two conserved motifs and hydrolyze phosphodiester bonds. TDP1 is a DNA repair enzyme that processes 3′ DNA end blocking lesions and a wide range of synthetic DNA adducts as a substrate. TDP1 hydrolyzes DNA-adducts via two coordinated S_N2 nucleophilic attacks mediated by the action of two histidine residues and leads to the formation of the covalent intermediate. Hydrolysis of this intermediate is proposed to be carried out by a water molecule that is activated by the His493 residue acting as a general base. It was known that phospholipase D enzymes are able to catalyze not only hydrolysis but also a transphosphatidylation reaction in the presence of primary alcohols in which they transfer the substrate to the alcohol instead of water. Here, we first demonstrated that TDP1 is able to undergo a "transphosphooligonucleotidation" reaction, transferring the substrate residue to the alcohol, thus inducing the formation of covalent DNA adducts with different primary alcohol residues. Such adducts can be accumulated in the conditions of high concentration of alcohol. We demonstrated that glycerol residue was efficiently cleaved from the 3′-end by TDP1 but not by its mutant form associated with the disease spinocerebellar ataxia with axonal neuropathy. Therefore, the second reaction step can be carried out not only by a water molecule but also by the other small nucleophilic molecules, e.g., glycerol and ethanol. Thus, in some cases, TDP1 can be regarded not only as a repair enzyme but also as a source of DNA damage especially in the case of mutation. Such damages can make a negative contribution to the stability of cell vitality.

Keywords: tyrosyl-DNA phosphodiesterase 1, 3′-phosphoglycolate, glycerol, alcohol, ethanol, spinocerebellar ataxia with axonal neuropathy type 1, DNA damage, DNA repair

INTRODUCTION

Tyrosyl-DNA phosphodiesterase 1 (TDP1) is an enzyme of the phospholipase D (PLD) superfamily (Interthal et al., 2001). Phospholipases hydrolyze phospholipids into fatty acids and other lipophilic substances. There are four major classes of phospholipases (A, B, C, and D) segregated by the catalyzed reaction type. PLD superfamily enzymes possess phosphodiesterase activity. Hydrolysis

of the abundant membrane phospholipid phosphatidylcholine with generation of choline and phosphatidic acid is the most commonly studied reaction of PLD enzymes. It is known that the PLD superfamily plays a central role in a variety of functions in prokaryotes, viruses, yeasts, fungi, plants, and eukaryotic species. Phosphatidic acid generated by PLD participates in vesicular trafficking, exocytosis, autophagy, and regulation of cellular metabolism, cytoskeletal reorganization, and tumorigenesis. PLD is a regulator of membrane remodeling, intercellular signaling, protein trafficking, and metabolic pathways; it may play a role in multiple sclerosis, cardiovascular, neurodegenerative, and infectious diseases, and in cell motility and migration, a critical step in the spread of cancer (Peng and Frohman, 2012; Bruntz et al., 2014; Frohman, 2015).

Historically, bacterial virulence factors that demonstrated the release of a choline were named PLDs for the function. Then, it was found that PLD enzymes can hydrolyze not only phosphatidylcholine but also other glycerophospholipids. In addition to hydrolyzing phospholipids, PLDs are able to catalyze a transphosphatidylation reaction in the presence of primary alcohols in which the phosphatidyl group from the hydrolysis of phosphatidylcholine is transferred to the alcohol instead of water, thus conducting headgroup exchange on phosphatidic acid at the terminal phosphodiester bond (Selvy et al., 2011).

PLD family members include not only phospholipases but also nucleases (Koonin, 1996; Ponting and Kerr, 1996) that contain HKD motifs (HxKxxxxD, where x is any amino acid) and hydrolyze phosphodiester bonds via a similar reaction mechanism (Koonin, 1996; Ponting and Kerr, 1996; Interthal et al., 2001; Selvy et al., 2011; Bruntz et al., 2014). TDP1 was the first eukaryotic PLD for which the crystal structure was obtained in 2002 by Davies et al. (2002b). TDP1 enzymatic activity was first found in yeast *Saccharomyces cerevisiae* as repairing the covalently linked adducts of DNA topoisomerase I (TOP1) by catalyzing the hydrolysis of the phosphodiester bond between the tyrosine residue of TOP1 peptide and the 3′ phosphate of DNA. The result DNA product has a break with 3′ phosphate and 5′ hydroxyl groups (Yang et al., 1996; Pouliot et al., 1999). TDP1 possesses a unique HKD motif that differs from other PLD superfamily members, and its orthologs represent a distinct class within the PLD superfamily. TDP1 catalytic center contains two histidine residues His493 and His263 (Interthal et al., 2001). The His493Arg mutation in Tdp1 gene causes spinocerebellar ataxia with axonal neuropathy type 1 (SCAN1) by affecting neuronal cells (Takashima et al., 2002). TDP1 activity is not limited by the removal of cellular TOP1 adducts. TDP1 was shown to catalyze 3′ phosphoglycolate removal from a single-stranded oligonucleotide and a single strand overhangs of DNA double-strand breaks (Inamdar et al., 2002; Raymond et al., 2005). TDP1 is now regarded as a general 3′ DNA end-processing enzyme that acts within the single-strand break repair complex to remove adducts and to prepare the DNA ends bearing 3′ phosphate group for further processing by DNA repair enzymes (Rass et al., 2007). TDP1 also possesses a DNA and RNA 3′-nucleosidase activity that removes from the 3′-end of the substrate a single nucleoside, as well as nucleoside analogs terminating DNA synthesis and widely used as antiviral and anticancer agents and a variety of synthetic DNA adducts for example with molecules, such as biotin and various fluorophores (Dexheimer et al., 2008; Murai et al., 2012; Huang et al., 2013; Dyrkheeva et al., 2018; Brettrager and van Waardenburg, 2019). TDP1 can also process other 3′ DNA end blocking lesions as a substrate: 3′ abasic sites (tetrahydrofuran and α,β-unsaturated aldehyde) and different bulky substituents (Hawkins et al., 2009; Interthal et al., 2005a; Zhou et al., 2005). TDP1 can reverse not only 3′-TOP1-DNA cross-linked bonds but also it is able to release different DNA-protein cross-links. It was found that both human and yeast TDP1 proteins have the ability to process 5′-phosphotyrosyl and 5′-phosphotyrosyl-linked peptide substrates, thus indicating that they can hydrolyze covalently linked adducts of DNA with TOP2 (Nitiss et al., 2006; Murai et al., 2012; Zhang et al., 2020). It also works on the other large adducts including protein fragments (peptides) as a result of failed Schiff base linked proteins, such as proteolytically processed poly(ADP-ribose) polymerase 1 (PARP1)-DNA adducts. These different protein-DNA adducts can be stabilized by chemotherapeutic compounds, e.g., camptothecins, etoposide, and local DNA perturbations introduced by irradiation and endogenous reactive oxygen species (Brettrager and van Waardenburg, 2019).

We have previously shown that human TDP1 can also cleave an apurinic/apyrimidinic (AP) site and its synthetic analogs located inside DNA strand with the formation of 3′ phosphate termini. This observation allows suggesting a novel pathway of AP site repair independent of AP endonuclease 1 (APE1) (Lebedeva et al., 2011, 2012, 2013; Kuznetsov et al., 2017). In contrast to APE1, TDP1 more effectively hydrolyzes AP sites in single-stranded DNA than in DNA duplex (Lebedeva et al., 2012). This suggests that TDP1 may be involved in the repair of AP sites in single-stranded genomic DNA regions that occur in all the major processes of DNA metabolism: replication, transcription, recombination, and repair.

We revealed that no cleavage product was detected for natural AP site in the case of SCAN1 (Lebedeva et al., 2012), whereas non-nucleotide insertions mimicking the AP site were cleaved by this mutant, although with lower efficiency than by wild-type (WT) TDP1 (Lebedeva et al., 2015; Kuznetsov et al., 2017). Moreover, we found that in the reaction catalyzed by SCAN1, two bands were observed on the gel when DNA with synthetic AP site mimetics was used as the substrate. One band corresponded to TDP1 cleavage product, whereas the second one migrated slower in the gel. As TDP1 belongs to the PLD family, we suggested that it can catalyze an equivalent "transferring" reaction in the presence of primary alcohols. Here, we analyze the second reaction product and reveal evidently that it corresponds to DNA fragment with 3′ phosphoglycerol residue. It can be generated because glycerol acts as a nucleophile on the second step of the reaction. Thus, we first demonstrated that TDP1, the same as other PLD enzymes, is able to undergo a reaction transferring the substrate residue to the alcohol instead of water. Also, we could see this second product on the gel with other alcohols including ethanol. This product is generated by SCAN1 and WT TDP1 in the presence of high alcohol concentration. Therefore, the second reaction step can be carried out not only by a water

molecule but also by the other small nucleophilic molecules, e.g., glycerol and ethanol.

RESULTS

Tyrosyl-DNA Phosphodiesterase 1 Wild Type and His493Arg Tyrosyl-DNA Phosphodiesterase 1 Mutant (SCAN1) Activity on Hairpin Substrate Containing Non-nucleotide Insertion

A fluorophore quencher-coupled DNA-biosensor with high sensitivity and specificity for real-time measurement of TDP1 cleavage activity was designed previously in our laboratory (Lebedeva et al., 2015). This biosensor is a short hairpin oligonucleotide with a 1,12-dodecanediol loop, a 5′-fluorescein 5(6)-amide (FAM) fluorophore, and a 3′-BHQ1 (black hole quencher 1) quencher. Specific phosphodiesterase activity of TDP1 is able to remove the quencher from the 3′-end (Lebedeva et al., 2015; Kuznetsov et al., 2017; Komarova et al., 2018; Mamontova et al., 2020). The biosensor contained tetramethyl phosphoryl guanidine (Tmg) group between the 3′-end of DNA and the quencher (**Figure 1A**, uncleavable Tmg group is designated as p*). This Tmg group is resistant to 3′-phosphodiesterase cleavage. We use it to ensure that the BHQ1-group is not cleaved from the 3′-terminus by the phosphodiesterase activity of TDP1. We used in this work similar hairpin oligonucleotide structures containing different non-nucleotide insertions (X) at the center of the 5′-FAM-GGAAGA-X-TCTTCC-p*-BHQ-3′ chain (**Table 1** and **Figure 1A**; upper oligonucleotide structure). In the previous studies, we found (Lebedeva et al., 2015; Kuznetsov et al., 2017) that TDP1 hydrolyzed phosphodiester bond at the center of the chain 5′ to dodecanediol non-nucleotide insertion. We investigated the TDP1 activity on this substrate by real-time fluorescence intensity measurement and by analysis of the reaction products in polyacrylamide gel with 7 M urea (PAAG). Previously, we have already observed in the gel a weak amount of the second band (Lebedeva et al., 2015; Kuznetsov et al., 2017) in the reaction with hairpin substrate catalyzed by SCAN1. Here, when we analyzed the reaction products of hairpin substrate hydrolysis catalyzed by TDP1 mutant SCAN1 in PAAG, we found two product bands on the gel picture with different mobilities (**Figure 1B**; P1 and P2). We revealed that the intensity of the second upper product band (P2) decreases in the time course and finally disappears after 30 min (**Figure 1B**).

We assumed that the band P2 could correspond to the oligonucleotide that appears as a result of TDP1 cleavage 3′ to the non-nucleotide insertion (**Figure 1A**, bold arrow). We supposed that this band eventually disappears, since TDP1 and SCAN1 first hydrolyze the phosphodiesterase bond to the 3′ side and then from the 5′ side of the insert. To test this hypothesis, we synthesized a set of oligonucleotides with different non-nucleotide insertions, including two decandiol residues (**Figure 1A**). In **Figure 1A**, the bold arrows indicate the prospective positions of oligonucleotide hydrolysis with TDP1

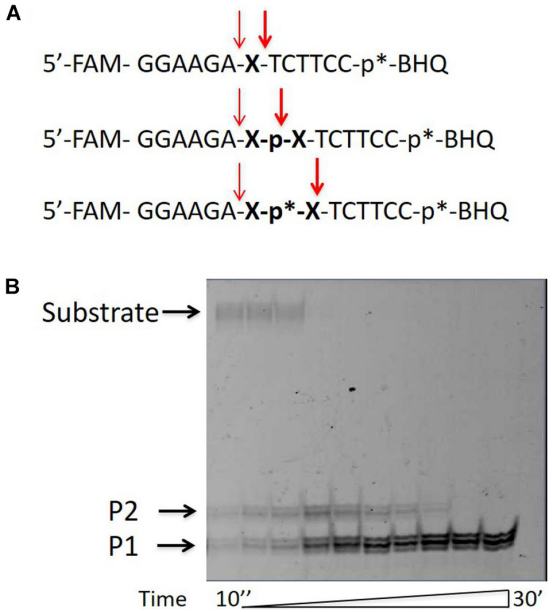

FIGURE 1 | Tyrosyl-DNA phosphodiesterase 1 (TDP1) mutant [spinocerebellar ataxia with axonal neuropathy type 1 (SCAN1)] activity on hairpin substrate containing non-nucleotide insertion. **(A)** Oligonucleotide substrates. BHQ1, Black Hole Quencher 1; FAM, 5(6)-carboxyfluorescein label; non-nucleotide insertions (X); p*, 1,3-dimethyl-2-(phosphorylimino)imidazolidine group (Dmi) group. **(B)** Electrophoretic analyses of SCAN1 (100 nM) reaction products with ïligonucleotide substrate containing non-nucleotide insertion (100 nM) (first substrate in panel **A**). Enzyme and substrate were incubated in the reaction buffer (50 mM Tris-HCl, pH 8.0, 50 mM NaCl, 7 mM β-mercaptoethanol) for time indicated at 37°C. The reaction products were separated by 20% polyacrylamide gel electrophoresis under denaturing conditions.

and SCAN1, giving presumably the second upper product in the picture. The thin fine arrows indicate the hydrolysis position corresponding to the usual lower reaction product (P1). For the entire set of oligonucleotides, the lower products should have identical mobility in the gel, and the mobility of the upper products, presumably, should be different. However, when the products of the reaction were separated in PAAG, we found that the mobility of the second upper product is also the same for oligonucleotides of different structures (**Supplementary Figure S1**, P2). That is why in the next step, we tried to identify the product of the upper band (P2).

Identification of the Upper Band Reaction Product by Matrix-Assisted Laser Desorption/Ionization–Mass Spectrometry

We obtained a product corresponding to the upper product band (P2) in an amount required to analyze the composition of the product by mass spectrometry (MS). The oligonucleotide product was purified by gel electrophoresis and chromatography and analyzed by matrix-assisted laser desorption/ionization (MALDI)-MS. The resulting spectrum is shown in **Supplementary Figure S2**. The spectrum was

analyzed, and the main peak of the spectrum corresponded to the lower oligonucleotide product with an "additive" with a molecular weight of 92 g/mol. Such a molecular weight did not correspond to the products that we expected (**Figure 1A**) but corresponded to the glycerol present in the reaction mixture. Thus, we assumed that the second upper product (P2) of the reaction is the lower product (Pl) with the attached glycerol residue. Since we knew that other phospholipases are capable of catalyzing the transfer reaction, we came up with the conclusion that TDP1 can also catalyze this type of reaction using glycerol as a nucleophile.

In order to check whether the upper product of the reaction is the lower product with the attached glycerol residue, we added glycerol to the reaction mixture in a concentration of 0–50%. **Figure 2** shows that for two substrates with different non-nucleotide insertions, the portion of the upper product increases as compared to the lower product with increasing glycerol concentration.

Tyrosyl-DNA Phosphodiesterase 1 Excises Glycerol Residue From DNA 3′-End

We took the TDP1 reaction product P2 as a purified oligonucleotide to test the activity of TDP1 and SCAN1 on such an oligonucleotide with a "glycerol" attached at the 3′-end. **Figure 3A** demonstrates that "glycerol" was efficiently cleaved from the 3′-end by TDP1 (lanes 2, 3), but not SCAN1 in these reaction conditions (lanes 4–8). The efficiency of the product formation (P1) depends on TDP1 concentration (**Figure 3A**, lanes 2 and 3, and **Figure 3B**). This TDP1 activity efficiently transforms the substrate up to 50% at a concentration of TDP1 1 μM in 10 s (**Figure 3B**).

Dye-labeled substrates were subjected to fluorescence resonance energy transfer (FRET) analysis of DNA cleavage reaction in the reaction buffer with or without glycerol. As illustrated in **Figure 4A**, the changes in FAM fluorescence during the interaction of TDP1 with the FAM-X-p*-BHQ substrate led to an increase in the FRET signal. The increase in FAM fluorescence intensity most likely reflects a release of the cleaved DNA product from the complex with the enzyme that leads to an increase of the distance between FAM and BHQ1 residues. It should be noted that in the presence of 15% glycerol, the observed rate was higher by 2.6-fold then in the case of glycerol-free reaction (0.128 and 0.048 s^{-1}, respectively, **Figure 4A**).

The fluorescence traces obtained for TDP1 upon the interaction with P1 and P2 purified oligonucleotides uncovered an increase in the FAM fluorescence intensity only in the case of P2 (**Figure 4B**). This difference can indicate that interaction of TDP1 with P1 and P2 oligonucleotides leads to formation of different complexes. Indeed, TDP1 interacts with P2 to produce a catalytic complex that leads to removing of glycerol residue at the 3′-end, whereas P1 represents the final product of an enzyme action. It is interesting to note that the observed rate constants of cleavage of FAM-X-p*-BHQ and P2 are very close (0.048 and 0.035 s^{-1}, respectively), indicating that the structure of DNA and nature of the modification are not significantly affected in catalytic reactions.

Tyrosyl-DNA Phosphodiesterase 1 Catalyzes Transferring Reaction With Other Alcohols and on Other DNA Substrates

We added to the reaction mixture, instead of glycerol, other low-molecular weight organic compounds with hydroxyl groups: alcohols (ethanol, methanol, isopropanol, ethylene glycol, and xylitol) and sugars (glucose and trehalose). The upper second product (P2) was detected in TDP1 and SCAN1 catalyzed reactions with ethanol and methanol (**Supplementary Figure S3A**), and with a dihydric alcohol–ethylene glycol (**Supplementary Figure S3A**), and was not detected in reaction with isopropanol and more bulky compounds, polyhydric alcohol xylitol and sugars (data not shown). The formation of the upper product was also demonstrated for the double-stranded oligonucleotide substrate containing the same non-nucleotide insertion (**Supplementary Figure S3B**) and for single-stranded DNA without the insertion where BHQ was hydrolyzed from 3′-end by TDP1 (**Supplementary Figure S3C**). We usually use this substrate for TDP1 inhibitor screening (Zakharenko et al., 2019).

It is interesting to note that while we revealed that the intensity of the second upper product band (P2) decreases in the time course and finally disappears after 30 min in the presence of the glycerol in the reaction mixture (**Figure 2**), in the presence of ethanol, this P2 product remained stable up to 60 min of the reaction time course (**Figure 5**).

Tyrosyl-DNA Phosphodiesterase 1 Catalyzes Transferring Reaction in the Cell Extracts

We checked whether the substrate (a short hairpin oligonucleotide with non-nucleotide insertion) is cleaved in whole-cell extracts of various types of cells: TK6 (human lymphoblastoid), HEK293 (human embryonic kidney), HeLa (cervical cancer)–WT and TDP1-deficient ($TDP1^{-/-}$), HCT116 (human colon carcinoma), and MCF-7 (human breast adenocarcinoma). The storage buffer of the extracts contained 50% glycerol. The second upper product was present when the substrate was cleaved in cell extracts (**Supplementary Figure S4A**, lanes 3 and 5–7, and **Supplementary Figure S4B**, lanes 4, 6, 8, 10, and 11), as in the reaction with the purified recombinant protein SCAN1 (**Supplementary Figure S4A**, lane 2) and TDP1 in the presence of glycerol (**Supplementary Figure S4B**, lane 3). At the same time, in WT HeLa, HCT116, and MCF-7, we observed other upper products perhaps corresponding to the other nucleophiles except glycerol presenting in these cell extracts (**Supplementary Figure S4A**, lanes 6 and 7, **Supplementary Figure S4B**, lanes 8, 10, and 11). There were no reaction products for TDP1-deficient cell extracts (**Supplementary Figure S4A**, lane 4, **Supplementary Figure S4B**, lanes 5, 7, and 9), since hairpin oligonucleotide is a specific TDP1 substrate.

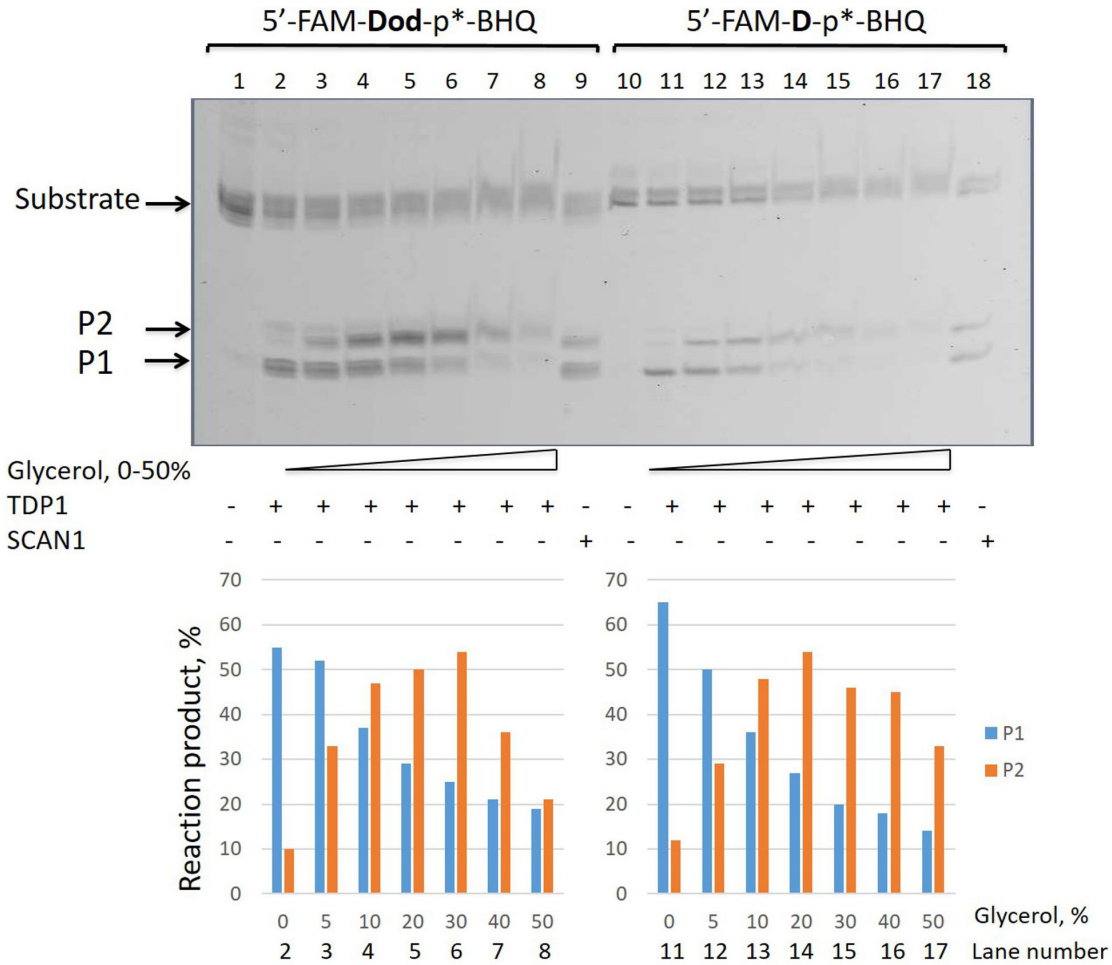

FIGURE 2 | Formation of the upper band tyrosyl-DNA phosphodiesterase 1 (TDP1) reaction product (P2) in the presence of glycerol. Electrophoretic analyses of TDP1 (50 nM) and spinocerebellar ataxia with axonal neuropathy type 1 (SCAN1) (100 nM) reaction products with îligonucleotide substrates containing two different non-nucleotide insertions: D, 1,10-decanediol phosphate; Dod, 1,12-dodecanediol phosphate (100 nM). Enzyme and substrate were incubated in the reaction buffer (50 mM Tris-HCl, pH 8.0, 50 mM NaCl, 7 mM β-mercaptoethanol) for 15 min at 37°C. Schematic representations of DNA substrates (**Figure 1** and **Table 1**) are shown at the top of the gel. The reaction products were separated by 20% polyacrylamide gel electrophoresis under denaturing conditions. The typical representative gel is given on the upper panel. The quantitaion of the reaction products for this gel is on the lower panel. p* – position of a 1,3-dimethyl-2-(phosphorylimino)imidazolidine group (Dmi) group.

DISCUSSION

Both phospholipases and nucleases of PLD superfamily hydrolyze phosphodiester bonds via a similar reaction mechanism. They contain paired catalytic histidine and lysine residues within two conserved HKD motifs (HxKxxxxD, where x is any amino acid) (Koonin, 1996; Ponting and Kerr, 1996; Interthal et al., 2001; Selvy et al., 2011; Bruntz et al., 2014). First, crystal structures for PLD enzymes were obtained for a bacterial PLD, *Streptomyces* sp. *strain PMF* (Leiros et al., 2000). Then, protein crystals of other PLD superfamily members have been reported, including endonucleases and several bacterial enzymes, and for human PLD (Bowling et al., 2020; Metrick et al., 2020). PLD enzymes act in two steps. In the first one, the histidine residue from one HKD motif serves as a nucleophile to attack the phosphate group of the substrate. The histidine from the second HKD domain donates proton to the leaving group. Functioning as nucleophiles, the constituent imidazole moieties of the histidines form transient covalent bonds with the substrate, producing an intermediate that can be hydrolyzed next. The second histidine extracts proton from water (or other nucleophile), and the activated molecule hydrolyzes the intermediate (Stuckey and Dixon, 1999; Davies et al., 2002a; Leiros et al., 2000; Selvy et al., 2011; Bruntz et al., 2014).

TDP1 possesses a unique HKD motif that differs from other PLD superfamily members, and its orthologs represent a distinct class within the PLD superfamily (Interthal et al., 2001). TDP1 hydrolyzes DNA adducts containing phosphotyrosyl bond between DNA 3′ phosphate termini and TOP1 residual peptide via two coordinated S_N2 nucleophilic attacks mediated

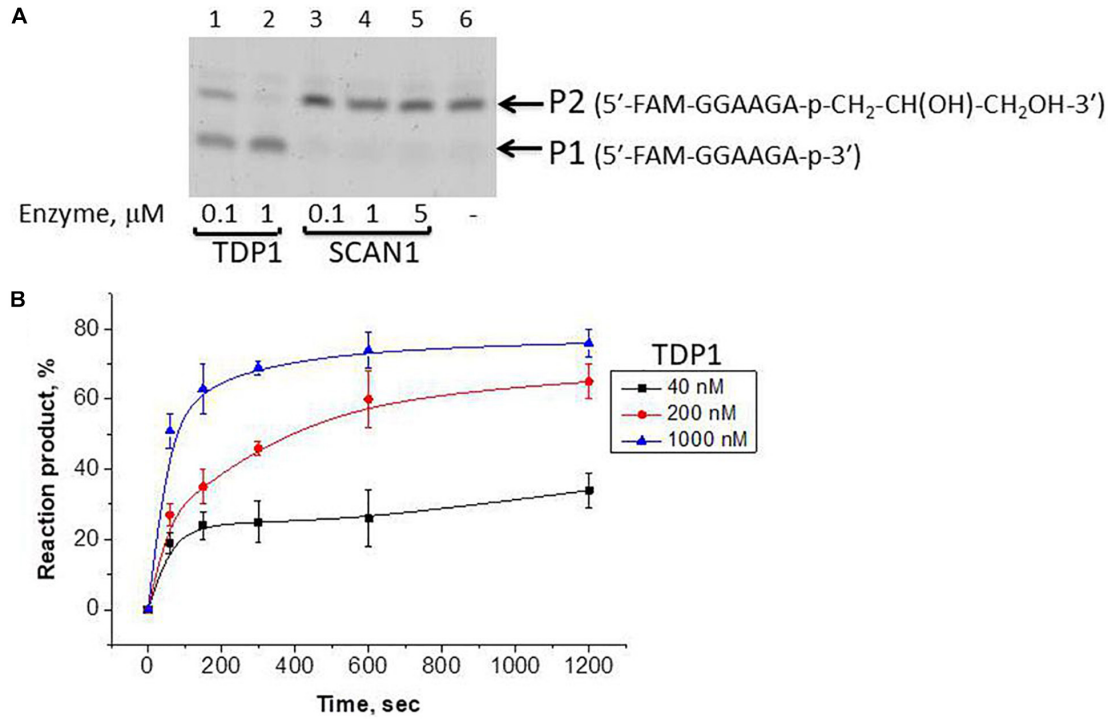

FIGURE 3 | Tyrosyl-DNA phosphodiesterase 1 (TDP1) excises glycerol residue from DNA 3′-end. Enzyme and substrate were incubated in the reaction buffer (50 mM Tris-HCl, pH 8.0, 50 mM NaCl, 7 mM β-mercaptoethanol) for time indicated at 37°C. **(A)** Electrophoretic analyses of TDP1 and spinocerebellar ataxia with axonal neuropathy type 1 (SCAN1) reaction products for 20 min reaction with purified P2 oligonucleotide (100 nM). **(B)** Time dependence of P2 to P1 conversion catalyzed by TDP1 with purified P2 oligonucleotide. Values of the reaction product (%) are the mean (±SD) of three independent experiments. The reaction products were separated by 20% polyacrylamide gel electrophoresis under denaturing conditions.

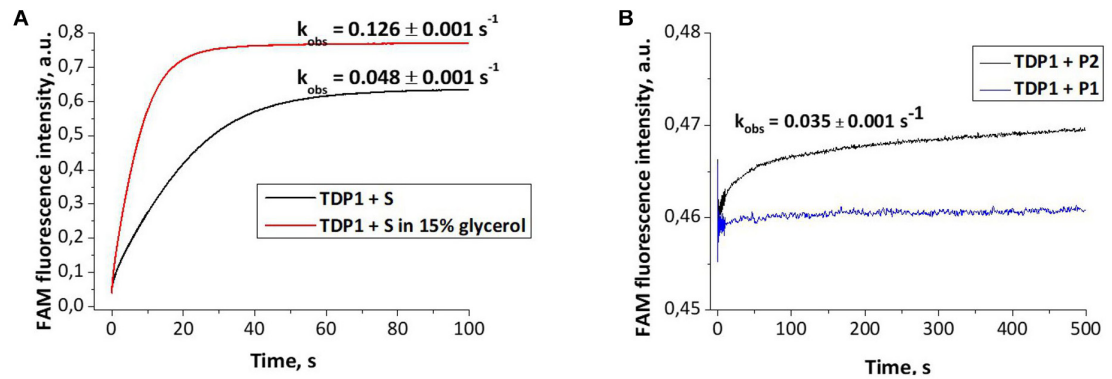

FIGURE 4 | Experimental fluorescence traces revealing the conformational changes during interaction of different oligonucleotides with tyrosyl-DNA phosphodiesterase 1 (TDP1) [(TDP1) = (oligonucleotides) = 1 μM]. **(A)** Interaction of S (FAM- GGAAGA-D-TCTTCC-p*-BHQ) with TDP1. **(B)** Interaction of P1 (5′-FAM-GGAAGA-p-3′) or P2 [5′-FAM-GGAAGA-p-CH2-CH(OH)-CH2OH-3′] purified oligonucleotides with TDP1.

by the action of two histidine residues like other PLD superfamily enzymes. Initially, the imidazole N1 atom of the His263 residue attacks the phosphotyrosyl bond and then the His493 can act as a general acid, which donates a proton to the tyrosine-containing peptide-leaving group. This results in the formation of a transient phosphoryl imidazole bond between N1 atom of His263 and the 3′-end of the DNA. Hydrolysis of this covalent intermediate is proposed to be carried out by a water molecule that is activated by the His493 residue acting as a general base (Davies et al., 2002a). The only known genetic defect in *Tdp1* gene is the A–G mutation. This homozygous recessive mutation A1478G that results in the substitution His493Arg is associated with the disease SCAN1 (Takashima et al., 2002). It was identified in a genome of the members of one family affected with SCAN1 (Takashima et al., 2002).

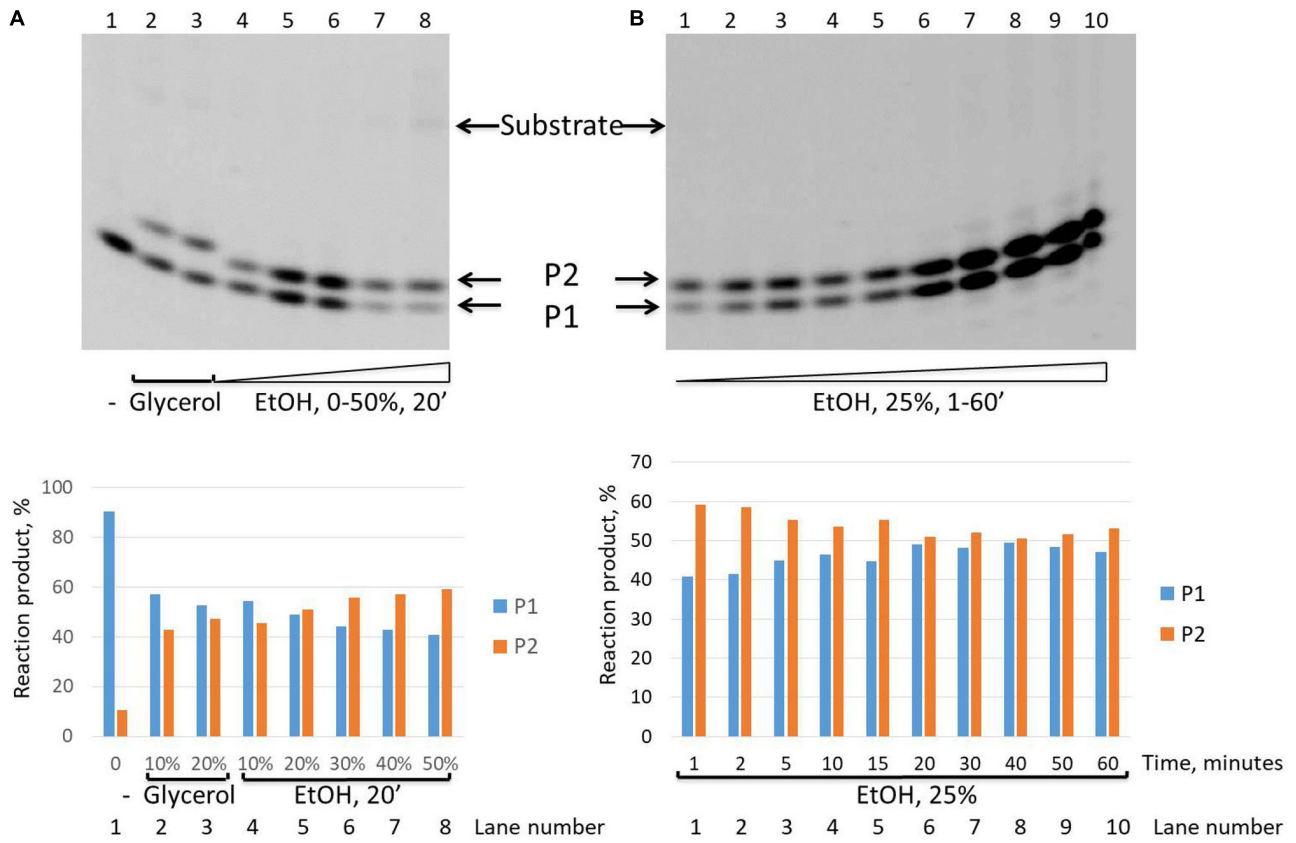

FIGURE 5 | Formation of the upper band tyrosyl-DNA phosphodiesterase 1 (TDP1) reaction product (P2) in the presence of ethanol. Electrophoretic analyses of TDP1 (100 nM) reaction products with îligonucleotide substrate containing non-nucleotide insertion 5′-FAM-D-p*-BHQ (100 nM). Enzyme and substrate were incubated in the reaction buffer (50 mM Tris-HCl, pH 8.0, 50 mM NaCl, 7 mM β-mercaptoethanol) for time indicated at 37°C. **(A)** P2 product formation in dependence of glycerol (lanes 2 and 3) or ethanol (lanes 4–8) concentration. **(B)** Time dependence of P2 product formation. The reaction products were separated by 20% polyacrylamide gel electrophoresis under denaturing conditions. The typical representative gels are given on the upper panels. The quantitaions of the reaction products for the corresponding gels are on the lower panels **(A,B)**.

Cells with a SCAN1 mutation showed increased sensitivity to camptothecin, an anticancer drug, that inhibits TOP1 (Takashima et al., 2002; Hirano et al., 2007). *In vitro* biochemical studies with TDP1 mutant SCAN1 revealed that this mutation reduces enzyme activity ∼25-fold and causes the accumulation of the TDP1–DNA covalent reaction intermediate, supporting the existence of the second S_N2 reaction step in the TDP1 catalytic mechanism (Interthal et al., 2005a,b).

TDP1 is a DNA repair enzyme that is able to remove a variety of natural and synthetic adducts including stalled TOP1-DNA complexes from 3′ DNA ends preparing the 3′-ends for further processing by DNA polymerases and ligases to complete the repair process and restore the DNA chain (Zakharenko et al., 2019). Other TDP1 substrates can be divided into two groups: small adducts consisting of damaged nucleotides, DNA inserted ribonucleotides, and noncanonical nucleotide/nucleoside analogs and large covalent protein-DNA adducts (Brettrager and van Waardenburg, 2019). Thus, TDP1 is able to remove a variety of adducts from 3′ DNA ends during DNA repair (Dexheimer et al., 2008; Murai et al., 2012; Huang et al., 2013; Dyrkheeva et al., 2018; Brettrager and van Waardenburg, 2019). TDP1 also could be involved in the repair of AP sites in single-stranded genomic DNA regions (Rechkunova et al., 2015).

Over the past years, we investigated the functions of TDP1 and SCAN1 in the DNA repair process (Zakharenko et al., 2019). It is known that for phospholipases, transphosphatidylation is more favored in the presence of a primary alcohol since generally short-chain primary alcohols are more nucleophilic than water (Bruntz et al., 2014). As proof of the two-step reaction mechanism with the formation of phosphatidyl-enzyme intermediate, the phosphorus chirally labeled substrate with oxygen isotopes at its phosphorus atom was used (Bruzik and Tsai, 1984). Analysis of the stereoconfiguration of the phosphorus before and after the enzymatic reaction by 31P-NMR revealed retention of the configuration, which supported the two-step SN2 reaction mechanism both for transphosphatidylation and hydrolysis reactions catalyzed by cabbage PLD. The formation of intermediate and thus the proof of the two-step reaction mechanism was also given by

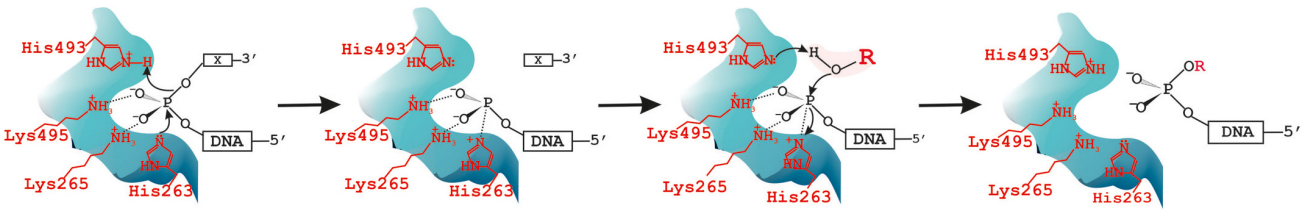

FIGURE 6 | Tyrosyl-DNA phosphodiesterase 1 (TDP1) catalytic cycle: it catalyzes not only hydrolysis but also transferring reaction. X = DNA 3′-end modification [non-nucleotide insertion (**Figures 1**, **2**, **5**) or black hole quencher (BHQ) (**Supplementary Figure S3B**) or glycerol/alcohol (**Figure 2**)]. R = H in the case of hydrolysis reaction or alcohol: C_2H_5-, -C_2H_4OH, $OHCH_2$-CH(OH)-CH_2- in the case of transferring reaction catalyzed by TDP1–"transphosphooligonucleotidation."

detecting the phosphatidyl-imidazole intermediate using MS (Orth et al., 2010). We observed two reaction products on the gel in the cleavage of oligonucleotide substrates with non-nucleotide insertion reactions catalyzed by SCAN1 and TDP1 (Kuznetsov et al., 2017). Then we suggested that TDP1 can possess also transferring activity the same as other PLD enzymes. In the present work, we found that the second product with a lower mobility in polyacrylamide gel is generated by WT TDP1 in the presence of high glycerol concentration. We concluded that this product can be generated because glycerol presents in the enzyme solution that was added to the reaction mixture. Next, we purified this oligonucleotide product and confirmed by MALDI-MS that this upper product is a glycerol residue covalently attached to the 3′-end of the lower oligonucleotide product. Thus, we concluded that the second reaction step of TDP1 can be carried out not only by a water molecule but also by the other small nucleophilic molecules, e.g., glycerol, and TDP1 as other PLD family members is able to undergo not only hydrolysis but also transferring reaction. It is known that PLD is able to catalyze synthesis of phosphatidylglycerol by head group exchange of a phosphatidylcholine. The researchers even tried to find the conditions for the preparation of "commercial industrial grades" of phosphatidylglycerol as surfactant/lubricant with unique properties for therapeutic practices for relief of diseases, such as neonatal respiratory distress syndrome (Piazza and Marmer, 2007). We found first that TDP1 as other PLD enzymes catalyzes transferring reaction. According to these results, we proposed a new step of "transphosphooligonucleotidation" analogous to PLDs' "transphosphatidylation" to the scheme of the reaction catalyzed by TDP1 (**Figure 6**) and the next step of hydrolysis. The model describing TDP1 catalytic mechanism was suggested in the work of Davies et al. (2002a). In this work, two crystal structures of TDP1 bound to the phosphate transition state analogs, vanadate and tungstate, were solved. It is interesting to note that glycerol molecule from the cryoprotectant solution was found in the structure bound to either vanadate or tungstate inhibitor molecules (Davies et al., 2002a).

We could see the second upper product on the gel not only with glycerol but also with other alcohols including ethanol (**Figure 5**). It could cause the formation of covalent DNA adducts with different primary alcohol residues in the cell. Such adducts can be accumulated in the conditions of high concentration of alcohol. We demonstrated that glycerol residue was efficiently cleaved from the 3′-end by TDP1 but not by SCAN1 (**Figure 3**). Thus, in some cases, TDP1 can be regarded not only as a repair enzyme but also as a source of DNA damages especially in the cases of its reduced enzyme activity, for example, in the case of mutations in the *Tdp1* gene. Such damages can make a negative contribution to the stability of cell vitality.

Ethanol is the most frequently used compound with psychoactive and narcotic effects among humans that inhibits the human central nervous system. It is important that it forms solutions in a wide range of proportions with both water and fats probably that is why ethanol has multiple effects on the body. Long-term ethanol consumption can contribute to the development of many diseases, including cardiovascular and cancer. Ethanol can cause oxidative damage to neurons in the brain and their death (Muneer et al., 2011). At the cell nucleus level, ethanol is able to alter access to the cell nucleus by changing the nuclear envelope structure, a double-layered lipid bilayer, penetrated by nuclear pore complexes, thus, the nuclear envelope becomes less permeable for diffusible ions and macromolecules. This could explain altered signaling to and communication with the cell nucleus in the pathophysiology of alcohol abuse (Schäfer et al., 2007). A large body of evidence has shown that alcohol and especially chronic alcohol use can have epigenetic effects, namely, site-selective acetylation, methylation, and phosphorylation in histone, nucleosomal remodeling via histone modifications and DNA methylation (Shukla et al., 2008; Tulisiak et al., 2017; Ciafrè et al., 2019). To date, studies of DNA modifications have primarily looked at global methylation profiles in human liver, brain, and blood, gene-specific methylation profiles in animal models, and methylation changes associated with prenatal ethanol exposure. Our finding of the possibility of direct covalent binding of ethanol to 3′-end of DNA by TDP1 and its mutant form SCAN1 presents a novel insight toward defining the molecular actions of ethanol. Future studies will show the meaning of this fact on cellular and nucleosomal levels. It is known that TDP1 is required for neural homeostasis and acts as a critical survival factor for neuronal development and homeostasis (Katyal et al., 2007; Van Waardenburg, 2016). Though TDP1, like most DNA repair-associated proteins, is not essential

for cell viability, TDP1 dysfunction results in SCAN1, a neurodegenerative syndrome. Most researchers investigate TDP1 neuroprotective property with connection to SCAN1 and stabilization of the TDP1 catalytic enzyme-DNA covalent complex, but we could say that in the context of alcoholism and chronic exposure of the nervous system to ethanol, TDP1 neuroprotective property is also important and requires a special detailed study.

MATERIALS AND METHODS

Expression and Purification of Wild-Type and Mutant (SCAN1) Human Tyrosyl-DNA Phosphodiesterase 1 Proteins

The recombinant N-terminally His-tagged TDP1 and the mutant form of TDP1 (SCAN1) with substitution (H493R) were expressed in *Escherichia coli* BL21 (DE3) cells. The plasmids pET16B-TDP1 and pET16B-SCAN1 were kindly provided by Dr. K. W. Caldecott, University of Sussex, United Kingdom, and by Dr. S. El-Khamisy, University of Sheffield, United Kingdom. Plasmids were transformed into BL21 cells by electroporation, and the cells were grown in LB medium at pH 7.5 with 100 mg/ml ampicillin at 30°C. Two hours after induction with 1 mM isopropyl β-d-1-thiogalactopyranoside (IPTG), cells were harvested. Cell pellets were thawed on ice, resuspended in binding buffer (0.5 M NaCl, 5% glycerol, 20 mM Tris-HCl, pH 8.0, mixture of protease inhibitors), and broken by sonication. After centrifugation, 10 mM imidazole was added to the supernatant. The Ni Sepharose column (GE Healthcare, United Kingdom) was washed with binding buffer (0.5 M NaCl, 10 mM imidazole, 20 mM Tris-HCl, pH 8.0). Elution of the proteins was carried out with elution buffer (0.5 M NaCl, 500 mM imidazole, 20 mM Tris-HCl, pH 8.0, protease inhibitors), and the eluate was loaded to the heparin Sepharose column (GE Healthcare, United Kingdom). Elution of the proteins was carried out with NaCl gradient 0.1–1 M in 20 mM Tris-HCl pH 8.0 with protease inhibitors. The proteins TDP1 and SCAN1 were stored in 50 mM NaCl, 50 mM Tris-HCl pH 8.0, 1 mM ethylenediaminetetraacetic acid (EDTA), 2 mM dithiothreitol (DTT), and 50% glycerol at -20°C. The enzyme samples were estimated to be more than 90% pure. Enzyme concentrations were estimated by Bradford assay. Coomassie-stained protein gels are shown in **Supplementary Figure S5**.

Oligonucleotide Substrate Preparation

Oligonucleotides were synthesized on a Biosset ASM-800 automated DNA synthesizer (Russia) on 200-nmol scale using β-cyanoethyl phosphoramidite chemistry. Here, 1,10-decanediol residue (D) and 1,12-dodecanediol residue (Dod) were introduced via the corresponding dimethoxytrityl phosphoramidite prepared as described previously (Durand et al., 1990). 5(6)-FAM phosphoramidite for FAM labeling and a solid support 3′-BHQ-1 CPG for attachment of a Black Hole QuencherTM BHQ-1 residue were generous gifts of Dr. Vladimir Ryabinin (ICBFM, Novosibirsk). Incorporation of a 1,3-dimethyl-2-(phosphorylimino)imidazolidine (Dmi) group was performed as described (Stetsenko et al., 2014). After the completion of solid-phase synthesis, polymer support from the column was transferred to a plastic tube and treated with 200 μl of concentrated (ca. 25%) aqueous ammonia solution per 5 mg of support at 55°C for 16 h. After deprotection, the supernatant was evaporated in vacuo using a Thermo Fisher Scientific SpeedVac concentrator (United States), 400 μl of 20 mM triethylammonium acetate (pH 7.0) was added, and supernatant was removed by centrifugation. Oligonucleotides were purified by reverse-phased (RP) high-performance liquid chromatography (HPLC) on an Agilent 1200 series HPLC system (United States) equipped with a Zorbax SB-C18 (5 μm) column (4.6 mm × 150 mm) using a gradient of acetonitrile from 0 to 40% in 0.02 M triethylammonium acetate pH 7.0 for 30 min, flow rate 2 ml/min. Denaturing gel electrophoresis in 20% polyacrylamide gel was used to check the purity of oligonucleotides with band visualization by staining with Stains-All (Sigma). Molecular masses of modified oligonucleotides were confirmed by electrospray ionization (ESI) mass spectra recorded on an Agilent G6410A LC-MS/MS triple quadrupole ESI mass spectrometer (United States) in the MS scan mode with negative ion detection. The oligonucleotides were dissolved to 0.1 mM concentration in 20 mM triethylammonium acetate containing 60% acetonitrile for direct injection (10 μl). Elution was made by 80% acetonitrile in isocratic mode, flow rate 0.1 ml/min. Default parameters for ESI and MS were used for all the experiments: nebulizer gas pressure was 30 psi (207 kPa), drying gas (nitrogen) flow rate was 9 L/min and temperature 340°C, capillary voltage was 4,000 V, detected mass range was from m/z 105 to 1,600. Molecular masses of oligonucleotides were calculated uzing experimental m/z values, obtained for each sample.

Molecular masses of modified oligonucleotides were confirmed byMALDI-time of flight (MALDI-TOF) mass spectra recorded in either negative or positive ion mode on a Bruker Reflex III Autoflex Speed mass spectrometer (Germany) using 3-hydroxypicolinic acid as a matrix.

Structures of the chemical modifications used in this study are depicted in **Supplementary Figure S6**. Sequences and ESI MS data of the oligonucleotides are given in **Table 1**.

TABLE 1 | Designations and sequences of oligonucleotide substrates.

No.	Designation	Sequence, 5′–3′
1	FAM-D-p*BHQ	FAM-GGAAGA**D**TCTTCCp*-BHQ1
2	FAM-DD-p*BHQ	FAM-GGAAGA**DD**TCTTCCp*-BHQ1
3	FAM-Dp*D-p*BHQ	FAM-GGAAGA**D**p*TCTTCCp*-BHQ1
4	FAM-Dod-p*BHQ	FAM-GGAAGA**Dod**TCTTCCp*-BHQ1
5	FAM-BHQ	FAM-AACGTCAGGGTCTTCC-BHQ1
6	dsFAM-Dod-p*BHQ	5′-FAM-GGAAG**Dod**CCCTGACGTTp*-BHQ1-3′ 3′-CCTTC-**T**-GGGACTGCAA-5′

BHQ1, Black Hole Quencher 1; FAM, 5(6)-carboxyfluorescein label; non-nucleotide insertions (X); D, 1,10-decanediol phosphate; Dod, 1,12-dodecanediol phosphate; p*, position of a 1,3-dimethyl-2-(phosphorylimino)imidazolidine group (Dmi) group. See **Supplementary Figure S6** for all the structures.

Gel-Based Tyrosyl-DNA Phosphodiesterase 1 Assay

TDP1 gel-based assays were performed using 100 nM substrate incubated with the indicated amount of recombinant human TDP1 or SCAN1 or cell extract for time indicated at 37°C in a buffer containing 50 mM Tris-HCl, pH 8.0, 50 mM NaCl, and 7 mM β-mercaptoethanol. To avoid the formation of the upper oligonucleotide product with attached glycerol residue from the enzyme solution, we purified TDP1 and SCAN1 solution on the SuperSpin Desaltor (Biotoolmics) columns. Reactions were terminated by the addition of gel loading buffer (TBE, 10% formamide, 7 M carbamide, 0.1% xylene cyanol, and 0.1% bromophenol blue, 20 mM EDTA). The samples were heated before loading at 90°C for 7 min. The products were analyzed by electrophoresis in a 20% denaturing polyacrylamide gel with 7 M urea. Gel images were scanned using a Typhoon FLA 9500 (GE Healthcare, United Kingdom) and calculated using a QuantityOne 4.6.7 software. The reaction product yields (%) were calculated as the percentage of the fluorescent signal of the product band to the total signal of the bands in the lane.

Stopped-Flow Fluorescence Measurements

Kinetic studies of the reactions were carried out using an SX.18MV stopped-flow spectrometer (Applied Photophysics, United Kingdom). The efficiency of energy transfer in the FAM/BHQ1 FRET pair was recorded with fluorescence excitation in the FAM dye at 494 nm. Fluorescence of the FAM dye was recorded at wavelengths more than 515 nm using an OG-515 filter (Schott, Germany). The dead time of the device is 1.4 ms. Each kinetic curve was averaged over at least four experimental curves. All experiments were performed at 37°C in the buffer solution containing 50 mM Tris-HCl, pH 8.0, 50 mM NaCl. In the course of FRET experiments, the enzyme and DNA concentrations were 1.0 μ M.

The solution of TDP1 was placed in one instrument's syringe and rapidly mixed in the reaction chamber with the substrate from another syringe. The reported concentrations of reactants are those in the reaction chamber after mixing. Typically, each trace shown in the figures is the average of four or more fluorescence traces recorded in individual experiments. FRET analysis revealed changes in the distance between the dye and quencher in the processes of DNA cleavage reaction.

DATA AVAILABILITY STATEMENT

The original contributions presented in the study are included in the article/**Supplementary Material**, further inquiries can be directed to the corresponding author/s.

AUTHOR CONTRIBUTIONS

ND and NL did all the experiments except stopped flow. ND and RA purified the recombinant proteins. MK synthesized the oligonucleotides. RA and MK did MALDI-MS decoding. AK and NK did the stopped flow experiments. ND, RA, NR, and OL designed the study. All authors contributed to the results discussion and manuscript writing.

FUNDING

The work was supported by the Russian Science Foundation (Grant No. 19-14-00204).

ACKNOWLEDGMENTS

MALDI-MS analysis of the protein samples was done in the Core Facility of Mass Spectrometric Analysis of ICBFM, SB RAS, Novosibirsk, Russia, by MK. The plasmids pET16B-TDP1 and pET16B-SCAN1 were kindly provided by K. W. Caldecott, University of Sussex, United Kingdom, and by S. El-Khamisy, University of Sheffield, United Kingdom. TDP1 WT and knockout cells for the cell extracts were kindly provided by S. El-Khamisy, University of Sheffield, United Kingdom [TK6 cells (human lymphoblastoid)], O. Kantidze, IGB, RAS, Moscow, Russia [HeLa cells (cervical cancer)], and S. Zakiyan, ICG, SB RAS, Novosibirsk, Russia [HEK293 cells (human embryonic kidney)].

SUPPLEMENTARY MATERIAL

The Supplementary Material for this article can be found online at: https://www.frontiersin.org/articles/10.3389/fcell.2020.604732/full#supplementary-material

REFERENCES

Bowling, F. Z., Salazar, C. M., Bell, J. A., Huq, T. S., Frohman, M. A., and Airola, M. V. (2020). Crystal structure of human PLD1 provides insight into activation by PI(4,5)P2 and RhoA. *Nat. Chem. Biol.* 16, 400–407. doi: 10.1038/s41589-020-0499-8

Brettrager, E. J., and van Waardenburg, R. C. A. M. (2019). Targeting Tyrosyl-DNA phosphodiesterase I to enhance toxicity of phosphodiester linked DNA-adducts. *Cancer Drug Resist.* 2, 1153–1163. doi: 10.20517/cdr.2019.91

Bruntz, R. C., Lindsley, C. W., and Brown, H. A. (2014). Phospholipase D signaling pathways and phosphatidic acid as therapeutic targets in cancer. *Pharmacol. Rev.* 66, 1033–1079. doi: 10.1124/pr.114.009217

Bruzik, K., and Tsai, M. D. (1984). Phospholipids chiral at phosphorus. Synthesis of chiral phoshatidylcholine and stereochemistry of phospholipase D. *Biochemistry* 23, 1656–1661. doi: 10.1021/bi00303a012

Ciafrè, S., Carito, V., Ferraguti, G., Greco, A., Chaldakov, G. N., Fiore, M., et al. (2019). How alcohol drinking affects our genes: an epigenetic point of view. *Biochem. Cell Biol.* 97, 345–356. doi: 10.1139/bcb-2018-0248

Davies, D. R., Interthal, H., Champoux, J. J., and Hol, W. G. J. (2002a). Insights into substrate binding and catalytic mechanism of human tyrosyl-DNA phosphodiesterase (TDP1) from vanadate and tungstate-inhibited structures. *J. Mol. Biol.* 324, 917–932. doi: 10.1016/s0022-2836(02)01154-3

Davies, D. R., Interthal, H., Champoux, J. J., and Hol, W. G. J. (2002b). The crystal structure of human tyrosyl-DNA phosphodiesterase. Tdp1. *Structure* 10, 237–248. doi: 10.1016/s0969-2126(02)00707-4

Dexheimer, T. S., Antony, S., Marchand, C., and Pommier, Y. (2008). Tyrosyl-DNA phosphodiesterase as a target for anticancer therapy. *Anticancer Agents Med. Chem.* 8, 381–389. doi: 10.2174/187152008784220357

Durand, M., Chevrie, K., Chassignol, M., Thuong, N. T., and Maurizot, J. C. (1990). Circular dichroism studies of an oligodeoxyribonucleotide containing a hairpin loop made of a hexaethylene glycol chain: conformation and stability. *Nucleic Acids Res.* 18, 6353–6359. doi: 10.1093/nar/18.21.6353

Dyrkheeva, N. S., Lebedeva, N. A., Sherstyuk, Y. V., Abramova, T. V., Silnikov, V. N., and Lavrik, O. I. (2018). Excision of carbohydrate-modified dNMP analogues from DNA 3′ end by human apurinic/apyrimidinic endonuclease 1 (APE1) and Tyrosyl-DNA Phosphodiesterase 1 (TDP1). *Mol. Biol.* 52, 1066–1073. doi: 10.1134/S002689841806006X

Frohman, M. A. (2015). The phospholipase D superfamily as therapeutic targets. *Trends Pharmacol Sci.* 36, 137–144. doi: 10.1016/j.tips.2015.01.001

Hawkins, A. J., Subler, M. A., Akopiants, K., Wiley, J. L., Taylor, S. M., Rice, A. C., et al. (2009). In vitro complementation of TDP1 deficiency indicates a stabilized enzyme-DNA adduct from tyrosyl but not glycolate lesions as a consequence of the SCAN1 mutation. *DNA Repair.* 8, 654–663. doi: 10.1016/j.dnarep.2008.12.012

Hirano, R., Interthal, H., Huang, C., Nakamura, T., Deguchi, K., Choi, K., et al. (2007). Spinocerebellar ataxia with axonal neuropathy: consequence of a Tdp1 recessive neomorphic mutation? *EMBO J.* 26, 4732–4743. doi: 10.1038/sj.emboj.7601885

Huang, S. Y., Murai, J., Dalla Rosa, I., Dexheimer, T. S., Naumova, A., Gmeiner, W. H., et al. (2013). TDP1 repairs nuclear and mitochondrial DNA damage induced by chain-terminating anticancer and antiviral nucleoside analogs. *Nucleic Acids Res.* 41, 7793–7803. doi: 10.1093/nar/gkt483

Inamdar, K. V., Pouliot, J. J., Zhou, T., Lees-Miller, S. P., Rasouli-Nia, A., and Povirk, L. F. (2002). Conversion of phosphoglycolate to phosphate termini on 3′ overhangs of DNA double strand breaks by the human tyrosyl-DNA phosphodiesterase hTdp1. *J. Biol. Chem.* 277, 27162–27168. doi: 10.1074/jbc.M204688200

Interthal, H., Chen, H. J., and Champoux, J. J. (2005a). Human TDP1 cleaves a broad spectrum of substrates, including phosphoamide linkages. *J. Biol. Chem.* 280, 36518–36528. doi: 10.1074/jbc.M508898200

Interthal, H., Chen, H. J., Kehl-Fie, T. E., Zotzmann, J., Leppard, J. B., and Champoux, J. J. (2005b). SCAN1 mutant TDP1 accumulates the enzyme–DNA intermediate and causes camptothecin hypersensitivity. *EMBO J.* 24, 2224–2233. doi: 10.1038/sj.emboj.7600694

Interthal, H., Pouliot, J. J., and Champoux, J. J. (2001). The tyrosyl-DNA phosphodiesterase TDP1 is a member of the phospholipase D superfamily. *Proc. Natl. Acad. Sci. U.S.A.* 98, 12009–12014. doi: 10.1073/pnas.211429198

Katyal, S., el-Khamisy, S. F., Russell, H. R., Li, Y., Ju, L., Caldecott, K. W., et al. (2007). TDP1 facilitates chromosomal single-strand break repair in neurons and is neuroprotective in vivo. *EMBO J.* 26, 4720–4731. doi: 10.1038/sj.emboj.7601869

Komarova, A. O., Drenichev, M. S., Dyrkheeva, N. S., Kulikova, I. V., Oslovsky, V. E., Zakharova, O. D., et al. (2018). Novel group of tyrosyl-DNA-phosphodiesterase 1 inhibitors based on disaccharide nucleosides as drug prototypes for anti-cancer therapy. *J. Enzyme. Inhib. Med. Chem.* 33, 1415–1429. doi: 10.1080/14756366.2018.1509210

Koonin, E. V. (1996). A duplicated catalytic motif in a new superfamily of phosphohydrolases and phospholipid synthases that includes poxvirus envelope proteins. *Trends Biochem. Sci.* 21, 242–243. doi: 10.1016/s0968-0004(96)30024-8

Kuznetsov, N. A., Lebedeva, N. A., Kuznetsova, A. A., Rechkunova, N. I., Dyrkheeva, N. S., Kupryushkin, M. S., et al. (2017). Pre-steady state kinetics of DNA binding and abasic site hydrolysis by tyrosyl-DNA phosphodiesterase 1. *J. Biomol. Struct. Dyn.* 35, 2314–2327. doi: 10.1080/07391102.2016.1220331

Lebedeva, N. A., Anarbaev, R. O., Kupryushkin, M. S., Rechkunova, N. I., Pyshnyi, D. V., Stetsenko, D. A., et al. (2015). Design of a new fluorescent oligonucleotide-based assay for a highly specific real-time detection of apurinic/apyrimidinic site cleavage by Tyrosyl-DNA Phosphodiesterase 1. *Bioconjug. Chem.* 26, 2046–2053. doi: 10.1021/acs.bioconjchem.5b00451

Lebedeva, N. A., Rechkunova, N. I., El-Khamisy, S. F., and Lavrik, O. I. (2012). Tyrosyl-DNA phosphodiesterase 1 initiates repair of apurinic/apyrimidinic sites. *Biochimie* 94, 1749–1753. doi: 10.1016/j.biochi.2012.04.004

Lebedeva, N. A., Rechkunova, N. I., Ishchenko, A. A., Saparbaev, M., and Lavrik, O. I. (2013). The mechanism of human tyrosyl-DNA phosphodiesterase 1 in the cleavage of AP site and its synthetic analogs. *DNA Repair* 12, 1037–1042. doi: 10.1016/j.dnarep.2013.09.008

Lebedeva, N. A., Rechkunova, N. I., and Lavrik, O. I. (2011). AP-site cleavage activity of tyrosyl-DNA phosphodiesterase 1. *FEBS Lett.* 585, 683–686. doi: 10.1016/j.febslet.2011.01.032

Leiros, I., Secundo, F., Zambonelli, C., Servi, S., and Hough, E. (2000). The first crystal structure of a phospholipase D. *Structure* 8, 655–667. doi: 10.1016/s0969-2126(00)00150-7

Mamontova, E. M., Zakharenko, A. L., Zakharova, O. D., Dyrkheeva, N. S., Volcho, K. P., Reynisson, J., et al. (2020). Identification of novel inhibitors for the tyrosyl-DNA-phosphodiesterase 1 (Tdp1) mutant SCAN1 using virtual screening. *Bioorg. Med. Chem.* 28:115234. doi: 10.1016/j.bmc.2019.115234

Metrick, C. M., Peterson, E. A., Santoro, J. C., Enyedy, I. J., Murugan, P., Chen, T., et al. (2020). Human PLD structures enable drug design and characterization of isoenzyme selectivity. *Nat. Chem. Biol.* 16, 391–399. doi: 10.1038/s41589-019-0458-4

Muneer, P. M., Alikunju, S., Szlachetka, A. M., and Haorah, J. (2011). Inhibitory effects of alcohol on glucose transport across the blood-brain barrier leads to neurodegeneration: preventive role of acetyl-L-carnitine. *Psychopharmacology* 214, 707–718. doi: 10.1007/s00213-010-2076-4

Murai, J., Huang, S. Y., Das, B. B., Dexheimer, T. S., Takeda, S., and Pommier, Y. (2012). Tyrosyl-DNA phosphodiesterase 1 (TDP1) repairs DNA damage induced by topoisomerases I and II and base alkylation in vertebrate cells. *J. Biol. Chem.* 287, 12848–12857. doi: 10.1074/jbc.M111.333963

Nitiss, K. C., Malik, M., He, X., White, S. W., and Nitiss, J. L. (2006). Tyrosyl-DNA phosphodiesterase (Tdp1) participates in the repair of Top2-mediated DNA damage. *Proc. Natl. Acad. Sci. U.S.A.* 103, 8953–8958. doi: 10.1073/pnas.0603455103

Orth, E. S., Brandão, T. A. S., Souza, B. S., Pliego, J. R., Vaz, B. G., Eberlin, M. N., et al. (2010). Intramolecular catalysis of phosphodiester hydrolysis by two imidazoles. *J. Am. Chem. Soc.* 132, 8513–8523. doi: 10.1021/ja1034733

Peng, X., and Frohman, M. A. (2012). Mammalian phospholipase D physiological and pathological roles. *Acta Physiol.* 204, 219–226. doi: 10.1111/j.1748-1716.2011.02298.x

Piazza, G. J., and Marmer, W. N. (2007). Conversion of Phosphatidylcholine to Phosphatidylglycerol with Phospholipase D and Glycerol. *J. Am. Oil Chem. Soc.* 84, 645–651. doi: 10.1007/s11746-007-1081-1

Ponting, C. P., and Kerr, I. D. (1996). A novel family of phospholipase D homologues that includes phospholipid synthases and putative endonucleases: identification of duplicated repeats and potential active site residues. *Protein Sci.* 5, 914–922. doi: 10.1002/pro.5560050513

Pouliot, J. J., Yao, K. C., Robertson, C. A., and Nash, H. A. (1999). Yeast gene for a Tyr-DNA phosphodiesterase that repairs topoisomerase I complexes. *Science* 286, 552–555. doi: 10.1126/science.286.5439.552

Rass, U., Ahel, I., and West, S. C. (2007). Defective DNA repair and neurodegenerative disease. *Cell* 130, 991–1004. doi: 10.1093/nar/gkaa489

Raymond, A. C., Staker, B. L., and Burgin, A. B. Jr. (2005). Substrate specificity of tyrosyl-DNA phosphodiesterase I (Tdp1). *J. Biol. Chem.* 280, 22029–22035. doi: 10.1074/jbc.M502148200

Rechkunova, N. I., Lebedeva, N. A., and Lavrik, O. I. (2015). Tyrosyl-DNA phosphodiesterase 1 is a new player in repair of apurinic/apyrimidinic sites. *Bioorg. Khim.* 41, 531–538. doi: 10.1134/s106816201505012x

Schäfer, C., Ludwig, Y., Shahin, V., Kramer, A., Carl, P., Schillers, H., et al. (2007). Ethanol alters access to the cell nucleus. *Cell Mol. Physiol.* 453, 809–818. doi: 10.1007/s00424-006-0165-3

Selvy, P. E., Lavieri, R. R., Lindsley, C. W., and Brown, H. A. (2011). Phospholipase D: enzymology. functionality, and chemical modulation. *Chem. Rev.* 111, 6064–6119. doi: 10.1021/cr200296t

Shukla, S. D., Velazquez, J., French, S. W., Lu, S. C., Ticku, M. K., and Zakhari, S. (2008). Emerging role of epigenetics in the actions of alcohol. *Alcohol. Clin. Exp. Res.* 32, 1525–1534. doi: 10.1111/j.1530-0277.2008.00729.x

Stetsenko, D. A., Kupryushkin, M. S., and Pyshnyi, D. V. (2014). Modified oligonucleotides and methods for their synthesis. *International Patent No. WO2016028187A1*.

Stuckey, J. A., and Dixon, J. E. (1999). Crystal structure of a phospholipase D family member. *Nat. Struct. Biol.* 6, 278–284. doi: 10.1038/6716

Takashima, H., Boerkoel, C. F., John, J., Saifi, G. M., Salih, M. A., Armstrong, D., et al. (2002). Mutation of TDP1, encoding a topoisomerase I-dependent DNA damage repair enzyme, in spinocerebellar ataxia with axonal neuropathy. *Nat. Genet.* 32, 267–272. doi: 10.1038/ng987

Tulisiak, C. T., Harris, R. A., and Ponomarev, I. (2017). DNA modifications in models of alcohol use disorders. *Alcohology* 60, 19–30. doi: 10.1016/j.alcohol.2016.11.004

Van Waardenburg, R. C. A. M. (2016). Tyrosyl-DNA Phosphodiesterase I a critical survival factor for neuronal development and homeostasis. *J. Neurol. Neuromed.* 1, 25–29. doi: 10.29245/2572.942x/2016/5.1048

Yang, S. W., Burgin, A. B. Jr., Huizenga, B. N., Robertson, C. A., Yao, K. C., and Nash, H. A. (1996). A eukaryotic enzyme that can disjoin dead-end covalent complexes between DNA and type I topoisomerases. *Proc. Natl. Acad. Sci. U.S.A.* 93, 11534–11539. doi: 10.1073/pnas.93.21.11534

Zakharenko, A., Dyrkheeva, N., and Lavrik, O. (2019). Dual DNA topoisomerase 1 and tyrosyl-DNA phosphodiesterase 1 inhibition for improved anticancer activity. *Med. Res. Rev.* 39, 1427–1441. doi: 10.1002/med.21587

Zhang, H., Xiong, Y., and Chen, J. (2020). DNA-protein cross-link repair: what do we know now? *Cell Biosci.* 10:3. doi: 10.1186/s13578-019-0366-z

Zhou, T., Lee, J. W., Tatavarthi, H., Lupski, J. R., Valerie, K., and Povirk, L. F. (2005). Deficiency in 3′-phosphoglycolate processing in human cells with a hereditary mutation in tyrosyl-DNA phosphodiesterase (TDP1). *Nucleic Acids Res.* 33, 289–297. doi: 10.1093/nar/gki170

Conflict of Interest: The authors declare that the research was conducted in the absence of any commercial or financial relationships that could be construed as a potential conflict of interest.

frontiers in Cell and Developmental Biology

BRIEF RESEARCH REPORT
published: 11 January 2021
doi: 10.3389/fcell.2020.617301

Apurinic/Apyrimidinic Endonuclease 1 and Tyrosyl-DNA Phosphodiesterase 1 Prevent Suicidal Covalent DNA-Protein Crosslink at Apurinic/Apyrimidinic Site

*Natalia A. Lebedeva[1], Nadejda I. Rechkunova[1], Anton V. Endutkin[1] and Olga I. Lavrik[1,2]**

[1] Institute of Chemical Biology and Fundamental Medicine, Novosibirsk, Russia, [2] Department of Natural Sciences, Novosibirsk State University, Novosibirsk, Russia

OPEN ACCESS

Edited by:
Nikita Kuznetsov,
Institute of Chemical Biology and Fundamental Medicine (RAS), Russia

Reviewed by:
Valentyn Oksenych,
Norwegian University of Science and Technology, Norway
Luigi Xodo,
University of Udine, Italy

***Correspondence:**
Olga I. Lavrik
lavrik@niboch.nsc.ru

Specialty section:
This article was submitted to Cell Death and Survival, a section of the journal Frontiers in Cell and Developmental Biology

Received: 14 October 2020
Accepted: 30 November 2020
Published: 11 January 2021

Citation:
Lebedeva NA, Rechkunova NI, Endutkin AV and Lavrik OI (2021) Apurinic/Apyrimidinic Endonuclease 1 and Tyrosyl-DNA Phosphodiesterase 1 Prevent Suicidal Covalent DNA-Protein Crosslink at Apurinic/Apyrimidinic Site. Front. Cell Dev. Biol. 8:617301. doi: 10.3389/fcell.2020.617301

Bifunctional 8-oxoguanine-DNA glycosylase (OGG1), a crucial DNA-repair enzyme, removes from DNA 8-oxo-7,8-dihydroguanine (8-oxoG) with following cleavage of the arising apurinic/apyrimidinic (AP) site. The major enzyme in eukaryotic cells that catalyzes the cleavage of AP sites is AP endonuclease 1 (APE1). Alternatively, AP sites can be cleaved by tyrosyl-DNA phosphodiesterase 1 (TDP1) to initiate APE1-independent repair, thus expanding the ability of the base excision repair (BER) process. Poly(ADP-ribose) polymerase 1 (PARP1) is a regulatory protein of DNA repair. PARP2 is also activated in response to DNA damage and can be regarded as the BER participant. Here we analyze PARP1 and PARP2 interactions with DNA intermediates of the initial stages of the BER process (8-oxoG and AP-site containing DNA) and their interplay with the proteins recognizing and processing these DNA structures focusing on OGG1. OGG1 as well as PARP1 and PARP2 form covalent complex with AP site-containing DNA without borohydride reduction. AP site incision by APE1 or TDP1 removal of protein adducts but not proteins' PARylation prevent DNA-protein crosslinks.

Keywords: apurinic/apyrimidinic site, 8-oxoguanine-DNA glycosylase, AP endonuclease 1, tyrosyl-DNA phosphodiesterase 1, poly(ADP-ribose) polymerases, DNA-protein crosslinks

INTRODUCTION

Cellular DNA is continuously exposed to both endogenous and exogenous damaging agents. Oxidative stress arising from endogenous reactive oxygen species and some environmental factors, e.g., UV irradiation, is a major source of DNA damage. As a consequence, modified bases, apurinic/apyrimidinic (abasic or AP) sites, and single-strand breaks (SSBs) are generated (Cadet et al., 1999; Lesher et al., 2002). One of the major base lesions induced by oxidative stress is 8-oxoguanine (8-oxoG), which is recognized and excised by a specific DNA glycosylase, initiating the base excision repair (BER) pathway (Radicella et al., 1997). Human 8-oxoguanine-DNA glycosylase (OGG1) plays a major role in the BER pathway by removing 8-oxoguanine base lesions from oxidized G/C base pairs generated an abasic site as the major product, that is subsequently incised by AP-endonuclease 1 (APE1) and further processed by subsequent enzymes in the BER pathway (Brooks et al., 2013). Alternatively, AP site can be cleaved by tyrosyl-DNA-phosphodiesterase 1

(TDP1) to initiate APE1-independent repair, thus expanding the ability of the BER process (Lebedeva et al., 2011, 2013). In addition to the major glycosylase activity, OGG1 also possesses a minor AP lyase activity arising from the formation of a Schiff base linkage between a conserved active site lysine and the C1′ of the damaged site (Girard et al., 1997). The lyase activity eliminates the 3′ phosphate of the AP site and yields a single strand break, but this activity is thought be minor under physiological conditions (Vidal et al., 2001; Kuznetsov et al., 2005; Morland et al., 2005; Dalhus et al., 2011; Faucher et al., 2012).

AP-endonuclease 1 stimulates turnover of several glycosylases by accelerating rate-limiting product release (Esadze et al., 2017). A stimulation mechanism involving stable protein-protein interactions between free APE1 and OGG1, or the DNA bound forms, was excluded using protein crosslinking assays. APE1 capability to access the AP site without forming specific interactions with the glycosylase provides a simple and elegant mechanism to passing along unstable intermediates in BER (Esadze et al., 2017). AP-endonuclease activity of APE1 is essential for stimulation and direct interactions between APE1 and OGG1 facilitate displacement of OGG1 (Sidorenko et al., 2007, 2008).

Poly(ADP-ribose) polymerase 1 (PARP1) is a regulatory protein involved in many different processes of DNA and RNA metabolism, including DNA repair, especially those containing AP sites and strand breaks that are common intermediates in the BER pathway (Schreiber et al., 2006; Hassa and Hottiger, 2008). Upon binding to these lesions, PARP1 becomes activated for synthesis of poly(ADP-ribose) (PAR), and PARP1 can PARylate itself as well as other proteins involved in DNA metabolism (D'Amours et al., 1999). Previously, PARP1 was found capable of forming a covalent DNA-protein crosslink (DPC) at the AP site in double-stranded DNA (Khodyreva et al., 2010). The C1′ atom of the AP site participates in Schiff base formation with a lysine side chain in PARP1, and a covalent bond is formed upon reduction of the Schiff base.

8-oxoguanine-DNA glycosylase interacts with PARP1 (Hooten et al., 2011). Authors found that OGG1 binds directly to PARP1 through the N-terminal region of OGG1, and this interaction is enhanced by oxidative stress. Furthermore, OGG1 binds to PARP1 through its BRCA1 C-terminal (BRCT) domain. OGG1 stimulates the poly(ADP-ribosyl)ation activity of PARP1, which may explain the lack of poly(ADP-ribosyl)ation in cells with decreased level of OGG1. Alternatively, OGG1 expression may enhance only PARP1 automodification rather than influencing PAR formation on target proteins. Importantly, activated PARP1 inhibits OGG1. OGG1 binding to PARP1 plays a functional role in the repair of oxidative DNA damage.

PARP2 is also activated in response to DNA damage and can be regarded as the BER participant. Biochemical studies revealed that PARP2, like PARP1 (Moor et al., 2015), interacts with the BER repair factors XRCC1, DNA polymerase β and DNA ligase III (Amé et al., 1999; Schreiber et al., 2002). However, PARP2 role in the BER process is still under investigation. PARP1 and PARP2 can heterodimerize, but they recognize different targets within BER DNA intermediates (Schreiber et al., 2002; Sukhanova et al., 2019). PARP2 preferentially binds gaps or flap structures that allow suggesting PARP2 is probably involved in the later steps of the repair process (Mortusewicz et al., 2007).

Here we analyze PARP1 and PARP2 interactions with DNA intermediates of the initial stages of the BER process (8-oxoG and AP-site containing DNA) and their interplay with the proteins recognizing and processing these DNA structures focusing on OGG1. OGG1 as well as PARP1 and PARP2 form covalent complex with AP site-containing DNA without borohydride reduction. AP site incision by APE1 or TDP1 removal of protein adducts but not proteins' PARylation prevent DPC without borohydride trapping.

METHODS

Protein Crosslinking to AP Site

The reaction mixtures (10 μl) contained 10 nM 5′-[^{32}P]-labeled DNA substrate, 50 mM Tris–HCl (pH 7.5), 50 mM Na1Cl, 1 mM DTT, 50 nM OGG1 and different concentrations of APE1 or PARP1/2. DNA duplex containing dUMP was preliminary incubated with UDG (0.5 U/μl) for 15 min at 37°C to generate AP site. Reactions were carried out at 37°C for 30 min and stopped with Laemmli loading buffer containing 5% SDS, 5% 2-mercaptoethanol, 0.3 M Tris–HCl, pH 7.8, 50% glycerol and 0.015% bromophenol blue and heated for 5 min at 95°C. The reaction products were separated by Laemmli electrophoresis in a 10% SDS-PAG followed by autoradiography and visualized by phosphorimaging using a Biomolecular Imager Typhoon FLA 9500 (GE Healthcare).

The sequences of the oligonucleotides used in experiments were as follows:

AP-DNA	5′–*GGCGATTAAGTTGGG**U**AACGTCAGGGTCTTCC–3′
	3′– CCGCTAATTCAACCCGTTGCAGTCCCAGAAGG–5′
8-oxoG-DNA	5′–*CTCTCCCTTC**X**CTCCTTTCCTCT–3′
	3′–GAGAGGGAAGCGAGGAAAGGAGA–5′
	* – ^{32}P X = 8-oxoG

Protein Poly(ADP-ribosyl)ation

Poly(ADP-ribosyl)ation of the proteins was performed as described in Maltseva et al. (2018). The reaction mixtures (10 μl) containing 50 mM Tris–HCl (pH 7.5), 50 mM NaCl, 1 mM DTT, 2.5 μM [^{32}P]-NAD$^+$, 10 nM DNA, 100 nM PARP1/2 and the indicated concentrations of OGG1 and APE1 were incubated at 25°C for 20 min. Samples were supplemented with Laemmli loading buffer and heated. The reaction products were separated by Laemmli electrophoresis in a 10% SDS-PAG followed by autoradiography and visualized by phosphorimaging.

EMSA Analysis of DNA-Protein Complexes

Protein binding to 5′-[^{32}P]-DNA were analyzed in a mixture (10 μl) containing 50 mM Tris–HCl, pH 7.5, 50 mM NaCl,

10 nM 5′-[^{32}P]-DNA and indicated concentrations of PARP1/2 or OGG1. The reaction mixtures were incubated at 25°C for 20 min. Loading buffer (1/5 volume) containing 20% glycerol and 0.015% bromophenol blue was then added to the samples. The DNA-protein complexes were analyzed by electrophoresis in a 5% polyacrylamide gel (acrylamide/bis-acrylamide = 60:1) in TBE buffer at 4°C followed by phosphorimaging.

RESULTS

Influence of APE1 and PARP1/2 on the OGG1 Crosslinking to AP Site

8-oxoguanine-DNA glycosylase as well as PARP1 and PARP2 interact with the AP site forming Schiff base which reduction by $NaBH_4$ results in covalent adducts (Nazarkina et al., 2007; Khodyreva et al., 2010; Kutuzov et al., 2015). Besides, PARP1 was shown to form covalent complex with AP site-containing DNA without $NaBH_4$ reduction (Prasad et al., 2014). Here we examined whether formation of stable DNA-protein crosslink (DPC) in the absence of $NaBH_4$ is the unique feature of PARP1 or other AP site-binding proteins are also able to form such adducts.

8-oxoguanine-DNA glycosylase was incubated with the 5′-labeled DNA substrates containing an 8-oxoG or AP site generated after uracil removing by the UDG and the complex was analyzed without $NaBH_4$ reduction (**Figure 1**). Incubation of OGG1 with DNA substrate containing 8-oxoG lesion (8oxoG-DNA) revealed the formation of DNA-protein covalent adducts in the absence of $NaBH_4$ reflecting the formation of the intermediate of the DNA glycosylase/AP lyase reaction (**Figure 1A**). The addition of APE1 at concentrations 2 and 4 times higher than OGG1 decreased the amount of the crosslinking products (**Figures 1A**, lanes 2–4) which indicates a possible competition between proteins for the AP site arising from 8-oxoG excising by OGG1. The simultaneous addition of OGG1 and APE1, even at concentrations lower than OGG1, to the reaction mixture with DNA containing the AP site generated by UDG (AP-DNA) almost completely inhibited OGG1 crosslinking to DNA (**Figure 1B**, lanes 2–4). Under the same conditions, no APE1 crosslinks to DNA substrates were observed, which was expected because the enzyme has extremely high AP-endonuclease activity that led to almost instantaneous processing of the AP-DNA (**Supplementary Figure S1**).

Addition of PARP1 or PARP2 at the increased concentrations affects OGG1 crosslinking to the AP site. This effect was more pronounce in the case of AP-DNA than with the 8oxoG-DNA: both PARPs completely inhibited OGG1-AP-DNA crosslinking at 100 nM concentration, whereas in the case of 8oxoG-DNA OGG1-DNA adducts were observed even in the presence of 200 nM PARPs (compare corresponding lanes on **Figures 1A,B**). Although PARPs themselves effectively crosslink to the AP site generated both by OGG1 (**Figure 1A**) and by UDG (**Figure 1B**), they compete with OGG1 more efficiently on DNA with the pre-formed AP site that allows suggesting

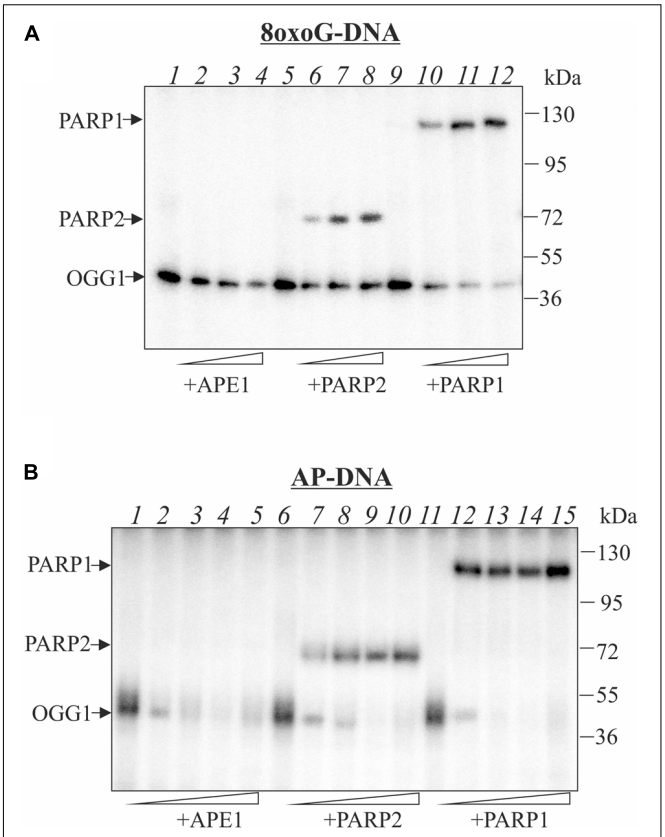

FIGURE 1 | Influence of APE1, PARP2, and PARP1 on the crosslinking of OGG1 to AP site-containing DNA. Phosphorimages of crosslinked proteins to ^{32}P-labeled 8-oxoG-containing DNA **(A)** and to AP site-containing DNA after treatment with UDG **(B)**. Reaction mixture included 10 nM DNA, 50 nM OGG1 and different concentrations of APE1 or PARP1/2 (50, 100, and 200 nM in **A**) and (10, 50, 100, and 200 nM in **B**). APE1, PARP1/2 were added to the reaction mixture simultaneously with OGG1.

PARPs facilitate OGG1 removal from its product. Neither OGG1 nor PARPs form crosslinks with intact DNA duplex (**Supplementary Figure S2**).

Effect of the TDP1 and APE1 on the OGG1 Crosslinking to AP Site

Earlier, we have shown that AP site is processed by tyrosyl-DNA phosphodiesterase 1 (Lebedeva et al., 2011) which can initiate APE1-independent BER pathway (Lebedeva et al., 2013). Here we performed comparative analysis of the TDP1 and APE1 effects on OGG1 crosslinking to AP site (**Figure 2**). Like APE1, TDP1 does not crosslink to AP site but competes with OGG1 for the AP site, thereby reducing the amount of the OGG1-DNA suicidal complexes especially on AP-DNA (**Figure 2** compare lanes 4–6 on A and B panels with lane 2). The addition of TDP1 to the reaction mixture after the formation of the OGG1-DNA adducts also led to a decrease in the observed OGG1 crosslinking products with both 8oxoG- and AP-DNA (lanes 7–9). We assume that TDP1 not only competes for DNA but also is able to remove OGG1 from the DNA-protein

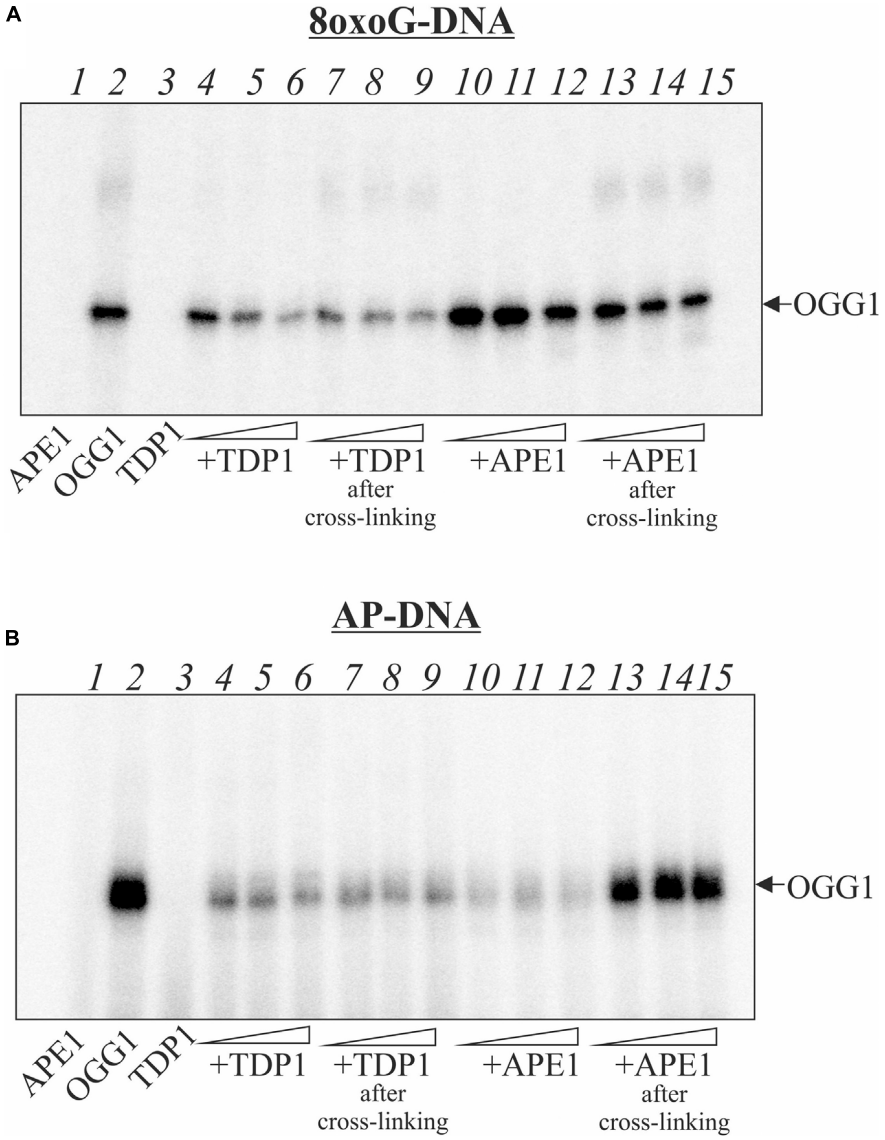

FIGURE 2 | Effect of the order of TDP1 and APE1 addition on the crosslinking of OGG1 to AP site-containing DNA. Phosphorimages of crosslinked proteins to ^{32}P-labeled 8-oxoG-containing DNA **(A)** and to AP site-containing DNA after treatment with UDG **(B)**. Reaction mixture included 10 nM DNA, 50 nM OGG1 and different concentrations (50, 100, and 200 nM) of TDP1 or APE1. TDP1 or APE1 were added to the reaction mixture simultaneously with OGG1 (lanes 4–6 and 10–12) or after incubation of DNA with OGG1 for 10 min (lanes 7–9 and 13–15). Lane 1 in **(A,B)** represent DNA substrate incubated with 200 nM APE1, lane 2 – DNA substrate incubated with 50 nM OGG1, lane 3 – DNA substrate incubated with 200 nM TDP1.

adduct. APE1 has less than TDP1 effect on 8oxoG-DNA both in the case of simultaneous addition and when it was added after OGG1-DNA crosslink formation (**Figure 2A**, compare lanes 10–12 with 4–6 and lanes 13–15 with 7–9). More visible decrease in the level of the OGG1-DNA products in the case of APE1 addition to pre-formed crosslinks (lanes 13–15) may be explained by the partial hydrolysis of AP sites generated by OGG1 before APE1 addition. In the case of AP-DNA, APE1 addition to the reaction mixture after the formation of the OGG1-DNA covalent complex has little effect on the product amount (**Figure 2B**, lanes 13–15) in comparison with simultaneous presence of both proteins (lanes 10–12) when crosslinking is dramatically reduced. This result reflects effective hydrolysis of AP site by APE1.

Effect of PARylation Catalyzed by PARP1/2 on the Protein Crosslinking to AP Site

The covalent attachment of OGG1 to AP site-containing DNA appears to be a suicidal event when BER is overwhelmed or disrupted. To investigate whether PARylation of OGG1 alters formation of the DPC, we performed crosslinking experiments in the presence of NAD^+ (**Figure 3**). The addition of NAD^+

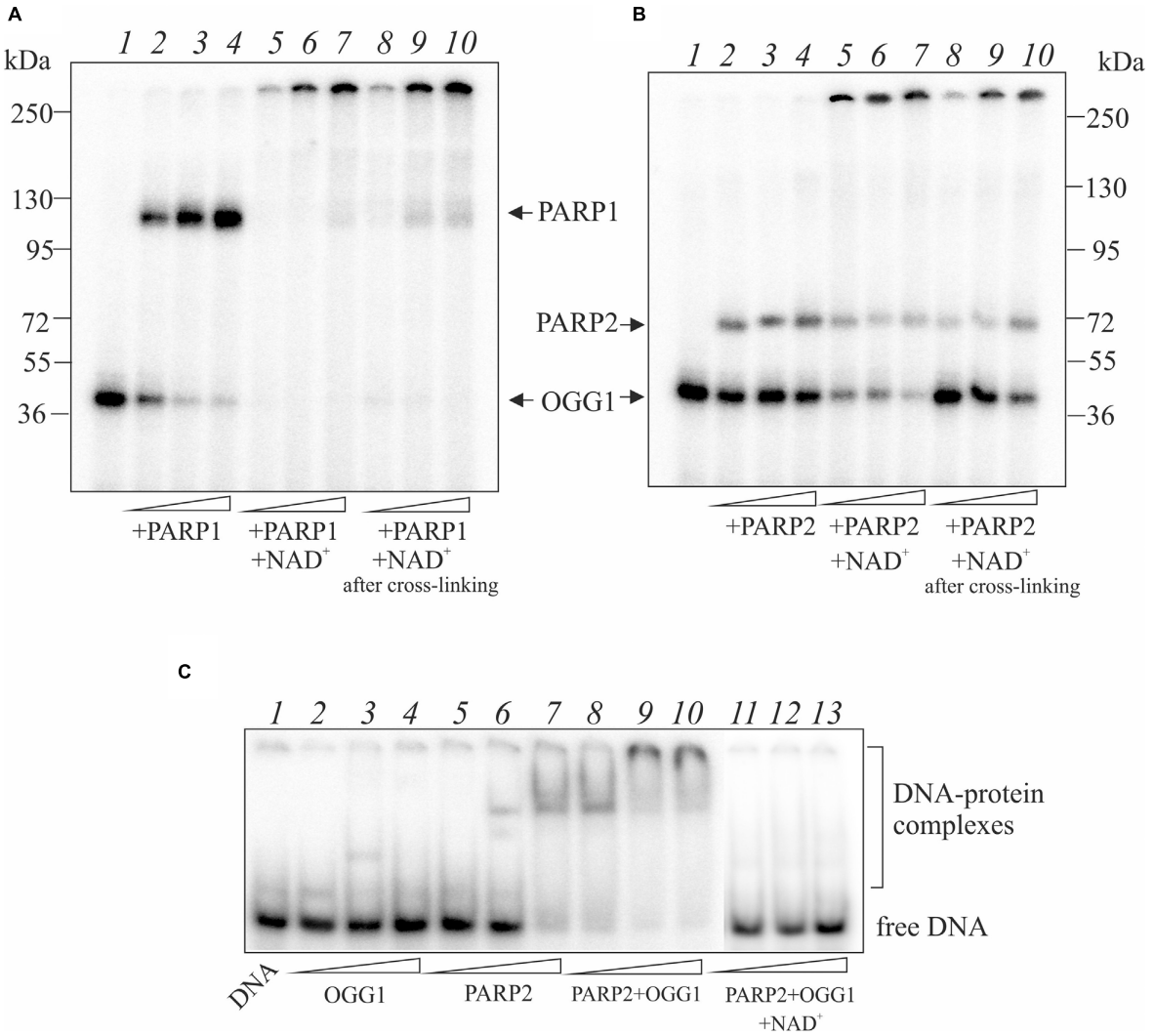

FIGURE 3 | Effect of NAD^+ addition on the crosslinking of OGG1 to AP site-containing DNA in the presence of PARP1 **(A)** and PARP2 **(B)**. Reaction mixture included 10 nM AP site-containing DNA after treatment with UDG, 50 nM OGG1 and different concentrations (50, 100, and 200 nM) of PARP1/2. NAD^+ at final concentration 1 mM was added to the reaction mixture simultaneously (lanes 5–7) or after incubation of OGG1 with PARP1/2 for 10 min (lanes 8–10). The EMSA analysis of ternary OGG1-PARP2-DNA complex formation **(C)**. AP-DNA after treatment with UDG was titrated by OGG1 (50, 100, and 200 nM) in the absence (lanes 2–4), in the presence of 100 nM PARP2 (lanes 8–10) or 100 nM PARP2 and 1 mM NAD^+ (lanes 11–13). Lanes 5–7 – AP-DNA titration with PARP2 (50, 100, and 200 nM) in the absence of OGG1. Lane 1 is DNA control.

to the reaction mixture with OGG1 and PARP1 led to the disappearance of OGG1 and PARP1 crosslinking to the AP-DNA (**Figure 3A**, lanes 5–7) and appearance of products with a low electrophoretic mobility, which suggests a possible DNA crosslinking with the PARylated OGG1 and/or PARP1. Moreover, addition of NAD^+ to the reaction mixture after crosslinking caused very similar products (lanes 8–10), consistent with PARylation of the crosslinked PARP1/DNA complex. These experiments indicate that PARP1 auto-PARylation has no significant effect on crosslinking and conversely, crosslinking has no significant effect on PARylation catalyzed by PARP1.

When NAD^+ was added to the reaction mixture with OGG1 and PARP2, a decrease in the amounts of crosslinked proteins was observed and products with a low electrophoretic mobility appeared (**Figure 3B**, lanes 5–7). The addition of NAD^+ after preliminary crosslinking practically did not influence on the OGG1 crosslinking (**Figure 3B**, lanes 8–10) whereas intensity of PARP2 crosslinking products decreased approximately in the same rate as in the case of simultaneous addition of all components (compare lanes 8–10 with 5–7). Using the EMSA method (**Figure 3C**), complexes of OGG1 (**Figure 3C**, lanes 2–4, **Supplementary Figure S3**) and PARP2 (lanes 5–7) with DNA as well as ternary OGG1-PARP2-DNA complexes (lanes 8–10) were detected, which were destroyed by the addition of NAD^+ (lanes 11–13). Taken together, data on PARP2/OGG1 interplay speak in favor of free but not crosslinked to DNA OGG1 is a target of PARylation catalyzed by PARP2.

Indeed, OGG1 is PARylated by both PARP1 and PARP2 (**Figure 4**). To examine whether OGG1 may be poly(ADP-ribosyl)ated by PARP1/2, [^{32}P]NAD$^+$ was used as substrate for PARylation. Using DNA structure containing an AP site after UDG treatment we observed low level of OGG1 PARylation by PARP2, since PARP2 is poorly activated on double stranded DNA without break (**Figure 4A**, lane 2). Under the same conditions, APE1 was PARylated effectively, since it cleaved the AP site and PARP2 was activated at the break. When APE1 and OGG1 were added simultaneously, the major products corresponded to OGG1 PARylation, despite APE1 concentration was higher than OGG1 (**Figure 4A**, lane 4). Similar result was obtained in the case of PARylation catalyzed by PARP1 (**Figure 4B**). When APE1 was added first, the product of OGG1 PARylation was less intensive than in the case of the simultaneous addition of the proteins (**Figure 4C**, compare lanes 2–5 and 7–10). The level of OGG1 modification practically did not depend on APE1 concentration up to 100 nM: it slightly decreased with increasing APE1 concentration added first (lanes 2–4) and increased in the case of simultaneous addition of both proteins (lanes 7–9). However, at 200 nM APE1 intensity of OGG1 PARylation product decreased significantly and PARylation of APE1 was observed (lanes 5, 10).

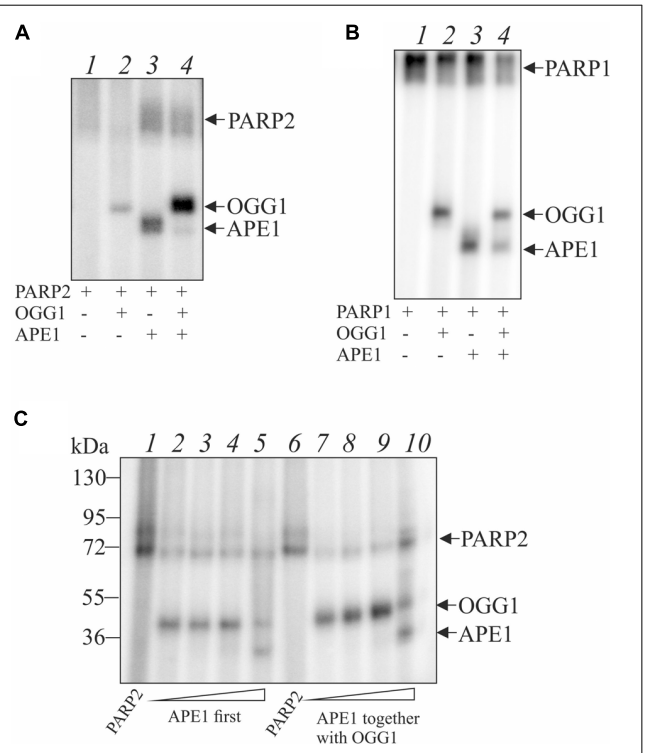

FIGURE 4 | Poly(ADP-ribosyl)ation of OGG1 catalyzed by PARP1 or PARP2 in the presence of AP site-containing DNA. The reaction mixtures containing 100 nM PARP2 **(A)** or 100 nM PARP1 **(B)**, 10 nM AP-DNA after treatment with UDG and 2.5 μM [^{32}P]-NAD$^+$ were incubated at 25°C for 20 min in the presence 50 nM OGG1 with or without 100 nM APE1 and analyzed by SDS-PAG electrophoresis. Influence of APE1 on the OGG1 poly(ADP-ribosyl)ation by PARP2 in the presence of AP site-containing DNA **(C)**. OGG1 at a final concentration 50 nM was added to the reaction mixture after PARP2 incubation with 10, 50, 100, and 200 nM APE1 (lanes 2–5) or simultaneously with APE1 (lanes 7–10).

DISCUSSION

Oxidative stress is one of the common sources to generate a large number of DNA damages, among DNA oxidative products 8-oxoG is the most abundant lesion, which is repaired by OGG1-initiated BER pathway. Although OGG1 is a bifunctional enzyme, its lyase activity is much lower than glycosylase that results in AP site accumulation. Recent study demonstrated that OGG1-initiated BER further increases the levels of DNA damage by generating repair intermediates, leading to PARP1 overactivation and cell death (Wang et al., 2018). In this study we show that OGG1 can generate additional DNA damages, namely DPC at AP site which form without borohydride reduction. Such DNA-protein adducts were earlier detected for PARP1 both with purified protein and in cell extracts (Prasad et al., 2014). These DNA–PARP1 crosslinks are associated with AP lyase reaction proceeding through the β-elimination (Khodyreva et al., 2010; Prasad et al., 2014). This reaction results in strand incision at C3′ and protein links to dRP group at the 3′ end. The authors have also analyzed other BER proteins including OGG1 but did not detect DPC in the absence of $NaBH_4$. In our study, PARP2 DPC was also detected. It should be noted that spontaneous formation of DPC at AP site incised by OGG1 was firstly detected for XRCC1 (Nazarkina et al., 2007). Therefore, not only PARP1 but also other proteins interacting with AP site and possess AP lyase activity can form DPC without $NaBH_4$ treatment.

Further, possible repair mechanism of the PARP1–DNA adducts was examined (Prasad et al., 2019). Neither APE1 no TDP1 were able to remove entire PARP1 from covalent complex with DNA. The authors proposed that proteasomal degradation of PARP1 is required for following enzymatic cleavage of covalent bond in DPC like it was earlier detected for topoisomerase 1–DNA adducts (Debethune et al., 2002). Indeed, the authors found that a proteasome inhibitor reduced repair resulting in accumulation of PARP1 DPC. Using a model DNA substrate mimicking the PARP1 DPC after proteasomal degradation, the authors demonstrated that repair was completed by the TDP1-mediated pathway of BER (Prasad et al., 2019). As OGG1 is less massive than PARP1, we proposed TDP1 capability to remove intact protein from OGG1–DNA adducts. Our results are in line with earlier observations on TDP1 implication in the release of SCAN1 mutant from the suicidal complex with DNA (Interthal et al., 2005; Kuznetsov et al., 2017). APE1 is not able to remove OGG1 from covalent complex with DNA but prevents its formation due to AP site hydrolysis (**Figure 2**). It was reported earlier that in the absence of $NaBH_4$, PARP1 DPC was not observed for 5′-dRP-DNA generated after AP site incision by APE1 as well as APE1 was not able to process PARP1 DPC after proteasomal degradation (Prasad et al., 2014). In the case of TDP1, the cleavage products of the AP site do not contain dRP residues (Lebedeva et al., 2013); therefore they are not reactive.

Tyrosyl-DNA phosphodiesterase 1 is regarded now as the highly potential target for inhibition in cancer cells

(Zakharenko et al., 2019). Commonly, TDP1 inhibitors are used in combination with Top1 poisons, thereby potentiating their effects. Our results allow speculating TDP1 inhibition as a factor to increase OGG1-mediated DNA damage in cancer cells which lost redox homeostasis resulting in oxidative DNA damage.

Poly(ADP-ribose) polymerase 1 and PARylation of repair proteins, including PARP1 itself, regulate their interaction with DNA and functional activity in the repair process. Although mutual influence of PARP1 and OGG1 was shown previously (Hooten et al., 2011), there were no data whether OGG1 is PARylated. Therefore, the present study firstly provides direct demonstration of OGG1 modification both by PARP1 and PARP2. This modification effects protein interaction with DNA but not prevent DPC formation at AP site. The model demonstrating interplay between OGG1 and APE1, TDP1, PARP1/2 on AP site-containing DNA can be hypothesized based on current observations (**Supplementary Figure S4**). Further investigation is required to reveal possible consequence of DPC formation in the cellular context and precise mechanism of the prevention/repair of these adducts by TDP1.

DATA AVAILABILITY STATEMENT

The original contributions presented in the study are included in the article/**Supplementary Material**, further inquiries can be directed to the corresponding author/s.

AUTHOR CONTRIBUTIONS

NL did all experiments. AE purified recombinant OGG1. NR and OL designed the study. All authors contributed to the results, discussion, and manuscript writing.

FUNDING

The work was supported by the Russian Science Foundation (grant no. 20-14-00086) and Russian State Funded Budget Project (grant number AAAA-A17-117020210022-4, for OL). The proteins' PARylation analysis was supported by the Russian Foundation for Basic Research (grant no. 19-04-00481).

ACKNOWLEDGMENTS

The authors are grateful to Dr. S. Khodyreva and Dr. M. Kutuzov (ICBFM SB RAS) for recombinant APE1 and PARP1/2 proteins, respectively.

SUPPLEMENTARY MATERIAL

The Supplementary Material for this article can be found online at: https://www.frontiersin.org/articles/10.3389/fcell.2020.617301/full#supplementary-material

REFERENCES

Amé, J. C., Rolli, V., Schreiber, V., Niedergang, C., Apiou, F., Decker, P., et al. (1999). PARP2. A novel mammalian DNA damage-dependent poly(ADP-ribose) polymerase. *J. Biol. Chem.* 274, 17860–17868. doi: 10.1074/jbc.274.25.17860

Brooks, S. C., Adhikary, S., Rubinson, E. H., and Eichman, B. F. (2013). Recent advances in the structural mechanisms of DNA glycosylases. *Biochim. Biophys. Acta* 1834, 247–271. doi: 10.1016/j.bbapap.2012.10.005

Cadet, J., Delatour, T., Douki, T., Gasparutto, D., Pouget, J. P., Ravanat, J. L., et al. (1999). Hydroxyl radicals and DNA base damage. *Mutat Res.* 424, 9–21. doi: 10.1016/s0027-5107(99)00004-4

Dalhus, B., Forsbring, M., Helle, I. H., Vik, E. S., Forstrom, R. J., Backe, P. H., et al. (2011). Separation-of-function mutants unravel the dual reaction mode of human 8-oxoguanine DNA glycosylase. *Structure* 19, 117–127. doi: 10.2210/pdb2XHI/pdb

D'Amours, D., Desnoyers, S., D'Silva, I., and Poirier, G. G. (1999). Poly(ADP-ribosyl)ation reactions in the regulation of nuclear functions. *Biochem. J.* 342(Pt. 2), 249–268. doi: 10.1042/0264-6021:3420249

Debethune, L., Kohlhagen, G., Grandas, A., and Pommier, Y. (2002). Processing of nucleopeptides mimicking the topoisomerase I-DNA covalent complex by tyrosyl-DNA phosphodiesterase. *Nucl. Acids Res.* 30, 1198–1204. doi: 10.1093/nar/30.5.1198

Esadze, A., Rodriguez, G., Cravens, S. L., and Stivers, J. T. (2017). AP-Endonuclease 1 accelerates turnover of human 8-Oxoguanine DNA glycosylase by preventing retrograde Binding to the Abasic-Site Product. *Biochemistry* 56, 1974–1986. doi: 10.1021/acs.biochem.7b00017

Faucher, F., Doublie, S., and Jia, Z. C. (2012). 8-Oxoguanine DNA Glycosylases: one Lesion. Three Subfamilies. *Int. J. Mol. Sci.* 13, 6711–6729. doi: 10.3390/ijms13066711

Girard, P. M., Guibourt, N., and Boiteux, S. (1997). The Ogg1 protein of Saccharomyces cerevisiae: a 7,8-dihydro-8-oxoguanine DNA glycosylase AP lyase whose lysine 241 is a critical residue for catalytic activity. *Nucl. Acids Res.* 25, 3204–3211. doi: 10.1093/nar/25.16.3204

Hassa, P. O., and Hottiger, M. O. (2008). The diverse biological roles of mammalian PARPS, a small but powerful family of poly-ADP-ribose polymerases. *Front. Biosci.* 13:3046–3082. doi: 10.2741/2909

Hooten, N. N., Kompaniez, K., Barnes, J., Lohani, A., and Evans, M. K. (2011). Poly(ADP-ribose) polymerase 1 (PARP1) binds to 8-oxoguanine-DNA glycosylase (OGG1). *J. Biol. Chem.* 286, 44679–44690. doi: 10.1074/jbc.M111.255869

Interthal, H., Chen, H. J., and Champoux, J. J. (2005). Human TDP1 cleaves a broad spectrum of substrates, including phosphoamide linkages. *J. Biol. Chem.* 280, 36518–36528. doi: 10.1074/jbc.M508898200

Khodyreva, S. N., Prasad, R., Ilina, E. S., Sukhanova, M. V., Kutuzov, M. M., Liu, Y., et al. (2010). Apurinic/apyrimidinic (AP) site recognition by the 5'-dRP/AP lyase in poly(ADP-ribose) polymerase-1 (PARP1). *Proc. Natl. Acad. Sci. U.S.A.* 107, 22090–22095. doi: 10.1073/pnas.1009182107

Kutuzov, M. M., Khodyreva, S. N., Ilina, E. S., Sukhanova, M. V., Amé, J. C., and Lavrik, O. I. (2015). Interaction of PARP2 with AP site containing DNA. *Biochimie* 112, 10–19. doi: 10.1016/j.biochi.2015.02.010

Kuznetsov, N. A., Koval, V. V., Zharkov, D. O., Nevinsky, G. A., Douglas, K. T., and Fedorova, O. S. (2005). Kinetics of substrate recognition and cleavage by human 8-oxoguanine-DNA glycosylase. *Nucl. Acids Res.* 33, 3919–3931. doi: 10.1093/nar/gki694

Kuznetsov, N. A., Lebedeva, N. A., Kuznetsova, A. A., Rechkunova, N. I., Dyrkheeva, N. S., Kupryushkin, M. S., et al. (2017). Pre-steady state kinetics of DNA binding and abasic site hydrolysis by tyrosyl-DNA phosphodiesterase 1. *J. Biomol. Struct. Dyn.* 35, 2314–2327. doi: 10.1080/07391102.2016.1220331

Lebedeva, N. A., Rechkunova, N. I., Ishchenko, A. A., Saparbaev, M., and Lavrik, O. I. (2013). The mechanism of human tyrosyl-DNA phosphodiesterase 1 in the cleavage of AP site and its synthetic analogs. *DNA Repair* 12, 1037–1042. doi: 10.1016/j.dnarep.2013.09.008

Lebedeva, N. A., Rechkunova, N. I., and Lavrik, O. I. (2011). AP-site cleavage activity of tyrosyl-DNA phosphodiesterase 1. *FEBS Lett.* 585, 683–686. doi: 10.1016/j.febslet.2011.01.032

Lesher, D. T., Pommier, Y., Stewart, L., and Redinbo, M. R. (2002). 8-Oxoguanine rearranges the active site of human topoisomerase I. *Proc. Natl. Acad. Sci. U.S.A.* 99, 12102–12107. doi: 10.1073/pnas.192282699

Maltseva, E. A., Krasikova, Y. S., Sukhanova, M. V., Rechkunova, N. I., and Lavrik, O. I. (2018). Replication protein A as a modulator of the poly(ADP-ribose)polymerase 1 activity. *DNA Repair* 72, 28–38. doi: 10.1016/j.dnarep.2018.09.010

Moor, N. A., Vasil'eva, I. A., Anarbaev, R. O., Antson, A. A., and Lavrik, O. I. (2015). Quantitative characterization of protein-protein complexes involved in base excision DNA repair. *Nucleic Acids Res.* 43, 6009–6022. doi: 10.1093/nar/gkv569

Morland, I., Luna, L., Gustad, E., Seeberg, E., and Bjoras, M. (2005). Product inhibition and magnesium modulate the dual reaction mode of hOgg1. *DNA Repair.* 4, 381–387. doi: 10.1016/j.dnarep.2004.11.002

Mortusewicz, O., Amé, J. C., Schreiber, V., and Leonhardt, H. (2007). Feedback-regulated poly(ADP-ribosyl)ation by PARP1 is required for rapid response to DNA damage in living cells. *Nucl. Acids Res.* 35, 7665–7675. doi: 10.1093/nar/gkm933

Nazarkina, Z. K., Khodyreva, S. N., Marsin, S., Lavrik, O. I., and Radicella, J. P. (2007). XRCC1 interactions with base excision repair DNA intermediates. *DNA Repair* 6, 254–264. doi: 10.1016/j.dnarep.2006.10.002

Prasad, R., Horton, J. K., Chastain, P. D. II, Gassman, N. R., Freudenthal, B. D., Hou, E. W., et al. (2014). Suicidal cross-linking of PARP1 to AP site intermediates in cells undergoing base excision repair. *Nucl. Acids Res.* 42, 6337–6351. doi: 10.1093/nar/gku288

Prasad, R., Horton, J. K., Dai, D. P., and Wilson, S. H. (2019). Repair pathway for PARP1 DNA-protein crosslinks. *DNA Repair* 73, 71–77. doi: 10.1016/j.dnarep.2018.11.004

Radicella, J. P., Dherin, C., Desmaze, C., Fox, M. S., and Boiteux, S. (1997). Cloning and characterization of hOGG1, a human homolog of the OGG1 gene of Saccharomyces cerevisiae. *Proc. Natl. Acad. Sci. U.S.A.* 94, 8010–8015. doi: 10.1073/pnas.94.15.8010

Schreiber, V., Amé, J. C., Dollé, P., Schultz, I., Rinaldi, B., Fraulob, V., et al. (2002). Poly(ADP-ribose) polymerase-2 (PARP2) is required for efficient base excision DNA repair in association with PARP1 and XRCC1. *J. Biol. Chem.* 277, 23028–23036. doi: 10.1074/jbc.M202390200

Schreiber, V., Dantzer, F., Ame, J. C., and de Murcia, G. (2006). Poly(ADP-ribose): novel functions for an old molecule. *Nat. Rev. Mol. Cell Biol.* 7, 517–528. doi: 10.1038/nrm1963

Sidorenko, V. S., Nevinsky, G. A., and Zharkov, D. O. (2007). Mechanism of interaction between human 8-oxoguanine-DNA glycosylase and AP endonuclease. *DNA Repair* 6, 317–328. doi: 10.1016/j.dnarep.2006.10.022

Sidorenko, V. S., Nevinsky, G. A., and Zharkov, D. O. (2008). Specificity of stimulation of human 8-oxoguanine-DNA glycosylase by AP endonuclease. *Biochem. Biophys. Res. Commun.* 368, 175–179. doi: 10.1016/j.bbrc.2008.01.076

Sukhanova, M. V., Hamon, L., Kutuzov, M. M., Joshi, V., Abrakhi, S., Dobra, I., et al. (2019). A Single-Molecule Atomic Force Microscopy Study of PARP1 and PARP2 Recognition of Base Excision Repair DNA Intermediates. *J. Mol. Biol.* 431, 2655–2673. doi: 10.1016/j.jmb.2019.05.028

Vidal, A. E., Hickson, I. D., Boiteux, S., and Radicella, J. P. (2001). Mechanism of stimulation of the DNA glycosylase activity of hOGG1 by the major human AP endonuclease: bypass of the AP lyase activity step. *Nucl. Acids Res.* 29, 1285–1292. doi: 10.1093/nar/29.6.1285

Wang, R., Li, C., Qiao, P., Xue, Y., Zheng, X., Chen, H., et al. (2018). OGG1-initiated base excision repair exacerbates oxidative stress-induced parthanatos. *Cell Death Dis.* 9:628. doi: 10.1038/s41419-018-0680-0

Zakharenko, A., Dyrkheeva, N., and Lavrik, O. (2019). Dual DNA topoisomerase 1 and tyrosyl-DNA phosphodiesterase 1 inhibition for improved anticancer activity. *Med. Res. Rev.* 39, 1427–1441. doi: 10.1002/med.21587

Conflict of Interest: The authors declare that the research was conducted in the absence of any commercial or financial relationships that could be construed as a potential conflict of interest.

The handling editor declared a shared affiliation and a past co-authorship with one of the authors OL at the time of review.

frontiers in Cell and Developmental Biology

ORIGINAL RESEARCH
published: 18 January 2021
doi: 10.3389/fcell.2020.617762

Interplay Between Mitophagy and Apoptosis Defines a Cell Fate Upon Co-treatment of Breast Cancer Cells With a Recombinant Fragment of Human κ-Casein and Tumor Necrosis Factor-Related Apoptosis-Inducing Ligand

Fabian Wohlfromm[1†], Max Richter[1†], Lado Otrin[2], Kamil Seyrek[1], Tanja Vidaković-Koch[2], Elena Kuligina[3], Vladimir Richter[3], Olga Koval[3] and Inna N. Lavrik[1]*

[1] Translational Inflammation Research, Medical Faculty, Otto von Guericke University, Magdeburg, Germany, [2] Max Planck Institute for Dynamics of Complex Technical Systems, Magdeburg, Germany, [3] Department of Biotechnology, Institute of Chemical Biology and Fundamental Medicine, Siberian Branch of Russian Academy of Sciences (SB RAS), Novosibirsk, Russia

A recombinant fragment of human κ-Casein, termed RL2, induces cell death of breast cancer cells; however, molecular mechanisms of RL2-mediated cell death have remained largely unknown. In the current study, we have decoded the molecular mechanism of the RL2-mediated cell death and found that RL2 acts via the induction of mitophagy. This was monitored by the loss of adenosine triphosphate production, LC3B-II generation, and upregulation of BNIP3 and BNIP3L/NIX, as well as phosphatase and tensin homolog-induced kinase 1. Moreover, we have analyzed the cross talk of this pathway with tumor necrosis factor-related apoptosis-inducing ligand (TRAIL)-induced apoptosis upon combinatorial treatment with RL2 and TRAIL. Strikingly, we found two opposite effects of this co-treatment. RL2 had inhibitory effects on TRAIL-induced cell death upon short-term co-stimulation. In particular, RL2 treatment blocked TRAIL-mediated caspase activation, cell viability loss, and apoptosis, which was mediated via the downregulation of the core proapoptotic regulators. Contrary to short-term co-treatment, upon long-term co-stimulation, RL2 sensitized the cells toward TRAIL-induced cell death; the latter observation provides the basis for the development of therapeutic approaches in breast cancer cells. Collectively, our findings have important implications for cancer therapy and reveal the molecular switches of the cross talk between RL2-induced mitophagy and TRAIL-mediated apoptosis.

Keywords: apoptosis, mitophagy, RL2, TOM70, TRAIL, lactaptin, milk proteins and peptides

OPEN ACCESS

Edited by:
Jianke Zhang,
Thomas Jefferson University,
United States

Reviewed by:
Ming-Zong Lai,
Academia Sinica, Taiwan
Elodie Lafont,
INSERM U1242 Laboratoire COSS, France

***Correspondence:**
Inna N. Lavrik
inna.lavrik@med.ovgu.de

† These authors have contributed equally to this work

Specialty section:
This article was submitted to Cell Death and Survival, a section of the journal Frontiers in Cell and Developmental Biology

Received: *15 October 2020*
Accepted: *09 December 2020*
Published: *18 January 2021*

Citation:
Wohlfromm F, Richter M, Otrin L, Seyrek K, Vidaković-Koch T, Kuligina E, Richter V, Koval O and Lavrik IN (2021) Interplay Between Mitophagy and Apoptosis Defines a Cell Fate Upon Co-treatment of Breast Cancer Cells With a Recombinant Fragment of Human κ-Casein and Tumor Necrosis Factor-Related Apoptosis-Inducing Ligand. Front. Cell Dev. Biol. 8:617762. doi: 10.3389/fcell.2020.617762

INTRODUCTION

Apoptosis is a program of cell death that is essential for all multicellular organisms (Krammer et al., 2007; Lavrik and Krammer, 2012). Its deregulation is associated with several diseases, including cancer. Several programs of cell death have been discovered to date (Galluzzi et al., 2018). Cross talk between different cell death modalities plays a key role in shaping life/death decisions in the cell. Furthermore, the success of anticancer therapies strongly depends on the efficiency of cell death induction and intrinsic cross talk of several cell death modalities. However, it is well known that many combinatorial treatments can also induce strong antiapoptotic responses. This can prevent apoptosis by upregulation of antiapoptotic genes and, hence, counteract the effect of anticancer therapies (Buchbinder et al., 2018). Accordingly, the detailed analysis of the cell death network upon administration of several cell death stimuli plays a key role in the development of contemporary anticancer therapies.

Tumor necrosis factor-related apoptosis-inducing ligand (TRAIL)-based agents are promising anticancer therapeutics that are in clinical trials for several cancer therapies, including breast cancer (Lemke et al., 2014; von Karstedt et al., 2017). TRAIL is a member of the death ligand family (Lafont et al., 2017). Binding of TRAIL to the specific receptors (TRAILR1/2) leads to the formation of the death-inducing signaling complex (DISC) and initiation of the extrinsic apoptosis pathway as well as caspase activation (Sprick et al., 2000; Spencer et al., 2009; Lafont et al., 2017). TRAIL receptors 1 and 2 belong to the death receptor family and are also named death receptors 4 and 5. In addition to the receptors, the adaptor protein Fas-associated protein with death domain (FADD), the initiator procaspase-8a/b (p55/p53), procaspase-10, and cellular FADD-like interleukin-1β-converting enzyme-inhibitory protein (c-FLIP) are part of the DISC (Sprick et al., 2000; Walczak and Haas, 2008). After recruitment to the DISC, procaspase-8a/b builds death effector domain (DED) filaments, formed via homotypic interactions between the DEDs of individual procaspase-8 molecules (Dickens et al., 2012; Schleich et al., 2012; Fu et al., 2016). This provides the platform for homodimerization of procaspase-8 molecules, its subsequent activation and processing of procaspase-8a/b to p43/p41, p30, and formation of caspase-8 heterotetramers $p10_2$-$p18_2$ (Lavrik et al., 2003; Hoffmann et al., 2009; Dickens et al., 2012). The activation of procaspase-8 is blocked by c-FLIP proteins (Hughes et al., 2016; Hillert et al., 2020).

There are two types of TRAIL signaling downstream of the DISC, which take place in the so-called type I and type II cells (Aldridge et al., 2011; von Karstedt et al., 2017). In type I cells, a high amount of the TRAIL DISC is formed, followed by the generation of high amounts of caspase-8 and subsequent cell death. In type II cells, smaller quantities of caspase-8 are formed at the DISC, and, accordingly, the propagation of cell death requires the mitochondrial amplification loop, which is mediated via Bid cleavage to tBid, translocation of tBid to mitochondria, cytochrome C release from the mitochondria, and caspase-9 activation (von Karstedt et al., 2017). Apoptosis induction in type II cells is controlled by X-linked inhibitor of apoptosis protein/caspase-3 ratios and can be blocked by overexpression of Bcl-2/Bcl-XL (Scaffidi et al., 1998; Aldridge et al., 2011; Kaufmann et al., 2012).

Lactaptin is the proteolytic fragment of the human milk protein κ-Casein (Semenov et al., 2010). A recombinant analog of lactaptin, the peptide RL2 (recombinant lactaptin 2), which comprises amino acid 23-134 of human κ-Casein, has been described to induce cell death of breast carcinoma cells (Semenov et al., 2010). In particular, this peptide was shown to induce cell death in MDA-MB-231 and MCF-7 cells and suppress tumor growth in mice models (Koval et al., 2012, 2014). RL2 was reported to modulate the expression of apoptotic proteins and induce autophagy in MDA-MB-231 cells (Koval et al., 2014; Bagamanshina et al., 2019). RL2 acts in monomeric, dimeric, and oligomeric forms; the latter are formed via cysteine bridges (Chinak et al., 2019). Moreover, recently, it has been shown that RL2 mediates cell death, which was accompanied by the loss of mitochondrial membrane potential and intracellular adenosine triphosphate (ATP) loss (Richter et al., 2020). Mass spectrometry-based screening of RL2 interactome identified the mitochondrial import protein TOM70 as an interaction partner of RL2. Further, it was unveiled that RL2 is targeted to the mitochondria after internalization into the cells (Richter et al., 2020). The requirement for TOM70/RL2 interaction in RL2-induced reduction of intracellular ATP levels was validated by downregulation of TOM70, resulting in partial rescue of the intracellular ATP yield. Taken together, it was shown that RL2-mediated cell death is mediated via mitochondria, in particular via interactions with TOM70. However, the detailed mechanisms of RL2 action at mitochondria leading to cell death needs to be further investigated. In particular, it remains unknown which molecular pathway plays a major role in RL2-mediated ATP loss and RL2-induced cell death.

In the current study, we uncover that RL2 acts via induction of mitophagy, leading to the ATP down-modulation. Moreover, we have analyzed the cross talk of this pathway with TRAIL-induced apoptosis and the effects of RL2 on TRAIL-induced apoptotic signaling. To this end, we addressed the interplay of extrinsic apoptosis and mitophagy upon co-administration of TRAIL and RL2 in breast cancer cells and delineated the major molecular switches between these pathways. Both agents are considered potent cell death inducers in breast cancer cells, and therefore, their combination is highly promising due to its putative therapeutic applications. Therefore, the current study leading to the understanding of the molecular mechanism of RL2/TRAIL co-treatment plays an important role in developing new therapeutic approaches for breast cancer.

RESULTS

RL2 Blocks Tumor Necrosis Factor-Related Apoptosis-Inducing Ligand-Induced Cell Viability Loss in Breast Cancer Cells

RL2 treatment alone induces cell viability loss of breast cancer cells (**Figure 1A**), whereas TRAIL treatment alone causes the

cell death of TRAIL-sensitive cells (Sprick et al., 2000; von Karstedt et al., 2017; Richter et al., 2020). To analyze the effects of RL2/TRAIL coadministration on cell viability, the treatment of MDA-MB-231 breast carcinoma cells with RL2, TRAIL, or their combination was carried out (**Figure 1B**). RL2 treatment alone caused only a slight cell viability loss, which was measured by metabolic assays, in the 6 h after its administration (**Figures 1A,B**). This was in line with previous reports (Richter et al., 2020). TRAIL addition alone led to a more pronounced cell viability loss compared with RL2. Already 4 h after TRAIL-only administration, the cell viability was strongly down-modulated compared with RL2-only treatment (**Figure 1B**). Strikingly, the coadministration of RL2 blocked TRAIL-mediated cell viability loss upon short-term treatment. In particular, 4 h after RL2/TRAIL co-stimulation, only a slight reduction in cell viability loss was observed, which was in contrast to the strong TRAIL-induced cell viability loss observed during this time interval (**Figure 1B**). However, the inhibitory effects of RL2 disappeared after longer stimulation of MDA-MB-231 cells. Moreover, 24 h after stimulation, RL2/TRAIL-induced cell viability loss was stronger than that mediated by TRAIL only or RL2 only (**Figure 1B**).

RL2 treatment of breast carcinoma cells induces the intracellular ATP loss that accompanies RL2-mediated cell death (Richter et al., 2020). The ATP loss might be considered as an indirect indication of cell viability loss. Hence, next, we analyzed the effects of RL2/TRAIL co-treatment on MDA-MB-231 cells via measuring intracellular ATP content (**Figure 1C**). In these experiments, in accordance with previous reports, RL2 treatment alone led to ATP down-modulation (Richter et al., 2020). Similarly, TRAIL treatment alone also led to strong ATP loss. Moreover, similar to the effects observed in **Figure 1B**, RL2/TRAIL co-treatment led to the inhibitory action of RL2 on TRAIL-induced ATP loss in MDA-MB-231 cells upon short-term treatment (**Figure 1C**). Strikingly, similar inhibitory effects of RL2 on TRAIL-induced cell viability loss were also observed on the other cell lines, such as ovarian carcinoma CAOV-4 cells (**Supplementary Figure 1**). Furthermore, analogous to the observations made using metabolic assays on MDA-MB-231 cells (**Figure 1B**), the inhibitory effects of RL2 disappeared after longer stimulation intervals (**Figure 1C**). Taken together, these experiments suggest that TRAIL and RL2 co-treatment blocks short-term and promotes long-term TRAIL-induced cell viability and ATP loss. Next, we aimed at uncovering the mechanisms behind these observed effects.

Mitochondrial respiratory complexes drive ATP production. RL2 blocks intracellular ATP production (**Figure 1C**), which might occur via perturbing the function of the mitochondrial respiratory chain. However, it is known that cells with compromised respiration might shift energy production to anaerobic glycolysis. The latter might take place upon RL2 treatment of the cells. To test this hypothesis, the oxygen consumption rate of MDA-MB-231 cells upon RL2 treatment was measured using a Clark-type electrode (**Figures 1D,E**). Strikingly, no alterations in the oxygen consumption were detected upon RL2 treatment (**Figure 1E**). This allows us to conclude that RL2 action does not directly involve perturbation of the mitochondrial respiratory chain, and other mechanisms leading to the ATP loss upon RL2 treatment were further investigated.

RL2 Blocks Tumor Necrosis Factor-Related Apoptosis-Inducing Ligand-Induced Caspase-8 Activation at the Death-Inducing Signaling Complex

TRAIL treatment leads to induction of the extrinsic apoptosis pathway, which is orchestrated by caspase activation. Caspase-8 is an apical or initiator caspase of TRAIL-induced apoptosis, triggering the effector caspase cascade. To find out whether inhibition of effector caspases occurs already at the level of initiator caspase activation, caspase-8 activity in MDA-MB-231 cells upon RL2, TRAIL, or RL2/TRAIL treatment for 3 h was measured (**Figure 2A**). TRAIL-only treatment resulted in a strong induction of caspase-8 activity after TRAIL stimulation, which is in line with previous reports (Sprick et al., 2000, 2002). RL2 alone did not cause any increase in caspase-8 activity. Moreover, the addition of RL2 strongly blocked the induction of caspase-8 activity induced by TRAIL (**Figure 2A**). These findings were further supported by a Western blot analysis of procaspase-8a/b processing, which indicated that RL2 co-treatment strongly diminished TRAIL-induced procaspase-8a/b processing to p43/p41, p30, and p18 (**Figure 2B**). Taken together, these results indicate that RL2 inhibits TRAIL-induced caspase activation already at the level of initiator caspase-8.

Upon TRAIL stimulation, caspase-8 is activated at the TRAIL DISC, comprising TRAILR1/2, FADD, procaspase-8/10, and c-FLIP proteins (Sprick et al., 2000; von Karstedt et al., 2017). In addition, caspase-8 has been reported to be activated in complex IIa, which also comprises the core components of the DISC: FADD, procaspase-8/10, and c-FLIP proteins (Lafont et al., 2017; von Karstedt et al., 2017). Because caspase-8 activation was inhibited upon RL2/TRAIL co-treatment, the next step was to test whether RL2 is recruited to the macromolecular complexes formed upon TRAIL stimulation and thereby interferes with caspase-8 activation. To this point, caspase-8 and FADD co-immunoprecipitations (co-IPs) were carried out with MDA-MB-231 cells using anti-caspase-8 and anti-FADD antibodies, respectively. These co-IPs should pull-down both complex II and DISC. RL2 stimulation alone did not trigger the association of FADD, procaspase-8, and c-FLIP proteins (**Supplementary Figures 2A,B**). TRAIL-only stimulation led to the association of procaspase-8, FADD, and c-FLIP, which were detected in both FADD co-IP (**Supplementary Figure 2A**) and caspase-8 co-IP (**Supplementary Figure 2B**). However, no association of RL2 with the core TRAIL DISC components was observed upon RL2/TRAIL co-treatment, neither in the FADD co-IP (**Supplementary Figure 2A**) nor in the caspase-8 co-IP (**Supplementary Figure 2B**). Moreover, the levels of association between FADD, procaspase-8, and c-FLIP were not changed

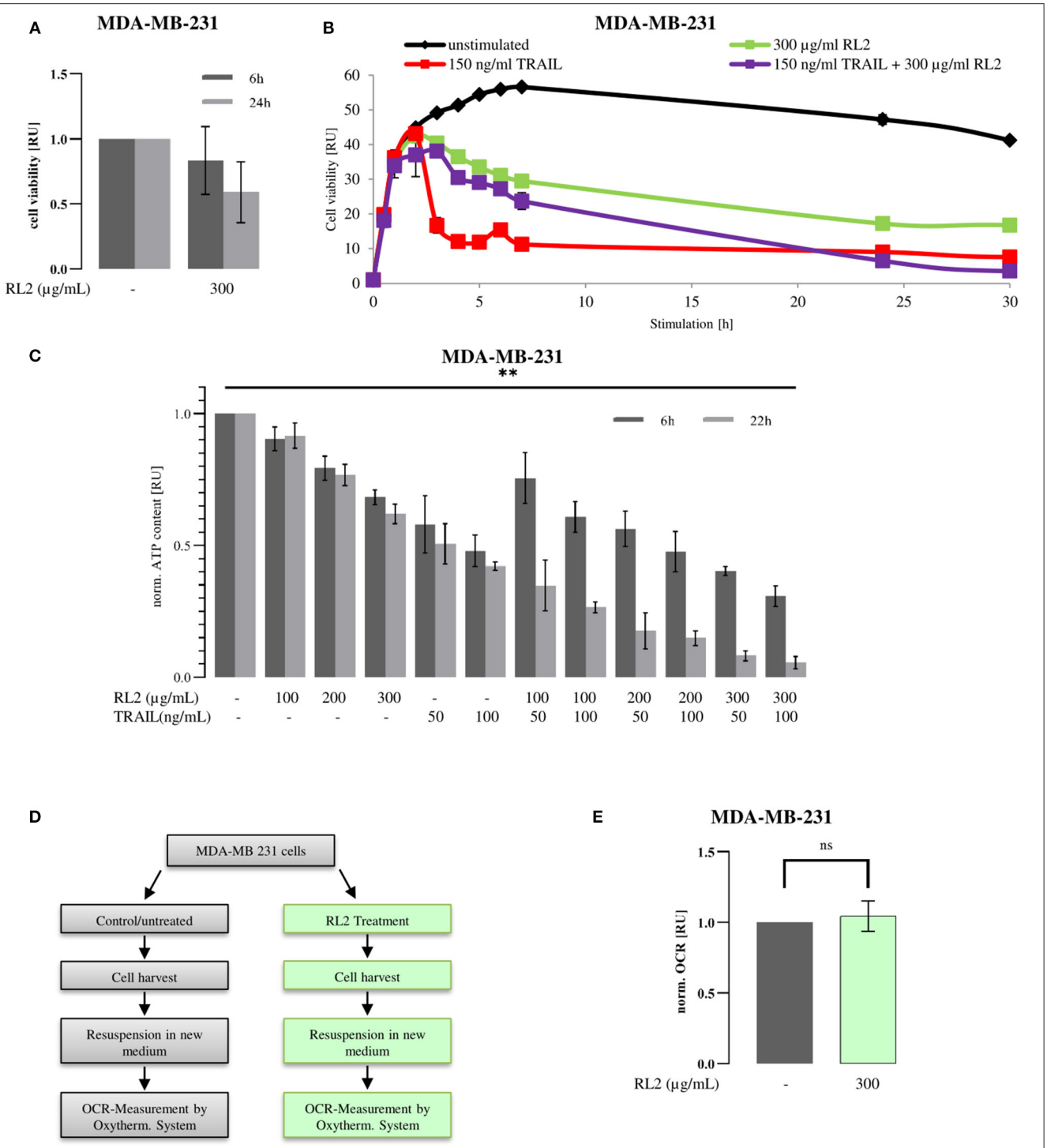

FIGURE 1 | RL2 inhibits TRAIL-induced cell viability loss in MDA-MB-231 cells during the first hours of TRAIL stimulation. MDA-MB-231 cells were treated with indicated concentrations of RL2, TRAIL, or their combination for 6–48 h. **(A,B)** Cell viability was measured using the metabolic RealTime-Glo MT Cell Viability Assay. **(C)** Cellular ATP levels were measured using CellTiter-Glo Luminescent Cell Viability Assay/CellTiter-Glo Substrate, and cell viabilities are normalized to the ones of non-treated cells and presented in relative units. Mean and standard deviations are shown ($n = 3$). Statistical analysis was performed for 6 and 22 h by ANOVA test **(C)**. **(D)** Workflow for oxygen consumption rate (OCR) measurement after RL2 treatment. Cells were treated (green) or remained untreated (gray) for 8 h. Then, medium was aspirated, and cells were harvested. Cells were resuspended in fresh media, and OCR was measured by Oxytherm System (Hansatech Instruments Ltd, Norfolk, UK). **(E)** OCR measurements on RL2-treated MDA-MB-231 cells. Mean and standard deviations are shown ($n = 3$). Statistical analysis was performed by Student's *t*-test.

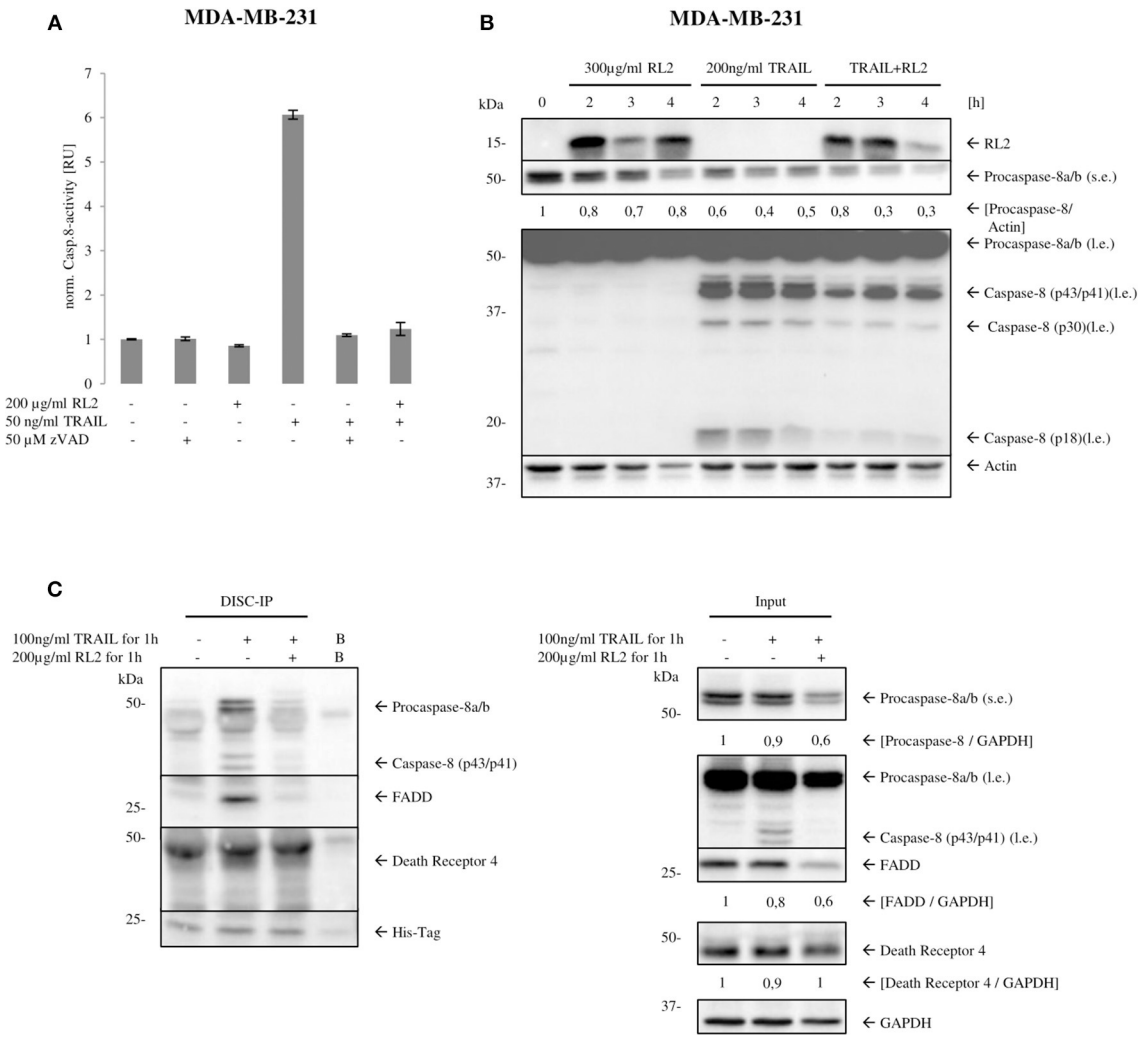

FIGURE 2 | RL2 reduces caspase-8 activity at the DISC. **(A)** MDA-MB-231 cells were treated with 200 µg/ml RL2, 50 ng/ml of TRAIL, or their combination for 3 h. Samples, which were pretreated with 50-µM pan-caspase inhibitor zVAD-fmk for 1 h, were used as a negative control. Caspase-8 activity was determined using Caspase-Glo 8 Assay. Caspase activity is normalized against untreated sample, and activity is shown in relative units. One representative assay of three independent ones is shown. **(B)** MDA-MB-231 cells were treated with 300 µg/ml RL2, 200 ng/ml TRAIL, or their combination for indicated time points and subjected to Western blot analysis with indicated antibodies. Procaspase-8 cleavage products p43/p41, p30, and p18 are indicated. One representative Western blot of two independent experiments is shown. l.e., long exposure; s.e., short exposure. Protein expression was quantified and normalized to actin. Quantification is shown under the specific bands. **(C)** MDA-MB-231 cells were treated with the indicated TRAIL, RL2, and RL2/TRAIL concentrations for 1 h. Co-IPs were performed with 5-µg anti-6 x His-Tag antibody (DISC-IP). Lysate (input) and DISC-IP were analyzed by Western blot for the indicated proteins. "Bead control" **(B)**: IP without any antibody addition. One representative experiment of two is shown.

upon the addition of RL2. These results strongly indicate that RL2 is not directly associated with FADD, procaspase-8, or c-FLIP. However, these results do not exclude that the composition of the TRAIL DISC upon RL2 co-stimulation might be different, as co-IP via FADD and procaspase-8 might result in the different ratios of these proteins than in the native DISC complex.

To check this hypothesis, we performed DISC co-IP (**Figure 2C**). This co-IP was performed via the His-tagged TRAIL, which allowed to pull-down FADD, procaspase-8, and TRAILR upon TRAIL stimulation (**Figure 2C**). Indeed, in accordance with our suggestion, the ratios of these proteins were different at the DISC from the complex II. In particular, upon RL2/TRAIL co-treatment, decreased amounts of procaspase-8a/b and FADD at the TRAIL DISC were observed compared with TRAIL only treatment (**Figure 2C**). Furthermore, we have detected the downregulation of FADD and procaspase-8 in the corresponding cellular lysates upon RL2 treatment, whereas the amounts of TRAILR1 remained unchanged in similar conditions (**Figure 2C**). This allowed us to draw a conclusion that RL2 treatment leads to the decrease of procaspase-8 and FADD amounts, which results in the less efficient DISC formation and caspase-8 activation.

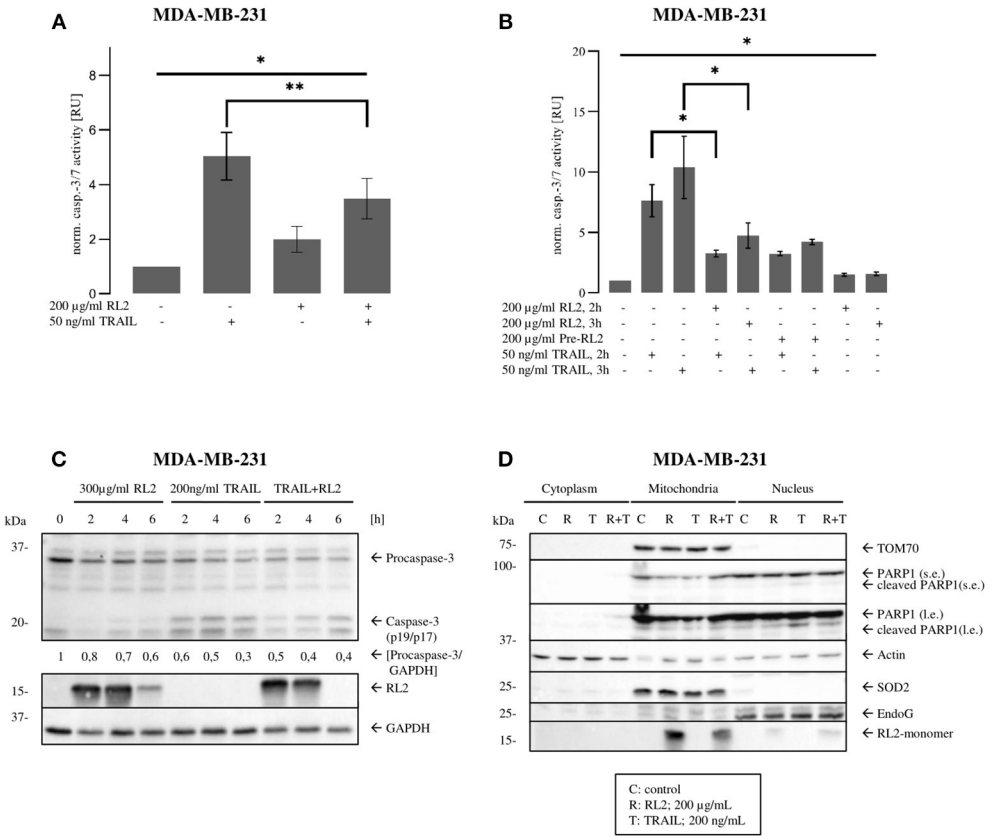

FIGURE 3 | RL2 inhibits TRAIL-induced effector caspase activity in MDA-MB-231 cells during first hours after TRAIL stimulation. **(A,B)** MDA-MB-231 cells were treated with indicated concentrations of RL2, TRAIL, the combination of both, or 2-h pretreatment by RL2 for 3 h. Caspase-3/-7-activity was determined using Caspase-Glo3/7 Assay. Caspase activities are normalized to the non-treated cells and presented in relative units. Mean and standard deviations are shown ($n = 3$). Statistical analysis was performed by ANOVA test (upper lane) or by paired Students *t*-test (angular area). **(C)** MDA-MB-231 cells were treated with 300 µg/ml RL2, 200 ng/ml TRAIL, or their combination for indicated time points and subjected to Western blot analysis with the indicated antibodies. Caspase-8 cleavage products p43/p41and caspase-3 cleavage products are indicated. One representative Western blot of two independent experiments is shown. Quantification of the protein expression was normalized to GAPDH. Quantification is shown under specific areas. **(D)** MDA-MB 231 cells were treated with 200 µg/ml RL2 ("R"), 100 ng/ml TRAIL ("T"), their combination ("R + T"), or left untreated ("C") for 1 h. Cells were separated into "Cytoplasm," "Mitochondria," and "Nucleus" fractions. Fractions were analyzed by Western blot with indicated antibodies. SOD2, Actin, and EndoG were used as fraction controls. One representative Western blot of three is shown. Quantification of three independent Western blots for this experiment is shown in **Supplementary Figure 3**. l.e., long exposure; s.e., short exposure.

RL2 Blocks Tumor Necrosis Factor-Related Apoptosis-Inducing Ligand-Induced Effector Caspase Activation

Caspase-8 triggers the effector caspase cascade. Accordingly, next, we analyzed whether RL2 treatment impinges on TRAIL-induced effector caspase activity. To this point, caspase-3/7 activation in MDA-MB-231 cells upon RL2, TRAIL, or their co-treatment was investigated. In concordance with the results of cell viability and caspase-8 activity assays, TRAIL treatment alone induced strong caspase-3/7 activity after stimulation for 3 h. This effector caspase activity was inhibited by RL2 co-treatment (**Figure 3A**). The same inhibitory effects of RL2 on TRAIL-induced caspase-3/7 activity were observed within 2 h after co-stimulation (**Figure 3B**). Interestingly, the pretreatment of MDA-MB-231 cells with RL2 for 2 h did not modulate its inhibitory action on TRAIL-induced caspase activity (**Figure 3B**). These findings were supported by a Western blot analysis of procaspase-3 processing, which demonstrated that RL2 co-treatment inhibits TRAIL-induced procaspase-3 processing (**Figure 3C**). In particular, downregulation of procaspase-3 and subsequently of its active subunits was observed. Hence, it might be concluded that RL2 inhibits TRAIL-induced effector caspase activation.

Our previous reports have demonstrated that RL2 is targeted to mitochondria, where it interacts with TOM70 (Richter et al., 2020). To check whether there is any alteration in mitochondrial localization of RL2 after co-stimulation with TRAIL, a cellular fractionation was carried out. In line with our previous reports, RL2 was found largely in the mitochondrial fraction under both stimulation conditions: upon single treatment and upon RL2/TRAIL co-treatment (**Figure 3D**). This allowed us

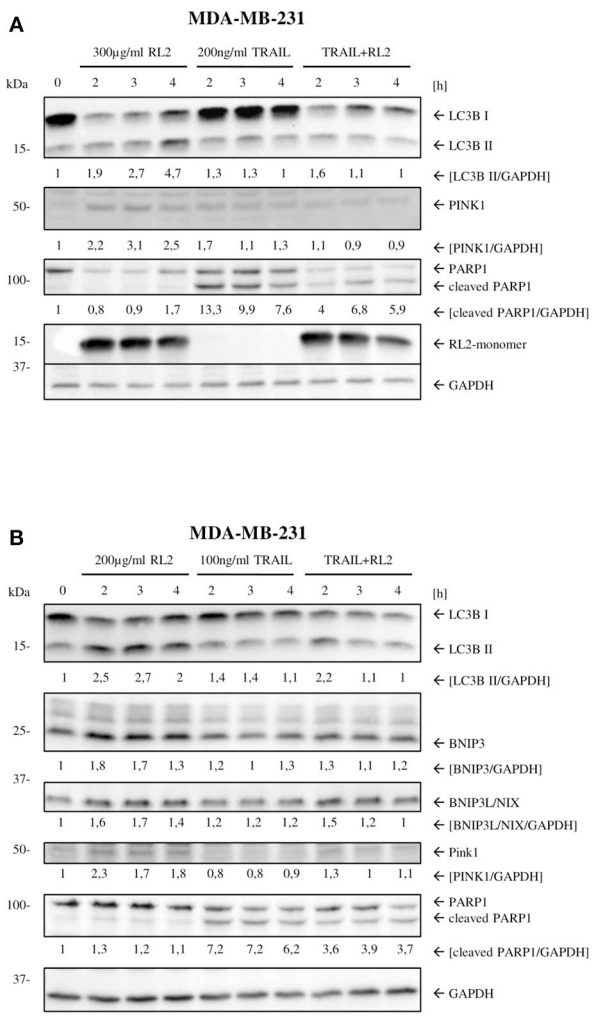

FIGURE 4 | RL2 induces mitophagy during first hours after stimulation. **(A)** MDA-MB-231 cells were treated with 300 µg/ml RL2, 200 ng/ml TRAIL, or the combination of both for indicated time intervals and subjected to Western blot analysis with the indicated antibodies. One representative Western blot of three independent experiments is shown. **(B)** MDA-MB-231 cells were treated with 200 µg/ml RL2 for indicated time intervals and subjected to Western blot analysis with the indicated antibodies. One representative Western blot of three independent experiments is shown. Quantification of three independent Western blots for this experiment is shown in **Supplementary Figure 4**. Quantification of the protein expression was normalized to GAPDH.

to conclude that RL2 is also targeted to mitochondria upon RL2/TRAIL co-treatment and might act in a similar fashion as upon single treatment.

Activation of effector caspases leads to the cleavage of their substrates, which is leading to the demolition of the cells. One of the caspase substrates, poly (adenosine diphosphate ribose) polymerase 1 (PARP1), has been described to serve as a key marker of effector caspase activation. The analysis of PARP1 cleavage in the nuclear fraction upon RL2/TRAIL co-treatment for 1 h demonstrated that this process is strongly inhibited by RL2 compared with single TRAIL treatment for 1 h (**Figure 3D** and **Supplementary Figure 3**). This further supports the inhibitory role of RL2 in TRAIL-induced apoptosis upon short-term treatment. Collectively, these findings indicate that RL2 impairs TRAIL-induced caspase activation at the level of both initiator and effector caspases.

RL2 Induces Mitophagy and Down-Modulation of Key Apoptotic Proteins

We have previously shown that RL2 interacts with TOM70 at mitochondria (Richter et al., 2020). Moreover, TOM70 serves as a receptor for phosphatase and tensin homolog-induced kinase 1 (PINK1), which is a key initiator protein of mitophagy (Kato et al., 2013). Mitophagy is a selective form of autophagy that is responsible for the removal of damaged mitochondria (Lazarou et al., 2015). The blockage of PINK1 interactions with TOM complex and TOM70 has been reported to induce mitophagy due to the impaired mitochondrial import of PINK1 (Youle and Narendra, 2011). Accordingly, we suggested that RL2 interaction with TOM70 might impair PINK1 import and lead to the induction of mitophagy, which is naturally accompanied by a loss of ATP and mitochondrial membrane potential (Youle and Narendra, 2011; Hamacher-Brady and Brady, 2016). To test this hypothesis, we analyzed the expression of key mitophagy markers (Hamacher-Brady and Brady, 2016) in MDA-MB-231 cells upon RL2 and RL2/TRAIL treatment using Western blot. Already 2 h after RL2 treatment, an increased signal of LC3B-II was detected along with the upregulation of BNIP3, BNIP3L, and PINK1 (**Figures 4A,B**; **Supplementary Figures 4A,B**). The same pattern was observed in co-stimulatory treatment with RL2/TRAIL (**Figures 4A,B**; **Supplementary Figures 4A,B**). Interestingly, the peak increase in mitophagy markers was observed after approximately 2 h of RL2 treatment, followed by their slow decrease. Moreover, this decrease was more prominent upon co-stimulatory treatment with RL2/TRAIL. The down-modulation of mitophagy markers fits well with the degradation of RL2 in MDA-MB-231 cells (**Figures 4A,B**). Importantly, upon TRAIL treatment, no increase in LC3B-II was detected, and the upregulation of BNIP3, BNIP3L, and PINK1 was not observed either. Thus, it might be concluded that both RL2 and RL2/TRAIL co-treatment induced mitophagy in MDA-MB-231 cells during short-term treatment.

Next, we checked whether mitophagy induction by RL2 leads to the down-modulation of core proapoptotic regulators in MDA-MB-231 cells. MDA-MB-231 are classified as type II cells (Aldridge et al., 2011). Therefore, they are dependent on caspase-8-mediated Bid cleavage and tBid generation for the propagation of TRAIL-induced apoptosis. Subsequently, the expression of procaspase-8 and Bcl-2 family members in parallel to LC3 processing was analyzed by Western blot (**Figure 5A**). RL2 treatment led to the downregulation of proapoptotic Bcl-2 family members Bid and Bax (**Figure 5A**). In accordance with (**Figures 2B,C**), procaspase-8a/b down-modulation was observed upon RL2 treatment also in these experiments (**Figure 5A**). These processes took place strictly in parallel to LC3 processing (**Figure 5A**). Importantly, the same effects

were observed upon RL2/TRAIL co-stimulation (**Figure 5B**). Indeed, down-modulation of procaspase-8 (**Figures 2B,C**) and Bax along with LC3 processing (**Figure 5B**) were monitored upon RL2/TRAIL co-treatment. This suggests that mitophagy-mediated downregulation of key apoptotic proteins blocks TRAIL signaling (**Figure 5B**). In particular, downregulation of Bid, which serves as a key link between activation of procaspase-8 at the DISC and amplification of the apoptotic signal in mitochondria of type II cells, might significantly contribute to the inhibition of TRAIL-induced apoptosis by RL2 co-treatment. Furthermore, a slight upregulation of Bcl-2 has been observed upon both RL2 and RL2/TRAIL co-treatment (**Figure 5**). Bcl-2 is a master regulator of life/death decision in type II cells (Scaffidi et al., 1998), and its upregulation might also contribute to the inhibitory effects of RL2 on TRAIL-induced apoptosis in MDA-MB-231 cells. Hence, this analysis demonstrates that the short-term RL2 treatment leads to downregulation of the core apoptotic regulators, including Bax and Bid, procaspases-8 and−3, and upregulation of antiapoptotic Bcl-2 protein and, accordingly, provides the basis for a diminished TRAIL signaling upon RL2/TRAIL stimulation.

Next, we checked whether the effect of RL2 on the expression of Bcl-2 family members could also be observed in other cell lines. The downregulation of Bax and Bid was also uncovered in MCF-7 cells; however, this downregulation was not as strong as in MDA-MB-231 cells, which is in line with the different sensitivity of these two cell lines toward RL2 treatment (Richter et al., 2020) (**Figure 5C**). These results suggest that RL2 treatment down modulates the key proapoptotic regulators of TRAIL-mediated apoptosis in breast cancer cells, possibly via mitophagy induction.

RL2/Tumor Necrosis Factor-Related Apoptosis-Inducing Ligand Co-treatment Inhibits Tumor Necrosis Factor-Related Apoptosis-Inducing Ligand-Mediated Cell Death Upon Short Term and Promotes Upon Long-Term Stimulation

RL2 co-treatment led to mitophagy induction upon short-term stimulation. To analyze RL2 effects on apoptotic cell death induced by TRAIL in MDA-MB-231 cells upon both short-term and long-term treatments, imaging flow cytometry and propidium iodide/annexin V staining were implemented (**Figures 6A–C**). TRAIL alone caused a strong increase in the amount of double-positive cells, which was observed already 6 h after TRAIL administration (**Figure 6A**). This indicates the induction of apoptosis, which was also consistent with the morphology of the TRAIL-treated cells (**Figure 6C**) (Pietkiewicz et al., 2015). In particular, the formation of apoptotic blebs was observed and typical nuclear changes occurring upon apoptosis induction (Pietkiewicz et al., 2015). The coadministration of RL2 inhibited TRAIL-mediated apoptosis in MDA-MB-231 cells upon short-term treatment (**Figure 6A**). This was in accordance with data on the inhibitory effects of RL2 on cell viability loss and caspase activity in MDA-MB-231 cells shortly after RL2/TRAIL co-stimulation. Moreover, in line with the observed effects of RL2 on cell viability loss upon the long-term treatment, RL2/TRAIL co-treatment for 48 h resulted in a higher number of dying cells compared with TRAIL-only treatment (**Figure 6B**). Consistent with the lower sensitivity of MCF-7 cells toward RL2 treatment (Richter et al., 2020), the inhibitory effects of RL2 on apoptosis in MCF-7 cells were observed at later time points (**Supplementary Figures 5A,B**). Taken together, RL2 inhibited TRAIL-induced apoptosis in MDA-MB-231 and MCF-7 cells upon short-term co-treatment and enhanced cell death upon long-term co-treatment.

DISCUSSION

Cross talk between different cell death modalities plays a key role in life/death decisions in the cell. Furthermore, the outcome of anticancer therapies strongly depends on the efficiency of cell death induction and the molecular balance of different cell death programs. Importantly, the outcome of combinatory effects upon treatment with several cell death stimuli is essential for the development of efficient anticancer therapies. Here, we addressed the interplay of cell death programs upon coadministration of TRAIL and RL2 to breast cancer cells. Both agents are considered promising cell death inducers in breast cancer cells, and, therefore, their combination is deemed highly important due to its putative therapeutic applications.

We have analyzed two major pathways involved in cell death regulation upon RL2 and TRAIL coadministration: mitophagy and apoptosis. TRAIL induces apoptosis, whereas RL2 induces mitophagy. Mitophagy results in the cellular ATP loss and downregulation of key proapoptotic proteins, which, in turn, leads to apoptosis inhibition. Moreover, two phases appear to be characteristic of the interplay between mitophagy and apoptosis. Initially, RL2-mediated mitophagy blocks apoptosis induction via downregulation of the core proapoptotic regulators, whereas at the later stages, apoptosis takes over. The latter might be connected to the proteolytic degradation of RL2 that was observed in this study and previous reports (Richter et al., 2020). Moreover, the ATP loss induced by mitophagy might lead to the ATP loss mediated necrosis on the single-cell level, which is likely contributing to the overall increase in the number of dying cells upon long-term RL2/TRAIL co-treatment. It has to be mentioned that autophagy induction by RL2 administration has been reported before (Bagamanshina et al., 2019). However, the recent attention toward the action of RL2 at mitochondria (Richter et al., 2020) allowed to suggest in the current study the contribution of mitophagy to RL2-mediated cell death. Moreover, the data presented in this study suggest that the autophagy markers, which were detected previously upon addition of RL2 (Bagamanshina et al., 2019), correspond to mitophagy induction. Hence, our current findings seem to be in accordance with previous reports.

Importantly, our study for the first time decoded the molecular mechanism of the RL2-mediated cell death and demonstrated that RL2 induces mitophagy. This allows solving the contradictions in the literature with respect to the possible mechanisms of RL2-mediated cell death. Furthermore, the

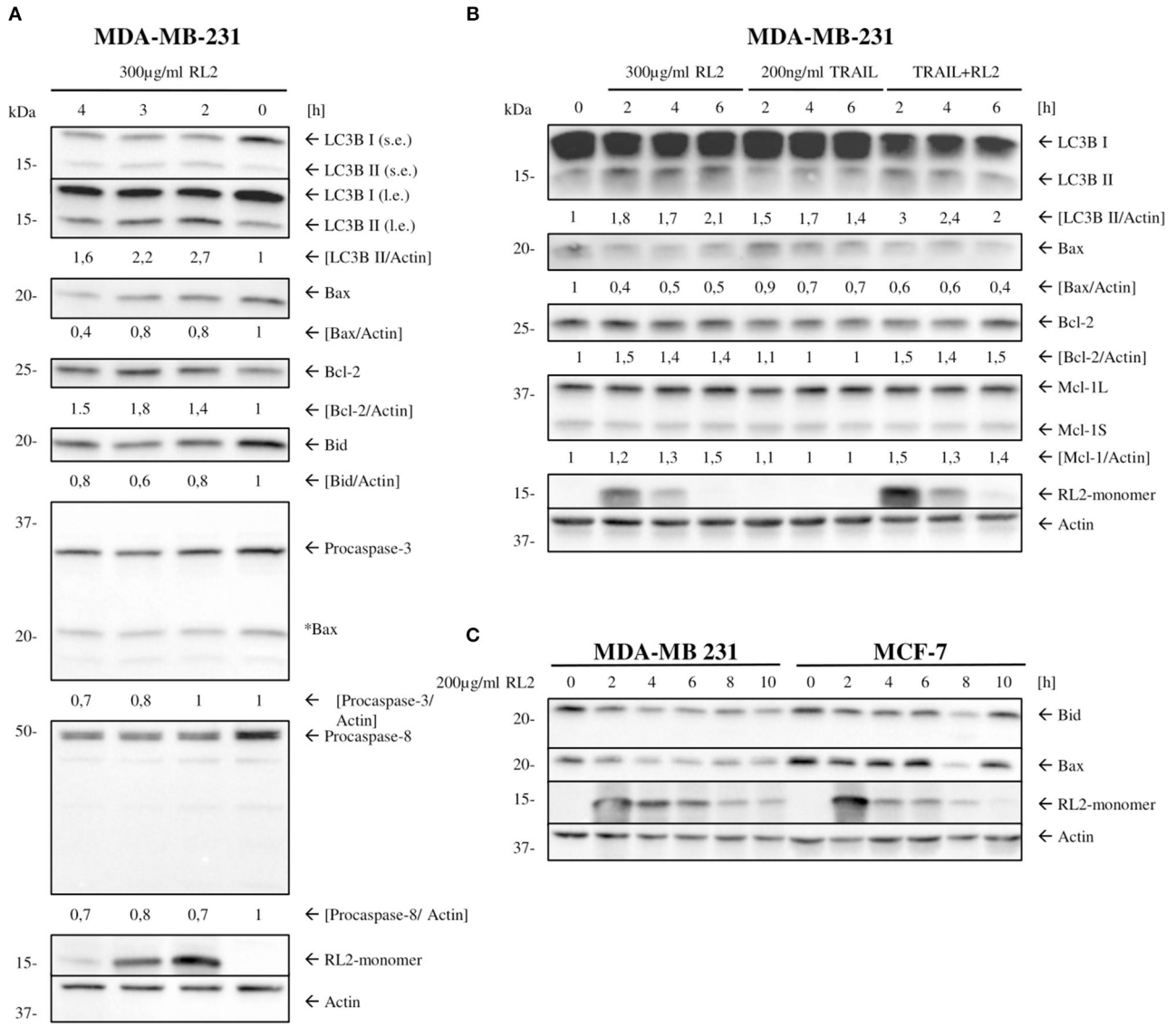

FIGURE 5 | RL2 changes the ratio between antiapoptotic vs. proapoptotic Bcl-2 protein family members. **(A,B)** MDA-MB-231 cells were treated with 300 µg/ml RL2, 200 ng/ml TRAIL, or the combination of both for indicated time intervals and subjected to Western blot analysis with the indicated antibodies. One representative Western blot of three independent experiments is shown. Quantification of the protein expression was normalized to actin. Quantification is shown under specific areas. **(C)** MDA-MB-231 and MCF-7 cells were treated with 200 µg/ml RL2 for indicated time intervals and subjected to Western blot analysis with the indicated antibodies. One representative Western blot of two independent experiments is shown.

interactome analysis of RL2, which deciphered the proteins of the TOM complex and, in particular, TOM70 as a key interaction partner of RL2, serves as important evidence hinting at RL2-induced mitophagy (Richter et al., 2020). TOM70 serves as a receptor for PINK1, which is a key inducer of mitophagy (Kato et al., 2013). The blockage of PINK1 interactions with TOM complex and TOM70 has been reported to induce mitophagy due to the impaired mitochondrial import of PINK1 (Youle and Narendra, 2011). As a result, PINK1 is not processed by PARL within mitochondria and accumulated at the outer mitochondrial membrane, leading to the recruitment of PARKIN that triggers mitophagy (Lazarou et al., 2015). Subsequently, we suggest that RL2 interaction with TOM70 serves as a blocker of TOM70 and thereby impairs PINK1 import. Hence, the induction of mitophagy via RL2 also supports the role of TOM70 and the TOM complex in PINK1 mitochondrial import.

Moreover, the induction of mitophagy provides an explanation for the drop of the mitochondrial membrane and potential ATP synthesis, occurring in the course of mitophagy (Youle and Narendra, 2011), that are observed upon

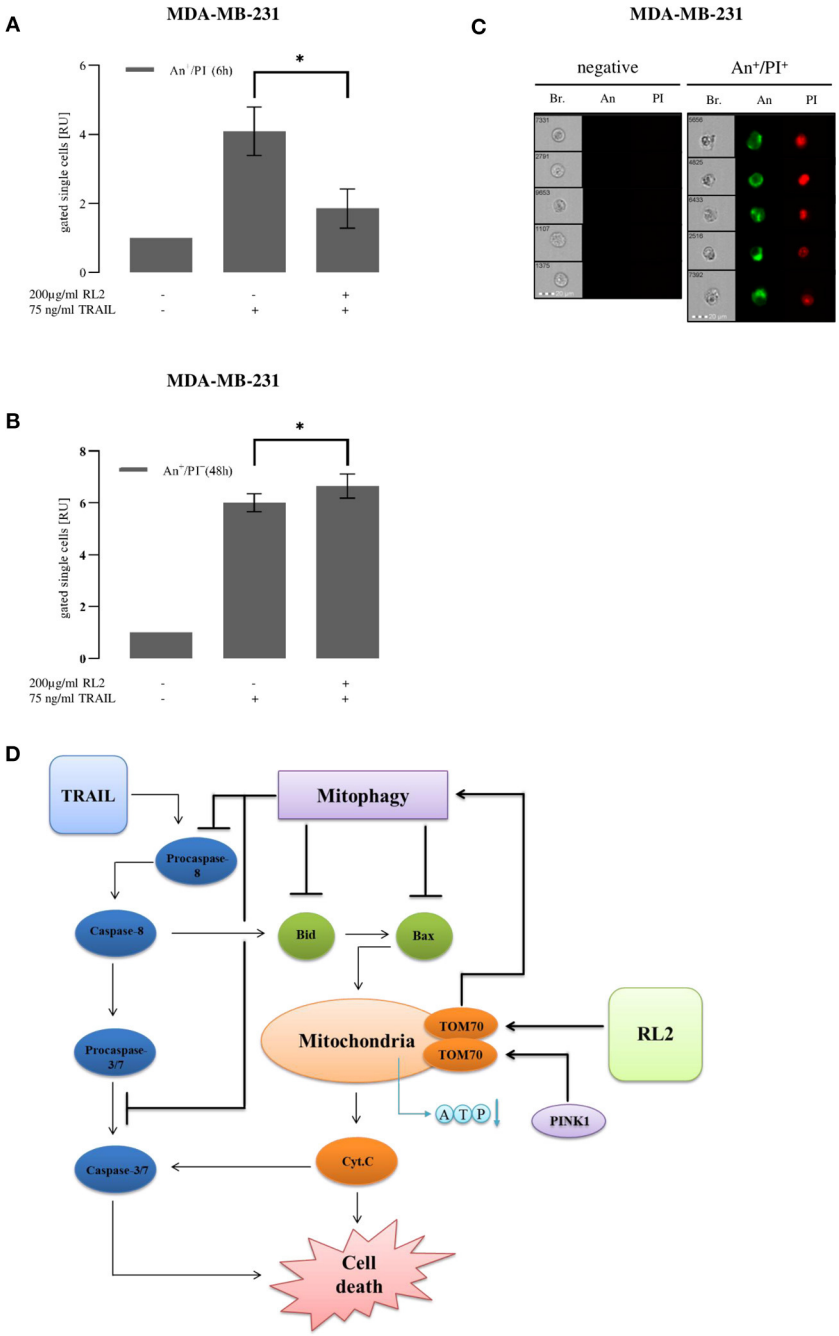

FIGURE 6 | RL2 decreases TRAIL-induced cell death in first hours after TRAIL stimulation and sensitizes cells in long-term treatments. MDA-MB-231 cells were stimulated with indicated concentrations of TRAIL or RL2/TRAIL combination for 6 h **(A)** or 48 h **(B)**. Cell death was measured using annexin V (An)/propidium iodide (PI) staining and analyzed with FlowSight. Amount of double-positive An^+/PI^+ cells calculated from three independent experiments are shown in relative units. Statistical analysis was performed by paired Student's *t*-test **(A,B)**. **(C)** Five representative images of double-negative An^-/PI^- (viable) and double-positive An^+/PI^+ cells are shown. Abbreviations: Brightfield (Br.), annexin V (An), and propidium iodide (PI). **(D)** Cross talk of RL2- and TRAIL-induced mitophagy and caspase-8 apoptotic cascade.

addition of RL2 to the cells in this study as well as in previous studies (Richter et al., 2020). It was suggested previously that the ATP loss upon RL2 administration might be resulting from perturbations of the mitochondrial respiratory chain (Richter et al., 2020). To test this hypothesis, we considered that cells with compromised respiration might shift the energy production to anaerobic glycolysis, and therefore, in this study, oxygen consumption was measured. Importantly, we did not

find any changes in oxygen consumption between treated and untreated cells, indicating that the ATP drop is not explained by perturbation of the mitochondrial respiratory chain. Hence, we rather suggest that the ATP loss observed upon RL2 treatment is based on mitophagy induction.

Taken together, we suggest the following scheme for the cross talk between RL2 and TRAIL stimulation (**Figure 6D**). TRAIL stimulation leads to DISC formation, caspase-8 activation, and apoptosis induction. Furthermore, after the penetration into the cells, RL2 is targeting mitochondria, where it binds to TOM70. This interaction blocks PINK1 transport leading to its accumulation at the outer mitochondrial membrane, loss of mitochondrial membrane potential, and induction of mitophagy. Further, PINK1 accumulation and its consequences result in decreased ATP synthesis and down-modulation of several key proapoptotic regulators, in particular, Bax and Bid, which are key players of the proapoptotic pathway. Moreover, the upregulation of Bcl-2 has been observed upon RL2 treatment, which is a key inhibitor of apoptotic response in type II cells (Scaffidi et al., 1998). This, in turn, might contribute to the down-modulation of TRAIL-induced apoptosis. Importantly, the same inhibitory effects on TRAIL signaling were observed on the other type II cells, ovarian carcinoma CAOV-4 cells. This suggests that RL2 might interfere with TRAIL-induced apoptosis in type II cells. However, all these effects are observed only within the first hours after RL2 administration, as, apparently, at the later time points, RL2 is degraded, and mitophagy is stopped, as was observed by the time-dependent decrease of mitophagy markers along with the decrease in RL2 levels.

The reports on the role of FADD and procaspase-8 in mitophagy and autophagy are still rather incoherent. In the current study, we have observed the downregulation of these two DED proteins leading to the decrease of TRAIL DISC formation and caspase-8 activation (**Figure 2**). Interestingly, in the previous reports, autophagy has been reported both to promote caspase-8 activity (Laussmann et al., 2011) as well as to down modulate the active caspase-8 (Hou et al., 2010). Moreover, FADD and procaspase-8 were reported to play a suppressor role in autophagy in proliferating T cells (Bell et al., 2008). Further, the formation of iDISC comprising FADD and procaspase-8, leading to caspase-8 activation at the autophagosomal membrane, was reported and interactions of FADD with ATG5 (Gordy and He, 2012). This shows that likely the effects of FADD and procaspase-8 on the mitophagy machinery might be cell-type and time-dependent, and further insights into these processes are required in future studies.

Importantly, upon long-term co-treatment, additive effects of TRAIL and RL2 administration were detected that led to the enhanced loss of cell viability and cell death. As discussed earlier, we suggest that this takes place in the second phase of RL2/TRAIL co-treatment when the effects of mitophagy are down-modulated. The detailed molecular mechanism of combinatorial effects of RL2 and TRAIL has to be addressed in future studies. These pathways might involve the Bcl-2-mediated down-modulation of mitophagy or mitophagy-induced priming of procaspase-8 activity at the later time points similar to the mechanisms mentioned earlier (Laussmann et al., 2011; Hamacher-Brady and Brady, 2016). Our findings demonstrate the potential of the RL2/TRAIL combination for therapeutic applications and the development of new anticancer therapeutic approaches. Moreover, the deregulation of mitophagy has been reported to be a feature of breast cancer cells leading to their resistant phenotype (Bernardini et al., 2017). In particular, the ablation of PINK1/Parkin-mediated mitophagy was reported to regulate the progression of breast cancers. Hence, the possibility of targeting breast cancer cells via administration of RL2 opens new therapeutic opportunities for breast cancer treatment. Moreover, the development of combinatorial treatments on the basis of RL2 might present a perspective approach for other therapeutic strategies for cancers associated with defects in mitophagy.

Taken together, we have further identified the molecular mechanisms of RL2 action in breast cancer cells. Our findings uncovered the molecular details of the cross talk between RL2-induced mitophagy and TRAIL-initiated apoptosis. We have identified that the interplay between mitophagy and TRAIL signaling inhibits cell death in the first stage and promotes it in the second stage. We conclude that the presented findings are likely to have important implications for cancer therapy and might pave the way toward the development of new therapeutic approaches for treating breast cancer.

MATERIALS AND METHODS

Cell Culture

Human adenocarcinoma cells MDA-MB-231 (#ACC 732, DSMZ, Germany) were maintained in Leibovitz L15 media (Gibco™), supplemented with 10% heat-inactivated fetal calf serum, 1% penicillin–streptomycin. Human adenocarcinoma cells MCF-7 (#ACC 115, DSMZ, Germany) were maintained in Roswell Park Memorial Institute 1640 medium (Thermo Fisher Scientific Inc., USA), supplemented with 10% heat-inactivated fetal calf serum, 1% penicillin–streptomycin, 1-mM sodium pyruvate, and 1× minimum essential medium nonessential amino acids in 5% carbon dioxide (CO_2). Human ovarian cancer cells CAOV-4, which is a kind gift of Prof. Zhivotovsky (Karolinska Institute, Stockholm, Sweden) (Zamaraev et al., 2018), were maintained in Dulbecco's modified Eagle medium/Ham's F-12 media (Pan-Biotech GmbH, Germany), supplemented with 10% heat-inactivated fetal calf serum, 1% penicillin–streptomycin, and 0.0001% puromycin in 5% CO_2.

Cell Viability Measurements by Adenosine Triphosphate Assay

MDA-MB-231 (1.2×10^4) or MCF-7 (2×10^5) cells were seeded in 96-well plates. Cells were stimulated in a volume of 50 µl. Measurements were performed according to the manufacturer's instructions (CellTiter-Glo® Luminescent Cell Viability Assay, Promega, Germany) with the addition of 50-µl CellTiter-Glo® solution to each well. The luminescence intensity was analyzed in duplicates using the microplate reader Infinite M200pro (Tecan, Switzerland). The values were normalized against the viability of untreated cells set as one relative unit (RU).

Cell Viability Measurements by Metabolic Assay

MDA-MB-231 (1.2×10^4) cells were seeded in 96-well plates. Cells were stimulated in a volume of 100 µl (50-µl medium + 50-µl metabolic substrate). Measurements were performed according to the instructions (RealTime-Glo™ MT cell Viability Assay, Promega Germany) with the addition of 50-µl metabolic substrate (2% MT cell viability substrate and 2% NanoLuc™Enzyme) to each well, directly before stimulation. The luminescence intensity was analyzed in duplicates using microplate reader Infinite M200pro (Tecan, Switzerland). The values were normalized against the viability of untreated cells that were set as one RU.

Caspase-3/7 Activity Assay

MDA-MB-231 (1.2×10^4) cells were seeded in 96-well plates. Cells were stimulated in a volume of 50 µl. Measurements were performed according to the manufacturer's instructions (Caspase-Glo® 3/7 Assay, Promega, Germany) with the addition 50 µl of the Caspase-Glo®3/7 solution to each well. The luminescence intensity was analyzed in duplicates by the microplate reader Infinite M200pro (Tecan, Switzerland). The values were normalized against caspase activity of non-treated cells and set as one RU.

Caspase-8 Activity Assay

MDA-MB-231 (1.2×10^4) cells were seeded in 96-well plates. Cells were stimulated with the indicated treatments in a volume of 50 µl. After 3 h incubation at 37°C and 5% CO_2, samples were measured according to the manufacturer's instructions (Caspase-Glo® 8 Assay, Promega, Germany) with the addition 50 µl of the Caspase-Glo®8 (with 0.3% MG-132-Inhibitor) solution to each well. The luminescence intensity was analyzed in duplicates by the microplate reader Infinite M200pro (Tecan, Switzerland). The values were normalized against caspase activity of non-treated cells and set as one RU.

Oxygen Consumption Rate Measurements

MDA-MB-231 (2.5×10^6) cells were seeded in 10-cm plates. Cells were stimulated with RL2 in a volume of 3 ml for 8 h. Subsequently, cells were trypsinated and resuspended in 500-µl fresh medium. Oxygen consumption rate (OCR) was measured by a Clark-type electrode in the Oxytherm System (Hansatech Instruments Ltd, Norfolk, UK). All samples were measured at 37°C and mixed continuously for ∼15 min. The baseline was recorded with 1 ml of fresh medium. Upon stable baseline (OCR < 0.4 nmol $\times$ min^{-1} $\times$ ml^{-1}), the cell samples were measured. Obtained data were fitted to linear regression, and the OCR was expressed in nmol O_2 $\times$ min^{-1} $\times$ ml^{-1}.

Cell Death Measurements by Imaging Flow Cytometry

Analysis of cell death induction was performed with FlowSight® Imaging Flow Cytometer (Amnis/MerckMillipore, USA). MDA-MB-231 cells were treated with RL2. Samples were stained with annexin V-fluorescein isothiocyante and propidium iodide. Data were analyzed with IDEAS software version 6.2 (Amnis/MerckMillipore, Darmstadt, Germany), as described previously (Pietkiewicz et al., 2015).

Western Blot Analysis and Co-immunoprecipitation

Cells ($1.25–2.5 \times 10^5$) were seeded in six-well plates. Cells were harvested, washed with phosphate-buffered saline (PBS), and lysed for 30 min on ice in lysis buffer (20-mM Tris-hydrochloride, pH 7.4, 137-mM sodium chloride, 2-mM ethylenediaminetetraacetic acid (EDTA), 10% glycerine, 1% Triton X-100, protease inhibitor mix (Roche, Mannheim, Germany) and subjected to Western blot analysis. Sodium dodecyl sulfate-polyacrylamide gel electrophoresis was performed with 12% sodium dodecyl sulfate gels. The TransBlot Turbo system (Biorad, Hercules, USA) was used to blot the gels to nitrocellulose membranes. The membranes were blocked with 5% nonfat dried milk in PBS with 0.05% Tween 20 for 1 h. Washing steps were performed with PBS-Tween three-fold for 5 min. Incubation with primary antibodies was performed overnight at 4°C in PBS-T. HRP-coupled isotype-specific secondary antibodies were incubated for 1 h at room temperature in 5% nonfat dried milk (SantaCruz, Dallas, USA). Chemiluminescence signal was produced with LuminataForte (MerckMillipore, Darmstadt, Germany) and detected with a ChemiDoc imaging system (Biorad, Hercules, USA). Caspase-8 and FADD co-IPs were performed with MDA-MB-231 cells upon RL2, RL2/TRAIL, or TRAIL stimulation. Stimulation was stopped by adding 10-ml cold PBS. Cells were centrifuged for 5 min at 500 $\times$ *g* and washed once with cold PBS. Cells were lysed in 500-µl lysis buffer for 30 min on ice and subsequently centrifuged for 15 min at 14,600 $\times$ *g*. Fifty-microliter supernatant was used as input control. The remaining supernatant of all samples was adjusted to the same protein concentration and used for immunoprecipitation. Five-microgram FADD or caspase-8 antibody was added to the lysate and incubated for 12 h at 4°C. Samples were subjected to Western blot analysis. DISC co-IP was performed with MDA-MB-231 cells after 1 h of TRAIL or RL2/TRAIL stimulation and via anti-6 x His-tag antibody directed against TRAIL (KillerTRAIL, Enzo Life Sciences). The lysis and co-IP steps were the same as for FADD- and caspase-8-co-IPs. Five-microgram anti-His-Tag antibody was used for each DISC co-IP.

Cellular Fractionation

MDA-MB-231 cells (2.5×10^6) were stimulated with 100 µg/ml RL2, 50 ng/ml TRAIL, TRAIL/RL2, or left untreated. All centrifugation steps in the following fractionation were performed at 17,000 $\times$ *g*. A swelling step was performed in swelling buffer [10-mM 4-(2-hydroxyethyl)-1-piperazineethanesulfonic acid, pH 7.6, 10-mM potassium chloride, 2-mM magnesium chloride, 0.1-mM EDTA, protease Inhibitor mix] for 5 min followed by addition of 0.3% NP-40 (Thermo Fisher Scientific Inc., USA) for 1 min. Centrifugation for 1 min resulted in a separation of the cytoplasmic fraction. The remaining pellet was resuspended in 500-µl swelling buffer and centrifuged for 15 s. The pellet was incubated for

30 min with 40-µl "nucleus buffer" [50-mM 4-(2-hydroxyethyl)-1-piperazineethanesulfonic acid, pH 7.8, 50-mM potassium chloride, 300-mM sodium chloride, 0.1-mM EDTA, 10% glycerol, protease Inhibitor mix], resuspended every 10 min, and centrifuged for 5 min. The nuclei-containing supernatant and mitochondria-containing pellet were separated and the pellet washed twice with PBS. The samples were subjected to Western blot analysis.

Statistics

Statistical analyses were performed with GraphPad Prism (Version 8.3.0). Paired Student *t*-test and one-way ANOVA test were performed as shown. *p*-Values are based on the following pattern: ns (not significant; $p > 0.05$), * (significant; $p < 0.05$), ** (significant; $p < 0.01$), *** (significant; $p < 0.005$), and **** (significant; $p < 0.001$).

Antibodies and Reagents

All chemicals were of analytical grade and purchased from AppliChem (Darmstadt, Germany), CarlRoth (Karlsruhe, Germany), Merck (Darmstadt, Germany), or Sigma-Aldrich (Taufkirchen, Germany). RL2 was purified as described previously (Koval et al., 2014). Z-VAD-FMK (N-1510, Bachem) and recombinant TRAIL (KillerTRAIL, Enzo Life Sciences) were given to cells in indicated concentrations. The following antibodies were used for Western blot analysis: polyclonal anti-Bax antibody (#5023), polyclonal anti-BID antibody (#2002), monoclonal anti-BNIP3 antibody (#44060), monoclonal anti-BNIP3/NIX antibody (#12396), polyclonal anti-caspase-3 antibody (#9662), monoclonal anti-Death Receptor 4 (D9S1T) antibody (#42533), polyclonal anti-endonuclease G (EndoG) antibody (#4969), polyclonal anti-LC3B antibody (#3868), polyclonal anti-PARP1 antibody (#9542), monoclonal anti-PINK1 antibody (#6946), and polyclonal anti-SOD2 antibody (#13194) from Cell Signaling Technology (USA); polyclonal anti-actin antibody (A2103) from Sigma-Aldrich, Germany; monoclonal anti-Bcl-2 antibody (sc-7382), polyclonal anti-GAPDH antibody (sc-48166), and polyclonal anti-Mcl-1 antibody (sc-819) from Santa Cruz Biotechnology (USA); polyclonal anti-κ-Casein antibody (#ab111406), polyclonal anti-6X His Tag antibody (ab9108), and polyclonal anti-TOM70 antibody (ab89624) from Abcam; and monoclonal anti-caspase-8 and anti-FADD antibodies (kindly provided by Prof. P. H. Krammer, DKFZ, Heidelberg). Horseradish peroxidase-conjugated goat anti-mouse immunoglobulins G1 and G2b and goat anti-rabbit and rabbit anti-goat were from Santa Cruz (California, USA).

DATA AVAILABILITY STATEMENT

The original contributions presented in the study are included in the article/**Supplementary Material**, further inquiries can be directed to the corresponding author/s.

AUTHOR CONTRIBUTIONS

FW, MR, and LO: experiments. FW: manuscript writing. LO, KS, TV-K, EK, VR, and OK: technologies and manuscript writing. IL: manuscript writing and supervision. All authors contributed to the article and approved the submitted version.

FUNDING

We acknowledge Volkswagen Foundation (VW90315), Wilhelm Sander-Stiftung (2017.008.02), Center of Dynamic Systems, funded by the European Union-programme European Regional Development Fund, and DFG (LA 2386) for supporting our work.

SUPPLEMENTARY MATERIAL

The Supplementary Material for this article can be found online at: https://www.frontiersin.org/articles/10.3389/fcell.2020.617762/full#supplementary-material

Figure S1 | RL2 inhibits TRAIL-induced cell viability loss in ovarian carcinoma CAOV-4 cells during the first hours of TRAIL stimulation Caov-4 cells were treated with indicated concentrations of RL2, TRAIL or their combination for 6 h. Cellular ATP levels were measured by using the CellTiter-Glo Luminescent Cell Viability Assay/ CellTiter-Glo Substrate and cell viabilities are normalized to the ones of non-treated cells and presented in relative units (RU). Mean and standard deviations are shown ($n = 2$). The statistical analysis was performed by Anova-test for 6 h.

Figure S2 | RL2 has no influence on TRAIL-induced complex II -formation (A, B) MDA-MB 231 cells were treated with the indicated TRAIL, RL2 and RL2/TRAIL concentrations for three hours. Immunoprecipitations (IPs) were done with **(A)** anti-FADD antibodies (FADD IP) and **(B)** anti-Caspase-8 antibodies (Casp.-8-IP). Both IPs were carried out with 5 ìg of the specific antibodies and analysed by Western Blot for the indicated proteins. Bead-control (Beads) were used as control without any antibody addition. One representative experiment out of two is shown for all experiments.

Figure S3 | RL2 inhibits TRAIL-induced PARP1 cleavage MDA-MB 231 cells were treated with 200 ìg/ml RL2, 100 ng/ml TRAIL or their combination for 1 h. The cells were separated in 'Cytoplasm', 'Mitochondria' and 'Nucleus' fractions. The fractions were analysed by Western Blot. Bands of cleaved-PARP were quantified against corresponding EndoG bands by ImageLab 5.1beta (Bio-Rad). Three independent Western Blot quantifications are shown.

Figure S4 | RL2 treatment induces autophagy/mitophagy **(A)** MDA-MB 231 cells were treated with 300 ìg/ml RL2, 200 ng/ml TRAIL or their combination for indicated time intervals and subjected to Western Blot analysis with the indicated antibodies. **(B)** MDA-MB 231 cells were treated with 200 ìg/ml RL2, 150 ng/ml TRAIL or the combination of both for indicated time intervals and subjected to Western Blot analysis with the indicated antibodies. Quantification of the Western Blot signals was carried out with ImageLab 5.1 beta. Three independent Western Blot quantifications are shown **(A, B)**.

Figure S5 | RL2 decreases TRAIL-induced cell death in the first hours after TRAIL stimulation (A,B) MCF-7 cells were stimulated with indicated concentrations of RL2, TRAIL or combination with RL2 for 24 h. Cell death was measured using Annexin V (An) /Propidium Iodide (PI) staining and analysed with FlowSight. **(A)** The amount of An-positive and PI positive cells of three independent experiments is shown in relative units (RU). The statistical analysis was performed by paired Student's t-test. **(B)**. Images of five representative cells for Brightfield (Br.) Annexin V (An) and Propidium Iodide (PI) are shown.

REFERENCES

Aldridge, B. B., Gaudet, S., Lauffenburger, D. A., and Sorger, P. K. (2011). Lyapunov exponents and phase diagrams reveal multi-factorial control over TRAIL-induced apoptosis. *Mol. Syst. Biol.* 7:553. doi: 10.1038/msb.2011.85

Bagamanshina, A. V., Troitskaya, O. S., Nushtaeva, A. A., Yunusova, A. Y., Starykovych, M. O., Kuligina, E. V., et al. (2019). Cytotoxic and antitumor activity of lactaptin in combination with autophagy inducers and inhibitors. *Biomed. Res. Int.* 2019:4087160. doi: 10.1155/2019/4087160

Bell, B. D., Leverrier, S., Weist, B. M., Newton, R. H., Arechiga, A. F., Luhrs, K. A., et al. (2008). FADD and caspase-8 control the outcome of autophagic signaling in proliferating T cells. *Proc. Natl. Acad. Sci. U. S. A.* 105, 16677–16682. doi: 10.1073/pnas.0808597105

Bernardini, J. P., Lazarou, M., and Dewson, G. (2017). Parkin and mitophagy in cancer. *Oncogene* 36, 1315–1327. doi: 10.1038/onc.2016.302

Buchbinder, J. H., Pischel, D., Sundmacher, K., Flassig, R. J., and Lavrik, I. N. (2018). Quantitative single cell analysis uncovers the life/death decision in CD95 network. *PLoS Comput. Biol.* 14:e1006368. doi: 10.1371/journal.pcbi.1006368

Chinak, O. A., Shernyukov, A. V., Ovcherenko, S. S., Sviridov, E. A., Golyshev, V. M., Fomin, A. S., et al. (2019). Structural and aggregation features of a human kappa-Casein fragment with antitumor and cell-penetrating properties. *Molecules* 24:2919. doi: 10.3390/molecules24162919

Dickens, L. S., Boyd, R. S., Jukes-Jones, R., Hughes, M. A., Robinson, G. L., Fairall, L., et al. (2012). A death effector domain chain DISC model reveals a crucial role for caspase-8 chain assembly in mediating apoptotic cell death. *Mol. Cell* 47, 291–305. doi: 10.1016/j.molcel.2012.05.004

Fu, T. M., Li, Y., Lu, A., Li, Z., Vajjhala, P. R., Cruz, A. C., et al. (2016). Cryo-EM structure of caspase-8 tandem DED filament reveals assembly and regulation mechanisms of the death-inducing signaling complex. *Mol. Cell* 64, 236–250. doi: 10.1016/j.molcel.2016.09.009

Galluzzi, L., Vitale, I., Aaronson, S. A., Abrams, J. M., Adam, D., Agostinis, P., et al. (2018). Molecular mechanisms of cell death: recommendations of the Nomenclature Committee on Cell Death 2018. *Cell Death Differ.* 25, 486–541. doi: 10.1038/s41418-017-0012-4

Gordy, C., and He, Y. W. (2012). The crosstalk between autophagy and apoptosis: where does this lead? *Protein Cell* 3, 17–27. doi: 10.1007/s13238-011-1127-x

Hamacher-Brady, A., and Brady, N. R. (2016). Mitophagy programs: mechanisms and physiological implications of mitochondrial targeting by autophagy. *Cell Mol. Life Sci.* 73, 775–795. doi: 10.1007/s00018-015-2087-8

Hillert, L. K., Ivanisenko, N. V., Espe, J., Konig, C., Ivanisenko, V. A., Kahne, T., et al. (2020). Long and short isoforms of c-FLIP act as control checkpoints of DED filament assembly. *Oncogene* 39, 1756–1772. doi: 10.1038/s41388-019-1100-3

Hoffmann, J. C., Pappa, A., Krammer, P. H., and Lavrik, I. N. (2009). A new C-terminal cleavage product of procaspase-8, p30, defines an alternative pathway of procaspase-8 activation. *Mol. Cell Biol.* 29, 4431–4440. doi: 10.1128/MCB.02261-07

Hou, W., Han, J., Lu, C., Goldstein, L. A., and Rabinowich, H. (2010). Autophagic degradation of active caspase-8: a crosstalk mechanism between autophagy and apoptosis. *Autophagy* 6, 891–900. doi: 10.4161/auto.6.7.13038

Hughes, M. A., Powley, I. R., Jukes-Jones, R., Horn, S., Feoktistova, M., Fairall, L., et al. (2016). Co-operative and hierarchical binding of c-FLIP and caspase-8: a unified model defines how c-FLIP isoforms differentially control cell fate. *Mol. Cell* 61, 834–849. doi: 10.1016/j.molcel.2016.02.023

Kato, H., Lu, Q., Rapaport, D., and Kozjak-Pavlovic, V. (2013). Tom70 is essential for PINK1 import into mitochondria. *PLoS ONE* 8:e58435. doi: 10.1371/journal.pone.0058435

Kaufmann, T., Strasser, A., and Jost, P. J. (2012). Fas death receptor signalling: roles of Bid and XIAP. *Cell Death Differ.* 19, 42–50. doi: 10.1038/cdd.2011.121

Koval, O. A., Fomin, A. S., Kaledin, V. I., Semenov, D. V., Potapenko, M. O., Kuligina, E. V., et al. (2012). A novel pro-apoptotic effector lactaptin inhibits tumor growth in mice models. *Biochimie* 94, 2467–2474. doi: 10.1016/j.biochi.2012.08.017

Koval, O. A., Tkachenko, A. V., Fomin, A. S., Semenov, D. V., Nushtaeva, A. A., Kuligina, E. V., et al. (2014). Lactaptin induces p53-independent cell death associated with features of apoptosis and autophagy and delays growth of breast cancer cells in mouse xenografts. *PLoS ONE* 9:e93921. doi: 10.1371/journal.pone.0093921

Krammer, P. H., Arnold, R., and Lavrik, I. N. (2007). Life and death in peripheral T cells. *Nat. Rev. Immunol.* 7, 532–542. doi: 10.1038/nri2115

Lafont, E., Kantari-Mimoun, C., Draber, P., De Miguel, D., Hartwig, T., Reichert, M., et al. (2017). The linear ubiquitin chain assembly complex regulates TRAIL-induced gene activation and cell death. *EMBO J.* 36, 1147–1166. doi: 10.15252/embj.201695699

Laussmann, M. A., Passante, E., Dussmann, H., Rauen, J. A., Wurstle, M. L., Delgado, M. E., et al. (2011). Proteasome inhibition can induce an autophagy-dependent apical activation of caspase-8. *Cell Death Differ.* 18, 1584–1597. doi: 10.1038/cdd.2011.27

Lavrik, I., Krueger, A., Schmitz, I., Baumann, S., Weyd, H., Krammer, P. H., et al. (2003). The active caspase-8 heterotetramer is formed at the CD95 DISC. *Cell Death Differ.* 10, 144–145. doi: 10.1038/sj.cdd.4401156

Lavrik, I. N., and Krammer, P. H. (2012). Regulation of CD95/Fas signaling at the DISC. *Cell Death Differ.* 19, 36–41. doi: 10.1038/cdd.2011.155

Lazarou, M., Sliter, D. A., Kane, L. A., Sarraf, S. A., Wang, C., Burman, J. L., et al. (2015). The ubiquitin kinase PINK1 recruits autophagy receptors to induce mitophagy. *Nature* 524, 309–314. doi: 10.1038/nature14893

Lemke, J., von Karstedt, S., Zinngrebe, J., and Walczak, H. (2014). Getting TRAIL back on track for cancer therapy. *Cell Death Differ.* 21, 1350–1364. doi: 10.1038/cdd.2014.81

Pietkiewicz, S., Schmidt, J. H., and Lavrik, I. N. (2015). Quantification of apoptosis and necroptosis at the single cell level by a combination of Imaging flow cytometry with classical annexin V/propidium iodide staining. *J. Immunol. Methods* 423, 99–103. doi: 10.1016/j.jim.2015.04.025

Richter, M., Wohlfromm, F., Kahne, T., Bongartz, H., Seyrek, K., Kit, Y., et al. (2020). The recombinant fragment of human kappa-casein induces cell death by targeting the proteins of mitochondrial import in breast cancer cells. *Cancers* 12:1427. doi: 10.3390/cancers12061427

Scaffidi, C., Fulda, S., Srinivasan, A., Friesen, C., Li, F., Tomaselli, K. J., et al. (1998). Two CD95 (APO-1/Fas) signaling pathways. *EMBO J.* 17, 1675–1687. doi: 10.1093/emboj/17.6.1675

Schleich, K., Warnken, U., Fricker, N., Ozturk, S., Richter, P., Kammerer, K., et al. (2012). Stoichiometry of the CD95 death-inducing signaling complex: experimental and modeling evidence for a death effector domain chain model. *Mol. Cell* 47, 306–319. doi: 10.1016/j.molcel.2012.05.006

Semenov, D. V., Fomin, A. S., Kuligina, E. V., Koval, O. A., Matveeva, V. A., Babkina, I. N., et al. (2010). Recombinant analogs of a novel milk pro-apoptotic peptide, lactaptin, and their effect on cultured human cells. *Protein J.* 29, 174–180. doi: 10.1007/s10930-010-9237-5

Spencer, S. L., Gaudet, S., Albeck, J. G., Burke, J. M., and Sorger, P. K. (2009). Non-genetic origins of cell-to-cell variability in TRAIL-induced apoptosis. *Nature* 459, 428–432. doi: 10.1038/nature08012

Sprick, M. R., Rieser, E., Stahl, H., Grosse-Wilde, A., Weigand, M. A., and Walczak, H. (2002). Caspase-10 is recruited to and activated at the native TRAIL and CD95 death-inducing signalling complexes in a FADD-dependent manner but can not functionally substitute caspase-8. *EMBO J.* 21, 4520–4530. doi: 10.1093/emboj/cdf441

Sprick, M. R., Weigand, M. A., Rieser, E., Rauch, C. T., Juo, P., Blenis, J., et al. (2000). FADD/MORT1 and caspase-8 are recruited to TRAIL receptors 1 and 2 and are essential for apoptosis mediated by TRAIL receptor 2. *Immunity* 12, 599–609. doi: 10.1016/S1074-7613(00)80211-3

von Karstedt, S., Montinaro, A., and Walczak, H. (2017). Exploring the TRAILs less travelled: TRAIL in cancer biology and therapy. *Nat. Rev. Cancer* 17, 352–366. doi: 10.1038/nrc.2017.28

Walczak, H., and Haas, T. L. (2008). Biochemical analysis of the native TRAIL death-inducing signaling complex. *Methods Mol. Biol.* 414, 221–239. doi: 10.1007/978-1-59745-339-4_16

Youle, R. J., and Narendra, D. P. (2011). Mechanisms of mitophagy. *Nat. Rev. Mol. Cell Biol.* 12, 9–14. doi: 10.1038/nrm3028

Zamaraev, A. V., Kopeina, G. S., Buchbinder, J. H., Zhivotovsky, B., and Lavrik, I. N. (2018). Caspase-2 is a negative regulator of necroptosis. *Int. J. Biochem. Cell Biol.* 102, 101–108. doi: 10.1016/j.biocel.2018.07.006

Conflict of Interest: The authors declare that the research was conducted in the absence of any commercial or financial relationships that could be construed as a potential conflict of interest.

frontiers in Cell and Developmental Biology

REVIEW
published: 22 January 2021
doi: 10.3389/fcell.2020.617884

Role of Base Excision Repair Pathway in the Processing of Complex DNA Damage Generated by Oxidative Stress and Anticancer Drugs

*Yeldar Baiken[1,2,3], Damira Kanayeva[1], Sabira Taipakova[4], Regina Groisman[5], Alexander A. Ishchenko[5], Dinara Begimbetova[2], Bakhyt Matkarimov[2] and Murat Saparbaev[4,5]**

[1] School of Sciences and Humanities, Nazarbayev University, Nur-Sultan, Kazakhstan, [2] National Laboratory Astana, Nazarbayev University, Nur-Sultan, Kazakhstan, [3] School of Engineering and Digital Sciences, Nazarbayev University, Nur-Sultan, Kazakhstan, [4] Department of Molecular Biology and Genetics, Faculty of Biology and Biotechnology, al-Farabi Kazakh National University, Almaty, Kazakhstan, [5] Groupe ≪Mechanisms of DNA Repair and Carcinogenesis≫, Equipe Labellisée LIGUE 2016, CNRS UMR9019, Université Paris-Saclay, Gustave Roussy Cancer Campus, Villejuif, France

OPEN ACCESS

Edited by:
Nikita Kuznetsov,
Institute of Chemical Biology and Fundamental Medicine (RAS), Russia

Reviewed by:
Gianluca Tell,
University of Udine, Italy
Nadezhda Rechkunova,
Institute of Chemical Biology and Fundamental Medicine (RAS), Russia

***Correspondence:**
Murat Saparbaev
murat.saparbaev@gustaveroussy.fr

Specialty section:
This article was submitted to Cell Death and Survival, a section of the journal Frontiers in Cell and Developmental Biology

Received: 15 October 2020
Accepted: 17 December 2020
Published: 22 January 2021

Citation:
Baiken Y, Kanayeva D, Taipakova S, Groisman R, Ishchenko AA, Begimbetova D, Matkarimov B and Saparbaev M (2021) Role of Base Excision Repair Pathway in the Processing of Complex DNA Damage Generated by Oxidative Stress and Anticancer Drugs. Front. Cell Dev. Biol. 8:617884. doi: 10.3389/fcell.2020.617884

Chemical alterations in DNA induced by genotoxic factors can have a complex nature such as bulky DNA adducts, interstrand DNA cross-links (ICLs), and clustered DNA lesions (including double-strand breaks, DSB). Complex DNA damage (CDD) has a complex character/structure as compared to singular lesions like randomly distributed abasic sites, deaminated, alkylated, and oxidized DNA bases. CDD is thought to be critical since they are more challenging to repair than singular lesions. Although CDD naturally constitutes a relatively minor fraction of the overall DNA damage induced by free radicals, DNA cross-linking agents, and ionizing radiation, if left unrepaired, these lesions cause a number of serious consequences, such as gross chromosomal rearrangements and genome instability. If not tightly controlled, the repair of ICLs and clustered bi-stranded oxidized bases via DNA excision repair will either inhibit initial steps of repair or produce persistent chromosomal breaks and consequently be lethal for the cells. Biochemical and genetic evidences indicate that the removal of CDD requires concurrent involvement of a number of distinct DNA repair pathways including poly(ADP-ribose) polymerase (PARP)-mediated DNA strand break repair, base excision repair (BER), nucleotide incision repair (NIR), global genome and transcription coupled nucleotide excision repair (GG-NER and TC-NER, respectively), mismatch repair (MMR), homologous recombination (HR), non-homologous end joining (NHEJ), and translesion DNA synthesis (TLS) pathways. In this review, we describe the role of DNA glycosylase-mediated BER pathway in the removal of complex DNA lesions.

Keywords: inter-strand DNA crosslink, bulky DNA adduct, base excision repair, DNA glycosylase, nucleotide excision repair, Fanconi anemia

INTRODUCTION

Endogenous oxidative stress and environmental factors induce multiple damage in cellular DNA, among them bulky DNA adducts, interstrand DNA cross-links (ICLs), and clustered DNA lesions (including double-strand breaks, DSBs), which are distinguished from singular lesions by their complex characters and structures (Deans and West, 2011; Yang et al., 2017; Mullins et al., 2019; Nickoloff et al., 2020) (**Figures 1A,B**). Complex DNA damage (CDD) is characterized by two important features: bulky character and the presence of more than one modification of one turn of the DNA helix. Although in general CDD constitutes a relatively minor share of the total DNA damage induced by chemo- and radiotherapy in treated cancer cells, they present daunting obstacles to DNA template scanning processes and if not repaired lead to cell death and gross chromosomal rearrangements. Among complex DNA lesions, ICLs are one of the most cytotoxic and difficult to repair, because they prevent DNA strand separation during DNA replication and transcription. To get insight into the biological roles of CDDs, it is important to comprehend the nature and mechanisms of their formation which often proceeds via interactions of DNA with endogenous reactive metabolites and various exogenous factors. Studies of the cellular defense mechanisms counteracting genotoxic effects of CDD revealed that the removal of complex lesions requires several distinct DNA repair pathways including global genome and transcription-coupled nucleotide excision repair (GG-NER and TC-NER, respectively), poly(ADP-ribose) polymerase (PARP)-mediated DNA strand break repair, base excision repair (BER), nucleotide incision repair (NIR), mismatch repair (MMR), non-homologous end joining (NHEJ), homologous recombination (HR), and translesion DNA synthesis (TLS) pathways. In this review, we attempt to enlighten the structural properties, mechanisms of formation of CDD, and role of recently discovered alternative DNA repair mechanisms. Due to the space constraints, the formation and repair of clustered DNA lesions will not be discussed in this review instead; we would recommend several excellent reviews on this topic (Cadet et al., 2012; Georgakilas et al., 2013; Sage and Shikazono, 2017; Mavragani et al., 2019).

COMPLEX DNA DAMAGE—NATURE, FORMATION, AND BIOLOGICAL ROLE

8,5′-Cyclopurine-2′-deoxynucleosides

Reactive oxygen species (ROS) are commonly responsible for the formation of non-bulky DNA base damage in cellular DNA (**Figure 1A**). Majority of ROS-induced DNA lesions are eliminated in the DNA glycosylase-initiated BER pathway. Nevertheless, ROS can generate CDDs, which can strongly perturb DNA replication and transcription in mammalian cells. 8,5′-Cyclopurine-2′-deoxynucleosides (cPus) can be formed as a result of endogenous oxidative stress and also by ionizing radiation under anoxic conditions (Xu et al., 2014). Bulky cPus adducts including diastereomeric (5′*S*)- and (5′*R*)-8,5′-*cyclo*-2′-deoxyadenosine (cdA) and 8,5′-*cyclo*-2′-deoxyguanosine (cdG) are generated by hydroxyl radical attack at C5′ sugar by hydrogen atom abstraction resulting in the formation of a covalent bond between the C5′ and C8 positions of the purine nucleoside (Dirksen et al., 1988; Kuraoka et al., 2000; Brooks, 2008) (**Figure 1B**). These nucleotide modifications can be referred to as a tandem lesion in which both sugar and base moieties have been damaged within distance of single nucleotides (Kuraoka et al., 2000; Merecz and Karwowski, 2016). The additional covalent bond in cPu hinders cleavage of the glycosidic bond by DNA glycosylases, making these lesions substrates for the NER pathway (Brooks et al., 2000; Kuraoka et al., 2000; Kropachev et al., 2014). It was demonstrated that Cockayne syndrome (CS) complementation group A (CSA) protein, a DNA excision repair protein involved in the TC-NER sub-pathway, is required for the removal of 5′S-cdA adducts in DNA from primary skin cells (D'Errico et al., 2007). The GG-NER pathway can remove cdA adducts with a similar efficiency as that of UV-induced CPDs but displays higher activity in excising the R-diastereomers as compared to S conformations (Brooks et al., 2000; Kuraoka et al., 2000). Hence, high levels of 5′S-cdA diastereomer in the nonexposed control group of mice compared to analogous 5′R-cdA might be due to the more efficient removal of 5′R-cdA by the GG-NER pathway (Wang et al., 2012; Chatgilialoglu et al., 2019). Several studies suggested that 5′R-cdA and 5′R-cdG adducts in DNA are better NER substrates than the 5′S-cdA and 5′S-cdG lesions (Kropachev et al., 2014; Cai et al., 2015; Shafirovich et al., 2019). In agreement with this, cdG and cdA adducts accumulate in DNA of keratinocytes from NER-deficient xeroderma pigmentosum (XP) complementation group C (XPC) and CSA patients exposed to X-rays and potassium bromate ($KBrO_3$) (D'Errico et al., 2006, 2007), as well as in organs of $CSB^{-/-}$ knockout mice (Wang et al., 2012; Chatgilialoglu et al., 2019). Kinetic assays showed the involvement of TLS DNA polymerases including Pol η, Pol κ, Pol ι, and Pol ζ in the replicative bypass of cPu lesions in human cells (You et al., 2013). Interestingly, Xu et al. (2014) revealed a novel repair pathway for cPu lesions that results in trinucleotide repeat (TNR) deletion *via* a unique DNA polymerase β (Polβ) lesion bypass during DNA replication and BER.

Aristolochic Acids and Their Association With Genotoxicity and Cancer Progression

Aristolochic acids (AAs) are a group of acids found in the flowering plant family *Aristolochiaceae* which are popular supplements in Chinese medicine. AAs are structurally diverse blends corresponding to nitrophenanthrene carboxylic acids composed of two main constituents: principally 8-methoxy-6-nitrophenanthro-(3,4-d)-1,3-dioxolo-5-carboxylic acid (AA-I, which is the most abundant one) and its 8-demethoxylated form (AA-II) (Dickman and Grollman, 2010). Consumption of AAs can lead to a rapid renal toxicity and, at certain levels, to liver (Ng et al., 2017; Lu et al., 2020) and kidney cancer (Vanherweghem et al., 1993; Debelle et al., 2008). Consumption of AAs-containing herbal remedies in South Asia remains a cause of serious concern for public health to date (Lu et al., 2020; Shan et al., 2020). Certain cases in Europe also have been registered in 1992; when several female patients in Belgium, after taking two Chinese

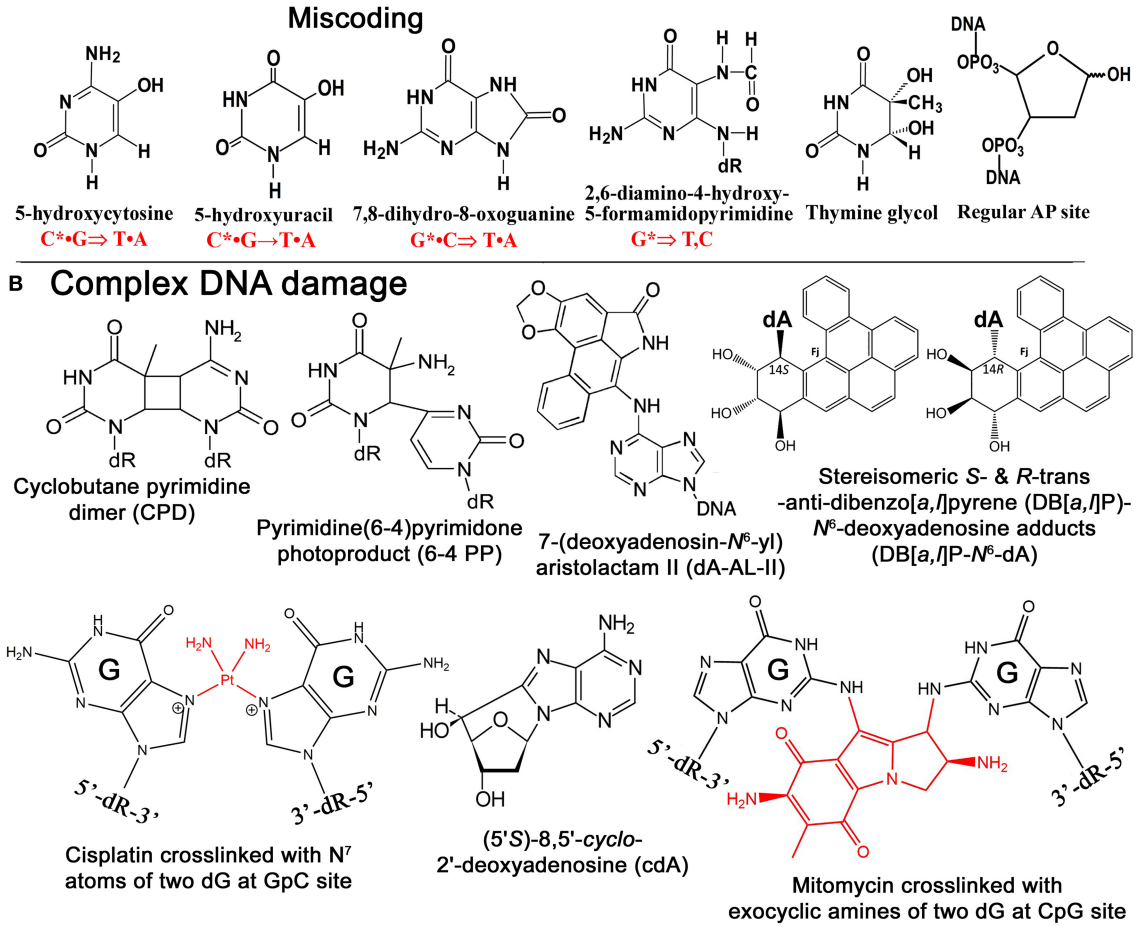

FIGURE 1 | Chemical structures of singular and complex DNA base damage. **(A)** Singular non-bulky oxidative DNA base lesions. **(B)** Complex DNA lesions including cisplatin-ICL, mitomycin-ICL, and bulky repair-resistant DNA base lesions.

herbs (*Stephania tetrandra* and *Magnolia officinalis*), as slimming treatment, suffered from rapidly progressive interstitial nephritis (Vanherweghem et al., 1993).

Although both AA-I and AA-II have analogous nephrotoxic and genotoxic effects in cells and animal models, carcinogenic mechanisms seem to be distinct (Schmeiser et al., 1986; Sato et al., 2004; Shibutani et al., 2007). It is noted that AA-I-induced nephrotoxicity has much severe consequences than the AA-II-induced one (Shibutani et al., 2007), even though AA-II can demonstrate greater genotoxicity and carcinogenic potential compared to AA-I (Shibutani et al., 2007; Xing et al., 2012). It was found that in the body aristolochic acids are activated by cellular nitroreductases, resulting in the formation of reactive intermediates that bind covalently to DNA to produce 7-(deoxyadenosin-N^6-yl)aristolactam (dA-AL) and 7-(deoxyguanosin-N^2-yl) aristolactam I (dG-AL) adducts (Bieler et al., 1997) (**Figure 1B**). The aristolactam-adenine adducts induce a unique mutational signature in tumors characterized by A•T→T•A transversions at dA residues located on the non-transcribed DNA strand (Moriya et al., 2011). This observation was further confirmed by Sidorenko et al., who demonstrated that dA-AL adducts are resistant to GG-NER, but can be efficiently removed by TC-NER (Sidorenko et al., 2012). Interestingly, the structural studies of damaged DNA have also revealed that the dA-AL adduct does not destabilize the DNA duplex, thus providing a structural basis for the mechanism of resistance of the bulky lesion to GG-NER (Lukin et al., 2012). Recently, it has been shown that translesion synthesis (TLS)-specific Y-family DNA polymerases, particularly Pol η, Pol ι, and Pol κ, are not required for the TLS across bulky dA-AL-I in mouse embryonic fibroblasts (MEFs), whereas Pol ζ, a B-family DNA polymerase, which is capable of bypassing the cyclobutane pyrimidine dimer (CPD), a common UV-induced lesion, catalyzes both insertion of dAMP and dTMP (Hashimoto et al., 2016).

Di-Benzopyrene DNA Adducts Are Highly Mutagenic Lesions

Bulky DNA adducts generated by environmental carcinogens cause mutations that often drive malignant transformation of

affected cells. As we described above, bulky DNA adducts are removed in the NER pathway; however, certain bulky DNA lesions that cause a minimal decrease, or an enhancement in the stabilities of the DNA duplex can be very resistant to the repair machinery. Benzo[a]pyrene (B[a]P) is a well-known representative of PAH carcinogens present in the environment (Luch, 2005). Primary sources of dibenzopyrenes in the environment are diesel and gasoline-fueled vehicle exhausts, tobacco smoke, other smoke sources such as grilling meat, coal gasification products, coal tar, and other substances produced by the incomplete combustion of organic matter (Luch, 2005; Bergvall and Westerholm, 2007; Kropachev et al., 2013). Cytochromes P450 1A1, 1A2, and 1B1 are responsible for the metabolic activation of PAHs by mono-oxygenation of hydrocarbons in cells to form epoxides (Luch et al., 1999; Straif et al., 2005; Sulc et al., 2016). Cellular metabolism of B[a]Ps produces a diol epoxide benzo[a]pyrene-7,8-dihydrodiol-9,10-oxide (BPDE), which can be hydrolyzed to BPDE tetrols and interact with guanines in DNA to form bulky B[*a*]P-N^2-dG adducts and B[*a*]P-N^6-dA adducts. B[a]Ps induces primarily guanine transversions (G•C → T•A).

Dibenzo[*a,l*]pyrene (DB[*a,l*]P), another PAH present in about ten-fold lower concentration in the environment, is 100 times more tumorigenic than B[*a*]P in rodent model systems (Cavalieri et al., 1991; Amin et al., 1995a,b; Prahalad et al., 1997; Luch, 2009; Zhang et al., 2011). The reactive diol epoxide intermediates of DB[*a,l*]P react with either N^6-adenine or N^2-guanine in DNA to form stable DB[*a,l*]P-N^6-dA and DB[*a,l*]P-N^2-dG adducts (Li et al., 1999a,b; Yagi et al., 2008) (**Figure 1B**). Remarkably, Kropachev et al. demonstrated that the *S* and *R* diastereoisomers of the DB[*a,l*]P-N^2-dG adduct are 15 and 35 times, respectively, more susceptible to removal by the GG-NER machinery as compared to the stereo-chemically identical DB[*a,l*]P- N^6-dA adduct (Kropachev et al., 2013). This observation suggests that the higher genotoxic activity of DB[*a,l*]P, as compared to B[*a*]P, might be due to the generation of repair-resistant and thus persistent DB[*a,l*]P-derived adenine adducts in exposed cells.

In summary, despite their bulky character, certain highly mutagenic DNA lesions can escape DNA damage surveillance and DNA excision repair. This repair-resistant DNA damage presents a challenge for the cell since it can persist in the genome and lead to the transcription and replication blockages and mutations. Nevertheless, these complex DNA lesions might be substrates for the TC-NER pathway, thus implying a possible existence of alternative DNA repair mechanisms that could remove damage in the non-transcribed part of genome.

Interstrand DNA Cross-Link (ICL)—Formation, Nature, and Use in Anticancer Therapies

Chemical agents such as bifunctional alkylating agents, platinum compounds, antitumor antibiotics, and furanocoumarins when reacting with DNA bases can generate a covalent bond between nucleotides on the opposite strands of a DNA duplex resulting in the formation of interstrand DNA cross-links (ICLs). ICLs are highly cytotoxic DNA lesions that prevent DNA strand separation during DNA replication, transcription, and recombination. Indeed, DNA cross-linking agents, like mitomycin C, cis-diamminedichloroplatinum(II), and melphalan, are widely used against hyperplastic diseases, such as cancer.

The formation of ICLs can also be the result of endogenously occurring reactive aldehydes such as malondialdehyde, a natural product of lipid peroxidation of polyunsaturated fatty acids, and nitric oxide, which may induce diazotization of exocyclic amine groups of the bases (Scharer, 2005). It was estimated that a single unrepaired ICL could kill a bacterial or yeast cell, while about 40 unrepaired ICLs could kill a mammalian cell (Magana-Schwencke et al., 1982; Lawley and Phillips, 1996). There are several types of ICLs that were discovered and characterized very early in 1960s. Cisplatin or cis-diamminedichloroplatinum(II) (*cis*-DDP) reacts with the N^7 atom of the deoxyguanosine residue forming initially one covalent bond with DNA then covalently binds to other neighboring guanine residues resulting in DNA cross-linking (Bancroft et al., 1990; Florea and Busselberg, 2011) (**Figure 1B**). Majority of *cis*-DDP-induced intra-strand DNA cross-links are between guanine residues in dGpG, dGpNpG, and between adenine and guanine in dApG sequences, and only a relatively minor portion of *cis*-DDP-induced ICLs are formed between two guanines in opposite strands at the dGpC context (Kartalou and Essigmann, 2001; Noll et al., 2006). The relative distribution of dGpG, dApG, and dGpNpG intra-strand cross-links, and dGpC ICLs, generated by *cis*-DDP is ∼65, 25, 5–10, and 2–5% of total adducts, respectively (Noll et al., 2006; Jung and Lippard, 2007; Enoiu et al., 2012).

Nitrogen mustards contain a reactive N,N-bis-(2-chloroethyl)amine functional group which reacts with guanine and adenine at the N^7 position with minor reaction at N^3-dC, N^1-dA, and O^6-dG (Osborne et al., 1995; Florea-Wang et al., 2009; Rojsitthisak et al., 2011). Derivatives of nitrogen mustards induce various DNA base modifications, and only 5% among them represent DNA cross-links between the N^7 position of two guanine bases on the opposite DNA strands (Kohn et al., 1966). Mustard derivatives such as chlorambucil, melphalan, cyclophosphamide, and bendamustine are widely used as chemotherapeutic agents that covalently cross-link two strands in the DNA duplex (Sunters et al., 1992; Chen et al., 2014).

Psoralens are a family of naturally occurring compounds known as the linear furanocoumarins linear furocoumarins found in leafy plants (mostly from *Apiaceae* and *Fabaceae*) (Scott et al., 1976). The hydrophobic and planar character of these molecules allows them to easily permeate the cell and then intercalate into the DNA duplex (Lopez-Martinez et al., 2016). Among several ICL-inducing agents, psoralens require UVA photoactivation following DNA intercalation to chemically react with DNA. 8-Methoxypsoralen (8-MOP), the most common form of psoralen frequently used for the treatments, is a planar, tricyclic compound that intercalates into the DNA duplex preferentially at 5′-TpA sites. Upon photoactivation, 8-MOP primarily photoalkylates DNA by cycloaddition to the 5,6-double bond of a thymine generating monoadducts (MA) with either the 4′,5′-double bond of the furan (MAf) or the 3,4-double bond of the pyrone (MAp) side of the psoralen (Cole, 1971). A unique

property of psoralen photochemistry is that the absorption of a second photon by the MAf leads to formation of a pyrone side 5,6-double bond adduct with a flanking thymine in the complementary strand, thus generating an ICL (Johnston and Hearst, 1981).

Mitomycin C (MMC) is a product of *Streptomyces caespitosus*, a species of actinobacteria, commonly used as antineoplastic chemotherapeutic agent against bladder, breast, colorectal, head and neck, cervical, and non-small cell lung cancers, and adenocarcinoma of stomach and pancreas. MMC contains a variety of functional groups, including three-membered heterocyclic rings: aminobenzoquinone- and aziridine-ring systems, one amine and two methylene bridges (Tomasz, 1995). Inert by its nature, MMC can be activated via chemical or enzymatic reduction of quinone ring and subsequently it covalently links to two guanine residues in complementary DNA strands of 5′-CpG sequences through binding to the DNA minor groove (Noll et al., 2006; Fan and Peng, 2016) (**Figure 1B**). Specifically, after two-electron reduction of the quinone ring, MMC loses its methoxy group resulting in the formation of the hydroquinone intermediate. Tautomerization succeeded by the reaction with the N^2-amino group of guanine results in monoadduct formation, whereas carbamoyl group elimination results in the formation of the highly reactive vinylogous hydroquinone methide intermediate, which subsequently alkylates the guanine on the opposite complementary DNA strand generating an ICL (Noll et al., 2006).

Repair-Resistant Complex DNA Lesions Induced by Nontherapeutic Factors

Apart from commonly used chemotherapeutic drug agents, there are other known carcinogenic compounds such as tobacco-specific N-nitrosamines, fluoranthenes, naphthol and binol derivatives, aflatoxin B1, and acetaldehydes which can induce bulky DNA adducts and ICLs. Aflatoxin B1 (AFB1), a potent carcinogen produced by Aspergillus species, mainly found as food contaminant in animal farms and poultry production through the diet. AFB1 exposure of infant mice induces hepatocellular carcinoma after reaching adulthood (Vesselinovitch et al., 1972). AFB1 is activated by cytochrome P450 1A2 and 3A4 to the 8,9-epoxide consequently forming AFB1-N^7-guanine adduct (Eaton and Gallagher, 1994). A relatively fast conversion rate of AFB1-N^7-guanine adduct to the ring-opened, formamidopyrimidine form (FAPY-AFB1) is an essential step in promoting aflatoxin carcinogenesis. The FAPY-AFB1 adduct seems to be the most stable of all AFB1-DNA adducts and is quite resistant to DNA repair machinery (Martin and Garner, 1977; Eaton and Gallagher, 1994).

Acetaldehydes, abundant organic compounds, are highly reactive due to the electrophilic nature of their carbonyl carbon, causing a variety of cellular and chromosomal aberrations in human cells. The partial oxidation of ethanol in the liver by alcohol dehydrogenase produces acetaldehyde, which is converted into acetic acid by acetaldehyde dehydrogenases (ALDHs). Half of the population of Northeast Asian descent and about 5–10% of Northern European descent harbor a dominant mutation in the ALDH2 gene, which greatly reduces the enzyme activity and leads to acetaldehyde accumulation after alcohol consumption. Individuals with a mutant form of ALDH2 have a greater risk of liver damage and susceptibility to many types of cancer (Seitz and Meier, 2007). Acetaldehyde can generate ICL and protein-DNA cross-links. N^2-Ethyl-2′-deoxyguanosine (N^2-ethyl-dG) and 1, N^2-propano-2'-deoxyguanosine (1, N^2-PdG) are major DNA adducts caused by acetaldehydes. Several studies indicated that endogenous aldehydes are a significant source of genotoxicity in the human hematopoietic system and that the presence of the proficient Fanconi anemia (FA) pathway is essential to protect cells from DNA damage induced by these reactive compounds. Hematopoietic stem cells (HSCs) are a primary target for aldehyde-induced DNA damage, and FA-deficient patients suffer from bone marrow failure due to p53/p21-mediated cell death and senescence (Ceccaldi et al., 2012). In agreement with this model, it was shown that the HSCs in *Aldh2*$^{-/-}$, *Fancd2*$^{-/-}$ double KO mice accumulate more DNA damage than HSCs in either of the single knockout mice (Garaycoechea et al., 2012). Formaldehyde, another highly reactive compound, can be generated from abundant folic acid consumption but would be effectively handled by a two-tier protection glutathione-dependent formaldehyde dehydrogenase (ADH5)/FANCD2 mechanism; however, DNA damage may still happen and lead to cytotoxic effects. Individuals affected by FA lack the defense system against formaldehyde and might be prone to the toxic compound exposure from folate decomposition (Burgos-Barragan et al., 2017). On the other side, a new strategy based on the delivery of a formaldehyde in the form of folate derivatives along with ADH5 inhibition that could effectively kill breast cancer cells deficient for BRCA1 and BRCA2 has been recently proposed (Burgos-Barragan et al., 2017).

ABERRANT REPAIR OF COMPLEX DNA LESIONS

Aberrant Repair of Bulky DNA Adducts

In general, DNA repair systems can discriminate between regular and modified bases. However, difficulties for the accurate discrimination between damaged and regular DNA strands do exist: DNA polymerase errors during replication and spontaneous conversion of 5-methylcytosine to thymine generate mismatched pairs between two regular bases. To thwart these mutagenic threats to genome integrity, cells have specific DNA repair mechanisms that can correct mismatched bases generated via spontaneous deamination or mis-incorporation during DNA replication. The mismatch-specific thymine- and adenine-DNA glycosylase (MBD4/TDG and MutY/MYH, respectively)-initiated BER and mismatch repair (MMR) pathway are able to eliminate normal DNA bases in mismatched DNA duplexes.

Evidences have accumulated that cellular response to DNA damage could lead to faulty DNA repair and contribute to age-related diseases such as cancer and brain disorder. In DNA repair-deficient cells and under certain circumstances, *E. coli* MutY and human MMR can act in an aberrant manner: MutY removes adenine (A) in a template strand

opposite to the misincorporated 8-oxoguanine residue (Fowler et al., 2003), and MMR removes thymine opposite to O^6-methylguanine (Hampson et al., 1997), leading to mutation and futile DNA repair cycles, respectively. These examples show that in the presence of unrepaired DNA lesions, the classic DNA repair mechanisms can act in an aberrant manner by targeting the nondamaged DNA strand and promote genome instability. Furthermore, the aberrant MMR and BER mechanisms acting upon oxidized guanine residues stimulate the trinucleotide expansion that underlies Huntington's disease, a severe hereditary neurodegenerative syndrome (Kovtun et al., 2007). The alkyl-purine DNA glycosylase (MPG/AAG/ANPG) initiates aberrant BER by removing regular purines from nondamaged DNA, and the increased level of MPG is associated with risk of lung cancer (Berdal et al., 1998; Leitner-Dagan et al., 2012). Actually, MMR is not capable of discriminating a particular strand in a DNA duplex harboring a mismatched base pair in absence of DNA replication (Pena-Diaz et al., 2012).

Previously, our laboratory showed that human TDG and MBD4 initiate aberrant repair by excising regular thymine (T) paired with a damaged adenine (A) residue in the DNA duplex (Talhaoui et al., 2014). TDG recognizes T in the nondamaged DNA strand opposite to 1, N^6-ethenoadenine (εA), hypoxanthine (Hx), 8-oxoA, and even abasic site in the TpG/CpX sequence context, where X is a modified residue. MBD4 removes T only when it pairs with εA, but not with Hx and other modified adenine residues. *In vitro* reconstitution demonstrated that TDG can catalyze aberrant removal of T in the specific sequence context that leads to TpG, CpA → CpG mutations (Talhaoui et al., 2014). As we described above, the highly mutagenic aristolactam-adenine adducts (dA-AL-I and dA-AL-II) generated in DNA by metabolic activation of aristolochic acids (AAs) are associated with urothelial carcinomas of the upper urinary tract and chronic kidney disease (Grollman et al., 2007; Chen et al., 2012). The urothelial carcinomas associated with AA exposure are characterized by A → T transversions (73% of all substitutions) preferentially occurring on the non-transcribed DNA strand (Hoang et al., 2013; Rosenquist and Grollman, 2016). Remarkably, a very particular mutational signature characterized by frequent CAG → CTG transversions in the 5′-CpApG trinucleotide context has been observed in tumor cells from upper urinary tract carcinoma associated with AA exposure (Rosenquist and Grollman, 2016; Ng et al., 2017). Based on these observations, we hypothesize that TDG initiates aberrant removal of T opposite to dA-AL-I and dA-AL-II in the 5′-CpA*pG context and promotes A → T transversions in human cells via error-prone DNA repair synthesis. Thus, it is tempting to speculate that specific inhibition of TDG activity in human cells may prevent genotoxic effects of AA exposure.

MYH (MUTYH) is a human mismatch-specific adenine-DNA glycosylase homologous to the *E. coli* MutY protein; both repair proteins display very similar DNA substrate specificities. Mutations in the MUTYH gene are associated with the familial colorectal cancer in the absence of a germline mutation in the *APC* gene and confer a spontaneous mutator phenotype in human and mice cell lines (Al-Tassan et al., 2002). Noteworthy, Vrouwe et al., demonstrated that UV irradiation of the noncycling NER-deficient XP-C and XP-A human fibroblasts generated persistent single-strand DNA breaks 24 h after exposure, and activated ATR-dependent DNA damage response (Vrouwe et al., 2011). Intriguingly, the formation of single-strand DNA breaks and DNA repair synthesis initiated at damage sites in XP fibroblasts did not lead to removal of UV lesions in cellular DNA, which is the feature of aberrant repair. Recently, Mazouzi et al. (2017) showed that MUTYH promotes an increased UV sensitivity of XP cells. The authors suggested that in NER-deficient cells, MUTYH might inhibit a hypothetical, alternative NER-independent repair of UV-induced DNA damage. Here, we hypothesize that the human adenine-DNA glycosylase when acting upon the DNA duplex containing UV adducts targets adenines in the nondamaged complementary DNA strand. This in turn leads to aberrant futile repair of the nondamaged DNA strand and subsequent usage of the UV damaged DNA strand as a template for repair synthesis and ligation. Therefore, we speculate that the severe UV-sensitive phenotype of XP patients is due to a DNA glycosylase-initiated aberrant repair of UV-induced DNA lesions in human cells that would lead to persistent DNA strand breaks and mutations in both proliferating and nondividing cells.

Aberrant Repair of Interstrand DNA Cross-Links

Similar to the alkyl-purine DNA glycosylases (AlkA and ANPG) which remove regular purines (Berdal et al., 1998), the NER machinery in bacterial and human cells can initiate futile DNA repair, during which regular oligonucleotide fragments are excised from undamaged DNA duplexes leading to the futile excision/re-synthesis cycles (Branum et al., 2001). Furthermore, mammalian NER machinery initiates futile repair when acting upon the DNA duplex, containing a single ICL, by excising a damage-free 22–28 mer oligomer near psoralen-induced DNA cross-link and generating a long gap (Bessho et al., 1997). Then, DNA repair synthesis fills the single-stranded gap and generates a non-ligatable nick without removing the ICL adduct (Mu et al., 2000). It is possible that in mammals the NER-mediated nonproductive repair of ICLs generates pro-apoptotic signals to eliminate cells containing nonrepaired or irreparable complex DNA lesions.

Cisplatin [*cis*-diamminedichloroplatinum(II)] is employed to treat various types of cancers, including lung, head and neck, ovarian, and other organs. Cisplatin interacts preferentially with guanine residues in DNA and generates mono-adducts and intra- and interstrand cross-links. Exposure of the cells to cisplatin triggers a strong DNA damage response signal, which often leads to the irreversible apoptosis. Studies of the roles of DNA glycosylases and other BER enzymes in the removal of ICL have generated conflicting results, suggesting that the involvement of a given DNA repair pathway strongly depends on cellular context and lesion structure. In cisplatin-ICL, the cytosine residues adjacent to the cross-linked guanines undergo extra-helical flipping which exposes them to water and subsequently stimulates spontaneous deamination and conversion of cytosines to uracils (Lukin and de Los Santos, 2006). A study performed by

Kothandapani et al. (2011) showed that the inhibition of human major AP endonuclease 1, APE1, combined with the knockdown of uracil-DNA glycosylase (UNG) and DNA polymerase β (Polβ), makes cancer cells more resistant to cisplatin. *In vitro* reconstitution of the repair of cisplatin-ICL in synthetic oligonucleotide revealed that despite the presence of ICL, UNG excises neighboring uracil residues to generate AP sites, which are then cleaved by APE1, followed by the Polβ-catalyzed gap-filling DNA repair synthesis (Kothandapani et al., 2011). This futile BER adjacent to cisplatin ICL sites initiated by the DNA glycosylase-mediated excision generates persistent DNA strand breaks, which would interfere with the productive repair of ICLs and increase cisplatin cytotoxicity (Kothandapani and Patrick, 2013). Several APE1 inhibitors have been generated and explored, which can specifically target either AP site cleavage activity [methoxyamine and APE1 inhibitor compound III (API3)] or redox regulation function (E3330 and Gossypol/AT101) of human enzyme (reviewed in Laev et al., 2017). A recent study demonstrated that the combination of cisplatin treatment with inhibition of the redox function of APE1 by E3330 decreased migration and invasion of lung cancer cells (Manguinhas et al., 2020). Another study showed that APE1 redox inhibitors in combination with cisplatin inhibit proliferation of bladder cancer cells more efficiently than cisplatin alone (Fishel et al., 2019). Currently, specific inhibitors against BER proteins such as Polβ, PNKP, FEN1, Ligase IIIα, and PARP1/PARG have been developed either to sensitize several cancers or to form synthetic lethal partnerships with common cancer mutations (reviewed in Grundy and Parsons, 2020).

The study of repair of trioxsalen (psoralen)-induced ICLs in living cells by McNeill et al. (2013) demonstrated a possible involvement of human endonuclease VIII-like DNA glycosylase 1 (NEIL1) in the aberrant repair of complex DNA lesions. Using fluorescently tagged fusion proteins and laser micro-irradiation coupled with confocal microscopy, the authors demonstrated that NEIL1 accumulates at sites of digoxigenin-tagged trioxsalen (psoralen)-induced ICLs. In addition, NEIL1 binds to duplex DNA containing ICL without exhibiting a DNA glycosylase activity; apparently, this abortive interaction interferes with the recruitment of the XPC protein, a NER factor, and removal of ICLs. The authors proposed that NEIL1 specifically recognizes psoralen-ICLs, and this can obstruct the efficient removal of these lethal DNA lesions *in vivo* (McNeill et al., 2013).

REMOVAL OF BULKY DNA ADDUCTS IN THE BASE EXCISION REPAIR PATHWAY

DNA glycosylases and AP endonucleases recognize and remove a variety of small non-bulky DNA base damages that in general have little influence on thermodynamic stability of the DNA helix (**Figure 2**). DNA glycosylases bind and flip out of the duplex the damaged nucleotide and insert it into the active site pocket, to stabilize the DNA substrate conformation enzyme fills the void left in the helix by inserting amino acid residues (Klimasauskas et al., 1994; Stivers, 2004; Hitomi et al., 2007). In general, the active sites of DNA glycosylases are small to accommodate large bulky base modifications; nevertheless, some observations indicate that DNA glycosylases can recognize and remove bulky DNA adducts despite steric constraints to fit these base lesions into their active site pockets. Earlier, it was shown that several DNA glycosylases such as *E. coli* Fpg, phage T4 endonuclease V, and human NEIL1 can excise the imidazole ring opened form of guanine-C8-N-hydroxy-2-aminofluorene adduct, UV-induced cyclobutane dimer, and psoralen-thymine monoadduct, respectively (Boiteux et al., 1989; Vassylyev et al., 1995; Couve-Privat et al., 2007). Bacterial Fpg accommodates bulky N^7-substituted FapydG derivatives of guanine lesion in its active site pocket by enabling the N^7-bulky group to stay outside of the protein surface (Coste et al., 2008) (**Figures 3A,B,E**). Studies of the crystal structure of T4 endonuclease V in complex with cyclobutane pyrimidine dimer (CPD) DNA showed that the enzyme kinks the DNA duplex and flips out the complementary adenine base in the opposite strand out of the DNA base stack, thus avoiding accommodation of bulky CPD within the protein surface (Vassylyev et al., 1995) (**Figures 3C,D,F**). At present, it is unclear how NEIL1 can recognize large voluminous DNA lesions such as psoralen-thymine, protein-DNA cross-links, and aflatoxin-Fapy-deoxyguanosine adducts (AFB1-Fapy-dG); we hypothesize that similar to bacterial Fpg, the human DNA glycosylase avoids steric hindrance by the exclusion of a bulky group from its active site pocket (Couve-Privat et al., 2007; McKibbin et al., 2013; Vartanian et al., 2017).

A new family of bacterial DNA glycosylases that use a non-base-flipping mechanism to recognize bulky DNA base damage and a certain type of ICL has been described recently (Mullins et al., 2015a,b; Mullins et al., 2017b). A distinct DNA glycosylase superfamily including AlkC and AlkD from *Bacillus cereus* (Alseth et al., 2006) can excise positively charged alkylpurines without inserting them into their active site pocket (Mullins et al., 2015b; Shi et al., 2018). Due to the absence of specific contacts between protein and damaged nucleobase, and the interaction with the deoxyribose-phosphate backbone, AlkD is capable of excising bulky DNA adducts such as pyridyloxobutyl (POB) adducts, products of cigarette-smoke carcinogen nitrosamine ketone, and N3-yatakemycinyl-adenine (YTMA) generated by yatakemycin (YTM), an extremely cytotoxic alkylating product (Xu et al., 2012; Mullins et al., 2015b, 2017a).

Azinomycin B (AZB), a secondary metabolite produced by soil-dwell bacteria *Streptomyces sahachiroi* and *Streptomyces griseofuscus*, induces ICLs in the DNA duplex by nucleophilic addition at the N7 positions of purines (Wang et al., 2016). Previously, it was shown that the coordinated action of the classical NER machinery and homologous recombination (HR) can efficiently remove ICLs in bacterial cells (Cheng et al., 1991). However, AlkZ DNA glycosylase of *Streptomyces sahachiroi* can unhook AZB-induced ICLs in the DNA duplex, thus establishing a new alternative ICL repair mechanism in this bacterium. AlkZ resolves AZB-ICLs through the cleavage of the N-glycosidic bond on both sides of the complementary DNA strands, where resultant AP sites can be repaired by bacterial AP endonuclease, Endo IV. This observation supports the hypothesis that the BER pathway alone can remove a certain type of bulky DNA

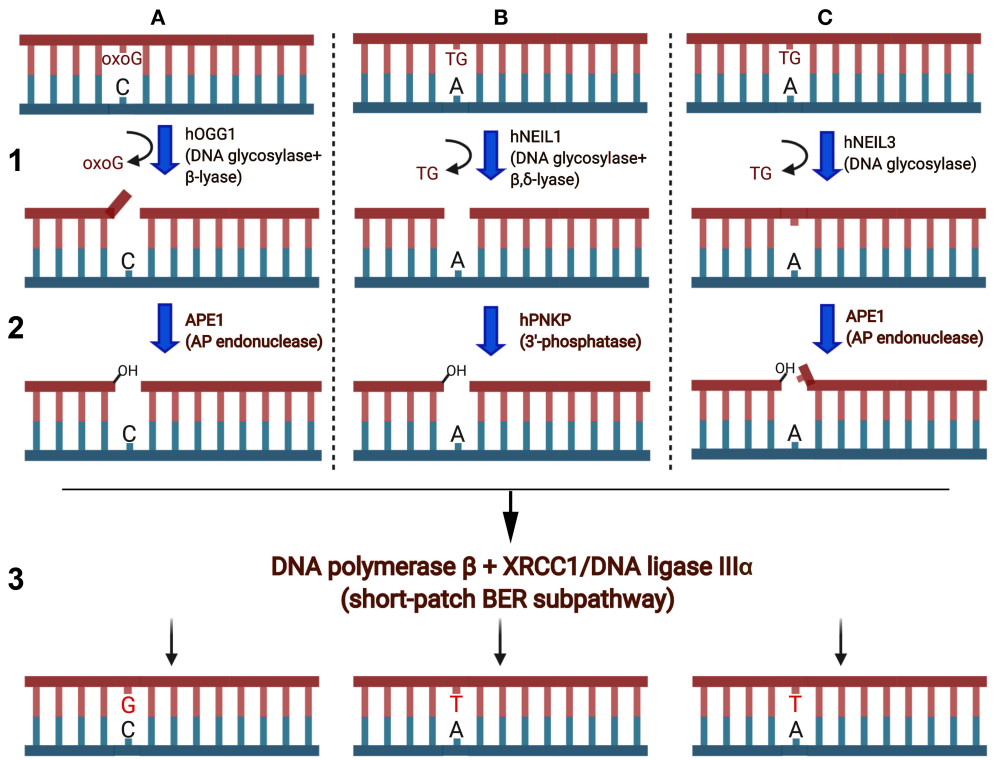

FIGURE 2 | Schematic presentation of the short-patch BER pathways. Oxygen free radicals induce oxidized guanines (oxoG) and thymine glycol (TG) in duplex DNA. **(A1)** Human OGG1 DNA glycosylase excises oxoG base in duplex DNA and cleaves abasic site via β-elimination reaction and generates single-strand break containing 3′-terminal α,β-unsaturated aldehyde (3′-PUA) and a 5′-terminal phosphate. **(A2)** 3′-PUA is removed by major human AP endonuclease 1 (APE1) to generate 3′-OH termini. **(B1)** NEIL1 excises TG and cleaves the remaining abasic site via β,δ-elimination and generates one nucleotide gap flanked with 3′-P and 5′-P. **(B2)** 3′-Phosphate is removed by hPNKP to generate 3′-OH termini. **(C1)** NEIL3 cleaves the N-glycosydic bond, releasing the TG and generating an AP site. **(C2)** The resulting AP sites are incised at 5′ by APE1, which generates a single-strand break with 3′-OH and a 5′-blocking deoxyribosophosphate (dRP) group. **(A3,B3,C3)** Finally, DNA polymerase β inserts one nucleotide (dG or dT) and removes if necessary the 5′-dRp group by its dRp-lyase activity and the remaining single-strand break is then sealed by XRCC1/Ligase IIIα complex.

lesions and ICLs (Noll et al., 2006; Huang and Li, 2013; Mullins et al., 2019). Consequently, cells lacking AlkZ are highly sensitive to AZB-induced ICLs, supporting the physiological relevance of AlkZ DNA glycosylase activity in *S. sahachiroi* (Wang et al., 2016). Both AlkD and AlkZ are DNA glycosylases that are able to recognize bulky and cross-linked DNA bases and play an important role in a toxin resistance mechanism in bacterial populations.

Recently, YcaQ, a new *E. coli* cationic alkylpurine DNA glycosylase homologous to AlkZ, has been identified. YcaQ can excise a broad range of DNA base lesions, including ICLs induced by nitrogen mustard. These studies demonstrate that the DNA glycosylase-initiated BER pathway is an alternative ICL repair pathway in bacteria, which may provide insight for potential mechanisms implicated in drug resistance in cancer cells (Martin et al., 2017; Mullins et al., 2017b).

The UV damage endonuclease (UVDE) is a DNA endonuclease that recognizes and incises DNA 5′ next to cyclobutane pyrimidine dimers (CPDs) and 6-4 photoproducts (6-4PPs) (Bowman et al., 1994; Yajima et al., 1995). In addition, UVDE can cleave the DNA duplex containing AP sites, cisplatin intra-strand DNA cross-links, uracil, and dihydrouracil and removes 3′-blocking groups at single strand break termini (Avery et al., 1999; Kanno et al., 1999). This UV DNA damage endonuclease activity is present in various eukaryotic microorganisms, including fungi *Schizosaccharomyces pombe* and *Neurospora crassa*, prokaryotes such as the Gram-positive bacteria *Bacillus subtilis* and *Deinococcus radiodurans* and Gram-negative bacteria *Thermus thermophilus*, and thermophilic archaeon *Sulfolobus acidocaldarius*. Meulenbroek et al. (2013) have resolved the crystal structure of *Sulfolobus acidocaldarius* UVDE (SacUVDE) in a pre-catalytic complex with DNA duplex containing a 6-4 photoproduct in the absence of divalent metal cations. This 3D structure revealed a novel dual dinucleotide flip mechanism for recognition of bulky cross-linked dipyrimidines. Archaeon SacUVDE flips the two purines opposite to the damaged pyrimidine bases into a dipurine-specific pocket, whereas the damaged pyrimidines are also flipped into another cleft (Meulenbroek et al., 2013).

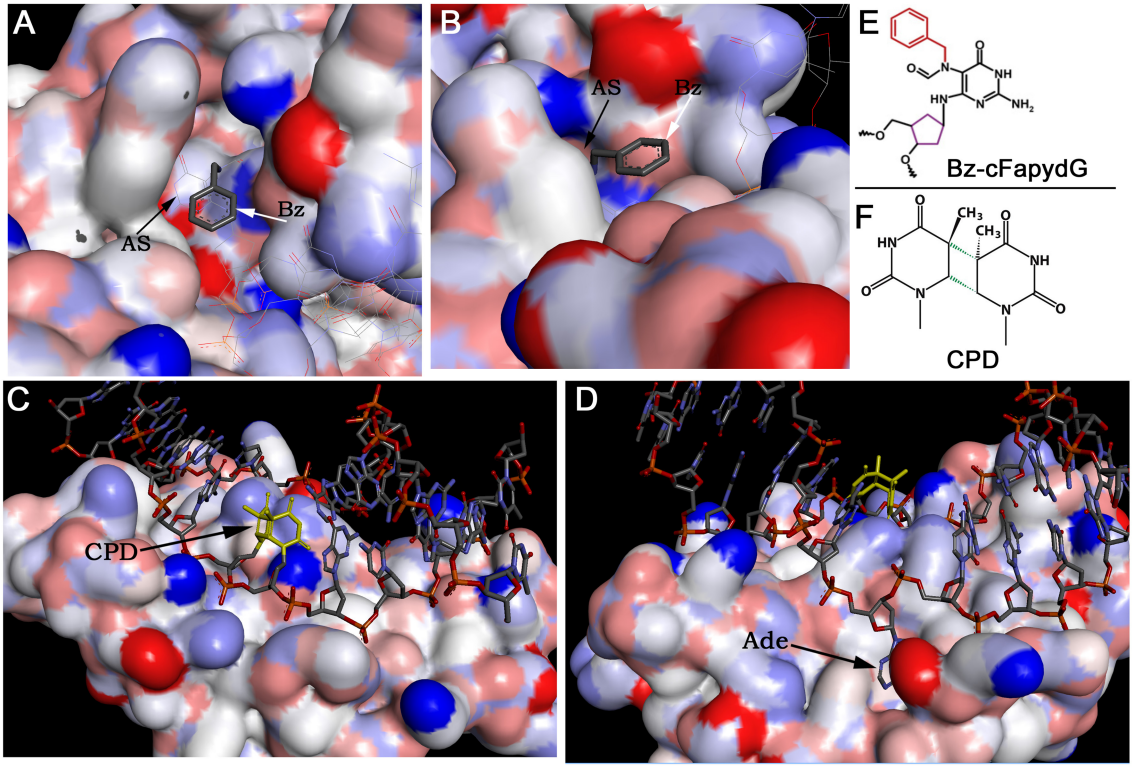

FIGURE 3 | The crystal structures of DNA glycosylases in complex with DNA duplexes containing bulky DNA base modifications. **(A,B)** Focus view of the Fpg binding pocket with the extrahelical Bz-cFapydG adduct. The 3D views of DNA glycosylase/substrate interactions derived from the PDB entry 3C58 (Coste et al., 2008). The benzyl group of the N^7-substituted cFapydG nucleoside is expelled from the binding pocket on the side of the flexible loop and thus allows the enzyme to accommodate the FapyG residue inside the active site pocket. **(C)** Focus view of the T4 endonuclease V catalytically active residues interacting with the phosphate backbones in the vicinity of the CPD. The 3D views of T4 Endo V/CPD interactions derived from the PDB entry 1vas (Vassylyev et al., 1995). **(D)** Focus view of the T4 endonuclease V-binding pocket with the extrahelical adenine residue. The adenine base complementary to 5′-CPD moiety is completely flipped out of the DNA duplex and trapped in a cavity on the protein surface. **(E)** Structure of the bulky N^7-benzyl-cFapydG nucleoside (Bz-cFapydG). **(F)** Structure of the cyclobutane pyrimidine dimer (CPD). "AS" denotes active site pocket of Fpg, "Bz" denotes benzyl group at the N^7 position of cFapydG, "CPD" denotes UV lesion, "Ade" denotes adenine residue in DNA.

ROLE OF NEI-LIKE DNA GLYCOSYLASES IN THE REPAIR OF ICLs

Mutations in genes responsible for counteracting ICL-mediated genotoxic effects can lead to Fanconi anemia (FA) disorder. FA is a recessive cancer-prone syndrome which is characterized with bone marrow failure and hypersensitivity to ICLs and, to a milder extension, to ionizing radiation and oxidative stress (Mace et al., 2005). Several lines of evidence indicate that in vertebrates, repair of ICLs is coupled to DNA replication and coordinated by the Fanconi anemia (FA) pathway. The stalled replication fork unhooks an ICL via dual incisions on both sides of the lesion by the scaffolding protein SLX4 and structure-specific endonuclease XPF/ERCC1, and this results in the generation of a double-strand break (DSB) (Hodskinson et al., 2014; Klein-Dowel et al., 2014). The unhooked ICL fragment swings free of the duplex exposing a single-stranded gap. Translesion synthesis (TLS)-specific DNA polymerases catalyze bypass of the gap and produce a three-stranded DNA repair intermediate that contains a short DNA fragment covalently attached to the duplex. It was proposed that this unhooked ICL fragment is removed in the classic NER pathway (Sancar et al., 2004; Cipak et al., 2006). However, work by Couve et al. (2009) revealed that the oxidative DNA glycosylase *E. coli* Nei and human NEIL1 excise with high efficiency the psoralen-induced bulky unhooked ICL oligomer within a three-stranded DNA structure. Three Nei-like (NEIL) DNA glycosylases are present in mammalian cells; these proteins show structural homology to the Fpg and Nei proteins of *Escherichia coli* and initiate the BER pathway to remove oxidized bases from DNA (Liu et al., 2013) (**Figures 2B,C**). Both NEIL1 and NEIL3 are cell cycle regulated with expression topping in the S phase and late S/G2, respectively, whereas NEIL2 is expressed throughout the cell cycle in a constitutive manner (Neurauter et al., 2012; Hegde et al., 2013). NEIL1 and NEIL2 contain a highly efficient β/δ-lyase activity, whereas NEIL3 exhibit a very weak β lyase function. All three mammalian Nei-like DNA glycosylases demonstrate an unusual preference for single-stranded DNA substrates and other open DNA conformations such as bubbles, loops, and recessed DNA duplexes generated during DNA replication and transcription. NEIL3 is perhaps the

most intriguing of the three due, (i) to its large structure that includes an extended C-terminal domain containing additional zinc finger motifs, (ii) the replacement of the usual proline residue as the nucleophile with valine, and (iii) its restricted expression pattern in mammalian cells (Liu et al., 2013). The observation that Nei-like proteins from *E. coli* to human cells can excise bulky unhooked psoralen-induced ICLs via simple one-step hydrolysis of the glycosidic bond between cross-linked base and deoxyribose sugar provides an alternative heuristic solution for the removal of complex DNA lesions. Complete reconstitution of the repair of unhooked ICL demonstrated that this bulky adduct can be processed in a short-patch BER pathway (**Figures 2B,C**). Based on these data, a model for the mechanism of ICL repair in mammalian cells that implicates the DNA glycosylase activity of NEIL1 downstream of XPF/ERCC1 and TLS repair steps was proposed (Couve et al., 2009).

Recent progress in understanding the repair mechanism of ICLs in vertebrates has revealed the existence of a DNA strand incision-independent repair mechanism. *In vitro* reconstitution of the ICL repair using plasmid DNA and cell-free extracts from *Xenopus* eggs revealed the DNA replication-coupled repair of ICL, which results in the formation of an X-shaped DNA structure due to convergence of two replication forks on the lesion (Raschle et al., 2008). Interestingly, when only one fork was stalled at the ICL in egg extracts, no ICL repair was observed suggesting that the convergence of two forks is required for the removal of the blocking lesion (Zhang et al., 2015). At the same time, using mammalian cells and DNA combing, Huang et al. (2013) investigated the collision of replication forks with fluorescently marked psoralen ICLs to visualize the process. The results showed that in the S phase the majority of psoralen-induced ICLs are bypassed through a replication-traverse pathway to resume DNA replication on the other side without removal of the blocking lesions. Thus, the dual-fork convergence and replication fork traverse, and an X-shaped DNA structure is produced around the ICL (Zhang and Walter, 2014). Noteworthily, these remaining ICLs are removed after DNA replication and no DSB formation is observed (Huang et al., 2013). Subsequently, Semlow et al. (2016) have shown that NEIL3 from *Xenopus laevis* can excise ICLs induced by psoralen and abasic site in X-shaped dsDNA structures through a DNA strand incision-independent repair mechanism, implying that this repair function may be one of the many roles of NEIL3 in highly proliferating cells. Following work by Martin et al. (2017) demonstrated that the purified human NEIL3 can cleave psoralen-induced ICL in single-stranded, three-stranded, and four-stranded DNA structures to produce long unhooked DNA oligomers containing either an AP site or a psoralen-thymine monoadduct. Furthermore, *E. coli* Nei and human NEIL1, similar to NEIL3, excise a psoralen-induced four-stranded DNA substrate to generate two unhooked DNA duplexes but with a nick. Noteworthily, the unusual DNA substrate specificities of these highly evolutionary conserved Nei-like enzymes imply the occurrence of very long three- and four-stranded cross-linked DNA–DNA structures that may originate *in vivo* via completion of DNA replication and TLS bypass of an unhooked ICL. In this hypothetical model, Martin et al. proposed that FANCM catalyze replication fork traverse through an unhooked ICL, without incision-mediated unhooking; this may produce either three- or four-stranded DNA molecules with a duplex cross-linked to long ssDNA or dsDNA molecules. Finally, these putative three- or four-stranded DNA structures can be excised by the Nei-like DNA glycosylases in the BER pathway; this alternative mechanism avoids formation of highly genotoxic DSB.

Recently, Li et al. (2020) have demonstrated that the NEIL3-catalyzed repair of psoralen-induced ICLs is physiologically relevant in mammalian cells. The authors found that NEIL3 plays a major role in the repair of psoralen-induced ICLs in mammalian cells, which is non-epistatic with the Fanconi anemia (FA) pathway, whereas the FA pathway is primarily responsible for the repair of ICLs induced by anticancer drugs such as MMC and cisplatin and proceeds via generation of DSBs. Noteworthily, PARP1 recruits NEIL3 to psoralen-induced ICLs in rapid manner, and PARP1 inhibitors block NEIL3 repair (Li et al., 2020). NEIL3 specifically interacts with the RUVBL1/2 complex (RuvB-like AAA ATPase 1 and 2), which function in both NEIL3 and FA pathways of ICL repair. The RING-type E3 ubiquitin ligase TRAIP (TRAF-interacting protein), which is essential for cell proliferation and replication fork progression through ICL, requires the recruitment of NEIL3 and depletion of TRAIP switch ICL repair to the FA-dependent incision repair pathway. Similar to the RuvBL1/2 complex, TRAIP functions upstream of NEIL3 and FA pathways for ICL repair.

As we described above, acetaldehyde, an endogenous and alcohol-derived metabolite, produced upon alcohol consumption induces DNA cross-links and provokes bone marrow failure in FA patients. A new excision-independent repair pathway, which functions in addition to the FA system, to resolve acetaldehyde-induced ICLs has been identified recently (Hodskinson et al., 2020). This new repair mechanism, similar to NEIL3 and FA pathways, requires replication fork convergence but catalyzes direct DNA damage reversal which leads to the breakage of the acetaldehyde cross-link, without excision of the lesion. After ICL breakage, the repair of remaining acetaldehyde-guanine mono-adduct requires TLS DNA polymerases REV1 and Pol ζ resulting in a distinct mutational spectrum (Hodskinson et al., 2020).

It should be noted that despite structural similarities among various ICLs, the level of distortion of the DNA duplex and choice of DNA repair mechanism would strongly depend on the chemical nature of ICL. The incision-dependent Fanconi anemia-coordinated network which proceeds via generation of DSB is a preferred repair pathway for cisplatin and nitrogen mustard-induced ICLs (Cipak et al., 2006; Raschle et al., 2008). On the other hand, ICLs generated by photoactivated psoralen and abasic sites would be preferentially repaired via DNA glycosylase-mediated excision of ICL (Semlow et al., 2016; Martin et al., 2017; Imani Nejad et al., 2020). Noteworthily, mouse embryonic fibroblast (MEF) knockout for NEIL3 exhibit modest sensitivity to cisplatin (Rolseth et al., 2013), suggesting that some cisplatin-induced ICLs might be processed via the BER pathway, as a backup repair system for FA and NER. It should be noted that DNA glycosylase-dependent repair of ICLs seems to be more mutagenic as compared to the versatile Fanconi anemia system (Semlow et al., 2016).

CONCLUDING REMARKS AND FUTURE PERSPECTIVES

Continuous damage of cellular DNA together with repair deficiency results in genome instability and cancer. Majority of DNA damage: non-bulky base modifications, abasic sites, and single-strand breaks with 3′-blocking groups are removed in DNA glycosylase and AP endonuclease-initiated BER and NIR pathways, respectively, without significant activation of DNA damage signaling pathways and cell cycle checkpoints, whereas complex DNA damage such as bulky DNA adducts and interstrand DNA cross-links, which constitute only a minor fraction of total DNA damage, presents a major challenge for DNA repair and cell fate. To counteract complex DNA lesions, the cell employs specific DNA damage signaling systems and several distinct DNA repair pathways acting in a highly coordinated manner. The chemical nature of complex DNA lesions and the extent of helix distortion their produce play important roles in DNA damage signaling, repair, and mutagenesis. Typically, complex DNA lesions are handled in the classical NER pathway, which can be coupled to transcription. Contrary to DNA glycosylases, NER machinery does not have specificity to a base modification *per se* but rather recognizes a DNA helix distortion, whereas DNA glycosylases are highly specific to the base modifications, because a damaged base should fit into their active site pocket. Intriguingly, certain types of DNA glycosylases are involved in the repair of bulky DNA adducts and ICLs, which cannot be accommodated inside the enzyme body. As a solution to this problem, T4 endonuclease V DNA glycosylase and UVDE endonuclease interact not with a UV pyrimidine dimer but with opposite adenine bases by inserting them into their specific pockets. The NER machinery cannot efficiently recognize bulky DNA adducts which do not distort DNA helix conformation and do not destabilize thermodynamic stability of the duplex (e.g., aristolactam-DNA adducts and dibenzopyrine-adenine adducts). In addition, the mammalian NER pathway is not efficient when acting upon ICLs, for the reason that both strands in duplex DNA are damaged and that the repair proteins cannot discriminate between two strands to excise the lesion (Mu et al., 2000), whereas Nei-like family DNA glycosylases recognize the adducted nucleobase but expel the bulky cross-linked moiety out of the active site pocket (Coste et al., 2008; Couve et al., 2009). NEIL1 and NEIL3 can excise ICL in both DNA strands in a sequential manner; importantly, NEIL3 does not cleave the DNA strand after base excision and thus does not generate toxic DSB (Semlow et al., 2016; Martin et al., 2017).

Mismatch-specific DNA glycosylases such as *E. coli* MutY and human TDG and MBD4 are prone to aberrant repair. In addition, cisplatin-induced ICLs can be processed in a futile uracil-DNA glycosylase-initiated BER, which exacerbates a cytotoxic effect of this drug. Thus, unrepaired bulky DNA adducts and ICLs might be processed by DNA glycosylases in an aberrant manner by removing nondamaged DNA bases, which are either opposite to modified DNA bases or in close proximity to an ICL. The question why aberrant DNA repair is evolutionarily conserved from *E. coli* to human remains pertinent. Plausible interpretations of this could be that (i) aberrant repair via stimulation of mutations in the specific regulatory regions of genome could play a capacitor role in evolution of warm-blood animals (Talhaoui et al., 2014) and (ii) aberrant removal of nondamaged bases prevents mutations since it triggers a strong cellular response, which in turn induces apoptosis or senescence in cells that accumulate unrepaired DNA lesions.

NEIL3 is a particular DNA glycosylase that possesses an extended C-terminal domain, containing three additional zinc finger-binding domains that specifically interact with ssDNA and ADP-ribose polymers (Chen et al., 2020). NEIL3 plays an important role in the repair of psoralen-induced ICLs in mammalian cells (Li et al., 2020). Nevertheless, NEIL3 DNA glycosylase-mediated repair of ICLs might be error-prone, as compared to the classic Fanconi anemia pathway, because of the generation of unrepaired AP sites in single-stranded DNA, which are protected from cleavage by the AP endonuclease (Ha et al., 2020) and can induce mutations (Semlow et al., 2016). Alternative DNA glycosylase-dependent repair of complex DNA lesions can be activated in cancer cells to promote genome instability and resistance to chemotherapy. Therefore, inhibition of DNA glycosylase activities in tumor cells offers a new strategy to combat anticancer therapy resistance.

AUTHOR CONTRIBUTIONS

YB, DK, AAI, DB, and MS wrote the nature of DNA damage part of the review. YB, ST, RG, BM, and MS wrote the DNA repair part of the review. YB, AAI, and MS prepared figures. All authors discussed and contributed to analysis of published literature and to writing the manuscript.

FUNDING

This research was supported by grants to Murat Saparbaev from la Ligue National Contre le Cancer Equipe Labellisee LIGUE 2016 (https://www.ligue-cancer.net) and Electricité de France (RB 2020-02) (http://www.edf.fr); to AAI from the French National Research Agency (ANR-18-CE44-0008) and Fondation ARC (PJA-20181208015); to BM from Nazarbayev University Oak Ridge Associated Universities (ORAU) grant 091019CRP2111; to YB from the Ministry of Education and Science of the Republic of Kazakhstan Grant No. AP08053387; and to ST from the Committee of Science of the Ministry of Education and Science of the Republic of Kazakhstan Grant No. AP05131478. YB and ST were supported by a doctoral fellowship from Nazarbayev University and post-doctoral fellowship from Al-Farabi Kazakh National University, respectively.

REFERENCES

Alseth, I., Rognes, T., Lindbäck, T., Solberg, I., Robertsen, K., Kristiansen, K. I., et al. (2006). A new protein superfamily includes two novel 3-methyladenine DNA glycosylases from *Bacillus cereus*, AlkC and AlkD. *Mol. Microbiol.* 59, 1602–1609. doi: 10.1111/j.1365-2958.2006.05044.x

Al-Tassan, N., Chmiel, N. H., Maynard, J., Fleming, N., Livingston, A. L., Williams, G. T., et al. (2002). Inherited variants of MYH associated with

somatic G:C–>T:A mutations in colorectal tumors. *Nat. Genet.* 30, 227–232. doi: 10.1038/ng828

Amin, S., Desai, D., Dai, W., Harvey, R. G., and Hecht, S. S. (1995a). Tumorigenicity in newborn mice of fjord region and other sterically hindered diol epoxides of benzo[g]chrysene, dibenzo[a,l]pyrene (dibenzo[def,p]chrysene), 4H-cyclopenta[def]chrysene and fluoranthene. *Carcinogenesis* 16, 2813–2817. doi: 10.1093/carcin/16.11.2813

Amin, S., Krzeminski, J., Rivenson, A., Kurtzke, C., Hecht, S. S., and el-Bayoumy, K. (1995b). Mammary carcinogenicity in female CD rats of fjord region diol epoxides of benzo[c]phenanthrene, benzo[g]chrysene and dibenzo[a,l]pyrene. *Carcinogenesis* 16, 1971–1974. doi: 10.1093/carcin/16.8.1971

Avery, A. M., Kaur, B., Taylor, J. S., Mello, J. A., Essigmann, J. M., and Doetsch, P. W. (1999). Substrate specificity of ultraviolet DNA endonuclease (UVDE/Uve1p) from Schizosaccharomyces pombe. *Nucleic Acids Res.* 27, 2256–2264. doi: 10.1093/nar/27.11.2256

Bancroft, D. P., Lepre, C. A., and Lippard, S. J. (1990). Pt-195 Nmr kinetic and mechanistic studies of cis-diamminedichloroplatinum and trans-diamminedichloroplatinum(Ii) binding to DNA. *J. Am. Chem. Soc.* 112, 6860–6871. doi: 10.1021/ja00175a020

Berdal, K. G., Johansen, R. F., and Seeberg, E. (1998). Release of normal bases from intact DNA by a native DNA repair enzyme. *Embo J.* 17, 363–367. doi: 10.1093/emboj/17.2.363

Bergvall, C., and Westerholm, R. (2007). Identification and determination of highly carcinogenic dibenzopyrene isomers in air particulate samples from a street canyon, a rooftop, and a subway station in Stockholm. *Environ. Sci. Technol.* 41, 731–737. doi: 10.1021/es062232p

Bessho, T., Mu, D., and Sancar, A. (1997). Initiation of DNA interstrand cross-link repair in humans: the nucleotide excision repair system makes dual incisions 5' to the cross-linked base and removes a 22- to 28-nucleotide-long damage-free strand. *Mol. Cell. Biol.* 17, 6822–6830. doi: 10.1128/MCB.17.12.6822

Bieler, C. A., Stiborova, M., Wiessler, M., Cosyns, J. P., van Ypersele de Strihou, C., and Schmeiser, H. H. (1997). 32P-post-labelling analysis of DNA adducts formed by aristolochic acid in tissues from patients with Chinese herbs nephropathy. *Carcinogenesis* 18, 1063–1067. doi: 10.1093/carcin/18.5.1063

Boiteux, S., Bichara, M., Fuchs, R. P., and Laval, J. (1989). Excision of the imidazole ring-opened form of N-2-aminofluorene-C(8)-guanine adduct in poly(dG-dC) by *Escherichia coli* formamidopyrimidine-DNA glycosylase. *Carcinogenesis* 10, 1905–1909. doi: 10.1093/carcin/10.10.1905

Bowman, K. K., Sidik, K., Smith, C. A., Taylor, J. S., Doetsch, P. W., and Freyer, G. A. (1994). A new ATP-independent DNA endonuclease from Schizosaccharomyces pombe that recognizes cyclobutane pyrimidine dimers and 6-4 photoproducts. *Nucleic Acids Res.* 22, 3026–3032. doi: 10.1093/nar/22.15.3026

Branum, M. E., Reardon, J. T., and Sancar, A. (2001). DNA repair excision nuclease attacks undamaged DNA. A potential source of spontaneous mutations. *J. Biol. Chem.* 276, 25421–25426. doi: 10.1074/jbc.M101032200

Brooks, P. J. (2008). The 8,5'-cyclopurine-2'-deoxynucleosides: candidate neurodegenerative DNA lesions in xeroderma pigmentosum, and unique probes of transcription and nucleotide excision repair. *DNA Repair* 7, 1168–1179. doi: 10.1016/j.dnarep.2008.03.016

Brooks, P. J., Wise, D. S., Berry, D. A., Kosmoski, J. V., Smerdon, M. J., Somers, R. L., et al. (2000). The oxidative DNA lesion 8,5'-(S)-cyclo-2'-deoxyadenosine is repaired by the nucleotide excision repair pathway and blocks gene expression in mammalian cells. *J. Biol. Chem.* 275, 22355–22362. doi: 10.1074/jbc.M002259200

Burgos-Barragan, G., Wit, N., Meiser, J., Dingler, F. A., Pietzke, M., Mulderrig, L., et al. (2017). Mammals divert endogenous genotoxic formaldehyde into one-carbon metabolism. *Nature* 548, 549–554. doi: 10.1038/nature23481

Cadet, J., Ravanat, J. L., TavernaPorro, M., Menoni, H., and Angelov, D. (2012). Oxidatively generated complex DNA damage: tandem and clustered lesions. *Cancer Lett.* 327, 5–15. doi: 10.1016/j.canlet.2012.04.005

Cai, Y., Kropachev, K., Terzidis, M. A., Masi, A., Chatgilialoglu, C., Shafirovich, V., et al. (2015). Differences in the access of lesions to the nucleotide excision repair machinery in nucleosomes. *Biochemistry* 54, 4181–4185. doi: 10.1021/acs.biochem.5b00564

Cavalieri, E. L., Higginbotham, S., RamaKrishna, N. V., Devanesan, P. D., Todorovic, R., Rogan, E. G., et al. (1991). Comparative dose-response tumorigenicity studies of dibenzo[alpha,l]pyrene versus 7,12-dimethylbenz[alpha]anthracene, benzo[alpha]pyrene and two dibenzo[alpha,l]pyrene dihydrodiols in mouse skin and rat mammary gland. *Carcinogenesis* 12, 1939–1944. doi: 10.1093/carcin/12.10.1939

Ceccaldi, R., Parmar, K., Mouly, E., Delord, M., Kim, J. M., Regairaz, M., et al. (2012). Bone marrow failure in Fanconi anemia is triggered by an exacerbated p53/p21 DNA damage response that impairs hematopoietic stem and progenitor cells. *Cell Stem Cell* 11, 36–49. doi: 10.1016/j.stem.2012.05.013

Chatgilialoglu, C., Ferreri, C., Geacintov, N. E., Krokidis, M. G., Liu, Y., Masi, A., et al. (2019). 5',8-Cyclopurine lesions in DNA damage: chemical, analytical, biological, and diagnostic significance. *Cells* 8:513. doi: 10.3390/cells8060513

Chen, C. H., Dickman, K. G., Moriya, M., Zavadil, J., Sidorenko, V. S., Edwards, K. L., et al. (2012). Aristolochic acid-associated urothelial cancer in Taiwan. *Proc. Natl. Acad. Sci. U. S. A.* 109, 8241–8246. doi: 10.1073/pnas.1119920109

Chen, Q., Bian, C., Wang, X., Liu, X., Ahmad Kassab, M., Yu, Y., et al. (2020). ADP-ribosylation of histone variant H2AX promotes base excision repair. *EMBO J.* e104542. doi: 10.15252/embj.2020104542. [Epub ahead of print].

Chen, W., Han, Y., and Peng, X. (2014). Aromatic nitrogen mustard-based prodrugs: activity, selectivity, and the mechanism of DNA cross-linking. *Chemistry* 20, 7410–7418. doi: 10.1002/chem.201400090

Cheng, S., Sancar, A., and Hearst, J. E. (1991). RecA-dependent incision of psoralen-crosslinked DNA by (A)BC excinuclease. *Nucleic Acids Res.* 19, 657–663. doi: 10.1093/nar/19.3.657

Cipak, L., Watanabe, N., and Bessho, T. (2006). The role of BRCA2 in replication-coupled DNA interstrand cross-link repair *in vitro*. *Nat. Struct. Mol. Biol.* 13, 729–733. doi: 10.1038/nsmb1120

Cole, R. S. (1971). Psoralen monoadducts and interstrand cross-links in DNA. *Biochim. Biophys. Acta* 254, 30–39. doi: 10.1016/0005-2787(71)90111-0

Coste, F., Ober, M., Le Bihan, Y. V., Izquierdo, M. A., Hervouet, N., Mueller, H., et al. (2008). Bacterial base excision repair enzyme Fpg recognizes bulky N7-substituted-FapydG lesion via unproductive binding mode. *Chem. Biol.* 15, 706–717. doi: 10.1016/j.chembiol.2008.05.014

Couve, S., Mace-Aime, G., Rosselli, F., and Saparbaev, M. K. (2009). The human oxidative DNA glycosylase NEIL1 excises psoralen-induced interstrand DNA cross-links in a three-stranded DNA structure. *J. Biol. Chem.* 284, 11963–11970. doi: 10.1074/jbc.M900746200

Couve-Privat, S., Mace, G., Rosselli, F., and Saparbaev, M. K. (2007). Psoralen-induced DNA adducts are substrates for the base excision repair pathway in human cells. *Nucleic Acids Res.* 35, 5672–5682. doi: 10.1093/nar/gkm592

Deans, A. J., and West, S. C. (2011). DNA interstrand crosslink repair and cancer. *Nat. Rev. Cancer* 11, 467–480. doi: 10.1038/nrc3088

Debelle, F. D., Vanherweghem, J. L., and Nortier, J. L. (2008). Aristolochic acid nephropathy: a worldwide problem. *Kidney Int.* 74, 158–169. doi: 10.1038/ki.2008.129

D'Errico, M., Parlanti, E., Teson, M., de Jesus, B. M., Degan, P., Calcagnile, A., et al. (2006). New functions of XPC in the protection of human skin cells from oxidative damage. *Embo J.* 25, 4305–4315. doi: 10.1038/sj.emboj.7601277

D'Errico, M., Parlanti, E., Teson, M., Degan, P., Lemma, T., Calcagnile, A., et al. (2007). The role of CSA in the response to oxidative DNA damage in human cells. *Oncogene* 26, 4336–4343. doi: 10.1038/sj.onc.1210232

Dickman, K., and Grollman, A. (2010). 7.18 - nephrotoxicity of natural products: aristolochic acid and fungal toxins. *Compreh. Toxicol.* 7, 433–458. doi: 10.1016/B978-0-08-046884-6.00823-X

Dirksen, M. L., Blakely, W. F., Holwitt, E., and Dizdaroglu, M. (1988). Effect of DNA conformation on the hydroxyl radical-induced formation of 8,5'-cyclopurine 2'-deoxyribonucleoside residues in DNA. *Int. J. Radiat. Biol.* 54, 195–204. doi: 10.1080/09553008814551631

Eaton, D. L., and Gallagher, E. P. (1994). Mechanisms of aflatoxin carcinogenesis. *Annu. Rev. Pharmacol. Toxicol.* 34, 135–172. doi: 10.1146/annurev.pa.34.040194.001031

Enoiu, M., Jiricny, J., and Scharer, O. D. (2012). Repair of cisplatin-induced DNA interstrand crosslinks by a replication-independent pathway involving transcription-coupled repair and translesion synthesis. *Nucleic Acids Res.* 40, 8953–8964. doi: 10.1093/nar/gks670

Fan, H. P., and Peng, X. (2016). Novel DNA cross-linking reagents. *Adv. Mol. Toxicol.* 10, 235–292. doi: 10.1016/B978-0-12-804700-2.00006-4

Fishel, M. L., Xia, H., McGeown, J., McIlwain, D. W., Elbanna, M., Craft, A. A., et al. (2019). Antitumor activity and mechanistic characterization of

APE1/Ref-1 inhibitors in bladder cancer. *Mol. Cancer Ther.* 18, 1947–1960. doi: 10.1158/1535-7163.MCT-18-1166

Florea, A. M., and Busselberg, D. (2011). Cisplatin as an anti-tumor drug: cellular mechanisms of activity, drug resistance and induced side effects. *Cancers* 3, 1351–1371. doi: 10.3390/cancers3011351

Florea-Wang, D., Pawlowicz, A. J., Sinkkonen, J., Kronberg, L., Vilpo, J., and Hovinen, J. (2009). Reactions of 4-[Bis(2-chloroethyl)amino]benzenebutanoic acid (chlorambucil) with DNA. *Chem. Biodivers* 6, 1002–1013. doi: 10.1002/cbdv.200800327

Fowler, R. G., White, S. J., Koyama, C., Moore, S. C., Dunn, R. L., and Schaaper, R. M. (2003). Interactions among the *Escherichia coli* mutT, mutM, and mutY damage prevention pathways. *DNA Repair* 2, 159–173. doi: 10.1016/S1568-7864(02)00193-3

Garaycoechea, J. I., Crossan, G. P., Langevin, F., Daly, M., Arends, M. J., and Patel, K. J. (2012). Genotoxic consequences of endogenous aldehydes on mouse haematopoietic stem cell function. *Nature* 489, 571–575. doi: 10.1038/nature11368

Georgakilas, A. G., O'Neill, P., and Stewart, R. D. (2013). Induction and repair of clustered DNA lesions: what do we know so far? *Radiat Res.* 180, 100–109. doi: 10.1667/RR3041.1

Grollman, A. P., Shibutani, S., Moriya, M., Miller, F., Wu, L., Moll, U., et al. (2007). Aristolochic acid and the etiology of endemic (Balkan) nephropathy. *Proc. Natl. Acad. Sci. U. S. A.* 104, 12129–12134. doi: 10.1073/pnas.0701248104

Grundy, G. J., and Parsons, J. L. (2020). Base excision repair and its implications to cancer therapy. *Essays Biochem.* 64, 831–843. doi: 10.1042/EBC20200013

Ha, A., Lin, Y., and Yan, S. (2020). A non-canonical role for the DNA glycosylase NEIL3 in suppressing APE1 endonuclease-mediated ssDNA damage. *J. Biol. Chem.* 295, 14222–14235. doi: 10.1074/jbc.RA120.014228

Hampson, R., Humbert, O., Macpherson, P., Aquilina, G., and Karran, P. (1997). Mismatch repair defects and O6-methylguanine-DNA methyltransferase expression in acquired resistance to methylating agents in human cells. *J. Biol. Chem.* 272, 28596–28606. doi: 10.1074/jbc.272.45.28596

Hashimoto, K., Bonala, R., Johnson, F., Grollman, A. P., and Moriya, M. (2016). Y-family DNA polymerase-independent gap-filling translesion synthesis across aristolochic acid-derived adenine adducts in mouse cells. *DNA Repair* 46, 55–60. doi: 10.1016/j.dnarep.2016.07.003

Hegde, M. L., Hegde, P. M., Bellot, L. J., Mandal, S. M., Hazra, T. K., Li, G. M., et al. (2013). Prereplicative repair of oxidized bases in the human genome is mediated by NEIL1 DNA glycosylase together with replication proteins. *Proc. Natl. Acad. Sci. U. S. A.* 110, E3090–3099. doi: 10.1073/pnas.1304231110

Hitomi, K., Iwai, S., and Tainer, J. A. (2007). The intricate structural chemistry of base excision repair machinery: implications for DNA damage recognition, removal, and repair. *DNA Repair* 6, 410–428. doi: 10.1016/j.dnarep.2006.10.004

Hoang, M. L., Chen, C. H., Sidorenko, V. S., He, J., Dickman, K. G., Yun, B. H., et al. (2013). Mutational signature of aristolochic acid exposure as revealed by whole-exome sequencing. *Sci. Transl. Med.* 5:197ra102. doi: 10.1126/scitranslmed.3006200

Hodskinson, M. R., Bolner, A., Sato, K., Kamimae-Lanning, A. N., Rooijers, K., Witte, M., et al. (2020). Alcohol-derived DNA crosslinks are repaired by two distinct mechanisms. *Nature* 579, 603–608. doi: 10.1038/s41586-020-2059-5

Hodskinson, M. R., Silhan, J., Crossan, G. P., Garaycoechea, J. I., Mukherjee, S., Johnson, C. M., et al. (2014). Mouse SLX4 is a tumor suppressor that stimulates the activity of the nuclease XPF-ERCC1 in DNA crosslink repair. *Mol. Cell* 54, 472–484. doi: 10.1016/j.molcel.2014.03.014

Huang, J., Liu, S., Bellani, M. A., Thazhathveetil, A. K., Ling, C., de Winter, J. P., et al. (2013). The DNA translocase FANCM/MHF promotes replication traverse of DNA interstrand crosslinks. *Mol. Cell* 52, 434–446. doi: 10.1016/j.molcel.2013.09.021

Huang, Y., and Li, L. (2013). DNA crosslinking damage and cancer - a tale of friend and foe. *Transl. Cancer Res.*2, 144–154. doi: 10.3978/j.issn.2218-676X.2013.03.01

Imani Nejad, M., Housh, K., Rodriguez, A. A., Haldar, T., Kathe, S., Wallace, S. S., et al. (2020). Unhooking of an interstrand cross-link at DNA fork structures by the DNA glycosylase NEIL3. *DNA Repair* 86:102752. doi: 10.1016/j.dnarep.2019.102752

Johnston, B. H., and Hearst, J. E. (1981). Low-level psoralen–deoxyribonucleic acid cross-links induced by single laser pulses. *Biochemistry* 20, 739–745. doi: 10.1021/bi00507a012

Jung, Y., and Lippard, S. J. (2007). Direct cellular responses to platinum-induced DNA damage. *Chem. Rev.* 107, 1387–1407. doi: 10.1021/cr068207j

Kanno, S., Iwai, S., Takao, M., and Yasui, A. (1999). Repair of apurinic/apyrimidinic sites by UV damage endonuclease; a repair protein for UV and oxidative damage. *Nucleic Acids Res.* 27, 3096–3103. doi: 10.1093/nar/27.15.3096

Kartalou, M., and Essigmann, J. M. (2001). Recognition of cisplatin adducts by cellular proteins. *Mutat. Res.* 478, 1–21. doi: 10.1016/S0027-5107(01)00142-7

Klein-Dowel, D., Boonen, R. A., Long, D. T., Szypowska, A. A., Raschle, M., Walter, J. C., et al. (2014). XPF-ERCC1 acts in unhooking DNA interstrand crosslinks in cooperation with FANCD2 and FANCP/SLX4. *Mol. Cell* 54, 460–471. doi: 10.1016/j.molcel.2014.03.015

Klimasauskas, S., Kumar, S., Roberts, R. J., and Cheng, X. (1994). HhaI methyltransferase flips its target base out of the DNA helix. *Cell* 76, 357–369. doi: 10.1016/0092-8674(94)90342-5

Kohn, K. W., Spears, C. L., and Doty, P. (1966). Inter-strand crosslinking of DNA by nitrogen mustard. *J. Mol. Biol.* 19, 266–288. doi: 10.1016/S0022-2836(66)80004-9

Kothandapani, A., Dangeti, V. S., Brown, A. R., Banze, L. A., Wang, X. H., Sobol, R. W., et al. (2011). Novel role of base excision repair in mediating cisplatin cytotoxicity. *J. Biol. Chem.* 286, 14564–14574. doi: 10.1074/jbc.M111.225375

Kothandapani, A., and Patrick, S. M. (2013). Evidence for base excision repair processing of DNA interstrand crosslinks. *Mutat. Res.* 743–744, 44–52. doi: 10.1016/j.mrfmmm.2012.11.007

Kovtun, I. V., Liu, Y., Bjoras, M., Klungland, A., Wilson, S. H., and McMurray, C. T. (2007). OGG1 initiates age-dependent CAG trinucleotide expansion in somatic cells. *Nature* 447, 447–452. doi: 10.1038/nature05778

Kropachev, K., Ding, S., Terzidis, M. A., Masi, A., Liu, Z., Cai, Y., et al. (2014). Structural basis for the recognition of diastereomeric 5',8-cyclo-2'-deoxypurine lesions by the human nucleotide excision repair system. *Nucleic Acids Res.* 42, 5020–5032. doi: 10.1093/nar/gku162

Kropachev, K., Kolbanovskiy, M., Liu, Z., Cai, Y., Zhang, L., Schwaid, A. G., et al. (2013). Adenine-DNA adducts derived from the highly tumorigenic Dibenzo[a,l]pyrene are resistant to nucleotide excision repair while guanine adducts are not. *Chem. Res. Toxicol.* 26, 783–793. doi: 10.1021/tx400080k

Kuraoka, I., Bender, C., Romieu, A., Cadet, J., Wood, R. D., and Lindahl, T. (2000). Removal of oxygen free-radical-induced 5',8-purine cyclodeoxynucleosides from DNA by the nucleotide excision-repair pathway in human cells. *Proc. Natl. Acad. Sci. U. S. A.* 97, 3832–3837. doi: 10.1073/pnas.070471597

Laev, S. S., Salakhutdinov, N. F., and Lavrik, O. I. (2017). Inhibitors of nuclease and redox activity of apurinic/apyrimidinic endonuclease 1/redox effector factor 1 (APE1/Ref-1). *Bioorg. Med. Chem.* 25, 2531–2544. doi: 10.1016/j.bmc.2017.01.028

Lawley, P. D., and Phillips, D. H. (1996). DNA adducts from chemotherapeutic agents. *Mutat. Res.* 355, 13–40. doi: 10.1016/0027-5107(96)00020-6

Leitner-Dagan, Y., Sevilya, Z., Pinchev, M., Kramer, R., Elinger, D., Roisman, L. C., et al. (2012). N-methylpurine DNA glycosylase and OGG1 DNA repair activities: opposite associations with lung cancer risk. *J. Natl. Cancer Inst.* 104, 1765–1769. doi: 10.1093/jnci/djs445

Li, K. M., Byun, J., Gross, M. L., Zamzow, D., Jankowiak, R., Rogan, E. G., et al. (1999a). Synthesis and structure determination of the adducts formed by electrochemical oxidation of Dibenzo[a,l]pyrene in the presence of adenine. *Chem. Res. Toxicol.* 12, 749–757. doi: 10.1021/tx9801965

Li, K. M., George, M., Gross, M. L., Lin, C. H., Jankowiak, R., Small, G. J., et al. (1999b). Structure elucidation of the adducts formed by fjord region Dibenzo[a,l]pyrene-11,12-dihydrodiol 13,14-epoxides with deoxyguanosine. *Chem. Res. Toxicol.* 12, 778–788. doi: 10.1021/tx980234k

Li, N., Wang, J., Wallace, S. S., Chen, J., Zhou, J., and D'Andrea, A. D. (2020). Cooperation of the NEIL3 and Fanconi anemia/BRCA pathways in interstrand crosslink repair. *Nucleic Acids Res.* 48, 3014–3028. doi: 10.1093/nar/gkaa038

Liu, M., Doublie, S., and Wallace, S. S. (2013). Neil3, the final frontier for the DNA glycosylases that recognize oxidative damage. *Mutat. Res.* 743–744, 4–11. doi: 10.1016/j.mrfmmm.2012.12.003

Lopez-Martinez, D., Liang, C. C., and Cohn, M. A. (2016). Cellular response to DNA interstrand crosslinks: the Fanconi anemia pathway. *Cell Mol. Life Sci.* 73, 3097–3114. doi: 10.1007/s00018-016-2218-x

Lu, Z. N., Luo, Q., Zhao, L. N., Shi, Y., Wang, N., Wang, L., et al. (2020). The mutational features of aristolochic acid-induced mouse and human liver cancers. *Hepatology* 71, 929–942. doi: 10.1002/hep.30863

Luch, A. (2005). Nature and nurture - lessons from chemical carcinogenesis. *Nat. Rev. Cancer* 5, 113–125. doi: 10.1038/nrc1546

Luch, A. (2009). On the impact of the molecule structure in chemical carcinogenesis. *EXS* 99, 151–179. doi: 10.1007/978-3-7643-8336-7_6

Luch, A., Schober, W., Soballa, V. J., Raab, G., Greim, H., Jacob, J., et al. (1999). Metabolic activation of dibenzo[a,l]pyrene by human cytochrome P450 1A1 and P450 1B1 expressed in V79 Chinese hamster cells. *Chem. Res. Toxicol.* 12, 353–364. doi: 10.1021/tx980240g

Lukin, M., and de Los Santos, C. (2006). NMR structures of damaged DNA. *Chem. Rev.* 106, 607–686. doi: 10.1021/cr0404646

Lukin, M., Zaliznyak, T., Johnson, F., and de los Santos, C. (2012). Structure and stability of DNA containing an aristolactam II-dA lesion: implications for the NER recognition of bulky adducts. *Nucleic Acids Res.* 40, 2759–2770. doi: 10.1093/nar/gkr1094

Mace, G., Bogliolo, M., Guervilly, J. H., Dugas du Villard, J. A., and Rosselli, F. (2005). 3R coordination by Fanconi anemia proteins. *Biochimie* 87, 647–658. doi: 10.1016/j.biochi.2005.05.003

Magana-Schwencke, N., Henriques, J. A., Chanet, R., and Moustacchi, E. (1982). The fate of 8-methoxypsoralen photoinduced crosslinks in nuclear and mitochondrial yeast DNA: comparison of wild-type and repair-deficient strains. *Proc. Natl. Acad. Sci. U. S. A.* 79, 1722–1726. doi: 10.1073/pnas.79.6.1722

Manguinhas, R., Fernandes, A. S., Costa, J. G., Saraiva, N., Camoes, S. P., Gil, N., et al. (2020). Impact of the APE1 redox function inhibitor E3330 in non-small cell lung cancer cells exposed to cisplatin: increased cytotoxicity and impairment of cell migration and invasion. *Antioxidants* 9:550. doi: 10.3390/antiox9060550

Martin, C. N., and Garner, R. C. (1977). Aflatoxin B -oxide generated by chemical or enzymic oxidation of aflatoxin B1 causes guanine substitution in nucleic acids. *Nature* 267, 863–865. doi: 10.1038/267863a0

Martin, P. R., Couv,é, S., Zutterling, C., Albelazi, M. S., Groisman, R., Matkarimov, B. T., et al. (2017). The Human DNA glycosylases NEIL1 and NEIL3 Excise Psoralen-Induced DNA-DNA Cross-Links in a Four-Stranded DNA Structure. *Sci. Rep.* 7:17438. doi: 10.1038/s41598-017-17693-4

Mavragani, I. V., Nikitaki, Z., Kalospyros, S. A., and Georgakilas, A. G. (2019). Ionizing radiation and complex DNA damage: from prediction to detection challenges and biological significance. *Cancers* 11:1789. doi: 10.3390/cancers11111789

Mazouzi, A., Battistini, F., Moser, S. C., Ferreira da Silva, J., Wiedner, M., Owusu, M., et al. (2017). Repair of UV-induced DNA damage independent of nucleotide excision repair is masked by MUTYH. *Mol. Cell* 68, 797–807.e797. doi: 10.1016/j.molcel.2017.10.021

McKibbin, P. L., Fleming, A. M., Towheed, M. A., Van Houten, B., Burrows, C. J., and David, S. S. (2013). Repair of hydantoin lesions and their amine adducts in DNA by base and nucleotide excision repair. *J. Am. Chem. Soc.* 135, 13851–13861. doi: 10.1021/ja4059469

McNeill, D. R., Paramasivam, M., Baldwin, J., Huang, J., Vyjayanti, V. N., Seidman, M. M., et al. (2013). NEIL1 responds and binds to psoralen-induced DNA interstrand crosslinks. *J. Biol. Chem.* 288, 12426–12436. doi: 10.1074/jbc.M113.456087

Merecz, A., and Karwowski, B. T. (2016). DNA tandem lesion: 5',8-cyclo-2'-deoxyadenosine. The influence on human health. *Mol. Biol.* 50, 899–905. doi: 10.1134/S0026893316050125

Meulenbroek, E. M., Peron Cane, C., Jala, I., Iwai, S., Moolenaar, G. F., Goosen, N., et al. (2013). UV damage endonuclease employs a novel dual-dinucleotide flipping mechanism to recognize different DNA lesions. *Nucleic Acids Res.* 41, 1363–1371. doi: 10.1093/nar/gks1127

Moriya, M., Slade, N., Brdar, B., Medverec, Z., Tomic, K., Jelakovic, B., et al. (2011). TP53 Mutational signature for aristolochic acid: an environmental carcinogen. *Int. J. Cancer* 129, 1532–1536. doi: 10.1002/ijc.26077

Mu, D., Bessho, T., Nechev, L. V., Chen, D. J., Harris, T. M., Hearst, J. E., et al. (2000). DNA interstrand cross-links induce futile repair synthesis in mammalian cell extracts. *Mol. Cell. Biol.* 20, 2446–2454. doi: 10.1128/MCB.20.7.2446-2454.2000

Mullins, E. A., Rodriguez, A. A., Bradley, N. P., and Eichman, B. F. (2019). Emerging roles of DNA glycosylases and the base excision repair pathway. *Trends Biochem. Sci.* 44, 765–781. doi: 10.1016/j.tibs.2019.04.006

Mullins, E. A., Shi, R., and Eichman, B. F. (2017a). Toxicity and repair of DNA adducts produced by the natural product yatakemycin. *Nat. Chem. Biol.* 13, 1002–1008. doi: 10.1038/nchembio.2439

Mullins, E. A., Shi, R., Kotsch, L. A., and Eichman, B. F. (2015a). A new family of HEAT-like repeat proteins lacking a critical substrate recognition motif present in related DNA glycosylases. *PLoS ONE* 10:e0127733. doi: 10.1371/journal.pone.0127733

Mullins, E. A., Shi, R., Parsons, Z. D., Yuen, P. K., David, S. S., Igarashi, Y., et al. (2015b). The DNA glycosylase AlkD uses a non-base-flipping mechanism to excise bulky lesions. *Nature* 527, 254–258. doi: 10.1038/nature15728

Mullins, E. A., Warren, G. M., Bradley, N. P., and Eichman, B. F. (2017b). Structure of a DNA glycosylase that unhooks interstrand cross-links. *Proc. Natl. Acad. Sci. U. S. A.* 114, 4400–4405. doi: 10.1073/pnas.1703066114

Neurauter, C. G., Luna, L., and Bjoras, M. (2012). Release from quiescence stimulates the expression of human NEIL3 under the control of the Ras dependent ERK-MAP kinase pathway. *DNA Repair* 11, 401–409. doi: 10.1016/j.dnarep.2012.01.007

Ng, A. W. T., Poon, S. L., Huang, M. N., Lim, J. Q., Boot, A., Yu, W., et al. (2017). Aristolochic acids and their derivatives are widely implicated in liver cancers in Taiwan and throughout Asia. *Sci. Transl. Med.* 9:eaan6446. doi: 10.1126/scitranslmed.aan6446

Nickoloff, J. A., Sharma, N., and Taylor, L. (2020). Clustered DNA double-strand breaks: biological effects and relevance to cancer radiotherapy. *Genes* 11:99. doi: 10.3390/genes11010099

Noll, D. M., Mason, T. M., and Miller, P. S. (2006). Formation and repair of interstrand cross-links in DNA. *Chem. Rev.* 106, 277–301. doi: 10.1021/cr040478b

Osborne, M. R., Wilman, D. E., and Lawley, P. D. (1995). Alkylation of DNA by the nitrogen mustard bis(2-chloroethyl)methylamine. *Chem. Res. Toxicol.* 8, 316–320. doi: 10.1021/tx00044a018

Pena-Diaz, J., Bregenhorn, S., Ghodgaonkar, M., Follonier, C., Artola-Boran, M., Castor, D., et al. (2012). Noncanonical mismatch repair as a source of genomic instability in human cells. *Mol. Cell* 47, 669–680. doi: 10.1016/j.molcel.2012.07.006

Prahalad, A. K., Ross, J. A., Nelson, G. B., Roop, B. C., King, L. C., Nesnow, S., et al. (1997). Dibenzo[a,l]pyrene-induced DNA adduction, tumorigenicity, and Ki-ras oncogene mutations in strain A/J mouse lung. *Carcinogenesis* 18, 1955–1963. doi: 10.1093/carcin/18.10.1955

Raschle, M., Knipsheer, P., Enoiu, M., Angelov, T., Sun, J., Griffith, J. D., et al. (2008). Mechanism of replication-coupled DNA interstrand crosslink repair. *Cell* 134, 969–980. doi: 10.1016/j.cell.2008.08.030

Rojsitthisak, P., Jongaroonngamsang, N., Romero, R. M., and Haworth, I. S. (2011). HPLC-UV, MALDI-TOF-MS and ESI-MS/MS analysis of the mechlorethamine DNA crosslink at a cytosine-cytosine mismatch pair. *PLoS ONE* 6:e20745. doi: 10.1371/journal.pone.0020745

Rolseth, V., Krokeide, S. Z., Kunke, D., Neurauter, C. G., Suganthan, R., Sejersted, Y., et al. (2013). Loss of Neil3, the major DNA glycosylase activity for removal of hydantoins in single stranded DNA, reduces cellular proliferation and sensitizes cells to genotoxic stress. *Biochim. Biophys. Acta* 1833, 1157–1164. doi: 10.1016/j.bbamcr.2012.12.024

Rosenquist, T. A., and Grollman, A. P. (2016). Mutational signature of aristolochic acid: clue to the recognition of a global disease. *DNA Repair* 44, 205–211. doi: 10.1016/j.dnarep.2016.05.027

Sage, E., and Shikazono, N. (2017). Radiation-induced clustered DNA lesions: repair and mutagenesis. *Free Radic. Biol. Med.* 107, 125–135. doi: 10.1016/j.freeradbiomed.2016.12.008

Sancar, A., Lindsey-Boltz, L. A., Unsal-Kacmaz, K., and Linn, S. (2004). Molecular mechanisms of mammalian DNA repair and the DNA damage checkpoints. *Annu. Rev. Biochem.* 73, 39–85. doi: 10.1146/annurev.biochem.73.011303.073723

Sato, N., Takahashi, D., Chen, S. M., Tsuchiya, R., Mukoyama, T., Yamagata, S., et al. (2004). Acute nephrotoxicity of aristolochic acids in mice. *J. Pharm. Pharmacol.* 56, 221–229. doi: 10.1211/0022357023051

Scharer, O. D. (2005). DNA interstrand crosslinks: natural and drug-induced DNA adducts that induce unique cellular responses. *Chembiochem* 6, 27–32. doi: 10.1002/cbic.200400287

Schmeiser, H. H., Pool, B. L., and Wiessler, M. (1986). Identification and mutagenicity of metabolites of aristolochic acid formed by rat liver. *Carcinogenesis* 7, 59–63. doi: 10.1093/carcin/7.1.59

Scott, B. R., Pathak, M. A., and Mohn, G. R. (1976). Molecular and genetic basis of furocoumarin reactions. *Mutat. Res.* 39, 29–74. doi: 10.1016/0165-1110(76)90012-9

Seitz, H. K., and Meier, P. (2007). The role of acetaldehyde in upper digestive tract cancer in alcoholics. *Transl. Res.* 149, 293–297. doi: 10.1016/j.trsl.2006.12.002

Semlow, D. R., Zhang, J., Budzowska, M., Drohat, A. C., and Walter, J. C. (2016). Replication-dependent unhooking of DNA interstrand cross-links by the NEIL3 glycosylase. *Cell* 167, 498–511.e414. doi: 10.1016/j.cell.2016.09.008

Shafirovich, V., Kolbanovskiy, M., Kropachev, K., Liu, Z., Cai, Y., Terzidis, M. A., et al. (2019). Nucleotide excision repair and impact of site-specific 5',8-cyclopurine and bulky DNA lesions on the physical properties of nucleosomes. *Biochemistry* 58, 561–574. doi: 10.1021/acs.biochem.8b01066

Shan, H., Tian, W., Hong, Y., Xu, B., Wang, C., Yu, B., et al. (2020). Clinicopathologic characteristics and prognosis of upper tract urothelial carcinoma complicated with aristolochic acid nephropathy after radical nephroureterectomy. *BMC Complement. Med. Ther.* 20:166. doi: 10.1186/s12906-020-2861-5

Shi, R., Mullins, E. A., Shen, X. X., Lay, K. T., Yuen, P. K., David, S. S., et al. (2018). Selective base excision repair of DNA damage by the non-base-flipping DNA glycosylase AlkC. *EMBO J.* 37, 63–74. doi: 10.15252/embj.201797833

Shibutani, S., Dong, H., Suzuki, N., Ueda, S., Miller, F., and Grollman, A. P. (2007). Selective toxicity of aristolochic acids I and II. *Drug Metab. Dispos.* 35, 1217–1222. doi: 10.1124/dmd.107.014688

Sidorenko, V. S., Yeo, J. E., Bonala, R. R., Johnson, F., Scharer, O. D., and Grollman, A. P. (2012). Lack of recognition by global-genome nucleotide excision repair accounts for the high mutagenicity and persistence of aristolactam-DNA adducts. *Nucleic Acids Res.* 40, 2494–2505. doi: 10.1093/nar/gkr1095

Stivers, J. T. (2004). Site-specific DNA damage recognition by enzyme-induced base flipping. *Prog. Nucleic Acid Res. Mol. Biol.* 77, 37–65. doi: 10.1016/S0079-6603(04)77002-6

Straif, K., Baan, R., Grosse, Y., Secretan, B., El Ghissassi, F., Cogliano, V., et al. (2005). Carcinogenicity of polycyclic aromatic hydrocarbons. *Lancet Oncol.* 6, 931–932. doi: 10.1016/S1470-2045(05)70458-7

Sulc, M., Indra, R., Moserova, M., Schmeiser, H. H., Frei, E., Arlt, V. M., et al. (2016). The impact of individual cytochrome P450 enzymes on oxidative metabolism of benzo[a]pyrene in human livers. *Environ. Mol. Mutagen.* 57, 229–235. doi: 10.1002/em.22001

Sunters, A., Springer, C. J., Bagshawe, K. D., Souhami, R. L., and Hartley, J. A. (1992). The cytotoxicity, DNA crosslinking ability and DNA sequence selectivity of the aniline mustards melphalan, chlorambucil and 4-[bis(2-chloroethyl)amino] benzoic acid. *Biochem. Pharmacol.* 44, 59–64. doi: 10.1016/0006-2952(92)90038-K

Talhaoui, I., Couve, S., Gros, L., Ishchenko, A. A., Matkarimov, B., and Saparbaev, M. K. (2014). Aberrant repair initiated by mismatch-specific thymine-DNA glycosylases provides a mechanism for the mutational bias observed in CpG islands. *Nucleic Acids Res.* 42, 6300–6313. doi: 10.1093/nar/gku246

Tomasz, M. (1995). Mitomycin C: small, fast and deadly (but very selective). *Chem. Biol.* 2, 575–579. doi: 10.1016/1074-5521(95)90120-5

Vanherweghem, J. L., Depierreux, M., Tielemans, C., Abramowicz, D., Dratwa, M., Jadoul, M., et al. (1993). Rapidly progressive interstitial renal fibrosis in young women: association with slimming regimen including Chinese herbs. *Lancet* 341, 387–391. doi: 10.1016/0140-6736(93)92984-2

Vartanian, V., Minko, I. G., Chawanthayatham, S., Egner, P. A., Lin, Y. C., Earley, L. F., et al. (2017). NEIL1 protects against aflatoxin-induced hepatocellular carcinoma in mice. *Proc. Natl. Acad. Sci. U. S. A.* 114, 4207–4212. doi: 10.1073/pnas.1620932114

Vassylyev, D. G., Kashiwagi, T., Mikami, Y., Ariyoshi, M., Iwai, S., Ohtsuka, E., et al. (1995). Atomic model of a pyrimidine dimer excision repair enzyme complexed with a DNA substrate: structural basis for damaged DNA recognition. *Cell* 83, 773–782. doi: 10.1016/0092-8674(95)90190-6

Vesselinovitch, S. D., Mihailovich, N., Wogan, G. N., Lombard, L. S., and Rao, K. V. (1972). Aflatoxin B 1, a hepatocarcinogen in the infant mouse. *Cancer Res.* 32, 2289–2291.

Vrouwe, M. G., Pines, A., Overmeer, R. M., Hanada, K., and Mullenders, L. H. (2011). UV-induced photolesions elicit ATR-kinase-dependent signaling in non-cycling cells through nucleotide excision repair-dependent and -independent pathways. *J. Cell Sci.* 124, 435–446. doi: 10.1242/jcs.075325

Wang, J., Clauson, C. L., Robbins, P. D., Niedernhofer, L. J., and Wang, Y. (2012). The oxidative DNA lesions 8,5'-cyclopurines accumulate with aging in a tissue-specific manner. *Aging Cell* 11, 714–716. doi: 10.1111/j.1474-9726.2012.00828.x

Wang, S., Liu, K., Xiao, L., Yang, L., Li, H., Zhang, F., et al. (2016). Characterization of a novel DNA glycosylase from *S. sahachiroi* involved in the reduction and repair of azinomycin B induced DNA damage. *Nucleic Acids Res.* 44, 187–197. doi: 10.1093/nar/gkv949

Xing, G., Qi, X., Chen, M., Wu, Y., Yao, J., Gong, L., et al. (2012). Comparison of the mutagenicity of aristolochic acid I and aristolochic acid II in the gpt delta transgenic mouse kidney. *Mutat. Res.* 743, 52–58. doi: 10.1016/j.mrgentox.2011.12.021

Xu, H., Huang, W., He, Q. L., Zhao, Z. X., Zhang, F., Wang, R., et al. (2012). Self-resistance to an antitumor antibiotic: a DNA glycosylase triggers the base-excision repair system in yatakemycin biosynthesis. *Angew. Chem. Int. Ed. Engl.* 51, 10532–10536. doi: 10.1002/anie.201204109

Xu, M., Lai, Y., Jiang, Z., Terzidis, M. A., Masi, A., Chatgilialoglu, C., et al. (2014). A 5', 8-cyclo-2'-deoxypurine lesion induces trinucleotide repeat deletion via a unique lesion bypass by DNA polymerase beta. *Nucleic Acids Res.* 42, 13749–13763. doi: 10.1093/nar/gku1239

Yagi, H., Frank, H., Seidel, A., and Jerina, D. M. (2008). Revised assignment of absolute configuration of the cis- and trans-N6-deoxyadenosine adducts at C14 of (+/-)-11beta,12alpha-dihydroxy-13alpha,14alpha-epoxy-11,12,13,14-tetrahydrodibenz o[a,l]pyrene by stereoselective synthesis. *Chem. Res. Toxicol.* 21, 2379–2392. doi: 10.1021/tx800268f

Yajima, H., Takao, M., Yasuhira, S., Zhao, J. H., Ishii, C., Inoue, H., et al. (1995). A eukaryotic gene encoding an endonuclease that specifically repairs DNA damaged by ultraviolet light. *Embo J.* 14, 2393–2399. doi: 10.1002/j.1460-2075.1995.tb07234.x

Yang, Z., Nejad, M. I., Varela, J. G., Price, N. E., Wang, Y., and Gates, K. S. (2017). A role for the base excision repair enzyme NEIL3 in replication-dependent repair of interstrand DNA cross-links derived from psoralen and abasic sites. *DNA Repair* 52, 1–11. doi: 10.1016/j.dnarep.2017.02.011

You, C., Swanson, A. L., Dai, X., Yuan, B., Wang, J., and Wang, Y. (2013). Translesion synthesis of 8,5'-cyclopurine-2'-deoxynucleosides by DNA polymerases eta, iota, and zeta. *J. Biol. Chem.* 288, 28548–28556. doi: 10.1074/jbc.M113.480459

Zhang, J., Dewar, J. M., Budzowska, M., Motnenko, A., Cohn, M. A., and Walter, J. C. (2015). DNA interstrand cross-link repair requires replication-fork convergence. *Nat. Struct. Mol. Biol.* 22, 242–247. doi: 10.1038/nsmb.2956

Zhang, J., and Walter, J. C. (2014). Mechanism and regulation of incisions during DNA interstrand cross-link repair. *DNA Repair* 19, 135–142. doi: 10.1016/j.dnarep.2014.03.018

Zhang, S. M., Chen, K. M., Aliaga, C., Sun, Y. W., Lin, J. M., Sharma, A. K., et al. (2011). Identification and quantification of DNA adducts in the oral tissues of mice treated with the environmental carcinogen dibenzo[a,l]pyrene by HPLC-MS/MS. *Chem. Res. Toxicol.* 24, 1297–1303. doi: 10.1021/tx200188j

Conflict of Interest: The authors declare that the research was conducted in the absence of any commercial or financial relationships that could be construed as a potential conflict of interest.

frontiers in Cell and Developmental Biology

BRIEF RESEARCH REPORT
published: 11 March 2021
doi: 10.3389/fcell.2021.617160

The Interaction Efficiency of XPD-p44 With Bulky DNA Damages Depends on the Structure of the Damage

Irina Petruseva[1†], Natalia Naumenko[1†], Jochen Kuper[2], Rashid Anarbaev[1], Jeannette Kappenberger[2], Caroline Kisker[2] and Olga Lavrik[1]*

[1] Laboratory of Bioorganic Chemistry of Enzymes, Institute of Chemical Biology and Fundamental Medicine SB RAS, Novosibirsk, Russia, [2] Rudolf Virchow Center for Integrative and Translational Bioimaging, University of Wuerzburg, Wuerzburg, Germany

OPEN ACCESS

Edited by:
Nikita Kuznetsov, Institute of Chemical Biology and Fundamental Medicine (RAS), Russia

Reviewed by:
Nicholas Geacintov, New York University, United States
Jung-Hyun Min, Baylor University, United States

***Correspondence:**
Olga Lavrik
lavrik@niboch.nsc.ru

[†]These authors share first authorship

Specialty section:
This article was submitted to Cell Death and Survival, a section of the journal Frontiers in Cell and Developmental Biology

Received: 14 October 2020
Accepted: 22 February 2021
Published: 11 March 2021

Citation:
Petruseva I, Naumenko N, Kuper J, Anarbaev R, Kappenberger J, Kisker C and Lavrik O (2021) The Interaction Efficiency of XPD-p44 With Bulky DNA Damages Depends on the Structure of the Damage. Front. Cell Dev. Biol. 9:617160. doi: 10.3389/fcell.2021.617160

The successful elimination of bulky DNA damages via the nucleotide excision repair (NER) system is largely determined by the damage recognition step. This step consists of primary recognition and verification of the damage. The TFIIH helicase XPD plays a key role in the verification step during NER. To date, the mechanism of damage verification is not sufficiently understood and requires further detailed research. This study is a systematic investigation of the interaction of ctXPD *(Chaetomium thermophilum)* as well as ctXPD-ctp44 with model DNAs, which contain structurally different bulky lesions with previously estimated NER repair efficiencies. We have used ATPase and DNA binding studies to assess the interaction of ctXPD with damaged DNA. The result of the analysis of ctXPD-ctp44 binding to DNA containing fluorescent and photoactivatable lesions demonstrates the relationship between the affinity of XPD for DNAs containing bulky damages and the ability of the NER system to eliminate the damage. Photo-cross-linking of ctXPD with DNA probes containing repairable and unrepairable photoactivatable damages reveals differences in the DNA interaction efficiency in the presence and absence of ctp44. In general, the results obtained indicate the ability of ctXPD-ctp44 to interact with a damage and suggest a significant role for ctp44 subunit in the verification process.

Keywords: nucleotide excision repair, XPD helicase, DNA damage, protein-DNA interaction, bulky damages recognition, photo-cross-linking

INTRODUCTION

The nucleotide excision repair (NER) pathway removes a wide range of bulky DNA damages with high accuracy. Damages appear as a result of various chemical and physical impacts with most of them being adducts of nitrogenous bases, that cause significant distortions of the regular double-stranded DNA structure. Eukaryotic NER involves about 30 proteins, which sequentially form complexes of different compositions on DNA. To date, significant progress has been made toward our understanding of the multi-stage NER mechanism but an important step in the process, i.e., the damage verification step, is still poorly understood. In particular, the rates of removal of bulky

damages vary by orders of magnitude, but the reason for these variations are insufficiently clear so far, although the basic principles of their recognition and the criteria for repair susceptibility are formulated (Mu et al., 2018).

Damage recognition is a key stage of the NER process that largely determines the rate of DNA repair (Schärer, 2013). It can be described as a step-by-step process that includes the primary recognition of damage and its subsequent verification. The XPC-HR23B-Centrin2 complex, which performs primary damage recognition for bulky lesions, is sensitive to distortions of the regular double helix structure and interacts with regions with disturbed and destabilized hydrogen bonds with increased affinity. With respect to a less distorting lesion, i.e., cyclo-butane pyrimidine dimers (CPDs) caused by UV light, the XPC-HR23B-Centrin2 complex requires in addition the UV-DDB complex for damage detection (Compe and Egly, 2016).

According to the generally accepted model of "indirect recognition," XPC-HR23B does not directly recognize the damage (Min and Pavletich, 2007; Jain et al., 2013; Schärer, 2013), rather the damage topology and induced distortions of the regular DNA structure affect the efficiency of the formation of productive XPC-DNA complexes (Reeves et al., 2011; Mu et al., 2018). The initial recognition stage is followed by the "contact" stage, i.e., verification of the presence of a bulky modification. This is the catalytic stage that involves the ATP-dependent helicase subunits of the TFIIH factor, which display an increased affinity for the XPC-DNA complexes (Araújo et al., 2001). One of the key players in this verification stage is the 5′→3′ helicase XPD. It is assumed that XPD within TFIIH engages with DNA. Subunit p44 directly stimulates XPD's 5′ to 3′ helicase function. When XPD encounters the damage, its helicase activity is inhibited and XPD is immobilized on DNA, thus finally marking the damage (Naegeli et al., 1993; Coin et al., 2007; Oksenych and Coin, 2010; Buechner et al., 2014; Wirth et al., 2016).

XPD belongs to the SF2B family of helicases and consists of two RecA like helicase domains (HD1 and HD2), an Arch-domain, and a 4Fe4S-cluster domain. A significant understanding of the structural organization and mechanism of the action of human XPD was achieved through the analysis of its archaeal orthologs.

The structural and biochemical analysis of the complex of XPD from the *Thermoplasma acidophilum* protein (taXPD) with DNA in combination with functional mutagenesis made it possible to propose a model of DNA binding in which DNA binds parallel to the HD1 and HD2 domains. HD2 contains a high-affinity ssDNA binding site that might serve as an initial binder. The continuation of the strand toward HD1 leads the DNA to a pore-like feature, which has been suggested to assume the function of a lesion recognition sensor and is formed by HD1, the Arch domain, and the 4Fe4S domain. After passing the pore, DNA may further bind to a basic groove that is formed by HD1 and the 4Fe4S domain (Kuper et al., 2012; Pugh et al., 2012; Constantinescu-Aruxandei et al., 2016). Recently, this model was further validated by a cryo-EM structure, where human XPD assumed a similar orientation with a bound DNA fragment, thus indicating that DNA binding to XPD is highly conserved (Kokic et al., 2019). Based on these analyses, it has been proposed that the rate of DNA unwinding decreases when the damaged unit of the strand interacts with the sensor pocket, i.e., an "immobilization" of XPD takes place at this point. The effect of the damage-induced decrease in the helicase activity was first demonstrated for its yeast homolog Rad3 (Naegeli et al., 1993). Further comparative mutagenesis studies showed that the location of the sensory pocket in human XPD (hXPD) coincided with its location in taXPD (Mathieu et al., 2013). However, some data suggest that bulky damages do not affect the archaeal helicase activity (Rudolf et al., 2009). There may be several reasons for this discrepancy. Despite the similarity of the domain architecture, XPDs from archaea function as isolated monomers, whereas eukaryotic lesion verification requires the presence of the multiprotein complex TFIIH, with XPD being one of the subunits in this complex.

The XPD helicase from the eukaryotic fungus *Chaetomium thermophilum* was recently utilized as a model to study hsXPD. This helicase, like the human protein, functions as a part of the protein TFIIH complex. It has been shown that the activity of ctXPD is tightly regulated by the interaction with the TFIIH subunits ctp44 and MAT1 (Kuper et al., 2014; Peissert et al., 2020). Ctp44 directly activates the ATPase function of ctXPD; meanwhile the presence of ctp44 does not alter the ctXPD affinity for DNA significantly (Kuper et al., 2014).

In this work, we characterized the interaction of ctXPD and the ctXPD-ctp44 complex with model DNA substrates, which contained bulky damages in the translocated strand. The structures of the DNA model lesions are shown in **Supplementary Figure 1S** and the DNA sequences are listed in **Supplementary Table 1S**. Our data indicate that the high efficiency of the NER-catalyzed excision of the bulky damage from DNA are associated with a high affinity of ctXPD to the damaged translocated strand. The experiments were performed using DNA that contained photoactivatable bulky damages. Our data show that both ctXPD and ctp44 interacted with the damage in the translocated strand and formed covalent adducts with the damage, which indicates that also the latter TFIIH subunit might assume additional functions at the stage of damage verification.

MATERIALS AND METHODS

Materials

All synthetic oligonucleotides were synthesized in the Laboratory of Biomedical Chemistry (ICBFM SB RAS, Russia). Amidophosphites for nFlu- and nAnt-containing oligonucleotides were synthesized as described (Evdokimov et al., 2013). [γ-^{32}P]ATP (3000 Ci/mmol), [α-^{32}P]ATP (3000 Ci/mmol) was from the Laboratory of Biotechnology (ICBFM SB RAS, Russia). T4 polynucleotide kinase, Taq polymerase, and T4 DNA ligase were from Biosan (Novosibirsk). Fab(g)-dCTP and Fap-dCTP were synthesized as described (Dezhurov et al., 2005; Safronov et al., 1997). Recombinant rat DNA polymerase β (Pol β) was purified mainly according to Goldman and Baseman (1980) using plasmid kindly gifted by Dr. S. H. Wilson (National Institute of Environmental Health Sciences, NIH, NC, United States).

5′-End ^{32}P-Labeling and Purification of Oligodeoxyribonucleotides

γ-[^{32}P]-ATP (3000 Ci/mmol) was produced at ICBFM SB RAS. Oligodeoxyribonucleotides were 5′-[^{32}P] phosphorylated with T4 polynucleotide kinase and purified by polyacrylamide 7.0 M urea gel electrophoresis as described in Evdokimov et al. (2013) and Lukyanchikova et al. (2018) followed by electroelution and precipitation with 2% solution of $LiClO_4$ in acetone. The precipitated oligodeoxyribonucleotides were dissolved in 10 mM Tris-HCl (pH 8.0) and 1 mM EDTA. A NER-competent extract of CHO cells was isolated mainly according to (Reardon and Sancar, 2006).

Protein Expression and Purification

CtXPD was cloned in the pBADM11vector and ctp44 (1–285, in the following referred to as ctp44) was cloned in the pETM11vector (EMBL-Heidelberg). Both proteins were expressed as N-terminally His-tagged proteins in *Escherichia coli* CodonPlus (DE3)-RIL cells (Stratagene). For expression, ctXPD cells were grown in TB medium at 37°C until they reached an OD_{600} value of 1.2–1.4. Expression was initiated with the addition of 0.02% L-arabinose and performed at 15°C for 18 h.

The cells for expression of ctp44 (1–285) were grown as described for ctXPD and expression was started by adding 0.5 mM IPTG at an OD_{600} value of 1.1–1.2 and performed at 15°C for 18 h.

CtXPD and ctp44 were purified using the chromatographic procedures described previously (Kuper et al., 2014) with several modifications. For the ctXPD purification, all buffers were degassed with argon. Metal affinity chromatography (HisTrap HP column, GE Healthcare) was performed followed by size exclusion chromatography (Sephacryl 16/60, GE Healthcare) (20 mM HEPES pH 7.5, 150 mM NaCl) and an additional anion exchange chromatography (AEC) step in the case of ctXPD. AEC was performed using a MonoQ 5/50 GL column (GE Healthcare) with 20 mM HEPES, pH 7.5, 50 mM NaCl, and 1 mM TCEP as loading buffer. The same buffer containing 1 M NaCl was used for gradient elution (0–50%) using 40 column volumes. The final buffer after AEC contained 20 mM HEPES, pH 7.5, 250 mM NaCl, and 1 mM TCEP.

Fluorescence Anisotropy Assay

DNA binding was analyzed by fluorescence anisotropy measurements using the DNA substrates shown in **Supplementary Table 1SA**. The assay was carried out in a buffer containing 20 mM HEPES pH 7.5, 30 mM KCl, 5 mM $MgCl_2$, and 1 mM TCEP supplemented with 10 nM DNA at room temperature. CtXPD and ctp44 were used at a 1:1 stoichiometric ratio at concentrations of 5 to 1500 nM as indicated. Fluorescence was detected at an excitation wavelength of 540 nm and an emission wavelength of 590 nm with a Clariostar plate reader (BMG Labtech, Germany).

The estimations have been performed according to the formula:

$$P = 1000 * \frac{I|| - I\perp}{I|| \, I\perp},$$

where P is Polarization (mP), I|| is the intensity of the detected light when the excitation and emission polarization is parallel and I⊥ is the intensity of detected light when the excitation and emission polarization is perpendicular.

In vitro ATPase Assay

CtXPD ATPase activity was measured with the *in vitro* ATPase assay, in which ATP consumption is coupled to the oxidation of NADH via pyruvate kinase and lactate dehydrogenase activities (Kuper et al., 2014). The activity profiles were measured at 37°C in 100 μL solution containing 1.5 U pyruvate kinase, 1.9 U lactate dehydrogenase, 2 mM phosphoenolpyruvate, and 0.15 mM NADH, 10 mM KCl, 1 mM $MgCl_2$, 1 mM TCEP, and 20 mM Tris-HCl (pH 8.0). We used different damage containing DNA substrates with a 5′-overhang and a Cy3 label at the 3'-end of the translocated strand and a Dabcyl modification at the 5′-end of the opposite strand (**Supplementary Table 1SB**). DNA was added at a final concentration of 250 nM.

The assay was carried out at saturating concentrations of ATP (2 mM). CtXPD and ctp44 were used at a 1:1 stoichiometric ratio with final concentrations of 250 nM. The reaction was initiated by the addition of ATP. For the ctXPD activation by ctp44 increasing concentrations of ctp44 (4 to 1000 nM) were added to 250 nM ctXPD in the presence of 1 μM ssDNA substrate. The activity profiles were measured at 340 nm using a Clariostar plate reader (BMG Labtech). The initial rates were recorded and the ATP consumption was determined using the molar extinction coefficient of NADH. The measurements were carried out in triplicates with at least two different protein batches. The MARS software package (BMG Labtech) was used for the analysis of the data.

Photo-Cross-Linking of ctXPD and ctp44 to Photoactivatable DNA Probes

Photo-cross-linking was performed in the reaction mixture (20–30 μL) that contained a photoreactive 120–250 nM 5′-[^{32}P]-labeled DNA probe (**Supplementary Table 1SC**), 200–500 nM ctXPD, and 100–200 nM ctp44 in the buffer for modification (20 mÌ HEPES, pH 7.5, 50 mÌ KCl, 5 mM $MgCl_2$, and 1 mM TCEP). The experiments were carried out both in the presence and in the absence of 2.5 mM ATP. The samples were exposed to UV irradiation (312 nm) in a BIO-LINK®BLX (Vilber Lourmat, France) for 10 min at 1 J/cm^2*min. The mixtures were supplemented with 4x Laemmli loading buffer, heated to 90°C for 10 min and the products were analyzed by SDS-PAGE (Laemmli, 1970). The gels were dried and subjected to autoradiography for quantification using a Typhoon FLA 9500 (GE Healthcare) and the Quantity One software.

RESULTS

Affinity of ctXPD-ctp44 for Damaged DNAs

The quantification of the interaction of ctXPD-ctp44 with model ssDNA was obtained by fluorescence anisotropy measurements

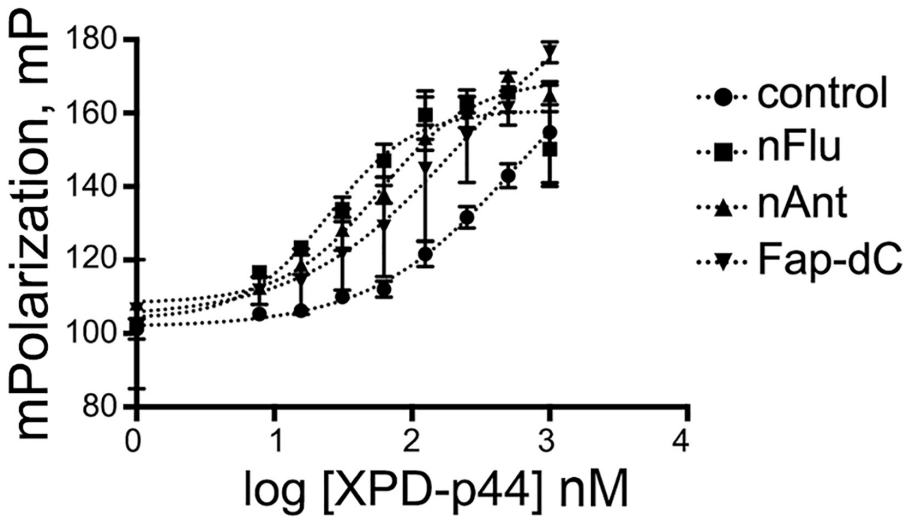

FIGURE 1 | Affinity of ctXPD-ctp44 to ssDNAs containing bulky damages. Fluorescence polarization measurements were used to determine the affinity of various DNA substrates to ctXPD at increasing concentrations. Data were plotted and fitted in GraphPad and presented here as normalized values with error bars representing the SD from at least three repeats.

(**Figure 1**). The introduction of bulky damages into DNA increased the affinity of ctXPD-ctp44 for modified DNA as compared to control DNA containing no damage. The EC_{50} values are presented in **Table 1**. CtXPD-ctp44 exhibits an EC_{50} of 500 for undamaged DNA. A 2.5 fold affinity increase was observed for ss-Fap-dC-DNA with a EC_{50} of 200 nM. Ss-nAnt-DNA led to an almost 8-fold higher affinity with a EC_{50} of 63 nM. Noteworthy, the tightest binding with a 166-fold higher affinity (3 nM) was observed with ssDNA containing the nFlu damage.

In a separate series of experiments, we compared the binding affinity of ctXPD-ctp44 for ss-Fab(g)-dC- and ss-Fap-dC-DNA. The EC_{50} values obtained are presented in **Supplementary Table 2S**; the titration curves and the experiment description are presented in **Supplementary Figure 3S**.

ATPase Activity of ctXPD-ctp44 Relative to Damaged DNA Substrates

To investigate the influence of the modified DNA on ctXPD activity, we performed ATPase studies with the modified DNA as substrate. To ensure that under the investigated conditions ctXPD and ctp44 form a productive complex, we titrated increasing amounts of ctp44 onto 250 nM ctXPD in the presence of 1 μM DNA. The resulting activation curve yielded an EC_{50} of 82 nM and full ctXPD activation at equimolar conditions indicating full complex formation (**Figure 2**). We therefore performed the subsequent experiments using equimolar concentrations of ctp44 and ctXPD. Interestingly, the ATPase activity of ctXPD-ctp44 was only slightly increased in the presence of damaged DNA compared to undamaged DNA (**Table 1**). This indicates that ATPase activity is not negatively affected by DNA damage. The minor change in activation depending on the used substrate could indicate that XPDs ATPase might be further stimulated by the modified DNA which would be in line with the enhanced binding of the substrate.

Affinity Modification of ctXPD and ctp44 Proteins Using Photoactivatable DNA Probes

To select reaction conditions for the photo-cross-linking experiments, we first examined ctXPD binding to modified and unmodified ss- and ds-DNAs by EMSA (**Supplementary Figure 2S**). Based on the data obtained, the range of ctXPD concentrations was selected for affinity modification experiments.

We compared the cross-linking efficiency of ctXPD to DNA probes containing the unrepairable and repairable photoactivatable damages, i.e., Fap-dC and Fab(g)-dC, respectively (**Figure 3A**). The photo-cross-linking of ctXPD to ss- and ds-DNA demonstrated that the products of ctXPD-DNA photo-cross-linking were formed three times more efficiently when the ssDNA probes were used. A higher yield

TABLE 1 | Characteristics of the interaction of ctXPD and ctp44 with DNAs containing bulky lesions, eliminated by NER with different efficiencies.

DNA damage	EC_{50} (ctXPD-ctp44-ssDNA), nM	ATPase activity, relative units	NER catalyzed specific excision, 137 bp dsDNA relative units
umDNA	500 ± 3	1	0
Fap-dC	200 ± 2	1.1 ± 0.2	0 *
nFlu	3 ± 1	1.3 ± 0.1	1.0**
nAnt	63 ± 1	1.4 ± 0.3	1.2**

Maltseva et al. (2007).
***Evdokimov et al. (2013).*

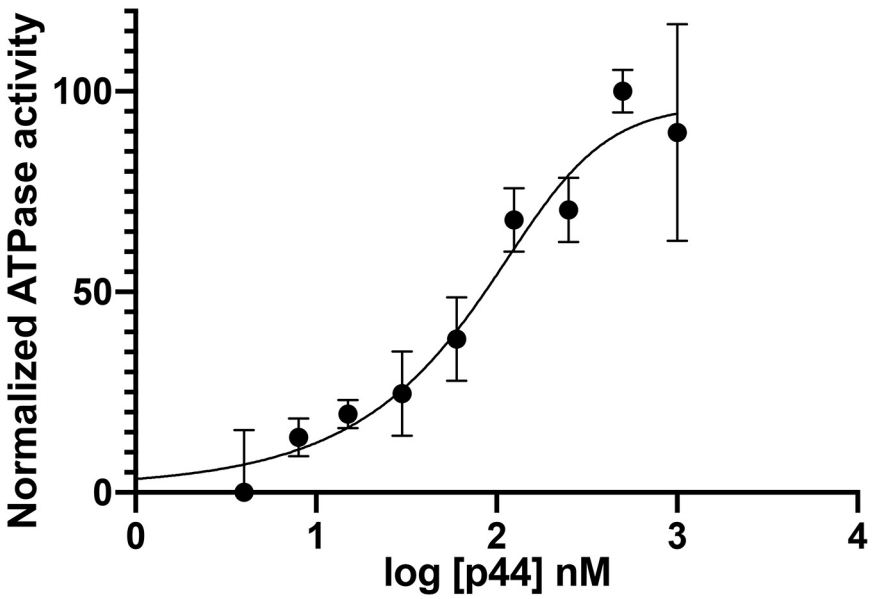

FIGURE 2 | Ctp44 activation of ctXPD. Increasing amounts of ctp44 were titrated onto ctXPD resulting in ctXPD activation. The data were fitted with the GraphPad Prism software resulting in an EC_{50} of 82 nM for ctp44. Error bars represent the SD from at least three repeats. Optimal conditions were then used to perform further experiments.

of cross-linked ctXPD when using a single-stranded DNA probe is a rather expected result, since the higher affinity of ctXPD for single-stranded DNA is accompanied by a longer residence time of the protein on the ssDNA probe. Next, we analyzed the cross-linking of the proteins with fs-Fap-dC- and fs-Fab(g)-dC-DNA probes with a 5′-overhang (16 nt) and ds fragment (38 bp) containing the photoactivatable damages (fs designates "fork structure"). The [^{32}P]-label was attached to the 5′-end of the ss 5′-overhang.

Under the conditions used, ctXPD formed a major covalent adduct with the fs probes, which displayed the same electrophoretic mobility both in the presence and in the absence of ATP and ctp44 (**Figure 3B**). In all the experiments DNA bearing the repairable Fab(g)-dC were more effective as cross-linking probes. The level of ctXPD cross-linking was influenced by the presence of ATP and ctp44.

The minimal levels of ctXPD cross-linking with fs DNA probes in the absence of both ATP and ctp44 (**Figure 3B**, lanes 2, 8; 3C) presumably results from ctXPD interaction with photoactivatable damages located in the double stranded area of the DNAs. Addition of ATP to ctXPD increased the level of the ctXPD adducts formed with fs-Fab(g)-DNA by a factor of 2.1 but did not enhance ctXPD adduction with fs-Fap-dC-DNA (**Figure 3B**, lanes 3, 9; 3C). Addition of ATP to ctXPD-ctp44 promoted the cross-linking of ctXPD to fs-Fap-dC-DNA (by a factor of 2.6) and, to a lesser extent, to fs-Fab(g)-dC (by a factor of 1.8) (**Figure 3B**, lanes 5, 6, 11, 12; 3C).

Our analysis also showed, that the ctp44 protein formed adducts with both photoactivatable fs-DNAs with high efficiency in the absence of ctXPD and ATP in the reaction mixtures. The presence of ctXPD decreased the photo-cross-linking of ctp44 in the absence of ATP. However, in the presence of ATP and ctXPD, the efficiency of the cross-linking of ctp44 increased by a factor of about 2.0 compared to that in the mixture without ATP (**Figure 3B**, lanes 5–6, 11–12).

DISCUSSION

The NER system exhibits an extremely broad substrate specificity, wherein the efficiency of the damage removal varies by orders of magnitude. The study of the relationship between the structure of the damages and the rate of its elimination is important both for the prevention of accelerated accumulation of mutations in the cells and the development of methods to increase the effectiveness of chemotherapy or complex cancer therapy by the accumulation of induced DNA damages (Kiwerska and Szyfter, 2019).

In this work, we studied the efficiency of protein-DNA interaction utilizing a series of different bulky DNA damages and the ctXPD-ctp44 protein complex from *C. thermophilum* (Kuper et al., 2014). XPD is thought to be the main sensor for the verification of bulky damages. However, the important role in the damage verification process is distributed between the subunits of core TFIIH including p44, which directly interacts with XPD and modulates its activity (Coin et al., 1998; Kuper et al., 2014).

A comparison of the binding of ctXPD-ctp44 to ssDNAs that contained the Fap-dC, nAnt, and nFlu damages to unmodified DNA (umDNA) showed that the affinity of ctXPD-ctp44 for these DNAs (**Table 1**) increased as follows: umDNA < Fap-dC-DNA < nAnt-DNA < < nFlu-DNA. These results correlate well with the reported removal of these damages within the NER cascade. Recently it has been shown that the efficiency of

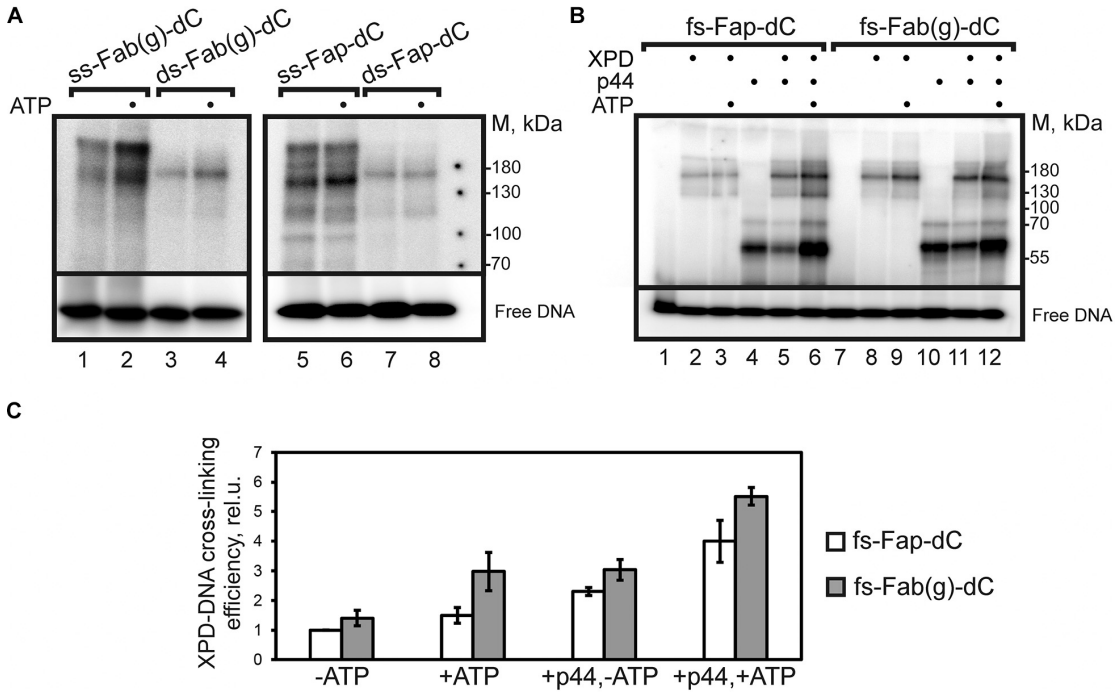

FIGURE 3 | Photo-cross-linking of DNA probes to ctXPD and ctp44. **(A)** *Autoradiogram of a SDS-PAGE gel after ctXPD cross-linking product separation. ss- or ds-Fab(g)- dC-, ss- or ds-Fap-dC-DNA were used as DNA probes. Reaction mixtures containing 200 nM ctXPD, 100 nM ss-Fab(g)-dC (lanes 1, 2), ds-Fab(g)-dC (lanes 3, 4), ss-Fap-dC (lanes 5, 6) or ds-Fap-dC (lanes 7, 8), 2.5 mM ATP (lanes 2, 4, 6, 8), and buffer components were analyzed by electrophoresis in a 10% polyacrylamide gel.* **(B)** *Autoradiogram of a SDS-PAGE gel after ctXPD /ctp44 cross-linking products separation. fs-Fap-dC- or fs-Fab(g)-dC-DNA were used as DNA probes. Reaction mixtures contained 120 nM fs-Fap-dC- (lanes 1–6) or fs-Fab(g)-dC-DNA probe (lanes 7–12), 200 nM ctXPD (lanes 2, 3, 5, 6, 8, 9, 11, 12), 200 nM ctp44 (lanes 4–6, 10–12) and buffer components. The experiments were carried out both in the presence (lanes 3, 6, 9, 12) and absence of 2.5 mM ATP. The samples were analyzed by electrophoresis in a 10% polyacrylamide gel.* **(C)** The dependence of photo-cross-linking efficiency of ctXPD on the type of DNA probe and the presence/absence of ctp44 and ATP in the reaction mixture. The efficiency of ctXPD cross-linking to fs-Fap-dC-DNA in the absence of ctp44 and ATP was taken as 1. Error bars represent the SD from triplicate measurements.

the removal of Fab(g)-dC from DNA was about half of that observed for the nFlu and nAnt damages (Lukyanchikova et al., 2016), and the Fap-dC damage was almost unrepaired (excision efficiency increased in a row: umDNA≈Fap-dC-DNA < < nFlu-DNA < nAnt-DNA (Evdokimov et al., 2011, 2018). The NER system removes the bulky nFlu and nAnt damages from DNA with almost the same high efficiency. However, the data obtained in this work have shown that the affinity of ctXPD-ctp44 for ss-nFlu-DNA (EC_{50}≈3 nM) is much higher than for ss-nAnt-DNA (EC_{50}≈60 nM). According to the results of computer simulations, the presence of the Flu moiety in dsDNA can lead to several changes in the DNA structure, which reduce the likelihood of a productive XPC-DNA complex formation (Evdokimov et al., 2018).

Thus, it can be assumed that good substrate properties of nFlu-containing DNA in the NER process are determined by the high affinity of ctXPD-ctp44 for DNA containing this damage. Despite the fact that the ATPase activity of ctXPD-ctp44 was increased in the presence of damaged DNA compared to undamaged DNA, the observed differences are small. In the case of ssDNA induced ATPase activities the small changes that we observed could hint at different ATPase activation, but the major information regarding specificity should be inferred from the binding data.

Affinity cross-linking of ctXPD and ctp44 with DNA probes of different structures containing the photoactivatable damages revealed different interaction capabilities of these proteins with Fap-dC-DNA and Fab(g)-dC-DNA. The results on the photo-cross-linking of ctXPD to ss- and ds-Fap-dC-DNA correlate well with the data on the higher affinity of ctXPD to ssDNA (Kuper et al., 2014). The increased affinity permits a longer residence time of XPD on the ssDNA probe, which promotes the formation of covalent adducts. In contrast to unrepaired Fap-dC, the Fab(g)-dC damage is removed from DNA quite effectively (Evdokimov et al., 2011). The simultaneous presence of ATP and ctp44, which promotes the activity of ctXPD by about an order of magnitude (Kuper et al., 2014), levels the difference between the yields of ctXPD adduction. The increase of the proteins photo-cross-linking level may result from specific structural changes in the ctXPD-ctp44 complex.

Our results confirm the important role of p44 in the verification of damaged DNA by XPD. These results indicate that p44 interacts with damaged DNAs. This assumption is partially supported by the recently published data (Barnett et al., 2019) on the interaction of the ð44–p62 heterodimer with DNA and will be the subject of further research.

DATA AVAILABILITY STATEMENT

The original contributions presented in the study are included in the article/**Supplementary Material**, further inquiries can be directed to the corresponding author.

AUTHOR CONTRIBUTIONS

IP, JoK, JeK, NN, and RA conducted the experiments. IP, JoK, and RA designed the model DNA structures. IP, JoK, and CK conceived the project. IP, NN, JoK, CK, and OL analyzed the data and wrote the manuscript. All authors contributed to the article and approved the submitted version.

FUNDING

This study was supported by the Russian Foundation for Basic Research (Project No. 19-04-00018) and Russian State Funded Project (No. 0245-2021-0009). The synthetic oligonucleotides were purchased with funds of the Russian Science Foundation (Project No. 19-74-10056).

SUPPLEMENTARY MATERIAL

The Supplementary Material for this article can be found online at: https://www.frontiersin.org/articles/10.3389/fcell.2021.617160/full#supplementary-material

REFERENCES

Araújo, S. J., Nigg, E. A., and Wood, R. D. (2001). Strong functional interactions of TFIIH with XPC and XPG in human DNA nucleotide excision repair, without a preassembled repairosome. *Mol. Cell. Biol.* 21, 2281–2291. doi: 10.1128/mcb.21.7.2281-2291.2001

Barnett, J., Kuper, J., Koelmel, W., Kisker, C., Kad, N., and Version, D. (2019). The TFIIH subunits p44/p62 act as a damage sensor during nucleotide excision repair. *bioRxiv* [preprint] doi: 10.1101/643874 bioRxiv: 643874,

Buechner, C., Heil, K., Michels, G., Carell, T., Kisker, C., and Tessmer, I. (2014). Strand-specific recognition of DNA damages by XPD provides insights into nucleotide excision repair substrate versatility. *J. Biol. Chem.* 289, 3613–3624. doi: 10.1074/jbc.M113.523001

Coin, F., Marinoni, J. C., Rodolfo, C., Fribourg, S., Pedrini, A. M., and Egly, J. M. (1998). Mutations in the XPD helicase gene result in XP and TTD phenotypes, preventing interaction between XPD and the p44 subunit of TFIIH. *Nat. Genet.* 20, 184–188. doi: 10.1038/2491

Coin, F., Oksenych, V., and Egly, J. M. (2007). Distinct roles for the XPB/p52 and XPD/p44 subcomplexes of TFIIH in damaged DNA opening during nucleotide excision repair. *Mol. Cell* 26, 245–256. doi: 10.1016/j.molcel.2007.03.009

Compe, E., and Egly, J. M. (2016). Nucleotide excision repair and transcriptional regulation: TFIIH and beyond. *Annu. Rev. Biochem.* 85, 265–290. doi: 10.1146/annurev-biochem-060815-014857

Constantinescu-Aruxandei, D., Petrovic-Stojanovska, B., Penedo, J. C., White, M. F., and Naismith, J. H. (2016). Mechanism of DNA loading by the DNA repair helicase XPD. *Nucleic Acids Res.* 44, 2806–2815. doi: 10.1093/nar/gkw102

Dezhurov, S. V., Khodyreva, S. N., Plekhanova, E. S., and Lavrik, O. I. (2005). A new highly efficient photoreactive analogue of dCTP. Synthesis, characterization, and application in photoaffinity modification of DNA binding proteins. *Bioconjug. Chem.* 16, 215–222. doi: 10.1021/bc0497867

Evdokimov, A., Petruseva, I., Tsidulko, A., Koroleva, L., Serpokrylova, I., Silnikov, V., et al. (2013). New synthetic substrates of mammalian nucleotide excision repair system. *Nucleic Acids Res.* 41:e123. doi: 10.1093/nar/gkt301

Evdokimov, A. N., Petruseva, I. O., Pestryakov, P. E., and Lavrik, O. I. (2011). Photoactivated DNA analogs of substrates of the nucleotide excision repair system and their interaction with proteins of NER-competent HeLa cell extract. *Biochemistry* 76, 188–200. doi: 10.1134/S0006297909050034

Evdokimov, A. N., Tsidulko, A. Y., Popov, A. V., Vorobiev, Y. N., Lomzov, A. A., Koroleva, L. S., et al. (2018). Structural basis for the recognition and processing of DNA containing bulky lesions by the mammalian nucleotide excision repair system. *DNA Repair (Amst.)* 61, 86–98. doi: 10.1016/j.dnarep.2017.10.010

Goldman, W. E., and Baseman, J. B. (1980). Selective isolation and culture of a proliferating epithelial cell population from the hamster trachea. *In Vitro* 16, 313–319.

Jain, V., Hilton, B., Lin, B., Patnaik, S., Liang, F., Darian, E., et al. (2013). Unusual sequence effects on nucleotide excision repair of arylamine lesions: DNA bending/distortion as a primary recognition factor. *Nucleic Acids Res.* 41, 869–880. doi: 10.1093/nar/gks1077

Kiwerska, K., and Szyfter, K. (2019). DNA repair in cancer initiation, progression, and therapy—a double-edged sword. *J. Appl. Genet.* 60, 329–334. doi: 10.1007/s13353-019-00516-9

Kokic, G., Chernev, A., Tegunov, D., Dienemann, C., Urlaub, H., and Cramer, P. (2019). Structural basis of TFIIH activation for nucleotide excision repair. *Nat. Commun.* 10:2885. doi: 10.1038/s41467-019-10745-5

Kuper, J., Braun, C., Elias, A., Michels, G., Sauer, F., Schmitt, D. R., et al. (2014). In TFIIH, XPD helicase is exclusively devoted to DNA repair. *PLoS Biol.* 12:e1001954. doi: 10.1371/journal.pbio.1001954

Kuper, J., Wolski, S. C., Michels, G., and Kisker, C. (2012). Functional and structural studies of the nucleotide excision repair helicase XPD suggest a polarity for DNA translocation. *EMBO J.* 31, 494–502. doi: 10.1038/emboj.2011.374

Laemmli, U. K. (1970). Cleavage of structural proteins during the assembly of the head of bacteriophage T4. *Nature* 227, 680–685. doi: 10.1038/227680a0

Lukyanchikova, N. V., Petruseva, I. O., Evdokimov, A. N., Koroleva, L. S., and Lavrik, O. I. (2018). DNA bearing bulky fluorescent and photoreactive damage in both strands as substrates of the nucleotide excision repair system. *Mol. Biol.* 52, 237–246. doi: 10.1134/S0026893318020061

Lukyanchikova, N. V., Petruseva, I. O., Evdokimov, A. N., Silnikov, V. N., and Lavrik, O. I. (2016). DNA with damage in both strands as affinity probes and nucleotide excision repair substrates. *Biochemistry (Mosc.)* 81, 386–400. doi: 10.1134/S0006297916030093

Maltseva, E. A., Rechkunova, N. I., Gillet, L. C., Petruseva, I. O., Schärer, O. D., and Lavrik, O. I. (2007). Crosslinking of the NER damage recognition proteins XPC-HR23B, XPA and RPA to photoreactive probes that mimic DNA damages. *Biochim. Biophys. Acta Gen. Subj.* 1770, 781–789. doi: 10.1016/j.bbagen.2007.01.007

Mathieu, N., Kaczmarek, N., Rüthemann, P., Luch, A., and Naegeli, H. (2013). DNA quality control by a lesion sensor pocket of the xeroderma pigmentosum group D helicase subunit of TFIIH. *Curr. Biol.* 23, 204–212. doi: 10.1016/j.cub.2012.12.032

Min, J., and Pavletich, N. P. (2007). Recognition of DNA damage by the Rad4 nucleotide excision repair protein. *Nature* 449, 570–575. doi: 10.1038/nature06155

Mu, H., Zhang, Y., Geacintov, N. E., and Broyde, S. (2018). Lesion sensing during initial binding by yeast XPC/Rad4: toward predicting resistance to nucleotide excision repair. *Chem. Res. Toxicol.* 31, 1260–1268. doi: 10.1021/acs.chemrestox.8b00231

Naegeli, H., Modrich, P., and Friedberg, E. C. (1993). The DNA helicase activities of Rad3 protein of *Saccharomyces cerevisiae* and helicase II of *Escherichia coli* are differentially inhibited by covalent and noncovalent DNA modifications. *J. Biol. Chem.* 268, 10386–10392.

Oksenych, V., and Coin, F. (2010). The long unwinding road: XPB and XPD helicases in damaged DNA opening. *Cell Cycle* 9, 90–96. doi: 10.4161/cc.9.1.10267

Peissert, S., Sauer, F., Grabarczyk, D. B., Braun, C., Sander, G., Poterszman, A., et al. (2020). In TFIIH the Arch domain of XPD is mechanistically essential

for transcription and DNA repair. *Nat. Commun.* 11:1667. doi: 10.1038/s41467-020-15241-9

Pugh, R. A., Wu, C. G., and Spies, M. (2012). Regulation of translocation polarity by helicase domain 1 in SF2B helicases. *EMBO J.* 31, 503–514. doi: 10.1038/emboj.2011.412

Reardon, J. T., and Sancar, A. (2006). Purification and characterization of *Escherichia coli* and human nucleotide excision repair enzyme systems. *Methods Enzymol.* 408, 189–213. doi: 10.1016/S0076-6879(06)08012-8

Reeves, D. A., Mu, H., Kropachev, K., Cai, Y., Ding, S., Kolbanovskiy, A., et al. (2011). Resistance of bulky DNA lesions to nucleotide excision repair can result from extensive aromatic lesion-base stacking interactions. *Nucleic Acids Res.* 39, 8752–8764. doi: 10.1093/nar/gkr537

Rudolf, J., Rouillon, C., Schwarz-Linek, U., and White, M. F. (2009). The helicase XPD unwinds bubble structures and is not stalled by DNA lesions removed by the nucleotide excision repair pathway. *Nucleic Acids Res.* 38, 931–941. doi: 10.1093/nar/gkp1058

Safronov, I. V., Shcherbik, N. V., Khodyreva, S. N., Vlasov, V. A., Dobrikov, M. I., Shishkin, G. V., et al. (1997). New photoreactive N(4)-substituted dCTP analogues:synthesis, photochemical characteristics, and substrate properties in HIV-1 reverse transcriptase catalyzed DNA synthesis. *Russ. J. Bioorg. Chem.* 23, 531–539.

Schärer, O. D. (2013). Nucleotide excision repair in Eukaryotes. *Cold Spring Harb. Perspåct. Biol.* 5:a012609. doi: 10.1101/cshperspect.a012609

Wirth, N., Gross, J., Roth, H., Buechner, C., Kisker, C., and Tessmer, I. (2016). Conservation and divergence in nucleotide excision repair lesion recognition. *J. Biol. Chem.* 291, 18932–18946. doi: 10.1074/jbc.M116.739425

Conflict of Interest: The authors declare that the research was conducted in the absence of any commercial or financial relationships that could be construed as a potential conflict of interest.

The handling editor declared a shared affiliation and a past co-authorship with one of the authors OL at the time of review.

frontiers in Cell and Developmental Biology

ORIGINAL RESEARCH
published: 26 March 2021
doi: 10.3389/fcell.2021.617161

The Enigma of Substrate Recognition and Catalytic Efficiency of APE1-Like Enzymes

Anastasiia T. Davletgildeeva[1,2], Alexander A. Ishchenko[3], Murat Saparbaev[3], Olga S. Fedorova[1] and Nikita A. Kuznetsov[1]**

[1] Institute of Chemical Biology and Fundamental Medicine, Siberian Branch of the Russian Academy of Sciences, Novosibirsk, Russia, [2] Department of Natural Sciences, Novosibirsk State University, Novosibirsk, Russia, [3] Group "Mechanisms of DNA Repair and Carcinogenesis", Equipe Labellisée LIGUE 2016, CNRS UMR 9019, Université Paris-Saclay, Villejuif, France

OPEN ACCESS

Edited by:
Alexey Moskalev,
Komi Scientific Center (RAS), Russia

Reviewed by:
Todd Hsu,
National Taiwan Ocean University, Taiwan
Daniela Marasco,
University of Naples Federico II, Italy
Somsubhra Nath,
Saroj Gupta Cancer Centre and Research Institute, India

***Correspondence:**
Olga S. Fedorova
fedorova@niboch.nsc.ru
Nikita A. Kuznetsov
nikita.kuznetsov@niboch.nsc.ru

Specialty section:
This article was submitted to Cell Death and Survival, a section of the journal Frontiers in Cell and Developmental Biology

Received: 14 October 2020
Accepted: 22 February 2021
Published: 26 March 2021

Citation:
Davletgildeeva AT, Ishchenko AA, Saparbaev M, Fedorova OS and Kuznetsov NA (2021) The Enigma of Substrate Recognition and Catalytic Efficiency of APE1-Like Enzymes. Front. Cell Dev. Biol. 9:617161. doi: 10.3389/fcell.2021.617161

Despite significant achievements in the elucidation of the nature of protein-DNA contacts that control the specificity of nucleotide incision repair (NIR) by apurinic/apyrimidinic (AP) endonucleases, the question on how a given nucleotide is accommodated by the active site of the enzyme remains unanswered. Therefore, the main purpose of our study was to compare kinetics of conformational changes of three homologous APE1-like endonucleases (insect *Drosophila melanogaster* Rrp1, amphibian *Xenopus laevis* xAPE1, and fish *Danio rerio* zAPE1) during their interaction with various damaged DNA substrates, i.e., DNA containing an F-site (an uncleavable by DNA-glycosylases analog of an AP-site), 1,N^6-ethenoadenosine (εA), 5,6-dihydrouridine (DHU), uridine (U), or the α-anomer of adenosine (αA). Pre-steady-state analysis of fluorescence time courses obtained for the interaction of the APE1-like enzymes with DNA substrates containing various lesions allowed us to outline a model of substrate recognition by this class of enzymes. It was found that the differences in rates of DNA substrates' binding do not lead to significant differences in the cleavage efficiency of DNA containing a damaged base. The results suggest that the formation of enzyme–substrate complexes is not the key factor that limits enzyme turnover; the mechanisms of damage recognition and cleavage efficacy are related to fine conformational tuning inside the active site.

Keywords: DNA repair, apurinic/apyrimidinic endonuclease, abasic site, target nucleotide recognition, pre-steady state kinetics

INTRODUCTION

The maintenance of DNA integrity is ensured by repair enzymes that recognize, remove, and restore the structure of damaged DNA regions (Friedberg et al., 2006). One way to remove nonbulky damaged bases is the base excision repair (BER) pathway, which is initiated by numerous damage-specific DNA glycosylases (Gros et al., 2002; Fromme et al., 2004). The removal of damaged bases from DNA in the first step of BER is coupled to the second step (catalyzed by an AP endonuclease), intended to remove apurinic/apyrimidinic (AP) sites and 3′-blocking sugar phosphate groups by the hydrolysis of the phosphodiester bond on the 5′ side of the lesion (Demple and Sung, 2005; Li and Wilson, 2014). As the result of AP endonuclease action, the formation of a single-nucleotide gap with 3′-OH and 5′-phosphate end groups takes place, which is necessary for DNA template-directed

incorporation of an intact nucleotide by DNA polymerase and DNA ligation of the strand break. It is also known that AP endonucleases can recognize not only AP-sites but also various damaged nucleotides such as 5,6-dihydrouridine (DHU), α-anomers of nucleotides, 1,N^6-ethenoadenosine (εA), uracil (U), and other modified residues (Gros et al., 2004). In addition, AP endonucleases have 3′-5′-exonuclease (Chou and Cheng, 2003; Wong et al., 2003; Kuznetsova et al., 2018a) and endoribonuclease (Barzilay and Hickson, 1995; Berquist et al., 2008; Barnes et al., 2009; Kuznetsova et al., 2020) activities.

A major human AP endonuclease, human APE1 (hAPE1) is one of the most studied AP endonucleases. Indeed, multiple structural data (Gorman et al., 1997; Mol et al., 2000a,b; Beernink et al., 2001; Manvilla et al., 2013; Tsutakawa et al., 2013; Freudenthal et al., 2015), kinetic studies (Timofeyeva et al., 2009; Miroshnikova et al., 2016a,b; Alekseeva et al., 2019a), and a mutational analysis (Erzberger and Wilson, 1999; Alekseeva et al., 2020) have made it possible to identify the key stages of the interaction of hAPE1 with a damaged DNA harboring an AP site or with damaged (Timofeyeva et al., 2011; Timofeyeva and Fedorova, 2016; Kuznetsova et al., 2018b; Bulygin et al., 2020) or undamaged (Kuznetsova et al., 2018a, 2020) nucleotides.

Of note, at present, no three-dimensional structure of an hAPE1 complex with a DNA substrate containing a damaged base is available. Nevertheless, crystal structures of hAPE1 bound to a DNA substrate containing an F-site (an uncleavable-by-DNA-glycosylases analog of an AP-site) allow to outline amino acid network contacts that sculpt the DNA conformation in the DNA-binding site as well as to reveal the amino acid residues participating in the catalytic reaction (**Figure 1**; Mol et al., 2000a,b; Tsutakawa et al., 2013; Freudenthal et al., 2015). The DNA-binding site consists of Arg73, Ala74, Lys78, Tyr128, Arg156, Arg181, Asn222, Asn226, and Thr268, which preferentially form hydrogen bonds and electrostatic contacts with DNA. These contacts induce F-site eversion from the double helix into the active site of the enzyme. Two amino acid residues, Arg177 and Met270, are inserted into the DNA helix after the F-site eversion and stabilize the extrahelical state of the damage. The damaged nucleotide is placed in the pocket formed by Asn174, Asn229, Ala230, Phe266, and Trp280. Another set of amino acid residues (Asp70, Glu96, Tyr171, Asp210, Asn212, Asp308, and His309) is responsible for the coordination of the cofactor Mg^{2+} and scissile phosphate group of the damaged nucleotide. The role of Mg^{2+} ions in the DNA binding and catalytic mechanism is still debated (Gorman et al., 1997; Masuda et al., 1998; Erzberger and Wilson, 1999; Mol et al., 2000b; Beernink et al., 2001; Oezguen et al., 2007; Lipton et al., 2008; Manvilla et al., 2013; He et al., 2014; Miroshnikova et al., 2016b; Alekseeva et al., 2020).

It was demonstrated earlier (Kanazhevskaya et al., 2012) that the kinetic mechanism of the interaction between hAPE1 and an abasic DNA involves a two-step equilibrium process. Thermodynamic analysis of DNA-binding stages (Miroshnikova et al., 2016a) revealed that the formation of the primary enzyme–substrate complex includes desolvation of polar groups at the DNA–protein interface and the removal of highly ordered molecules of "crystalline water" from DNA grooves. It was assumed that at this stage, bonds are formed between the DNA and amino acid residues Arg73, Ala74, Lys78, Asn222, Asn226, Asn229, and Trp280 of the DNA-binding site. Additionally, intercalating amino acid residues Arg177 and Met270 get inserted into the DNA grooves. The second stage includes a specific rearrangement of the initial complex, e.g., flipping of the F-site into the enzyme active site and stabilization of this state by residues Arg177 and Met270 via their full insertion into the major and minor DNA grooves, respectively. Later, it was reported (Kuznetsova et al., 2018b) that after the insertion of such damaged nucleotides as εA, α-anomer of adenine (αA), DHU, and F-site into the enzyme active site, no damage-specific contacts in the binding pocket are formed between amino acid residues and the damaged DNA base. Therefore, it has been suggested that the substrate specificity of hAPE1 is governed by the ability of a damaged nucleotide to flip out from the DNA duplex in response to an enzyme-induced DNA distortion (Kuznetsova et al., 2018b). Recently, it was demonstrated by molecular dynamics simulations (Bulygin et al., 2020) that the protein loop containing Asn229/Thr233/Glu236 undergoes significant damage-dependent reorganization, indicating an important role of this loop in the recognition of a damaged nucleotide. Indeed, destabilization of the α-helix containing Thr233 and Glu236 via a loss of the interaction between these residues greatly increases the plasticity of the damaged nucleotide-binding pocket and increases the ability of the hAPE1 active site to accommodate structurally different damaged nucleotides.

Despite significant achievements in the elucidation of the mechanisms of target nucleotide recognition by AP endonucleases and in the understanding of the nature of protein–DNA contacts that control the specificity of these enzymes vis-à-vis regular and various damaged nucleotides, the question of how a particular nucleotide is recognized by the active site of the enzyme remains unanswered. Therefore, the main purpose of our study was to compare the kinetics of conformational changes of three homologous APE1-like endonucleases (insect *Drosophila melanogaster* Rrp1, amphibian *Xenopus laevis* xAPE1, and fish *Danio rerio* zAPE1) during their interaction with various damaged DNA substrates. As model damaged substrates, we used DNA duplexes containing an F-site, εA, αA, DHU, or uridine. It is noteworthy that the catalytic domains of Rrp1, xAPE1, and zAPE1 all have high amino acid sequence identity with the catalytic domain of hAPE1, thereby allowing to compare newly obtained data with the mechanism of substrate specificity control assumed earlier for hAPE1 (Kuznetsova et al., 2018b; Bulygin et al., 2020).

MATERIALS AND METHODS

Buffers

Buffers were prepared from reagent-grade chemicals using double-distilled water. BER buffer consisting of 50 mM Tris-HCl (pH 7.5), 50 mM KCl, 5 mM $MgCl_2$, 1 mM dithiothreitol, 1 mM EDTA, and 7% of glycerol (v/v). Nucleotide incision repair (NIR) buffer was composed of 50 mM Tris-HCl (pH 7.5 at 25°C),

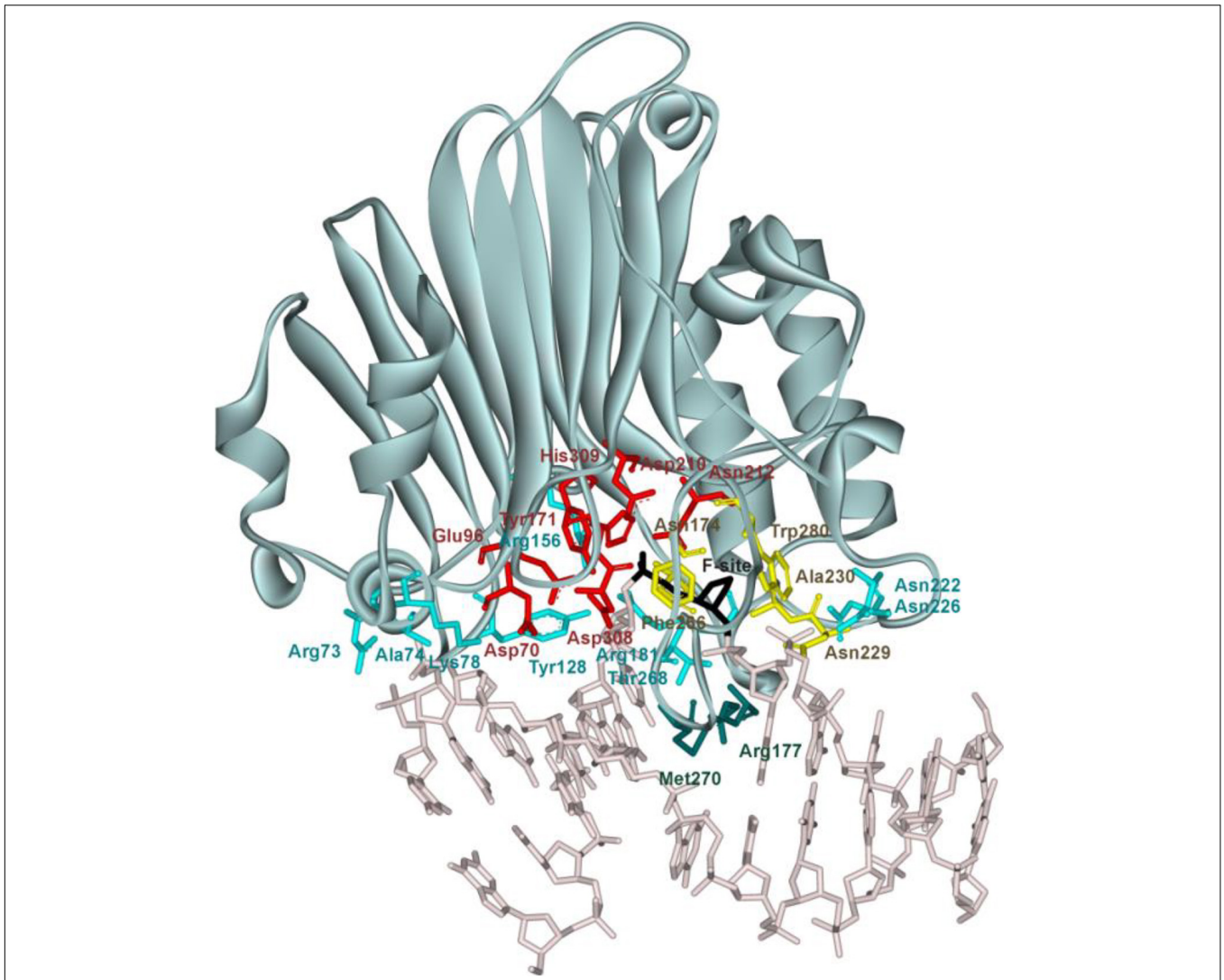

FIGURE 1 | The structure of hAPE1 complexed with DNA containing an F-site (Protein Data Bank ID 1DE8). Catalytic amino acid residues Asp70, Glu96, Tyr171, Asp210, Asn212, Asp308, and His309 (red); amino acid residues of the DNA-binding site Arg73, Ala74, Lys78, Tyr128, Arg156, Arg181, Asn222, Asn226, and Thr268 (blue); intercalating amino acids Met270 and Arg177 (green); and residues Asn174, Asn229, Ala230, Phe266, and Trp280 forming a damaged base-binding pocket (yellow) are highlighted, as is the F-site (black).

50 mM KCl, 1 mM $MgCl_2$, 1 mM dithiothreitol, 1 mM EDTA, and 7% of glycerol (v/v). All the experiments were carried out at 25°C.

Oligonucleotides

The synthesis of the oligonucleotides (**Table 1**) was carried out on an ASM-800 DNA/RNA synthesizer (Biosset, Russia) by means of standard commercial phosphoramidites and CPG solid supports from the Glen Research (United States). The oligonucleotides were deprotected according to the manufacturer's protocols and were purified by high-performance liquid chromatography. Oligonucleotide homogeneity was checked by denaturing 20% polyacrylamide gel electrophoresis (PAGE). Concentrations of oligonucleotides were calculated from their absorbance at 260 nm (A_{260}). Oligonucleotide duplexes were prepared by annealing oligonucleotide strands at a 1:1 molar ratio.

Enzyme Purification

hAPE1 was expressed and purified in its native form without tags or other modifications as described previously (Daviet et al., 2007). The enzymes Rrp1 (*D. melanogaster*), xAPE1 (*X. laevis*), and zAPE1 (*D. rerio*) were isolated from *Escherichia coli* Rosetta2 (DE3) cells transformed with plasmid pET28c carrying an N-terminal His_6 and a relevant gene. To purify these enzymes expressed as recombinant proteins, 1 L of culture [in Luria–Bertani (LB) broth] of *E. coli* cells carrying the required encoding vector construct was grown with 50 μg/ml of kanamycin at 37°C until A_{600} reached 0.6–0.7; the expression of the enzymes was induced overnight with 0.3 mM isopropyl β-D-1-thiogalactopyranoside. The cells were harvested by centrifugation (5,000 × *g*, 10 min) and then resuspended in a buffer (20 mM HEPES-KOH pH 7.8, 40 mM NaCl, and 0.1% of NP40) followed

TABLE 1 | DNA substrates used in this study.

Shorthand	Sequence
F-substrate	5′-GCTCAFGTACAGAGCTG-3′ 3′-CGAGTGCATGTCTCGAC-5′
F-aPu-substrate	5′-GCTCAF(aPu)TACAGAGCTG-3′ 3′-CGAGTGTATGTCTCGAC-5′
FRET-X-substrate X = F-site, DHU or U	5′-FAM-GCTCAXGTACAGAGCTG-3′ 3′-CGAGTGCATGTCTCGAC-BHQ1-5′
FRET-Y-substrate Y = αA, εA	5′-FAM-GCTCAYGTACAGAGCTG-3′ 3′-CGAGTTCATGTCTCGAC-BHQ1-5′
Nondamaged DNA	5′-FAM-GCTCACGTACAGAGCTG-3′ 3′-CGAGTGCATGTCTCGAC-BHQ1-5′

by cell lysis by means of the French press. All the purification procedures were carried out at 4°C. Each homogenate was centrifuged at 40,000 × *g* for 40 min, NaCl concentration in the supernatant was brought to 250 mM (400 mM in the case of Rrp1), and the supernatant was passed through a column packed with 30 ml of Q-Sepharose Fast Flow (Cytiva, GE Healthcare Life Sciences, United States) pre-equilibrated in the same buffer. The flow-through fractions containing an enzyme were pooled, supplemented with 20 mM imidazole, and loaded on a 1-ml HiTrap-Chelating^{TM} column (Cytiva GE Healthcare Life Sciences, United States). Bound proteins were eluted with a linear 20 → 500 mM gradient of imidazole. The protein concentration was measured by the Bradford method; the stock solution was stored at −20°C.

PAGE Experiments

6-Carboxyfluorescein (FAM)-5′-labeled oligonucleotides were subjected to experiments on separation of cleavage products by PAGE. AP endonuclease assays with all DNA substrates were carried out at 25°C in 10 μl reactions containing BER reaction buffer (in the case of the F-site-containing DNA) or NIR reaction buffer (in case of αA-, εA-, DHU-, or U-containing DNA). The substrate concentration chosen for comparing the activity of the enzymes was 1.0 μM, and the concentration of each enzyme was 1.0 μM as well. The reaction was initiated by the addition of the enzyme. Aliquots of the reaction mixture were withdrawn, immediately quenched with 10 μl of a gel-loading dye containing 7 M urea and 25 mM EDTA, followed by heating at 95°C for 3 min, and were loaded on a 20% (w/v) polyacrylamide/7 M urea gel. PAGE (gel concentration, 20%) was performed under denaturing conditions (7 M urea) at 55°C and a voltage of 200–300 V. The gels were visualized using an E-Box CX.5 TS gel-documenting system (Vilber Lourman, France), and the bands were quantified by scanning densitometry in the Gel-Pro Analyzer software, v.4.0 (Media Cybernetics, United States).

Fluorescence Stopped-Flow Experiments

Pre-steady-state kinetics were studied by the stopped-flow technique using an SX20 stopped-flow spectrometer (Applied Photophysics Ltd., Leatherhead, United Kingdom). The fluorescence of FAM was excited at 494 nm, and the Förster resonance energy transfer (FRET) signal was monitored at wavelengths ≥530 nm by means of an OG-530 filter (Schott, Mainz, Germany). Trp was excited at 290 nm, and its fluorescence emission was monitored at wavelengths ≥320 nm using a WG-320 filter (Schott, Mainz, Germany). 2-Aminopurine (aPu) fluorescence was excited at 310 nm, and its emission was monitored at wavelengths ≥370 nm with an LG-370 Corion filter. The dead time of the instrument is 1.4 ms. Typically, each trace shown is an average of three or more individual experiments. Experimental error was less than 5%. Experiments with α-A-, ε-A-, DHU-, and U-containing DNA substrates were conducted in NIR buffer. Experiments with the F-site-containing DNA (F-substrate) and a nondamaged DNA duplex were performed in BER buffer. The solutions containing the enzyme and substrate were loaded into two separate syringes of the stopped-flow instrument and were incubated for an additional 3 min at 25°C prior to mixing. The reported concentrations of reactants are those in the reaction chamber after mixing.

Analysis of the Kinetic Data

The sets of kinetic curves obtained at different concentrations of the F-substrate during interactions with an enzyme (zAPE1, xAPE1, or Rrp1) were fitted to the following exponential equation (Eq. 1) with amplitudes A_1 and A_2 and first-order rate constants k_{obs1} and k_{obs2}, respectively, in the Origin software (Originlab Corp.):

$$y = A_1 \exp\left(-k_{obs1}t\right) + A_2 \exp\left(-k_{obs2}t\right) + \text{offset} \quad (1)$$

For the linear fits of the change in observed rate constants (k_{obs}), Eqs 2 and 3 were used:

$$k_{obs1} = k_1[\text{E}] + k_{-1} \quad (2)$$

where k_1 and k_{-1} are rate constants for the forward and reverse reaction, and [E] is the enzyme concentration;

$$k_{obs2} = k_{cat}[\text{E}] \quad (3)$$

where k_{cat} is the rate constant of the irreversible catalytic step of the enzymatic reaction, and [E] denotes the concentration of the enzyme.

The sets of kinetic curves obtained at different concentrations of the non-specific DNA during interactions with an enzyme (hAPE1, zAPE1, xAPE1, or Rrp1) were analyzed in the DynaFit software (BioKin, Pullman, WA) (Kuzmic, 1996) as described elsewhere (Kuznetsov et al., 2012a,b, 2014; Kladova et al., 2018b).

The kinetic curves represent changes in the FRET signal in the course of the reaction owing to sequential formation and subsequent transformation of the DNA–enzyme complex and its conformers. The stopped-flow fluorescence traces were directly fitted to fluorescence intensity (F) at any reaction time point (t) as the sum of the intensities of background fluorescence and fluorescence of each intermediate complex formed by the enzyme with DNA:

$$F = F_b + \sum_{i=0}^{n} f_i \times [\text{ES}]_i \quad (4)$$

where F_b is the background fluorescence or the equipment-related photomultiplier parameter ("noise"), and f_i is the

molar response coefficient of the i-th intermediate ES_i ($i = 0$ corresponds to the free protein and $i > 0$ to the enzyme–DNA complexes).

Concentrations of each species in the mechanisms are described by a set of differential equations according to a kinetic scheme (see section "Results"). The software performs numerical integration of a system of ordinary differential equations with subsequent nonlinear least-squares regression analysis. In the fits, the values of all relevant rate constants for the forward and reverse reactions are optimized, as are the specific molar "response factors" for all intermediate complexes.

RESULTS AND DISCUSSION

The Rationale

Previously, it has been proposed that the key factor responsible for DNA substrate specificity of hAPE1 is the ability of a damaged nucleotide to get everted from a double helix and to get inserted into the damaged nucleotide-binding pocket (Kuznetsova et al., 2018b; Bulygin et al., 2020). To verify whether this mechanism is a common feature of other APE1-like enzymes, three AP endonucleases from different species were chosen on the basis of high identity of their C-terminal catalytic domain with hAPE1 (**Figure 2**).

Notably, the N-terminal domains of APE1-like enzymes substantially vary in size (**Figure 2**). Among the tested enzymes, the largest domain (consisting of 417 amino acid residues) was found in Rrp1. Moreover, the numbers of basic residues in N-terminal domains are also considerably higher in Rrp1 than in the other tested enzymes: 20 arginines and 74 lysines in Rrp1, two arginines and nine lysines in hAPE1, five arginines and nine lysines in zAPE1, and one arginine and nine lysines in xAPE1. Analysis of N-truncated variants of hAPE1 revealed that this lysine-rich region might act by stabilizing the non-specific association with nucleic acids through electrostatic interactions (Fantini et al., 2010; Poletto et al., 2013). A loss of the N-terminal domain influences the stability of both enzyme–substrate and enzyme–product complexes (Izumi and Mitra, 1998; Chattopadhyay et al., 2006) but does not affect the rates of initial complex formation or catalysis (Timofeyeva et al., 2009) in the case of abasic DNA cleavage. By contrast, this domain affects both the rate of formation and the stability of the initial complex in the cases of NIR and $3' \rightarrow 5'$ exonuclease activities (Gros et al., 2004; Daviet et al., 2007; Timofeyeva et al., 2009). Multiple studies also underscore that the N-terminal domain may functionally interact with different proteins involved in DNA repair (Kladova et al., 2018a; Moor et al., 2020; Popov et al., 2020), transcription (Georgiadis et al., 2008; Kelley et al., 2011; Bazlekowa-Karaban et al., 2019), and RNA metabolism (Vascotto et al., 2009; Tell et al., 2010; Poletto et al., 2013). Summarizing the literature data, we can conclude that the N-terminal domain may be required for the preliminary low-affinity binding process in search of the proper lesion in DNA or a cleavage site in RNA and protein–protein interactions. Therefore, in the present study, we compare properties of APE1-like enzymes taking into account differences in the C-terminal catalytic domain, which is responsible for the specific DNA binding.

An alignment of sequences of the C-terminal catalytic domain of the four AP endonucleases revealed that almost all DNA-binding amino acid residues are identical among all these enzymes, except Arg181 (amino acid numbering corresponding to hAPE1 sequence), which is replaced by Asn in Rrp1, and Asn229 is replaced by Thr in xAPE1. Intercalating and catalytic residues are identical too, with a single substitution of Asp70, which coordinates a Mg^{2+} ion, by Ala in the case of Rrp1. It is worth noting that two amino acid residues of the damaged base-binding pocket (Asn229 and Ala230) are replaced by Thr and Pro in xAPE1.

To examine the kinetics of interactions of the AP endonucleases under study with different DNA substrates, we employed the stopped-flow fluorescence method. This method is applied to the research on pre-steady-state kinetics of different enzymatic systems using various types of fluorescence (Fischer et al., 2004; Toseland and Webb, 2013; Kuznetsova et al., 2018b; Kladova et al., 2019). It is important to choose an appropriate system with which to follow the conformational changes of the DNA substrate or the enzyme. This is because the fluorescence signal change resulting from the interactions between the enzyme and substrate can be rather complex and likely will differ from one type of fluorescence to another. Accordingly, it is always useful to study the same reaction by following the changes in several types of fluorescence. Previously, a significant amount of data has been obtained on the kinetics of hAPE1 interacting with different substrates by means of the fluorescence of Trp residues in the enzyme (Timofeyeva et al., 2009, 2011; Kuznetsova et al., 2018b; Alekseeva et al., 2019b) and also DNA substrates that contain aPu as a fluorescent nucleotide analog (Kanazhevskaya et al., 2012; Kuznetsova et al., 2014, 2018a) or an emitter/quencher pair of dyes to measure FRET (Miroshnikova et al., 2016b; Alekseeva et al., 2019a, 2020). It was tempting to use the data known for hAPE1 as a reference of all APE1-like enzymes tested in the present study. Nonetheless, we were unable to detect significant changes in own Trp fluorescence intensity of xAPE1, zAPE1, and Rrp1 in the reactions with the F-substrate (**Figure 3A**). Indeed, the amplitude of changes in the fluorescence intensity of Trp residues during the interactions of the AP endonucleases under study with the F-substrate was extremely small or absent at all when compared with hAPE1. Of note, hAPE1 contains seven Trp residues (Trp67, Trp75, Trp83, Trp119, Trp188, Trp267, and Trp280) that are absolutely conserved in all the tested AP endonucleases (**Figure 2**), except for the absence of Trp83 in Rrp1. It has been suggested previously that observed changes in Trp fluorescence of hAPE1 most likely reflect conformational changes near the Trp280 residue, which is situated in the active site of hAPE1 (Miroshnikova et al., 2016a,b; Kuznetsova et al., 2018b). Even though Trp residues are conserved in all enzymes, and Trp280 is believed to make a major contribution to alterations in the intensity of the protein's own fluorescence during the enzymatic reaction with a DNA substrate, the weak changes in the signal most likely indicate a difference in the conformational mobility of the parts of protein molecules that contain Trp residues. It can also be assumed

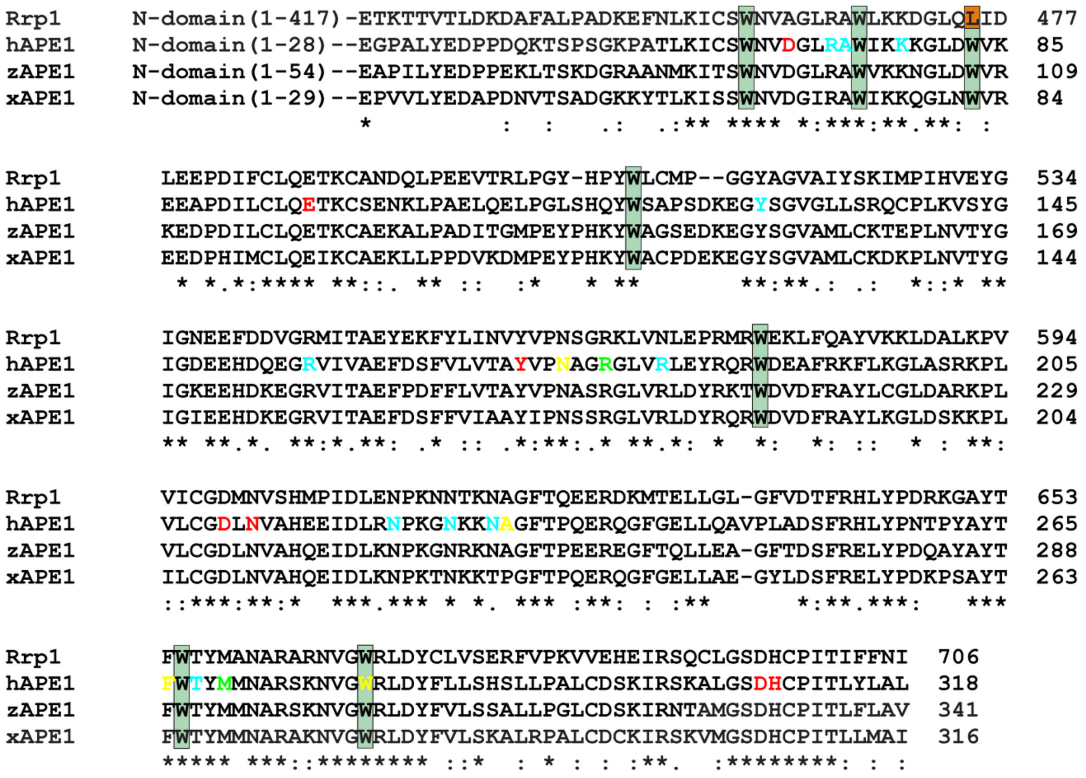

FIGURE 2 | An alignment of sequences of hAPE1, xAPE1, zAPE1, and Rrp1. Catalytic amino acid residues Asp70, Glu96, Tyr171, Asp210, Asn212, Asp308, and His309 (red); amino acid residues of the DNA-binding site Arg73, Ala74, Lys78, Tyr128, Arg156, Arg181, Asn222, Asn226, Asn229, and Thr268 (blue); intercalating amino acid residues Met270 and Arg177 (light green); and residues Asn174, Asn229, Ala230, Phe266, and Trp280 forming the damaged base-binding pocket (yellow) are highlighted. Conserved Trp residues are indicated by dark green boxes. Asterisks indicate identical residues, colons denote conserved residues, and dots are residues with at least some physicochemical properties conserved.

that the difference in Trp fluorescence intensity behavior is dependent on the features of non-specific DNA binding by the N-terminal domain of enzymes. The role of the N-terminal domain in damage-specific recognition and formation of the catalytic complex remains elusive.

The pilot experiments with the F-aPu-substrate containing aPu next to the F-site (**Figure 3B**) revealed an increase in the fluorescence intensity of aPu within the initial 1-s period. The increase in the fluorescence intensity of aPu during DNA substrate cleavage was reported earlier for hAPE1 (Kanazhevskaya et al., 2012). Therefore, the obtained traces for xAPE1 and zAPE1 are consistent with fast cleavage of the F-site by these enzymes. In the case of Rrp1 from *D. melanogaster*, the increase phase was slower and finalized only during 300 s, implying that Rrp1 possesses a much weaker AP endonuclease activity.

To follow the conformational changes in DNA by detecting changes in the FRET signal, we used the FRET-F-duplex with FAM attached to the 5′ end of the damaged strand and a BHQ1 quencher residue attached to the 5′ end of the complementary strand. It should be noted that FRET detection has been previously utilized for the analysis of DNA cleavage activity of hAPE1 (Alekseeva et al., 2019a, 2020; Kladova et al., 2020). As shown in **Figure 3C**, FRET detection revealed a significant increase in the signal that corresponds to catalytic cleavage of the F-site for all the tested AP endonucleases. As in the previous case, F-site cleavage by Rrp1 was notably slower than that by other AP endonucleases.

Overall, the comparative analysis of kinetic traces, which reflect (i) potential conformational variation of the enzyme molecule after catalytic activity, (ii) environment changes for a single aPu residue in the substrate, and (iii) the distance between terminal fluorophores in the duplex substrate, revealed a difference among the enzymes from the insect *D. melanogaster*, amphibian *X. laevis*, and fish *D. rerio* and well-studied human APE1. Despite high identity of the functionally characterized amino acid residues among all the enzymes, it was found that Rrp1 has a considerably lower AP endonuclease activity. There are several possible reasons for the slower Rrp1 activity in comparison with xAPE1 and zAPE1. First of all, analysis of the amino acid residues in the DNA-binding site revealed that Arg181 (conserved among the tested APE1-like enzymes, **Figure 2**) is substituted by Asn in the case of Rrp1. On the other hand, Rrp1 features a substitution of the conserved Asp70 residue by Ala. Finally, the difference in Trp fluorescence intensity changes—between the proteins (hAPE1 and the tested enzymes) with identical spatially located Trp residues in the catalytic domain—suggests that the N-terminal domain may

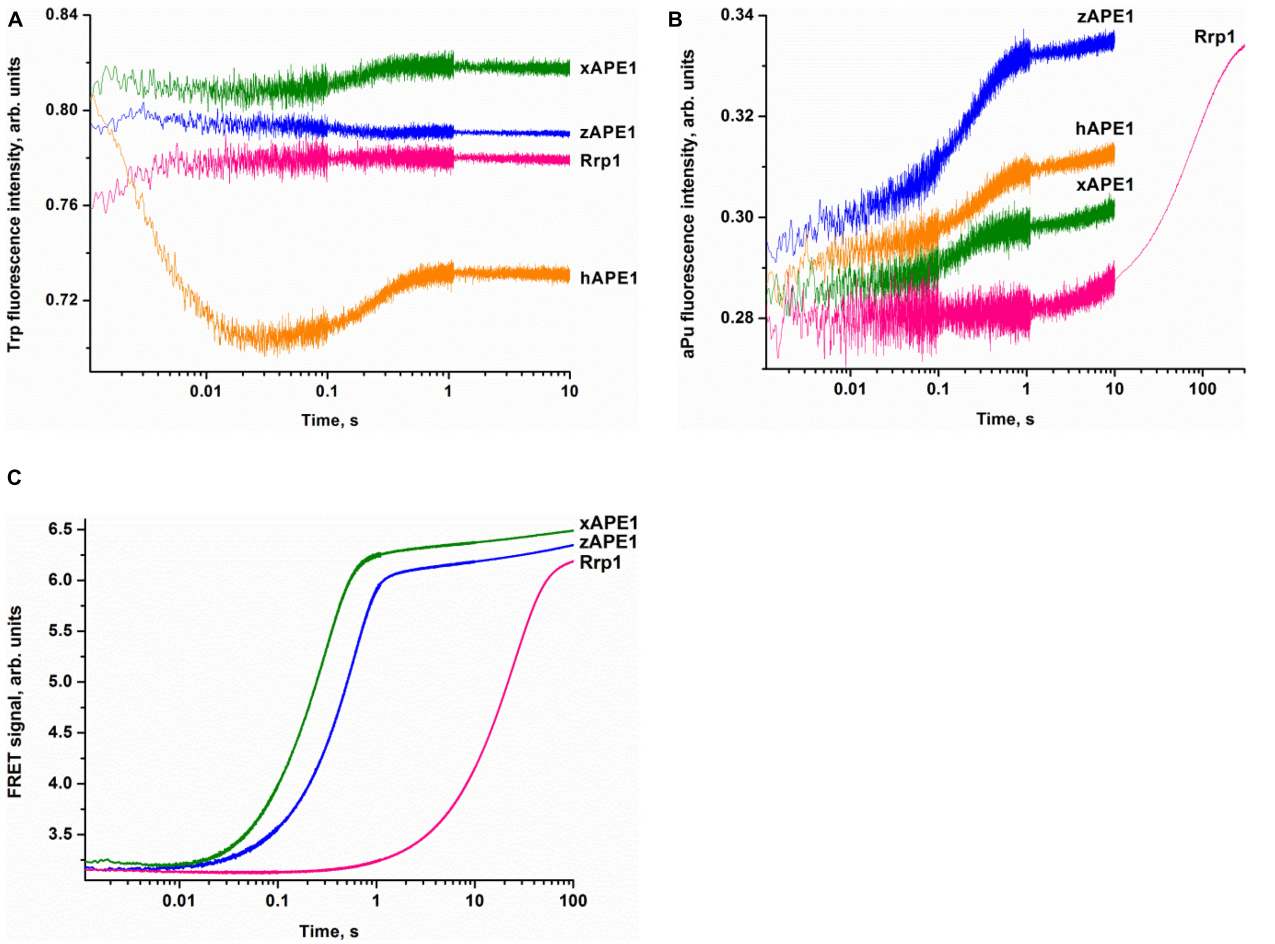

FIGURE 3 | Interactions of AP endonucleases with DNA containing an F-site, as monitored by changes in the fluorescence intensity of Trp **(A)**, aPu **(B)**, or FRET signal **(C)**. (DNA substrate) = (enzyme) = 1.0 μM.

affect conformational mobility of the full-length enzyme. Indeed, even though the role of the N-terminal domain is unclear, it should be noted that the slowest enzyme Rrp1 has the largest N-terminal domain among the tested enzymes.

Interaction With a DNA Oligo Containing an F-Site

To determine the kinetics of interactions between the DNA substrate containing an F-site (a stable synthetic analog of an AP-site) and an AP endonuclease (zAPE1, xAPE1, or Rrp1), a fixed concentration of the FRET-F-substrate was rapidly mixed with various concentrations of an enzyme by the stopped-flow apparatus, and fluorescence was recorded for some time (**Figure 4**). All three enzymes yielded similar patterns of the kinetic traces: a short lag was followed by a fast increase (in the FRET signal owing to the growing distance between FAM and BHQ1 residues) corresponding to the catalytic stage of the enzymatic reaction, and then all fluorescence curves reached a plateau. It must be noted that the FRET curves in case of xAPE1 featured a small but real instant decrease in the signal in the initial part of curves up to 10–20 ms (**Figure 4A**). This decrease phase most likely reflects the formation of the enzyme–substrate complex. Nevertheless, a substantial amplitude of the increase in the signal (reflecting the process of F-site cleavage) made it difficult to detect changes in the FRET signal (much weaker in amplitude) related to processes of substrate–enzyme complex formation in the cases of zAPE1 and Rrp1 (**Figures 4C,E**). This observation also implies that xAPE1 induces greater bending of the DNA substrate during the complex formation, and thus the convergence of FAM and BHQ1 residues makes the decrease in the FRET signal more detectable.

The enzymatic cleavage of the FRET-F-substrate was generally completed by 1.0 s in the case of zAPE1 and xAPE1 and continued up to 100 s in the case of Rrp1. The traces were well fitted to a double exponential Eq. 1 giving both observed rate constants being linearly dependent on the enzyme concentration. This fitting yielded the kinetic model depicted in **Scheme 1**. This kinetic model is consistent with the time courses in **Figure 4** and contains one equilibrium stage of the substrate binding and an irreversible catalytic stage. All rate and equilibrium constants corresponding to this mechanism are given in **Table 2**. Although

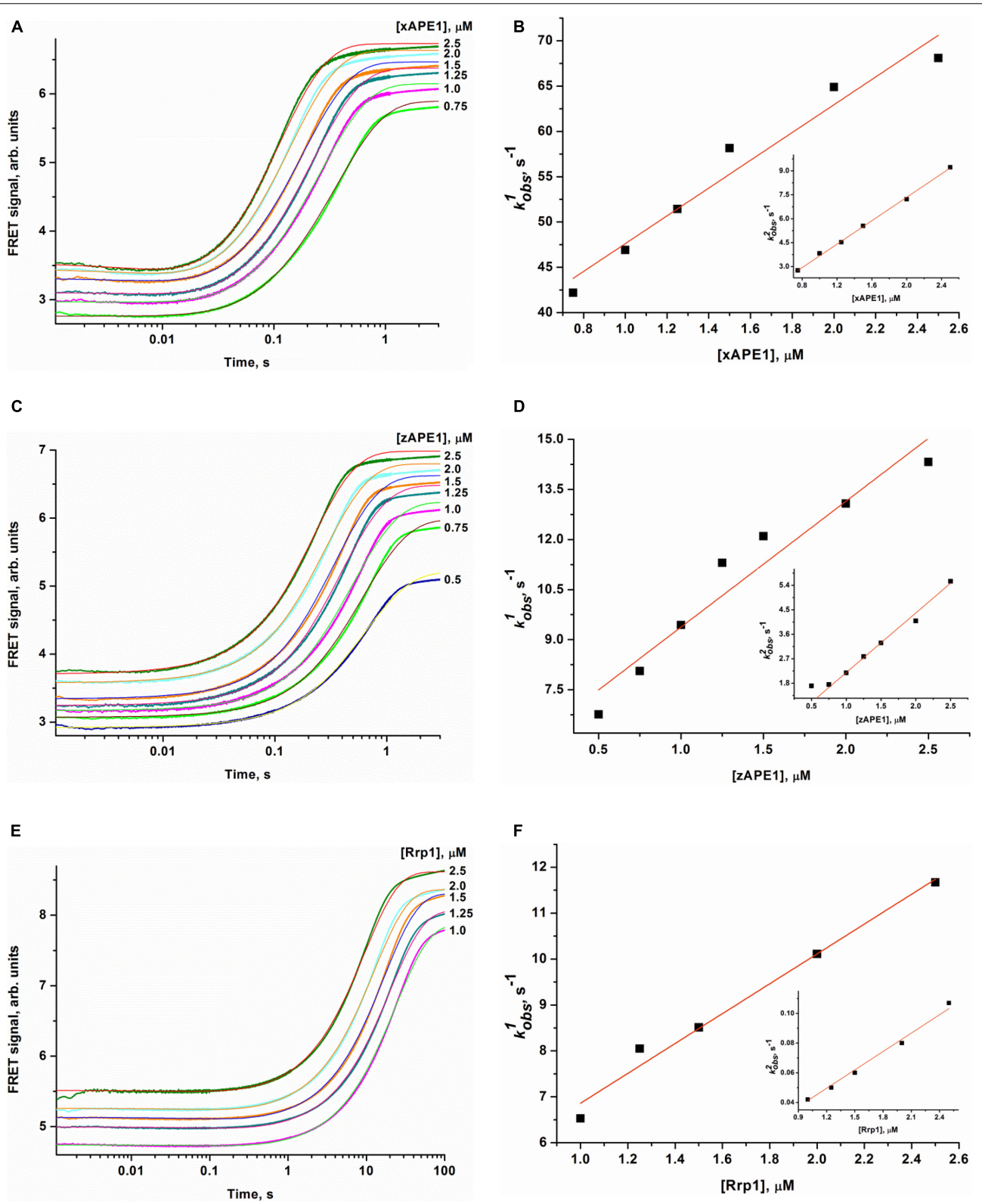

FIGURE 4 | Changes in the FRET signal during the interaction of xAPE1 **(A,B)**, zAPE1 **(C,D)**, or Rrp1 **(E,F)** with the FRET-F-substrate. (FRET-F) = 1.0 μM, and concentrations of enzymes are shown on the right in the panel. Individual traces were fitted to double-exponential Eq. 1, and the dependences of the observed rate constants k_{obs1} and k_{obs2} on enzyme concentration were linearly fitted to Eqs 2 and 3, respectively.

$$E + S \underset{k_{-1}}{\overset{k_1}{\rightleftharpoons}} E{\bullet}S \xrightarrow{k_{cat}} E + P$$

E, enzyme; S, FRET-F-substrate; E•S, enzyme–substrate complex; P, reaction product.

SCHEME 1 | Recognition of the FRET-F-substrate by AP endonucleases.

the rate constants obtained for the enzyme–substrate complex formation gave rather similar binding constants K_1 for the three enzymes, there were significant differences among their catalytic rate constants. The most rapid k_{cat} was observed for the xAPE1 enzyme ($3.7 \pm 0.1\ s^{-1}$), and this constant was only slightly faster than that obtained for zAPE1 ($2.2 \pm 0.1\ s^{-1}$). Rate constant k_{cat} characterizing catalytic cleavage of the F-site by Rrp1 turned out to be two orders of magnitude slower: $0.040 \pm 0.001\ s^{-1}$. Thus, despite the finding that the overall FRET-F-substrate-binding process takes place with similar efficacy for zAPE1, xAPE1, and Rrp1, the catalytic stage of the cleavage reaction is dramatically slowed down in the interactions with Rrp1. Probably, this loss of catalytic efficiency is associated with the lack of the Asp70 residue in the active site of Rrp1; this residue is essential for proper coordination of Mg^{2+}. This assumption is in agreement with the reported moderate reduction in hAPE1 AP endonuclease activity after site-directed mutation D70A is introduced (Erzberger and Wilson, 1999).

Our data allow us to conclude that the difference in the N-terminal domain among the enzymes has no effect on the catalytic complex formation with F-site-containing DNA, in good agreement with the results obtained previously for the wild type and an N-terminally truncated version of hAPE1 (Izumi and Mitra, 1998; Chattopadhyay et al., 2006; Timofeyeva et al., 2009). Moreover, the similarity of binding constants (**Table 2**) among all these enzymes indicates that the R181N substitution in the DNA-binding site of Rrp1 is also not essential for the catalytic complex formation with F-site-containing DNA. These findings are consistent with one study (Freudenthal et al., 2015), which revealed that wild-type and R181A hAPE1 bind to the substrate with similar affinity. Nonetheless, their binding analysis with product DNA indicates that the mutant (R181A) enzyme binds with approximately threefold weaker affinity than that of the wild-type enzyme, implying that Arg181 participates in product DNA binding.

TABLE 2 | Rate and equilibrium constants of the interaction of AP endonucleases with the FRET-F-substrate.

Constant	zAPE1	xAPE1	Rrp1
$k_1 \times 10^{-6}$, $M^{-1}s^{-1}$	3.8 ± 0.4	15 ± 2	3.3 ± 0.2
k_{-1}, s^{-1}	5.6 ± 0.7	32 ± 3	3.6 ± 0.4
$K_1 \times 10^{-6}$, M^{-1}	0.7 ± 0.2	0.5 ± 0.1	0.9 ± 0.2
k_{cat}, s^{-1}	2.2 ± 0.1	3.7 ± 0.1	0.040 ± 0.001

Data are presented as mean ± SD.
$K_1 = k_1/k_{-1}$.

Binding of Nondamaged DNA

Crystal structures have shown that in the catalytic complex, hAPE1 induces DNA bending by approximately 35° (Mol et al., 2000a,b; Tsutakawa et al., 2013; Freudenthal et al., 2015). Damaged DNA bending has also been detected in solution by PELDOR spectroscopy and FRET analysis (Kuznetsova et al., 2018b; Alekseeva et al., 2019a). Therefore, to resolve the nondamaged DNA-binding stage, we recorded time-dependent changes of the FRET signal during DNA binding under the same conditions as those used for the FRET-F-substrate. For the nondamaged DNA, changes in the FRET signal were associated with changes in the distance between the emitter and quencher, which are located at the opposite ends of the duplex. The FRET pair of dyes could be spatially close during "endonuclease-type" complex formation in the same manner as with the damaged duplex that would lead to DNA bending. Another possible reason for the FRET signal change is the end of the binding process resulting in the formation of a "3′-5′ exonuclease-type" enzyme–DNA complex, which causes displacement of the dyes on both sides of the duplex. On the other hand, the 3′-5′ exonuclease degradation of the duplex was not observed in the selected time range (10 s, **Figure 5**), in line with the very slow processing rate of the blunt-end duplex compared with recessed DNA (Kuznetsova et al., 2018a; Liu et al., 2021).

When a fixed concentration of the intact DNA duplex was mixed with various concentrations of the enzymes, an initial decrease in the FRET signal was observed that was followed by an increase in the signal for zAPE1, hAPE1, and Rrp1 but not for xAPE1 (**Figure 5**). The experiments with well-studied hAPE1 have been conducted to obtain the reference data under the conditions closest to those used for the enzymes being tested. In the assay of xAPE1, only a decrease in the FRET signal was detectable; it manifested the biggest amplitude change among all the enzymes, suggesting that the DNA binding by xAPE1 leads to more pronounced bending of the DNA structure.

Inspection of the time courses obtained for nondamaged-DNA binding by the AP endonucleases zAPE1, xAPE1, and hAPE1 revealed that the process was essentially completed within 1 s. The time courses of interactions between intact DNA and Rrp1 reach a plateau at time points exceeding 10 s, meaning that the process of DNA binding by Rrp1 proceeded more slowly than that of the other APE1-like enzymes.

The kinetic curves (**Figure 5**) were fitted in DynaFit to calculate rate constants of the DNA-binding steps. The analysis yielded a minimal kinetic mechanism containing two reversible steps in the case of enzymes hAPE1, zAPE1, and Rrp1 (**Scheme 2**) but only one-step binding for xAPE1 (**Scheme 3**). Rate

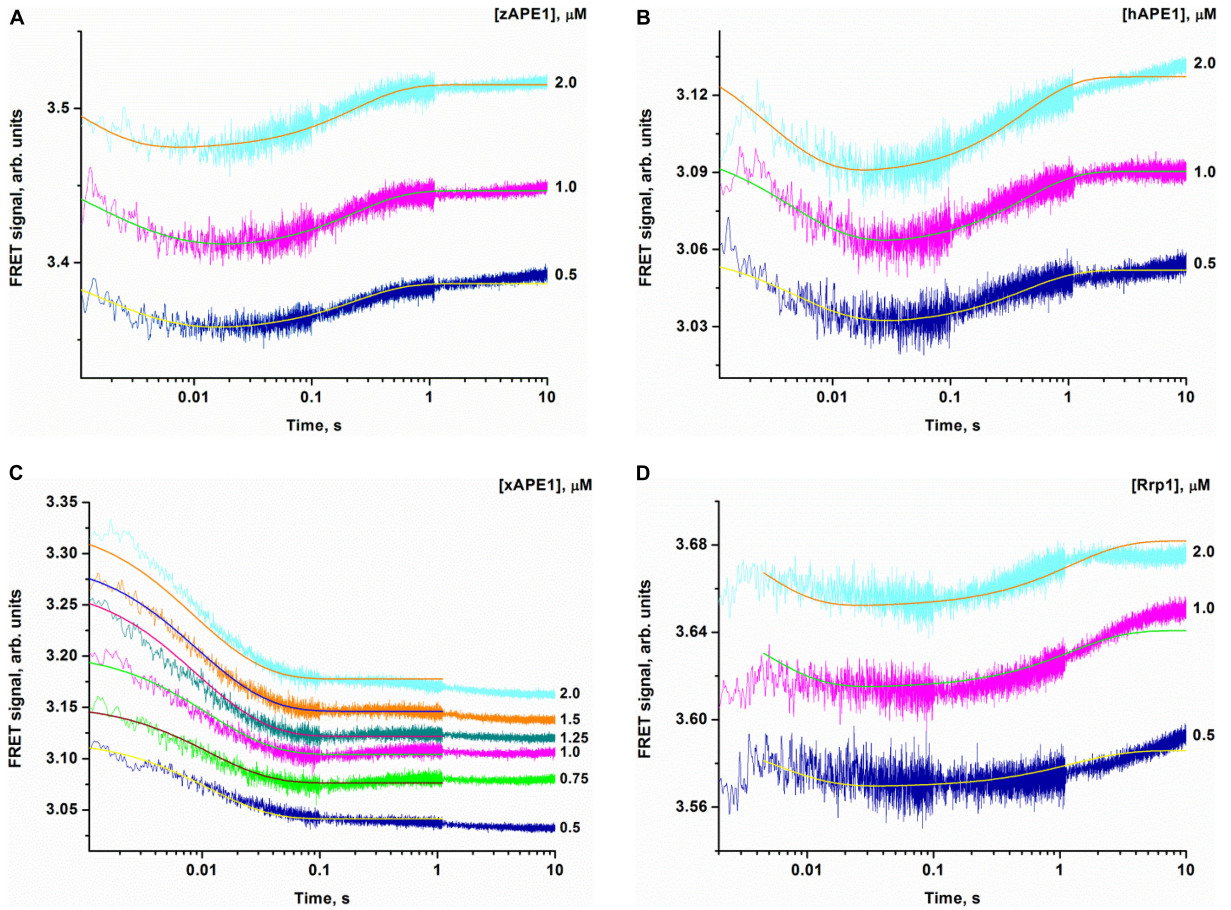

FIGURE 5 | Changes in the FRET signal during the interaction of zAPE1 **(A)**, hAPE1 **(B)**, xAPE1 **(C)**, or Rrp1 **(D)** with the nondamaged DNA. (DNA) = 1.0 μM, and concentrations of enzymes are shown on the right in the panel. Traces were fitted by nonlinear least-squares regression analysis.

constants of forward and reverse reactions in **Schemes 2**, **3** as well as the equilibrium constants calculated as the ratio of k_i to k_{-i} ($K_i = k_i/k_{-i}$) and the overall association constants $K_{ass} = K_1 \times K_2$ (if there are any) are presented in **Table 3**.

The formation of the primary enzyme–substrate complex $(E\bullet S)_1$ was most effective for zAPE1 because forward-reaction constant k_1 was the fastest among the enzymes under study (790×10^6 $M^{-1}s^{-1}$) and because reverse reaction constant k_{-1} [characterizing the stability of the $(E\bullet S)_1$ complex] was relatively slow (7.0 s^{-1}). Another enzyme showing approximately the same low k_{-1} value (5.0 s^{-1}) was xAPE1. Nonetheless, for xAPE1, forward reaction constant k_1 (70×10^6 $M^{-1}s^{-1}$) was one order of magnitude lower compared with zAPE1, thus making association constant K_1 14×10^6 M^{-1} for xAPE1, while K_1 for zAPE1 was almost eifgtfold higher (110×10^6 M^{-1}). Forward reaction constants k_1 for Rrp1 and hAPE1 were quite similar (120×10^6 and 180×10^6 $M^{-1}s^{-1}$, respectively) giving the lowest values of initial DNA-binding constant K_1 2.0×10^6 and 6.0×10^6 M^{-1}, respectively.

Thus, the $(E\bullet S)_1$ complex resulting from the binding of the nondamaged DNA by the zAPE1 enzyme turned out to be formed much more efficiently and was the most stable, with its association constant K_1 being an order of magnitude higher when compared with the other enzymes. Association constants K_1 are similar between hAPE1 and xAPE1, but K_1 for Rrp1 is the smallest one. These differences are seen in FRET signal time courses of these enzymes. The phase of the initial decrease in the FRET signal ended approximately within 0.02, 0.04, and 0.1 s, respectively, for zAPE1, hAPE1, and Rrp1. Even though the phase of fluorescence declines in the case of xAPE1 finished rather late (compared with the other enzymes), this phenomenon is associated with the absence of a pronounced phase of a subsequent increase in the FRET signal characterizing the transformation of the $(E\bullet S)_1$ complex to the $(E\bullet S)_2$ complex. Indeed, the nature of complex $(E\bullet S)_2$ requires additional elucidation because the formation of this complex is not a universal feature of the tested APE1-like enzymes. Probably, in the interaction with nondamaged DNA, this complex characterizes the efficiency of enzymes' binding to the 3′ end of the duplex in an attempt to start 3′-5′-exonuclease degradation of the DNA.

Of note, although the forward and reverse constants [characterizing the transformation of the enzyme–substrate complex $(E\bullet S)_1$ into $(E\bullet S)_2$] showed almost ninefold differences

$$E + S \underset{k_{-1}}{\overset{k_1}{\rightleftharpoons}} (E\bullet S)_1 \underset{k_{-2}}{\overset{k_2}{\rightleftharpoons}} (E\bullet S)_2$$

E, enzyme; S, nondamaged DNA; $(E\bullet S)_i$, different enzyme–substrate complexes.

SCHEME 2 | Binding of the nondamaged DNA by AP endonucleases hAPE1, zAPE1, and Rrp1.

$$E + S \underset{k_{-1}}{\overset{k_1}{\rightleftharpoons}} (E\bullet S)_1$$

E, enzyme; S, nondamaged DNA; $(E\bullet S)_1$, enzyme–substrate complex.

SCHEME 3 | Recognition of the intact DNA by xAPE1.

TABLE 3 | Rate and equilibrium constants of the interaction of AP endonucleases with the nondamaged DNA as determined by nonlinear least-squares regression analysis of the FRET traces.

Constant	zAPE1	xAPE1	Rrp1	hAPE1
$k_1 \times 10^{-6}$, $M^{-1}s^{-1}$	790 ± 60	70 ± 5	120 ± 30	180 ± 20
k_{-1}, s^{-1}	7.0 ± 0.8	5.0 ± 2.0	60 ± 20	30 ± 7
$K_1 \times 10^{-6}$, M^{-1}	110 ± 20	14 ± 7	2.0 ± 1.0	6.0 ± 2.0
k_2, s^{-1}	0.18 ± 0.03	–	0.02 ± 0.01	0.08 ± 0.01
k_{-2}, s^{-1}	4.1 ± 0.2	–	0.8 ± 0.1	2.3 ± 0.1
K_2	0.04 ± 0.01	–	0.03 ± 0.01	0.04 ± 0.01
$K_{ass} \times 10^{-6}$, M^{-1}	5.0 ± 2.0	–	0.06 ± 0.05	0.2 ± 0.1

*$K_i = k_i/k_{-i}$, $K_{ass} = K_1 \times K_2$.

from the k_2 constant, K_2 was roughly similar among all the enzymes except for xAPE1. As a result, differences in total association constant K_{ass} are completely explained by the differences in association constant K_1 (characterizing the efficiency of the initial DNA binding). Overall, it can be concluded that for Rrp1, the formation of the $(E\bullet S)_2$ enzyme–substrate complex was the least efficient among the tested enzymes; this finding may be related to a possible effect of the largest N-terminal domain or of substitution R181N in the DNA-binding site of Rrp1. Therefore, these features of Rrp1 could play some role in the primary-complex transformation during the interaction with the nondamaged DNA. Nevertheless, in the case of binding of the DNA containing the F-site (**Table 2**), the efficiency of catalytic-complex formation was quite similar among all the APE1-like enzymes, suggesting that the efficiency of formation of different complexes and their conformational transformation are dependent on the nature of the DNA bound by these enzymes.

Interaction With DNA Containing a Damaged Base

First of all, the cleavage efficiency of DNA substrates containing αA, εA, DHU, or uracil (U) by the three nonhuman AP endonucleases was analyzed by PAGE (**Figures 6A–D**). As shown in **Figure 6E**, all APE1-like enzymes are able to cleave DNA substrates containing DHU, εA, or U. Unexpectedly, it was found that Rrp1 is inactive toward αA-containing DNA, whereas xAPE1 and zAPE1 can still recognize this lesion as a substrate. Regarding the activity of hAPE1 toward various target nucleotides, it has been reported (Prorok et al., 2013; Kuznetsova et al., 2018b; Bulygin et al., 2020) that αA is a better substrate than εA and U. These findings indicate that despite the high identity of active-site residues among all the tested APE1-like enzymes, they have individual features of substrate recognition.

To clarify DNA conformational changes in the course of substrate binding, fluorescence curves reflecting the interactions of AP endonucleases with different DNA substrates (containing αA, εA, DHU, or U) were recorded by the stopped-flow kinetic method (**Figure 7**). A very low rate of site-specific DNA cleavage together with interference with 3′–5′ exonuclease degradation of DNA substrates under some conditions with long reaction time did not let us register the full enzyme cycle, which includes DNA binding, cleavage, and product dissociation. Therefore, the experimental limitations did not allow us to identify a kinetic model for damaged DNA substrates. All time courses are presented in time intervals up to 10 s corresponding only to DNA-binding steps because—as was demonstrated by PAGE—no significant cleavage of these DNA substrates occurs in the given time interval. Thus, all changes in the FRET signal depicted in **Figure 7** characterize only the initial binding of the DNA substrate by the enzymes and subsequent conformational transformation of the enzyme–substrate complexes. The complexity of the obtained time courses and a low signal-to-noise ratio in some cases did not permit precise fitting of the kinetic curves.

The fluorescence time courses recorded for interactions between the AP endonucleases and DHU-containing DNA substrate revealed a decrease in the FRET signal followed by a subsequent increase as in the case of nondamaged DNA (**Figure 7A**). The most pronounced changes in the FRET signal were observed when the DHU-substrate was bound by zAPE1 and xAPE1. The fast initial decrease in the FRET signal that proceeds within 0.02 s most likely reflects the

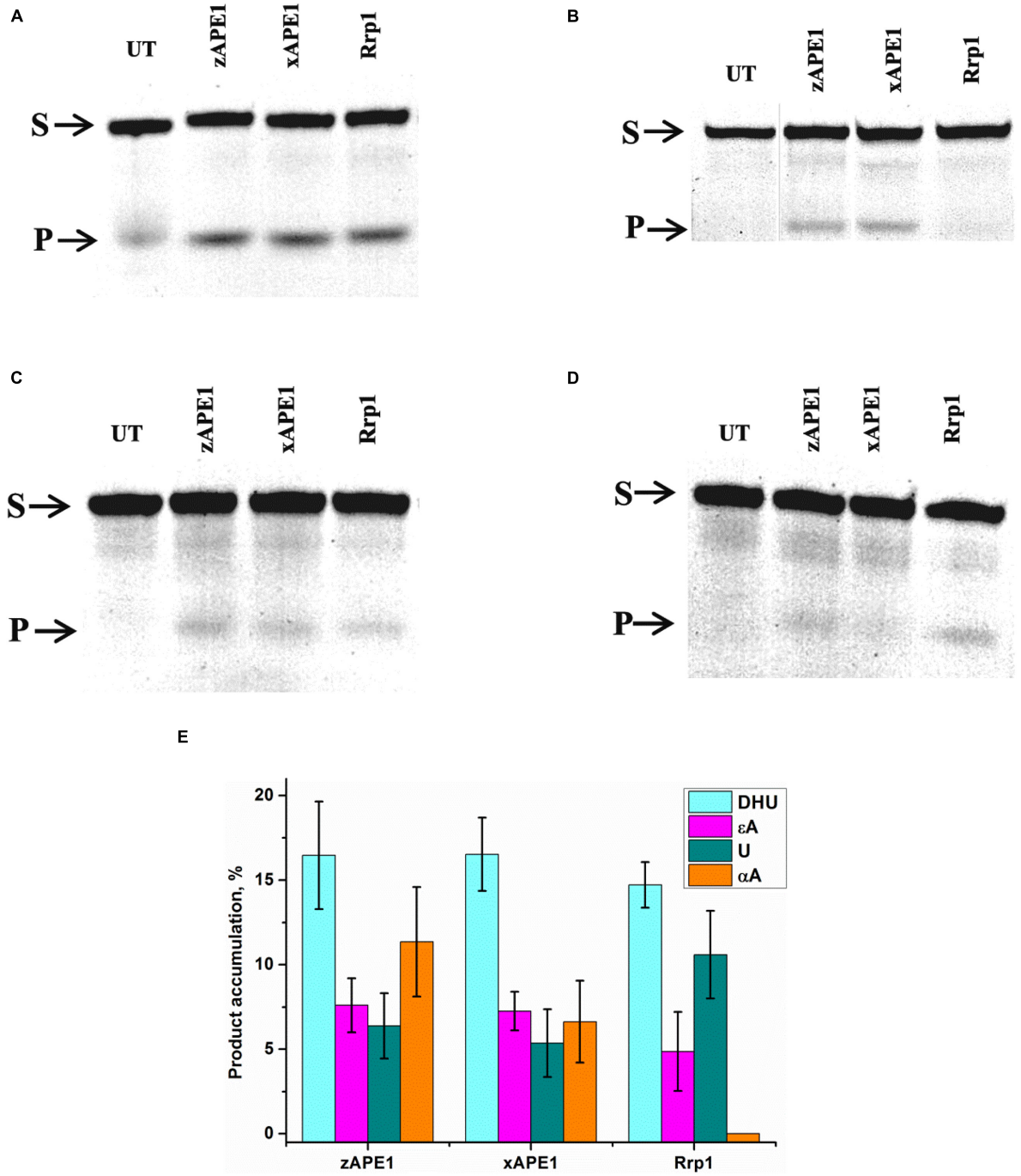

FIGURE 6 | PAGE analysis of DNA cleavage by APE1-like enzymes during an interaction with the FRET–DHU-substrate **(A)**, FRET–αA-substrate **(B)**, FRET–εA-substrate **(C)**, or FRET-U-substrate **(D)**. A comparison of efficacy of model DNA substrates' cleavage by APE1-like enzymes **(E)**. (Enzyme) = (DNA substrate) = 1.0 μM. T = 25°C, reaction time = 2 h. S is a substrate, P is a product of DNA chain cleavage, and UT is a sample untreated with an enzyme.

emergence of the primary enzyme–substrate complex. This phase for Rrp1 was at least 10-fold slower and finalized only at time point "0.3 s." Because of the slow rate of primary-complex formation, the second phase of the FRET signal increase was also significantly slower for Rrp1 when compared with xAPE1 and zAPE1.

Fluorescence time courses obtained for the interactions of zAPE1 and xAPE1 with the εA-containing DNA substrate (**Figure 7B**) showed an initial decrease in the FRET signal up to time point 0.02 and 0.4 s, respectively, followed by an increase in the signal. For the Rrp1 interaction with the FRET-εA-substrate, only a decrease phase of up to the 10 s

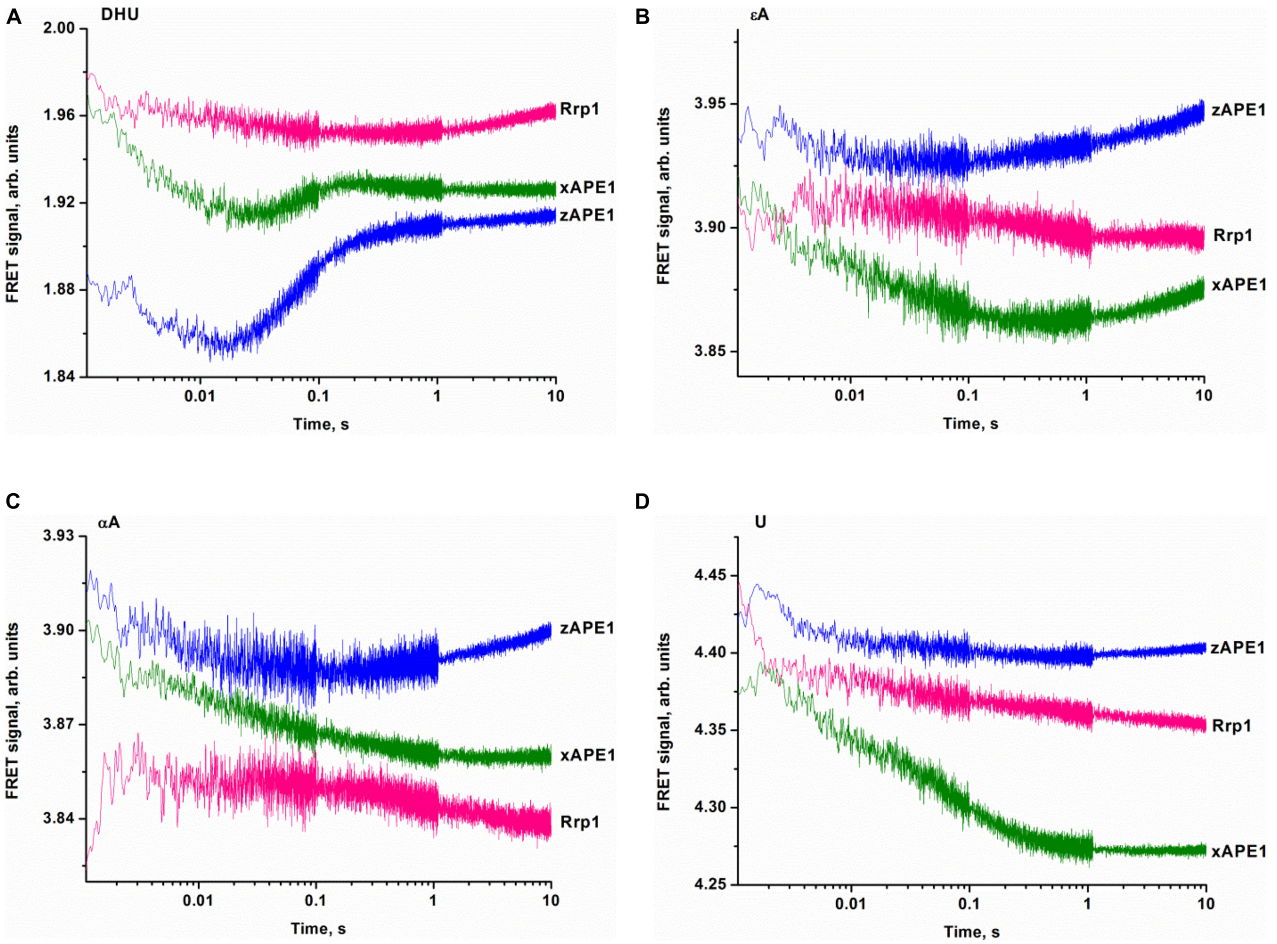

FIGURE 7 | Binding of APE1-like enzymes with the FRET–DHU-substrate **(A)**, FRET–εA-substrate **(B)**, FRET–αA-substrate **(C)**, or FRET–U-substrate **(D)**. (Enzyme) = (DNA substrate) = 1.0 μM.

was detectable. These data revealed that the larger εA base than DHU base is recognized by APE1-like enzymes with completely different efficiency. In the assessment of εA-DNA recognition by Rrp1, the initial binding step was expectedly slower compared with the other enzymes, in agreement with the data on the nondamaged DNA. Nevertheless, the 20-fold rate difference between zAPE1 and xAPE1 revealed a significant disturbance of εA base recognition in comparison with the DHU base (**Figures 7A,B**). As recently reported regarding hAPE1 (Bulygin et al., 2020), accommodation of a damaged base in the active-site pocket is associated with a significant disturbance of the "damage recognition loop," which includes residues Asn229, Thr233, and Glu236. An alignment of amino acid sequences of the tested enzymes (**Figure 2**) revealed that Thr233 and Glu236 are fully conserved, whereas Asn229 is substituted by Thr in xAPE1. It is also worth noting that the human APE1 Asn229 mutant shows significantly weaker binding to a damaged DNA substrate (Shen and Loeb, 2003; Izumi et al., 2004). Moreover, Ala230—forming the wall of the damaged base-binding pocket—is also substituted by the rigid Pro residue only in xAPE1. Therefore, when interacting with an abasic nucleotide or even DHU-containing DNA, highly similar zAPE1 and xAPE1 significantly differ in the rate of formation of the initial complex and its subsequent transformation during an interaction with a larger damaged nucleotide containing the εA base. Moreover, the data obtained about the αA- and U-containing DNA substrates (**Figures 7C,D**) uncovered slower initial complex formation for xAPE1 in comparison with zAPE1. Indeed, on the one hand, molecular dynamics simulations (Bulygin et al., 2020) indicate that during the recognition of various damaged nucleotides, the DNA-binding site of APE1-like enzymes must undergo conformational changes to accommodate the nucleotide containing a damaged base. On the other hand, as reported (Bulygin et al., 2020), the cleavage of αA- and εA-substrates is more or less efficient because the position of these bases in the binding pocket does not correspond to optimal distances between the scissile phosphate group and catalytic amino acid residues.

The detailed molecular mechanism underlying the control of specificity to a damaged base requires additional investigation including site-directed mutational analysis of some enzymes and global evolutionary analysis of these enzymes to identify possible

roles of amino acid residues of the enzyme in the mechanism of substrate recognition. Moreover, the impact of the N-terminal domain on the DNA-binding properties and ability of enzymes to recognize different types of damaged bases should be researched further. Nevertheless, the obtained data support the idea that the NIR activity of AP endonucleases is a generic function of these enzymes.

CONCLUSION

In general, our examination of fluorescence time courses—obtained for the interaction of several APE1-like enzymes with DNA substrates containing various lesions and a FRET dye pair—allows us to outline a model of substrate recognition by this class of enzymes. Binding constants for F-site-containing DNA proved to be similar among all the assayed AP endonucleases, suggesting that abasic site recognition by these enzymes most likely is based on a combination of three "whales": DNA flexibility, the ability of the F-site to get flipped out from the duplex, and the absence of steric hindrances throughout the trajectory of eversion into the active site of the enzymes. However, Rrp1 manifested a significantly slower rate of the catalytic reaction with F-site-containing DNA compared with zAPE1 and xAPE1. This effect is possibly related to the loss of Asp70, one of the residues that coordinate cofactor Mg^{2+} in the active site. This assumption is in agreement with the moderately lower AP endonuclease activity of hAPE1 carrying site-directed mutation D70A (Erzberger and Wilson, 1999).

The binding processes leading to the changes in the FRET signal during interactions with nondamaged DNA and DNA substrates containing damaged bases are the fastest for zAPE1, and the rates of these processes are comparable to those of hAPE1 reported previously (Kuznetsova et al., 2018b; Bulygin et al., 2020). Of note, the substitution of two amino acid residues in the damaged base-binding pocket (Asn229Thr and Ala230Pro) in xAPE1 in comparison with the other APE1-like enzymes (hAPE1, zAPE1, and Rrp1) leads to significant differences in the rates of formation of the initial complex with DNA containing αA, εA, or U but not the less rigid F-site or the nonplanar DHU base. For Rrp1, the binding of nondamaged DNA and DNA substrates containing damaged bases was the slowest. Even though the substitution of Arg181 in the DNA-binding site by the Asn residue does not affect catalytic complex formation in the case of F-site-containing DNA, this mutation may alter the non-specific binding and recognition of bulkier nucleotides containing a damaged base. Another possible factor that could influence the DNA-binding process is the N-terminal domain of the enzymes under study. Although the role of N-terminal domains in the DNA binding and recognition of a damaged base is outside the scope of this study, it is likely that the lower DNA-binding affinity for nondamaged DNA and DNA substrates containing damaged bases is linked with differences in this domain. As suggested for hAPE1, the N-terminal domain influences the rate of formation of the enzyme–substrate complex in NIR and $3'\rightarrow5'$ exonuclease reactions (Gros et al., 2004; Daviet et al., 2007; Timofeyeva et al., 2009) but not in the case of abasic-DNA cleavage (Izumi and Mitra, 1998; Chattopadhyay et al., 2006).

Unexpectedly, the differences in the rates of DNA substrates' binding do not cause significant differences in the cleavage efficiency of the DNA containing a damaged base, suggesting that the formation of enzyme–substrate complexes is not the key factor that limits the enzyme turnover. From this standpoint, individual site-directed mutations in the active site or the whole N-domain are not important for the ability of the enzyme to recognize a damaged base; they can only affect the rate of complex formation. Our results suggest that the nature of damage recognition and cleavage efficacy have something to do with the fine conformational tuning inside the active site. In this regard, our results on APE1-like enzymes are in agreement with our findings about hAPE1 (Bulygin et al., 2020): the location of αA and εA in the binding pocket does not correlate with the conformation of amino acid residues optimal for catalysis. Therefore, the conformational rearrangements inside the active site must be the driving force behind the processes catalyzed by APE1-like enzymes.

Taken together, our results mean that the activity of AP endonucleases toward a damaged base-containing DNA is a common feature of AP endonucleases from evolutionarily distant species, as initially reported for Nfo from *E. coli* (Ide et al., 1994; Ischenko and Saparbaev, 2002; Ishchenko et al., 2004) and later described for hAPE1 (Gros et al., 2004). It is well known that hAPE1 is an essential enzyme for abasic-site cleavage in the BER pathway and in transcriptional regulation of genes. Moreover, a knockout of the *APE1* gene in mice or even a knockdown of APE1 activity increases the sensitivity to oxidative stress and promotes cell death (Xanthoudakis, 1996; Meira et al., 2001; Huamani et al., 2004; Fung and Demple, 2005; Unnikrishnan et al., 2009) implying importance of this enzyme. On the other hand, at present, it is still unclear whether inactivation of which function of this multifunctional enzyme has such serious consequences. Therefore, our data suggest that the NIR activity of AP endonucleases is conserved among insects (*D. melanogaster*), amphibians (*X. laevis*), fishes (*D. rerio*), and humans, indicating its high importance for cellular processes.

DATA AVAILABILITY STATEMENT

The original contributions presented in the study are included in the article/supplementary material, further inquiries can be directed to the corresponding authors.

AUTHOR CONTRIBUTIONS

ATD conducted the experiments. AAI, MS, and NAK conceived and designed the experiments. AID, NAK, and OSF analyzed the data. AAI, MS, NAK, and OSF contributed to the reagents, materials, and/or analytical tools. ATD, NAK, MS, and OSF wrote the manuscript. All authors contributed to the article and approved the submitted version.

FUNDING

The part of the work involving enzyme cloning, purification, and kinetic analysis was supported by the Russian Science Foundation grant no. 19-74-10034. Partial governmental support for equipment use was received from the Russian Ministry of Science and Higher Education project # AAAA-A17-117020210022-4. ATD is supported by Ph.D. grant 20-34-90008 from Russian Foundation for Basic Research. This work was also supported by grants from the La Ligue Nationale Française Contre le Cancer «Equipe LNCC 2016» (https://www.ligue-cancer.net) and the Electricité de France RB 2020-02 (http://www.edf.fr) to MS and from the French National Research Agency (ANR-18-CE44-0008) and Foundation ARC (PJA-20181208015) to AAI.

REFERENCES

Alekseeva, I. V., Bakman, A. S., Vorobjev, Y. N., Fedorova, O. S., and Kuznetsov, N. A. (2019a). Role of ionizing amino acid residues in the process of DNA binding by human AP endonuclease 1 and in its catalysis. *J. Phys. Chem. B* 123, 9546–9556. doi: 10.1021/acs.jpcb.9b07150

Alekseeva, I. V., Davletgildeeva, A. T., Arkova, O. V., Kuznetsov, N. A., and Fedorova, O. S. (2019b). The impact of single-nucleotide polymorphisms of human apurinic/apyrimidinic endonuclease 1 on specific DNA binding and catalysis. *Biochimie* 163, 73–83. doi: 10.1016/j.biochi.2019.05.015

Alekseeva, I. V., Kuznetsova, A. A., Bakman, A. S., Fedorova, O. S., and Kuznetsov, N. A. (2020). The role of active-site amino acid residues in the cleavage of DNA and RNA substrates by human apurinic/apyrimidinic endonuclease APE1. *Biochim. Biophys. Acta Gen. Subj.* 1864, 129718. doi: 10.1016/j.bbagen.2020.129718

Barnes, T., Kim, W. C., Mantha, A. K., Kim, S. E., Izumi, T., Mitra, S., et al. (2009). Identification of Apurinic/apyrimidinic endonuclease 1 (APE1) as the endoribonuclease that cleaves c-myc mRNA. *Nucleic Acids Res.* 37, 3946–3958. doi: 10.1093/nar/gkp275

Barzilay, G., and Hickson, I. D. (1995). Structure and function of apurinic/apyrimidinic endonucleases. *Bioessays* 17, 713–719. doi: 10.1002/bies.950170808

Bazlekowa-Karaban, M., Prorok, P., Baconnais, S., Taipakova, S., Akishev, Z., Zembrzuska, D., et al. (2019). Mechanism of stimulation of DNA binding of the transcription factors by human apurinic/apyrimidinic endonuclease 1, APE1. *DNA Repair (Amst.)* 82:102698. doi: 10.1016/j.dnarep.2019.102698

Beernink, P. T., Segelke, B. W., Hadi, M. Z., Erzberger, J. P., Wilson, D. M. III, and Rupp, B. (2001). Two divalent metal ions in the active site of a new crystal form of human apurinic/apyrimidinic endonuclease, Ape1: implications for the catalytic mechanism. *J. Mol. Biol.* 307, 1023–1034. doi: 10.1006/jmbi.2001.4529

Berquist, B. R., McNeill, D. R., and Wilson, D. M. III (2008). Characterization of abasic endonuclease activity of human Ape1 on alternative substrates, as well as effects of ATP and sequence context on AP site incision. *J. Mol. Biol.* 379, 17–27. doi: 10.1016/j.jmb.2008.03.053

Bulygin, A. A., Kuznetsova, A. A., Vorobjev, Y. N., Fedorova, O. S., and Kuznetsov, N. A. (2020). The role of active-site plasticity in damaged-nucleotide recognition by human apurinic/apyrimidinic endonuclease APE1. *Molecules* 25:3940. doi: 10.3390/molecules25173940

Chattopadhyay, R., Wiederhold, L., Szczesny, B., Boldogh, I., Hazra, T. K., Izumi, T., et al. (2006). Identification and characterization of mitochondrial abasic (AP)-endonuclease in mammalian cells. *Nucleic Acids Res.* 34, 2067–2076. doi: 10.1093/nar/gkl177

Chou, K.-M., and Cheng, Y.-C. (2003). The exonuclease activity of human apurinic/apyrimidinic endonuclease (APE1). Biochemical properties and inhibition by the natural dinucleotide Gp4G. *J. Biol. Chem.* 278, 18289–18296. doi: 10.1074/jbc.M212143200

Daviet, S., Couve-Privat, S., Gros, L., Shinozuka, K., Ide, H., Saparbaev, M., et al. (2007). Major oxidative products of cytosine are substrates for the nucleotide incision repair pathway. *DNA Repair* 6, 8–18. doi: 10.1016/j.dnarep.2006.08.001

Demple, B., and Sung, J.-S. (2005). Molecular and biological roles of Ape1 protein in mammalian base excision repair. *DNA Repair* 4, 1442–1449.

Erzberger, J. P., and Wilson, D. M. III (1999). The role of Mg2+ and specific amino acid residues in the catalytic reaction of the major human abasic endonuclease: new insights from EDTA-resistant incision of acyclic abasic site analogs and site-directed mutagenesis. *J. Mol. Biol.* 290, 447–457. doi: 10.1006/jmbi.1999.2888

Fantini, D., Vascotto, C., Marasco, D., D'Ambrosio, C., Romanello, M., Vitagliano, L., et al. (2010). Critical lysine residues within the overlooked N-terminal domain of human APE1 regulate its biological functions. *Nucleic Acids Res.* 38, 8239–8256. doi: 10.1093/nar/gkq691

Fischer, C. J., Maluf, N. K., and Lohman, T. M. (2004). Mechanism of ATP-dependent translocation of E. coli UvrD monomers along single-stranded DNA. *J. Mol. Biol.* 344, 1287–1309. doi: 10.1016/j.jmb.2004.10.005

Freudenthal, B. D., Beard, W. A., Cuneo, M. J., Dyrkheeva, N. S., and Wilson, S. H. (2015). Capturing snapshots of APE1 processing DNA damage. *Nat. Struct. Mol. Biol.* 22, 924–931. doi: 10.1038/nsmb.3105

Friedberg, E. C., Roger, A. S., Wolfram, S., Graham, C. W., Tom, E., and Richard, D. W. (2006). *DNA Repair and Mutagenesis, Second Edition*. Washington, DC: American Society of Microbiology, doi: 10.1128/9781555816704

Fromme, J. C., Banerjee, A., and Verdine, G. L. (2004). DNA glycosylase recognition and catalysis. *Curr. Opin. Struct. Biol.* 14, 43–49.

Fung, H., and Demple, B. (2005). A vital role for Ape1/Ref1 protein in repairing spontaneous DNA damage in human cells. *Mol. Cell* 17, 463–470. doi: 10.1016/j.molcel.2004.12.029

Georgiadis, M. M., Luo, M., Gaur, R. K., Delaplane, S., Li, X., and Kelley, M. R. (2008). Evolution of the redox function in mammalian apurinic/apyrimidinic endonuclease. *Mutat. Res.* 643, 54–63. doi: 10.1016/j.mrfmmm.2008.04.008

Gorman, M. A., Morera, S., Rothwell, D. G., de La Fortelle, E., Mol, C. D., Tainer, J. A., et al. (1997). The crystal structure of the human DNA repair endonuclease HAP1 suggests the recognition of extra-helical deoxyribose at DNA abasic sites. *EMBO J.* 16, 6548–6558. doi: 10.1093/emboj/16.21.6548

Gros, L., Ishchenko, A. A., Ide, H., Elder, R. H., and Saparbaev, M. K. (2004). The major human AP endonuclease (Ape1) is involved in the nucleotide incision repair pathway. *Nucleic Acids Res.* 32, 73–81. doi: 10.1093/nar/gkh165

Gros, L., Saparbaev, M. K., and Laval, J. (2002). Enzymology of the repair of free radicals-induced DNA damage. *Oncogene* 21, 8905–8925.

He, H., Chen, Q., and Georgiadis, M. M. (2014). High-resolution crystal structures reveal plasticity in the metal binding site of apurinic/apyrimidinic endonuclease I. *Biochemistry* 53, 6520–6529. doi: 10.1021/bi500676p

Huamani, J., McMahan, C. A., Herbert, D. C., Reddick, R., McCarrey, J. R., MacInnes, M. I., et al. (2004). Spontaneous mutagenesis is enhanced in apex heterozygous mice. *Mol. Cell. Biol.* 24, 8145–8153. doi: 10.1128/MCB.24.18.8145-8153.2004

Ide, H., Tedzuka, K., Shimzu, H., Kimura, Y., Purmal, A. A., Wallace, S. S., et al. (1994). α-Deoxyadenosine, a major anoxic radiolysis product of adenine in DNA, is a substrate for *Escherichia coli* endonuclease IV. *Biochemistry* 33, 7842–7847. doi: 10.1021/bi00191a011

Ischenko, A. A., and Saparbaev, M. K. (2002). Alternative nucleotide incision repair pathway for oxidative DNA damage. *Nature* 415, 183–187. doi: 10.1038/415183a

Ishchenko, A. A., Ide, H., Ramotar, D., Nevinsky, G., and Saparbaev, M. (2004). α-anomeric deoxynucleotides, anoxic products of ionizing radiation, are substrates for the endonuclease IV-type AP endonucleases. *Biochemistry* 43, 15210–15216.

Izumi, T., and Mitra, S. (1998). Deletion analysis of human AP-endonuclease: minimum sequence required for the endonuclease activity. *Carcinogenesis* 19, 525–527. doi: 10.1093/carcin/19.3.525

Izumi, T., Schein, C. H., Oezguen, N., Feng, Y., and Braun, W. (2004). Effects of backbone contacts 3′ to the abasic site on the cleavage and the product binding by human apurinic/apyrimidinic endonuclease (APE1). *Biochemistry* 43, 684–689. doi: 10.1021/bi0346190

Kanazhevskaya, L. Y., Koval, V. V., Vorobjev, Y. N., and Fedorova, O. S. (2012). Conformational dynamics of abasic DNA upon interactions with AP endonuclease 1 revealed by stopped-flow fluorescence analysis. *Biochemistry* 51, 1306–1321. doi: 10.1021/bi201444m

Kelley, R. M., Georgiadis, M. M., and Fishel, L. M. (2011). APE1/Ref-1role in redox signaling: translational applications of targeting the redox function of the DNA repair/redox protein APE1/Ref-1. *Curr. Mol. Pharmacol.* 5, 36–53. doi: 10.2174/1874467211205010036

Kladova, O. A., Bazlekowa-Karaban, M., Baconnais, S., Piétrement, O., Ishchenko, A. A., Matkarimov, B. T., et al. (2018a). The role of the N-terminal domain of human apurinic/apyrimidinic endonuclease 1, APE1, in DNA glycosylase stimulation. *DNA Repair (Amst).* 64, 10–25. doi: 10.1016/j.dnarep.2018.02.001

Kladova, O. A., Grin, I. R., Fedorova, O. S., Kuznetsov, N. A., and Zharkov, D. O. (2019). Conformational dynamics of damage processing by human DNA glycosylase NEIL1. *J. Mol. Biol.* 431, 1098–1112. doi: 10.1016/j.jmb.2019.01.030

Kladova, O. A., Iakovlev, D. A., Groisman, R., Ishchenko, A. A., Saparbaev, M. K., Fedorova, O. S., et al. (2020). An assay for the activity of base excision repair enzymes in cellular extracts using fluorescent DNA probes. *Biochemistry (Moscow)* 85, 480–489. doi: 10.1134/S0006297920040082

Kladova, O. A., Krasnoperov, L. N., Kuznetsov, N. A., and Fedorova, O. S. (2018b). Kinetics and thermodynamics of DNA processing by wild type DNA-glycosylase endo III and its catalytically inactive mutant forms. *Genes (Basel)* 9:190. doi: 10.3390/genes9040190

Kuzmic, P. (1996). Program DYNAFIT for the analysis of enzyme kinetic data: application to HIV proteinase. *Anal. Biochem.* 237, 260–273. doi: 10.1006/abio.1996.0238

Kuznetsov, N. A., Koval, V. V., Zharkov, D. O., and Fedorova, O. S. (2012a). Conformational dynamics of the interaction of *Escherichia coli* endonuclease VIII with DNA substrates. *DNA Repair* 11, 884–891. doi: 10.1016/j.dnarep.2012.08.004

Kuznetsov, N. A., Kuznetsova, A. A., Vorobjev, Y. N., Krasnoperov, L. N., and Fedorova, O. S. (2014). Thermodynamics of the DNA damage repair steps of human 8-oxoguanine DNA glycosylase. *PLoS One* 9:e98495. doi: 10.1371/journal.pone.0098495

Kuznetsov, N. A., Vorobjev, Y. N., Krasnoperov, L. N., and Fedorova, O. S. (2012b). Thermodynamics of the multi-stage DNA lesion recognition and repair by formamidopyrimidine-DNA glycosylase using pyrrolocytosine fluorescence–stopped-flow pre-steady-state kinetics. *Nucleic Acids Res.* 40, 7384–7392. doi: 10.1093/nar/gks423

Kuznetsova, A. A., Fedorova, O. S., and Kuznetsov, N. A. (2018a). Kinetic Features of 3′-5′ exonuclease activity of human AP-Endonuclease APE1. *Molecules* 23:2101. doi: 10.3390/molecules23092101

Kuznetsova, A. A., Kuznetsov, N. A., Ishchenko, A. A., Saparbaev, M. K., and Fedorova, O. S. (2014). Pre-steady-state fluorescence analysis of damaged DNA transfer from human DNA glycosylases to AP endonuclease APE1. *Biochim. Biophys. Acta* 1840, 3042–3051. doi: 10.1016/j.bbagen.2014.break07.016

Kuznetsova, A. A., Matveeva, A. G., Milov, A. D., Vorobjev, Y. N., Dzuba, S. A., Fedorova, O. S., et al. (2018b). Substrate specificity of human apurinic/apyrimidinic endonuclease APE1 in the nucleotide incision repair pathway. *Nucleic Acids Res.* 46, 11454–11465. doi: 10.1093/nar/gky912

Kuznetsova, A. A., Novopashina, D. S., Fedorova, O. S., and Kuznetsov, N. A. (2020). Effect of the substrate structure and metal ions on the hydrolysis of undamaged RNA by human AP endonuclease APE1. *Acta Nat.* 2, 33–44.

Li, M., and Wilson, D. M. III (2014). Human apurinic/apyrimidinic endonuclease 1. *Antioxid Redox Signal* 20, 678–707. doi: 10.1089/ars.2013.5492

Lipton, A. S., Heck, R. W., Primak, S., McNeill, D. R., Wilson, D. M. III, and Ellis, P. D. (2008). Characterization of Mg2+ binding to the DNA repair protein apurinic/apyrimidic endonuclease 1 via solid-state 25Mg NMR spectroscopy. *J. Am. Chem. Soc.* 130, 9332–9341. doi: 10.1021/ja0776881

Liu, T. C., Lin, C. T., Chang, K. C., Guo, K. W., Wang, S., Chu, J. W., et al. (2021). APE1 distinguishes DNA substrates in exonucleolytic cleavage by induced space-filling. *Nat. Commun.* 12:601. doi: 10.1038/s41467-020-20853-2

Manvilla, B. A., Pozharski, E., Toth, E. A., and Drohat, A. C. (2013). Structure of human apurinic/apyrimidinic endonuclease 1 with the essential Mg2+ cofactor. *Acta Crystallogr. D Biol. Crystallogr.* 69, 2555–2562. doi: 10.1107/S0907444913027042

Masuda, Y., Bennett, R. A., and Demple, B. (1998). Rapid dissociation of human apurinic endonuclease (Ape1) from incised DNA induced by magnesium. *J. Biol. Chem.* 273, 30360–30365.

Meira, L. B., Devaraj, S., Kisby, G. E., Burns, D. K., Daniel, R. L., Hammer, R. E., et al. (2001). Heterozygosity for the mouse Apex gene results in phenotypes associated with oxidative stress. *Cancer Res.* 61, 5552–5557.

Miroshnikova, A. D., Kuznetsova, A. A., Kuznetsov, N. A., and Fedorova, O. S. (2016a). Thermodynamics of damaged DNA binding and catalysis by human AP endonuclease 1. *Acta Nat.* 8, 103–110.

Miroshnikova, A. D., Kuznetsova, A. A., Vorobjev, Y. N., Kuznetsov, N. A., and Fedorova, O. S. (2016b). Effects of mono- and divalent metal ions on DNA binding and catalysis of human apurinic/apyrimidinic endonuclease 1. *Mol. BioSyst.* 12, 1527–1539. doi: 10.1039/c6mb00128a

Mol, C. D., Hosfield, D. J., and Tainer, J. A. (2000a). Abasic site recognition by two apurinic/apyrimidinic endonuclease families in DNA base excision repair: the 3′ ends justify the means. *Mutat. Res.* 460, 211–229.

Mol, C. D., Izumi, T., Mitra, S., and Tainer, J. A. (2000b). DNA-bound structures and mutants reveal abasic DNA binding by APE1 and DNA repair coordination. *Nature* 403, 451–456. doi: 10.1038/35000249

Moor, N., Vasil'eva, I., and Lavrik, O. (2020). Functional role of N-terminal extension of human ap endonuclease 1 in coordination of base excision dna repair via protein–protein interactions. *Int. J. Mol. Sci.* 21:3122. doi: 10.3390/ijms21093122

Oezguen, N., Schein, C. H., Peddi, S. R., Power, T. D., Izumi, T., and Braun, W. (2007). A "moving metal mechanism" for substrate cleavage by the DNA repair endonuclease APE-1. *Proteins* 68, 313–323. doi: 10.1002/prot.21397

Poletto, M., Vascotto, C., Scognamiglio, P. L., Lirussi, L., Marascod, D., and Tell, G. (2013). Role of the unstructured N-terminal domain of the hAPE1 (human apurinic/apyrimidinic endonuclease 1) in the modulation of its interaction with nucleic acids and NPM1 (nucleophosmin). *Biochem. J.* 452, 545–557. doi: 10.1042/BJ20121277

Popov, A. V., Grin, I. R., Dvornikova, A. P., Matkarimov, B. T., Groisman, R., Saparbaev, M., et al. (2020). Reading targeted DNA damage in the active demethylation pathway: role of accessory domains of eukaryotic AP endonucleases and thymine-DNA glycosylases. *J. Mol. Biol.* doi: 10.1016/j.jmb.2019.12.020 [Epub ahead of print],

Prorok, P., Alili, D., Saint-Pierre, C., Gasparutto, D., Zharkov, D. O., Ishchenko, A. A., et al. (2013). Uracil in duplex DNA is a substrate for the nucleotide incision repair pathway in human cells. *Proc. Natl. Acad. Sci. U.S.A.* 110, E3695–E3703. doi: 10.1073/pnas.1305624110

Shen, J. C., and Loeb, L. A. (2003). Mutations in the α8 loop of human APE1 alter binding and cleavage of DNA containing an abasic site. *J. Biol. Chem.* 278, 46994–47001. doi: 10.1074/jbc.M309362200

Tell, G., Wilson, D. M., and Lee, C. H. (2010). Intrusion of a DNA repair protein in the RNome world: is this the beginning of a new era? *Mol. Cell. Biol.* 30, 366–371. doi: 10.1128/mcb.01174-09

Timofeyeva, N. A., and Fedorova, O. S. (2016). A kinetic mechanism of repair of DNA containing alpha-anomeric deoxyadenosine by human apurinic/apyrimidinic endonuclease 1. *Mol. Biosyst.* 12, 3435–3446. doi: 10.1039/c6mb00511j

Timofeyeva, N. A., Koval, V. V., Ishchenko, A. A., Saparbaev, M. K., and Fedorova, O. S. (2011). Kinetic mechanism of human apurinic/apyrimidinic endonuclease action in nucleotide incision repair. *Biochemistry* 76, 273–281.

Timofeyeva, N. A., Koval, V. V., Knorre, D. G., Zharkov, D. O., Saparbaev, M. K., Ishchenko, A. A., et al. (2009). Conformational dynamics of human AP endonuclease in base excision and nucleotide incision repair pathways. *J. Biomol. Struct. Dyn.* 26, 637–652. doi: 10.1080/07391102.2009.10507278

Toseland, C. P., and Webb, M. R. (2013). ATPase mechanism of the 5′-3′ DNA helicase, RecD2. *J. Biol. Chem.* 288, 25183–25193. doi: 10.1074/jbc.M113.484667

Tsutakawa, S. E., Shin, D. S., Mol, C. D., Izumi, T., Arvai, A. S., Mantha, A. K., et al. (2013). Conserved structural chemistry for incision activity in structurally non-homologous apurinic/apyrimidinic endonuclease APE1 and endonuclease IV DNA repair enzymes. *J. Biol. Chem.* 288, 8445–8455.

Unnikrishnan, A., Raffoul, J. J., Patel, H. V., Prychitko, T. M., Anyangwe, N., Meira, L. B., et al. (2009). Oxidative stress alters base excision repair pathway and increases apoptotic response in apurinic/apyrimidinic endonuclease 1/redox factor-1 haploinsufficient mice. *Free Radic. Biol. Med.* 46, 1488–1499. doi: 10.1016/j.freeradbiomed.2009.02.021

Vascotto, C., Fantini, D., Romanello, M., Cesaratto, L., Deganuto, M., Leonardi, A., et al. (2009). APE1/Ref-1 Interacts with NPM1 within nucleoli and plays a role in the rRNA quality control process. *Mol. Cell. Biol.* 29, 1834–1854. doi: 10.1128/MCB.01337-08

Wong, D., DeMott, M. S., and Demple, B. (2003). Modulation of the 3′→5′-exonuclease activity of human apurinic endonuclease (Ape1) by its 5′-incised abasic DNA product. *J. Biol. Chem.* 278, 36242–36249. doi: 10.1074/jbc.M306065200

Xanthoudakis, S. (1996). The redox/DNA repair protein, Ref-1, is essential for early embryonic development in mice. *Proc. Natl. Acad. Sci. U.S.A.* 93, 8919–8923. doi: 10.1073/Pnas.93.17.8919

Conflict of Interest: The authors declare that the research was conducted in the absence of any commercial or financial relationships that could be construed as a potential conflict of interest.

Advantages of publishing in Frontiers

OPEN ACCESS
Articles are free to read for greatest visibility and readership

FAST PUBLICATION
Around 90 days from submission to decision

HIGH QUALITY PEER-REVIEW
Rigorous, collaborative, and constructive peer-review

TRANSPARENT PEER-REVIEW
Editors and reviewers acknowledged by name on published articles

Frontiers
Avenue du Tribunal-Fédéral 34
1005 Lausanne | Switzerland

Visit us: www.frontiersin.org
Contact us: frontiersin.org/about/contact

REPRODUCIBILITY OF RESEARCH
Support open data and methods to enhance research reproducibility

DIGITAL PUBLISHING
Articles designed for optimal readership across devices

FOLLOW US
@frontiersin

IMPACT METRICS
Advanced article metrics track visibility across digital media

EXTENSIVE PROMOTION
Marketing and promotion of impactful research

LOOP RESEARCH NETWORK
Our network increases your article's readership